UNIVERSITY OF LIVERPOOL

Modulating Docetaxel Encapsulation and Release from Branched Vinyl Copolymer Nanoparticles Formed *via* Co-nanoprecipitation

Thesis submitted in accordance with the requirements of the University of Liverpool for the degree of Doctor in Philosophy

Sean Flynn

September 2019

Acknowledgements

I would like to start by thanking my mum, Toula, for her constant love, support and relentless determination to give me and my brother the best opportunities in life. It was her encouragement to pursue the best education I could that convinced me to go to university and has since opened up opportunities beyond either of our expectations. The journey to this point hasn't been direct and definitely wasn't always smooth however, I have always been safe in the knowledge that I could count on her support at every step along the way. I only hope that I can show the same level of support to my children as she has to hers and if I can, I will be as proud of myself as I am of her today.

I would like to take this opportunity to thank my PhD supervisor, Prof. Steve Rannard, for giving me the opportunity to conduct my PhD research under his guidance. Steve has been a fantastic supervisor who has helped me discover my research interests, develop and pursue ideas and grasp opportunities, both in and outside of this research project. I have thoroughly enjoyed my PhD and I am truly grateful for everything that Steve has taught me.

I'd also like to thank every member of the Rannard group, past and present, who have made my PhD studies such an enjoyable experience. Special thanks go to Dr. Andrew Dwyer and Dr. Pierre Chambon who both have made significant contributions to this research and have had a huge impact on my development as a scientist over the past 5 years. I've studied alongside Dr. Stephanie Edwards every day of my 8 years at the University of Liverpool; throughout this time she has been a great friend and I am in no doubt that this will continue beyond our time as students.

The submission of this thesis would not have been possible without the encouragement and support of my loving girlfriend, Helen. The phrase "every step of the way" is often overused however, in this case, it could not be more fitting. From literally helping me conduct experiments to assisting with the preparation of this thesis she has had an immeasurable influence on my ability to complete and communicate this research. Furthermore, her emotional support has made the good times great and the tough times bearable. Outside of the laboratory, I couldn't have asked for a better partner over the previous 5 years; her caring and thoughtful nature gives me the inspiration to rise and meet any challenge whilst her playful sense of humour and strong wit never allow me to get too far off the ground. Helen, I will be forever grateful for the unfaltering support you have given me and I now look forward to spending more time with you and continuing to build our future together.

It is important for me acknowledge all of the teachers and staff at Holy Family Catholic High School who supported me immensely during my time there as a student. I would especially like to thank David Holmes (and of course Sheila) for his advice, support and, often, patience over the years. His stabilising influence always kept me on track, his advice helped me make some of the big decisions and he has become a great friend who I truly value. Special thanks also go to Alan Lowndes for inspiring my interest in Chemistry and providing me with a solid foundation of scientific knowledge which has served me well throughout my later studies. I'd also like to thank Matt Symes, Mark Kinsella, Helen Sawyer and Shabari Shields who all played fundamental roles in my academic and personal development throughout this time. Holy Family's motto is "be the best you can be" and there is no doubt in my mind that the support I received from its teachers and staff has enabled me to do so.

Finally, there are hundreds, if not thousands, of people whose individual actions, small or large, have helped me on my journey through academia to the point of submitting this thesis. There are, of course, too many to name individually however, I want to make it clear that these actions did not go unnoticed and that I will be forever grateful for each and every one of them.

ABSTRACT

***Sean Flynn* – Modulating docetaxel encapsulation and release from branched vinyl copolymer nanoparticles formed *via* co-nanoprecipitation**

The acute toxicity and inherent low water solubility of many chemotherapeutics often prevent such drugs from achieving the optimal therapeutic effect in a clinical setting. Branched vinyl copolymer nanoparticles have been investigated as potential drug delivery vehicles for the controlled release of docetaxel, a commercially available hydrophobic anti-cancer drug. Branched vinyl copolymer nanoparticles were produced *via* co-nanoprecipitation; this relatively new nanoformulation technique involved the simultaneous nanoprecipitation of high molecular weight, hydrophobic branched copolymers with their corresponding amphiphilic AB block copolymers, through a rapid manipulation of their solvent environment. This approach was used to entrap docetaxel molecules within the hydrophobic cores of branched vinyl copolymer nanoparticles during the co-nanoprecipitation process.

A comprehensive study was undertaken to expand the scope of branching vinyl copolymer nanoparticles that can be produced *via* co-nanoprecipitation, beyond the limited number of nanomaterials that have been reported to date. This involved co-nanoprecipitation of a large number of hydrophobic and amphiphilic polymers which possessed a wide range of different chemical and physical properties. This required the development of an unlikely synthetic approach, copper-catalysed reversible-deactivation radical polymerisation in anhydrous alcoholic media, for the development of novel hydrophobic polymeric materials. Fundamental studies were conducted to understand the experimental factors which influence nanoparticle formation during co-nanoprecipitation and, where possible, these factors were used as leavers to influence nanoparticle characteristics.

Promising branched vinyl copolymer nanoparticle candidates were taken forward to drug encapsulation and release studies. This involved the use of radiometric techniques to quantify the encapsulation and release of docetaxel from branched vinyl copolymer nanoparticles. Docetaxel loadings of up to 25 weight % of the total nanoparticle mass and encapsulation efficiencies of up to 97 % were achieved during co-nanoprecipitation. The properties of the polymers used to construct branched vinyl copolymer nanoparticles also had a significant impact on docetaxel release. The impact of nanoparticle properties, including core polarity and viscosity, on the levels of docetaxel entrapment during co-nanoprecipitation and the rate of docetaxel release will be presented. The suitability of leading nanoparticle candidates as prospective drug nanocarriers *in vivo* will be discussed.

Contents

Chapter 1 1
1.1 Cancer 2
1.1.1 Conventional Cancer Treatments 2
1.2 Nanomedicine 5
1.2.1 Enhanced Drug Delivery 6
1.2.2 Physiological Barriers and Opportunities for DNC Systems 9
1.2.2.1 Interactions with Blood Components within Systemic Circulation 10
1.2.2.2 Clearance Mechanisms of the Liver, Kidneys and Spleen 13
1.2.2.3 Targeted Delivery to Cancer Cells at Tumour Sites 13
1.2.2.4 Extra-Cellular Barriers for DNC Systems 15
1.2.2.5 Intra-Cellular Barriers for DNC Systems 20
1.2.2.6 Clinical Application of DNC Systems for the Treatment of Cancer 21
1.3 Polymer Chemistry 24
1.3.1 Reversible-Deactivation Radical Polymerisation 24
1.3.1.1 Polymer Architecture 27
1.3.1.2 Polymer Functionality 31
1.3.1.3 Stimuli-Responsive Polymers 35
1.4 Synthetic Approaches for the Generation of Polymer-Based Nanoparticles 39
1.4.1 Block Copolymer Self-Assembly 39
1.4.1.1 In-Situ Nanoparticle Forming Techniques 40
1.4.2 Nanoprecipitation 43
1.4.2.1 The Nanoprecipitation Process 43
1.5 Smart Nanomaterials *via* Macromolecular Design 46
1.5.1 Tailoring Nanoparticle Chemistry 46
1.5.2 Responsive Nanocarriers 47
1.6 Research Aims 48
1.7 References 50
Chapter 2 64
2.1 Introduction 65
2.1.1 Copper-Catalysed Reversible-Deactivation Radical Polymerisation 65
2.1.2 Conventional Copper-Catalysed Atom Transfer Radical Polymerisation 66
2.1.3 Varying Polymer Architecture Using Cu-RDRP 68
2.1.3.1 Block Copolymers 68
2.1.3.2 Branched Statistical Copolymers 71
2.1.4 RDRP of Hydrophobic Monomers in Polar Solvents 75

2.1.5 Chapter Aims 76
2.2 Expanding the Scope of Cu-RDRP in Alcoholic Media 77
2.2.1 Feasibility Studies 77
2.2.2 Linear Polymerisation of Hydrophobic Methacrylates in Anhydrous Alcohols 80
2.2.2.1 Synthesis of an Initiator for Cu-RDRP, Benzyl 2-Bromoisobutyrate 80
2.2.2.2 Cu-RDRP of Hydrophobic Methacrylates in Anhydrous Methanol 82
2.2.2.3 Kinetics Studies of the Cu-RDRP of nHMA in Anhydrous Methanol 86
2.2.2.4 Cu-RDRP of Hydrophobic Methacrylates in Isopropyl Alcohol 89
2.2.2.5 Comparison of Cu-RDRP in Anhydrous MeOH and Anhydrous IPA 91
2.3 Amphiphilic AB Block Copolymers *via* Cu-RDRP in Alcoholic Media 93
2.3.1 Synthesis of a Poly(ethylene glycol) Macro-initiator 94
2.3.2 Polymerisation from PEG_{45}-Br *via* Cu-RDRP in Anhydrous Alcohols 96
2.4 Branched Statistical Copolymers *via* Cu-RDRP in Anhydrous Alcohols 99
2.4.1 Statistical Copolymerisations of Hydrophobic Methacrylates with EGDMA *via* Cu-RDRcP in Anhydrous Alcohols 99
2.4.2 Mark-Houwink-Sakurada Analysis of Branched Statistical Copolymers and Linear Homologues 107
2.4.3 Understanding the Factors Affecting Branching During Cu-RDRcP 110
2.4.4 Comparison of Branching Observed Between Monomer-Solvent Systems 113
2.5 Conclusions 120
2.6 References 121
Chapter 3 125
3.1 Introduction 126
3.1.1 Co-nanoprecipitation 126
3.1.2 Chapter Aims 128
3.2 Selection of Polymers for use in (Co)nanoprecipitation Studies 129
3.3 Nanoprecipitation Studies 131
3.3.1 Preliminary Nanoprecipitation Studies 131
3.4 Co-nanoprecipitation Studies 135
3.4.1 Initial Co-nanoprecipitation Studies 136
3.4.2 Encapsulation of a Hydrophobic Molecule during Co-nanoprecipitation 142
3.4.2.1 Impact of a Guest Molecule on the (Co)nanoprecipitation process 142
3.4.2.2 Evaluation of Nanoparticle Core Polarity using Fluorescence Emission Spectroscopy 145
3.4.3 Factors Affecting Co-nanoprecipitation 148
3.4.3.1 Nanoparticle Composition 149
3.4.3.2 Impact of Initial Polymer Concentration on Co-nanoprecipitation 158
3.4.4 Nanoparticle Stability 165

3.4.4.1 Nanoparticle Stability to Dilution 165
3.4.4.2 Nanoparticle Stability to Salt 167
3.5 Conclusions 170
3.6 References 171
Chapter 4 173
4.1 Introduction 174
4.1.1 Docetaxel Anticancer Chemotherapeutic Drug 174
4.1.2 Docetaxel Nanoformulation 176
4.1.3 Chapter Aims 177
4.2 Docetaxel Encapsulation *via* Co-nanoprecipitation 178
4.3 Quantitative Analysis of Docetaxel Encapsulation and Release from Branched Vinyl Copolymer Nanoparticles formed *via* Co-Nanoprecipitations 186
4.3.1 Quantification of Docetaxel Encapsulation Efficiency and Drug Loading achieved during Nanoparticle Formation *via* Co-Nanoprecipitation 186
4.3.1.1 Quantifying the EE and DL of ^{3}H -labelled Docetaxel during Co-Nanoprecipitation 187
4.3.2 Monitoring Docetaxel Release *via* ^{3}H Radio-dialysis 192
4.4 Conclusions 208
4.5 References 209
Chapter 5 212
5.1 Conclusions 213
5.1.1 Chapter 2 213
5.1.2 Chapter 3 215
5.1.3 Chapter 4 217
5.2 Future Work 219
5.2.1 Further Development of the Research Conducted in this Thesis 219
5.2.1.1 Chapter 2 – Polymer Chemistry 219
5.2.1.2 Chapter 3 – Nanoparticle Formation via (Co)nanoprecipitation 220
5.2.1.3 Chapter 4 – Understanding Drug Encapsulation and Release 222
5.2.2 Alternative Approaches to Manipulation of Nanoparticle Properties 223
5.2.2.1 Optimisation of Nanoparticle Properties using Bespoke Copolymers 223
5.2.2.2 Copolymer End-Groups to Modulate Docetaxel Release 231
5.2.2.3 Alternative Block Copolymers to Modify Nanoparticle Shell Functionality 235
5.3 References 239
Chapter 6 241
6.1 Materials 242
6.2 Characterisation 242
6.3 Methods 243

6.3.1 Chapter 2 243
6.3.1.1 Monomer-Alcohol Miscibility Studies 243
6.3.1.2 Pyrene Fluorescence Emission Spectroscopy of Monomer, Solvent and Monomer-Alcohol Solutions 243
6.3.1.3 Synthesis of Benzyl Initiator 244
6.3.1.4 Synthesis of Poly(Ethylene Glycol) Macro-Initiator (PEG_{45}-Br) 244
6.3.1.5 General Procedure for the Synthesis of Linear Homopolymers by Cu-RDRP (MMA, EMA, nBMA, tBMA, nHMA, CHMA, BzMA, EHMA, LMA and SMA) 245
6.3.1.6 Kinetic Studies of the Cu-RDRP of nHMA at 60 °C in MeOH 247
6.3.1.7 General Procedure for the Synthesis of AB Block Copolymers by Cu-RDRP (MMA, EMA, nBMA, tBMA, nHMA, CHMA, BzMA, EHMA, LMA and SMA) 248
6.3.1.8 General Procedure for the Synthesis of Branched Statistical Copolymers by Cu-RDRP (MMA, EMA, nBMA, tBMA, nHMA, CHMA, BzMA, EHMA, LMA and SMA) 248
6.3.1.9 Analysis of Branched Copolymer Architecture by TD-SEC 250
6.3.2 Chapter 3 251
6.3.2.1 Polymer Solubility Studies 251
6.3.2.2 Initial Nanoprecipitation Studies 251
6.3.2.3 Initial Co-Nanoprecipitation Studies 251
6.3.2.4 Nanoparticle Imaging via Scanning Electron Microscopy 252
6.3.2.5 Pyrene Encapsulation Studies 252
6.3.2.6 Nanoparticle Composition Co-Nanoprecipitation Studies 253
6.3.2.7 Co-Nanoprecipitation Concentration Studies 253
6.3.2.8 Nanoparticle Stability to Dilution Studies 254
6.3.2.9 Nanoparticle Salt Stability Studies 255
6.3.3 Chapter 4 255
6.3.3.1 Initial Docetaxel Encapsulation Study 255
6.3.3.2 Calculation of Drug Loading via ^{1}H NMR Spectroscopy 256
6.3.3.3 Calculation of Drug Loading via Ultraviolet-Visible Spectroscopy 258
6.3.3.4 Assessment of ^{3}H-Labelled Radio Purity via Radio Thin-Layer Chromatography 259
6.3.3.5 Preparation of ^{3}H-Docetaxel Loaded Branched Vinyl Copolymer Nanoparticles via Co-Nanoprecipitation 259
6.3.3.6 Measurement of Encapsulation Efficiency and Drug Loading of ^{3}H-Labelled Docetaxel Using Radiometric Analysis 260
6.3.3.7 Monitoring Release of ^{3}H-Labelled Docetaxel from Branched Vinyl Copolymer Nanoparticles during Radio-Dialyses 261
6.3.3.8 Determination of Branched Copolymer Complex Viscosities Using Rheological Analysis 261
6.3.4 Chapter 5 262

6.3.4.1 Preparation of Branched Statistical Copolymers of HPMA, EHMA and EGDMA via Cu-RDRP at 60 °C in Anhydrous Methanol....262
6.3.4.2 Preparation of Statistical AB Block Copolymers of PEG_{45} EHMA and HPMA via Cu-RDRP at 60 °C in Anhydrous Methanol....262
6.3.4.3 Rheological Analyses of Branched Statistical Copolymers....263
6.3.4.4 Co-nanoprecipitations of Statistical Branched and AB Block Copolymers....263
6.3.4.5 Monitoring ^{3}H-Docetaxel Release from Branched Vinyl Copolymer Nanoparticles during Radio-Dialyses....264
6.3.4.6 Preparation of a Docetaxel Based Macro-Initiator....264
6.3.4.7 Linear Polymerisation of nHMA via Cu-RDRP at 60 °C in Anhydrous Methanol using a Docetaxel Based Macro-Initiator....264
6.3.4.8 Branched Copolymerisation of nHMA and EGDMA via Cu-RDRP at 60 °C in Anhydrous Methanol using a Docetaxel Based Macro-Initiator....265
6.3.4.9 Co-Nanoprecipitation of Branched Docetaxel Copolymer Conjugates and Amphiphilic AB Block Copolymers....266
6.3.4.10 Preparation of a p(nHMA) Based Macro-RAFT Agent....266
6.3.4.11 Chain Extension of a $p(nHMA)_{122}$ Macro-RAFT Agent....267
6.3.4.12 Sole Nanoprecipitations of Amphiphilic AB Block Copolymers....267
6.3.4.13 Co-nanoprecipitations of $p(nHMA_{68}$-co-$EGDMA_{1.03})$ with Amphiphilic AB Block Copolymers....268
6.4 References....268
Appendix....269

List of Abbreviations

ATRA	Atom Transfer Radical Addition
ATRP	Atom Transfer Radical Polymerisation
BFM	Bi-Functional Monomers
CIE	Clathrin-Independent Endocytosis
CME	Clathrin-Mediated Endocytosis
CRP	Conventional Radical Polymerisation
CuRDRcP	Copper-Catalysed Reversible-Deactivation Radical Copolymerisation
CuRDRP	Copper-Catalysed Reversible-Deactivation Radical Polymerisation
Đ	Dispersity
DB	Degree Of Branching
DCR	Derived Count Rate
DL	Drug Loading
DLCA	Diffusion-Limited Cluster-Cluster Aggregation
DLS	Dynamic Light Scattering
DNC	Drug Nanocarrier System
DP_n	Number-Average Degree Of Polymerisation
DSC	Differential Scanning Calorimetry
EE	Encapsulation Efficiency
EGF	Epidermal Growth Factor
EGFR	Epidermal Growth Factor Receptor
EPR	Enhanced Permeability And Retention
ETFD	Emulsion Template Freeze-Drying
IV	Intravenous
LSC	Liquid Scintillation Counting
MHS	Mark-Houwink-Sakurada
M_n	Number-Average Molecular Weight
M_n theory	Theoretical Number Average Molecular Weights
MPS	Mononuclear Phagocytic System
NET	Neutrophil Extracellular Trap
NMP	Nitroxide-Mediated Radical Polymerisation
NMR	Nuclear Magnetic Resonance
PISA	Polymerisation-Induced Self-Assembly
PRINT	Particle Replication In Non-Wetting Templates
RAFT	Reversible Addition-Fragmentation Chain Transfer
RALS	Right-Angle Light Scattering
RBC	Red Blood Cells
RDRP	Reversible Deactivation Radical Copolymerisation
R_h	Hydrodynamic Radius
RI	Refractive Index
RME	Receptor-Mediated Endocytosis
ROMP	Ring-Opening Metathesis Polymerisation
SCVP	Self-Condensing Vinyl Polymerisation
SEC	Size Exclusion Chromatography

SET-LRP	Single Electron Transfer Living Radical Polymerisation
SLN	Solid Lipid Nanoparticles
SPARC	Secreted Protein Acidic Rich In Cysteine
TD-SEC	Triple Detection Size Exclusion Chromatography
T_g	Glass Transition Temperature
TLC	Thin Layer Chromatography
UCST	Upper Critical Solution Temperature
WBC	White Blood Cells

List of Chemical Abbreviations

^3H	Tritium
bpy	2-2' Bipyridine
BzBiB	Benzyl 2-Bromoisobutyrate
BzMA	Benzyl Methacrylate
$CDCl_3$	Deuterated Chloroform
CHMA	Cyclohexyl Methacrylate
Cu	Copper
DCM	Dichloromethane
DMAEMA	2(Dimethyl Amino) Ethyl Methacrylate
DMAP	4-(Dimethyl Amino) Pyridine
DSDMA	Disulphide Based Dimethacrylate
EGDMA	Ethylene Glycol Dimethacrylate
EHMA	2-Ethyl Hexyl Methacrylate
EMA	Ethyl Methacrylate
EtOH	Ethanol
HEMA	Hydroxyethyl Methacrylate
HPMA	2-Hydroxypropyl Methacrylate
IPA	Isopropyl Alcohol
LMA	Lauryl Methacrylate
MeOH	Methanol
MMA	Methyl Methacrylate
NaCl	Sodium Chloride
*n*BMA	N-Butyl Methacrylate
*n*HMA	N-Hexyl Methacrylate
NIPAAM	N-Isopropylacrylamide
N_2	Nitrogen
OEGMA	Oligo(Ethylene Glycol) Monomethacrylate
PEG	Poly(Ethylene Glycol)
PEG_{45}-Br	Poly(Ethylene Glycol) Macroinitiator
PEG_{45}-OH	Methoxy Terminated Poly(Ethylene Glycol)
SMA	Stearyl Methacrylate
*t*BMA	*tert*-Butyl Methacrylate
TEA	Triethyl Amine
THF	Tetrahydrofuran

Chapter 1

Bespoke Drug Nanocarriers *via* Macromolecular Design: The Next Generation of Smart Nanomedicines for the Treatment of Cancer

1.1 Cancer

Over the remainder of the 21st century cancer is expected to become the leading cause of death and the largest barrier to increasing life expectancy in every country across the globe.[1] In 2015, the World Health Organisation (WHO) estimated that cancer was the first or second leading cause of death in adults below the age of 70, in 91 of the 172 countries studied; furthermore, cancer was in the top four most prevalent causes of death in an additional 22 countries.[2] Cancer has increasing prevalence in highly economically developed countries which have higher life expectancies. The American Cancer Society estimated that 606,880 cancer related deaths occurred in 2019;[3] in the UK, there were an estimated 363,484 new cancer diagnoses each year between 2014 and 2016, with a subsequent 163,000 cancer related deaths reported in 2016.[4] The increased prevalence of cancer in the UK precipitated a coordinated response from cancer charities, healthcare professionals and national government which resulted in the launch of a National Cancer Strategy by the Department for Health and Social Care in 2011.[5] This strategy takes a multi-faceted approach by targeting: (1) cancer prevention, by reducing risk factors such as unhealthy lifestyles and occupational exposures to harmful substances. (2) Early detection, by increasing cancer awareness and screening services and (3) Improving the range and efficacy of cancer treatments available by funding fundamental research for the development and translation of novel cancer treatments. Whilst preventative strategies may go a long way to reduce the number of cancer diagnoses in the future, the versatile and complex nature of existing cancers will likely always drive clinical demand for novel therapies which can save, or improve the quality of, the lives of cancer patients.

1.1.1 Conventional Cancer Treatments

There are a wide range of treatments available to either halt or slow the growth of cancerous tumours (Table 1.1). In cases where tumours are concentrated in one area and can be accessed without high levels of risk, they can be removed with surgery; this approach can also be used to ‘debulk’ tumours in order to increase the effectiveness of other cancer treatments. Whilst the acute risk of continued growth or even spreading of tumours often justifies the need for surgery, this invasive technique can cause patient discomfort and lead to complications such as infection. Radiotherapy is another treatment which can be used against localised cancer cells. This involves treating a tumour with a beam of ionising radiation which causes damage to the cell DNA and subsequently inhibits cell replication processes, resulting in cell death. A key drawback of radiotherapy is that it is non-specific and therefore can also damage non-cancerous cells surrounding the tumour causing a range of undesirable side effects. In recent years the development of Proton Beam Therapy has provided radiotherapists with the ability to deliver doses of ionising radiation over a narrow depth range; this allows specific targeting of tumours whilst minimising damage to the surrounding healthy cells.[6]

Table 1.1 A general overview of conventional cancer therapies, including the associated: cancer forms/ areas treated, advantages, disadvantages and common side effects.

Treatment	Cancer Form	Advantages	Disadvantages	Side Effects
Surgery	Wide ranging, solid tumours, localised.	Tumour removal Reduce tumour size Eases symptoms	Intrusive, limited accessibility.	Pain, infection, bleeding.
Radiation Therapy	Brain, breast, chest, head and neck, pelvis, rectum, stomach and abdomen.	Kills cancer cells.	Non-specific.	Fatigue, hair loss, nausea/ vomiting, skin changes, diarrhoea, taste changes, headaches, urinary and bladder changes, swelling.
Chemotherapy	Wide ranging.	Kills cancer cells, can prolong patient survival.	Non-specific, toxic, strong side effects, cumulative impact.	Anaemia, appetite loss, constipation, delirium, diarrhoea, fertility issues, hair loss, infection, nausea/vomiting, nerve problems, inflammation, pain, skin changes, urinary and bladder changes.
Immunotherapy	Wide-ranging	Enhanced immune system's ability to fight cancer.	Limited availability, limited success.	Pain, skin changes, flu-like symptoms, low/high blood pressure, nausea/vomiting, swelling, heart palpitations, diarrhoea, infection, inflammation.
Targeted Therapy	Wide ranging.	Targets specific cancer cell growth/ replication functions.	Biopsy required, requires bespoke drug synthesis, cancer cells develop drug resistance.	Drug dependent. Diarrhoea, liver problems, fatigue, blood clotting, high blood pressure, fatigue, mouth sores, nail changes, loss of hair colour, skin changes, gastrointestinal problems.
Hormone Therapy	Prostate and breast cancers.	Reduced tumour size, reduce possibility of cancer return.	Limited drug availability, possible weight gain (prostate cancer).	Low libido, poor body temperature regulation, weakened bones, diarrhoea, nausea/ vomiting, fatigue, mood changes, menstrual cycle disruption, vaginal dryness.
Stem Cell	Leukaemia, lymphoma, neuroblastoma and multiple myeloma.	Aides recovery, improved cardiovascular and immune systems.	Dietary impact, long winded, very expensive, can impact immune system.	Bleeding, increased risk of infection, damage to skin, liver, intestines and other organs (graft-versus-host disease).

Some less common but equally important cancer treatments include immunotherapy, targeted therapy, hormone therapy and stem cell treatment. Immunotherapies make use of the body's immune system to identify and subsequently destroy cancerous cells; this can be achieved by attaching markers to cancer cells, making it easier for the immune system to identify and subsequently destroy them. Alternatively, they can also be used to trigger an immune response, this increases the sensitivity of the immune system which also aides the identification of cancerous cells. Hormonal treatment is used to target cancers in which cell growth is reliant

on naturally occurring hormones; these are particularly relevant for prostate and breast cancers.[7] Treatments aim to prevent growth of cancerous cells either by halting hormone production or by influencing the way hormones behave in the body. Targeted therapies are a form of precision medicine which rely on a detailed understanding of the specific cell biology and tumour formation processes which occur in individual forms of cancer. A plethora of precision medicine approaches are currently being studied for the treatment of cancer.

Stem cell transplants are another form of treatment received by cancer patients. Often used to offset the detrimental side-effects of cancer therapies, stem cell treatment involves the injection of blood stem cells which can promote the production of red blood cells (RBC), white blood cells (WBC) and platelets. For example, patients suffering from the side-effects of toxic chemotherapeutics often receive stem cell treatment to strengthen their cardiovascular and immune systems. Whilst primarily used to aid patient recovery, allogenic stem cell transplants have also shown direct impact against cancer *via* the 'graft *vs.* tumour effect' in which graft WBCs, formed by external donor stem cells, attack tumour cells.[8] However, graft WBCs have also been known to attack healthy tissues therefore causing undesirable patient side-effects.

Chemotherapy is perhaps the most well-known cancer treatment. It involves the administration of anti-cancer drugs, herein referred to as chemotherapeutics, within systemic circulation in order to treat, or to suppress the symptoms of, a wide range of cancers. Whilst the specific mechanisms of action for individual chemotherapeutics are as varied as the drugs themselves, chemotherapeutics are generally cytotoxic to cancer cells and typically induce apoptosis *via* interference in the processes of cell division, which characteristically proceed at higher mitotic rates compared with healthy cells. The indiscriminate nature of chemotherapy often results in chemotherapeutics being taken up by healthy tissues. Cells containing high mitotic activity, such as those in bone marrow, hair follicles and gut epithelium, are particularly sensitive to chemotherapy and their uptake of chemotherapeutics cause detrimental side-effects for cancer patients.[9]

The complex and diverse range of the physiological barriers which chemotherapeutics must overcome in order to perform their anti-cancer functions *in vivo* has significantly hindered the translation of many promising therapeutic candidates to a clinical setting.[10] This has driven clinical demand for novel technological interventions which can increase the efficacy and thus economic viability of the next generation of chemotherapy treatments. In recent years this has inspired scientists to explore the next generation of cancer based research which includes the application of nanomedicine in the detection, imaging and treatment of cancer.

1.2 Nanomedicine

Nanomedicine is a developing field which has evolved from the significant advances made in the area of nanotechnology over the last quarter of a century. It combines nanotechnology with the pharmacological and biomedical sciences in order to generate novel solutions for the diagnosis, imaging and treatment of existing and emerging global healthcare issues.[11] This is typically achieved by the construction of nanomaterials, using either top-down or bottom-up approaches, with sizes ranging from 1-1000 nm (Figure 1.1). Such materials can be designed to possess bespoke chemical and physical properties which enable them to perform precise functions when applied within a biological or clinical setting. There are many advantages to working at the nanoscale. The small size of nanomaterials can provide them with desirable behaviours *in vivo*; such nanomaterials also possess high surface functionality, compared with their bulk materials, as a result of their significantly larger surface-to-volume ratios. Nanomedicine utilises a wide range of nanomaterials including: dendrimers, polymer-conjugates, inorganic nanoparticles as well as a range of polymer and drug-based nano-assemblies. These materials are employed across many nanomedicine disciplines, including drug delivery, bio-imaging, bio-sensing, blood purification, tissue engineering and medical devices.[12] Nanomedicine has proven an effective tool in the fight against cancer; in particular, is has been used to improve the imaging and treatment of tumours within clinical settings.[13] Given the vast scope of research covered by nanomedicine and the specific nature of this thesis, the focus will be the drug delivery aspect of nanomedicine which will be discussed herein.

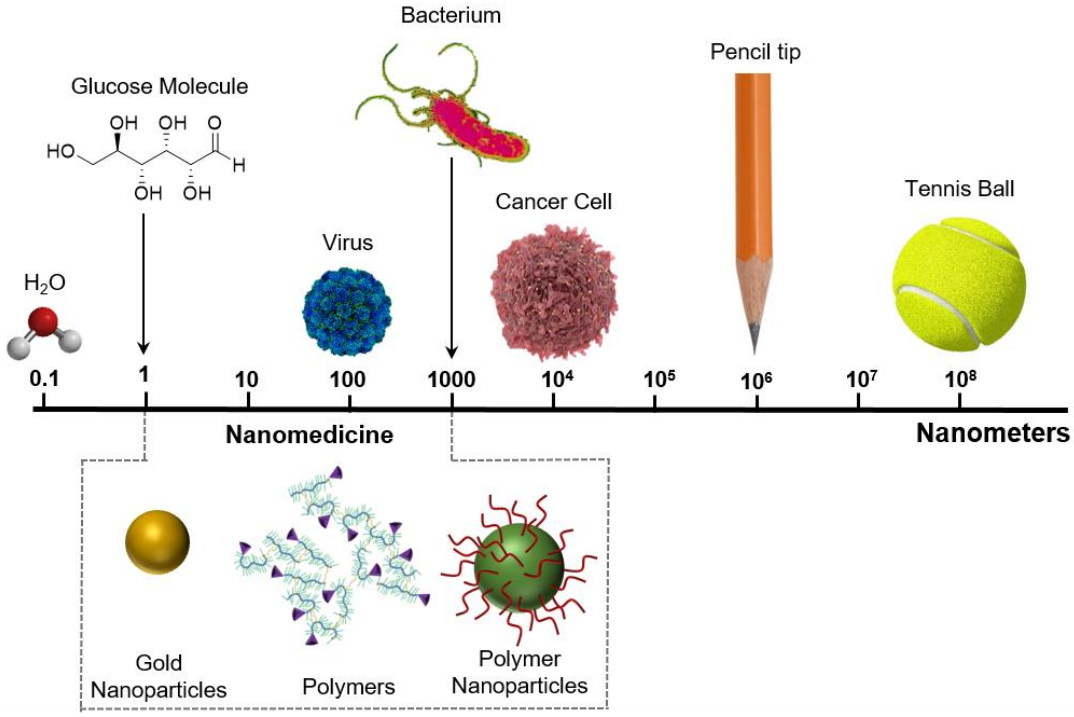

Figure 1.1 Illustration of the size scale at which nanomedicine research is conducted.

1.2.1 Enhanced Drug Delivery

In order to achieve their desired therapeutic effect, chemotherapeutics must be selectively taken up by cancer cells at the site of a tumour. This requires such chemotherapeutics to be administered and travel to a target site. A key issue with many chemotherapeutics is that they exhibit low solubility in biological fluids, are difficult to formulate and creating particles out of them can lead to aggregation. In addition, particles are readily cleared from systemic circulation *via* the mononuclear phagocytic system (MPS). This significantly hinders their uptake within target cells and thus limits their therapeutic effect.

In response to the clinical need to overcome such issues, the development of drug nanocarrier systems (DNC) has become one of the leading areas of research in nanomedicine. The concept of a DNC involves the formation of a stable nanosuspension either containing or solely consisting of the pharmacologically active compound. The use of a DNC system enables many pharmacological factors, such as the biodistribution and plasma drug concentration, to be manipulated in order to produce a desired therapeutic effect. Many formulation strategies have been employed in the quest to produce stable nanoparticle dispersions; an overview of some of the leading strategies is presented in Figure 1.2. These include lipid based nanocarriers, block copolymer self-assemblies, drug-polymer composites and drug nanocrystals.

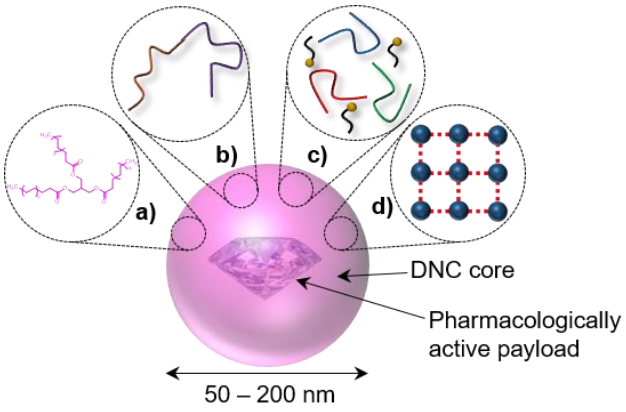

Figure 1.2 General overview of the diverse range of DNC classes currently being researched in nanomedicine. DNC systems consist of a pharmacologically active payload encapsulated within a nanocarrier system consisting of: a) Lipids, including solid lipid nanoparticles and liposomes. b) Block copolymers, including micelles and vesicles. c) Synthetic polymers and surfactants, such as solid drug nanoparticles and nanoprecipitates and d) Drug colloids such as nanocrystals.[14,15]

Numerous lipid based DNCs have been developed for the encapsulation of pharmacologically active payloads; these include liposomes and solid lipid nanoparticles (SLN).[16–19] Liposomes have often been referred to as the "gold standard" of lipid-based drug delivery systems. These phospholipid based vesicular systems are capable of loading both hydrophilic and hydrophobic drugs within their aqueous core and lipophilic bilayer respectively. The fact that they are constructed of highly biocompatible lipids means that liposomes are typically non-immunogenic which has allowed them to be used as chemotherapeutic nanocarriers within

a clinical setting.[20,21] In contrast, SLNs contain a solid hydrophobic core, consisting of lipids, stabilised by a range of polymer and small molecule based surfactants. The term lipid is used more liberally when discussing SLNs, as a number of hydrophobic compounds have been used to construct such nanomaterials, including triglycerides, partial glycerides, fatty acids, waxes, and steroids.[22] Whilst the static nature of their core provides SLNs with increased stability and controlled drug release profiles, it has also been a barrier to achieving high drug loadings during SLN formation.[23,24] Nonetheless, SLNs still remain the subject of significant amounts of nanomedicine research which targets the development of novel cancer treatments.[25–27]

The self-assembly of amphiphilic block copolymers offers another synthetic strategy for the generation of DNC systems. Amphiphilic block copolymers contain segmented hydrophilic and hydrophobic blocks. Micelles and vesicles are formed when amphiphilic block copolymers undergo self-assembly in water in order to minimise energetically unfavourable hydrophobe-water interactions. The morphology of these materials is dependent on their respective block lengths and can be tuned to generate either spherical or cylindrical micelles, or vesicles containing a tuneable membrane thickness. It is possible to encapsulate hydrophobic drug molecules within either the micelle core or vesicle membrane during the self-assembly of such nanostructures. This has led to such materials being studied as DNC systems for the encapsulation and release of a range of hydrophobic drug payloads.[28]

A wide range of formulation strategies have been used to developed drug-polymer nanocomposites which can act as a DNC system *in vivo*.[29] Such strategies typically use polymers and surfactants to generate stable aqueous nanosuspensions containing high levels of a therapeutic compound. Perhaps the most predominant formulation strategy involves a technique known as nanoprecipitation.[30] This approach involves displacement of a good solvent from a solution of a particle forming substance, typically a polymer, with a miscible non-solvent. The process of nanoprecipitation is well studied and this will be discussed in more detail in Chapter 3 Section 3.1. Briefly, nanoprecipitation proceeds as a three-stage process, involving the nucleation, growth and aggregation of polymers following a rapid change to their solvent environment. The relative contributions of these stages dictate nanoparticle size, stability and uniformity and, when optimised, can result in the formation of highly monodisperse polymer-based nanoparticles of tuneable size. The facile nature of the nanoprecipitation process allows the production of nanoparticles to be scaled up with relative ease; as a result, many high throughput and continuous production processes have been employed for nanoprecipitation based research.[30] The incorporation of hydrophobic drugs within the nanoprecipitation process has enabled their encapsulation within polymer-based nanoparticles and has led to the study of such materials as prospective DNC systems for the treatment of a range of diseases.[31]

An alternative drug-polymer composite formulation strategy, which has been used to generate solid drug nanoparticles (SDN), is the emulsion template freeze-drying (ETFD) approach.[32-35] SDNs consist of a solid particle core, consisting of an active pharmaceutical ingredient, typically a drug, stabilised by a matrix of polymers and surfactants. They are typically generated using a three-stage process.[36,37] The first stage involves the formation of an oil-in-water emulsion. This is achieved *via* emulsification of an aqueous solution of water-soluble polymers and surfactants with a water-immiscible organic solvent, in which the hydrophobic drug is dissolved. The drug-loaded emulsion is then rapidly frozen, typically under liquid nitrogen, to entrap droplets within a solid emulsion template; both the aqueous and non-aqueous phases are then removed by freeze-drying to leave a monolith of water soluble polymer, surfactants and the active pharmaceutical payload. This monolith can then be dispersed in water to form a colloidally stable aqueous nanodispersion of the active pharmaceutical.[37] Similar nanomaterials have also been formulated using spray drying based techniques.[38–41] SDNs have been generated using a range of pharmaceutically active compounds, in particular, as DNCs of chemotherapeutics and antiretrovirals for the treatment of cancer and the human immunodeficiency virus (HIV).[42–44]

The final class of DNC system to be discussed here is drug nanocrystals. These are solid crystals of pharmaceutically active drugs with sizes ranging from 1-1000 nm. The main advantage of drug nanocrystals is that they solely consist of the active drug and therefore theoretically contain optimal drug loadings; however, in practice, surfactants and stabilisers are often required in order to prevent further crystallisation/aggregation processes.[45] Nanocrystals can be produced using either top-down or bottom-up based formulation strategies. Top-down strategies are typically attrition-based mechanical processes, such as high shear homogenisation or wet milling, which employ high levels of stress in order to break down large drug crystals into their nanosized equivalents.[46] In contrast, bottom-up approaches typically involve the building of nanostructures from individual drug molecules. This is often achieved *via* nanocrystallisation of drugs through manipulation of their solvent environment and requires the use of surfactants and stabilisers to cap the crystallisation process at the nanoscale. Known as combinations approaches, combinations of top-down and bottom-up techniques have also been used to generate drug nanocrystals.[47] The ability to generate stable nanocrystals of pharmaceutically active drugs has attracted significant research interest and as a result drug nanocrystals are considered one of the leading DNC systems for clinical translation.[48,49]

Whilst significant progress has been made towards the design of a range of DNC systems, capable of encapsulating high amounts of therapeutically active payloads, many prospective DNC systems have been found unsuitable for translation to their chosen nanomedicine

application. This has often occurred as a result of DNC systems being unable to overcome a range of physiological barriers, such as removal from systemic circulation and selective uptake within target tissues, *in vivo*. As a result, despite the ability to encapsulate high drug loadings, some DNC systems have proved ineffective in the delivery of pharmacologically active payloads and have thus been unable to produce the desired therapeutic response.[50]

1.2.2 Physiological Barriers and Opportunities for DNC Systems

In order to achieve the desired therapeutic effect, DNCs must deliver their pharmacologically active payloads to a desired location, typically a tumour site, in a concentration which exceeds the therapeutic dose required. To achieve this, DNCs must overcome a wide range of physiological hurdles which include a number of vascular, extracellular and intracellular barriers.[51–53] It is therefore essential that such barriers are taken into account when designing the chemical and structural properties of new DNC systems.[54] This has opened up a new field of research in the design of biocompatible nanomaterials which can overcome a diverse range of physiological barriers in order to carry out specific functions in nanomedicine.[55]

Although it is the most common drug delivery route, oral administration presents numerous challenges which DNCs must overcome before entering systemic circulation.[14,15,56,57] The harsh acidic conditions within the gastrointestinal (GI) tract can cause the structural integrity of the DNC to become compromised and subsequently enable chemical degradation of the pharmacologically active payload.[58] In order to enter systemic circulation, DNCs must also pass through an epithelial membrane of the small intestine wall. This process is significantly hindered by the presence of a layer of mucus, a viscoelastic mucin fibre hydrogel, which sits on top of the endothelial membrane.[59,60] Mucus layers trap and rapidly clear pathogens and foreign particulates to prevent their entry into systemic circulation *via* absorption through the small intestine wall. This has been highlighted as a significant barrier to nanoparticle entry into systemic circulation.[61–69] As a result, despite the formulation of poorly soluble drugs into DNC systems, oral administration can still result in low bioavailability of the active pharmacological compounds.[70–72]

The physiological barriers associated with oral administration can be avoided *via* direct intravenous (IV) administration of the DNC into systemic circulation. IV administration offers the most efficient and reproducible way to deliver DNCs into systemic circulation and overcome issues such as low drug bioavailability. Once in the blood stream, DNCs are faced with further obstacles, including retaining colloidal stability within the blood, opsonisation and subsequent removal *via* the MPS, as well as other physiological filtration mechanisms within the cardiovascular system, and ensuring delivery of the active payload specifically to a tumour site.

1.2.2.1 Interactions with Blood Components within Systemic Circulation

IV administration causes a substantial change to the media in which DNCs are suspended and poses a significant risk to the colloidal stability of DNC systems. Blood consists of erythrocytes and leukocytes, also known as RBCs and WBCs respectively, along with thrombocytes (platelets), suspended in a solution of proteins and low molecular weight solutes known as plasma. Minimal interactions occur between DNCs and non-phagocytic species such as RBCs and platelets within systemic circulation;[73] this is also true for the majority of WBCs which require activation before their defence mechanisms take effect.[74] However, alternative WBC dependent responses have proven effective defence mechanisms against pathogens. For example, following exposure to pathogens, neutrocytes can secrete granule proteins and chromatin in order to nullify and kill invading pathogens.[75] Known as neutrophil extracellular traps (NET), such responses have been identified *in vivo* and have also proven an effective defence mechanism for the entrapment of bacteria within septic blood.[76,77] Such cellular defence mechanisms present complex obstacles for DNC systems and can potentially limit their lifetime within systemic circulation. NETs formed by neutrocytes, monocytes and macrophages *in vitro* have proven an effective clearance mechanism for the removal of Au-NPs, of varying sizes and shapes.[78]

Blood plasma contains a range of proteins which are capable of interacting with foreign species such as DNCs. The level of interaction which occurs between plasma proteins and DNCs is highly dependent on the physiochemical properties of the DNC; in particular in the particle size, shape and surface properties, including charge and chemical functionality.[79–81] The extent of protein adsorption can significantly impact a nanoparticle's lifetime within systemic circulation as well as its subsequent biodistribution.[82,83] Human albumin is the most abundant protein found in blood plasma. Responsible for the regulation of osmotic pressure and for the transportation of hydrophobic molecules within systemic circulation, albumin interacts with DNCs *via* a number of ionic and hydrophobic interactions.[82,83] The coating of albumin on nanoparticle surfaces is a dynamic process, in which weakly-bound albumin rapidly undergoes reversible adsorption and desorption processes. Albumin can therefore be displaced at the surface of DNC systems by proteins that possess higher binding affinities.[82,83] As a result, the dysopsonic benefits of albumin binding to DNC systems is somewhat limited; for example, pre-binding of albumin, to the surface of 50 nm polystyrene-based nanoparticles, showed only modest increases in nanoparticle circulation times following IV administration to Wistar rats.[84]

Albumin also presents opportunities for DNC systems. Due to its macromolecular structure (67 kDa), albumin binding results in a significant increase to the nanoparticle's hydrodynamic radius (R_h); such increases are particularly beneficial to small nanocarrier systems ($\leq$ 6 nm),

such as: small molecules, polymer-drug conjugates, inorganic nanoparticles and block copolymer micelles, which are vulnerable to, R_h dependent, glomerular filtration mechanisms.[85,86] In addition to improved colloidal stability, albumin coating of DNCs have also been shown to increase patient tolerance to potent taxane-derived chemotherapeutics, which resulted in a 1.71 fold increase in the maximum tolerated dose during human clinical trials.[85,86] Albumin has a binding affinity for the glycoprotein receptor, GP60, located on the surface of the endothelial cells which line the blood vessels surrounding solid tumours. Albumin coating of DNCs therefore also provides an additional entry route into the interstitium of solid tumours. Interaction between albumin bound nanoparticles and GP60 results in the activation of caveolin-1 and promotes transcytosis of the intact nanoparticles across the cell membrane. Once located within the tumour, albumin-bound nanoparticles benefit from a tumour selective targeting process induced by interactions with Secreted Protein Acidic Rich in Cysteine (SPARC).[87] SPARC is a protein which is released in order to modulate interactions between cells and species dissolved/suspended within the extracellular matrix.[88] Whilst not unique to cancer cells,[89] high levels of SPARC are commonly associated with advanced stages of tumours formed by a range of head and neck, non-small cell lung and breast cancers.[90–93] Following release into the extracellular matrix, the strong affinity between SPARC and albumin leads to the formation of a SPARC-albumin-DNC complex. This complex accumulates at the membrane of tumour cells where the reversible albumin-DNC binding process facilitates diffusion of the active chemotherapeutic into the intracellular compartments of cancer cells promoting selective apoptosis. These albumin-mediated transport and cancer targeting mechanisms provide unique opportunities to incorporate albumin binding in the design of DNCs systems capable of overcoming the physiological barriers associated with the specific targeting of tumours.

The complement system presents another physiological barrier which can reduce the circulation time of DNCs within systemic circulation. The complement system is responsible for enhancing the ability of the immune system, using both the adaptive and innate immune systems, to clear microbes and damaged cells from an organism.[94,95] The complement system consists of more than 30 dormant enzyme precursors and membrane-bound proteins which, once activated, can trigger a cascade of protein cleavage reactions in a process known as complement activation. Activation can be achieved *via* classical, alternative and lectin binding pathways and result in the clearance of pathogens *via* either i) enhanced pathogen recognition by the MPS following opsonisation processes or ii) formation of a membrane attack complex which facilitates an uncontrolled influx of intracellular fluids causing the swelling and subsequent lysis of pathogens. Whilst an effective defence mechanism against a range of pathogens, strict regulation over cascade processes prevent uncontrolled attacks on host cells

by the immune system.[96] The complement system therefore offers an additional clearance/ destruction pathway which must be avoided by DNCs within systemic circulation.

High plasma concentrations of proteins involved in the complement system lead to a multitude of interactions with circulating DNCs;[80,97,98] the binding of such proteins initiates an amplification process which promotes further opsonisation and subsequently results in the phagocytosis of DNC systems.[73] Activation of the complement system by DNCs is highly dependent upon the surface properties of the nanocarrier. The adsorption of proteins of the complement system is typically promoted by nanoparticles which contain: a significant negative or positive surface charges, high levels of hydrophobicity and/or an irregular surface topology.[99–101] The nature of nanoparticle surface charge has been shown to influence the complement activation pathway; negatively charged nanoparticles have been shown to activate the complement system *via* the classical pathway, whereas positively charged species induce alternative activation pathways.[102] Nanoparticle size, and subsequently the radius of curvature, is another factor which influences the extent of absorption of proteins of the complement system.[103] Larger nanoparticles (R_h > 200 – 800 nm) that possess low curvature allow high levels of opsonisation by proteins of the complement system in comparison to their smaller analogues. The level of opsonisation therefore decreases with nanoparticle size as the radius of curvature increases. However, the extent of nanoparticle removal *via* complement mediated phagocytosis is dependent upon the extent of nanoparticle opsonisation rather than nanoparticle size.[102] Efforts to reduce the opsonisation and subsequent removal of nanoparticles *via* the complement system involve coating nanoparticles with chemically inert, hydrophilic polymers. Such polymers, which will be discussed later in this Chapter, can significantly reduce the level of non-specific deposition of proteins of the complement system and thus increase the circulation times of PEGylated nanoparticles *in vivo*.[104–108]

In addition to the physiological barriers presented by the binding of albumin and proteins of the complement system, nanoparticles also face challenges which arise as a result of the adsorption of other plasma proteins. Lipoproteins are assemblies of cholesterol esters, phospholipids, triacylglycerides and a range of apolipoproteins which are responsible for the transport of lipids within systemic circulation.[109,110] Lipoproteins and apolipoproteins can interact with DNCs within systemic circulation;[109,111] for example, phospholipid exchange with lipoproteins can disrupt the colloidal stability of unilamellar vesicles, resulting in the premature release of their calcein payload.[112] Alternatively, apolipoproteins can displace albumin from the surface of circulating nanoparticles;[79] this can influence the biodistribution of nanoparticles specifically towards hepatocytes and tissues rich in lipoprotein receptors.[113-115] Immunoglobulins are large Y-shaped proteins which facilitate the neutralisation of pathogens within systemic circulation. Although always present within

systemic circulation their secretion by plasma cells is accelerated during an immunogenic response.[116,117] Immunoglobulin adsorption onto the surface of DNCs can occur though either specific recognition of nanoparticle surface chemistries or *via* hydrophobic interactions.[118] Such interactions can increase the rate at which nanoparticles are cleared through cooperative effects with the complement system.[119] Nanoparticle systems may interact with a range of other plasma proteins, such as fibronectin, fibrinogen and C-reactive protein.[120] Such interactions can influence nanoparticle lifetimes in systematic circulation as well as their subsequent tissue deposition *via* combinations of complement activation and receptor-mediated internalisation mechanisms.[121]

1.2.2.2 Clearance Mechanisms of the Liver, Kidneys and Spleen

DNCs that can maintain their colloidal stability whilst remaining inert to protein adsorption and subsequent clearance mechanisms are able to travel around the body within the vascular system. Whilst in systemic circulation they are subjected to many size-dependent filtration mechanisms in the liver, kidneys and spleen.[122] Nanoformulation of chemotherapeutics within DNC systems allows such filtration mechanisms to be by-passed and can therefore can be used to increase drug half-lives within systemic circulation.[123]

1.2.2.3 Targeted Delivery to Cancer Cells at Tumour Sites

One challenge facing chemotherapy nanomedicines is the ability to deliver their drug payloads specifically to tumour sites. Human tumours are complex and heterogeneous; as a result, significant variations arise in the tumour formation processes which occur between patients, multiple tumours within the same patient and microenvironments within a single tumour site.[124–127] As a result, chemotherapy regimens often require optimisation in order to overcome the heterogeneous nature of such tumours.[128] DNCs must overcome vascular and interstitial barriers in order to permeate tumour tissues.[129–131] Firstly, they must transude from systemic circulation, through a layer of endothelial cells which line the vascular system, in order to permeate the micro-environment within a tumour. Despite the complex and heterogeneous nature of cancers there are many commonalities in tumour formation processes. These include enhanced proliferation and growth rates, impacts on the immune system and the induction of angiogenesis (blood vessel formation), all of which provide opportunities for chemotherapy nanomedicines.[132,133]

Since the 1950s, *in vivo* studies have shown that small molecule dyes, administered IV into animals bearing tumours, are extravasated from systemic circulation and subsequently accumulate in tumour tissues.[134–136] Further studies have shown that this occurs as a result of two key physiological changes which take place during tumour formation: (i) deformation of blood vessels' endothelial membrane at the tumour site, creating so called "leaky vasculature" which promotes diffusion into the tumour;[137] (ii) impairment of the lymphatic system, typically responsible for the clearance of macromolecules, resulting in poor lymphatic drainage from tumour tissues.[138] These physiological changes form the basis of what is known as the enhanced permeability and retention (EPR) effect (Figure 1.4).[138] The EPR effect has been highlighted as one of the key physiological opportunities for the passive targeting of tumours by DNC systems. The EPR effect is particularly relevant for large macromolecules (> 50 kDa) and nanoparticles which typically exhibit longer plasma half-lives.[139] It typically takes at least six hours within systemic circulation before nanoparticle accumulation is observed at a tumour site.[140] This rules out many small molecule chemotherapeutics which are typically removed from systemic circulation shortly following IV administration. It is therefore essential that DNC systems, which aim to target tumours using the EPR effect, are able to avoid the wide range of clearance mechanisms, including but not limited to those described above. Providing they can remain stable and avoid clearance from systemic circulation, nanoparticles are able to accumulate within tumours at concentrations significantly higher than that in the plasma and with high specificity over non-cancerous tissues.[141] This raised the possibility of enhanced and specific delivery to tumours and led to the EPR effect being referred to as the "gold standard" of new anti-cancer agents.[142]

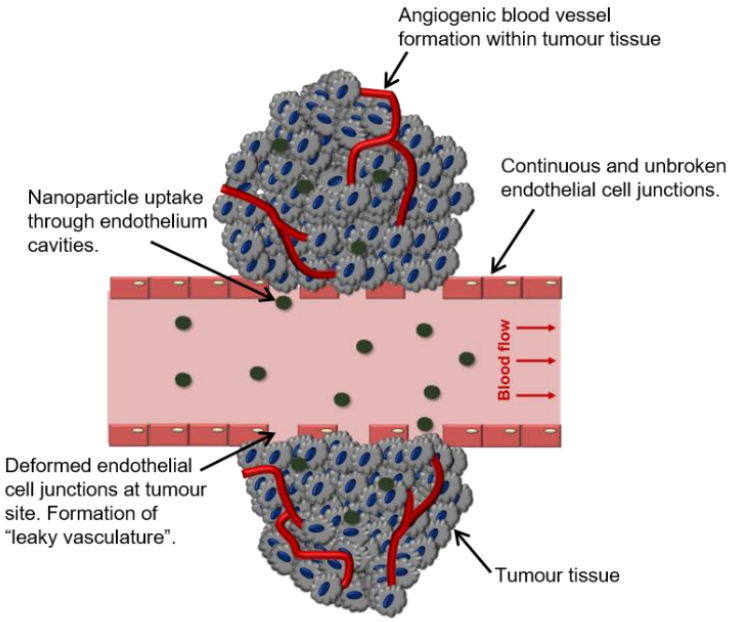

Figure 1.4 The enhanced permeability and retention (EPR) effect. Schematic representation of the extravasation of nanoparticles through leaky vasculature in endothelial membranes. This facilitates the accumulation of nanoparticles within tumour tissues as a result of poor lymphatic drainage.

Whilst the EPR effect has since been the subject of copious amounts of research, the vast majority of *in vivo* studies have been conducted using tumours transplanted into small animal models. The relevance of such studies have been the subject of considerable debate.[143–147] Whilst many have identified the EPR effect as an opportunity for the passive targeting of tumours, others have questioned its relevance in the treatment of human cancers within a clinical setting.[54,148,149] The accumulation of nanoparticles within human tumours *via* the EPR effect has been studied extensively;[150–154] however, little is known regarding the variability in nanoparticle accumulation in solid tumours, observed between different patients and cancer types. The extent of nanoparticle accumulation, *via* the EPR effect, has been linked to the degree of deformation caused to endothelial membranes during angiogenesis. For example, in the case of Kaposi's sarcoma, deformation of the endothelial membrane was sufficient enough to allow RBCs (*ca.* 8 μm) to escape the vascular system.[155] In this case, the use of nanoformulated doxorubicin proved a more effective therapy than the conventional chemotherapy treatment;[156] whereas the same formulation proved less effective at permeating breast cancer tumours possessing "less leaky" vasculature.[157] The heterogeneity of the EPR effect has been further demonstrated in recent *in vivo* studies using larger animal models to provide "comparative oncology". Nanoparticle uptake within tumours was significantly higher in dogs with carcinomas (85 % of the sample) (leaky vasculature) compared with dogs with sarcomas (25 % of the sample).[158–160] Similar effects have been observed in clinical studies.[161] These results demonstrate that the EPR effect only provides therapeutic benefits for a limited number of cancers and highlights the need to explore alternative tumour-specific permeation mechanisms.

1.2.2.4 Extra-Cellular Barriers for DNC Systems

Once located within the micro-environment of a tumour, nanocarriers must undergo cellular internalisation in order to have their desired therapeutic effect. This can occur *via* a number of non-targeted and receptor mediated cellular internalisation mechanisms. Such mechanisms are outlined in Figure 1.5 and include clathrin-independent endocytosis, clathrin-mediated endocytosis, micropinocytosis, caveolin-dependent endocytosis, phagocytosis, and receptor-mediated endocytosis. Whilst the biological interactions associated with each mechanism remain unique, there are many similarities between each of the cellular internalisation mechanisms described above. They all involve interactions between nanoparticles and the outer surface of cells, leading to the formation of internalised vesicles which vary in their size and internal environment. The cellular internalisation mechanism taken is largely dependent on the nanoparticle's physical and chemical properties, including size, charge, morphology and surface functionality, as well as the nature of the cell-type being targeted.

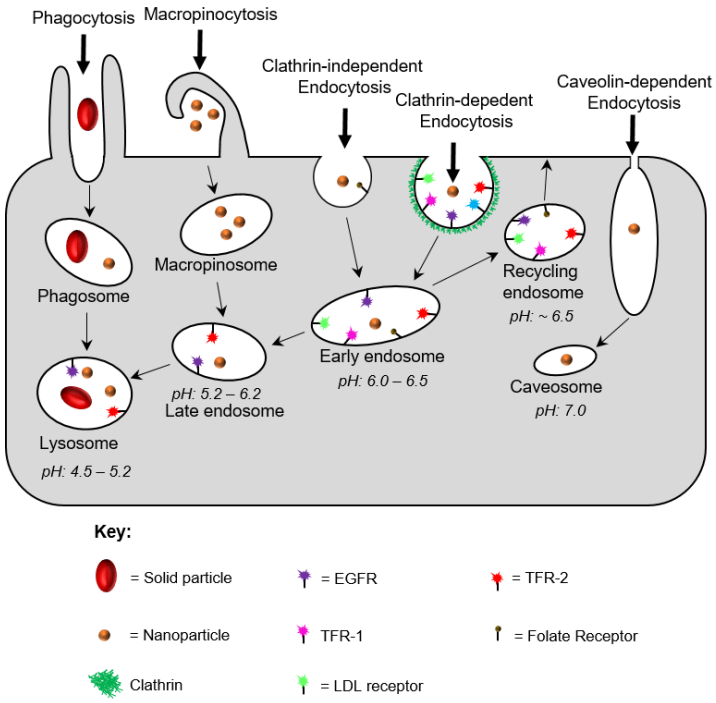

Figure 1.5 An overview of passive cellular internalisation mechanisms. a) Clathrin-independent endocytosis, b) Caveolin-dependent endocytosis, c) Phagocytosis, d) Micropinocytosis and e) Receptor-mediated endocytosis.

Clathrin-mediated endocytosis (CME) is a complex endocytic pathway which involves intracellular signalling, membrane recycling and nutrient uptake.[162] Vesicle formation is initiated when complex protein assemblies cause a curvature in a cell membrane, resulting in the formation of a spherical, clathrin-coated pit at the surface of a cell.[163–170] The vesicle formation process is completed when the neck of the clathrin-coated pit is resealed by the protein, GTPase, to reform the cell-membrane whilst simultaneously releasing the vesicle into the cell cytoplasm.[171–173] CME has been highlighted as an effective cellular internalisation mechanism for non-targeted nanoparticles with sizes of ~100 nm.[171–173] In particular, non-targeted nanoparticles possessing positive charges particularly favour CME; this is possibly due to electrostatic interactions with the negatively charged cell membrane. Whilst little detail is known about the mechanistic detail behind CME, it appears to be the predominant cellular internalisation pathway for non-targeted nanoparticles. Alternatively, cells which are devoid of clathrin rely on clathrin-independent endocytotic pathways for the uptake of nutrients and growth hormones from the extracellular environment.[174,175] In particular, folic acid is known to be taken up by clathrin-independent endocytosis. Given their high proliferation and mitotic rates, cancer cells typically have high demand for folic acid.[176] Nanoparticle functionalisation with folic acid has therefore provided an opportunity to achieve enhanced levels of nanoparticle cellular internalisation *via* clathrin-independent endocytosis.

Caveolae-dependent endocytosis (CDE) is an important factor in many biological functions such as cell signalling, transcytosis and lipid regulation and is thought to play a role in many types of disease. CDE involves the formation of an oval shaped invagination, typically < 80 nm in size. The lines of the invagination are lined with caveolin, a dimeric protein responsible for their characteristic oval shapes, which are stabilised by another caveolin protein known as Caveolin 2, amongst many others.[177–179] The CDE pathway has proven a useful opportunity for DNC systems; in particular, Abraxane, a commercially available chemotherapeutic nanoformulation has been reported to be taken up in cancer cells *via* CDE. Furthermore, the albumin corona, which possesses a high affinity for the GP60 receptor present in caveolae endothelial cells, facilitated the transcytosis of Abraxane into the interstitial tumour environment.[180] One advantage of this cellular internalisation pathway is the neutral pH within caveosomes can facilitate the internalisation of pH-sensitive materials during premature triggering responses such as nanocarrier degradation or drug release.[180]

Micropinocytosis involves the formation of a large membrane extension from cell surface out into the extracellular space. These membrane extensions then collapse back onto the cell surface and create a large vesicle (>1 μm) whilst entrapping a large "gulp" of the extra-cellular fluid.[181] Any particles, dissolved molecules, or nutrients within the engulfed extra-cellular fluid are taken into the endocytic vesicle known as a macropinosome. This is a non-specific bulk uptake and is not impacted by non-specific interactions or ligand-receptor binding. Given the larger size of micropinosomes, in comparison with endosomes and caveosomes, micropinocytosis offers a feasible cellular internalisation mechanism for the uptake of larger particles which are unable enter cells through either clathrin or caveolae dependent endocytosis.[182] However this route also offers a portal for many pathogens, including bacteria and viruses.[183]

Phagocytosis is an endocytic process which facilitates the breakdown of pathogens and cell debris *via* the binding, internalisation and subsequent digestion of large particles which arrive at a cell surface.[184] A key characteristic of phagocytosis is the large size (>250 nm) of the internal vesicles formed, known as phagosomes, which allows the internalisation of larger species that typically cannot be taken up *via* alternative cellular internalisation mechanisms.[184] Phagocytosis can be triggered by specific interactions between cell-surface receptors and ligands attached on the surface of a nanoparticles.[185–188] Alternatively, nanoparticle opsonisation with plasma proteins and the subsequent activation of the complement system can also accelerate phagocytosis rates, as described in Section 1.2.2.1.[189,190] Whilst the shape and size of large particles can influence the extent of phagocytosis,[191–193] the sizes required to promote particle uptake *via* this mechanism is typically much greater than those exhibited in many chemotherapy based DNC formulations.

Alternatively enhanced cellular internalisation can be achieved using active targeting strategies such as receptor mediated endocytosis (RME). RME involves the targeting of over-expressed receptors specifically located on the surface of cancer cells.[194] This is achieved by the attachment of ligands, which are complementary to the target cell receptor, to the surface of a DNC system in order to promote nanoparticle-receptor interactions thus boosting cellular internalisation *via* RME (Figure 1.6). As a result, it is possible to minimise toxicity to non-cancerous cells and thus reduce the undesired side effects associated with the active therapeutic compound. This approach has been used for the delivery of small molecule therapeutics, DNA, siRNA and miRNA specifically to cancer cells using a wide range of cell targeting ligands; such as highly abundant small molecules, peptides, aptamers and antibodies.[195]

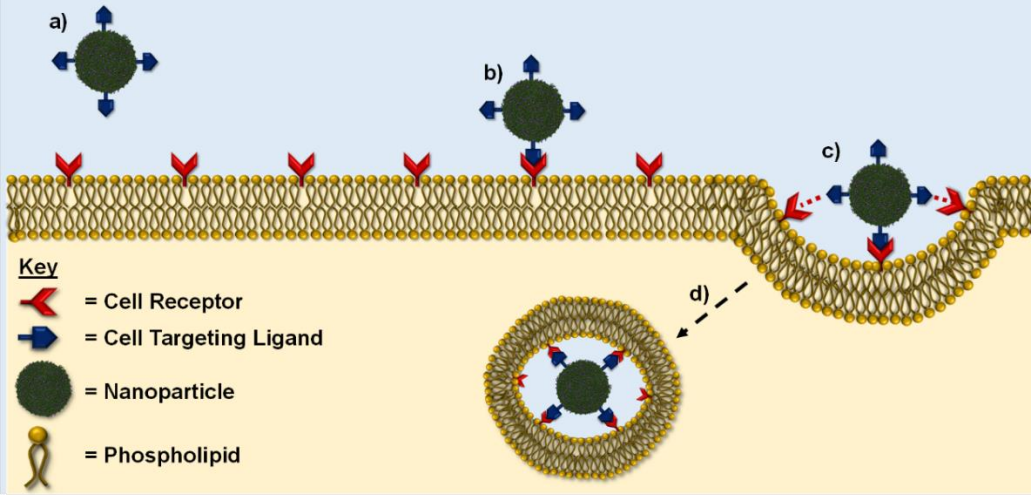

Figure 1.6 Graphical representation of the cellular internalisation of nanoparticles *via* receptor-mediated endocytosis. a) Nanoparticles, which containing a cell-targeting ligand, approach the cell membrane. b) Specific interactions arise between nanoparticle surface ligands and receptors expressed on the cell surface. c) Nanoparticles are engulfed during vesicle formation. d) Internalised nanoparticles are directed towards early endosomes.

Folate receptors are macromolecular glycoproteins which are over-expressed on the surface of a wide range of cancers.[196] Folic acid is a small molecule (441 g mol^{-1}) water-soluble B vitamin with a high affinity for folate receptors. Functionalisation of DNCs with folic acid can facilitate the selective delivery of drug payloads to cancer cells which over-express folate receptors.[196] Folate-conjugated DNC systems have demonstrated higher efficacies than their non-targeting analogues in both *in vitro* and *in vivo* studies.[197–200] However, folate receptors are also expressed by non-cancerous cells, including epithelial cells in the kidney and activated macrophages, which can hinder the selectivity of DNC uptake.[201,202]

Transferrin is a macromolecular glycoprotein responsible for the uptake and transport of iron across cell membranes and subsequently plays a crucial role in cell growth.[203–205] Although it is also expressed on the surface of a range of healthy cell types, transferrin receptors exist in

significantly higher concentrations on the surface of many cancer cell lines. This has made transferrin receptor-mediated endocytosis the target of copious amounts of DNC research; in particular this has been achieved *via* surface functionalisation of a range of DNC systems with ligands, such as human transferrin and transferring binding single-chain antibody fragments, which are capable of facilitating transferrin-mediated endocytosis.[206–212] One barrier to targeted delivery of DNC systems *via* the transferrin-mediated endocytic pathway is the "neutralisation" of targeting ligands following the adsorption of plasma proteins within biological fluids. Study of the cellular uptake of transferrin-coated silica nanoparticles within A549 lung epithelial cells, which over-express transferrin receptors, demonstrated that specific cell-targeting is supressed within physiological fluids.[213] This reduced cell specificity, in comparison to experiments conducted in buffered media, was attributed to neutralisation of targeting ligands by interaction with solutes present within the complex biological milieu. The inability to differentiate between target and non-target cells would result in DNC accumulation within healthy tissues and fail to reduce the toxic side effects of future chemotherapy based nanomedicines. This therefore raises questions over the suitability of this strategy within a clinical setting.

The epidermal growth factor receptor (EGFR) is a transmembrane protein capable of cellular signalling and is responsible for initiating cell growth and replication functions.[214,215] Epidermal growth factors (EGF) are macromolecular proteins capable of binding to the extracellular component of an EGFR. Binding of EGFs to EGFR dimers formed at the cell surface, whether *via* homodimerisation of EGFR or heterodimerisation with another member of the ErbB tyrosine kinase family, play an important role in stabilisation of EGFR dimers and the ensuing cellular signalling processes which take place following their formation. EGFRs are overexpressed on a range of tumours including brain, breast, colorectal, ovarian, pancreatic and prostate cancers.[214,215] The EGFR therefore offers another opportunity for the specific targeting of cancer cells using a DNC system. Again, this can be achieved by attachment of ligands, which are capable of EGFR binding, to the surface of a DNC. A wide range of species are capable of binding to EGFR and may therefore prove useful in the design of EGFR-targeted nanomaterials, these include betacellulin, EGF, epigen, epiregulin, transforming growth factor-α and heparin binding EGF-like growth factor.[216–222] Ligand functionalised nanoparticles are capable of binding to and therefore stabilising EGFR dimers complexes on the surface of cancer cells. The formation of the ligand-stabilised EGFR dimer complexes initiate cellular signalling processes following which the ligand-EGFR dimer complexes are internalised *via* clathrin-mediated endocytosis.[223] A number of DNC systems have been developed to target cellular internalisation *via* EGFR-mediated endocytosis.[224,225] This has been achieved by conjugation of EGF to the surface of nanoparticles; for example

functionalisation of superparamagnetic iron oxide nanoparticles with EGF showed improved magnetic resonance imaging properties to their non-targeted analogues.[226] Similarly, EGF-functionalised gelatin based nanoparticles have shown enhanced targeting of highly EGFR expressing A549 cells over HFL1 (low EGFR expression) *in vivo*; such nanoparticles were also able to target tumours using EGFRs in an *in vivo* tumour-bearing mouse model.[227]

Whether achieved *via* passive or active targeting strategies, ensuring cellular internalisation is an essential function of a DNC. The physiological barriers and therefore the role of the DNC system are, however, not complete once cellular internalisation has been achieved. Once located within a cell, DNC systems are faced with a range of intracellular barriers which they must overcome in order to ensure that they achieve their desired therapeutic effect.

1.2.2.5 Intra-Cellular Barriers for DNC Systems

DNCs which undergo cellular internalisation *via* CIM, CIE and receptor-mediated endocytosis are held within endosomes. Escape from such endosomes is essential in order to avoid lysosomal degradation, facilitated by the high enzyme concentrations and/or the low pH within lysosomes. Failure to achieve endosomal escape can also allow exocytosis of the DNC systems and thus their therapeutic purposes cannot be realised.[228] The maturation of early endosomes into late endosomes is accompanied by a significant reduction in pH. DNC systems must therefore be resistant to changes in pH in order to maintain their colloidal stability and must also avoid premature release of their therapeutic payloads. This observed change in pH has been exploited as an opportunity to promote endosomal escape; in particular, by functionalisation of nanomaterials with pH responsive moieties which, following a decrease in pH, are capable of inducing endosomolysis and thus causing the release of the DNC system into the cytosol.[229–231] Only once DNC systems are within the cytosol must they release their drug payloads in order to have the desired therapeutic effect. Intracellular fluids such as cytosol contain high concentrations of glutathione, a thiol-containing amino acid, which can be used as a stimulus to trigger drug release from DNC systems.[232,233]

DNC systems internalised *via* caveolin-mediated endocytosis are localised in caveosomes. The neutral pH within caveosomes puts less demand on the colloidal stability of internalised DNC systems and also minimises enzyme- and acid- promoted hydrolysis reactions. Caveosomes therefore present a suitable route for the transport of DNC systems which are chemically active or susceptible to hydrolysis. It has been shown that caveosomes can facilitate the transcytosis of 15 nm gold nanoparticles across endothelial membranes.[234] Alternatively, the cargo held within caveosomes can be directed towards the Golgi apparatus and endoplasmic reticulum.[235,236] This highlights the possibility that the caveolin-mediated endocytic pathway can be exploited for two anti-cancer applications: i) DNC transport across endothelial

membranes, in order to access sub-endothelial tissues and ii) The delivery of targeted chemotherapeutics which aim to inhibit the biological functions of the Golgi apparatus and/or endoplasmic reticulum.

1.2.2.6 Clinical Application of DNC Systems for the Treatment of Cancer

Despite the large number of physiological barriers that must be overcome in order to achieve the desired therapeutic effect, many DNC systems have been studied as novel drug delivery strategies in the fight against cancer. The main types of materials which have been studied in clinical trials and subsequently approved for use as novel nanomedicine cancer therapies include lipid based nanomaterials, block copolymer self-assemblies, drug-polymer composites, drug nanocrystals and drug-conjugates. A list of DNC systems which are currently undergoing pre-clinical and clinical evaluation are presented in Table 1.2. Drug conjugates are not relevant to the nature of the research discussed in this thesis; the reader is directed to a number of excellent review articles which discuss this topic in more detail.[237–239]

Table 1.2 Examples of anti-cancer nanomedicines which are either approved for use or are currently undergoing clinical trials. Table adapted from Hare *et al.*[240] and Lu *et al.*[241]

DNC type	Drug	Product name/company	Target	Phase	Ref.
Liposomes	Doxorubicin	Myocet™/Teva UK	Metastatic breast cancer	Approved	[242]
		Doxil™/Janssen	Kaposi's sarcoma Ovarian cancer Multiple myeloma	Approved	[155]
		Thermodox™/Celsion	Primary hepatocellular carcinoma Refractory chest wall breast cancer Colorectal liver metastases	Phase III	[243,244]
		2B3–101/2-BBB Medicines BV	Brain metastases Glioma	Phase II	[245,246]
	Vincristine	Marqibo™/Spectrum Pharmaceuticals	Acute lymphoblastic leukaemia	Approved	[247–251]
	Daunorubicin	DaunoXome™/Galen	HIV-related Kaposi's sarcoma	Approved	[252–257]
	Cytarabine	Depocyt™/Pacira Pharmaceuticals	Lymphomatous meningitis	Approved	[258–260]
	Irinotecan	Onivyde™/ Merrimack Pharmaceuticals		Approved	[258–260]

Table 1.2 Continued

DNC type	Drug	Product name/company	Target	Phase	Ref.
Polymer micelles	Paclitaxel	Genexol-PM™/ Samyang Biopharmaceuticals	Breast cancer Non-small cell lung cancer Ovarian cancer	Approved	261–264
		NK105/NanoCarrier™	Stomach cancer Breast cancer	Phase III	265–269
		NC-4016/ NanoCarrier™	Solid tumours	Phase I	265,270
		Nanoxel™/Samyang Biopharmaceuticals	Advanced breast cancer	Phase I	271–274
	DACH-platin	NC-6004 Nanoplatin™ /NanoCarrier™	Pancreatic cancer Head and neck cancer Non-small cell lung cancer	Phase III	275–279
Drug-polymer composites	Docetaxel	BIND-014 (Accurin™)/BIND Therapeutics	Cholangiocarcinoma Cervical cancer Bladder cancer Head and neck cancer Non-small cell lung cancer subtypes	Phase II	280,281
Drug-polymer composites	AZD2811 (AZD1152 hydroxyquinazoline pyrazol anilide; Aurora-B Kinase Inhibitor)	AZD2811 (Accurin™) nanoparticle/AstraZeneca	Advanced solid tumours	Phase I	280,281
Drug nanocrystals	2-methoxyestradiol	Panzem®/EntreMed	Solid tumours	Phase II	282–286
	Paclitaxel	Paxceed®/Angiotech Pharmaceuticals	Solid Tumours	Phase II	287–289
	Thymectacin	Theralux®/Celmed BioSciences	Solid Tumours	Phase II	290

The majority of DNC systems currently undergoing pre-clinical and clinical development are not functionalised with cell-targeting ligands, therefore accumulation within tumour tissue relies on the EPR effect. Such DNCs are designed to improve drug efficacy and patient tolerability *via* manipulation of the pharmacokinetics and biodistribution of the active chemotherapeutic. Retention of the chemotherapeutic within the DNC system allows the maximum plasma concentration of free drug (C_{max}) to be reduced. This allows accumulation of the DNC system at the tumour site *via* the EPR effect and ensures that tumours receive

specific and prolonged exposure to therapeutic concentrations of the drug. DNC research is therefore focused on manipulation of DNC properties in order to ensure the stability and controlled release of their payloads in order to allow them to capitalise on the opportunity presented by the EPR effect. One key issue which has arisen during pre-clinical evaluation is the release of active payloads from DNC before accumulation within the tumour microenvironment takes place. A number of strategies have been employed to address this including covalent attachment or controlling drug diffusion through polymer matrices.[291–293]

Alternatively, some DNC systems currently undergoing clinical development have adopted active targeting strategies.[294] Another advantage of using DNC systems for the targeted delivery of toxic chemotherapeutic agents, specifically to a tumour site, is the ability to reduce the harsh side-effects experienced by patients undergoing chemotherapy regimens. For example, pre-clinical evaluation of a AZD-2811 nanoformulation showed that encapsulation of the active Aurora-B kinase inhibitor within a drug-polymer composite reduced dose toxicity to bone marrow.[241] As a result, doses of nanoformulated AZD-2811 could be administered in excess of the toxic dose limit typically shown by the unformulated chemotherapeutic. Alternatively, unformulated water-insoluble chemotherapeutics often require the use of excipients to increase their solubility in biological fluids. Such excipients often exhibit toxicity and, as a result, can also limit the dose of a chemotherapeutic which can be safely administered. This is demonstrated by the variation in the toxic dose limit observed between different paclitaxel nanoformulations. For example, higher doses of paclitaxel can be administered as the polymeric micelle-based nanoformulation, Genexol-PM™ compared to the excipient-stabilised paclitaxel solution, Taxol™.[295] This difference in toxicity has been attributed to the presence of the excipient Cremophor™ used to solubilise Paclitaxel in the Taxol™.[290] Achieving improved safety profiles using chemotherapeutic nanoformulations can therefore have significant impacts on the clinical performance and thus the outcome of chemotherapy treatments.

Although the development of chemotherapy based DNC systems has proven successful in the treatment of a wide range of cancers, the vast majority of cancer research has focused on a small range of nanomaterials and DNC platforms. This has limited chemists' abilities to respond to, and further their understanding of the barriers and opportunities presented by the vascular, extracellular and intracellular systems, as well as those which arise during tumour formation processes. Future research must utilise nanomaterials that have been specifically designed to study and/or exploit the opportunities identified by past research. Advances in the field of polymer chemistry has facilitated the generation of precise macromolecular structures which can be used to generate functional nanomaterials. Such nanomaterials will be instrumental in the development of the next generation of anti-cancer nanomedicines.

1.3 Polymer Chemistry

The field of polymer chemistry is of significant global importance; from the tyres on the cars that we drive to the clothes that we wear, polymers play a significant role in many aspects of our daily lives. Polymers can either be synthesised *via* chain growth or step growth polymerisation.[296] Briefly, chain growth polymerisations involve addition of individual monomers to a growing polymer chain, whereas step growth polymerisations involve combination of bifunctional monomers to form a series of dimers, trimers and oligomers which eventually combine to form long chain polymers. Until relatively recently, neither approach provided good control over the polymerisation processes or the properties of the polymers subsequently formed. As a result, chemists' abilities to design precise nanomaterials with pre-determined structures and control over polymer molecular weight was somewhat limited. Although such control could be achieved using living polymerisation methods, the limited monomer scope and its requirement for stringent polymerisation conditions, such as exclusion of moisture, have limited its adaptation by polymer chemists. In contrast, the discovery of reversible-deactivation radical polymerisation (RDRP) techniques in the last decade of the 20th century has revolutionised the field of polymer chemistry and opened up many new areas of polymer research.

1.3.1 Reversible-Deactivation Radical Polymerisation

The discovery and development of RDRP techniques has, without doubt, provided the most significant advancement in the field of polymer chemistry over the past quarter of a century. The aim of RDRP techniques is to facilitate the polymerisation of vinyl monomers whilst affording polymer chemists with a degree of control over polymer molecular weight whilst minimising the disparity between growing polymer chains. There are two key areas where RDRP techniques provide significant advances from the conventional radical polymerisation techniques. i) They are pseudo-living processes in which all polymer chains are initiated at the same time and continue to grow throughout polymerisation. ii) They suppress undesirable side reactions by using the RDRP process to minimise the concentration of active radicals during polymerisation. These two factors combined allow a known number of polymer chains to grow at equal rates with minimal disparity between polymer chain lengths. This has allowed polymers of pre-determined number-average molecular weights *(M_n)* to be produced containing significantly lower dispersity (Đ) values (Đ = 1.01 - 1.30) than those typically obtained for polymers produced using conventional radical polymerisation techniques.

Since the discovery of RDRP in the mid-1990s a plethora of synthetic techniques have been developed; however, nitroxide-mediated radical polymerisation (NMP),[297–300] atom transfer radical polymerisation (ATRP), single electron transfer living radical polymerisation (SET-LRP)[301,302] and reversible addition-fragmentation chain transfer (RAFT)[303]

polymerisation remain the four most popular techniques in use today. Whilst the subtle detail of each technique differ, they all share the same basic mechanistic principles of a reversible deactivation radical process. The RDRP process is based on the dynamic covalent affiliation between a labile end-group and the ω-terminus of a polymer chain (Figure 1.7). The chemical nature of the labile end-group is dependent upon the RDRP technique employed. In ATRP/ SET-LRP labile end-groups typically consist of halides. Alternatively, NMP uses nitroxides and RAFT polymerisation is facilitated by a range of thiocarbonyl based end-groups, including trithiocarbonates, dithioesters and dithiocarbonates (xanthates).[304–306] The specific mechanistic detail of individual RDRP techniques will be discussed in detail during the introduction sections of the relevant chapters.

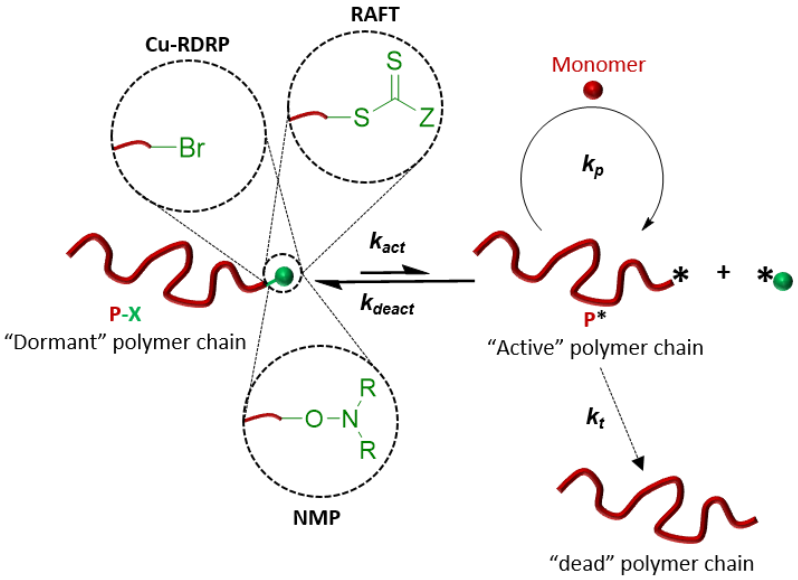

Figure 1.7 Schematic general representation of the dynamic equilibrium which forms the basis of RDRP techniques. This equilibrium exists between dormant (P-X), where X represents a labile group, and active (*P**) states in which polymers exist during RDRP. P-X undergoes activation (k_{act}) to form P*. P* can undergo propagation with monomer (k_p) to increase its degree of polymerisation or a termination reaction (k_t) to form a "dead" polymer chain.

The reversible attachment of labile end-groups to polymer chains means that polymer chains can exist in two forms during RDRP: i) as a "dormant chain" where a labile end-group is covalently attached to the ω-terminus of the polymer chain and ii) as an "active" chain, where homolysis of the labile covalent bond results in the formation of an active radical at the ω-terminus. The dormant state is chemically inert and is therefore unable to participate in chemical reactions such as propagation or chain termination. In contrast, the active state contains a reactive radical which is capable of facilitating chain growth *via* propagation with a monomer; this occurs with a rate constant k_p. Active radicals are also capable of participating in undesirable side reactions such as chain termination, occurring with a rate constant k_t, which irreversibly cap polymer chains and thus preventing their further growth *via* propagation. Growing polymer chains undergo constant transformation between their active and dormant

states throughout polymerisation; these occur *via* a series of activation and deactivation reactions which proceed with the rate constants k_{act} and k_{deact}, respectively.

RDRP processes are extremely effective in preventing undesirable side reactions, such as chain termination. Once an active species is generated, it can either undergo propagation with monomer, termination with another active radical or, most likely, the reverse deactivation process, *via* recombination with a labile end-group. This ensures that active radicals have short lifetimes and the fact that the RDRP equilibrium lies in favour of the dormant species also maintains a low concentration of active polymer chains throughout polymerisation. As a result polymerisations proceed in a pseudo-living manner and the formation of dead polymer chains, *via* radical-radical combination, is effectively suppressed by the RDRP process. This allows the majority of polymer chains to continue to grow unhindered throughout polymerisation.

Another key advance brought about by the discovery of RDRP is that it provided chemists with the ability to target the M_n prior to synthesis. Regardless of the technique employed, the labile end-group responsible for facilitating the RDRP process is incorporated into polymer chains during the initial stage of polymerisation. This is achieved by addition of a molecule capable of facilitating RDRP (the RDRP agent) into polymerisation reactions. The chemical functionalities of such RDRP agents are subsequently incorporated at either end of the polymer chain. As a result, control over the stoichiometry of the monomer and RDRP agent at the start of polymerisation allow desired polymer chain lengths to be targeted with relative ease. RDRP techniques also provide the ability to polymerise a wider scope of monomers in comparison to traditional living polymerisation techniques. Furthermore, a range of RDRP techniques have been developed which allow polymerisations to be conducted under mild conditions including in aqueous solution, at ambient temperature and in the presence of oxygen;[307–309] such advances have only helped to promote the industrial translation of such techniques and have increased the commercial viability of materials produced by RDRP.[310]

The ability to produce polymers of predetermined molecular weight whilst maintaining low dispersity between polymer chains was a huge step forward in the field of polymer chemistry. This has subsequently formed the basis of decades of research which has pushed the limits and scope of polymer science. The versatility of the RDRP process has since been used to generate a variety of novel polymer architectures which were previously unachievable using conventional radical polymerisation techniques.

1.3.1.1 Polymer Architecture

RDRP techniques have permitted the synthesis of a wide range of novel macromolecular architectures. Macromolecular architectures can vary in many ways including the number of monomer types within a polymer, their distribution within a polymer and the way in which polymer chains are arranged within a polymer structure (polymer topology). Some of the most studied polymer architectures which can be generated using RDRP include: linear homopolymers,[311] block copolymers,[312] multi-block copolymers,[313,314] graft copolymers,[315] star polymers,[316] branched polymers and hyper-branched polymers.[313,314] An overview of these macromolecular architectures is presented in Figure 1.8.

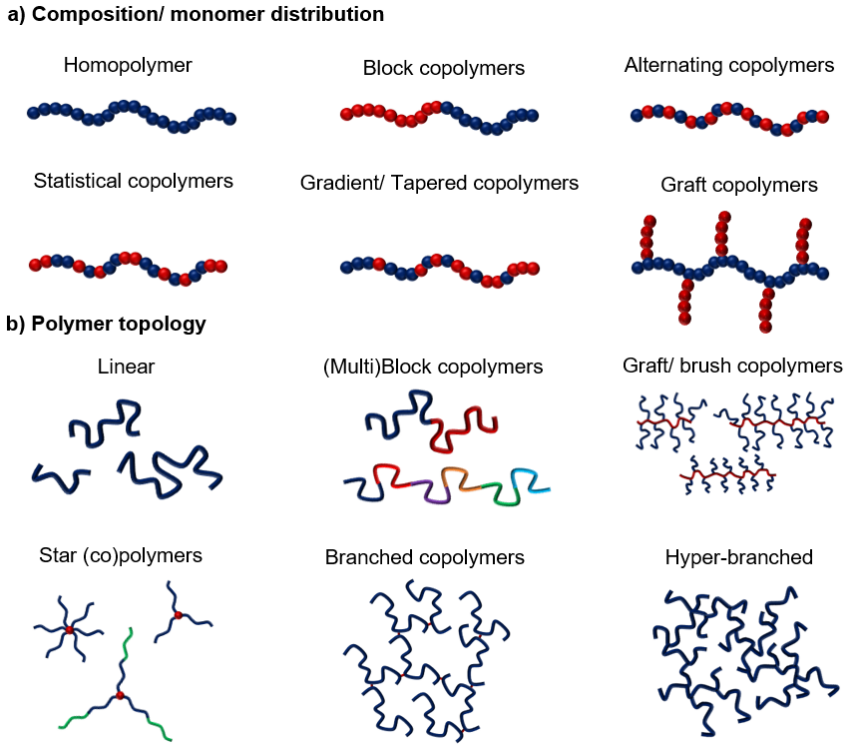

Figure 1.8 Examples of the macromolecular structures which can be generated using RDRP. a) Variations in the distribution of monomers in across the (co)polymer backbone. b) The wide range of polymer architectures which can be generated as a result of the enhanced control provided by RDRP.

As described in Section 1.3.2.1, RDRP allows the generation of well-defined polymers with controlled molecular weights. In cases where polymerisations are conducted using RDRP agents which contain a single functional group capable of facilitating RDRP, chain growth occurs in one direction. Perhaps considered the conventional RDRP approach, the architecture generated is known as a linear polymer. Where polymerisations contain only one type of monomer the resulting polymers generated are known as linear homopolymers. In contrast, copolymerisation of more than one monomer type generates a linear copolymer. The distribution of comonomers within linear copolymers architectures generated *via* RDRP can vary significantly. As a result of the pseudo-living nature of RDRP processes, the relative rates

of monomer consumption during copolymerisation are reflected by the comonomer distribution along each individual chain. As a result, not only do linear copolymers possess similar molecular weights, they also contain effectively identical compositional gradients along their copolymer backbone. The magnitude of the compositional gradient is highly dependent upon the relative reactivities of the two (or more) comonomers being polymerised.[317] In particular, this gives rise to the generation of statistical, alternating and gradient/tapered copolymer architectures that cannot be achieved using conventional radical polymerisation techniques.[318]

Copolymers in which monomers are compartmentalised into discrete regions along the copolymer backbone are known as block copolymers. The synthesis of such materials can be achieved *via* RDRP due to the retention of labile polymer end-groups following polymerisation. This allows such polymers to be used as macromolecular RDRP agents (macro-RDRP agent) in the polymerisation of a second monomer in a subsequent RDRP process. Known as a chain extension, this results in the complete segregation of the two monomer types across the block copolymer backbone.[319] Furthermore, the ability to target M_n also facilitates the creation of block copolymers with control over their respective block lengths. The high end-group fidelity which has been shown by many RDRP techniques means that multiple chain extensions to be conducted without loss of a polymer's labile end-group. This has allowed the creation of multi-block copolymers with as high as 10 different monomer segments across the multi-block copolymer backbone using various RDRP techniques.[320]

Alternatively, the synthesis of RDRP agents containing more than one moiety capable of facilitating RDRP has enabled the creation of multi-arm star polymers.[321] Polymerisation from such multifunctional RDRP agents promotes divergent growth in a number of directions proportional to the number of labile groups present. For example, the use of a trifunctional RDRP agent would promote chain growth in three directions, to form a 3-armed star, whereas the use of a hexafunctional RDRP agent would facilitate chain growth in six directions, forming a 6-armed star. RDRP therefore enables the construction of star polymers through what is known as a core-first approach.[322] RDRP also offers the ability to produce stars containing different arm lengths by controlling the stoichiometry between monomer and RDRP agent. Furthermore, the retention of labile end-groups on the polymer arms has allowed chain extension of multi-armed star polymers to generate multi-armed star block copolymers.[321]

Graft copolymers are another form of segmented copolymer where one monomer typically forms the copolymer backbone whilst the other monomer forms randomly distributed branches which protrude from the polymer backbone. Such materials are often referred to as comb- or

brush-like copolymers. There are three main synthetic approaches used for the generation of graft copolymers, these are often referred to as grafting-to, grafting-from and grafting-through approaches. The grafting-to approach typically involves a two-stage process. Firstly, a polymer backbone is synthesised containing one monomer type; this monomer typically contains pendant functional groups which are capable of participating in post-polymerisation modification reactions. A second step then involves post-polymerisation modification of the polymer backbone *via* covalent attachment of a second polymer to the pendant functional groups of the polymer backbone. This approach can be difficult as the production of a suitable polymer backbone typically requires bespoke monomer synthesis and post-polymerisation modification reactions must achieve high yields in order to obtain the desired graft copolymer architecture.

Alternatively, the grafting-from approach involves two sequential polymerisation reactions. The first reaction, similar to that described in the grafting-to approach, involves the synthesis of a polymer backbone containing pendant functional groups. However, in the grafting-from approach, these functional groups are in fact RDRP agents which act as "grafting points" from which the growth of the second component occurs. The grafting-through approach is perhaps the simplest synthetic approach for the generation of graft copolymers. Firstly, polymer chains are generated containing an end-group functionality which subsequently can be converted into a polymerisable group, to form what is known as a macromonomer. The polymerisation of such macromonomers therefore allows the generation of graft copolymers *via* a grafting through approach.[323] One advantage of this approach is that many macromonomers are now commercially available and this can therefore remove the necessity for macromonomer synthesis. RDRP techniques have provided a large degree of control over the graft copolymer architecture. The ability to control polymer chain lengths allows the length of both polymer backbone and polymer side-chains to be pre-determined prior to synthesis. Furthermore, addition of a non-functional comonomer during the synthesis of the copolymer backbone has allowed the grafting density of graft copolymers to be controlled.[324]

Branched and hyper-branched polymers have attracted significant attention since the discovery of RDRP.[313] The term branched polymer refers to polymers in which a proportion of the pendant groups of the polymer backbone either consist of, or are covalently-linked to, another polymer chain. The control provided by RDRP techniques has facilitated the generation of branched and hyper-branched polymer architectures which could not previously be obtained using conventional radical polymerisation techniques.[325] The key difference between branched and hyper-branched polymer architectures has been the topic of considerable debate;[325] to speak generally, polymer nomenclature is typically assigned based on the prevalence of branching within the macromolecular architecture. A number of approaches have been

developed to determine the prevalence of branching within a polymer. For example, the degree of branching (DB) is a quantitative measure of the number of branch points and terminal units in the whole polymer structure. Alternatively, others have reported the branching density within polymer structures, which represents the mass of branching units as a function of the total mass of the branched polymer.[326] Under these assessments, branched polymers typically exhibit lower degrees of branching/branching densities than hyper-branched polymers.

The main synthetic approach used for the generation of branched copolymers involves the copolymerisation of monofunctional and bifunctional monomers (BFM) *via* RDRP. BFMs are monomers which contain two functional groups capable of participating in propagation reactions; incorporation of each of these groups into separate growing polymer chains generates a branch point between the two chains. The resulting branched copolymers therefore consist of large numbers of primary chains covalently linked through BFMs which act as branch points within the branched macromolecular architecture. A detailed mechanistic insight into the formation of branched copolymers *via* copolymerisation of monofunctional and BFMs using RDRP is presented in Chapter 2, Section 2.1.3.2. The development of RDRP has aided the prevention of gelation in order to provide statistical incorporation of BFMs across all growing polymer chains; thus allowing such copolymerisations to conform to the Flory-Stockmayer theory of gelation.[327]

Alternatively, hyper-branched polymers contain much higher branching densities. The construction of hyper-branched polymer architectures has been greatly advanced by the use of RDRP. Self-condensing vinyl polymerisation (SCVP) is an approach which involves the polymerisation of inimers to generate hyper-branched polymer architectures.[328] Inimers are species which contain two chemical moieties capable of undergoing RDRP; these include a polymerisable group as well as an RDRP agent functionality. As a result, inimers act as both monomers and RDRP agents during SCVP. This allows them to be incorporated into a polymer backbone through their polymerisable group, whilst simultaneously grafting-from the polymer backbone *via* their RDRP agent functionality.[329] Whilst SCVP has been attempted using conventional radical polymerisation with only limited success, the application of RDRP techniques to SCVP have resulted in the production of hyper-branched architectures which exhibit exceptionally high DB values.[330] More recently, the construction of hyper-branched polymers has been achieved *via* homopolymerisation of BFMs using RDRP.[331] This approach has facilitated the production of densely-packed hyper-branched polymers with comparable DB values to those obtained *via* SCVP. RDRP plays an essential role in controlling polymer chain lengths in order to prevent the onset of gelation.

The wide range of polymer architectures which are now easily accessible to polymer chemists is another indication of the advances brought about by the discovery and development of RDRP techniques. High tolerance of many chemical functionalities has also allowed the production of functional macromolecules.[332] Furthermore, the use of a broad range of components in the design of complex macromolecules, such as monomers, RDRP agents, BFMs and inimers to name a few, allow functionality to be incorporated at specific locations on the (co)polymer architectures.

1.3.1.2 Polymer Functionality

The use of many different reaction components in RDRP, particularly in the construction of complex (co)polymer architectures, has allowed chemists to incorporate functionality into polymers with relative ease. The reaction components used in RDRP are dependent upon the polymer architecture being targeted; however, the most common functional handles through which functionality is incorporated into polymers include α-end-groups, monomers, ω-end-groups and branch points.[333] An overview of these functional handles and their locations within various macromolecular architectures is presented in Figure 1.9.

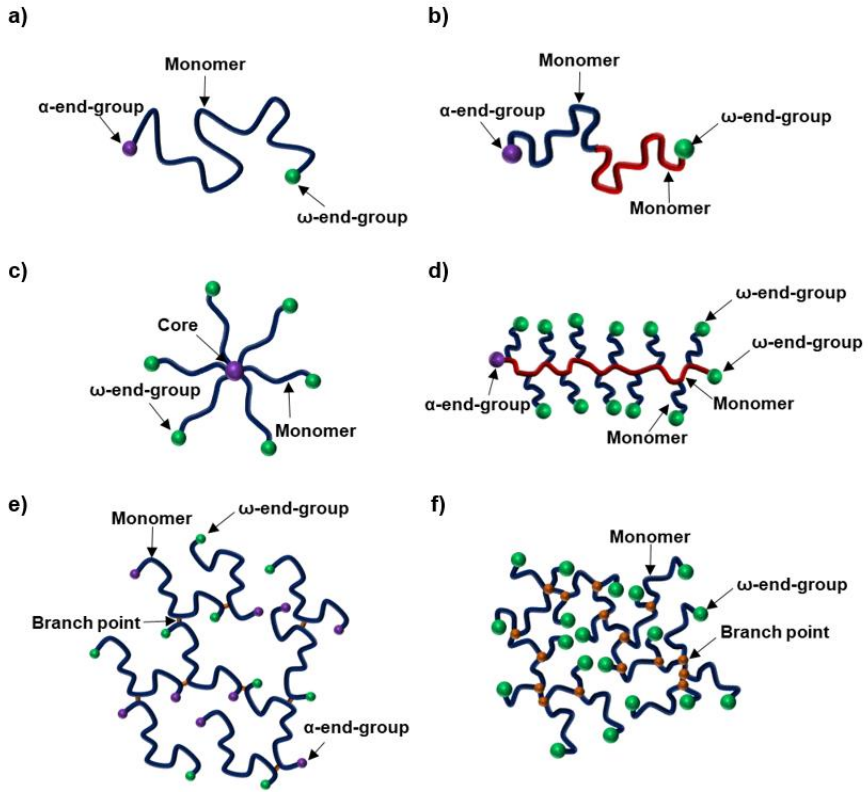

Figure 1.9 Schematic representation of the functional handles through which chemical functionality can be incorporated into polymer structures. Demonstration of the specific functional handles available for a range of polymer architectures, including: a) Linear homopolymers, b) Block copolymers, c) Star polymers, d) Graft copolymers, e) Branched copolymers and f) Hyper-branched polymers. Functional handles include: monomer (blue and red), α-end-group/core (purple), ω-end-group/RDRP agent (green) and branch points (orange) functionalities.

There are two main approaches through which functionality can be incorporated into polymers. Perhaps the easier of the two approaches, chemists can employ reaction components which already possess the desired chemical functionality in a RDRP; such functionalities are therefore incorporated into the polymer structure during polymerisation. Whilst the production of such reaction components can often require complex organic syntheses, this process offers a relatively facile approach to incorporate chemical functionality into a polymer.

Alternatively, a desired chemical functionality can be incorporated through post-polymerisation modification. This requires the use of reaction components which contain precursor moieties. This approach therefore uses polymers as macromolecular scaffolds through which desired chemical functionalities can be incorporated. Whilst this approach typically removes the need for complex synthesis of reaction components, its success is highly dependent upon the efficiency of the post-polymerisation modification reaction and can often require additional purification steps to remove side-products. The use of this approach has been accelerated by the discovery of click chemistry.[334] This term is given to chemical reactions which proceed with exceptionally high yields, do not generate side products and typically proceed without the need for a catalyst. This approach, including the areas of post-polymerisation modifications and click chemistry, lies beyond the scope of the work covered in this thesis and will therefore not be discussed herein; however, the reader is directed to a number of excellent review articles which discuss these topics in more detail.[335–338]

Monomer structure is perhaps the most utilised route through which functionality has been incorporated into polymers. Monomers typically make up the majority of the overall polymer mass, and therefore have a significant impact on the overall properties of the resulting polymer. In particular, monomer chemistry is often used to control macroscopic polymer properties such as water solubility and thermal properties such as the glass transition temperature (T_g). For example, water-soluble polymers can be produced through selection of water-soluble monomers, such as those containing: acidic, cationic, anionic, zwitterionic,[339,340] short water-soluble polymers such as poly(ethylene glycol) (PEG)[323] as well as a range of other polar functional groups.[341] In contrast, selections of hydrophobic monomers such as those containing pendant alkyl, aromatic or lipid-based functional groups generate hydrophobic polymers which are insoluble in water.[342] A number of bespoke monomers have been generated to produce polymers containing precise chemical functionalities which are suited towards a chosen application. Known as polymer conjugates, such approaches have seen the production of polymers functionalised with drugs, carbohydrates, fluorophores, chromophores, deoxynucleic acids (DNA) and amino acids.[343–346] The extent to which functional groups are incorporated into polymers is often controlled by copolymerisation with a relatively benign comonomer. For example, 6-O-vinyladipoyl-D-glucose was copolymerised with the

hydrophilic comonomer N-isoproylacrylamide (NIPAAm) to generate a series of water-soluble glycopolymers *via* RDRP.[347]

Chemical functionality can be incorporated at polymer end-groups through the use of functional RDRP agents. As mentioned above, RDRP agents are incorporated at either end of polymer chains during the initial stages of polymerisation. The labile end-group functionality of an RDRP agent is located at the ω-end-group, where it facilitates chain growth *via* the RDRP process, whereas the remainder of the RDRP agent forms the polymer's α-terminus and has no influence of the polymerisation process. The design and use of functional RDRP agents therefore provides an opportunity to integrate chemical functionality at the α-terminus of a polymer chain. This approach has been adopted by chemists using different RDRP techniques *via* the creation and use of functional RDRP agents.[348] Functional RDRP agents have been used to achieve complex macromolecular architectures using relatively simple polymerisation techniques. For example, the use of macro-RDRP agents has allowed the production of AB diblock and ABA triblock copolymers in a one pot-synthesis.[349] In other cases the use of dendron-based RDRP agents has enabled the production of linear-dendritic hybrid, dendronised polymers and hyper-branched polydendrons.[350] Although a relatively facile way to incorporate functionality into polymer structures, the main limitations of this approach are: i) the possible complexity associated with the synthesis of functional RDRP agents and ii) that polymer end-groups typically only make up a small fraction of the overall polymer mass. Despite these limitations, end-group functionalisation has attracted significant attention in nanomedicine based polymer research.[351]

Polymers generated using RDRP typically retain their labile end-group (RDRP agent) functionality at their ω-terminus following polymerisation. These functional groups offer another handle through which further functionality can be introduced. In the case of RAFT polymerisation, remaining ω-end-groups, which typically consist of dithioester- or trithiocarbonate-based compounds, can undergo a selection of removal, transformation or functionalisation reactions with relative ease.[352] A similar series of reactions have also been established for the modification of the alkyl halide ω-end-group, which is typically retained by polymers produced using ATRP and SET-LRP techniques.[353] Perhaps the most effective use of remaining RDRP agent functionalities has been the chain extension with a second monomer. In many cases this has done to influence the polymer's physical properties; for example, in the chain extension of hydrophilic polymers with hydrophobic monomers in order to generate amphiphilic block copolymers.[354–356] In other cases chain extensions have been used to incorporate functional monomers at the ω-terminus of a polymer. For example, the chain extension of an amphiphilic block copolymer with glyco-monomer to incorporate cell-targeting functionality at the fore-end of the copolymer chain; this subsequently facilitated

the receptor-mediated endocytosis of the resulting block copolymer micelles formed.[357] This approach has also been used to generate novel macromolecular architectures;[330,358] for example, the chain extension of hyper-branched polymers has generated hyp-star materials which consist of a hydrophobic hyper-branched polymer core and high numbers of hydrophilic linear arms. Such materials have been coined 'unimolecular micelles' as they remain as individual nanoparticles in aqueous solution possessing a hydrodynamic radius of approximately 20 nm.

Branch points offer another handle through which chemical functionality can be incorporated into branched and hyper-branched polymers. Until recently, the vast majority of (hyper)branched polymer research had focused on the discovery, understanding and development of novel synthetic strategies for the production of such materials.[330,359,360] As a result, the use of branch points as a means to incorporate chemical functionality was relatively under-utilised. However, now that a number of synthetic strategies have been established, this area of research is receiving increased interest from polymer researchers. In particular research has involved the synthesis of functional BFMs and inimers which can then be incorporated into (hyper)branched polymer architectures. Due to the infancy of this research area the majority of publications have involved "proof of concept" studies to demonstrate the ability to introduce relatively benign chemical functionalities into (hyper)branched polymer structures.[328] However, more recently the introduction of chemical functionality at polymer branch points has yielded (hyper)branched materials with potential future applications. For example, the use of a macrocyclic ligands containing BFM, capable of chelating Gd^{3+} ions, facilitated the preparation of branched copolymers for application as MRI contrast agents and demonstration of this application in *in vivo* studies.[361] Alternatively, inimers containing labile covalent bonds as linker groups between their polymerisable and RDRP agent groups were used to produce degradable hyper-branched polymers using RDRP-mediated SCVP.[362]

Whilst branch points offer a suitable opportunity to generate functional polymers, their importance in the formation of (hyper)branched architectures must not be underestimated. The introduction of bulky substituents will increase the size and thus steric hindrance around a BFM/inimer and may therefore hinder their ability to participate in branching reactions and create the desired polymer architecture. This issue can be circumvented *via* the introduction of precursor functionalities at polymer branch points, which are then able to facilitate the introduction of more complex or bulkier functionalities through post-polymerisation modification. This was demonstrated by Gao and co-workers, who introduced azide functionalities at polymer branch points that subsequently facilitated the attachment of focal point alkyne functionalised, third generation dendrimers using a post-polymerisation azide-alkyne click reaction.[363]

The ability to incorporate chemical functionalities at precise locations on complex macromolecular structures has equipped chemists with the ability to influence the chemical and physical properties of polymers. Many chemical functionalities allow such polymeric materials to respond to changes in their chemical and physical environments. The use of such chemical functionalities is therefore useful in the design of responsive materials. This has attracted significant interest and has formed the basis of considerable amounts of polymer chemistry research.

1.3.1.3 Stimuli-Responsive Polymers

The ability to incorporate functionality into macromolecular architectures has enabled the creation of polymers capable of responding to a range of external stimuli. Stimulus-responsive materials typically rely on labile or dynamic covalent interactions, interactions of polymers with their external environment, for example the surrounding solvent, or even changes in their internal structures to facilitate such responses.[364] Stimulus-responsive materials with the capability to respond to a wide range of external stimuli have been produced using RDRP. These include pH,[365] temperature,[366] redox, light,[367] the presence of ions, and other chemicals ranging from small molecules to gases.[368] Whilst the specific chemical changes play a critical role in the facilitation of such responses, their mechanistic details are beyond the scope of the work covered in this thesis. The reader is directed to a number of review articles which discuss these topics in further detail.[365,369,370]

Of particular interest here is the impact that such chemical changes can have on the behaviour of polymers. The main types of polymer stimulus-responsive behaviour can be characterised as follows: i) chemical degradation of macromolecular structures,[371] ii) changes in aqueous solution behaviour, iii) chemical neutrality/ ionisation and iv) impacts on polymer rigidity/ viscosity. An overview of such stimulus-responsive behaviour is presented in Figure 1.10.

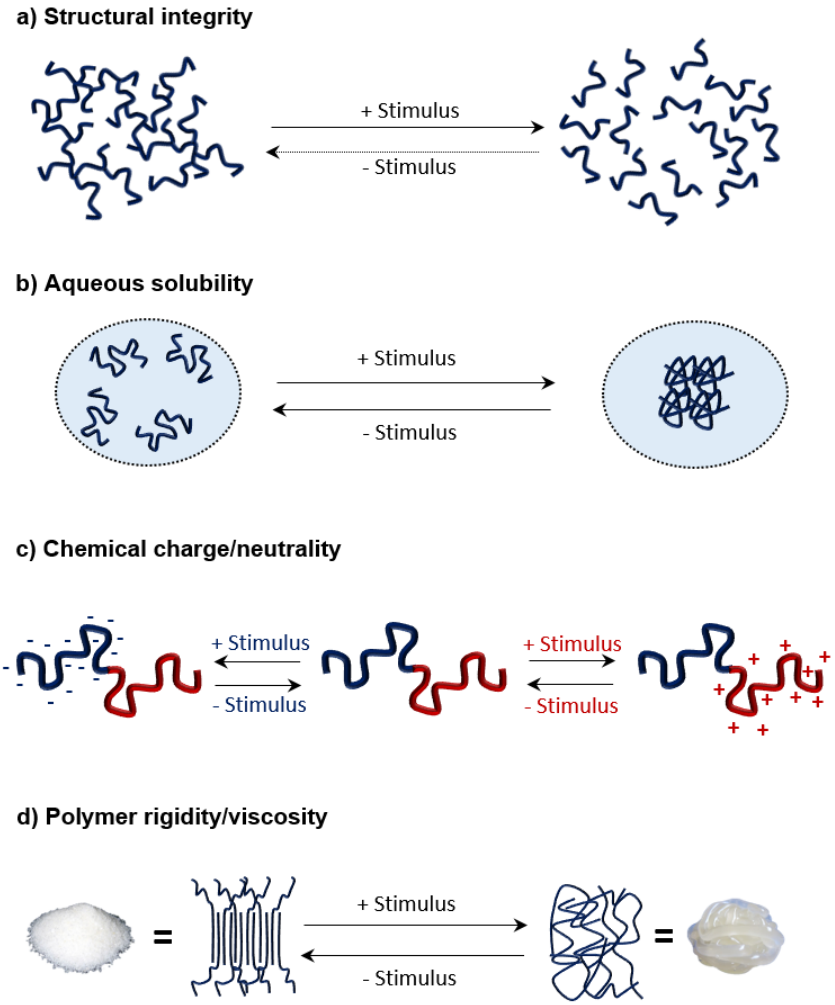

Figure 1.10 Schematic representation of the stimuli-responsive behaviours of polymers which can be induced by changes to their chemical and physical environment. These include effects on a) Structural integrity b) Aqueous solubility, c) Chemical charge and d) Polymer rigidity/ viscosity.

RDRP involves polymerisation of vinyl-based monomers and therefore typically generates polymers containing non-degradable aliphatic backbones. As a result, degradation of polymer backbones has, until recently, been considered to be an impossible task. In recent years, the radical ring opening polymerisation of cyclic ketene acetals, in particular the seven-membered 2-methylene-1,3dioxepane (MDO), has opened the door to the synthesis of degradable polymer backbones *via* radical polymerisation techniques.[334,372–380] The radical ring-opening of MDO places an ester within the backbone of the ensuing polymer, thus allowing polymer degradation *via* base-catalysed hydrolysis following addition of potassium hydroxide. This approach has been used to generate a range of macromolecular architectures containing degradable polymer backbones using RDRP.[381–385]Another approach which has been used to place a labile link within a polymer backbone and includes the use of bifunctional RDRP agents containing degradable linkers.[386–389] The use of a bifunctional RDRP agent places it in the centre of the polymer chain. Subsequent cleavage can therefore facilitate polymer degradation, which can be triggered by a range of external stimuli.

In the cases of branched and hyper-branched polymers, branch points provide another opportunity to incorporate labile linkers into macromolecular architectures. This has been achieved by the incorporation of labile groups into BFMs and inimers thus forming weak links throughout the resulting hyper(branched) structures.[328,390] This has allowed the production of (hyper)branched materials whose degradation can be triggered by a range of external stimuli, including pH, temperature, UV light and the presence of reducing agents.[391–393] It is important to note that despite the fact that many of the chemical changes which induce stimulus-responsive behaviour are reversible, the reformation of the polymer architectures is not. The stimulus-responsive degradation of polymers are therefore typically considered as irreversible processes. However, in some cases, polymer architectures can be reformed through the reversal of the degradation process. For example, in the case of hyper-branched polymers held together by thermo-responsive Diels-Alder linkers, ^{1}H NMR analysis showed 71 % of polymer branch points had reformed on cooling just 48 hours after thermally-triggered polymer degradation.[390]

Polymer solution behaviours are highly dependent upon the level of interaction between polymers and their surrounding solvent. Chemical and physical changes to polymers, which arise as a result of stimulus-responsive behaviours, can therefore have significant impacts on polymer solution behaviour; generally speaking, they can either have beneficial or detrimental effects. Many polymers possess thermally-responsive behaviour in aqueous solution.[394] In particular, polymers derived from NIPAAm and PEG-based monomers have been produced in order to exploit their lower-critical solution (LCST) behaviour. The term LCST refers to the temperature at which a polymer precipitates from solution. This is the result of the Gibbs free energy (ΔG) of aqueous mixing passing through zero within a practical temperature range; for example poly(NIPAAm) and poly((oligoethylene glycol) methacrylate) have LCSTs of 32 °C and 90 °C respectively.[395] The construction of copolymers containing varying compositions of monomers that possess contrasting aqueous solution behaviour has enabled the tuning of polymer LCSTs.[396] Furthermore, polymer LCST behaviour is also dependent on many other conditions, including concentration, molecular weight, polymer architecture and the concentration of salts within aqueous solution.[397] The phase transition which occurs when an aqueous solution of polymer is heated above its LCST can easily be reversed by cooling the solution;[323,398–403] although in some cases a difference can occur between the transition temperature obtained between heating and cooling cycles of aqueous solutions containing complex macromolecular architectures.[356,404–406]

In other cases, pH-responsive monomers can be used to influence polymer aqueous solution behaviour. This typically involves incorporation of ionisable groups into a polymer which can undergo reversible chemical transformations following changes to the environmental pH. This

has generally been achieved using carboxylic acid and amine based polymers which become ionised at high and low pH respectively.[407,408] In their neutral forms, such polymers typically exhibit low water solubility; however, polymer ionisation has an impact on the nature of polymer-solvent interactions, typically *via* the establishment of cation/anion-hydrogen bonding, and thus significantly increases the aqueous solubility of such polymers.[409] In other cases, quaternisation of tertiary amines groups, typically *via* alkylation using alkyl halides, has been used to generate cationic charges;[410] such reactions are typically irreversible and they can have a dramatic impact on aqueous solubility.

Thermo-responsive behaviour can also have a significant impact on the physical properties of polymers. In particular, temperature has a significant influence on polymer rigidity or viscosity in the bulk. These properties are typically linked to the physical state, degree of entanglement and strength of intermolecular forces, acting on polymer chains within the bulk material.[411] Polymers are typically characterised as either semi-crystalline or amorphous materials. Semi-crystalline polymers have regions in which polymer chains are held in highly ordered arrangements, which maximise non-covalent interactions between them, known as crystalline regions. Sections of the bulk material which do not adopt such highly ordered arrangements are known as amorphous regions. Semi-crystalline polymers have both crystalline and amorphous regions and, as a result, are typically brittle solids when below their melting points (T_m) and T_g. In contrast, polymers which do not possess crystalline regions are known as amorphous. They are held together by chain entanglements and intermolecular forces which act between the large macromolecules; however, these forces are typically much weaker than those present in the highly ordered structures of semi-crystalline materials.[412] Amorphous polymers typically exhibit rigid/ "glassy" behaviour when below their T_g, above which they become soft and flexible. Although possessing greater chain mobility, polymers still behave as rubbery solids above their T_g due to strong intermolecular forces still present between polymer chains.[413] As a result polymer viscosity typically decreases with temperature as chains acquire sufficient energy to overcome the intermolecular forces acting between them. The thermal transitions and melt viscosities of polymers are highly dependent upon many polymer properties, including molecular weight, monomer type, copolymer composition and polymer architecture. Polymer melting and glass transitions are both reversible processes and therefore temperature can be used as a stimulus to trigger the hardening/softening of polymers in their bulk state.[414] The use of polymers which are capable of responding to external stimuli can bring an additional dimension to the nanomaterials that they are used to construct. This has particular relevance to the field of nanomedicine, and in particular targeted drug delivery, where nanoparticles may be required to adapt in order to overcome a particular physiological barrier or capitalise on a specific opportunity. If used correctly, stimulus-responsive materials can be

incorporated into the design of DNC systems in order to equip them with the ability to respond to the physiological challenges presented by the vascular, extracellular and intracellular environments; this may ultimately improve their efficacy in delivering chemotherapeutics directly to cancer cells.

1.4 Synthetic Approaches for the Generation of Polymer-Based Nanoparticles

The advances made in the field of polymer chemistry has facilitated similar progress in the field of nanotechnology. In particular, the ability to control the molecular weight, macromolecular architecture and chemical functionality of polymers has allowed the construction of nanomaterials from well-defined building blocks. Furthermore, this has allowed the chemical and physical properties of such polymers to be translated into macroscopic behaviours of the resulting nanomaterials. One area which is of particular interest to the development of novel DNC systems is the generation of polymer-based nanoparticles *via* the formulation of synthetic polymers. In general, significant advances have been observed in two areas of polymer nanotechnology; these are the formation of amphiphilic block copolymer self-assemblies and the formation of polymer-based nanoparticles *via* nanoprecipitation.

1.4.1 Block Copolymer Self-Assembly

Amphiphilic block copolymers readily undergo self-assembly in water to avoid high energy water-hydrophobe interactions and thus minimise free energy. Incompatibility of one (or more) of the copolymer blocks with water typically drive the hydrophobic domains of numerous block copolymers together to form core-shell structures, where the core consists of hydrophobic domains with the hydrophilic domains facing outwards into the aqueous medium. The energetics of self-assembly are also driven by the formation of favourable non-covalent interactions between hydrophobic domains within the core of the self-assembly. The hydrophobic core-forming block also plays an important role in the formation, and stabilisation of block copolymer self-assemblies. Extending from the hydrophobic core, hydrophilic domains form a dense hydrated corona which provides steric stabilisation. The energetics of block copolymer self-assembly are beyond the scope of this thesis. However, the reader is directed to a number of excellent review articles which discuss this topic in considerable detail.[415,416]

Block copolymer self-assemblies can adopt a number of morphologies, including spherical micelles, cylindrical/worm-like micelles and polymersomes. Theoretically, the morphology adopted by block copolymer self-assemblies can be related to the free energy per chain, which consists of the free energy contributions of the hydrophobic and hydrophilic blocks as well as that of the core-corona interface.[417–419] Numerous experimental factors can also impact the

morphology adopted by block copolymer self-assemblies.[420–423] In practice, however, a simplified approach, known as the packing parameter ($P = v/a_o l_c$) is often used to explain the morphology adopted by block copolymer self-assemblies in aqueous solution.[424] This approach is presented in Figure 1.11. The packing parameter (P) determines the interfacial curvature at the core-corona interface of block copolymer self-assemblies in the state of minimum energy and thus dictate the copolymer morphology. The parameter, P, is depends on a number of factors, such as the volume ratio of the hydrophobic and hydrophilic domains, the extent of core hydration and the conformation adopted by the core forming block.[425] As a result, block copolymer self-assembly can be directed by careful selection of the relative degrees of polymerisation of both the hydrophobic and hydrophilic blocks.

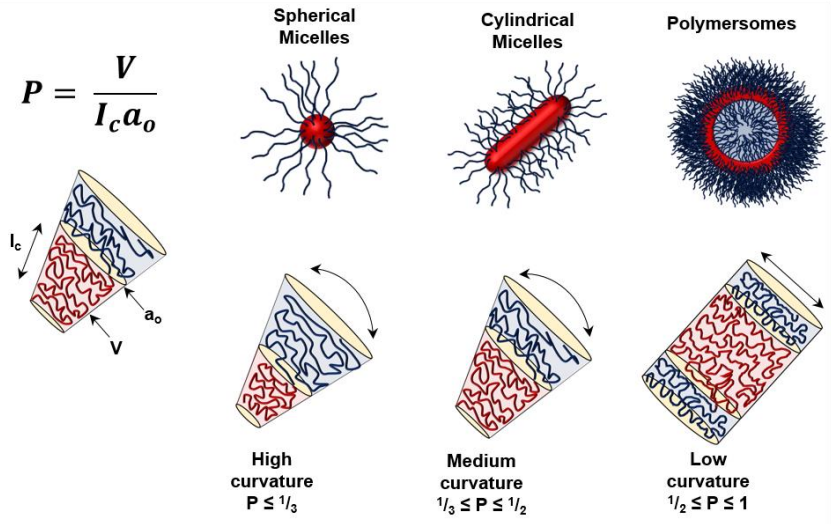

Figure 1.11 The influence of the packing parameter (P) on the morphology of amphiphilic block copolymer self-assemblies, where V is the hydrophobic chain volume, a_0 is the interfacial area per chain and I_c is the hydrophobic chain length. Schematic representation of spherical micelles, cylindrical/work-like micelles and polymersomes. Figure adapted from reference[426].

1.4.1.1 In-Situ Nanoparticle Forming Techniques

Block copolymer nanoparticle research initially involved the post-polymerisation self-assembly of block copolymers generated using, often complex, multi-step polymer syntheses. In recent years research focus has switched towards the *in situ* generation of self-assembled block copolymers nanostructures during RDRP. In particular, this has involved the development of two synthetic approaches; polymerisation-induced self-assembly (PISA) and emulsion-based RDRP. An overview of these approaches is presented in Figure 1.12. The two approaches build on the success of emulsion-RDRP techniques which have been used to generate block copolymer nanoparticles *via* the chain extension of water-soluble macro-RDRP agents with water-immiscible hydrophobic monomers in aqueous emulsion.[427–430]

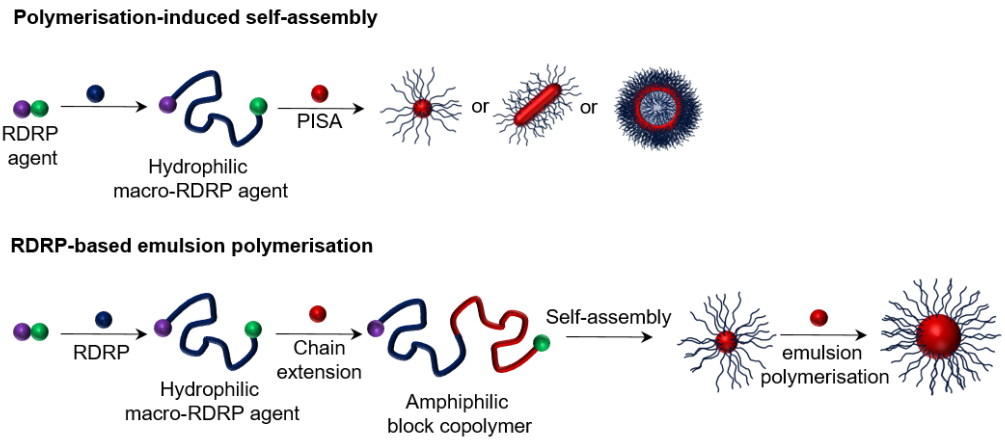

Figure 1.12 A general overview of the two predominant synthetic approaches used for the *in-situ* generation of block copolymer nanoparticles using RDRP. (Top) polymerisation-induced self-assembly (PISA). (Bottom) RDRP-based emulsion polymerisation.

PISA is a relatively new phenomenon in which aqueous nanoparticle dispersions are formed through the *in situ* self-assembly of propagating block copolymer chains during aqueous RDRP.[431] This allowed the preparation of aqueous nanoparticle dispersions at much higher concentrations than can be achieved through post-polymerisation processing methods (up to 50 %).[432] There are two critical criteria which must be met in order for an aqueous dispersion RDRP to proceed *via* PISA: i) the polymerisation must involve the chain extension of a water soluble polymer; ii) polymerisations are limited to monomers which are themselves water-miscible yet subsequently form water-insoluble polymers. Aqueous PISA is therefore limited to a small number of water-miscible vinyl monomers and requires the use of RDRP techniques to facilitate the chain extension of a soluble polymer.[433–440] As a result of using both a water-soluble macro-RDRP agent and monomer, chain extensions proceed in an identical manner to typical homogeneous polymerisations during the early stages of polymerisation. However, once the chain length of the water-insoluble block exceeds the limit at which polymer solubility can be maintained, the onset of micellar nucleation occurs. This would usually result in the macroscopic phase separation between the aqueous and hydrophobic polymer phases; however, the presence of the water-soluble block provides steric stabilisation and allows the *in situ* formation of block copolymer nanoparticles *via* PISA.[441,442] The onset of PISA can be observed by a characteristic increase in rate of polymerisation; this is caused by a relatively local high monomer concentration which arises due to monomer diffusion into the core of block copolymer nanoparticles formed.[443] Continued monomer consumption following the onset of nucleation facilitates the generation of amphiphilic block copolymers of controlled molecular weight. PISA has been used to generate aqueous nanoparticle dispersions containing various morphology including spherical and cylindrical micelles as well as polymersomes.[444]

Alternatively, emulsion-based RDRP has also been used to generate block copolymer nanoparticles *in situ*.[445–449] Aqueous emulsion-based RDRP involves the use of block

copolymer self-assemblies as nanoreactors for the polymerisation of water-immiscible monomers in aqueous emulsion. Amphiphilic block copolymers fulfil two roles in this synthetic approach, they act as both macro-RDRP agents and polymeric stabilisers during the aqueous emulsion polymerisation.[450] Preparation of block copolymer nanoparticles using emulsion-based RDRP first requires the synthesis of an amphiphilic block copolymer. This is typically achieved *via* preparation of a hydrophilic macro-RDRP agent and subsequent chain extension with a hydrophobic monomer; the blocking order employed is of crucial importance here in order to ensure that the labile end-group is located at the growing end of the hydrophobic block.[450] These amphiphilic block copolymers can then undergo self-assembly in water to form aqueous block copolymer nanodispersions. The corresponding water-immiscible monomer and initiator are added to aqueous nanoparticle dispersions to facilitate a second chain extension. Diffusion of the water-immiscible monomer into the hydrophobic core causes swelling of block copolymer nanoparticles which therefore act as polymerisation nanoreactors during the ensuing emulsion-based RDRP. Once polymerisation is complete, the hydrodynamic diameter (D_H) of block copolymer nanoparticles are larger than that of the self-assembly prior to polymerisation of the third block. The magnitude of the change in D_H is proportional to the ratio of monomer to macro-RDRP agent at the start of polymerisation and therefore allows tuning of the size of block copolymer nanoparticles.[451]

Block copolymer self-assemblies offer a robust nanoparticle platform with the potential to act as DNC systems *in vivo*.[452] Regardless of the synthetic approach employed, hydrophobic guest molecules can easily be encapsulated within the core of block copolymer nanoparticles. In the case of the post-polymerisation formulation of amphiphilic block copolymers, hydrophobic guest molecules can be encapsulated simply by including them in the self-assembly process.[453] Hydrophobic guest molecules can also been incorporated into block copolymer nanoparticles using *in situ* nanoparticle forming techniques by addition of guest molecules during the various polymerisation processes.[454–458] However, the encapsulation of hydrophobic drugs by physical entrapment through PISA has typically shown low encapsulation efficiencies and drug loadings.[459] Alternatively, a number of post-polymerisation processing procedures have been developed to load hydrophobic drugs into block copolymer nanoparticles. These approaches have shown high levels of success, particularly in cases where favourable interactions exists between guest molecules and the hydrophobic cores of block copolymer nanoparticles.[460–463] In other cases drugs have been incorporated into block copolymer nanoparticles using prodrug monomers, which contain cleavable covalent linkers, during PISA; this has allowed quantitative encapsulation of camptothecin *via* the use of a reduction cleavable camptothecin monomer.[464]

1.4.2 Nanoprecipitation

Nanoprecipitation is an alternative formulation approach which can be used to generate aqueous nanoparticle dispersions of synthetic polymers.[465] It is an easy and reproducible post-polymerisation formulation technique which has been applied to a wide range of polymers and has allowed the encapsulation of numerous hydrophobic guest molecules.[466] Nanoprecipitation has therefore attracted significant interest within nanomedicine research.[467]

1.4.2.1 The Nanoprecipitation Process

Preparation of polymer-based nanoparticle dispersions *via* nanoprecipitation involves the rapid mixing of a hydrophobic polymer, dissolved within a water-miscible organic solvent, with a large amount of an anti-solvent, typically water. The rapid diffusion of the bad solvent into the organic phase triggers a significant change in the solvent environment in which the polymer is dissolved. As a result, the polymer concentration within the nanoprecipitation medium usually exceeds the thermodynamic solubility limit, creating what is known as a state of supersaturation. The extent of supersaturation can be represented by the supersaturation ratio ($S_r = C/C_{eq}$) which, in the case of polymer nanoprecipitation, is defined as the ratio between the polymer concentration in the nanoprecipitation medium (C) and that at the thermodynamic equilibrium solubility limit (C_{eq}).[468] When the supersaturation limit is exceeded ($S_r > 1$) polymer chains collapse, in order to minimise high energy interactions with surrounding anti-solvent, causing the spontaneous formation of nuclei.

The formation of polymer nanoparticles *via* nanoprecipitation can occur through two different growth mechanisms. These mechanisms are known as nucleation and diffusion-limited growth and diffusion-limited cluster-cluster aggregation (DLCA).[469] Schematic representations of the nucleation and growth mechanisms which occur during the nanoprecipitation of polymers are presented in Figure 1.13.

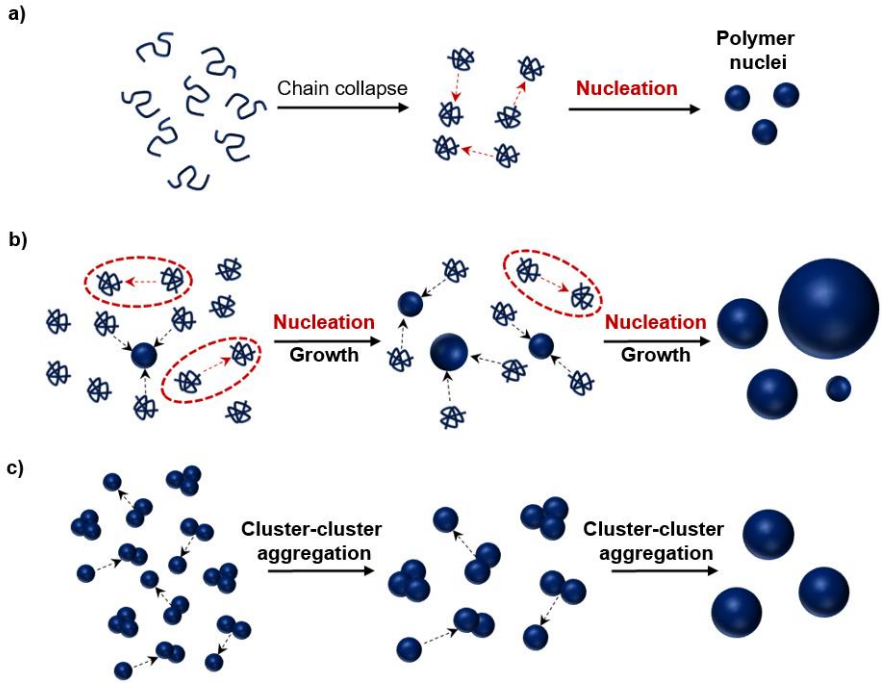

Figure 1.13 Schematic representation of the nucleation and growth mechanisms by which polymeric nanoparticles are formed during nanoprecipitation. a) The collapse and subsequent nucleation of polymer chains to form nuclei which occurs in a state of supersaturation. b) Formation of polymeric nanoparticles *via* a nucleation and diffusion limited growth mechanism. c) Formation of polymeric nanoparticles *via* a diffusion limited cluster-cluster aggregation mechanism.

The mechanism taken is highly dependent upon the nuclei concentration and by extent the degree of supersaturation.[470] Low degrees of supersaturation result in the formation of few stable nuclei, in such cases nanoparticle growth typically occurs through fusion of solute molecules to the surface of polymer nuclei until the amount of polymer within the nanoprecipitation medium has decreased to the thermodynamic equilibrium concentration. Under these conditions, nanoparticle growth is therefore limited by both the rate of nucleation and the rate at which polymer solutes diffuse to the surface of polymer nuclei through the nanoprecipitation medium. In contrast, high levels of supersaturation enhance the rate of polymer nucleation. High concentrations of polymer nuclei promote nanoparticle growth predominantly through random collisions of existing nuclei in a process known as DLCA. The probability of collisions between nuclei increase in proportion to the square of the number of nuclei present. The DLCA mechanism is therefore favoured under conditions of homogeneous nucleation. Collisions generally result in aggregation of the particles as typically soft nanoparticles rearrange to form dense structures which typically possess spherical morphologies. The growth mechanism has a profound impact on the dispersity of the nanoparticle size distribution and the segregation of nucleation and growth stages is considered crucial for the generation of monodisperse nanoparticles.[471,472] Regardless of the growth mechanisms adopted, nanoparticles continue to grow until colloidal stability is achieved or, undesirably, macroscopic precipitation takes place.[473]

The stabilisation of growing nuclei is essential to generate nanoparticles possessing hydrodynamic diameters in the nanometer size range and to also prevent excessive growth which will eventually lead to larger unstable aggregates. Nanoparticle stabilisation can be provided by either charge or steric stabilisation. Both mechanisms ensure that the repulsive forces acting between nanoparticles exceed the attractive Van der Waals forces which seek to fuse nanoparticle clusters together to form larger aggregates. Schematic representations of the repulsive forces provided by charge and steric stabilisation are presented in Figure 1.14.

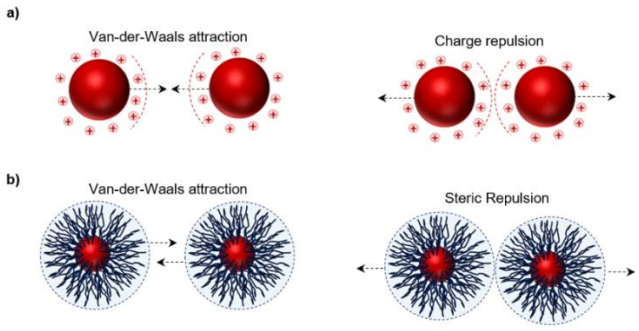

Figure 1.14 Schematic representation of nanoparticle stabilisation mechanisms. a) Charge repulsion between two nanoparticles possessing cationic charge. b) Steric repulsion between the overlapping hydrated shells of nanoparticles stabilised using amphiphilic polymeric stabilisers.

Charged nanoparticles typically possess a surrounding electrical double layers. This causes nanoparticles to repel each other and thus prevent aggregation in a process known as electrostatic repulsion. Electrostatic repulsion becomes significant when the electrical double layer of two (or more) individual nanoparticles come into contact as nanoparticles approach each other. The balance between the electrostatic repulsion pushing nanoparticles apart and the attractive Van der Waals forces is explained by the DLVO theory, established by Derjaguin, Landau, Verwey, and Overbeek.[474,475] In cases where the level of electrostatic repulsion is sufficient to overcome Van der Waals attraction, aggregation is avoided and nanoparticle dispersions remain stable. In contrast, weak repulsive forces are unable prevent nanoparticle aggregation.

Alternatively, steric stabilisation is provided when nanoparticles contain a solvated shell of adsorbed polymer chains that prevent nanoparticle-nanoparticle aggregation through steric repulsive forces. Steric repulsion is driven by osmotic pressure as the concentration of polymer chains increases in the overlap zone.[476] Steric stabilisation can be achieved by conducting nanoprecipitation in the presence of suitable stabilisers such as low molecular weight surfactants or amphiphilic copolymers. Alternatively, nanoprecipitation of polymers which themselves contain hydrophilic moieties do not require addition of such stabiliser molecules. It is possible to combine charge and steric stabilisation *via* nanoprecipitation of polymers which possess both amphiphilic and polyelectrolyte properties.[477] Both stabilisation mechanisms play an essential role in capping nanoparticle growth during nanoprecipitation.

Nanoparticle growth ceases once repulsive forces between nanoparticle clusters become sufficient to outweigh the attractive forces bringing them together. The stabiliser concentration can therefore be used to influence the extent of growth through cluster-cluster aggregation and thus provide control over nanoparticle size.[478]

Nanoprecipitation has been used to generate aqueous nanoparticle dispersions using a wide range of synthetic polymers and recent research has focused on tailoring nanoprecipitation conditions in order to achieve optimal nucleation, growth and stabilisation mechanisms which promote the formation of monodisperse nanoparticles with control over their hydrodynamic diameter. The use of bespoke synthetic polymers has also allowed the construction of functional nanoparticles possessing specific chemical and physical properties. Furthermore, the addition of hydrophobic small molecules during nanoprecipitation has facilitated the encapsulation of such guest molecules within nanoparticle cores.[479] Nanoprecipitation therefore offers an exciting formulation platform for the generation of novel DNC systems for the delivery of chemotherapeutics.

1.5 Smart Nanomaterials *via* Macromolecular Design

The ability to generate bespoke polymers, with high levels of control over their chemical functionality and macromolecular architecture, combined with the ability to formulate such polymers into well-ordered nanomaterials, has enabled such nanomaterials to be designed at a molecular level. In recent years this bottom-up approach has facilitated the preparation of new nanoparticles equipped with the ability to perform a range of specific functions. In particular, such approaches have been used to control both the internal and surface chemistry of a variety of nanoparticle types and has also facilitated the preparation of functional materials.

1.5.1 Tailoring Nanoparticle Chemistry

The incorporation of specific chemical functionalities during nanoparticle formation has been an effective strategy to control the macroscopic properties of the resulting nanoparticles. Nanoparticle mechanical properties are an important factor which must be considered when selecting nanoparticles for applications in nanomedicine. Nanoparticle rigidity can influence its ability to function a DNC system in biological/ physiological environments. In particular, it can influence nanoparticle: removal from systemic circulation *via* biological filtration mechanisms, biodistribution, tumour penetration and interaction with cancer cells.[480] Nanoparticle morphology is also an important factor in controlling the outcome of the application of nanoparticles within biological and physiological environments. For example, Li et al. reported that the extent and mechanism of mannose surface-functionalised nanoparticle macrophage uptake was significantly higher for spherical nanoparticles than that observed for their cylindrical/ worm-like equivalents.[480]

Rannard and co-workers have used end-group chemistry to influence the surface and core chemistry of branched vinyl copolymer nanoparticles.[350,481,482] Known as hyper-branched polydendrons, the use of dendritic initiators in the preparation of branched copolymers *via* ATRP of hydrophobic monomers has allowed dendron surface functionalities to be incorporated at each α-terminus on the resulting branched copolymers. Subsequent nanoprecipitation of these materials has produced nanoparticles possessing such dendritic functionalities both within the core and on the surface of the nanoparticles. Furthermore, co-initiation of dendritic initiators containing different surface functionalities has allowed systematic variation of nanoparticle functionality. Manipulation of nanoparticle functionality have resulted in tuneable permeation through model gut epithelium, influence over nanoparticle core hydrophobicity and selective binding of Au nanoparticles. Alternatively, other researchers have conjugated cell-targeting ligands at the end-groups of polymers used in nanoparticle formation to promote enhanced nanoparticle cellular internalisation *via* receptor-mediated endocytosis.[483]

1.5.2 Responsive Nanocarriers

In contrast to the modulation of drug release through manipulation of nanoparticle core chemistry, the use of stimulus-responsive polymers has enabled the design of nanoparticles capable of facilitating triggered burst release following application of an external stimulus. DNC systems have been designed to respond to a wide range of external stimuli, including pH, temperature, redox potential, enzymes, magnetic fields, light and sonication.[484] Burst release is typically triggered by rapid disassembly of the DNC system caused by the chemical changes induced by an external stimulus; this has allowed specific design of DNC systems to capitalise on many physiological opportunities presented *in vivo*. For example, Xu *et al.* demonstrated the ability to trigger the release of hydrophobic payloads from pH-sensitive core cross-linked ABC triblock copolymer micelles using reversible imine chemistry.[485] The pH sensitive cross-links were readily cleaved following a reduction in pH to below 5.5; this DNC system is therefore specifically designed to release its encapsulated payload within early endosomes shortly after cellular internalisation.[486] Alternatively, similar approaches have been employed using redox-sensitive disulphide chemistry within cross-linked block copolymer micelles; this has allowed such materials to utilise intracellular levels of glutathione to trigger burst release of encapsulated payloads within the cell cytoplasm.[487] In another approach, stimuli-responsive chemical linkers have enabled the cleavage of drugs from nanoparticles comprising polymer prodrugs containing labile conjugation chemistries.[488] This has been demonstrated, for example, by Jin *et al.* who generated amphiphilic block copolymers containing the anti-cancer drug, 5-fluorouracil (5 FU), *via* a UV-sensitive covalent linker.[489]

Self-assembly of these block copolymer conjugates generated spherical micelles capable of facilitating the burst release of 5-FU under UV irradiation (254 nm).

The simultaneous advances in the fields of polymer chemistry and nanotechnology have provided chemists with the ability to construct precise nanomaterials whose properties can be predetermined prior to synthesis. Researchers must therefore pay considerable attention to the materials they use when designing new nanomaterials platforms for application as prospective drug nanocarrier systems. Understanding of the chemical and physical properties of such materials will not only help achieve improved research outcomes but will also allow a deeper understanding of the applications for which such materials have been constructed.

1.6 Research Aims

Ultimately, the aim of this research was to develop a novel polymer-based nanoparticle platform which can demonstrate controlled encapsulation and release of the hydrophobic chemotherapeutic, docetaxel. An important aspect of this work was to ensure that such a nanoparticle platform has the potential to be used as a DNC system *in vivo*.

The production of such a DNC system required the development of a novel synthetic approach for the generation of branched vinyl copolymer nanoparticles, known as co-nanoprecipitation.[490] In order to expand the scope of co-nanoprecipitation, the generation of a library of hydrophobic polymers containing various (co)polymer architectures was required. This research aimed to build on previously established RDRP techniques, namely copper-catalysed RDRP (Cu-RDRP) of hydrophobic methacrylates in anhydrous alcohols, to generate this polymer library. Whilst this may be considered an unusual solvent choice for the preparation of hydrophobic (co)polymers, this synthetic approach was selected in order to explore the potential of Cu-RDRP in anhydrous alcohols for the generation of complex polymer architectures. In particular, this work targeted the preparation of linear homopolymers, amphiphilic AB block copolymers and branched statistical copolymers. We also aimed to discover the scope and limitations which were expected to arise in what would appear a complex and possibly even incompatible synthetic platform.

The materials generated were used to prepare branched copolymer nanoparticles *via* co-nanoprecipitation. We aimed to extend the scope of materials used in co-nanoprecipitation with the desire to influence, or even control, nanoparticle properties through careful selection of the polymers from which they are constructed. The functional handles through which the chemical and physical properties of AB block and branched copolymers have been controlled in this research are presented in Figure 1.15. Co-nanoprecipitation was therefore attempted using combinations of polymers possessing different chemical and physical properties. We wished to understand factors which influence the co-nanoprecipitation process and where

possible were linked to the macroscopic properties and behaviour of the branched copolymer nanoparticles formed. The ability to influence nanoparticle core polarity was considered an important factor which could influence drug release rates; we therefore explored the ability to influence nanoparticle core polarity through selection of the polymers used in co-nanoprecipitation. Furthermore, we aimed to demonstrate the encapsulation of hydrophobic guest molecules during co-nanoprecipitation and thus highlight the potential of such materials to act as DNC systems.

Promising candidates were then advanced to drug encapsulation studies in order to evaluate their ability to incorporate docetaxel, a hydrophobic chemotherapeutic, during co-nanoprecipitation. Docetaxel encapsulation experiments were designed to explore the drug loading capabilities of co-nanoprecipitation and understand the role that Docetaxel plays in the co-nanoprecipitation process. Comparative drug-release and encapsulation efficiency experiments were attempted using radiometric analyses. Such experiments were designed to develop an understanding of the relationships between the physical properties of branched copolymer nanoparticles and the encapsulation efficiency and release rates of docetaxel.

Efforts were made to control drug release rates through systematic variation in the physical and chemical properties of the polymers from which branched copolymer nanoparticles were constructed. This was attempted *via* the generation of statistical copolymers in order to create incremental changes in polymer properties through comonomer composition. Co-nanoprecipitations, drug encapsulation and release experiments aimed to evaluate the impact of such changes on the macroscopic behaviours of branched copolymer nanoparticles. Finally, we also looked to exploit the numerous functional handles available to incorporate functionality into AB block and branched statistical copolymers in order to manipulate the chemical and physical properties of nanoparticles subsequently formed through their co-nanoprecipitation. The impact of the introduction of such chemical functionalities on the chemical and physical properties of branched copolymer nanoparticles was investigated.

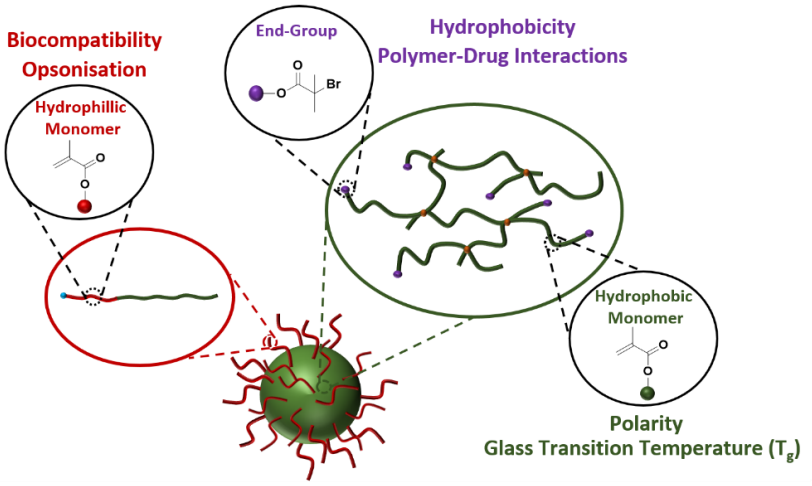

Figure 1.15 Schematic representation of the aims of this research project showing the various functional handles at which the properties of nanoparticles, formed *via* co-nanoprecipitation of AB block and branched copolymers, can be modified.

1.7 References

1 World Health Organization. Global Health Observatory., Geneva: World Health Organization;, who.int/gho/database/%0Aen/, (accessed 21 June 2018).

2 F. Bray, J. Ferlay, I. Soerjomataram, R. L. Siegel, L. A. Torre and A. Jemal, *CA. Cancer J. Clin.*, 2018, **68**, 394–424.

3 R. L. Siegel, K. D. Miller and A. Jemal, *CA. Cancer J. Clin.*, 2019, **69**, 7–34.

4 C. R. UK, Cancer Statistics for the UK, https://www.cancerresearchuk.org/health-professional/cancer-statistics-for-the-uk#heading-Zero, (accessed 16 June 2019).

5 D. of Health, *Improving Outcomes: A Strategy for Cancer*, 2011.

6 M. Durante, *Br. J. Cancer*, 2019, **120**, 777–778.

7 M. Ulm, A. V Ramesh, K. M. McNamara, S. Ponnusamy, H. Sasano and R. Narayanan, *Endocr. Connect.*, 2019, **8**, R10–R26.

8 Y. M. Hawsawi, F. Al-Zahrani, C. H. Mavromatis, M. A. Baghdadi, S. Saggu and A. A. A. Oyouni, *Technol. Cancer Res. Treat.*, 2018, **17**, 1–12.

9 R. Oun, Y. E. Moussa and N. J. Wheate, *Dalt. Trans.*, 2018, **47**, 6645–6653.

10 E. Blanco, H. Shen and M. Ferrari, *Nat. Biotechnol.*, 2015, **33**, 941.

11 Y. S. Youn and Y. H. Bae, *Adv. Drug Deliv. Rev.*, 2018, **130**, 3–11.

12 J. Shi, P. W. Kantoff, R. Wooster and O. C. Farokhzad, *Nat. Rev. Cancer*, 2016, **17**, 20.

13 F. Mottaghitalab, M. Farokhi, Y. Fatahi, F. Atyabi and R. Dinarvand, *J. Control. Release*, 2019, **295**, 250–267.

14 B. E. Rabinow, *Nat. Rev. Drug Discov.*, 2004, **3**, 785–796.

15 T. Vasconcelos, B. Sarmento and P. Costa, *Drug Discov. Today*, 2007, **12**, 1068–1075.

16 M. Danaei, M. Dehghankhold, S. Ataei, F. Hasanzadeh Davarani, R. Javanmard, A. Dokhani, S. Khorasani and M. R. Mozafari, *Pharmaceutics*, 2018, **10**, 57–74.

17 G. Graverini, V. Piazzini, E. Landucci, D. Pantano, P. Nardiello, F. Casamenti, D. E. Pellegrini-Giampietro, A. R. Bilia and M. C. Bergonzi, *Colloids Surfaces B Biointerfaces*, 2018, **161**, 302–313.

18 A. Garcês, M. H. Amaral, J. M. Sousa Lobo and A. C. Silva, *Eur. J. Pharm. Sci.*, 2018, **112**, 159–167.

19 H. M. Abdelaziz, M. Gaber, M. M. Abd-Elwakil, M. T. Mabrouk, M. M. Elgohary, N. M. Kamel, D. M. Kabary, M. S. Freag, M. W. Samaha, S. M. Mortada, K. A. Elkhodairy, J. Y. Fang and A. O. Elzoghby, *J. Control. Release*, 2018, **269**, 374–392.

20 N. V. Koshkina, E. Golunski, L. E. Roberts, B. E. Gilbert and V. Knight, *J. Aerosol Med. Depos. Clear. Eff. Lung*, 2004, **17**, 7–14.

21 G. Mainelis, S. Seshadri, O. B. Garbuzenko, T. Han, Z. Wang and T. Minko, *J. Aerosol Med. Pulm. Drug Deliv.*, 2013, **26**, 345–354.

22 S. Martins, B. Sarmento, D. C. Ferreira and E. B. Souto, *Int. J. Nanomedicine*, 2007, **2**, 595–607.

23 R. K. Subedi, K. W. Kang and H. K. Choi, *Eur. J. Pharm. Sci.*, 2009, **28**, 508–513.

24 W. Mehnert and K. Mäder, *Adv. Drug Deliv. Rev.*, 2012, **25**, 165–196.
25 M. Videira, A. J. Almeida and N. Fabra, *Nanomedicine Nanotechnology, Biol. Med.*, 2012, **8**, 1208–1215.
26 N. Naseri, H. Valizadeh and P. Zakeri-Milani, *Adv. Pharm. Bull.*, 2015, **5**, 305–313.
27 L. Hu and Y. Jia, *Die Pharm. Int. J. Pharm. Sci.*, 2010, **65**, 585–587.
28 H. Cabral, K. Miyata, K. Osada and K. Kataoka, *Chem. Rev.*, 2018, **118**, 6844–6892.
29 H. He, L. Liu, E. E. Morin, M. Liu and A. Schwendeman, *Acc. Chem. Res.*, 2019, **52**, 2445–2461.
30 W. S. Saad and R. K. Prud'Homme, *Nano Today*, 2016, **11**, 212–227.
31 P. Xue, J. Wang, X. Han and Y. Wang, *Colloids Surfaces B Biointerfaces*, 2019, **180**, 202–211.
32 U. Wais, A. W. Jackson, T. He and H. Zhang, *Nanoscale*, 2016, **8**, 1746–1769.
33 L. M. Tatham, S. P. Rannard and A. Owen, *Ther. Deliv.*, 2015, **6**, 469–490.
34 H. Zhang, D. Wang, R. Butler, N. L. Campbell, J. Long, B. Tan, D. J. Duncalf, A. J. Foster, A. Hopkinson, D. Taylor, D. Angus, A. I. Cooper and S. P. Rannard, *Nat. Nanotechnol.*, 2008, **3**, 506–511.
35 U. Wais, A. W. Jackson, Y. Zuo, Y. Xiang, T. He and H. Zhang, *J. Control. Release*, 2016, **222**, 141–150.
36 J. J. Hobson, A. Al-khouja, P. Curley, D. Meyers, C. Flexner, M. Siccardi, A. Owen, C. F. Meyers and S. P. Rannard, *Nat. Commun.*, 2019, **10**, 1413–1423.
37 N. Grant and H. Zhang, *J. Colloid Interface Sci.*, 2011, **356**, 573–578.
38 R. Rosière, M. Gelbcke, V. Mathieu, P. Van Antwerpen, K. Amighi and N. Wauthoz, *Int. J. Oncol.*, 2015, **47**, 1131.
39 K. Tomoda, T. Ohkoshi, K. Hirota, G. S. Sonavane, T. Nakajima, H. Terada, M. Komuro, K. Kitazato and K. Makino, *Colloids Surfaces B Biointerfaces*, 2009, **71**, 177–182.
40 D. K. Jensen, L. B. Jensen, S. Koocheki, L. Bengtson, D. Cun, H. M. Nielsen and C. Foged, *J. Control. Release*, 2012, **157**, 141–148.
41 X. Guo, X. Zhang, L. Ye, Y. Zhang, R. Ding, Y. Hao, Y. Zhao, Z. Zhang and Y. Zhang, *J. Drug Target.*, 2014, **22**, 421–427.
42 L. M. Tatham, A. C. Savage, A. Dwyer, M. Siccardi, T. Scott, M. Vourvahis, A. Clark, S. P. Rannard and A. Owen, *Eur. J. Pharm. Biopharm.*, 2019, **138**, 92–98.
43 R. P. Bakshi, L. M. Tatham, A. C. Savage, A. K. Tripathi, G. Mlambo, M. M. Ippolito, E. Nenortas, S. P. Rannard, A. Owen and T. A. Shapiro, *Nat. Commun.*, 2018, **9**, 315–323.
44 T. O. Mcdonald, M. Giardiello, P. Martin, M. Siccardi, N. J. Liptrott, D. Smith, P. Roberts, P. Curley, A. Schipani, S. H. Khoo, J. Long, A. J. Foster, S. P. Rannard and A. Owen, *Adv. Healthc. Mater.*, 2014, **3**, 400–411.
45 L. Peltonen and J. Hirvonen, *Int. J. Pharm.*, 2018, **537**, 73–83.
46 C. M. Keck and R. H. Müller, *Eur. J. Pharm. Biopharm.*, 2006, **62**, 3–16.
47 K. M. Raghava Srivalli and B. Mishra, *Saudi Pharm. J.*, 2016, **24**, 386–404.
48 X. Miao, W. Yang, T. Feng, J. Lin and P. Huang, *Wiley Interdiscip. Rev. Nanomedicine Nanobiotechnology*, 2018, **10**, e1499.
49 J. P. Möschwitzer, *Int. J. Pharm.*, 2013, **453**, 142–156.
50 F. Alexis, E. Pridgen, L. K. Molnar and O. C. Farokhzad, *Mol. Pharm.*, 2008, **5**, 505–515.
51 J. Bourquin, A. Milosevic, D. Hauser, R. Lehner, F. Blank, A. Petri-Fink and B. Rothen-Rutishauser, *Adv. Mater.*, 2018, **30**, 1704307.
52 H. Chen, W. Zhang, G. Zhu, J. Xie and X. Chen, *Nat. Rev. Mater.*, 2017, **2**, 17024.
53 C. von Roemeling, W. Jiang, C. K. Chan, I. L. Weissman and B. Y. S. Kim, *Trends Biotechnol.*, 2017, **35**, 159–171.
54 T. J. Anchordoquy, Y. Barenholz, D. Boraschi, M. Chorny, P. Decuzzi, M. A. Dobrovolskaia, Z. S. Farhangrazi, D. Farrell, A. Gabizon, H. Ghandehari, B. Godin, N. M. La-Beck, J. Ljubimova, S. M. Moghimi, L. Pagliaro, J.-H. Park, D. Peer, E. Ruoslahti, N. J. Serkova and D. Simberg, *ACS Nano*, 2017, **11**, 12–18.
55 Y. Lu, A. A. Aimetti, R. Langer and Z. Gu, *Nat. Rev. Mater.*, 2016, **2**, 16075.
56 Y. S. Youn, J. Y. Jung, S. H. Oh, S. D. Yoo and K. C. Lee, *J. Control. release*, 2006, **114**, 334–342.
57 M. Sugawara, S. Kadomura, X. He, Y. Takekuma, N. Kohri and K. Miyazaki, *Eur. J. Pharm. Sci.*, 2005, **26**, 1–8.
58 M. W. Tibbitt, J. E. Dahlman and R. Langer, *J. Am. Chem. Soc.*, 2016, **138**, 704–717.
59 L. M. Ensign, R. Cone and J. Hanes, *Adv. Drug Deliv. Rev.*, 2012, **64**, 557–570.
60 V. V Khutoryanskiy, *Adv. Drug Deliv. Rev.*, 2018, **124**, 140–149.

61 W. Shan, X. Zhu, M. Liu, L. Li, J. Zhong, W. Sun, Z. Zhang and Y. Huang, *ACS Nano*, 2015, **9**, 2345–2356.
62 A. Banerjee, J. Qi, R. Gogoi, J. Wong and S. Mitragotri, *J. Control. Release*, 2016, **238**, 176–185.
63 Y. Wang, S. K. Lai, J. S. Suk, A. Pace, R. Cone and J. Hanes, *Angew. Chemie Int. Ed.*, 2008, **47**, 9726–9729.
64 M. Yang, S. K. Lai, Y. Wang, W. Zhong, C. Happe, M. Zhang, J. Fu and J. Hanes, *Angew. Chemie Int. Ed.*, 2011, **50**, 2597–2600.
65 J. S. Suk, S. K. Lai, Y.-Y. Wang, L. M. Ensign, P. L. Zeitlin, M. P. Boyle and J. Hanes, *Biomaterials*, 2009, **30**, 2591–2597.
66 B. C. Tang, M. Dawson, S. K. Lai, Y.-Y. Wang, J. S. Suk, M. Yang, P. Zeitlin, M. P. Boyle, J. Fu and J. Hanes, *Proc. Natl. Acad. Sci.*, 2009, **106**, 19268–19273.
67 R. A. Cone, *Adv. Drug Deliv. Rev.*, 2009, **61**, 75–85.
68 S. K. Lai, Y.-Y. Wang and J. Hanes, *Adv. Drug Deliv. Rev.*, 2009, **61**, 158–171.
69 J. S. Suk, S. K. Lai, N. J. Boylan, M. R. Dawson, M. P. Boyle and J. Hanes, *Nanomedicine*, 2011, **6**, 365–375.
70 D. Gardner, R. Casper, F. Leith and I. R. Wilding, *Pharm. Tech. Eur*, 1997, **9**, 46–53.
71 J. Desai, K. Alexander and A. Riga, *Int. J. Pharm.*, 2006, **308**, 115–123.
72 A. Streubel, J. Siepmann and R. Bodmeier, *Curr. Opin. Pharmacol.*, 2006, **6**, 501–508.
73 M. J. Hickey and P. Kubes, *Nat. Rev. Immunol.*, 2009, **9**, 364.
74 S. Gordon and P. R. Taylor, *Nat. Rev. Immunol.*, 2005, **5**, 953.
75 V. Brinkmann, U. Reichard, C. Goosmann, B. Fauler, Y. Uhlemann, D. S. Weiss, Y. Weinrauch and A. Zychlinsky, *Science.*, 2004, **303**, 1532–1535.
76 T. A. Fuchs, A. Brill, D. Duerschmied, D. Schatzberg, M. Monestier, D. D. Myers, S. K. Wrobleski, T. W. Wakefield, J. H. Hartwig and D. D. Wagner, *Proc. Natl. Acad. Sci.*, 2010, **107**, 15880–15885.
77 S. R. Clark, A. C. Ma, S. A. Tavener, B. McDonald, Z. Goodarzi, M. M. Kelly, K. D. Patel, S. Chakrabarti, E. McAvoy and G. D. Sinclair, *Nat. Med.*, 2007, **13**, 463.
78 M. Bartneck, H. A. Keul, G. Zwadlo-Klarwasser and J. Groll, *Nano Lett.*, 2009, **10**, 59–63.
79 T. Cedervall, I. Lynch, M. Foy, T. Berggård, S. C. Donnelly, G. Cagney, S. Linse and K. A. Dawson, *Angew. Chemie Int. Ed.*, 2007, **46**, 5754–5756.
80 M. Lundqvist, J. Stigler, G. Elia, I. Lynch, T. Cedervall and K. A. Dawson, *Proc. Natl. Acad. Sci.*, 2008, **105**, 14265 LP – 14270.
81 S. R. Saptarshi, A. Duschl and A. L. Lopata, *J. Nanobiotechnology*, 2013, **11**, 26.
82 S. C. Semple, A. Chonn and P. R. Cullis, *Adv. Drug Deliv. Rev.*, 1998, **32**, 3–17.
83 D. E. Owens III and N. A. Peppas, *Int. J. Pharm.*, 2006, **307**, 93–102.
84 K. Ogawara, K. Furumoto, S. Nagayama, K. Minato, K. Higaki, T. Kai and T. Kimura, *J. Control. Release*, 2004, **100**, 451–455.
85 F. Kratz, *J. Control. Release*, 2008, **132**, 171–183.
86 G. Hartung, G. Stehle, H. Sinn, A. Wunder, H. H. Schrenk, S. Heeger, M. Kränzle, L. Edler, E. Frei and H. H. Fiebig, *Clin. Cancer Res.*, 1999, **5**, 753–759.
87 K. Motamed, *Int. J. Biochem. Cell Biol.*, 1999, **31**, 1363–1366.
88 R. A. Brekken and E. H. Sage, *Matrix Biol.*, 2001, **19**, 815–827.
89 O. L. Podhajcer, L. G. Benedetti, M. R. Girotti, F. Prada, E. Salvatierra and A. S. Llera, *Cancer Metastasis Rev. VO - 27*, 2008, 691.
90 D. Chin, G. M. Boyle, R. M. Williams, K. Ferguson, N. Pandeya, J. Pedley, C. M. Campbell, D. R. Theile, P. G. Parsons and W. B. Coman, *Int. J. Cancer*, 2005, **113**, 789–797.
91 N. Desai, V. Trieu, B. Damascelli and P. Soon-Shiong, *Transl. Oncol.*, 2009, **2**, 59–64.
92 M. I. Koukourakis, A. Giatromanolaki, R. A. Brekken, E. Sivridis, K. C. Gatter, A. L. Harris and E. H. Sage, *Cancer Res.*, 2003, **63**, 5376 LP – 5380.
93 G. Watkins, A. Douglas-Jones, R. Bryce, R. E Mansel and W. G. Jiang, *Prostaglandins, Leukot. Essent. Fat. Acids*, 2005, **72**, 267–272.
94 M. J. Walport, *N. Engl. J. Med.*, 2001, **344**, 1058–1066.
95 D. Ricklin, G. Hajishengallis, K. Yang and J. D. Lambris, *Nat. Immunol.*, 2010, **11**, 785–797.
96 P. F. Zipfel and C. Skerka, *Nat. Rev. Immunol.*, 2009, **9**, 729–740.
97 S. M. Moghimi, A. C. Hunter and J. C. Murray, *Pharmacol. Rev.*, 2001, **53**, 283–318.
98 G. Gaucher, K. Asahina, J. Wang and J.-C. Leroux, *Biomacromolecules*, 2009, **10**, 408–416.
99 S. C. Semple, A. Chonn and P. R. Cullis, *Biochemistry*, 1996, **35**, 2521–2525.
100 A. Gessner, R. Waicz, A. Lieske, B.-R. Paulke, K. Mäder and R. H. Müller, *Int. J. Pharm.*, 2000, **196**, 245–249.

101 D. V Devine, K. Wong, K. Serrano, A. Chonn and P. R. Cullis, *Biochim. Biophys. Acta - Biomembr.*, 1994, **1191**, 43–51.
102 A. Chonn, P. R. Cullis and D. V Devine, *J. Immunol.*, 1991, **146**, 4234 LP – 4241.
103 A. Vonarbourg, C. Passirani, P. Saulnier, P. Simard, J. C. Leroux and J. P. Benoit, *J. Biomed. Mater. Res. A*, 2006, **78**, 620–628.
104 A. Vonarbourg, C. Passirani, P. Saulnier and J.-P. Benoit, *Biomaterials*, 2006, **27**, 4356–4373.
105 S. M. Moghimi and J. Szebeni, *Prog. Lipid Res.*, 2003, **42**, 463–478.
106 I. Hamad, O. Al-Hanbali, A. C. Hunter, K. J. Rutt, T. L. Andresen and S. M. Moghimi, *ACS Nano*, 2010, **4**, 6629–6638.
107 J. M. Harris and R. B. Chess, *Nat. Rev. Drug Discov.*, 2003, **2**, 214–221.
108 K. Knop, R. Hoogenboom, D. Fischer and U. S. Schubert, *Angew. Chemie Int. Ed.*, 2010, **49**, 6288–6308.
109 K. M. Wasan, D. R. Brocks, S. D. Lee, K. Sachs-Barrable and S. J. Thornton, *Nat. Rev. Drug Discov.*, 2008, **7**, 84–99.
110 L. S. Kumpula, J. M. Kumpula, K. Kaski, M. Ala-Korpela, M.-R. Taskinen and M. Jauhiainen, *Chem. Phys. Lipids*, 2008, **155**, 57–62.
111 W. V Rodrigueza, M. C. Phillips and K. J. Williams, *Adv. Drug Deliv. Rev.*, 1998, **32**, 31–43.
112 T. M. Allen, *Biochim. Biophys. Acta - Biomembr.*, 1981, **640**, 385–397.
113 J. Kreuter, T. Hekmatara, S. Dreis, T. Vogel, S. Gelperina and K. Langer, *J. Control. Release*, 2007, **118**, 54–58.
114 P. C. N. Rensen, M. C. M. Van Dijk, E. C. Havenaar, M. K. Bijsterbosch, J. K. Kruijt and T. J. C. Van Berkel, *Nat. Med.*, 1995, **1**, 221–225.
115 A. Akinc, W. Querbes, S. De, J. Qin, M. Frank-Kamenetsky, K. N. Jayaprakash, M. Jayaraman, K. G. Rajeev, W. L. Cantley, J. R. Dorkin, J. S. Butler, L. Qin, T. Racie, A. Sprague, E. Fava, A. Zeigerer, M. J. Hope, M. Zerial, D. W. Y. Sah, K. Fitzgerald, M. A. Tracy, M. Manoharan, V. Koteliansky, A. de Fougerolles and M. A. Maier, *Mol. Ther.*, 2010, **18**, 1357–1364.
116 J. A. Hubbell, S. N. Thomas and M. A. Swartz, *Nature*, 2009, **462**, 449–460.
117 M. A. Dobrovolskaia and S. E. McNeil, *Nat. Nanotechnol.*, 2007, **2**, 469–478.
118 E. AlléAaemann, P. Gravel, J. Leroux, L. Balant and R. Gurny, *J. Biomed. Mater. Res.*, 1997, **37**, 229–234.
119 M. R. Ehrenstein and C. A. Notley, *Nat. Rev. Immunol.*, 2010, **10**, 778–786.
120 H. Chen, S. Kim, W. He, H. Wang, P. S. Low, K. Park and J.-X. Cheng, *Langmuir*, 2008, **24**, 5213–5217.
121 P. Aggarwal, J. B. Hall, C. B. McLeland, M. A. Dobrovolskaia and S. E. McNeil, *Adv. Drug Deliv. Rev.*, 2009, **61**, 428–437.
122 N. Bertrand and J.-C. Leroux, *J. Control. Release*, 2012, **161**, 152–163.
123 T. M. Allen, C. Hansen, F. Martin, C. Redemann and A. Yau-Young, *Biochim. Biophys. Acta - Biomembr.*, 1991, **1066**, 29–36.
124 A. A. Alizadeh, V. Aranda, A. Bardelli, C. Blanpain, C. Bock, C. Borowski, C. Caldas, A. Califano, M. Doherty, M. Elsner, M. Esteller, R. Fitzgerald, J. O. Korbel, P. Lichter, C. E. Mason, N. Navin, D. Pe'er, K. Polyak, C. W. M. Roberts, L. Siu, A. Snyder, H. Stower, C. Swanton, R. G. W. Verhaak, J. C. Zenklusen, J. Zuber and J. Zucman-Rossi, *Nat. Med.*, 2015, **21**, 846–853.
125 B. Vogelstein, N. Papadopoulos, V. E. Velculescu, S. Zhou, L. A. Diaz Jr and K. W. Kinzler, *Science*, 2013, **339**, 1546–1558.
126 P. L. Bedard, A. R. Hansen, M. J. Ratain and L. L. Siu, *Nature*, 2013, **501**, 355.
127 C. E. Meacham and S. J. Morrison, *Nature*, 2013, **501**, 328.
128 M. R. Junttila and F. J. de Sauvage, *Nature*, 2013, **501**, 346.
129 R. K. Jain, *Cancer Metastasis Rev.*, 1990, **9**, 253–266.
130 S. N. Ekdawi, D. A. Jaffray and C. Allen, *Nano Today*, 2016, **11**, 402–414.
131 T. Stylianopoulos and R. K. Jain, *Nanomedicine*, 2015, **11**, 1893–1907.
132 W. A. Flavahan, E. Gaskell and B. E. Bernstein, *Science*, 2017, **357**, eaal2380.
133 D. Hanahan and R. A. Weinberg, *Cell*, 2011, **144**, 646–674.
134 R. J. Goldacre and B. Sylven, *Br. J. Cancer*, 1962, **16**, 306–322.
135 L. N. Owen, *Nature*, 1960, **187**, 795–796.
136 R. J. Goldacre and B. Sylven, *Nature*, 1959, **184**, 63–64.
137 L. E. Gerlowski and R. K. Jain, *Microvasc. Res.*, 1986, **31**, 288–305.
138 Y. Matsumura and H. Maeda, *Cancer Res.*, 1986, **46**, 6387 LP – 6392.
139 H. Maeda, J. Wu, T. Sawa, Y. Matsumura and K. Hori, *J. Control. Release*, 2000, **65**, 271–

284.
140 H. Maeda, *Adv. Enzyme Regul.*, 2001, **41**, 189–207.
141 S. Tran, P.-J. DeGiovanni, B. Piel and P. Rai, *Clin. Transl. Med.*, 2017, **6**, 44–65.
142 S. K. Golombek, J.-N. May, B. Theek, L. Appold, N. Drude, F. Kiessling and T. Lammers, *Adv. Drug Deliv. Rev.*, 2018, **130**, 17–38.
143 Y. Nakamura, A. Mochida, P. L. Choyke and H. Kobayashi, *Bioconjug. Chem.*, 2016, **27**, 2225–2238.
144 E. Huynh and G. Zheng, *Nanomedicine*, 2015, **10**, 1993–1995.
145 U. Prabhakar, H. Maeda, R. K. Jain, E. M. Sevick-Muraca, W. Zamboni, O. C. Farokhzad, S. T. Barry, A. Gabizon, P. Grodzinski and D. C. Blakey, *Cancer Res.*, 2013, **73**, 2412–2417.
146 H. Nakamura, F. Jun and H. Maeda, *Expert Opin. Drug Deliv.*, 2015, **12**, 53–64.
147 J. W. Nichols and Y. H. Bae, *J. Control. Release*, 2014, **190**, 451–464.
148 A. J. Clark, D. T. Wiley, J. E. Zuckerman, P. Webster, J. Chao, J. Lin, Y. Yen and M. E. Davis, *Proc. Natl. Acad. Sci. U. S. A.*, 2016, **113**, 3850–3854.
149 F. Danhier, *J. Control. Release*, 2016, **244**, 108–121.
150 K. J. Harrington, S. Mohammadtaghi, P. S. Uster, D. Glass, A. M. Peters, R. G. Vile and J. S. W. Stewart, *Clin. Cancer Res.*, 2001, **7**, 243 LP – 254.
151 C. A. Presant, D. Blayney, P. Kennedy, C. Wiseman, K. Gala, S. L. Presant, R. T. Proffit, R. J. Crossley, S. J. Preiss, G. E. Ksionski, A. F. Turner, H. I. Nadel and L. E. Williams, *Lancet*, 1990, **335**, 1307–1309.
152 B. Briele, A. Hotze, P. Oehr, H. J. Biersack, F. Rosanowski, W. Gorgulla, C. Herberhold and J. P. Hartlapp, *Lancet*, 1990, **336**, 875–876.
153 A. Khalifa, D. Dodds, R. Rampling, J. Paterson and T. Murray, *Nucl. Med. Commun.*, 1997, **18**, 17–23.
154 C. A. Presant, R. T. Proffitt, A. F. Turner, L. E. Williams, D. Winsor, J. L. Werner, P. Kennedy, C. Wiseman, K. Gala, R. J. McKenna, J. D. Smith, S. A. Bouzaglou, R. A. Callahan, J. Baldeschwieler and R. J. Crossley, *Cancer*, 1988, **62**, 905–911.
155 Y. (Chezy) Barenholz, *J. Control. Release*, 2012, **160**, 117–134.
156 D. W. Northfelt, B. J. Dezube, J. A. Thommes, B. J. Miller, M. A. Fischl, A. Friedman-Kien, L. D. Kaplan, C. Du Mond, R. D. Mamelok and D. H. Henry, *J. Clin. Oncol.*, 1998, **16**, 2445–2451.
157 M. E. R. O'Brien, N. Wigler, M. Inbar, R. Rosso, E. Grischke, A. Santoro, R. Catane, D. G. Kieback, P. Tomczak, S. P. Ackland, F. Orlandi, L. Mellars, L. Alland and C. Tendler, *Ann. Oncol.*, 2004, **15**, 440–449.
158 A. K. LeBlanc, M. Breen, P. Choyke, M. Dewhirst, T. M. Fan, D. L. Gustafson, L. J. Helman, M. B. Kastan, D. W. Knapp, W. J. Levin, C. London, N. Mason, C. Mazcko, P. N. Olson, R. Page, B. A. Teicher, D. H. Thamm, J. M. Trent, D. M. Vail and C. Khanna, *Sci. Transl. Med.*, 2016, **8**, 324ps5 LP-324ps5.
159 A. K. LeBlanc, C. N. Mazcko and C. Khanna, *Clin. Cancer Res.*, 2016, **22**, 2133–2138.
160 A. E. Hansen, A. L. Petersen, J. R. Henriksen, B. Boerresen, P. Rasmussen, D. R. Elema, P. M. af Rosenschöld, A. T. Kristensen, A. Kjær and T. L. Andresen, *ACS Nano*, 2015, **9**, 6985–6995.
161 A. A. Natfji, D. Ravishankar, H. M. I. Osborn and F. Greco, *J. Pharm. Sci.*, 2017, **106**, 3179–3187.
162 T. Kirchhausen, *Annu. Rev. Biochem.*, 2000, **69**, 699–727.
163 E. M. Schmid and H. T. McMahon, *Nature*, 2007, **448**, 883–888.
164 F. Tebar, S. K. Bohlander and A. Sorkin, *Mol. Biol. Cell*, 1999, **10**, 2687–2702.
165 P. A. Vanlandingham, M. P. Barmchi, S. Royer, R. Green, H. Bao, N. Reist and B. Zhang, *Traffic*, 2014, **15**, 433–450.
166 W. M. Henne, H. M. Kent, M. G. J. Ford, B. G. Hegde, O. Daumke, P. J. G. Butler, R. Mittal, R. Langen, P. R. Evans and H. T. McMahon, *Structure*, 2007, **15**, 839–852.
167 E. Cocucci, F. Aguet, S. Boulant and T. Kirchhausen, *Cell*, 2012, **150**, 495–507.
168 B. R. Capraro, Z. Shi, T. Wu, Z. Chen, J. M. Dunn, E. Rhoades and T. Baumgart, *J. Biol. Chem.*, 2013, **288**, 12533–12543.
169 B. J. Peter, H. M. Kent, I. G. Mills, Y. Vallis, P. J. G. Butler, P. R. Evans and H. T. McMahon, *Science.*, 2004, **303**, 495 LP – 499.
170 M. G. J. Ford, I. G. Mills, B. J. Peter, Y. Vallis, G. J. K. Praefcke, P. R. Evans and H. T. McMahon, *Nature*, 2002, **419**, 361–366.
171 H. T. McMahon and E. Boucrot, *Nat. Rev. Mol. Cell Biol.*, 2011, **12**, 517–533.
172 M. H. B. Stowell, B. Marks, P. Wigge and H. T. McMahon, *Nat. Cell Biol.*, 1999, **1**, 27–32.

173 M. Marsh and H. T. McMahon, *Science.*, 1999, **285**, 215–220.
174 M. Kirkham, A. Fujita, R. Chadda, S. J. Nixon, T. V Kurzchalia, D. K. Sharma, R. E. Pagano, J. F. Hancock, S. Mayor and R. G. Parton, *J. Cell Biol.*, 2005, **168**, 465–476.
175 E.-M. Damm, L. Pelkmans, J. Kartenbeck, A. Mezzacasa, T. Kurzchalia and A. Helenius, *J. Cell Biol.*, 2005, **168**, 477 LP – 488.
176 L. E. Kelemen, *Int. J. Cancer*, 2006, **119**, 243–250.
177 L. Pelkmans and A. Helenius, *Traffic*, 2002, **3**, 311–320.
178 K. G. Rothberg, J. E. Heuser, W. C. Donzell, Y.-S. Ying, J. R. Glenney and R. G. W. Anderson, *Cell*, 1992, **68**, 673–682.
179 T. V Kurzchalia and R. G. Partan, *Curr. Opin. Cell Biol.*, 1999, **11**, 424–431.
180 G. Sahay, D. Y. Alakhova and A. V Kabanov, *J. Control. Release*, 2010, **145**, 182–195.
181 J. P. Lim and P. A. Gleeson, *Immunol. Cell Biol.*, 2011, **89**, 836–843.
182 D. A. Kuhn, D. Vanhecke, B. Michen, F. Blank, P. Gehr, A. Petri-Fink and B. Rothen-Rutishauser, *Beilstein J. Nanotechnol.*, 2014, **5**, 1625–1636.
183 C. C. Norbury, L. J. Hewlett, A. R. Prescott, N. Shastri and C. Watts, *Immunity*, 1995, **3**, 783–791.
184 A. Aderem and D. M. Underhill, *Annu. Rev. Immunol.*, 1999, **17**, 593–623.
185 Z. Cui and R. J. Mumper, *Int. J. Pharm.*, 2002, **238**, 229–239.
186 A. França, P. Aggarwal, E. V Barsov, S. V Kozlov, M. A. Dobrovolskaia and Á. González-Fernández, *Nanomedicine*, 2011, **6**, 1175–1188.
187 M. Cuna, M. Alonso-Sande, C. Remuñán-López, J. Pivel, J. Alonso-Lebrero and M. Alonso, *J. Nanosci. Nanotechnol.*, 2006, **6**, 2887–2895.
188 T. H. Kim, H. Jin, H. W. Kim, M.-H. Cho and C. S. Cho, *Mol. Cancer Ther.*, 2006, **5**, 1723 LP – 1732.
189 D. M. Underhill and H. S. Goodridge, *Nat. Rev. Immunol.*, 2012, **12**, 492–502.
190 D. E. Owens and N. A. Peppas, *Int. J. Pharm.*, 2006, **307**, 93–102.
191 Y. Geng, P. Dalhaimer, S. Cai, R. Tsai, M. Tewari, T. Minko and D. E. Discher, *Nat. Nanotechnol.*, 2007, **2**, 249–255.
192 J. A. Champion and S. Mitragotri, *Proc. Natl. Acad. Sci. U. S. A.*, 2006, **103**, 4930 LP – 4934.
193 J. A. Champion and S. Mitragotri, *Pharm. Res.*, 2009, **26**, 244–249.
194 I. Ojima, E. S. Zuniga, W. T. Berger and J. D. Seitz, *Future Med. Chem.*, 2012, **4**, 33–50.
195 A. Z. Wang, F. Gu, L. Zhang, J. M. Chan, A. Radovic-Moreno, M. R. Shaikh and O. C. Farokhzad, *Expert Opin. Biol. Ther.*, 2008, **8**, 1063–1070.
196 C. Müller and R. Schibli, *Front. Oncol.*, 2013, **3**, 249.
197 M. E. Werner, S. Karve, R. Sukumar, N. D. Cummings, J. A. Copp, R. C. Chen, T. Zhang and A. Z. Wang, *Biomaterials*, 2011, **32**, 8548–8554.
198 S. Jiang, X. Gong, X. Zhao and Y. Zu, *Drug Deliv.*, 2015, **22**, 206–213.
199 A. Gabizon, D. Tzemach, J. Gorin, L. Mak, Y. Amitay, H. Shmeeda and S. Zalipsky, *Cancer Chemother. Pharmacol.*, 2010, **66**, 43–52.
200 X. Zhao, H. Li and R. J. Lee, *Expert Opin. Drug Deliv.*, 2008, **5**, 309–319.
201 J. Shen, A. R. Hilgenbrink, W. Xia, Y. Feng, D. S. Dimitrov, M. B. Lockwood, R. J. Amato and P. S. Low, *J. Leukoc. Biol.*, 2014, **96**, 563–570.
202 P. S. Low and S. A. Kularatne, *Curr. Opin. Chem. Biol.*, 2009, **13**, 256–262.
203 M. B. Omary and I. S. Trowbridge, *J. Biol. Chem.*, 1981, **256**, 12888–12892.
204 C. Schneider, M. J. Owen, D. Banville and J. G. Williams, *Nature*, 1984, **311**, 675–678.
205 P. Ponka and C. N. Lok, *Int. J. Biochem. Cell Biol.*, 1999, **31**, 1111–1137.
206 J. Y. Yhee, S. J. Lee, S. Lee, S. Song, H. S. Min, S.-W. Kang, S. Son, S. Y. Jeong, I. C. Kwon, S. H. Kim and K. Kim, *Bioconjug. Chem.*, 2013, **24**, 1850–1860.
207 M. Hong, S. Zhu, Y. Jiang, G. Tang and Y. Pei, *J. Control. Release*, 2009, **133**, 96–102.
208 Y. Cui, Q. Xu, P. K.-H. Chow, D. Wang and C.-H. Wang, *Biomaterials*, 2013, **34**, 8511–8520.
209 C. H. J. Choi, C. A. Alabi, P. Webster and M. E. Davis, *Proc. Natl. Acad. Sci. U. S. A.*, 2010, **107**, 1235–1240.
210 R. van der Meel, L. J. C. Vehmeijer, R. J. Kok, G. Storm and E. V. B. van Gaal, *Adv. Drug Deliv. Rev.*, 2013, **65**, 1284–1298.
211 F. Danhier, O. Feron and V. Préat, *J. Control. Release*, 2010, **148**, 135–146.
212 F. S. Tabatabaei Mirakabad, K. Nejati-Koshki, A. Akbarzadeh, M. R. Yamchi, M. Milani, N. Zarghami, V. Zeighamian, A. Rahimzadeh, S. Alimohammadi, Y. Hanifehpour and S. W. Joo, *Asian Pacific J. Cancer Prev.*, 2014, **15**, 517–553.
213 A. Salvati, A. S. Pitek, M. P. Monopoli, K. Prapainop, F. B. Bombelli, D. R. Hristov, P. M.

Kelly, C. Åberg, E. Mahon and K. A. Dawson, *Nat. Nanotechnol.*, 2013, **8**, 137–143.
214 R. S. Herbst, *Int. J. Radiat. Oncol.*, 2004, **59**, S21–S26.
215 P. Seshacharyulu, M. P. Ponnusamy, D. Haridas, M. Jain, A. K. Ganti and S. K. Batra, *Expert Opin. Ther. Targets*, 2012, **16**, 15–31.
216 A. J. Dunbar, I. K. Priebe, D. A. Belford and C. Goddard, *Biochem. J.*, 1999, **344**, 713–721.
217 J. Massagué, *J. Biol. Chem*, 1990, **265**, 21393–21396.
218 M. Shoyab, V. L. McDonald, J. G. Bradley and G. J. Todaro, *Proc. Natl. Acad. Sci. U. S. A.*, 1988, **85**, 6528–6532.
219 H. Toyoda, T. Komurasaki, D. Uchida, Y. Takayama, T. Isobe, T. Okuyama and K. Hanada, *J. Biol. Chem.*, 1995, **270**, 7495–7500.
220 L. Strachan, J. G. Murison, R. L. Prestidge, M. A. Sleeman, J. D. Watson and K. D. Kumble, *J. Biol. Chem.*, 2001, **276**, 18265–18271.
221 S. Higashiyama, K. Lau, G. E. Besner, J. A. Abraham and M. Klagsbrun, *J. Biol. Chem.*, 1992, **267**, 6205–6212.
222 R. C. Harris, E. Chung and R. J. Coffey, *Exp. Cell Res.*, 2003, **284**, 2–13.
223 A. Citri and Y. Yarden, *Nat. Rev. Mol. Cell Biol.*, 2006, **7**, 505–516.
224 S.-M. Lee, H. Park, J.-W. Choi, Y. N. Park, C.-O. Yun and K.-H. Yoo, *Angew. Chemie Int. Ed.*, 2011, **50**, 7581–7586.
225 S. Acharya, F. Dilnawaz and S. K. Sahoo, *Biomaterials*, 2009, **30**, 5737–5750.
226 M. A. Shevtsov, B. P. Nikolaev, L. Y. Yakovleva, Y. Y. Marchenko, A. V Dobrodumov, A. L. Mikhrina, M. G. Martynova, O. A. Bystrova, I. V Yakovenko and A. M. Ischenko, *Int. J. Nanomedicine*, 2014, **9**, 273–287.
227 C.-L. Tseng, W.-Y. Su, K.-C. Yen, K.-C. Yang and F.-H. Lin, *Biomaterials*, 2009, **30**, 3476–3485.
228 Y. W. Cho, J.-D. Kim and K. Park, *J. Pharm. Pharmacol.*, 2003, **55**, 721–734.
229 E. Gallon, T. Matini, L. Sasso, G. Mantovani, A. Armiñan de Benito, J. Sanchis, P. Caliceti, C. Alexander, M. J. Vicent and S. Salmaso, *Biomacromolecules*, 2015, **16**, 1924–1937.
230 D. Mavrogiorgis, P. Bilalis, A. Karatzas, D. Skoulas, G. Fotinogiannopoulou and H. Iatrou, *Polym. Chem.*, 2014, **5**, 6256–6278.
231 A. J. Convertine, D. S. W. Benoit, C. L. Duvall, A. S. Hoffman and P. S. Stayton, *J. Control. Release*, 2009, **133**, 221–229.
232 J. F. Quinn, M. R. Whittaker and T. P. Davis, *Polym. Chem.*, 2017, **8**, 97–126.
233 M. Danial and A. Postma, *Ther. Deliv.*, 2017, **8**, 359–362.
234 P. Oh, P. Borgström, H. Witkiewicz, Y. Li, B. J. Borgström, A. Chrastina, K. Iwata, K. R. Zinn, R. Baldwin, J. E. Testa and J. E. Schnitzer, *Nat. Biotechnol.*, 2007, **25**, 327–337.
235 P. U. Le and I. R. Nabi, *J. Cell Sci.*, 2003, **116**, 1059 LP – 1071.
236 I. R. Nabi and P. U. Le, *J. Cell Biol.*, 2003, **161**, 673–677.
237 F. Canal, J. Sanchis and M. J. Vicent, *Curr. Opin. Biotechnol.*, 2011, **22**, 894–900.
238 F. Greco and M. J. Vicent, *Adv. Drug Deliv. Rev.*, 2009, **61**, 1203–1213.
239 Y. Wang, A. G. Cheetham, G. Angacian, H. Su, L. Xie and H. Cui, *Adv. Drug Deliv. Rev.*, 2017, **110**–**111**, 112–126.
240 J. I. Hare, T. Lammers, M. B. Ashford, S. Puri, G. Storm and S. T. Barry, *Adv. Drug Deliv. Rev.*, 2017, **108**, 25–38.
241 S. Ashton, Y. H. Song, J. Nolan, E. Cadogan, J. Murray, R. Odedra, J. Foster, P. A. Hall, S. Low, P. Taylor, R. Ellston, U. M. Polanska, J. Wilson, C. Howes, A. Smith, R. J. A. Goodwin, J. G. Swales, N. Strittmatter, Z. Takáts, A. Nilsson, P. Andren, D. Trueman, M. Walker, C. L. Reimer, G. Troiano, D. Parsons, D. De Witt, M. Ashford, J. Hrkach, S. Zale, P. J. Jewsbury and S. T. Barry, *Sci. Transl. Med.*, 2016, **8**, 325ra17.
242 R. C. F. Leonard, S. Williams, A. Tulpule, A. M. Levine and S. Oliveros, *The Breast*, 2009, **18**, 218–224.
243 P. C. Lyon, L. F. Griffiths, J. Lee, D. Chung, R. Carlisle, F. Wu, M. R. Middleton, F. V Gleeson and C. C. Coussios, *J. Ther. Ultrasound*, 2017, **5**, 28–36.
244 C. E. Swenson, D. Haemmerich, D. H. Maul, B. Knox, N. Ehrhart and R. A. Reed, *PLoS One*, 2015, **10**, e0139752–e0139752.
245 T. Birngruber, R. Raml, W. Gladdines, C. Gatschelhofer, E. Gander, A. Ghosh, T. Kroath, P. J. Gaillard, T. R. Pieber and F. Sinner, *J. Pharm. Sci.*, 2014, **103**, 1945–1948.
246 P. J. Gaillard, C. C. M. Appeldoorn, R. Dorland, J. van Kregten, F. Manca, D. J. Vugts, B. Windhorst, G. A. M. S. van Dongen, H. E. de Vries, D. Maussang and O. van Tellingen, *PLoS One*, 2014, **9**, e82331.
247 L. D. Kaplan, S. R. Deitcher, J. A. Silverman and G. Morgan, *Clin. Lymphoma, Myeloma*

Leuk., 2014, **14**, 37–42.
248 J. A. Silverman and S. R. Deitcher, *Cancer Chemother. Pharmacol.*, 2013, **71**, 555–564.
249 F. Hagemeister, M. A. Rodriguez, S. R. Deitcher, A. Younes, L. Fayad, A. Goy, N. H. Dang, A. Forman, P. McLaughlin, L. J. Medeiros, B. Pro, J. Romaguera, F. Samaniego, J. A. Silverman, A. Sarris and F. Cabanillas, *Br. J. Haematol.*, 2013, **162**, 631–638.
250 A. Y. Bedikian, J. A. Silverman, N. E. Papadopoulos, K. B. Kim, A. E. Hagey, A. Vardeleon, W.-J. Hwu, J. Homsi, M. Davies and P. Hwu, *J. Clin. Pharmacol.*, 2011, **51**, 1205–1212.
251 M. A. Rodriguez, R. Pytlik, T. Kozak, M. Chhanabhai, R. Gascoyne, B. Lu, S. R. Deitcher and J. N. Winter, *Cancer*, 2009, **115**, 3475–3482.
252 E. A. Forssen, *Adv. Drug Deliv. Rev.*, 1997, **24**, 133–150.
253 S. D. Fosså, N. Aass and G. Parö, *Eur. J. Cancer*, 1998, **34**, 1131–1132.
254 K. J. O'Byrne, A. L. Thomas, R. A. Sharma, M. DeCatris, F. Shields, S. Beare and W. P. Steward, *Br. J. Cancer*, 2002, **87**, 15–20.
255 J. R. Eckardt, E. Campbell, H. A. Bums, G. R. Weiss, G. I. Rodriguez, S. M. Fields, A. M. Thurman, N. W. Peacock, P. Cobb, M. L. Rothenberg, M. E. Ross and D. D. Von Hoff, *Am. J. Clin. Oncol.*, 1994, **17**, 498–501.
256 M. Offidani, L. Corvatta, R. Centurioni, F. Leoni, L. Malerba, A. Mele, M. Marconi, A. Scortechini, M. Masia and P. Leoni, *Hematol. J.*, 2003, **4**, 47–53.
257 S. Lowis, I. Lewis, A. Elsworth, C. Weston, F. Doz, G. Vassal, R. Bellott, J. Robert, F. Pein, S. Ablett, R. Pinkerton, D. Frappaz, U. K. C. C. S. G. (UKCCSG) N. Agents and S. F. d'Oncologie P. (SFOP) P. Group, *Br. J. Cancer*, 2006, **95**, 571–580.
258 M. J. Glantz, K. A. Jaeckle, M. C. Chamberlain, S. Phuphanich, L. Recht, L. J. Swinnen, B. Maria, S. LaFollette, G. B. Schumann, B. F. Cole and S. B. Howell, *Clin. Cancer Res.*, 1999, **5**, 3394 LP – 3402.
259 P. Beauchesne, M. Blonski and H. Brissart, *In Vivo*, 2011, **25**, 991–993.
260 S. Phuphanich, B. Maria, R. Braeckman and M. Chamberlain, *J. Neurooncol.*, 2007, **81**, 201–208.
261 H. K. Ahn, M. Jung, S. J. Sym, D. B. Shin, S. M. Kang, S. Y. Kyung, J.-W. Park, S. H. Jeong and E. K. Cho, *Cancer Chemother. Pharmacol.*, 2014, **74**, 277–282.
262 T.-Y. Kim, D.-W. Kim, J.-Y. Chung, S. G. Shin, S.-C. Kim, D. S. Heo, N. K. Kim and Y.-J. Bang, *Clin. Cancer Res.*, 2004, **10**, 3708 LP – 3716.
263 D.-W. Kim, S.-Y. Kim, H.-K. Kim, S.-W. Kim, S. W. Shin, J. S. Kim, K. Park, M. Y. Lee and D. S. Heo, *Ann. Oncol.*, 2007, **18**, 2009–2014.
264 W. T. Lim, E. H. Tan, C. K. Toh, S. W. Hee, S. S. Leong, P. C. S. Ang, N. S. Wong and B. Chowbay, *Ann. Oncol.*, 2009, **21**, 382–388.
265 Y. Fujiwara, H. Mukai, T. Saeki, J. Ro, Y.-C. Lin, S. E. Nagai, K. S. Lee, J. Watanabe, S. Ohtani, S. B. Kim, K. Kuroi, K. Tsugawa, Y. Tokuda, H. Iwata, Y. H. Park, Y. Yang and Y. Nambu, *Br. J. Cancer*, 2019, **120**, 475–480.
266 K. Kato, K. Chin, T. Yoshikawa, K. Yamaguchi, Y. Tsuji, T. Esaki, K. Sakai, M. Kimura, T. Hamaguchi, Y. Shimada, Y. Matsumura and R. Ikeda, *Invest. New Drugs*, 2012, **30**, 1621–1627.
267 S. Emoto, H. Yamaguchi, J. Kishikawa, H. Yamashita, H. Ishigami and J. Kitayama, *Cancer Sci.*, 2012, **103**, 1304–1310.
268 T. Hamaguchi, K. Kato, H. Yasui, C. Morizane, M. Ikeda, H. Ueno, K. Muro, Y. Yamada, T. Okusaka, K. Shirao, Y. Shimada, H. Nakahama and Y. Matsumura, *Br. J. Cancer*, 2007, **97**, 170–176.
269 I. Nakamura, E. Ichimura, R. Goda, H. Hayashi, H. Mashiba, D. Nagai, H. Yokoyama, T. Onda and A. Masuda, *Int. J. Nanomedicine*, 2017, **12**, 1293–1304.
270 T. Ueno, K. Endo, K. Hori, N. Ozaki, A. Tsuji, S. Kondo, N. Wakisaka, S. Murono, K. Kataoka, Y. Kato and T. Yoshizaki, *Int. J. Nanomedicine*, 2014, **9**, 3005–3012.
271 V. Q. Do, K.-H. Park, J.-M. Park and M.-Y. Lee, *Toxicol. Res.*, 2019, **35**, 201–207.
272 S.-W. Lee, M.-H. Yun, S. W. Jeong, C.-H. In, J.-Y. Kim, M.-H. Seo, C.-M. Pai and S.-O. Kim, *J. Control. Release*, 2011, **155**, 262–271.
273 A. Madaan, P. Singh, A. Awasthi, R. Verma, A. T. Singh, M. Jaggi, S. K. Mishra, S. Kulkarni and H. Kulkarni, *Clin. Transl. Oncol.*, 2013, **15**, 26–32.
274 A. A. Ranade, D. A. Joshi, G. K. Phadke, P. P. Patil, R. B. Kasbekar, T. G. Apte, R. R. Dasare, S. D. Mengde, P. M. Parikh, G. S. Bhattacharyya and G. L. Lopes, *Ann. Oncol.*, 2013, **24**, v6–v12.
275 V. Subbiah, J. E. Grilley-Olson, A. J. Combest, N. Sharma, R. H. Tran, I. Bobe, A. Osada, K. Takahashi, J. Balkissoon, A. Camp, A. Masada, D. J. Reitsma and L. A. Bazhenova, *Clin.*

Cancer Res., 2018, **24**, 43 LP – 51.
276 T. Shimizu and Y. Kato, *Drug Deliv. Syst.*, 2009, **24**, 45–53.
277 K. Endo, T. Ueno, S. Kondo, N. Wakisaka, S. Murono, M. Ito, K. Kataoka, Y. Kato and T. Yoshizaki, *Cancer Sci.*, 2012, **104**, 369–374.
278 T. Doi, T. Hamaguchi, K. Shitara, S. Iwasa, Y. Shimada, M. Harada, K. Naito, N. Hayashi, A. Masada and A. Ohtsu, *Cancer Chemother. Pharmacol.*, 2017, **79**, 569–578.
279 R. Plummer, R. H. Wilson, H. Calvert, A. V Boddy, M. Griffin, J. Sludden, M. J. Tilby, M. Eatock, D. G. Pearson, C. J. Ottley, Y. Matsumura, K. Kataoka and T. Nishiya, *Br. J. Cancer*, 2011, **104**, 593–598.
280 K. A. Autio, R. Dreicer, J. Anderson, J. A. Garcia, A. Alva, L. L. Hart, M. I. Milowsky, E. M. Posadas, C. J. Ryan, R. P. Graf, R. Dittamore, N. A. Schreiber, J. M. Summa, H. Youssoufian, M. J. Morris and H. I. Scher, *JAMA Oncol.*, 2018, **4**, 1344–1351.
281 D. D. Von Hoff, M. M. Mita, R. K. Ramanathan, G. J. Weiss, A. C. Mita, P. M. LoRusso, H. A. Burris, L. L. Hart, S. C. Low, D. M. Parsons, S. E. Zale, J. M. Summa, H. Youssoufian and J. C. Sachdev, *Clin. Cancer Res.*, 2016, **22**, 3157 LP – 3163.
282 J. James, D. J. Murry, A. M. Treston, A. M. Storniolo, G. W. Sledge, C. Sidor and K. D. Miller, *Invest. New Drugs*, 2007, **25**, 41–48.
283 M. R. Harrison, N. M. Hahn, R. Pili, W. K. Oh, H. Hammers, C. Sweeney, K. Kim, S. Perlman, J. Arnott, C. Sidor, G. Wilding and G. Liu, *Invest. New Drugs*, 2011, **29**, 1465–1474.
284 A. J. Tevaarwerk, K. D. Holen, D. B. Alberti, C. Sidor, J. Arnott, C. Quon, G. Wilding and G. Liu, *Clin. Cancer Res.*, 2009, **15**, 1460–1465.
285 D. Matei, J. Schilder, G. Sutton, S. Perkins, T. Breen, C. Quon and C. Sidor, *Gynecol. Oncol.*, 2009, **115**, 90–96.
286 M. H. Kulke, J. A. Chan, J. A. Meyerhardt, A. X. Zhu, T. A. Abrams, L. S. Blaszkowsky, E. Regan, C. Sidor and C. S. Fuchs, *Cancer Chemother. Pharmacol.*, 2011, **68**, 293–300.
287 J. Deng, L. Huang and F. Liu, *Int. J. Pharm.*, 2010, **390**, 242–249.
288 F. Liu, J.-Y. Park, Y. Zhang, C. Conwell, Y. Liu, S. R. Bathula and L. Huang, *J. Pharm. Sci.*, 2010, **99**, 3542–3551.
289 Y. Liu, L. Huang and F. Liu, *Mol. Pharm.*, 2010, **7**, 863–869.
290 R. Shegokar and R. H. Müller, *Int. J. Pharm.*, 2010, **399**, 129–139.
291 P. Chytil, S. Hoffmann, L. Schindler, L. Kostka, K. Ulbrich, H. Caysa, T. Mueller, K. Mäder and T. Etrych, *J. Control. Release*, 2013, **172**, 504–512.
292 J. Kopeček, *Adv. Drug Deliv. Rev.*, 2013, **65**, 49–59.
293 Q. Hu, E. V. B. van Gaal, P. Brundel, H. Ippel, T. Hackeng, C. J. F. Rijcken, G. Storm, W. E. Hennink and J. Prakash, *J. Control. Release*, 2015, **205**, 98–108.
294 J. Hrkach, D. Von Hoff, M. M. Ali, E. Andrianova, J. Auer, T. Campbell, D. De Witt, M. Figa, M. Figueiredo and A. Horhota, *Sci. Transl. Med.*, 2012, **4**, 128ra39.
295 Z. He, X. Wan, A. Schulz, H. Bludau, M. A. Dobrovolskaia, S. T. Stern, S. A. Montgomery, H. Yuan, Z. Li, D. Alakhova, M. Sokolsky, D. B. Darr, C. M. Perou, R. Jordan, R. Luxenhofer and A. V Kabanov, *Biomaterials*, 2016, **101**, 296–309.
296 T. Yokozawa and Y. Ohta, *Chem. Rev.*, 2016, **116**, 1950–1968.
297 C. J. Hawker, J. M. J. Frechet, R. B. Grubbs and J. Dao, *J. Am. Chem. Soc.*, 1995, **117**, 10763–10764.
298 G. Moad and E. Rizzardo, *Macromolecules*, 1995, **28**, 8722–8728.
299 M. K. Georges, R. P. N. Veregin, P. M. Kazmaier and G. K. Hamer, *Macromolecules*, 1993, **26**, 2987–2988.
300 C. J. Hawker, G. G. Barclay and J. Dao, *J. Am. Chem. Soc.*, 1996, **118**, 11467–11471.
301 M. Kato, M. Kamigaito, M. Sawamoto and T. Higashimura, *Macromolecules*, 1995, **28**, 1721–1723.
302 J.-S. Wang and K. Matyjaszewski, *J. Am. Chem. Soc.*, 1995, **117**, 5614–5615.
303 V. Percec, T. Guliashvili, J. S. Ladislaw, A. Wistrand, A. Stjerndahl, M. J. Sienkowska, M. J. Monteiro and S. Sahoo, *J. Am. Chem. Soc.*, 2006, **128**, 14156–14165.
304 G. Moad, E. Rizzardo and S. H. Thang, *Aust. J. Chem.*, 2005, **58**, 379–410.
305 G. Moad, E. Rizzardo and S. H. Thang, *Aust. J. Chem.*, 2009, **62**, 1402–1472.
306 E. Rizzardo, J. Chiefari, B. Y. K. Chong, F. Ercole, J. Krstina, J. Jeffery, T. P. T. Le, R. T. A. Mayadunne, G. F. Meijs, C. L. Moad, G. Moad and S. H. Thang, *Macromol. Symp.*, 1999, **143**, 291–307.
307 S. R. Samanta, V. Nikolaou, S. Keller, M. J. Monteiro, D. A. Wilson, D. M. Haddleton and V. Percec, *Polym. Chem.*, 2015, **6**, 2084–2097.
308 A. J. D. Magenau, N. C. Strandwitz, A. Gennaro and K. Matyjaszewski, *Science.*, 2011, **332**,

81–84.
309 A. Anastasaki, V. Nikolaou, Q. Zhang, J. Burns, S. R. Samanta, C. Waldron, A. J. Haddleton, R. McHale, D. Fox, V. Percec, P. Wilson and D. M. Haddleton, *J. Am. Chem. Soc.*, 2014, **136**, 1141–1149.
310 N. Chan, M. F. Cunningham and R. A. Hutchinson, *J. Polym. Sci. Part A Polym. Chem.*, 2013, **51**, 3081–3096.
311 D. A. Z. Wever, P. Raffa, F. Picchioni and A. A. Broekhuis, *Macromolecules*, 2012, **45**, 4040–4045.
312 R. Nicolaÿ, Y. Kwak and K. Matyjaszewski, *Chem. Commun.*, 2008, 5336–5338.
313 R. M. England and S. Rimmer, *Polym. Chem.*, 2010, **1**, 1533–1544.
314 B. Liu, A. Kazlauciunas, J. T. Guthrie and S. Perrier, *Polymer.*, 2005, **46**, 6293–6299.
315 H. Shinoda and K. Matyjaszewski, *Macromolecules*, 2001, **34**, 6243–6248.
316 R. Whitfield, A. Anastasaki, N. P. Truong, P. Wilson, K. Kempe, J. A. Burns, T. P. Davis and D. M. Haddleton, *Macromolecules*, 2016, **49**, 8914–8924.
317 S. Perrier, *Macromolecules*, 2017, **50**, 7433–7447.
318 S. B. Lee, A. J. Russell and K. Matyjaszewski, *Biomacromolecules*, 2003, **4**, 1386–1393.
319 D. J. Keddie, *Chem. Soc. Rev.*, 2014, **43**, 496–505.
320 C. Boyer, A. H. Soeriyadi, P. B. Zetterlund and M. R. Whittaker, *Macromolecules*, 2011, **44**, 8028–8033.
321 R. Aksakal, M. Resmini and C. R. Becer, *Polym. Chem.*, 2016, **7**, 171–175.
322 J. Xia, X. Zhang and K. Matyjaszewski, *Macromolecules*, 1999, **32**, 4482–4484.
323 J.-F. Lutz, *J. Polym. Sci. Part A Polym. Chem.*, 2008, **46**, 3459–3470.
324 Y. Deng, S. Zhang, G. Lu and X. Huang, *Polym. Chem.*, 2013, **4**, 1289–1299.
325 B. I. Voit and A. Lederer, *Chem. Rev.*, 2009, **109**, 5924–5973.
326 P. S. Eselem Bungu and H. Pasch, *Polym. Chem.*, 2018, **9**, 1116–1131.
327 T. C. Lubensky and J. Isaacson, *J. Phys. Fr.*, 1981, **42**, 175–188.
328 X. Wang and H. Gao, *Polymers.*, 2017, **9**, 188–210.
329 S. Pearson, C. St Thomas, R. Guerrero-Santos and F. D'Agosto, *Polym. Chem.*, 2017, **8**, 4916–4946.
330 R. W. Graff, X. Wang and H. Gao, *Macromolecules*, 2015, **48**, 2118–2126.
331 T. Zhao, Y. Zheng, J. Poly and W. Wang, *Nat. Commun.*, 2013, **4**, 1873.
332 D. N. Schulz and A. O. Patil, in *Functional Polymers*, American Chemical Society, Washington, 1998, vol. 704, p. 1.
333 K. Adachi and Y. Tsukahara, in *Encyclopedia of Polymeric Nanomaterials*, eds. S. Kobayashi and K. Müllen, Springer Berlin Heidelberg, Berlin, Heidelberg, 2015, pp. 1167–1175.
334 S. Maji, F. Mitschang, L. Chen, Q. Jin, Y. Wang and S. Agarwal, *Macromol. Chem. Phys.*, 2012, **213**, 1643–1654.
335 M. A. Gauthier, M. I. Gibson and H.-A. Klok, *Angew. Chemie Int. Ed.*, 2009, **48**, 48–58.
336 R. K. Iha, K. L. Wooley, A. M. Nyström, D. J. Burke, M. J. Kade and C. J. Hawker, *Chem. Rev.*, 2009, **109**, 5620–5686.
337 P. Thirumurugan, D. Matosiuk and K. Jozwiak, *Chem. Rev.*, 2013, **113**, 4905–4979.
338 C. E. Hoyle, A. B. Lowe and C. N. Bowman, *Chem. Soc. Rev.*, 2010, **39**, 1355–1387.
339 H. Willcock, A. Lu, C. F. Hansell, E. Chapman, I. R. Collins and R. K. O'Reilly, *Polym. Chem.*, 2014, **5**, 1023–1030.
340 S. Sakamoto, Y. Sanada, M. Sakashita, K. Nishina, K. Nakai, S. Yusa and K. Sakurai, *Polym. J.*, 2014, **46**, 617–622.
341 D. Heinz, E. Amado and J. Kressler, *Polymers.*, 2018, **10**, 960.
342 S. R. Tonge and B. J. Tighe, *Adv. Drug Deliv. Rev.*, 2001, **53**, 109–122.
343 Y. Ning, L. A. Fielding, K. E. B. Doncom, N. J. W. Penfold, A. N. Kulak, H. Matsuoka and S. P. Armes, *ACS Macro Lett.*, 2016, **5**, 311–315.
344 S. G. Roy and P. De, *J. Appl. Polym. Sci.*, , DOI:10.1002/app.41084.
345 Z. P. Tolstyka, H. Phillips, M. Cortez, Y. Wu, N. Ingle, J. B. Bell, P. B. Hackett and T. M. Reineke, *ACS Biomater. Sci. Eng.*, 2016, **2**, 43–55.
346 W. Sriprom, M. Néel, C. D. Gabbutt, B. M. Heron and S. Perrier, *J. Mater. Chem.*, 2007, **17**, 1885–1893.
347 K. Sun, S. W. A. Bligh, H. Nie, J. Quan and L. Zhu, *RSC Adv.*, 2014, **4**, 34912–34921.
348 K. Matyjaszewski and N. V Tsarevsky, *Nat. Chem.*, 2009, **1**, 276–288.
349 A. B. Dwyer, P. Chambon, A. Town, F. L. Hatton, J. Ford and S. P. Rannard, *Polym. Chem.*, 2015, **6**, 7286–7296.
350 F. L. Hatton, L. M. Tatham, L. R. Tidbury, P. Chambon, T. He, A. Owen and S. P. Rannard,

Chem. Sci., 2015, **6**, 326–334.
351 R. Tong, L. Tang, L. Ma, C. Tu, R. Baumgartner and J. Cheng, *Chem. Soc. Rev.*, 2014, **43**, 6982–7012.
352 H. Willcock and R. K. O'Reilly, *Polym. Chem.*, 2010, **1**, 149–157.
353 A. Anastasaki, J. Willenbacher, C. Fleischmann, W. R. Gutekunst and C. J. Hawker, *Polym. Chem.*, 2017, **8**, 689–697.
354 L. D. Blackman, D. B. Wright, M. P. Robin, M. I. Gibson and R. K. O'Reilly, *ACS Macro Lett.*, 2015, **4**, 1210–1214.
355 D. B. Wright, J. P. Patterson, N. C. Gianneschi, C. Chassenieux, O. Colombani and R. K. O'Reilly, *Polym. Chem.*, 2016, **7**, 1577–1583.
356 L. D. Blackman, M. I. Gibson and R. K. O'Reilly, *Polym. Chem.*, 2017, **8**, 233–244.
357 K. Babiuch, A. Dag, J. Zhao, H. Lu and M. H. Stenzel, *Biomacromolecules*, 2015, **16**, 1948–1957.
358 K. Min and H. Gao, *J. Am. Chem. Soc.*, 2012, **134**, 15680–15683.
359 I. Bannister, N. C. Billingham, S. P. Armes, S. P. Rannard and P. Findlay, *Macromolecules*, 2006, **39**, 7483–7492.
360 T. Zhao, Y. Zheng, J. Poly and W. Wang, *Nat. Commun.*, 2013, **4**, 1–8.
361 A. W. Jackson, P. Chandrasekharan, J. Shi, S. P. Rannard, Q. Liu, C.-T. Yang and T. He, *Int. J. Nanomedicine*, 2015, **10**, 5895–5907.
362 R. W. Graff, X. Wang and H. Gao, *Macromolecules*, 2015, **48**, 2118–2126.
363 R. W. Graff, Y. Shi, X. Wang and H. Gao, *Macromol. Rapid Commun.*, 2015, **36**, 2076–2082.
364 A. W. Jackson and D. A. Fulton, *Polym. Chem.*, 2013, **4**, 31–45.
365 G. Kocak, C. Tuncer and V. Bütün, *Polym. Chem.*, 2017, **8**, 144–176.
366 R. Hoogenboom, in *Smart Polymers and their Applications*, eds. M. R. Aguilar and J. B. T.-S. P. and their A. San Román, Woodhead Publishing, Cambridge, 2nd edn., 2014, pp. 15–44.
367 O. Bertrand and J.-F. Gohy, *Polym. Chem.*, 2017, **8**, 52–73.
368 H. Liu, S. Lin, Y. Feng and P. Theato, *Polym. Chem.*, 2017, **8**, 12–23.
369 M. Wei, Y. Gao, X. Li and M. J. Serpe, *Polym. Chem.*, 2017, **8**, 127–143.
370 G. Moad, *Polym. Chem.*, 2017, **8**, 177–219.
371 V. Delplace and J. Nicolas, *Nat. Chem.*, 2015, **7**, 771.
372 W. J. Bailey, Z. Ni and S. R. Wu, *Macromolecules*, 1982, **15**, 711–714.
373 S. Agarwal, *Polym. J.*, 2007, **39**, 163–174.
374 L. F. Sun, R. X. Zhuo and Z. L. Liu, *J. Polym. Sci. Part A Polym. Chem.*, 2003, **41**, 2898–2904.
375 J. Undin, A. Finne-Wistrand and A.-C. Albertsson, *Biomacromolecules*, 2014, **15**, 2800–2807.
376 J. Undin, A. Finne-Wistrand and A.-C. Albertsson, *Biomacromolecules*, 2013, **14**, 2095–2102.
377 W. J. Bailey, Z. Ni and S.-R. Wu, *J. Polym. Sci. Polym. Chem. Ed.*, 1982, **20**, 3021–3030.
378 S. Agarwal, R. Kumar, T. Kissel and R. Reul, *Polym. J.*, 2009, **41**, 650–660.
379 J. Undin, T. Illanes, A. Finne-Wistrand and A.-C. Albertsson, *Polym. Chem.*, 2012, **3**, 1260–1266.
380 S. Jin and K. E. Gonsalves, *Macromolecules*, 1997, **30**, 3104–3106.
381 G. G. Hedir, A. Pitto-Barry, A. P. Dove and R. K. O'Reilly, *J. Polym. Sci. Part A Polym. Chem.*, 2015, **53**, 2699–2710.
382 G. G. Hedir, M. C. Arno, M. Langlais, J. T. Husband, R. K. O'Reilly and A. P. Dove, *Angew. Chemie Int. Ed.*, 2017, **56**, 9178–9182.
383 C. A. Bell, G. G. Hedir, R. K. O'Reilly and A. P. Dove, *Polym. Chem.*, 2015, **6**, 7447–7454.
384 G. G. Hedir, C. A. Bell, R. K. O'Reilly and A. P. Dove, *Biomacromolecules*, 2015, **16**, 2049–2058.
385 G. G. Hedir, C. A. Bell, N. S. Ieong, E. Chapman, I. R. Collins, R. K. O'Reilly and A. P. Dove, *Macromolecules*, 2014, **47**, 2847–2852.
386 M. Rikkou-Kalourkoti, E. Loizou, L. Porcar, K. Matyjaszewski and C. S. Patrickios, *Polym. Chem.*, 2012, **3**, 105–116.
387 J. A. Johnson, M. G. Finn, J. T. Koberstein and N. J. Turro, *Macromolecules*, 2007, **40**, 3589–3598.
388 J. A. Syrett, G. Mantovani, W. R. S. Barton, D. Price and D. M. Haddleton, *Polym. Chem.*, 2010, **1**, 102–106.
389 N. V Tsarevsky and K. Matyjaszewski, *Macromolecules*, 2002, **35**, 9009–9014.
390 J. A. Alfurhood, P. R. Bachler and B. S. Sumerlin, *Polym. Chem.*, 2016, **7**, 3361–3369.
391 M. Zhang, H. Liu, W. Shao, K. Miao and Y. Zhao, *Macromolecules*, 2013, **46**, 1325–1336.
392 H. L. Cao, Y. X. Dong, A. Aied, T. Y. Zhao, X. Chen, W. X. Wang and A. Pandit, *Chem.*

Commun., 2014, **50**, 15565–15568.
393 C. Li, H. Liu, D. Tang and Y. Zhao, *Polym. Chem.*, 2015, **6**, 1474–1486.
394 S. Hocine and M.-H. Li, *Soft Matter*, 2013, **9**, 5839–5861.
395 Y. Kotsuchibashi and R. Narain, *Polym. Chem.*, 2014, **5**, 3061–3070.
396 H. M. L. Lambermont-Thijs, R. Hoogenboom, C.-A. Fustin, C. Bomal-D'Haese, J.-F. Gohy and U. S. Schubert, *J. Polym. Sci. Part A Polym. Chem.*, 2009, **47**, 515–522.
397 K. Bebis, M. W. Jones, D. M. Haddleton and M. I. Gibson, *Polym. Chem.*, 2011, **2**, 975–982.
398 J.-F. Lutz, Ö. Akdemir and A. Hoth, *J. Am. Chem. Soc.*, 2006, **128**, 13046–13047.
399 J.-F. Lutz and A. Hoth, *Macromolecules*, 2006, **39**, 893–896.
400 R. Hoogenboom, H. M. L. Thijs, M. J. H. C. Jochems, B. M. van Lankvelt, M. W. M. Fijten and U. S. Schubert, *Chem. Commun.*, 2008, 5758–5760.
401 H. Okamura, T. Mori, K. Minagawa, S. Masuda and M. Tanaka, *Polymer.*, 2002, **43**, 3825–3828.
402 S. Samanta, D. R. Bogdanowicz, H. H. Lu and J. T. Koberstein, *Macromolecules*, 2016, **49**, 1858–1864.
403 N. S. Ieong, M. Redhead, C. Bosquillon, C. Alexander, M. Kelland and R. K. O'Reilly, *Macromolecules*, 2011, **44**, 886–893.
404 H. Cheng, L. Shen and C. Wu, *Macromolecules*, 2006, **39**, 2325–2329.
405 C. Wu and X. Wang, *Phys. Rev. Lett.*, 1998, **80**, 4092–4094.
406 Y. Ding, X. Ye and G. Zhang, *Macromolecules*, 2005, **38**, 904–908.
407 C. Donini, D. N. Robinson, P. Colombo, F. Giordano and N. A. Peppas, *Int. J. Pharm.*, 2002, **245**, 83–91.
408 T. R. Kyriakides, C. Y. Cheung, N. Murthy, P. Bornstein, P. S. Stayton and A. S. Hoffman, *J. Control. Release*, 2002, **78**, 295–303.
409 K. M. Hutchins, *R. Soc. open Sci.*, 2018, **5**, 180564–180580.
410 M. Sawamoto and M. Ouchi, eds. S. Kobayashi and K. Müllen, Springer Berlin Heidelberg, Berlin, Heidelberg, 2015, pp. 320–324.
411 S. Napolitano, E. Glynos and N. Tito, *Reports Prog. Phys.*, 2017, **80**, 36602.
412 R. F. Boyer, *Polymer.*, 1976, **17**, 996–1008.
413 N. Padhye, D. M. Parks, B. L. Trout and A. H. Slocum, *Sci. Rep.*, 2017, **7**, 46405.
414 S. J. Garcia, *Eur. Polym. J.*, 2014, **53**, 118–125.
415 K. Kataoka, A. Harada and Y. Nagasaki, *Adv. Drug Deliv. Rev.*, 2012, **64**, 37–48.
416 I. K. Voets, A. de Keizer and M. A. Cohen Stuart, *Adv. Colloid Interface Sci.*, 2009, **147**–**148**, 300–318.
417 L. Zhang and A. Eisenberg, *Polym. Adv. Technol.*, 1998, **9**, 677–699.
418 A. Halperin, M. Tirrell and T. P. Lodge, Springer Berlin Heidelberg, Berlin, Heidelberg, 1992, pp. 31–71.
419 E. B. Zhulina and O. V Borisov, *Macromolecules*, 2012, **45**, 4429–4440.
420 M. Antonietti and S. Förster, *Adv. Mater.*, 2003, **15**, 1323–1333.
421 S. Förster and T. Plantenberg, *Angew. Chemie Int. Ed.*, 2002, **41**, 688–714.
422 K. Letchford and H. Burt, *Eur. J. Pharm. Biopharm.*, 2007, **65**, 259–269.
423 K. Yu, L. Zhang and A. Eisenberg, *Langmuir*, 1996, **12**, 5980–5984.
424 R. Nagarajan, *Langmuir*, 2002, **18**, 31–38.
425 Y. Mai and A. Eisenberg, *Chem. Soc. Rev.*, 2012, **41**, 5969–5985.
426 A. Blanazs, S. P. Armes and A. J. Ryan, *Macromol. Rapid Commun.*, 2009, **30**, 267–277.
427 J. Rieger, F. Stoffelbach, C. Bui, D. Alaimo, C. Jérôme and B. Charleux, *Macromolecules*, 2008, **41**, 4065–4068.
428 J. Rieger, G. Osterwinter, C. Bui, F. Stoffelbach and B. Charleux, *Macromolecules*, 2009, **42**, 5518–5525.
429 E. Groison, S. Brusseau, F. D'Agosto, S. Magnet, R. Inoubli, L. Couvreur and B. Charleux, *ACS Macro Lett.*, 2012, **1**, 47–51.
430 T. Boursier, I. Chaduc, J. Rieger, F. D'Agosto, M. Lansalot and B. Charleux, *Polym. Chem.*, 2011, **2**, 355–362.
431 M. J. Derry, T. Smith, P. S. O'Hora and S. P. Armes, *ACS Appl. Mater. Interfaces*, 2019, **11**, 33364–33369.
432 B. Karagoz, L. Esser, H. T. Duong, J. S. Basuki, C. Boyer and T. P. Davis, *Polym. Chem.*, 2014, **5**, 350–355.
433 Z. An, W. Tang, C. J. Hawker and G. D. Stucky, *J. Am. Chem. Soc.*, 2006, **128**, 15054–15055.
434 Z. An, Q. Shi, W. Tang, C.-K. Tsung, C. J. Hawker and G. D. Stucky, *J. Am. Chem. Soc.*, 2007, **129**, 14493–14499.

435 C. Grazon, J. Rieger, N. Sanson and B. Charleux, *Soft Matter*, 2011, **7**, 3482–3490.
436 G. Delaittre, M. Save and B. Charleux, *Macromol. Rapid Commun.*, 2007, **28**, 1528–1533.
437 G. Liu, Q. Qiu and Z. An, *Polym. Chem.*, 2012, **3**, 504–513.
438 G. Liu, Q. Qiu, W. Shen and Z. An, *Macromolecules*, 2011, **44**, 5237–5245.
439 A. Blanazs, A. J. Ryan and S. P. Armes, *Macromolecules*, 2012, **45**, 5099–5107.
440 W. Shen, Y. Chang, G. Liu, H. Wang, A. Cao and Z. An, *Macromolecules*, 2011, **44**, 2524–2530.
441 A. M. I. Ali, P. Pareek, L. Sewell, A. Schmid, S. Fujii, S. P. Armes and I. M. Shirley, *Soft Matter*, 2007, **3**, 1003–1013.
442 D. H. Napper and A. Netschey, *J. Colloid Interface Sci.*, 1971, **37**, 528–535.
443 A. Blanazs, J. Madsen, G. Battaglia, A. J. Ryan and S. P. Armes, *J. Am. Chem. Soc.*, 2011, **133**, 16581–16587.
444 E. R. Jones, M. Semsarilar, P. Wyman, M. Boerakker and S. P. Armes, *Polym. Chem.*, 2016, **7**, 851–859.
445 M. Chenal, L. Bouteiller and J. Rieger, *Polym. Chem.*, 2013, **4**, 752–762.
446 N. P. Truong, M. V Dussert, M. R. Whittaker, J. F. Quinn and T. P. Davis, *Polym. Chem.*, 2015, **6**, 3865–3874.
447 W. Zhang, F. D'Agosto, O. Boyron, J. Rieger and B. Charleux, *Macromolecules*, 2012, **45**, 4075–4084.
448 D. E. Ganeva, E. Sprong, H. de Bruyn, G. G. Warr, C. H. Such and B. S. Hawkett, *Macromolecules*, 2007, **40**, 6181–6189.
449 I. Chaduc, A. Crepet, O. Boyron, B. Charleux, F. D'Agosto and M. Lansalot, *Macromolecules*, 2013, **46**, 6013–6023.
450 X. Zhang, S. Boissé, W. Zhang, P. Beaunier, F. D'Agosto, J. Rieger and B. Charleux, *Macromolecules*, 2011, **44**, 4149–4158.
451 P. Gurnani, C. Sanchez-Cano, K. Abraham, H. Xandri-Monje, A. B. Cook, M. Hartlieb, F. Lévi, R. Dallmann and S. Perrier, *Macromol. Biosci.*, 2018, **18**, 1800213.
452 S. M. D'Addio, W. Saad, S. M. Ansell, J. J. Squiers, D. H. Adamson, M. Herrera-Alonso, A. R. Wohl, T. R. Hoye, C. W. Macosko, L. D. Mayer, C. Vauthier and R. K. Prud'homme, *J. Control. Release*, 2012, **162**, 208–217.
453 G. Gaucher, M.-H. Dufresne, V. P. Sant, N. Kang, D. Maysinger and J.-C. Leroux, *J. Control. Release*, 2005, **109**, 169–188.
454 B. Karagoz, C. Boyer and T. P. Davis, *Macromol. Rapid Commun.*, 2014, **35**, 417–421.
455 J. Madsen, S. P. Armes, K. Bertal, S. MacNeil and A. L. Lewis, *Biomacromolecules*, 2009, **10**, 1875–1887.
456 J. Madsen, S. P. Armes and A. L. Lewis, *Macromolecules*, 2006, **39**, 7455–7457.
457 M. Duval, G. Waton and F. Schosseler, *Langmuir*, 2005, **21**, 4904–4911.
458 A. Chatterjee, *J. Chem. Phys.*, 2010, **132**, 224905.
459 R. H. J. Otten and P. van der Schoot, *J. Chem. Phys.*, 2011, **134**, 94902.
460 D. Nguyen, H. S. Zondanos, J. M. Farrugia, A. K. Serelis, C. H. Such and B. S. Hawkett, *Langmuir*, 2008, **24**, 2140–2150.
461 W.-J. Zhang, C.-Y. Hong and C.-Y. Pan, *ACS Appl. Mater. Interfaces*, 2017, **9**, 15086–15095.
462 W.-J. Zhang, C.-Y. Hong and C.-Y. Pan, *Biomacromolecules*, 2017, **18**, 1210–1217.
463 L. Qiu, C.-R. Xu, F. Zhong, C.-Y. Hong and C.-Y. Pan, *ACS Appl. Mater. Interfaces*, 2016, **8**, 18347–18359.
464 W.-J. Zhang, C.-Y. Hong and C.-Y. Pan, *Biomacromolecules*, 2016, **17**, 2992–2999.
465 H. Fessi, F. Puisieux, J. P. Devissaguet, N. Ammoury and S. Benita, *Int. J. Pharm.*, 1989, **55**, R1–R4.
466 K. M. Pustulka, A. R. Wohl, H. S. Lee, A. R. Michel, J. Han, T. R. Hoye, A. V McCormick, J. Panyam and C. W. Macosko, *Mol. Pharm.*, 2013, **10**, 4367–4377.
467 C. E. Mora-Huertas, H. Fessi and A. Elaissari, *Int. J. Pharm.*, 2010, **385**, 113–142.
468 F. Shiba and Y. Okawa, *J. Phys. Chem. B*, 2005, **109**, 21664–21668.
469 E. Lepeltier, C. Bourgaux and P. Couvreur, *Adv. Drug Deliv. Rev.*, 2014, **71**, 86–97.
470 J. Aubry, F. Ganachaud, J.-P. Cohen Addad and B. Cabane, *Langmuir*, 2009, **25**, 1970–1979.
471 M. A. Watzky and R. G. Finke, *J. Am. Chem. Soc.*, 1997, **119**, 10382–10400.
472 H. Jun, T. Fabienne, M. Florent, P.-E. Coulon, M. Nicolas and S. Olivier, *Langmuir*, 2012, **28**, 15966–15974.
473 J. Pecher and S. Mecking, *Chem. Rev.*, 2010, **110**, 6260–6279.
474 B. Derjaguin and L. D. Landau, *Zhurnal Eksp. I Teor. Fiz.*, 1945, **15**, 663.
475 E. J. W. Verwey, *J. Phys. Colloid Chem.*, 1947, **51**, 631–636.

476 X.-Z. Cao, H. Merlitz, C.-X. Wu, S. A. Egorov and J.-U. Sommer, *Soft Matter*, 2013, **9**, 5916–5926.
477 Z. Zhu, K. Margulis-Goshen, S. Magdassi, Y. Talmon and C. W. Macosko, *J. Pharm. Sci.*, 2010, **99**, 4295–4306.
478 S. Mourdikoudis, R. M. Pallares and N. T. K. Thanh, *Nanoscale*, 2018, **10**, 12871–12934.
479 R. Ferrari, M. Sponchioni, M. Morbidelli and D. Moscatelli, *Nanoscale*, 2018, **10**, 22701–22719.
480 Y. Hui, X. Yi, F. Hou, D. Wibowo, F. Zhang, D. Zhao, H. Gao and C.-X. Zhao, *ACS Nano*, 2019, **13**, 7410–7424.
481 H. E. Rogers, P. Chambon, S. E. R. Auty, F. Y. Hern, A. Owen and S. P. Rannard, *Soft Matter*, 2015, **11**, 7005–7015.
482 F. Y. Hern, A. Hill, A. Owen and S. P. Rannard, *Polym. Chem.*, 2018, **9**, 1767–1771.
483 M. A. Quadir, S. W. Morton, L. B. Mensah, K. Shopsowitz, J. Dobbelaar, N. Effenberger and P. T. Hammond, *Nanomedicine*, 2017, **13**, 1797–1808.
484 S. Mura, J. Nicolas and P. Couvreur, *Nat. Mater.*, 2013, **12**, 991–1003.
485 X. Xu, J. D. Flores and C. L. McCormick, *Macromolecules*, 2011, **44**, 1327–1334.
486 S. Mukherjee, R. N. Ghosh and F. R. Maxfield, *Physiol. Rev.*, 1997, **77**, 759–803.
487 S. McRae Page, M. Martorella, S. Parelkar, I. Kosif and T. Emrick, *Mol. Pharm.*, 2013, **10**, 2684–2692.
488 J. Yu, X. Chu and Y. Hou, *Chem. Commun.*, 2014, **50**, 11614–11630.
489 Q. Jin, F. Mitschang and S. Agarwal, *Biomacromolecules*, 2011, **12**, 3684–3691.
490 J. Ford, P. Chambon, J. North, F. L. Hatton, M. Giardiello, A. Owen and S. P. Rannard, *Macromolecules*, 2015, **48**, 1883–1893.

Chapter 2

Utilising Copper-Catalysed Reversible Deactivation Radical Polymerisation of Hydrophobic Methacrylates in Alcoholic Media to Access a Variety of Polymer Architectures

Publications arising from this chapter:

"Expanding the monomer scope of linear and branched vinyl polymerisations via Copper catalysed reversible-deactivation radical polymerisation of hydrophobic methacrylates using anhydrous alcohol solvents"

S. Flynn, A. B. Dwyer, P. Chambon and S. Rannard

Polym. Chem., 2019, **10**, 5103

2.1 Introduction

2.1.1 Copper-Catalysed Reversible-Deactivation Radical Polymerisation

Copper (Cu)-catalysed reversible-deactivation radical polymerisation (Cu-RDRP) evolved after the development and successful implementation of transition metal complexes as catalysts in the atom transfer radical addition (ATRA) of olefins to alkyl halides.[1–3] The presence of halogen atoms within ATRA adducts demonstrated the ability to abstract the halogen atom from the transition metal complex. This raised the possibility of performing repetitive additions to an alkyl halide and formed the basis of the key principles which underpin Cu-RDRP. In 1994, Sawamoto and co-workers reported the first transition metal-catalysed polymerisation of methyl methacrylate (MMA). This was facilitated by a ligated ruthenium (II)-based transition metal complex, in combination with an aluminium-based Lewis acid, capable of reversible halogen abstraction.[4] Within a year, a report from Matyjaszewski and Wang demonstrated the first RDRP process facilitated solely by a transition metal complex. This Cu-based system utilised 2-2' bipyridine (bpy) ligands and facilitated the Cu-RDRP of methyl acrylate and styrene; such formulations conferred the ability to target molecular weight (M_w) and produce polymers of low dispersity (Đ) compared with those typically generated using conventional radical polymerisation.[5]

Since the discovery of Cu-RDRP, numerous techniques have emerged, including conventional atom transfer radical polymerisation (ATRP),[5] reverse ATRP,[6] simultaneous reverse and normally initiated ATRP,[7] activators (re)generated by electron transfer ATRP,[8,9] initiators for continuous activator regeneration ATRP,[10] supplemental activators and reducing agents (SARA) ATRP,[11] electrochemically-mediated ATRP,[12] single electron transfer(degenerative transfer)-living radical polymerisation (SET-LRP),[13] photoinitiated ATRP[14] and photoinitiated SET-LRP.[15,16] These techniques enable chemists to generate a range of functional polymers with precise control over M_w, chain lengths and architectures. The complex nature of each of these techniques goes beyond the scope of the work covered in this thesis. Therefore the reader is directed to an excellent review article which discusses each of these processes in more detail.[17] As the work in this Chapter utilises experimental procedures consistent with those described for conventional ATRP mediated by a $[Cu(bpy)_2]Cl$ catalytic system, this Cu-RDRP technique will be discussed in more detail.

2.1.2 Conventional Copper-Catalysed Atom Transfer Radical Polymerisation

Conventional Cu-catalysed ATRP utilises a reversible redox process, between ligated Cu^{I} and Cu^{II} complexes, to suppress the concentration of active radicals during polymerisation. In doing so, it is possible to significantly reduce the prevalence of undesirable side reactions, such as chain termination or chain transfer, which are commonly associated with conventional free radical polymerisation (FRP). Alkyl halides are typically employed as initiators in ATRP. In contrast to FRP, where radicals are constantly generated throughout polymerisation *via* thermal decomposition of an initiator, ATRP involves rapid homogeneous initiation. Halogen abstraction by the $[Cu(bpy)_2]Cl$ activator initially leads to a high radical concentration. The majority of radicals generated undergo rapid deactivation, facilitated by the newly-formed $[Cu(bpy)_2Br]Cl$ deactivating species, to regenerate the alkyl-halide. However, a small fraction of radical species are terminated *via* radical-radical combination. This leaves a residual amount of the deactivating species and allows the ATRP equilibrium to be established.

The conventional ATRP process facilitated by $[Cu(bpy)_2]Cl$/ $[Cu(bpy)_2Br]Cl$ catalytic system is represented in Scheme 2.1. Activation of a dormant polymer chain (P_n-Br) occurs following halogen abstraction by $[Cu(bpy)_2]Cl$. This activation proceeds with a rate constant k_{act}, resulting in the generation of an active polymer species (P_n•) and the subsequent oxidised halogenated $[Cu(bpy)_2Br]Cl$ complex. The most likely fate of the active polymer radical is to undergo deactivation (rate k_{deact}) by re-abstraction of the halogen atom from the $[Cu(bpy)_2Br]Cl$ complex, which itself undergoes a one-electron reduction, to regenerate a dormant polymer chain and the $[Cu(bpy)_2]Cl$ complex respectively. However, the polymer radicals can undergo chain growth *via* propagation with free monomer (M, rate constant k_p). Alternatively, a polymer radical could also undergo termination with another polymer radical (P_m•); this can occur either by combination with another radical species (rate constant k_{tc}) or through termination by disproportionation (rate constant k_{td}).

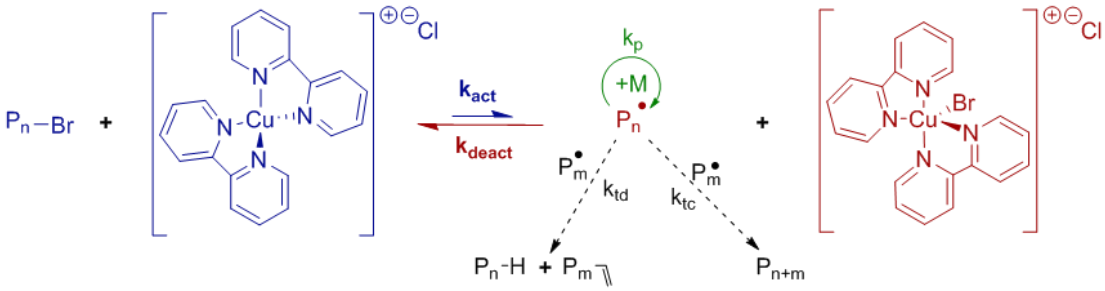

Scheme 2.1 Mechanism of conventional Cu-catalysed ATRP facilitated by CuCl/bpy as described by Matyjaszewski and co-workers.[5]

The dynamic ATRP equilibrium ensures that the concentration of active radical species remains both low and constant throughout polymerisation; this effectively prevents undesirable side reactions legitimising the assumption that the contribution of termination is negligible during ATRP. A fast equilibrium approximation, which is essential for the production of polymers of low Đ, can therefore be used to derive the apparent rate law for Cu-catalysed ATRP (Equation 2.1).

$$R_p = k_p[M][P^*] = k_p K_{eq}[M][I]_0 \times \left(\frac{[Cu^I]}{[X\text{-}Cu^{II}]} \right) \qquad \textbf{Equation 2.1}$$

The derived raw law for Cu-catalysed ATRP as reported by Matyjaszewski and co-workers.[18] R_p = observed propagation rate, k_p = propagation rate constant, [M] = monomer concentration, [P*] = radical concentration, K_{eq} = ATRP equilibrium constant = k_{act}/k_{deact} (see Scheme 2.1), $[I]_0$ = initiator concentration at t_0, $[Cu^I]$ = activator concentration and $[X\text{-}Cu^{II}]$ = deactivator concentration where X = halogen atom. Kinetic studies of the ATRP of styrenes,[19] acrylates,[20] and methacrylates[21,22] have shown that the R_p is first order with respect to the concentration of monomer, initiator and the Cu-complex. These observations are consistent with the derived rate law and are typically demonstrated by a linear evolution in monomer conversion with time when plotted using semi logarithmic co-ordinates (Figure 2.1a, red solid line). This also demonstrates the efficacy of the ATRP process in maintaining a constant $[P^{\cdot}]$ throughout polymerisation. Deviations from this behaviour can occur in cases where termination or self-initiation are prevalent during ATRP.

During ATRP, the evolution of M_n with monomer conversion is similar to those described for "living" polymerisation processes. The rapid, homogeneous initiation process ensures that all initiating moieties grow at the same time; this typically causes a linear increase in M_n with monomer conversion (Figure 2.1b, purple solid line). Increases in M_n are typically accompanied by a reduction in Đ as the ATRP proceeds (Figure 2.1b, green dashed line). In the early stages of polymerisation, the mass acquired following monomer addition, during activation/deactivation cycles, makes up a large proportion of the polymer M_n. As a result, relatively large discrepancies arise between the M_n of growing polymer chains and thus larger Đ values are obtained at low monomer conversion. As the reaction progresses, polymer chains become more uniform and propagation has a smaller impact on the M_n of larger polymer chains. This is particularly relevant in the ATRP of acrylic monomers which possess large k_p values. The relatively uniform chain growth process provides the ability to target M_n simply by manipulation of the molar ratio of monomer to initiator at the start of polymerisation, similar to the case and benefits of traditional ionic "living" polymerisation; this has allowed chemists to controllably produce linear homopolymers, copolymers and polymers of various architectures with M_n > 100,000 g mol^{-1} using ATRP.[23]

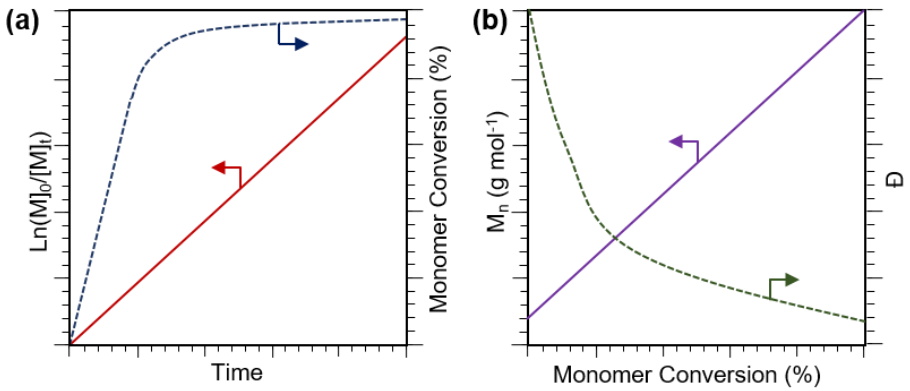

Figure 2.1 Graphical representations of the rate of monomer consumption and the evolution of the M_n distribution during Cu-RDRP. (a) Typical plots obtained for monomer conversion (dashed blue line) and ln([M]$_0$/[M]) (solid red line) *vs.* time. (b) The typical evolutions observed in the number average M_n (M_n, solid purple line) and polymer dispersity (Đ, dashed green line) with monomer conversion.

2.1.3 Varying Polymer Architecture Using Cu-RDRP

The degree of control exhibited over the polymerisation has allowed a wide range of polymer and copolymer architectures to be generated using Cu-RDRP. This has facilitated the generation of functional nanomaterials containing precise chemical structures with unique macroscopic behaviour; which has often made Cu-RDRP the synthetic tool of choice for the creation of bespoke (co)polymers for applications within fields such as bioengineering, medicine and nanotechnology.[24–29] Whilst any of the extensive list of (co)polymer architectures outlined in Chapter 1, Section 1.3.1.1, can be achieved using a well-controlled Cu-RDRP processes, the work in this thesis focuses on the generation of AB block copolymers and branched statistical copolymers. As a result, these copolymer architectures shall be discussed in more detail below. Should the reader be interested in the generation of alternative polymer architectures using Cu-RDRP, they are directed to an excellent review article which discusses this topic in detail.[29]

2.1.3.1 Block Copolymers

As discussed in Chapter 1, Section 1.3.1.1, the term ‘block copolymer’ refers to a copolymer in which comonomers are compartmentalised into discrete regions within a copolymer chain. The pseudo-living nature of Cu-RDRP along with its high end-group fidelity has made it a popular synthetic tool for the generation of block copolymers. As well as the ability to polymerise a broader range of monomer functionalities, Cu-RDRP offers a significant advantage over traditional “living” polymerisation techniques in that reactive end-group functionalities can be isolated and reinitiated with relative ease. There are two predominant synthetic routes used to generate block copolymers *via* Cu-RDRP. Both approaches involve growth from a polymeric species, often termed a macro-initiator. The key difference between these approaches involves the preparation of such macro-initiators (Figure 2.2).

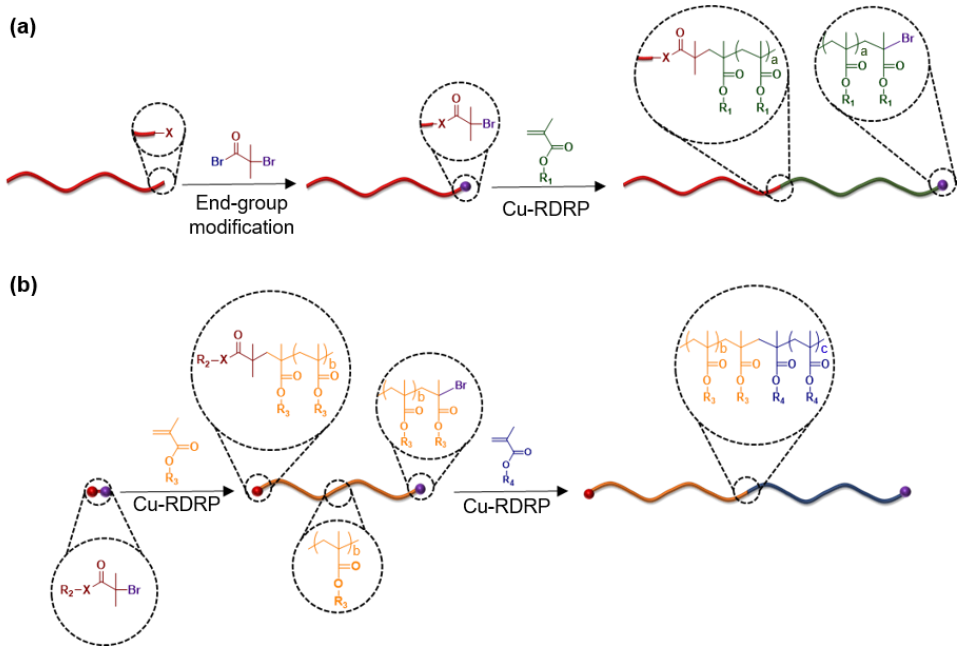

Figure 2.2 The predominant synthetic strategies used to generate block copolymers using Cu-RDRP. (a) Preparation of a macro-initiator *via* polymer end-group modification and subsequent growth of a secondary block using Cu-RDRP. (b) Utilising high end-group fidelity to generate a block copolymer *via* chain extension of a polymer, with a second monomer, using Cu-RDRP.

One approach involves the preparation of a macro-initiator *via* end-group modification of a polymer chain, usually generated in a separate polymerisation process, in order to equip it with a functional group capable of initiating Cu-RDRP. This enables such polymers to facilitate the growth of a second polymer block *via* Cu-RDRP (Figure 2.2a). One advantage of this approach is that it allows the combination of Cu-RDRP with polymer segments prepared using alternative polymerisation techniques. For example, this has allowed the preparation of macro-initiators from polymers prepared using step-growth, co-ordination, anionic and cationic vinyl polymerisation, ring-opening polymerisation, FRP and alternative RDRP techniques.[30–37] This approach has also been used to generate biopolymer conjugates *via* polymerisation from macro-initiators containing naturally-occurring polymers including polysaccharides, peptides, proteins and nucleic acids, using Cu-RDRP.[38] Furthermore, it can be adapted to generate ABA triblock copolymers using α,ω – homo bifunctional macro-initiators which facilitate chain growth in two directions.[39–42] The success of this approach relies heavily on the efficiency of the end-group modification. A low-efficiency end-group modification, which fails to equip all polymer chains with an initiating group, renders such chains incapable of facilitating Cu-RDRP. The presence of such "dead chains" can have drastic implications on the M_n targeting capabilities of subsequent polymerisations and can also require additional purification steps, such as dialysis, to remove unreacted polymer chains. End-group modification is therefore limited to either a small number of highly efficient coupling chemistries or require the use of excess reagents during end-group modifications.

Alternatively, polymers generated using Cu-RDRP that have retained their end-group functionality can also act as macro-initiators. Such macro-initiators can be used in a subsequent polymerisation of a second monomer, typically referred to as a chain extension, to generate block copolymers using Cu-RDRP (Figure 2.2b). Two crucial requirements for the synthesis of well-defined block copolymers are preservation of end-group functionality and an efficient (re)initiation/ cross-propagation process. Significant reductions in end-group fidelity have often been reported during ATRP at ≥ 60 % monomer conversion.[43,44] This has been attributed to the prevalence of undesirable side reactions including transfer to ligand and bimolecular termination reactions.[43] For example, analysis of the end-group fidelity during the ATRP of styrene at 90 °C showed that only 48 % of growing chains remained active at 92 % monomer conversion.[44] This significantly restricts the possibility of producing block copolymers using conventional ATRP and often requires polymerisations to be stopped at low monomer conversion in order to retain the active end-group responsible for facilitating the Cu-RDRP process. The development of alternative Cu-RDRP techniques include SET-LRP and SARA ATRP, which employ significantly lower amounts of the activating species in order to suppress the concentration of active radicals, have enabled the production of macro-initiators which retain quantitative end-group fidelity, even at high monomer conversions.[45,46] This has permitted the production of block and multi-block copolymers with precise control over the order, number, length and functionality of the component blocks.[45,47]

In general, when producing block copolymers using any RDRP technique, efficient re-initiation is essential to ensure that all macro-initiators undergo chain extension. The re-initiation efficiency is highly dependent on the monomer class of both the macro-initiator and the monomer selected for chain extension. It is therefore essential to follow a block order based on the reactivity of active chain-ends derived from each monomer. In Cu-RDRP, values of K_{eq} can be used to gauge macro-initiator end-group activity; this is typically dictated by a combination of electronic and steric effects and follows the order acrylonitrile > methacrylates > styrene ~ acrylates > acrylamides.[48] This typically hinders the chain extension of a macro-initiator with a monomer possessing higher activity. However, Cu-RDRP provides the unique ability to modify terminal alkylhalide end-group functionality *via* a halogen exchange reaction; this has allowed the efficient chain extension of relatively low activity acrylate-based macro-initiators with more active methacrylate monomers.[49,50] This unique ability to overcome block ordering constraints is one advantage of Cu-RDRP.

2.1.3.2 Branched Statistical Copolymers

The formation of branched copolymers *via* statistical Cu-catalysed reversible-deactivation radical copolymerisation (Cu-RDRcP) of monofunctional and bifunctional monomers (BFM) evolved logically from the 'Strathclyde Approach'[51–53] following its discovery shortly after the first reports of reversible deactivation radical copolymerisation (RDRcP) techniques emerged; as a result this techniques has often been coined 'A modified Strathclyde Approach'. The first synthesis of a branched polymer *via* copolymerisation of monofunctional and BFMs using RDRcP occurred in 2004 when Sherrington and co-workers reported the copolymerisation of MMA and ethylene glycol dimethacrylate (EGDMA) using both ATRP and group transfer polymerisation.[54] Since then, numerous branched copolymers have been reported using a variety of RDRP techniques, including ATRP,[55] RAFT,[56] nitroxide-mediated radical polymerisation[57] and reversible complexation mediated copolymerisation[58] as well as other polymerisation techniques such as ring-opening metathesis polymerisation (ROMP)[59] and the palladium-catalysed polymerisation of alkynes.[60]

The control afforded by RDRP techniques allows key features of the branched polymer architecture to be pre-determined prior to synthesis. RDRP techniques provide control over the number of repeat units per primary chain simply by increasing the concentration of monomer to initiator at the start of polymerisation ($[M]_0/[I]_0$). This has allowed the production of branched polymers containing from 10 to > 100 repeat units per primary chain. The combination of multiple primary chains result in the formation of high molecular weight branched polymers, with M_w > 100 kg mol^{-1} often reported;[61,62] these are significantly higher than those obtained for branched polymers produced *via* the "Strathclyde Approach". The extent of branching is dictated by the average number of BFMs incorporated per primary chain during copolymerisation and is dependent upon the relative concentrations of BFM and initiator at the start of polymerisation ($[B]_0/[I]_0$). Li and Armes studied the influence of $[B]_0/[I]_0$ on the molecular weight distributions of branched polymers isolated from the copolymerisation of 2-hydroxypropyl methacrylate (HPMA) and a disulphide-based dimethacrylate (DSDMA) using ATRP.[55] Increased M_w were observed as $[B]_0/[I]_0$ was increased from 0.00 – 0.95, due to a greater fraction of polymer chains which partake in branching reactions. Formation of an insoluble gel network occurred during copolymerisation where $[B]_0/[I]_0$ exceeded 1.00; this supported conclusions made by Wang and Zhu who conducted a similar ATRP study on the statistical copolymerisation of MMA and EGDMA.[63] Numerous groups have studied the critical $[B]_0/[I]_0$ ratio at which insoluble gel networks become unavoidable, commonly known as the theoretical gel point. This has been assessed both theoretically and experimentally and indicate that, as in the Strathclyde route, gelation can be avoided provided the number of BFMs per primary chain does not exceed unity.[56,64,65]

Significant research effort has focused on developing understanding of the branching process which occurs during statistical copolymerisation of monofunctional and BFMs. Bannister *et al.* studied the copolymerisation of HPMA and EGDMA using ATRP and identified that the copolymerisation proceeded in three stages (Figure 2.3).

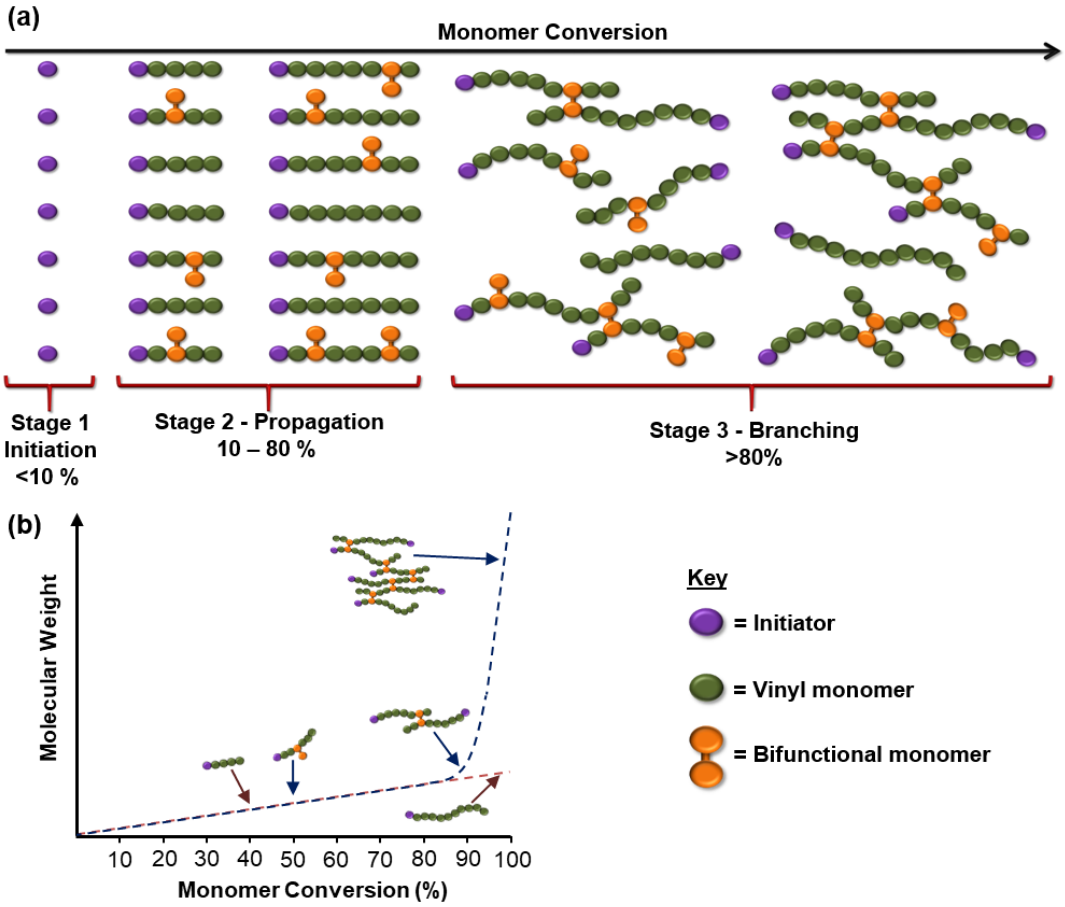

Figure 2.3 The evolution of branching during statistical RDRcP of monofunctional and bifunctional monomers. a) The stages of copolymerisation identified by Bannister et al. during the copolymerisation of HPMA and EGDMA by ATRP. b) Comparative illustrations of the evolution of M_w during linear homopolymerisation of monofunctional monomers (dashed red lines) and statistical copolymerisations of monofunctional and bifunctional monomers (dashed blue lines).

The initial stages of the copolymerisation of HPMA and EGDMA mimicked that of an ATRP conducted in the absence of EGDMA. Stage one involved activation and subsequent propagation of initiating moieties to form oligomers. During stage two, monofunctional and BFMs were statistically incorporated into propagating polymer chains, to produce low dispersity primary chains containing a pendant methacrylate group. The consumption of the pendant group was suppressed at low monomer conversion due to its low concentration relative to unreacted monomer. Consequently, during the early stages of polymerisation, the evolution of M_n with monomer conversion was in good agreement with that observed for a polymerisation conducted in the absence of a BFM. The polymerisation entered stage three as monomer conversion exceeded 70 %. At this point the M_w and dispersity deviated from those

obtained from linear polymerisations at similar monomer conversions. This occurred due to the presence of higher M_w species formed through coupling of primary chains *via* intermolecular branching reactions. Branching reactions became dominant at high monomer conversion (> 95 %) due to an increased relative concentration of the pendant vinyl group. As monomer conversion exceeded 95 % the polymerisation changed from a chain-growth to a pseudo-step-growth mechanism. This was evident from the exponential increase observed in both M_w and dispersity with monomer conversion which occurred due to statistical coupling of high M_w materials (Figure 2.3b).

The conclusions drawn by Bannister *et al.* were reinforced by a number of publications which reported the copolymerisation of a range of monofunctional and BFMs including methacrylates, acrylates, acrylamides and vinyl ethers using a range of RDRP techniques. Rosselgong and Armes later studied the copolymerisation of MMA and DSDMA using both ATRP and RAFT.[66] In this report it was demonstrated that the evolution of branching remained independent of the RDRP technique employed and provided further support of the statistical branching mechanism proposed previously. The use of DSDMA facilitated the reductive cleavage of all branch points by treatment of such branched copolymers with tributyl phosphine. Size exclusion chromatography (SEC) analysis before and after branch point cleavage revealed that branched polymers consisted of low dispersity primary chains, which resembled those produced from the polymerisation of MMA in the absence of DSDMA. This also demonstrated that the branching process has no detrimental effect on the control afforded by RDRP techniques.

Another crucial factor which influences the extent of branching during copolymerisation of monofunctional and BFMs is the concentration at which polymerisations are conducted. Armes and co-workers noted that soluble branched polymers could be obtained above the theoretical gel point ($[B]_0/[I]_0$ > 1.00) when polymerisations were conducted at low concentrations, even at exceptionally high monomer conversions (> 99 %).[56] The absence of gelation was attributed to a change in pendent methacrylate group consumption during polymerisation. Pendant methacrylate groups can be consumed either *via* intermolecular branching or intramolecular cyclisation reactions (Figure 2.4).

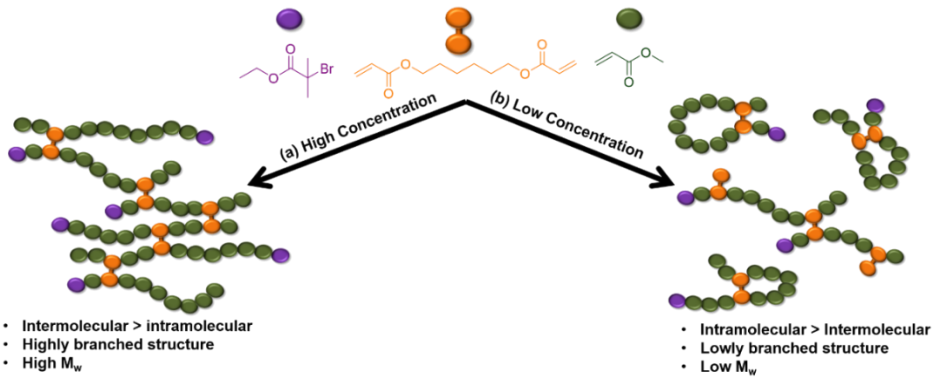

Figure 2.4 Impact of concentration on the nature of pendent methacrylate group consumption during copolymerisation. Illustration of the highly branched and lowly branched/ cyclised copolymer architectures generated during copolymerisations conducted at high (left) and low concentrations (right) respectively.

Intermolecular branching occurs when a propagating radical reacts with a pendent methacrylate group of another polymer chain, generating a branch point between the two primary chains. Intramolecular cyclisation occurs when both the reacting propagating radical and pendent methacrylate group belong to the same primary polymer chain, subsequently forming a cyclic structure within the polymer backbone. The ratio between intermolecular branching and intramolecular cyclisation has been studied theoretically and using both ^{1}H and ^{13}C nuclear magnetic resonance (NMR) spectroscopy.[67–69]

Rosselgong and Armes studied the statistical copolymerisation of MMA and DSDMA at various monomer concentrations using both ATRP and RAFT.[66] This work demonstrated that the extent of intramolecular cyclisation was highly dependent on the monomer concentration at which polymerisations were conducted. Intermolecular branching was favoured at high concentration due to increased proximity of polymer chains with their neighbours in solution. Consequently, intramolecular cyclisation was suppressed and intermolecular branching dominated consumption of pendant methacrylate groups. As a result, high M_w polymers with broad molecular weight distributions were obtained. In contrast, for polymerisations conducted at low monomer concentrations, consumption of pendent vinyl groups occurred predominantly by intramolecular cyclisation, resulting in low M_w, lightly branched and cyclic copolymer architectures. Consumption of pendent vinyl groups *via* intramolecular cyclisation increases the number of BFMs that can be tolerated within primary chains without any gelation. Soluble branched polymers containing an average of 5.00 DSDMA groups per primary chain were obtained from the RAFT copolymerisation of MMA and DSDMA conducted at 10 weight percent (wt %) solids content. Macroscopic gelation, however, was observed when polymerisations were attempted using as low as 1.60 and 0.95 equivalents of DSDMA per primary chain at 30 and 50 wt % solid contents respectively. These findings were supported in a publication by Zhu and co-workers.[70] In another publication, Rosselgong *et al.* showed that intramolecular cyclisation reactions can be suppressed by conducting

polymerisations at high monomer concentrations, which resulted in "near-ideal" branching behaviour.[71] Matyjaszewski and co-workers conducted a similar study which showed that intermolecular branching reactions can be completely suppressed when Cu-RDRcP is conducted under extreme dilution.[72]

2.1.4 RDRP of Hydrophobic Monomers in Polar Solvents

In recent years, there has been increasing interest in the RDRP of monomers within reaction media typically considered to be a poor solvent for the resulting polymer; many strategies have been developed to overcome polymer-solvent incompatibility. Percec and co-workers have demonstrated the ability to conduct SET-LRP of hydrophobic monomers in biphasic reaction mixtures to generate linear homopolymers of low dispersity with considerable control over M_n.[73–78] The biphasic nature of the solvent systems employed provided control over the levels of Cu(I) disproportionation, using a polar solvent phase, whilst maintaining polymer solubility within a water-immiscible non-polar phase. Additionally, polymerisation-induced self-assembly (PISA) has become established over recent years, facilitating the formation of amphiphilic block copolymers in solvents which are incompatible with one copolymer block segment;[79] growth of a solvent-incompatible second block drives the self-assembly of propagating polymer chains to form well-defined, sterically-stabilised block copolymer nanoparticles of varying size and morphology.[80–84] Whilst the majority of publications in this area rely on RAFT to facilitate RDRP, a wide range of research has been reported using PISA facilitated by Cu-RDRP processes. Alternatively, Gao and co-workers have used emulsion polymerisation to generate high M_w hyperbranched polymers *via* self-condensing vinyl polymerisation of water-immiscible acrylic and methacrylic inimers in aqueous emulsion.[85,86] Compartmentalisation of inimers within emulsion droplets has proved an effective technique to promote the formation of materials with higher M_w and greater degrees of branching than were produced in solution.[87]

Rannard and co-workers have previously reported the highly controlled nature of the Cu-RDRP of *n*-butyl methacrylate (*n*BMA) at elevated temperature in anhydrous methanol (MeOH; generally considered a poor solvent for the resulting polymer), to give *p*(*n*BMA) of controlled M_n and low dispersities ($Đ$ = 1.03 - 1.10).[88] These enhanced levels of control were attributed to two factors: a previously unreported upper critical solution temperature (UCST) and the impact of unreacted monomer on the solvent environment. Combined, these factors promoted *p*(*n*BMA) solubility in anhydrous MeOH at elevated temperatures and allowed polymerisations to remain as homogeneous mixtures throughout polymerisation. This technique has been used to generate a range of *p*(*n*BMA) architectures, including linear homopolymers, AB block copolymers, ABA triblock copolymers, branched statistical copolymers, branched statistical block copolymers and hyperbranched polydendrons.[89,90]

2.1.5 Chapter Aims

The synthesis of amphiphilic block copolymers was explored to develop a library of polymers which to study the generation of branched vinyl polymer nanoparticles *via* a co-nanoprecipitation strategy. This requires a robust RDRP process to be established which can facilitate the generation of well-defined linear homopolymers, amphiphilic block copolymers and branched statistical copolymers (Figure 2.5). Given its previous success, Cu-RDRP in anhydrous alcohols was selected. Specifically, this chapter aims to broaden the scope of hydrophobic monomers undergoing successful polymerisation *via* Cu-RDRP in anhydrous alcohol solvents to create a platform for later nanoparticle studies. In addition to those previously reported, methyl methacrylate (MMA), ethyl methacrylate (EMA), *tert*-butyl methacrylate (*t*BMA), *n*-hexyl methacrylate (*n*HMA), cyclohexyl methacrylate (CHMA), benzyl methacrylate (BzMA), 2-ethylhexyl methacrylate (EHMA), lauryl methacrylate (LMA) and stearyl methacrylate (SMA) were selected for polymerisation. Given the proposed role of unreacted monomer in the solvation of polymer chains, detailed studies were conducted in order to understand the impact of monomer on the solution properties of various polymerisation mixtures. Pyrene fluorescence emission spectroscopy was utilised to assess the relative polarity of homogeneous alcohol polymerisation mixtures across a range of methacrylate monomers and relate this to the controlled nature of Cu-RDRP in anhydrous MeOH or isopropyl alcohol (IPA) during linear polymerisations.

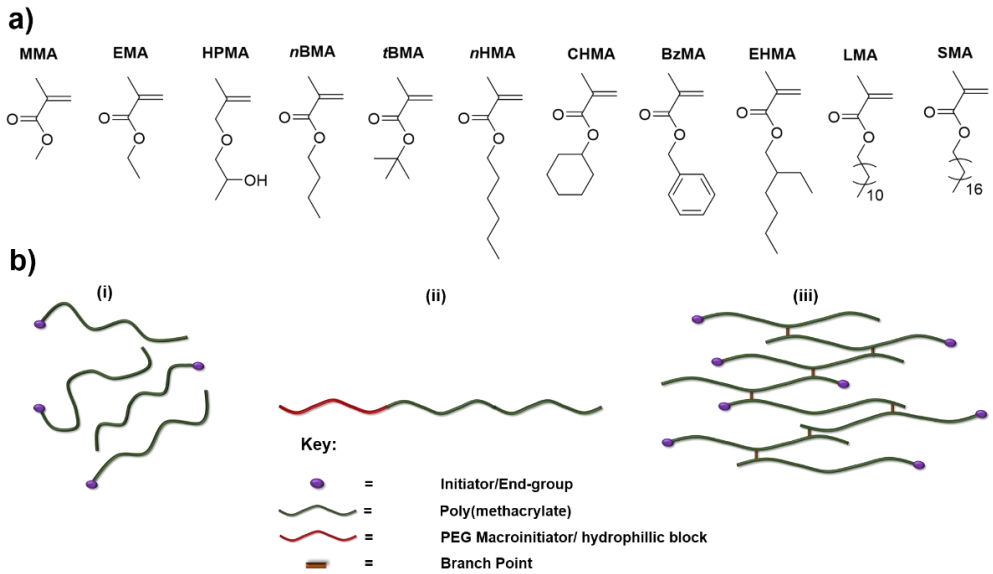

Figure 2.5 (a) Structural representation of hydrophobic methacrylate monomers chosen for Cu-RDRP in alcoholic media. (b) Schematic representation of polymer architectures targeted including: (i) linear homopolymers, (ii) amphiphilic block copolymers and (iii) branched statistical copolymers.

The generation of amphiphilic block copolymers was attempted *via* polymerisation from a macro-initiator with a range of hydrophobic monomers using Cu-RDRP. The statistical copolymerisation of hydrophobic methacrylates with a suitable BFM is the synthetic approach

selected to generate high M_w branched copolymers *via* Cu-RDRcP. This work aims to explore the possibility of creating branched statistical copolymers of hydrophobic monomers in anhydrous alcohols typically considered to be poor solvents for their resulting homopolymers. Triple-detection SEC analyses were utilised to evaluate the levels of branching which take place during copolymerisation. A number of reaction parameters were also studied to determine the key factors which govern the extent of branching occurring during Cu-RDRcP of hydrophobic methacrylates with a BFM in anhydrous alcohols.

2.2 Expanding the Scope of Cu-RDRP in Alcoholic Media

The success of the Cu-RDRP of *n*BMA in anhydrous MeOH has largely been attributed to the co-solvation of growing *p*(*n*BMA) chains by unreacted monomer. Whilst the control offered by this polymerisation technique combined with its facile synthetic and purification procedures has facilitated a substantial amount of research, little is yet known about the extent to which *n*BMA modifies reaction mixtures during polymerisation. With this in mind, along with the desire to expand the scope of this polymerisation process, a number of scoping studies were conducted to assess the impact of methacrylate monomers on the solution properties of polymerisation reaction mixtures.

2.2.1 Feasibility Studies

In order to increase the scope of hydrophobic methacrylate monomers which have been reported as polymerising in anhydrous MeOH, miscibility experiments were conducted; monomer concentrations similar to those used during Cu-RDRP were used. It was observed that MMA, HPMA, EMA, *n*BMA, *t*BMA, *n*HMA, CHMA, BzMA, EHMA and LMA all formed homogeneous methanolic solutions at a concentration of 50 wt % w.r.t. monomer, at both ambient and elevated temperatures (60 °C). When added to anhydrous MeOH, SMA remained an insoluble white powder at temperatures below its melting point (T_m = 18 – 20 °C) and formed a clear biphasic mixture when heated to 60 °C (Appendix, Figure A2.1). To facilitate the homogeneous polymerisation of SMA an alternative solvent, IPA, was selected due to its lower polarity index of 3.9 compared with 5.1 for MeOH.[91] On addition of SMA to anhydrous IPA at ambient temperature, rapid dissolution was observed and the mixture remained homogenous upon heating to 60 °C. Subsequent studies showed that IPA was a good solvent for all methacrylate monomers selected at a solvent concentration of 50 wt %.

The monomer co-solvency effect relies on the low polarity of methacrylate monomers to decrease the overall polarity of polymerisation mixtures, allowing retention of solubility of growing chains during polymerisation. Given the varied hydrophobicity of the monomers chosen for this study, it was expected that the extent of monomer co-solvency would vary between monomers thus allowing the homogeneous polymerisation of less polar methacrylate

monomers in alcoholic media. To evaluate the extent of monomer co-solvency in different monomer - alcohol mixtures, monomer polarities were quantified using fluorescence emission spectroscopy (Appendix Table A2.1). This was achieved by analysing the fluorescence emission of pyrene, in particular the relative intensities of the first (373 nm, I_1) and third (385 nm, I_3) vibrational bands, whilst dissolved in hydrophobic methacrylate monomers as well as for all miscible monomer – alcohol mixtures. This method is commonly used for the quantification of the polarity of organic solvents, with experimental I_1/I_3 ratios typically varying from 1.87 in protic solvents such as water to 0.58 in non-polar organic solvents such as hexane.[92] Experimental I_1/I_3 ratios obtained for pyrene (10 nM) dissolved in neat monomer showed that monomer polarity decreased in the order of HPMA (1.48), MMA (1.44), EMA (1.39), BzMA (1.39), *n*BMA (1.30), CHMA (1.27), *t*BMA (1.27), *n*HMA (1.23), EHMA (1.17), LMA (1.17), SMA (0.95) (Figure 2.6a (green bars) and bi). A general decrease in experimental I_1/I_3 ratios was observed from MMA to SMA, as the mass fraction of the lipophilic monomer side chain increased. Polar groups also had a significant impact on monomer polarity. The presence of the hydroxyl group in HPMA resulted in an I_1/I_3 higher than those obtained for MMA and EMA, which contain smaller lipophilic side chain weight fractions.

Experiments were conducted to understand the extent of monomer co-solvency upon the polarity of monomer – MeOH mixtures. An I_1/I_3 ratio of 1.53 was obtained for pyrene dissolved in anhydrous MeOH. A series of solutions were prepared containing pyrene dissolved in monomer – MeOH mixtures (50 wt %). Analysis of solution polarities gave I_1/I_3 ratios of 1.49, 1.49, 1.48, 1.46, 1.42, 1.41, 1.39, 1.37, 1.33 and 1.24 for methanolic solutions containing HPMA, MMA, EMA, BzMA, *n*BMA, *t*BMA, CHMA, *n*HMA, EHMA and LMA respectively (Figure 2.6a). Analyses were conducted using a range of common organic solvents. This showed that in cases where little difference was observed between monomer polarity and that of pure MeOH, the co-solvency effect had little impact on the polarity of polymerisation mixtures. This was particularly relevant for HPMA, MMA and EMA where monomer – MeOH mixtures showed comparable I_1/I_3 ratios to those obtained for pure MeOH. In contrast, monomer – MeOH mixtures containing less polar monomers saw a significant decrease in solution polarity, with the biggest impacts observed for LMA, EHMA and *n*HMA. It was not possible to measure the polarity of a SMA-MeOH mixture due to the bi-phasic nature of the monomer – MeOH mixture.

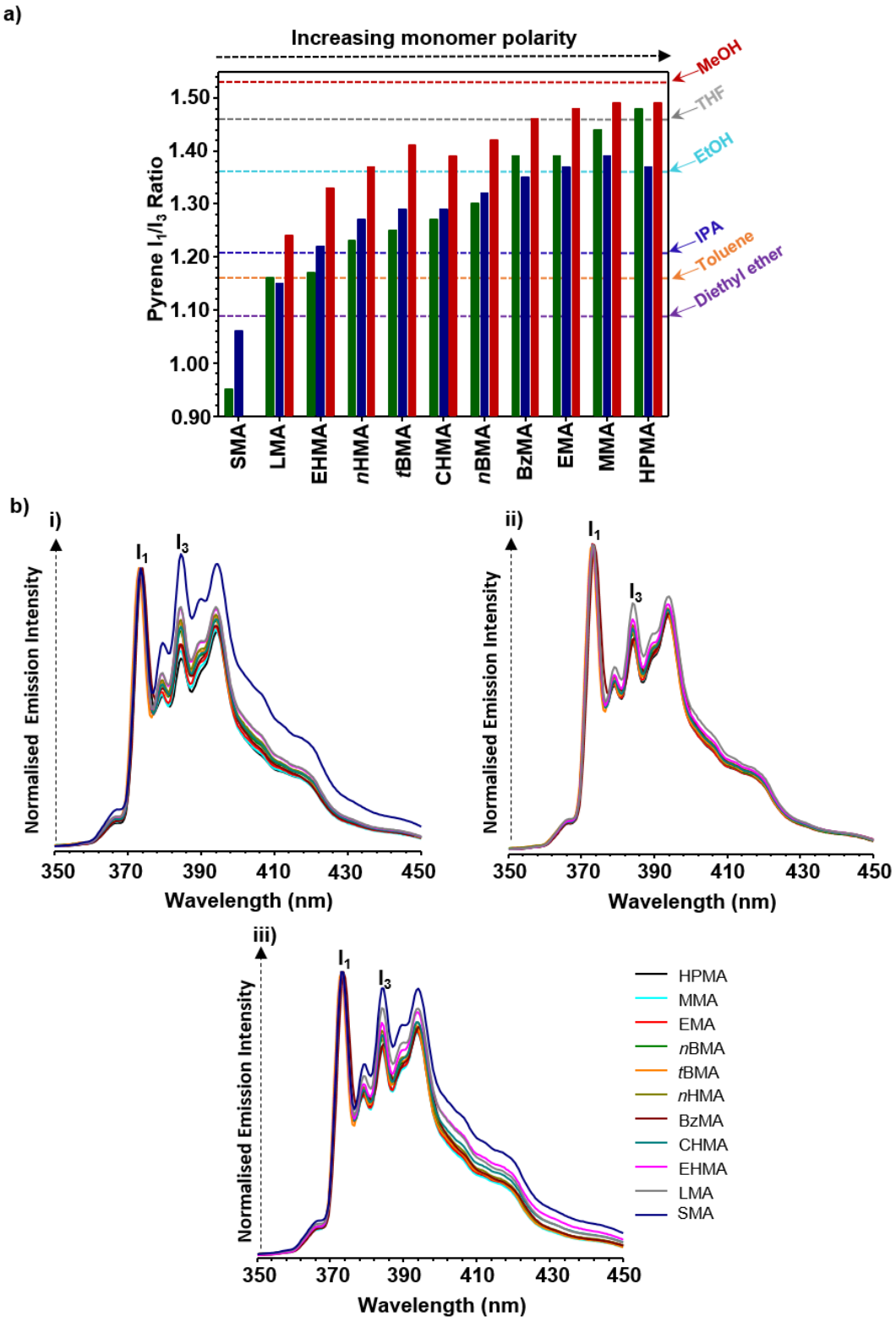

Figure 2.6. Evaluation of monomer polarity by fluorescence emission spectroscopy of pyrene in various monomer/ monomer-solvent environments. (a) Obtained I_1/I_3 ratios of pyrene dissolved in: MeOH (red dotted line), THF (grey dotted lines), ethanol (cyan dotted line), IPA (blue dotted line), toluene (orange dotted line), diethyl ether (purple dotted line), methacrylic monomers (green bars), methacrylic monomer-IPA mixtures (blue bars) and methacrylic monomer-MeOH mixtures (red bars). (b) Overlaid fluorescence emission spectra, normalised with respect to the emission at 373 nm (I_1), obtained for pyrene dissolved in: (i) methacrylic monomers (ii) methacrylic monomer-MeOH mixtures and (iii) methacrylic monomer-IPA mixtures.

To understand how the monomer co-solvency effect varies between different monomer-alcohol systems, a series of monomer – IPA solutions were also prepared containing pyrene (10 nM). The polarities of monomer – IPA solutions were also quantified by analysing the I_1/I_3 ratio of pyrene using fluorescence emission spectroscopy, and revealed values of 1.38, 1.37, 1.37, 1.35, 1.32, 1.29, 1.29, 1.27, 1.22, 1.15 and 1.06, for monomer – IPA solutions containing: MMA, EMA, HPMA, BzMA, *n*BMA, *t*BMA, CHMA, *n*HMA, EHMA, LMA and SMA respectively. In this study, the I_1/I_3 ratio for pyrene (10 nM) in pure IPA was recorded as 1.21. In contrast to the monomer – MeOH systems, solutions containing more polar monomers had lower I_1/I_3 ratios relative to that of the pure monomer as a result of the presence of IPA; whereas less polar monomers saw an increase in solution polarity on mixing with IPA. In all cases, I_1/I_3 ratios obtained for monomer – IPA solutions were 0.09 – 0.12 lower than those obtained for the same monomer – MeOH solutions. This consistent decrease confirmed that solution polarity could also be manipulated by exchanging MeOH for a less polar alcohol.

These results identified a variety of monomer – alcohol mixtures which form homogeneous solutions under typical Cu-RDRP conditions. Fluorescence emission spectroscopy proved a useful tool for quantification of both monomer and solution polarities and demonstrated that solution polarity is dependent on the nature of the methacrylate monomer chosen and thus highlighted the feasibility of extending the monomer co-solvency effect to a wider range of hydrophobic methacrylate monomers.

2.2.2 Linear Polymerisation of Hydrophobic Methacrylates in Anhydrous Alcohols

Linear polymerisations of hydrophobic methacrylates were conducted using Cu-RDRP in anhydrous MeOH and anhydrous IPA. Polymerisations were attempted using all of the hydrophobic monomers used in the monomer-alcohol miscibility and polarity studies discussed above. Firstly, this required the synthesis of a hydrophobic Cu-RDRP initiator which was soluble in both MeOH and IPA.

2.2.2.1 Synthesis of an Initiator for Cu-RDRP, Benzyl 2-Bromoisobutyrate

Benzyl 2-bromoisobutyrate (BzBiB) was selected as the initiator for Cu-RDRP polymerisation of hydrophobic methacrylates in anhydrous alcohols as it allowed quantification of the composition of polymerisation mixtures and the number average degree of polymerisation (DP_n) of the polymers subsequently formed. BzBiB was synthesised by esterification of benzyl alcohol with α-bromo isobutyrylbromide under an inert dry nitrogen atmosphere in the presence of triethyl amine (TEA) and 4-(dimethylamino)pyridine (DMAP), in anhydrous tetrahydrofuran (THF, Scheme 2.2).

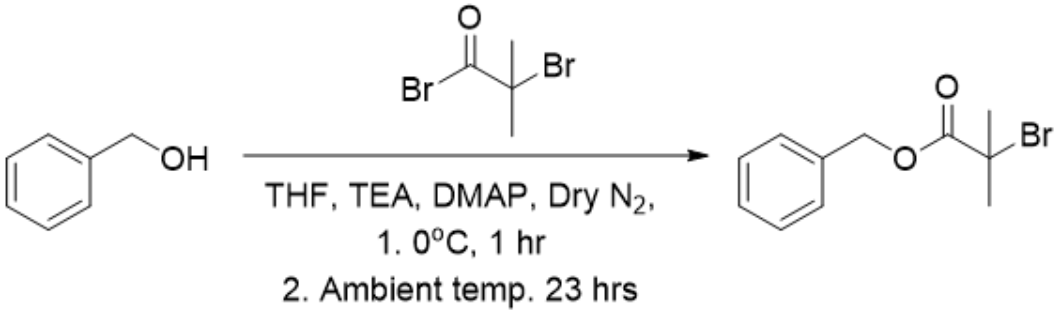

Scheme 2.2 Synthesis of benzyl 2-bromoisobutyrate (BzBiB).

The reaction was initiated by dropwise addition of a concentrated α-bromo isobutyrylbromide/ THF solution to a cooled solution of benzyl alcohol, DMAP and TEA in THF. The addition was completed using an ice bath in order to remove heat generated by the exothermic reaction. Once the addition was complete, the reaction was allowed to proceed at ambient temperature. After a total of 24 hours the reaction was quenched by addition of deionised H_2O, dried *in vacuo* and the product isolated in 81 % yield using silica gel column chromatography. The product was characterised using ^{1}H and ^{13}C NMR spectroscopy (Figures 2.7 and 2.8). The formation of the ester linkage was indicated by the chemical shift at ~170 ppm, characteristic of a carbonyl environment, in the ^{13}C NMR spectrum; this was supported by a absorption band at ~1750 cm^{-1} in the Fourier transform infrared (FTIR) spectrum.

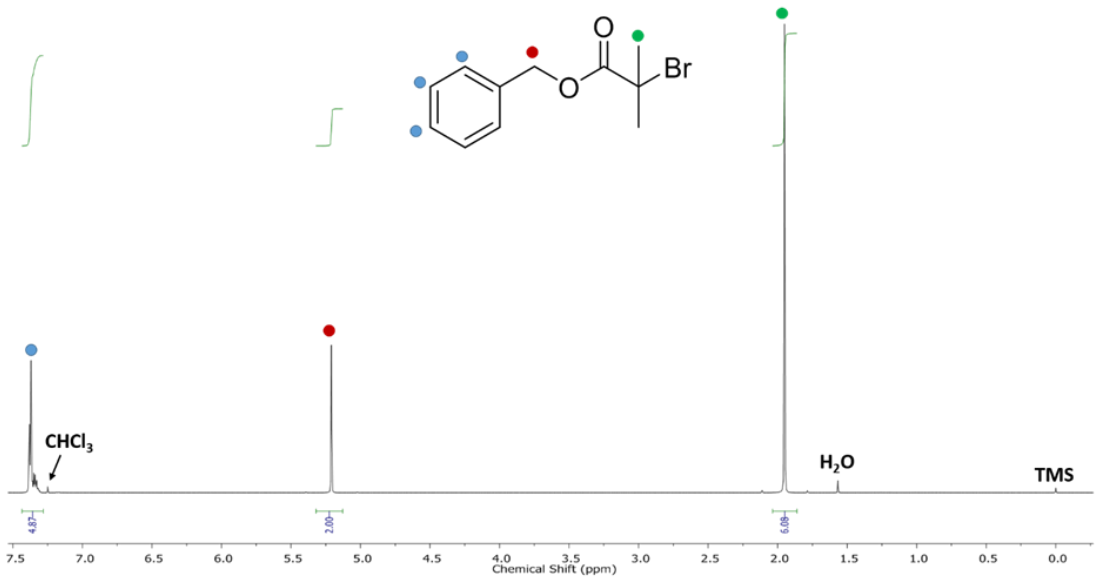

Figure 2.7 ^{1}H NMR (400 MHz, $CDCl_3$) spectrum of benzyl 2-bromoisobutyrate (BzBiB).

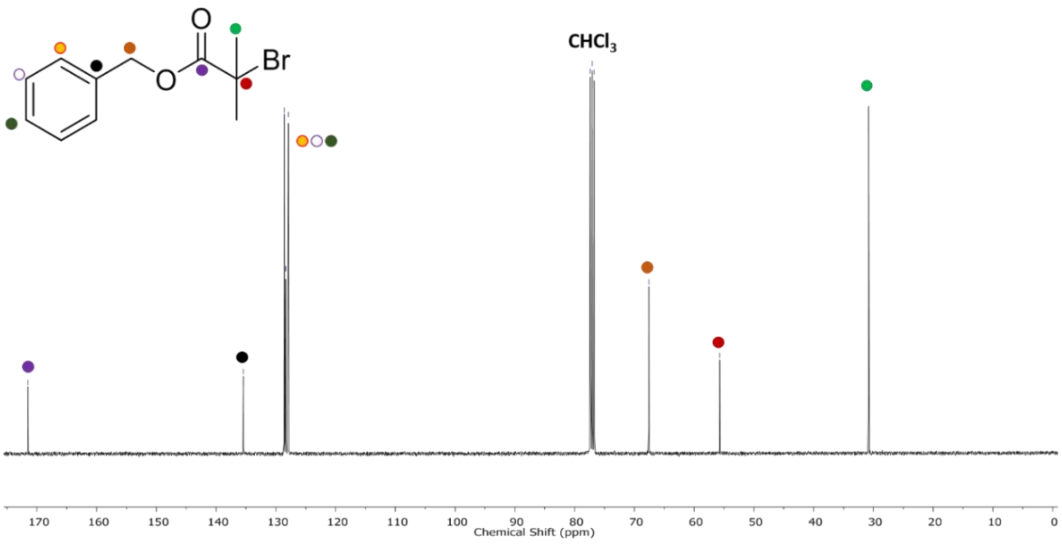

Figure 2.8 ^{13}C NMR spectrum (100 MHz, $CDCl_3$) of benzyl 2-bromoisobutyrate (BzBiB).

2.2.2.2 Cu-RDRP of Hydrophobic Methacrylates in Anhydrous Methanol

Homopolymerisations of hydrophobic methacrylate monomers were conducted using Cu-RDRP at 60 °C in anhydrous MeOH employing a Cu(I)Cl/ 2,2 – bipyridine (bpy) catalytic system (Scheme 2.3). Polymerisations targeted a DP_n of 60 monomer units, using an initial molar ratio of monomer: initiator: CuCl: bpy ($[M]_0$: $[I]_0$: $[Cu]_0$: $[bpy]_0$) of 60:1:1:2, at a MeOH concentration of 50 wt %. Polymerisations were allowed to proceed for 18 hours. Methanolic polymerisations were conducted using: MMA, EMA, *n*BMA, *n*HMA, CHMA, BzMA, EHMA and LMA. The polymerisations of SMA and *t*BMA were not attempted due to monomer-solvent immiscibility and previously reported unsuccessful polymerisations respectively.[90]

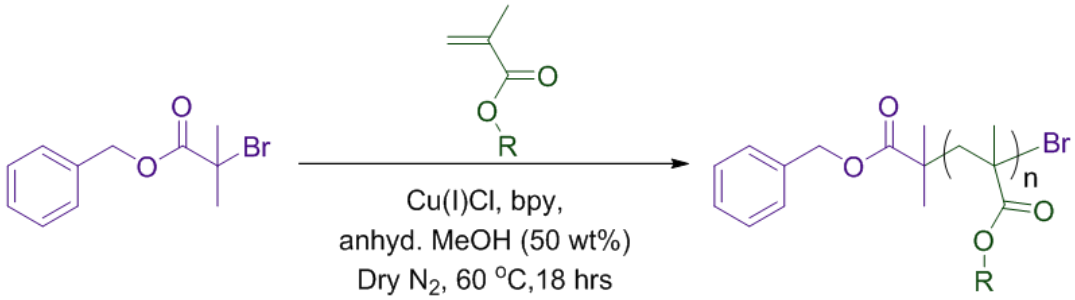

Scheme 2.3 Cu-RDRP of hydrophobic methacrylate monomers in anhydrous MeOH.

During initial stages of polymerisation all reactions appeared to proceed under controlled conditions, showing characteristic dark brown opaque homogeneous solutions commonly associated with Cu-RDRP. The polymerisations of MMA, EMA and *n*BMA remained as homogeneous solutions throughout the 18 hour polymerisation period until precipitation was observed upon cooling below 60 °C. The polymerisation of *n*HMA showed phase separation during polymerisation forming a biphasic polymerisation mixture containing an opaque dark

brown viscous polymer phase beneath a non-viscous, opaque dark brown liquid. Similar observations were made during the polymerisation of CHMA where the polymer phase formed an opaque brown solid, likely due to the glass transition temperature (T_g) of *p*(CHMA) exceeding the temperature of the reaction mixture. Conversely, BzMA, EHMA and LMA formed biphasic reaction mixtures within 3 hours of initiation. The contrasting homogeneities observed during polymerisation likely occurred due to combinations of monomer co-solvency and previously reported upper critical solution temperature (UCST) behaviour in MeOH.[93–95] In cases where polymers display UCST behaviour in MeOH, polymers remained solvated at elevated temperature despite the minimal monomer co-solvency effect at high conversion (Figure 2.9 bi). In contrast, whilst polymers which do not possess UCST behaviour in MeOH remain solvated during the early stages of polymerisation, depletion of the monomer concentration during polymerisation resulted in the onset of phase separation, as a diminished monomer co-solvency effect was no longer able to solvate growing polymer chains (Figure 2.9 bii).

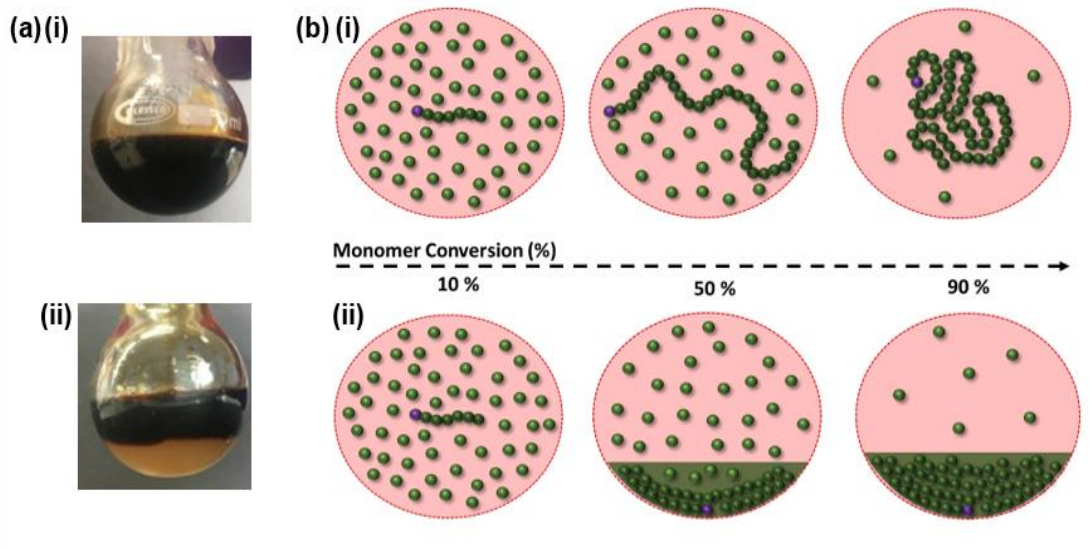

Figure 2.9 Comparison of polymerisation mixture homogeneity during Cu-RDRP of hydrophobic methacrylates in MeOH. (a) Photographs of exemplary (i) homogeneous (*p*(*n*BMA)) and (ii) biphasic (*p*(EHMA)) reaction mixtures after 18 hours. (b) Schematic representation of proposed co-solvency effects in (i) homogeneous and (ii) biphasic reaction mixtures.

After 18 hours polymerisations were terminated by exposure to air. This caused rapid poisoning of the $[Cu(I)(bpy)_2]Cl$ catalytic system, which was evident from a change in the colour of the polymerisation from an opaque dark brown to a transparent green solution due to the change in oxidation state of the Cu. Biphasic reaction mixtures were diluted with $CDCl_3$ until a homogeneous solution was formed. Polymers were then purified *via* a two-stage process: 1) The catalytic system was removed by passing the diluted reaction mixture through a neutral alumina column using either $CHCl_3$ or THF as the mobile phase, 2) Unreacted monomer, free ligand and initiator residues were removed *via* precipitation. Polymer solutions

were concentrated *in vacuo* and precipitated three times using cold MeOH or cold petroleum ether, depending on the nature of the polymer (see Chapter 6, Section 6.3.1.8). Polymers were then dried *in vacuo* at 40 °C for 48 hours to ensure complete solvent removal.

Selection of the BzBiB initiator allowed characterisation of polymerisation mixtures and purified polymers by ^{1}H NMR spectroscopy (see Chapter 6, Section 6.3.1.7). Analysis of polymerisation mixtures prior to initiation permitted determination of the ratio of monomer to initiator at the start of polymerisation ($[M]_0/[I]_0$) and quantification of monomer conversion (conv.) once polymerisations were complete; this subsequently allowed estimation of the theoretical number-average molecular weight (M_n theory). ^{1}H NMR analysis of purified polymers was also used to determine the purity, DP_n and subsequently the number-average molecular weight ($M_{n(NMR)}$) of purified polymers (Table 2.1). Analysis showed that all polymerisations had achieved high monomer conversion (92 - > 99 %) after 18 hours. This was somewhat surprising, especially in the polymerisations of *n*HMA, CHMA, BzMA, EHMA and LMA, given the observed phase separation which had occurred during polymerisation.

Table 2.1 Cu-RDRP of hydrophobic methacrylates in anhydrous methanol at 60 °C.

	^{1}H NMR ($CDCl_3$)						**TD-SEC (THF/TEA)[e]**		
	$[M]_0/[I]_0$[a]	**Conv (%)[b]**	**M_n Theory (g mol^{-1})[c]**	**DP_n[d]**	**M_n (g mol^{-1})**	**IE (%)**	**M_w (g mol^{-1})**	**M_n (g mol^{-1})**	**Đ**
p(MMA)$_{67}$	60	99	6 300	67	7 000	90	11 000	9 800	1.12
p(EMA)$_{64}$	60	97	6 900	64	7 600	91	10 800	8 900	1.21
p(*n*BMA)$_{74}$	62	99	9 100	74	10 800	84	13 000	11 600	1.12
p(*n*HMA)$_{67}$	60	>99	10 500	67	11 700	90	15 800	13 600	1.16
p(CHMA)$_{66}$	60	97	10 000	66	11 400	88	15 600	13 100	1.19
p(BzMA)$_{*}$	60	97	10 500	-*	-*	-*	17 000	13 700	1.24
p(EHMA)$_{65}$	60	99	12 000	65	13 100	92	18 400	14 500	1.26
p(LMA)$_{80}$	60	92	14 300	80	20 600	69	41 400	26 000	1.59

[a]Calculated by ^{1}H NMR spectroscopy ($CDCl_3$, 400 MHz) of polymerisation mixture at t = 0. [b]Calculated by ^{1}H NMR spectroscopy of polymerisation mixture at t = final. [c]M_n theory = (($[M]_0/[I]_0$ x Mr(monomer)) x conv.) + Mr(Initiator)) [d]Calculated by ^{1}H NMR spectroscopy of the purified polymer: M_n = (DP_n x Mr(monomer)) + Mr(initiator). [e]Calculated by TD-SEC (triple detection size exclusion chromatography) using THF/TEA mobile phase (98/2 v/v %) at 35 °C using a flow rate of 1 mL min^{-1}. *Characterisation of *p*(BzMA)$_{60}$ by ^{1}H NMR spectroscopy was not possible due to overlap between initiator and monomer resonances.

With the exception of *p*(LMA), ^{1}H NMR analysis of purified polymers showed good agreement between experimental and theoretical number-average molecular weights, with initiation efficiencies typically varying from 84 – 92 %. However, the methanolic Cu-RDRP of LMA demonstrated poor M_w targeting capability, with a significant discrepancy between the theoretical and experimental molecular weights obtained by ^{1}H NMR spectroscopy. The

removal of unreacted monomers, free ligand and initiator residues were confirmed by the absence of such resonances in the ^{1}H NMR spectra of the polymers after their precipitation.

Polymers were also characterised using triple-detection size exclusion chromatography in THF/TEA (98 / 2 v/v %) which showed mono-modal chromatograms for all polymers, again with the exception of *p*(LMA). Polymers possessed narrow molecular weight distributions ($Đ$ = 1.12 – 1.26) characteristic of those typically obtained by Cu-RDRP (Figure 2.10). In contrast, the TD-SEC (triple detection size exclusion chromatography) chromatogram obtained for *p*(LMA) contained a broad molecular weight distribution ($Đ$ = 1.59) and showed a low molecular weight shoulder likely due to termination of growing chains during polymerisation (Figure 2.10 (h)). It is possible that the occurrence of phase separation may have isolated some growing polymer chains during the early stages of polymerisation, leading to an increase in the dispersity of the *p*(LMA) sample obtained *via* the Cu-RDRP of LMA at 60 °C in anhydrous MeOH.

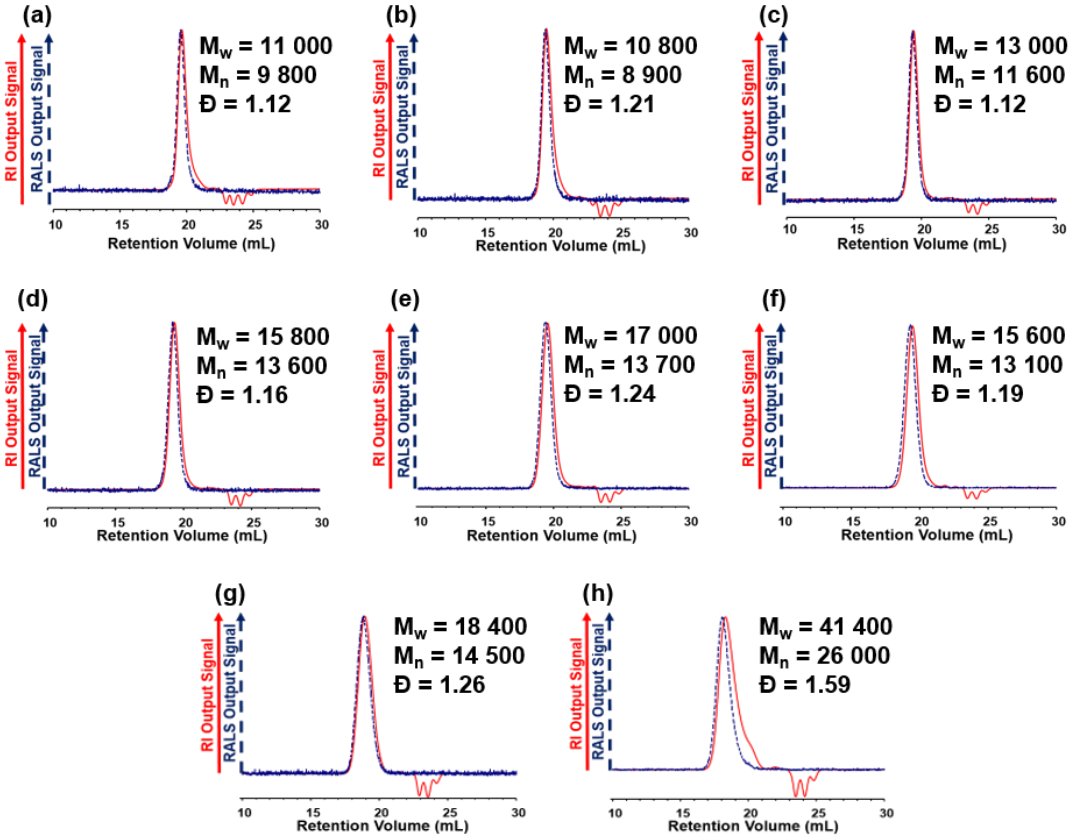

Figure 2.10 Refractive index (RI, red solid lines) and right-angle light scattering (RALS, blue dotted lines) chromatograms obtained by TD-SEC of polymers generated *via* Cu-RDRP at 60 °C in methanol. (a) *p*(MMA), (b) *p*(EMA), (c) *p*(*n*BMA), (d) *p*(*n*HMA), (e) *p*(BzMA), (f) *p*(CHMA), (g) *p*(EHMA), (h) *p*(LMA).

To summarise, Cu-RDRPs of MMA, EMA, *n*BMA, *n*HMA, CHMA, BzMA and EHMA in anhydrous MeOH at 60 °C were successful, therefore this approach offers a new synthetic

route for the generation of linear homopolymers with the ability to target M_n whilst maintaining a low dispersity. This is somewhat surprising given that polymerisations were conducted in a solvent typically considered to be an anti-solvent for the resultant polymers. Polymerisation homogeneity was highly monomer dependent as the polymerisations of MMA, EMA and *n*BMA remained homogeneous throughout polymerisation, whilst phase separation occurred during the polymerisations of *n*HMA, CHMA, BzMA and EHMA. In contrast, the Cu-RDRP of LMA lacked the control typically associated with an RDRP process and was therefore considered an unsuitable approach for the synthesis of *p*(LMA). Further studies are required to understand the impact of polymerisation induced phase separation on Cu-RDRP.

2.2.2.3 Kinetics Studies of the Cu-RDRP of nHMA in Anhydrous Methanol

As the role of phase separation during polymerisation remained unclear, kinetic studies were conducted in order to determine the impact of phase separation on the rate of formation and molecular weight distribution of polymer chains within a biphasic polymerisation. The Cu-RDRP of *n*HMA in anhydrous MeOH was selected as a model biphasic reaction mixture and their synthesis was conducted at a $[M]_0$:$[I]_0$:$[Cu]_0$:$[bpy]_0$ molar ratio of 60:1:1:2 and a MeOH concentration of 50 wt % (Scheme 2.4).

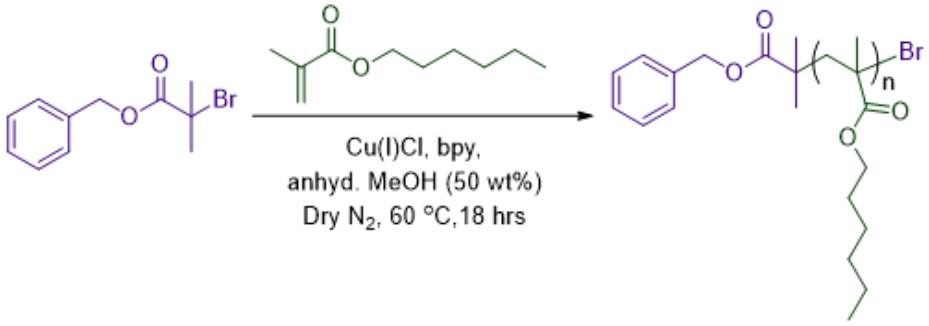

Scheme 2.4 Cu-RDRP of *n*HMA in anhydrous methanol at 60 °C.

The onset of phase separation made it difficult to obtain homogeneous aliquots of the reaction mixture using traditional methods of sampling of the reaction throughout polymerisation. To combat this, an experiment was designed to conduct the Cu-RDRP of *n*HMA in parallel reaction flasks, allowing for the isolation of heterogeneous samples at various time points throughout the polymerisation. To achieve this, a large scale Cu-RDRP of *n*HMA (25.0 g) was initiated and large aliquots (ca. 2 mL) were immediately transferred into separate reaction flasks under N_2. The reaction flasks were sealed and placed in an oil bath at 60 °C. Reaction flasks were removed at set time intervals and quenched by deactivation of the catalytic system using rapid cooling, dilution and exposure to oxygen. Reaction mixtures remained homogeneous during the early stages of polymerisation however, after 7 hours the onset of polymerisation induced phase separation occurred, resulting in the formation of a biphasic

reaction mixture containing a dark brown, non-viscous solvent phase resting above a dark brown, viscous polymer layer.

The use of parallel reaction flasks allowed kinetic sampling of polymerisation beyond the onset of phase separation. Biphasic samples were diluted with $CDCl_3$, in order to re-dissolve the polymer phase whilst simultaneously ensuring deactivation of the catalytic system, allowing determination of monomer conversion by ^{1}H NMR spectroscopy. Samples were then purified by passing the diluted solutions over neutral alumina to remove the catalytic system and subsequently precipitating into cold MeOH. Analysis of data obtained by ^{1}H NMR showed that the polymerisation had achieved near-quantitative monomer conversion after 18 hours (>99 %).

Kinetic plots were constructed using ^{1}H NMR data obtained throughout the polymerisation (Figure 2.11). Analysis of monomer conversion *vs.* time indicated that the polymerisation obeyed first order kinetics with respect to *n*HMA; this was confirmed when a linear plot was obtained following replotting of kinetic data in accordance with the first order integrated rate law. A plot of $\ln([M]_0/[M])$ *vs.* time demonstrated that the Cu-RDRP of *n*HMA in anhydrous MeOH proceeded with an apparent propagation rate constant of 5.34×10^{-3} min^{-1} at 60 °C. The fact that first order kinetics were obeyed throughout polymerisation demonstrated a constant radical concentration thus indicating that undesirable side reactions, such as termination, are negligible throughout this polymerisation. The final homogeneous sample of the polymerisation was obtained after 7 hours, shortly before the onset of phase separation, at which point the polymerisation had achieved 92 % monomer conversion. Beyond this point, the onset of phase separation had little effect on the rate of polymerisation which is somewhat surprising given the decreased mobility of growing chains.

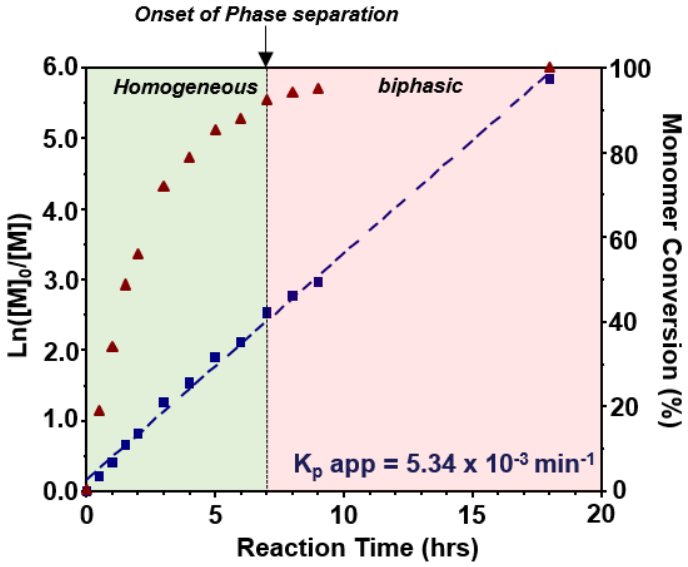

Figure 2.11 Monitoring of the Cu-RDRP of *n*HMA in anhydrous MeOH at 60 °C using ^{1}H NMR spectroscopy. Plots of monomer conversion (red triangles) and $\ln([M]_0/[M])$ (blue squares) *vs.* time.

The use of parallel reaction flasks allowed isolation of purified samples of *p*(*n*HMA) during polymerisation and allowed the evolution of the *p*(*n*HMA) molecular weight distribution to be studied using TD-SEC (Figure 2.12). A general increase in M_w was observed (Figure 2.12a), indicated by polymer elution at shorter retention volumes as the polymerisation proceeded. A plot of both $M_{n(\text{TD-SEC})}$ and $M_{n(\text{NMR})}$ *vs.* monomer conversion demonstrated linear increases in M_n with monomer conversion which is typical of a well-controlled RDRP (Figure 2.12b). The M_n obtained were slightly higher than expected for each of the given time points, likely due to termination of active radical species during establishment of the ATRP equilibrium; initiator efficiencies of 80 and 81 % were determined by TD-SEC and ^{1}H NMR spectroscopy respectively. Further analysis of the evolution of the molecular weight distribution throughout polymerisation showed a characteristic reducation in Đ with monomer conversion. Đ decreased from 1.36 to 1.18 as monomer conversion increased from 19 to >99 %.

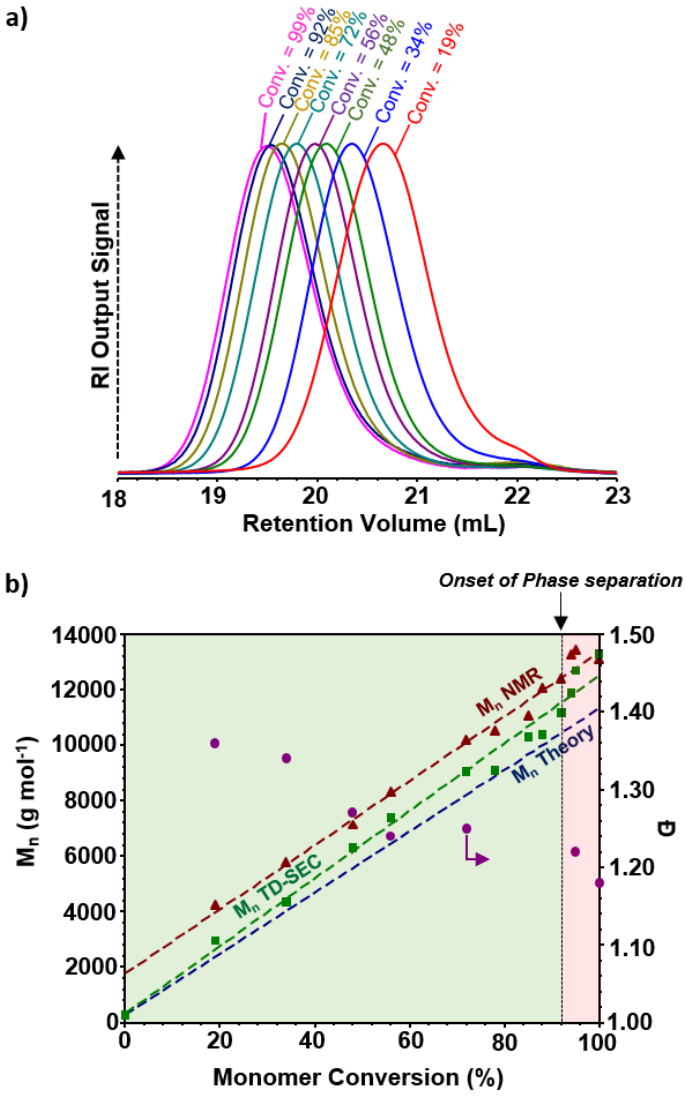

Figure 2.12 Analysis of the evolution of the molecular weight distribution during the Cu-RDRP of *n*HMA in anhydrous MeOH using TD-SEC. a) Overlaid RI traces for samples of *p*(*n*HMA) obtained at given monomer conversions. b) Plot of M_n determined by both TD-SEC and ^{1}H NMR *vs.* monomer conversion.

Analysis of the molecular weight distribution throughout polymerisation further substantiates the controlled nature of the Cu-RDRP of *n*HMA in anhydrous MeOH at 60 °C. Perhaps what is most surprising is the negligible impact that polymerisation-induced phase separation has on both the rate of polymerisation and the evolution of the molecular weight distribution. It is likely that any negative impact is diminished due to its occurrence during the latter stages of polymerisation (~ 90 % monomer conversion). As a result, growing chains have little opportunity to deviate from the trajectory taken during polymerisation under homogeneous conditions. It is also likely that residual monomer is soluble and can therefore partition into the polymer phase. It is also important to mention that the dark brown colour observed is highly indicative that both $[Cu(bpy)_2]^+$ and $[Cu(bpy)_2]^{2+}$ species are present within the polymer phase formed; it is therefore possible that the RDRP process can continue unhindered following the onset of polymerisation-induced phase separation.

Although biphasic polymerisations of *n*HMA, CHMA, and EHMA resulted in the formation of linear homopolymers with predetermined M_n whilst maintaining low dispersity between polymer chains, the polymerisation of LMA did not exhibit such control. Whilst the kinetic studies described above provide a detailed insight into the Cu-RDRP of *n*HMA at 60 °C in anhydrous MeOH, further studies are required to determine the impact of the onset of polymerisation-induced phase separation during the Cu-RDRP of other hydrophobic methacrylate monomers. It is possible that, in cases where phase separation occurs during the early stages of polymerisation, it allows significant deviation of the fate of propagating chains from that which would have occurred under a homogeneous, well-controlled RDRP process. In cases such as this, polymerisations may require an alternative solvent environment which could delay, or even prevent polymerisation-induced phase separation.

2.2.2.4 Cu-RDRP of Hydrophobic Methacrylates in Isopropyl Alcohol

In an attempt to delay or perhaps even prevent the onset of phase separation, a number of Cu-RDRP syntheses were conducted in anhydrous IPA for a subset of hydrophobic methacrylate monomers (Scheme 2.5). It was expected that conducting polymerisations within a less polar polymerisation mixture would provide a better solvent environment for hydrophobic propagating chains. Linear homopolymerisations of MMA, *t*BMA, CHMA, LMA and SMA were conducted at a total solids concentration of 50 wt % in anhydrous IPA, targeting a DP_n of 60 monomer units. MMA, CHMA and LMA were selected due to their contrasting phase behaviour during Cu-RDRP in anhydrous MeOH, representing successful homogeneous, successful biphasic and unsuccessful biphasic polymerisations respectively. Polymerisations of *t*BMA and SMA, which had not been attempted in anhydrous MeOH due to previously

reported unsuccessful polymerisation and monomer - MeOH immiscibility, were also attempted in anhydrous IPA.

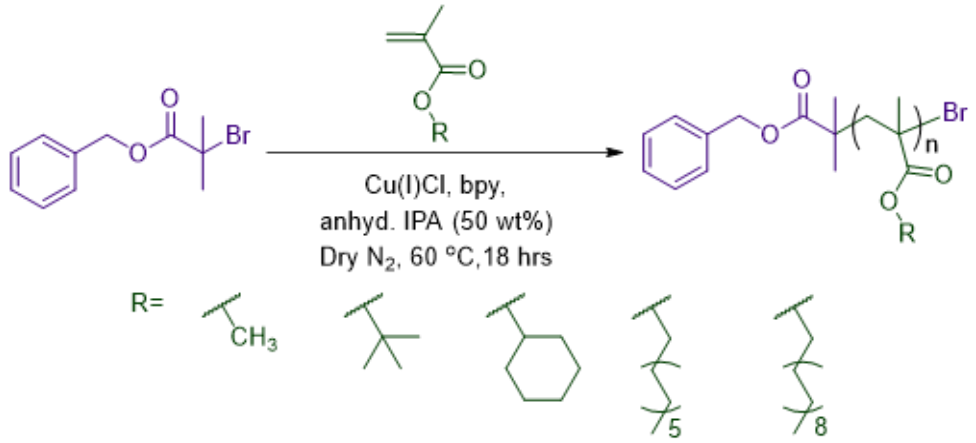

Scheme 2.5 Cu-RDRP of hydrophobic methacrylate monomers in anhydrous IPA.

All polymerisations and subsequent purification processes were conducted in accordance with those used for the generation of linear homopolymers *via* methanolic Cu-RDRP, described above. As was observed during Cu-RDRP in anhydrous MeOH, reaction mixtures showed varied phase behaviours during polymerisation. The polymerisations of MMA and *t*BMA remained homogeneous whilst, although they may have initially appeared homogeneous, phase separation occurred during polymerisations of CHMA, LMA and SMA within 3 hours of initiation. Despite these contrasting phase behaviours, ^{1}H NMR analysis of reaction mixtures after 18 hours showed that all polymerisations had achieved high monomer conversion (88->99 %). Polymers were purified *via* flash column chromatography over neutral alumina, subsequently precipitated into a suitable anti-solvent, and then dried *in vacuo* at 40 °C for 48 hours, facilitating characterisation using ^{1}H NMR spectroscopy and TD-SEC (Table 2.2).

Table 2.2 Cu-RDRP of hydrophobic methacrylates in anhydrous IPA at 60 °C.

	^{1}H NMR						**TD-SEC (THF/TEA)[e]**		
	$[M]_0$ / $[I]_0$[a]	**Conv. (%)[b]**	**M_n Theory (g mol^{-1})[c]**	**DP_n[d]**	**M_n (g mol^{-1})**	**IE (%)**	**M_w (g mol^{-1})**	**M_n (g mol^{-1})**	**Đ**
p(MMA)$_{70}$	60	>99	6 300	70	7 300	86	11 200	55 000	1.16
p(*t*BMA)$_{59}$	60	88	7 800	59	8 700	91	14 300	10 000	1.43
p(CHMA)$_{68}$	60	99	10 300	68	11 700	88	16 400	13 000	1.26
p(LMA)$_{66}$	60	97	15 100	66	17 000	89	24 400	17 800	1.37
p(SMA)$_{67}$	61	99	20 700	67	23 000	90	35 500	25 000	1.53

[a]Calculated by ^{1}H NMR spectroscopy of polymerisation mixture at t = 0. [b]Calculated by ^{1}H NMR spectroscopy of polymerisation mixture at t = final. [c]M_n Theory = (([M]$_0$/[I]$_0$ x Mr(monomer)) x conv.) + Mr(Initiator)) [d]Calculated by ^{1}H NMR spectroscopy of the purified polymer: M_n = (DP_n x Mr(monomer)) + Mr(initiator). [e]Calculated by TD-SEC using THF/TEA mobile phase (98/2 v/v %) at 35 °C using a flow rate of 1 mL min^{-1}.

End-group analyses were conducted using ^{1}H NMR spectroscopy and showed good agreement between theoretical and experimental number-average molecular weights. Initiation efficiencies ranged from 86 - 91 %, highlighting a strong M_w targeting capability of Cu-RDRP in anhydrous IPA. Molecular weight distributions were obtained using TD-SEC and displayed monomodal molecular weight distributions for all polymers with number-average molecular weights obtained by TD-SEC showing consistent agreement with those determined by ^{1}H NMR spectroscopy (Table 2.2). The absence of a low molecular weight shoulder in any of the RI chromatograms, as had been observed for *p*(LMA) obtained from Cu-RDRP in anhydrous MeOH, also indicated minimal chain termination during the early stages of polymerisation.

Despite the M_n targeting capabilities shown, some polymers generated using Cu-RDRP in anhydrous IPA contained broad molecular weight distributions. The Đ values of 1.43, 1.37 and 1.53 obtained for *p*(*t*BMA), *p*(LMA) and *p*(SMA) respectively were higher than those typically expected of a well-controlled RDRP process (Đ ≤ 1.30). This implies that in these cases, although Cu-RDRP in anhydrous IPA provides control over the DP_n of the polymers formed, the RDRP process is less effective in preventing undesirable side reactions, such as chain termination and/or chain transfer, than is typically experienced during Cu-RDRP in anhydrous MeOH. Many factors determine the level of control within Cu-RDRP, not least factors including monomer type, catalyst solubility and reaction homogeneity. It is therefore not sensible to directly compare the polymerisation of one monomer in anhydrous IPA with that of another monomer in anhydrous MeOH. For this reason, in order to understand the impact of exchanging the alcohol in which Cu-RDRP is conducted, direct comparisons between such polymerisations is required.

2.2.2.5 Comparison of Cu-RDRP in Anhydrous MeOH and Anhydrous IPA

The anhydrous MeOH and anhydrous IPA polymerisations of MMA, CHMA and LMA were compared due to their varying phase behaviours under these conditions (Figure 2.13). Analysis of the refractive index and right-angle light scattering chromatograms obtained by TD-SEC showed that the change in solvent had minimal impact on the overall polymer molecular weight distribution for *p*(MMA) and *p*(CHMA). Although a slight broadening was observed in both the RI and RALS chromatograms, accompanied by increased Đ values, for MMA and CHMA polymers obtained from anhydrous IPA polymerisations. It is important to note that whether conducted in anhydrous MeOH or anhydrous IPA, polymerisations of MMA and CHMA proceeded as homogeneous and biphasic polymerisations respectively, therefore it appeared that reaction mixture homogeneity had little impact on the control exhibited during Cu-RDRP. The slight broadening of the molecular weight distribution on switching from anhydrous MeOH to anhydrous IPA has previously been reported for the Cu-RDRP of *n*BMA

and had been attributed to the polymer conformation within a poor solvent environment.[88] Whilst this hypothesis can reasonably be applied to the polymerisations described here, it is also likely that a change in the reaction solvent would impact the RDRP equilibrium and thus affect the levels of control exhibited during polymerisation.

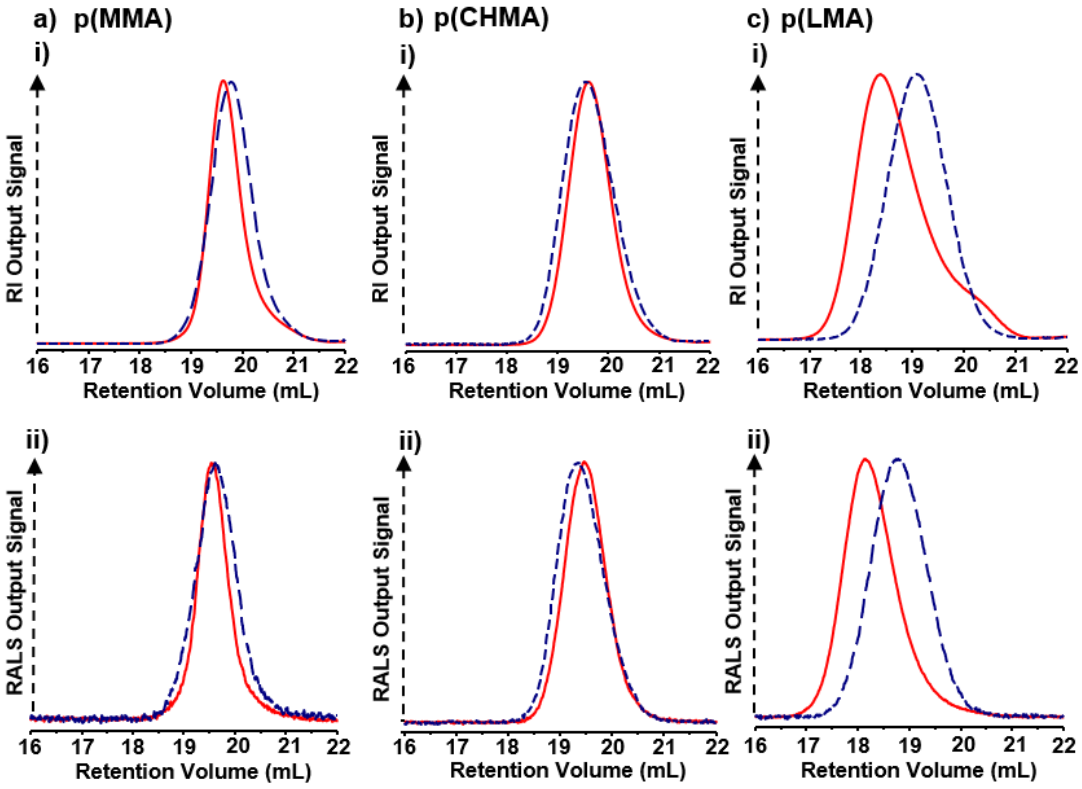

Figure 2.13 Molecular weight distributions of a) *p*(MMA), b) *p*(CHMA) and c) *p*(LMA) generated by Cu-RDRP in MeOH (red lines) and IPA (blue dotted lines). (i) Refractive index and (ii) right angle light scattering chromatograms obtained by TD-SEC in THF/TEA (92/2 v/v %) at a flow rate of 1 mL min^{-1}.

In contrast, considerable differences were observed between the molecular weight distributions of *p*(LMA) obtained by polymerisations in the different solvents (Figure 2.13, ci + ii). The polymerisation of LMA in MeOH yielded a polymer containing a broad molecular weight distribution (Đ = 1.59) with very low initiator efficiencies ($IE_{(TD\text{-}SEC)}$ = 55 %). Furthermore, the presence of a low molecular weight shoulder in the RI chromatogram (Figure 2.13ci - red line) demonstrated a lack of control during the polymerisation of LMA in anhydrous MeOH and suggests a level of termination during the early stages of polymerisation, possibly due to the onset of phase separation. Anhydrous IPA provided an improved environment for LMA polymerisation under these conditions ($IE_{(TD\text{-}SEC)}$ = 89 %) and examination of the RI chromatogram (Figure 2.13ci - blue dotted line) did not show the low molecular weight shoulder observed in MeOH reactions. It is possible that switching to a less polar reaction mixture may delay the point at which polymerisation-induced phase separation occurs thus preventing termination of oligomers in the early stages of polymerisation.

The level of control observed in polymerisations varied significantly between monomers. Đ values obtained by TD-SEC showed a moderate negative correlation with the polymerisation mixture polarities obtained using fluorescence emission spectroscopy, described in Section 2.2.1 (Figure 2.14). The contrast in reaction mixture polarity within MMA/MeOH and SMA/IPA polymerisations ($\Delta I_1/I_3$ = 0.43) was comparable to that measured between MeOH and diethyl ether ($\Delta I_1/I_3$ = 0.44). It is therefore highly likely that the monomer-controlled reaction mixture polarity induces variations in the solubility of the CuCl/bpy catalytic system thus limiting the ability of the RDRP process to prevent undesirable side reactions. Despite these negative implications, the Đ values obtained for *p*(LMA) and *p*(SMA) only just fall outside the scope of what is typically considered acceptable for a well-controlled RDRP process. This demonstrates that Cu-RDRP in anhydrous alcohols is a suitable synthetic route for the generation of linear homopolymers of targeted M_n and low to moderate Đ, for all of the monomers selected for study.

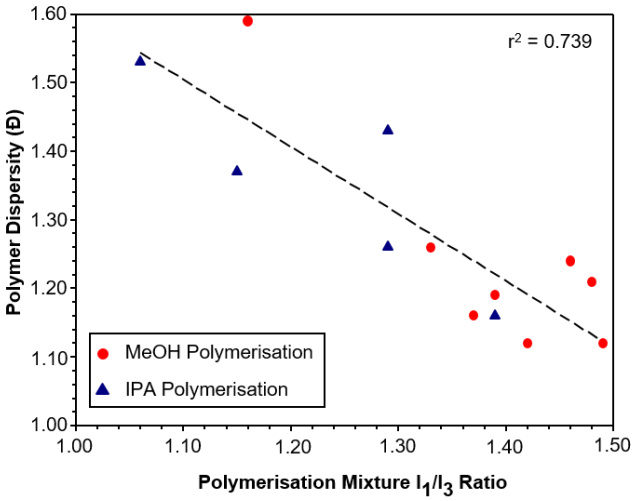

Figure 2.14 Graphical representation of the relationship between polymerisation mixture polarity, measured using fluorescence emission spectroscopy (as described in Section 2.2.1), and the Đ values obtained by TD-SEC analysis of polymers generated in THF/TEA (92/2 v/v %) at a flow rate of 1 mL min^{-1}.

2.3 Amphiphilic AB Block Copolymers *via* Cu-RDRP in Alcoholic Media

The discovery of suitable conditions for the polymerisation of all hydrophobic monomers targeted in this study provided a platform for the generation of additional polymer architectures using Cu-RDRP in anhydrous alcohols. The preparation of AB diblock copolymers was initially targeted due to the similarity in the polymerisation methods used to generate linear homopolymers; the only difference being that Cu-RDRP would be conducted using a polymer based macro-initiator, rather than BzBiB (Scheme 2.6). This approach consisted of two stages; firstly, a poly(ethylene glycol) (PEG) macro-initiator (PEG_{45}-Br) was synthesised *via* end-group modification of a methoxy-terminated poly(ethylene glycol) (PEG_{45}-OH) using α-bromoisobutyryl bromide. The second stage involved chain extension of

PEG_{45}-Br with a range of hydrophobic methacrylate monomers using Cu-RDRP in anhydrous alcohols to generate amphiphilic AB diblock copolymers which consisted of a hydrophilic PEG block covalently bonded to a hydrophobic methacrylic block.

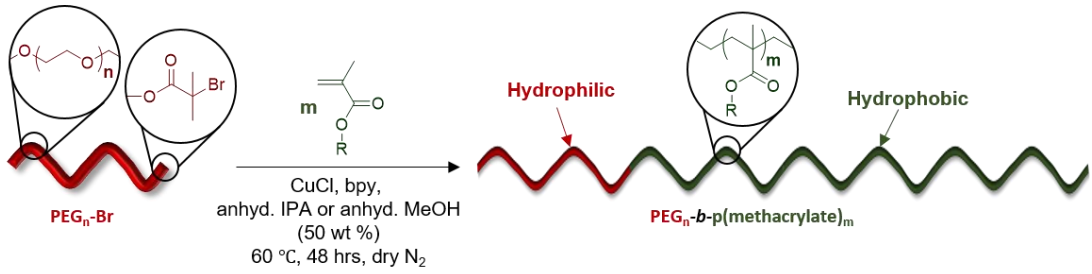

Scheme 2.6 Schematic representation of the proposed synthetic approach for the generation of amphiphilic block copolymers *via* polymerisation from a PEG macro-initiator using Cu-RDRP in anhydrous alcohols.

2.3.1 Synthesis of a Poly(ethylene glycol) Macro-initiator

The preparation of PEG based macro-initiators for use in Cu-RDRP has been widely reported.[61,89,96] Synthesis typically involves esterification between a PEG-OH and an acid bromide containing an alkyl bromide initiating moiety. The reaction is widely used not only due to the facile synthesis and purification procedures but also as a result of the wide range of acid bromides and methoxy-functional PEGs that are commercially available. The preparation of a PEG based initiator was achieved *via* esterification of PEG-OH, containing a M_n = 2000 g mol^{-1} with α-bromoisobutyryl bromide in DCM (Scheme 2.7). A DP_n of 45 monomer units was confirmed by end-group analysis of the starting material using ^{1}H NMR spectroscopy, giving a $M_{n(NMR)}$ = 2130 g mol^{-1}. The reaction was initiated by dropwise addition of a concentrated α-bromoisobutyrylbromide / DCM solution to a cooled DCM solution containing PEG_{45}-OH, DMAP and TEA. The addition was completed using an ice bath in order to remove heat generated by the exothermic reaction. Once the addition was complete the reaction was allowed to proceed at ambient temperature. After 24 hours the reaction was quenched by addition of deionised H_2O; the reaction mixture was then filtered and passed over a basic alumina flash column. The polymer was then purified by precipitation from DCM into cold petroleum ether (3 times).

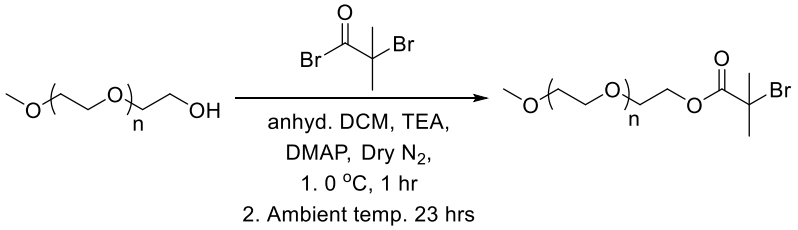

Scheme 2.7 Synthesis of a PEG_{45}-Br macro-initiator *via* esterification of PEG_{45}-OH with α-bromoisobutyryl bromide.

The PEG_{45}-Br macro-initiator was characterised using a number of analytical techniques. The end-group modification was confirmed by ^{1}H NMR analysis (Figure 2.15); in particular, by the appearance of a chemical shift for the methylene protons (h) at 1.96 ppm, this was accompanied by a downfield shift in the terminal ethylene protons (g) to 4.35ppm as a result of functionalisation with an α-bromoisobutyrate group at the ω-terminus. Comparison of the relative intensities of methyl (a) and isobutyryl (h) groups, located at the α- and ω- terminus respectively, indicated that > 99 % of hydroxyl end-groups had undergone functionalisation. Comparison between the relative intensity of chemical shifts attributed to PEG repeat units (b-f) with respect to polymer end-groups (h and a) reaffirmed a DP_n of 45 monomer units, confirming a slight increase in $M_{n(NMR)}$ to 2162 g mol^{-1} following end-group modification. The success of the reaction was further supported by ^{13}C NMR analysis, which showed new chemical shifts at 30, 57 and 174 ppm attributed to the methyl, quaternary and carbonyl carbons of the α-bromoisobutyryl group (Appendix, Figure A2.2). TD-SEC analysis demonstrated negligible difference in the molecular weight distributions of PEG_{45}-OH and PEG_{45}-Br; this confirmed that the structural integrity of the macro-initiator had not been compromised during either the end-group modification or the purification process that ensued. Thus a suitable PEG-based macro-initiator had been prepared for the generation of amphiphilic block copolymers *via* Cu-RDRP in anhydrous alcohols.

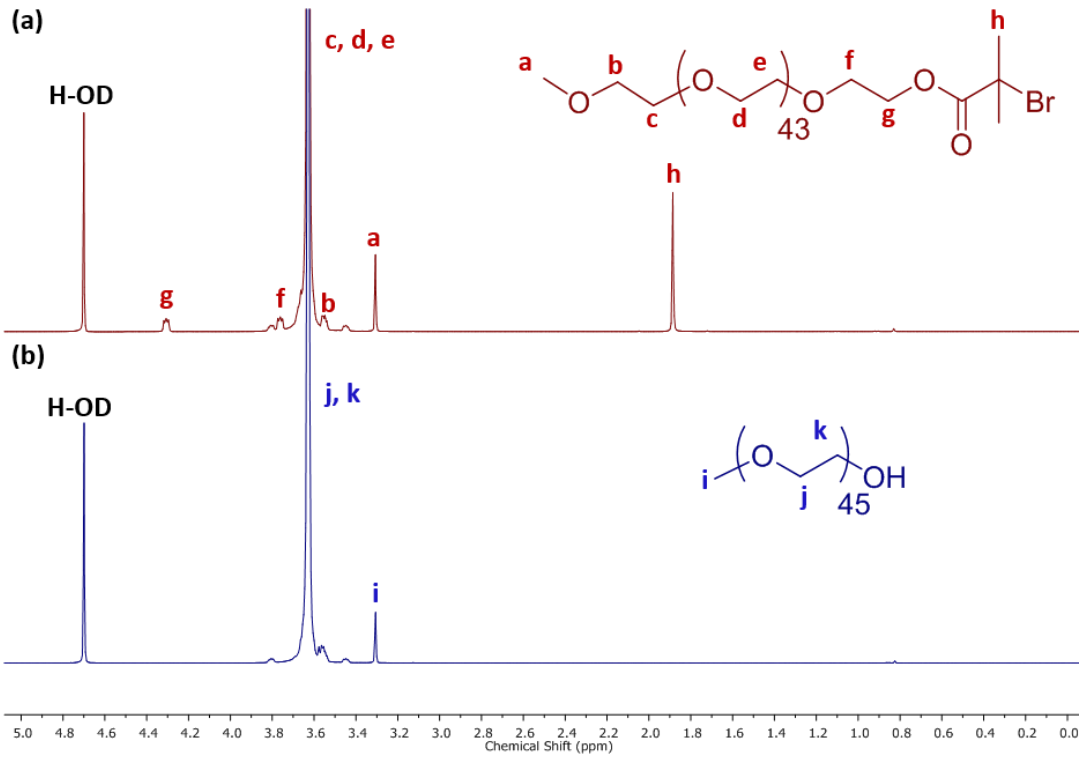

Figure 2.15 Overlaid ^{1}H NMR spectra (D_2O, 400 MHz) of (a) PEG_{45}-Br and (b) PEG_{45}-OH.

2.3.2 Polymerisation from PEG_{45}-Br *via* Cu-RDRP in Anhydrous Alcohols

Polymerisations from PEG_{45}-Br were conducted using Cu-RDRP in anhydrous alcohols in a similar manner to those used to generate linear homopolymers, described in section 2.2.2.2. A DP_n = 120 monomer units was targeted by ensuring a $[M]_0/[I]_0$ ratio of 120/1 at the start of polymerisation. Reactions were therefore allowed to proceed for 48 hours at 60 °C in order to achieve this higher targeted DP_n. The anhydrous alcohol-monomer pairings were decided based on the success of their linear homopolymerisations; polymerisations of MMA, EMA, *n*BMA, *n*HMA, CHMA, BzMA and EHMA were conducted in anhydrous MeOH whilst *t*BMA, LMA and SMA were polymerised using anhydrous IPA as the reaction solvent. Polymerisations were conducted at high solids (≥ 50 wt %) in order to maximise the impact of monomer co-solvency during polymerisation and to attempt to delay any onset of polymerisation-induced phase separation.

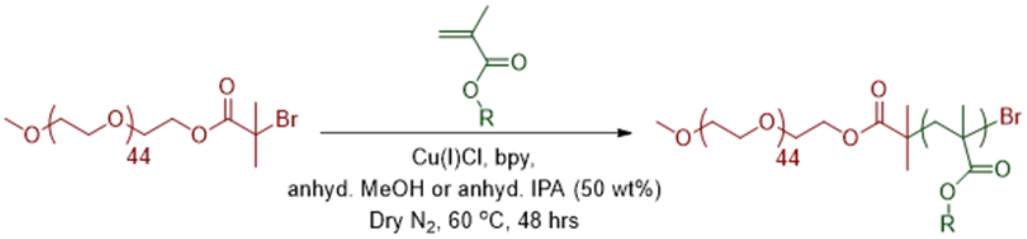

Scheme 2.8 Polymerisation from a PEG_{45}-Br macro-initiator with various hydrophobic methacrylate monomers *via* Cu-RDRP in anhydrous alcohols.

Interestingly, the phase behaviours observed during polymerisation were identical to those exhibited in the generation of linear homopolymers. Polymerisations of MMA, EMA, *n*BMA and *t*BMA remained homogeneous throughout polymerisation whereas biphasic reaction mixtures formed during polymerisations with: *n*HMA, CHMA, BzMA, EHMA, LMA and SMA. This was somewhat surprising as it had been expected that α-terminus functionalisation with an alcohol-soluble PEG chain may prevent phase separation due to increased polymer solubility in anhydrous alcohol or that it may even drive block copolymer self-assembly *in-situ*, forcing polymerisations to proceed *via* a polymerisation-induced self-assembly (PISA) process.

Regardless of polymerisation mixture homogeneity, ^{1}H NMR analysis showed that all polymerisations achieved high monomer conversion (≥ 94 %) after 48 hours. Polymerisations were then terminated through a combination of rapid cooling, dilution with THF/$CDCl_3$ (monomer dependent, see Chapter 7, Section 6.3.1.7) and deactivation of the copper catalyst *via* exposure to oxygen. The deactivated catalytic system was removed by passing polymer solutions over a neutral alumina flash column and the polymers were purified by precipitation (three times) from THF into a selected anti-solvent. Finally, residual solvent was removed *in vacuo* at 45 °C for 48 hours to give the purified amphiphilic AB block copolymers. Purified polymers were characterised using both ^{1}H NMR spectroscopy and TD-SEC (Table 2.3).

Table 2.3 Polymerisations from PEG_{45}-Br *via* Cu-RDRP of hydrophobic methacrylates at 60 °C using anhydrous alcohol solvents.

	^{1}H NMR						TD-SEC (THF/TEA)[e]		
	$[M]_0$ / $[I]_0$[a]	Conv. (%)[b]	M_n Theory (g mol^{-1})[c]	DP_n[d]	M_n (g mol^{-1})	Solvent	M_w (g mol^{-1})	M_n (g mol^{-1})	Đ
PEG_{45}-Br	-	-	-	45	2 150	-	-	-	-
PEG_{45}-*b*-*p*(MMA)$_{122}$	120	98	13 900	122	14 400	MeOH	19 800	17 700	1.12
PEG_{45}-*b*-*p*(EMA)$_{125}$	120	96	15 300	125	16 400	MeOH	21 500	17 700	1.21
PEG_{45}-*b*-*p*(*n*BMA)$_{125}$	120	98	18 900	125	19 900	MeOH	24 200	22 500	1.08
PEG_{45}-*b*-*p*(*t*BMA)$_{122}$	120	94	18 200	122	19 500	IPA	25 300	18 400	1.38
PEG_{45}-*b*-*p*(*n*HMA)$_{117}$	120	96	21 800	117	22 100	MeOH	29 300	25 700	1.14
PEG_{45}-*b*-*p*(CHMA)$_{123}$	120	95	21 300	123	22 300	MeOH	29 200	25 200	1.16
PEG_{45}-*b*-*p*(BzMA)$_{123}$	120	>99	23 300	123	23 800	MeOH	28 600	24 900	1.15
PEG_{45}-*b*-*p*(EHMA)$_{115}$	117	>99	25 400	115	25 000	MeOH	31 000	26 600	1.17
PEG_{45}-*b*-*p*(LMA)$_{121}$	120	>99	32 700	121	32 700	IPA	46 700	33 200	1.41
PEG_{45}-*b*-*p*(SMA)$_{122}$	120	99	42 400	122	43 500	IPA	63 900	43 700	1.46

[a]Calculated by ^{1}H NMR spectroscopy of polymerisation mixture at t = 0. [b]Calculated by ^{1}H NMR spectroscopy of polymerisation mixture at t = final. [c]M_n Theory = (($[M]_0/[I]_0$ x Mr(monomer)) x conv.) + M_n(Initiator)) [d]Calculated by ^{1}H NMR spectroscopy of the purified polymer: M_n = (DP_n x Mr(monomer)) + M_n(initiator). [e]Calculated by TD-SEC using THF/TEA mobile phase (98/2 v/v %) at 35 °C using a flow rate of 1 mL min^{-1}.

The $M_{n(NMR)}$ values obtained agreed with M_n theory values calculated based on monomer conversion. Calculated initiation efficiencies were in excess of 93 % which demonstrates that, despite the contrasting phase behaviours between monomer-alcohol pairings, a range of amphiphilic AB block copolymers can be generated with excellent control over M_w, using Cu-RDRP in anhydrous alcohols. This was supported when M_n values obtained by TD-SEC agreed with those obtained by ^{1}H NMR spectroscopy. The success of polymerisations from PEG_{45}-Br was supported when RI chromatograms obtained for each of the AB block copolymers were overlaid with that of the PEG_{45}-Br macro-initiator from which they were constructed (Figure 2.16). In all cases, monomodal M_w distributions were obtained showing elution of AB block copolymers at lower retention volumes relative to those of the PEG_{45}-Br macro-initiator, confirming the absence of macro-initiator residues in the purified samples.

Analysis of molecular weight distributions showed that all polymerisations conducted in anhydrous MeOH produced high M_n AB block copolymers with low $Đ$ values ($Đ$ = 1.08 – 1.21); this demonstrated a highly effective RDRP process capable of minimising undesirable side reactions. Whilst the $Đ$ values obtained for AB block copolymers were lower than those obtained for their linear homopolymers generated under identical conditions, the variation in DP_n targeted prohibits comparison between the level of control achieved for these polymerisations. Furthermore, the use of a PEG_{45}-Br macroinitiator would further mask the

impact of small discrepancies between polymer chain lengths on the overall dispersity of the AB block copolymer. Polymerisations conducted in anhydrous IPA produced polymers with $Đ$ values just outside what is typically expected of a well-controlled RDRP process ($Đ$ = 1.38-1.46). This reaffirms the hypothesis that the benefits of manipulating reaction mixture polarity, in order to suppress polymerisation-induced phase separation, are partially offset by a slight loss of control over the RDRP process which likely arises due to decreased catalyst solubility within the reaction media. However, these results demonstrate that the use of Cu-RDRP in anhydrous alcohols can easily generate amphiphilic AB block copolymers with good control over the molecular weight distribution.

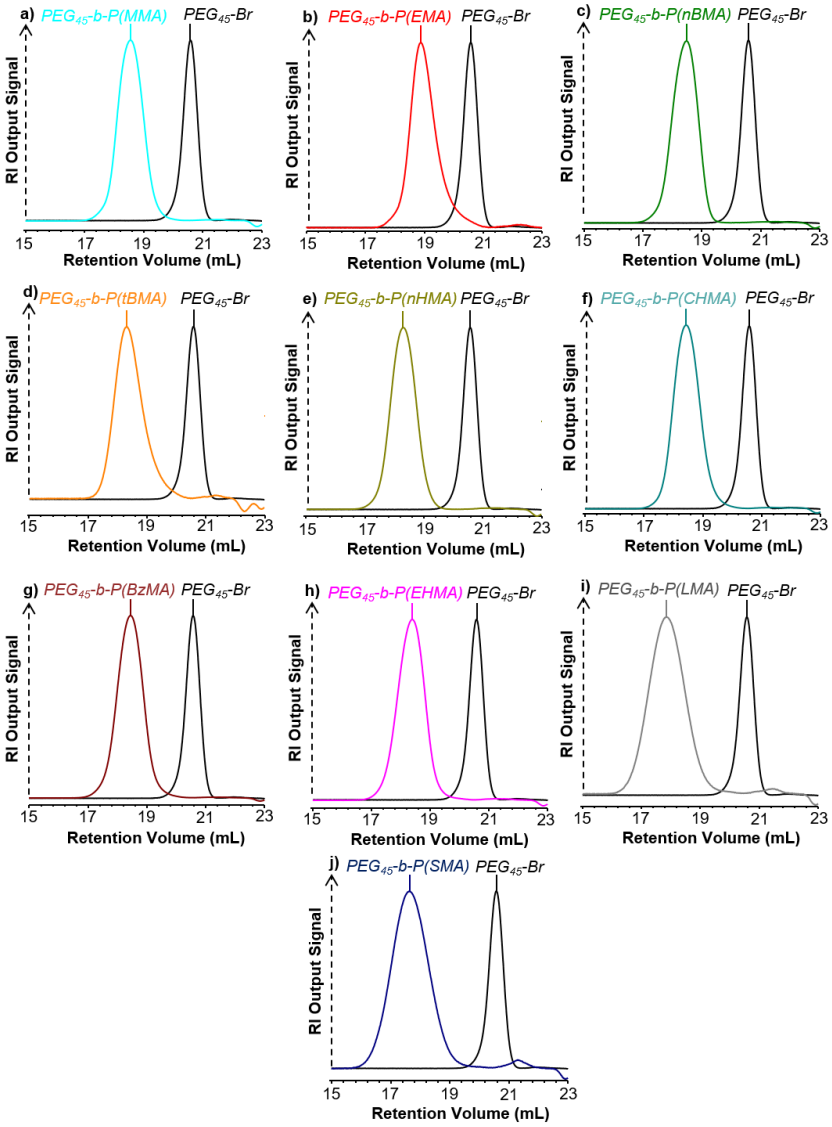

Figure 2.16 TD-SEC analysis of amphiphilic AB block copolymers generated *via* polymerisation from a PEG_{45}-Br macro initiator with hydrophobic methacrylate monomers using Cu-RDRP. Overlaid TD-SEC chromatograms showing molecular weight distributions of PEG_{45}-Br macro-initiator (black, a-j) with a) PEG_{45}-*b*-*p*(MMA) (cyan), b) PEG_{45}-*b*-*p*(EMA) (red), c) PEG_{45}-*b*-*p*(*n*BMA) (green), d) PEG_{45}-*b*-*p*(*t*BMA) (orange), e) PEG_{45}-*b*-*p*(*n*HMA) (gold), f) PEG_{45}-*b*-*p*(CHMA) (teal), g) PEG_{45}-*b*-*p*(BzMA) (dark red), h) PEG_{45}-*b*-*p*(EHMA) (pink), i) PEG_{45}-*b*-*p*(LMA) (dark grey), j) PEG_{45}-*b*-*p*(SMA) (blue).

2.4 Branched Statistical Copolymers *via* Cu-RDRP in Anhydrous Alcohols

Having established the viability of the Cu-RDRP of a range of hydrophobic methacrylate monomers in anhydrous alcohols, the synthesis of branched statistical copolymer architectures was investigated for each of the most successful monomer-alcohol combinations.

2.4.1 Statistical Copolymerisations of Hydrophobic Methacrylates with EGDMA *via* Cu-RDRcP in Anhydrous Alcohols

Cu-catalysed reversible-deactivation radical copolymerisations (Cu-RDRcP) were conducted in an identical manner to those described previously (Section 2.2.2.2) for the generation of linear homopolymers. As previously, a DP_n of 60 monomer units was targeted by ensuring a molar ratio of monomer to initiator of 60:1 prior to initiation ($[M]_0/[I]_0$ = 60); in addition, small amounts of the BFM, EGDMA, were added to generate branch points between the primary polymer chains (Scheme 2.9). BzBiB was selected as the initiator in order to allow ^{1}H NMR analysis of polymerisations as well as for characterisation of the branched statistical copolymers formed.

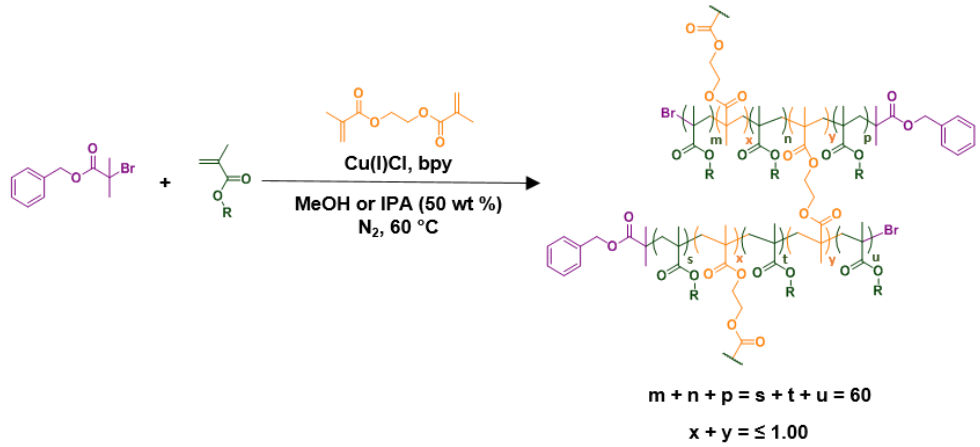

Scheme 2.9 Synthesis of branched statistical copolymers *via* statistical copolymerisation of hydrophobic methacrylate monomers with EGDMA by Cu-RDRcP using anhydrous alcohol solvents.

The formation of a 3D gelled network was avoided by ensuring that the nominal molar ratio of EGDMA to initiator did not exceed unity ($[B]_0/[I]_0 \leq 1.00$). A series of copolymerisations were conducted for each of the monomer-alcohol combinations using $[B]_0/[I]_0$ ratios varying from 0.59 to 0.97, as determined by ^{1}H NMR spectroscopy of the crude reaction mixtures (Chapter 6, Section 6.3.1.8). Polymerisations were allowed to proceed for 24 hours during which the phase behaviour observed for all monomer-alcohol systems was identical to their corresponding linear homopolymerisations described above. Analysis of polymerisation mixtures after 24 hours showed that all polymerisations had achieved high monomer conversion (97->99 %), which is essential to promote interchain branching and facilitate the

formation of high molecular weight branched copolymers using this approach. Following removal of the CuCl/bpy catalytic system *via* column chromatography and subsequent purification by multiple precipitations into a suitable anti-solvent (see Chapter 6, Section 6.3.1.7), branched copolymers were characterised using ^{1}H NMR spectroscopy to determine DP_n and $M_{n(\mathrm{NMR})}$ of the constituent primary chains within the complex branched copolymer architectures. Primary chain $M_{n(\mathrm{NMR})}$ values (Table 2.4 and 2.5) obtained in this way showed good agreement with $M_{n(\mathrm{NMR})}$ values obtained for their corresponding linear homologues generated in the absence of EGDMA (Section 2.2), indicating that the presence of EGDMA had negligible impact on primary chain formation during branching copolymerisations of hydrophobic methacrylate monomers with EGDMA *via* alcoholic Cu-RDRP.

The initiation efficiencies observed for branching copolymerisations were comparable to those observed during analogous linear homopolymerisations. Initiation efficiency was therefore also expected to impact the molar equivalents of the BFM, EGDMA, per propagating primary chain during copolymerisation. In order to estimate the actual ratio of BFM to initiator within branching copolymerisations, herein described as 'experimental $[B]_0/[I]_0$', nominal $[B]_0/[I]_0$ values obtained by ^{1}H NMR analysis of the polymerisation mixture at t_0 were modified in accordance with Equation 2.2. This provided accurate understanding of the actual composition of polymerisation mixtures (Table 2.4 and 2.5) as well as the number-average equivalents of EGDMA per primary chain within the final branched statistical copolymers. Taking one statistical copolymerisation of *n*BMA and EGDMA as an example (Table 2.4), analysis of the reaction mixture prior to initiation revealed a nominal $[B]_0/[I]_0$ value of 0.94; under identical conditions, the linear homopolymerisation of *n*BMA proceeded with an initiator efficiency of 84 %. Using these values, an experimental $[B]_0/[I]_0$ value of 1.12 was obtained, indicating incorporation of 1.12 EGDMA units per primary chain during copolymerisation. Analysis of the purified branched copolymer by ^{1}H NMR showed a primary chain DP_n of 73 *n*BMA units; the structure of this branched copolymer can therefore be expressed as *p*(*n*BMA$_{73}$-*co*-EGDMA$_{1.12}$). This nomenclature has been used throughout this work to express the composition of branched statistical copolymers generated *via* Cu-RDRcP.

Table 2.4 Branched copolymers generated by Cu-RDRP of hydrophobic methacrylate monomers and EGDMA in anhydrous methanol.

Polymer	^{1}H NMR ($CDCl_3$) – Primary chain analysis						TD-SEC (THF/TEA)			
	$[M]_0/[I]_0$	$[B]_0/[I]_0$	Exp. $[B]_0/[I]_0$	Conv. (%)	M_n (Theory) (g mol^{-1})	M_n (NMR) (g mol^{-1})	M_w (kg mol^{-1})	M_n (kg mol^{-1})	$Đ$	α
p(MMA$_{67}$-*co*-EGDMA$_{0.89}$)	60	0.80	0.89				Gelation Observed			
p(MMA$_{67}$-*co*-EGDMA$_{1.00}$)	61	0.90	1.00				Gelation Observed			
p(EMA$_{66}$-*co*-EGDMA$_{0.89}$)	59	0.81	0.89	99	7 000	7 800	179.3	30.0	5.97	0.384
p(EMA$_{68}$-*co*-EGDMA$_{0.93}$)	61	0.85	0.93	99	7 200	8 000	398.6	35.0	11.80	0.385
p(EMA$_{67}$-*co*-EGDMA$_{0.99}$)	59	0.90	0.99	99	7 000	7 900	538.2	44.4	17.43	0.386
p(EMA$_{67}$-*co*-EGDMA$_{1.04}$)	60	0.95	1.04	99	7 100	7 900	1 485	51.6	31.78	0.415
p(*n*BMA$_{70}$-*co*-EGDMA$_{0.95}$)	61	0.80	0.95	99	8 900	10 200	242.2	33.4	7.25	0.393
p(*n*BMA$_{73}$-*co*-EGDMA$_{1.01}$)	63	0.85	1.01	> 99	9 200	10 600	387.5	35.0	11.07	0.394
p(*n*BMA$_{72}$-*co*-EGDMA$_{1.07}$)	63	0.90	1.07	99	9 200	10 500	673.3	44.4	15.16	0.392
p(*n*BMA$_{73}$-*co*-EGDMA$_{1.12}$)	62	0.94	1.12	> 99	9 100	10 600	798.0	51.6	15.46	0.396
p(*n*HMA$_{65}$-*co*-EGDMA$_{0.87}$)	60	0.78	0.87	> 99	10 500	11 300	282.6	29.5	9.58	0.383
p(*n*HMA$_{67}$-*co*-EGDMA$_{0.94}$)	62	0.85	0.94	> 99	10 800	11 700	530.2	41.7	12.70	0.391
p(*n*HMA$_{65}$-*co*-EGDMA$_{0.98}$)	60	0.88	0.98	> 99	10 400	11 300	591.1	40.9	14.45	0.389
p(*n*HMA$_{68}$-*co*-EGDMA$_{1.03}$)	60	0.93	1.03	> 99	10 500	11 800	981.1	50.6	19.39	0.384
p(BzMA$_{78}$-*co*-EGDMA$_{0.91}$)*	60	0.70	0.91*	> 99	10 800	-*	303.5	31.4	9.66	0.390
p(BzMA$_{78}$-*co*-EGDMA$_{1.04}$)*	60	0.80	1.04*				Gelation Observed			
p(BzMA$_{78}$-*co*-EGDMA$_{1.17}$)*	60	0.90	1.17*				Gelation Observed			
p(EHMA$_{68}$-*co*-EGDMA$_{0.82}$)	62	0.75	0.82	> 99	12 600	13 700	246.2	42.1	5.84	0.390
p(EHMA$_{65}$-*co*-EGDMA$_{0.89}$)	60	0.82	0.89	> 99	12 200	13 100	313.1	31.5	9.94	0.392
p(EHMA$_{68}$-*co*-EGDMA$_{0.93}$)	63	0.86	0.93	> 99	12 800	13 700	879.7	52.0	16.93	0.398
p(EHMA$_{70}$-*co*-EGDMA$_{1.05}$)	64	0.97	1.05				Gelation Observed			
p(LMA$_{87}$-*co*-EGDMA$_{1.01}$)	60	0.70	1.01				Gelation Observed			
p(LMA$_{87}$-*co*-EGDMA$_{1.16}$)	60	0.80	1.16				Gelation Observed			
p(LMA$_{88}$-*co*-EGDMA$_{1.30}$)	61	0.90	1.30				Gelation Observed			

[a]Calculated by 1H NMR spectroscopy of polymerisation mixture at t = 0. [b]Calculated by 1H NMR spectroscopy of polymerisation mixture at tf. [c]M_n(Theory) = (([M]0/[I]0 x Mr(monomer)) x conv.) + Mr(Initiator)) [d]Calculated by ^{1}H NMR spectroscopy of the purified polymer: M_n (PC) = (DP_n x Mr(monomer)) + Mr(initiator). [e]Calculated by TD-SEC using THF/TEA mobile phase (98/2 v/v %) at 35 °C using a flow rate of 1 mL min^{-1}. * Characterisation of *p*(BzMA$_{60}$-*co*-EGDMA$_{0.70}$) by ^{1}H NMR spectroscopy was not possible due to overlap between initiator and monomer resonances.

Table 2.5 Branched copolymers generated by Cu-RDRP of hydrophobic methacrylate monomers and EGDMA in anhydrous IPA.

Polymer	^{1}H NMR ($CDCl_3$) – Primary chain analysis						TD-SEC (THF/TEA)			
	$[M]_0/[I]_0$	$[B]_0/[I]_0$	Exp. $[B]_0/[I]_0$	Conv. (%)	M_n (Theory) (g mol^{-1})	M_n (NMR) (g mol^{-1})	M_w (kg mol^{-1})	M_n (kg mol^{-1})	$Đ$	α
p(MMA$_{64}$-*co*-EGDMA$_{0.83}$)	56	0.71	0.83	>99	5 900	6 700	352.6	24.8	14.20	0.347
p(MMA$_{70}$-*co*-EGDMA$_{0.94}$)	62	0.81	0.94	>99	6 500	7 300	1 758	50.1	35.08	0.382
p(MMA$_{70}$-*co*-EGDMA$_{1.05}$)	60	0.90	1.05				Gelation Observed			
p(MMA$_{70}$-*co*-EGDMA$_{1.10}$)	60	0.95	1.10				Gelation Observed			
p(*t*BMA$_{68}$-*co*-EGDMA$_{0.77}$)	61	0.70	0.77	>99	8 900	9 900	66.5	31.8	2.09	0.471
p(*t*BMA$_{65}$-*co*-EGDMA$_{0.93}$)	60	0.85	0.93	98	8 800	9 500	94.1	29.4	3.20	0.431
p(*t*BMA$_{69}$-*co*-EGDMA$_{1.02}$)	63	0.93	1.02	97	9 200	10 100	150.7	64.0	2.35	0.432
p(*t*BMA$_{67}$-*co*-EGDMA$_{1.05}$)	60	0.96	1.05	98	8 800	9 800	163.2	45.3	3.60	0.422
p(CHMA$_{65}$-*co*-EGDMA$_{0.67}$)	59	0.59	0.67	> 99	10 200	11 200	45.5	17.3	2.34	0.415
p(CHMA$_{68}$-*co*-EGDMA$_{0.91}$)	60	0.80	0.91	> 99	10 400	11 700	102.9	23.5	4.38	0.403
p(CHMA$_{69}$-*co*-EGDMA$_{1.03}$)	60	0.91	1.03	> 99	10 400	11 900	227.1	33.5	6.70	0.391
p(CHMA$_{69}$-*co*-EGDMA$_{1.06}$)	60	0.93	1.06	> 99	10 400	11 900	273.2	35.6	7.68	0.398
p(LMA$_{72}$-*co*-EGDMA$_{0.88}$)	66	0.78	0.88	> 99	17 000	18 600	96.1	32.2	2.98	0.423
p(LMA$_{65}$-*co*-EGDMA$_{0.96}$)	60	0.85	0.96	> 99	15 500	16 800	111.1	33.4	3.32	0.407
p(LMA$_{64}$-*co*-EGDMA$_{1.01}$)	59	0.90	1.01	> 99	15 300	16 500	147.1	30.2	4.86	0.402
p(LMA$_{70}$-*co*-EGDMA$_{1.04}$)	64	0.93	1.04	> 99	16 500	18 100	294.4	54.0	5.46	0.386
p(SMA$_{72}$-*co*-EGDMA$_{0.89}$)	64	0.80	0.89	> 99	21 900	24 700	186.0	43.5	4.27	0.404
p(SMA$_{73}$-*co*-EGDMA$_{0.96}$)	65	0.85	0.94	> 99	22 200	24 900	208.0	39.6	5.24	0.399
p(SMA$_{68}$-*co*-EGDMA$_{1.00}$)	62	0.90	1.00	> 99	21 200	23 300	362.6	43.1	8.83	0.376
p(SMA$_{65}$-*co*-EGDMA$_{1.06}$)	60	0.95	1.06	> 99	20 600	22 300	352.4	53.1	6.63	0.392

[a]Calculated by 1H NMR spectroscopy of polymerisation mixture at t = 0. [b]Calculated by 1H NMR spectroscopy of polymerisation mixture at tf. [c]M_n(Theory) = (([M]0/[I]0 x Mr(monomer)) x conv.) + Mr(Initiator)) [d]Calculated by ^{1}H NMR spectroscopy of the purified polymer: M_n (PC) = (DP_n x Mr(monomer)) + Mr(initiator). [e]Calculated by TD-SEC using THF/TEA mobile phase (98/2 v/v %) at 35 °C using a flow rate of 1 mL min^{-1}. * Characterisation of *p*(BzMA$_{60}$-*co*-EGDMA$_{0.70}$) by ^{1}H NMR spectroscopy was not possible due to overlap between initiator and monomer resonances.

$$\text{Experimental}\,\frac{[B]_0}{[I]_0} = \frac{[B]_0}{[I]_0 \times IE_{(NMR)}} \qquad \textbf{Equation 2.2}$$

Calculation of the experimental ratio of BFM to initiator at the start of polymerisation, accounting for the impact of initiator efficiency. $[B]_0$ / $[I]_0$ represents the relative concentration of EGDMA to BzBiB as determined by ^{1}H NMR analysis of the reaction mixture prior to initiation. $IE_{(NMR)}$ represents the initiation efficiency, represented as a decimal, obtained by ^{1}H NMR spectroscopy from the analogous linear homopolymerisation (Appendix, Figure A2.3).

The formation of branched copolymer architectures was confirmed by TD-SEC. In all cases, both the M_w and M_n values obtained by TD-SEC (M_w up to 1,758 kg mol^{-1} and M_n up to 52.0 kg mol^{-1}) were significantly higher than those of their linear homologues, despite agreement between DP_n values obtained by ^{1}H NMR spectroscopy. This clearly indicated the formation of branched copolymers consisting of multiple primary chains which closely resemble the linear homopolymers described above.

TD-SEC chromatograms of branched copolymers also gave broad molecular weight distributions ($Đ$ = 2.09 – 35.08), indicating the deviation from conventional linear polymer synthesis and the considerable range of species present within the copolymer samples created by the statistical branching process. Overlay of the RI and RALS chromatograms obtained by TD-SEC show these differences clearly (Figure 2.17 and Appendix, Figure A2.4). The presence of high molecular weight species was evident from the difference between the respective chromatograms. A comparison of the RI chromatogram overlays also shows very close correlation of linear homopolymers and the low molecular weight fractions of the corresponding branched statistical copolymers, indicating the presence of the component linear homopolymer primary chains within the branched copolymer distributions, as has been previously reported.[97] This is supported by the $M_{n(NMR)}$ calculations and would suggest a near-identical number of primary chains are created in both polymerisations and that they propagate to near-identical chain lengths; M_w and dispersity differences are, therefore, simply due to the number and distribution of conjoined chains. The presence of some linear primary chains is the result of the statistical nature of intermolecular branching and is an intrinsic feature of such branching copolymerisations, either due to the lack of EGDMA incorporation within all chains or consumption of incorporated EGDMA functionality *via* intramolecular cyclisation.[98]

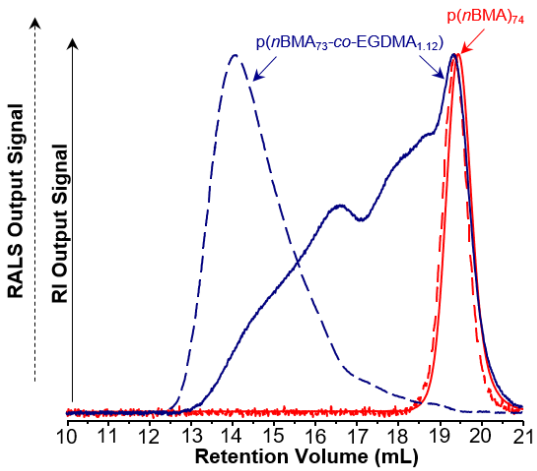

Figure 2.17 Comparison of linear and branched copolymer architectures by TD-SEC. Overlaid RI (solid lines) and RALS (dashed lines) chromatograms obtained for linear homopolymer, $p(n\text{BMA})_{74}$, (red lines) and branched statistical copolymer, $p(n\text{BMA}_{73}\text{-}co\text{-EGDMA}_{1.12})$ (blue lines).

Further TD-SEC analyses were conducted in order to compare the molecular weight distributions of linear homopolymers and branched statistical copolymers. Plots of cumulative weight fraction (cum. ω_f) *vs.* M_w can be easily obtained using TD-SEC. Overlaid plots obtained for the branched statistical copolymer, $p(n\text{BMA}_{73}\text{-}co\text{-EGDMA}_{1.12})$, and its corresponding linear homopolymers, $p(n\text{BMA})_{74}$, reiterated the formation of high molecular weight copolymers during Cu-RDRcP (Figure 2.18a). In the case of the $p(n\text{BMA})_{74}$ the top half of the cum. ω_f is occupied by species with absolute $M_w \geq 12\ 500$ g mol^{-1}; in contrast, analysis of $p(n\text{BMA}_{73}\text{-}co\text{-EGDMA}_{1.12})$ showed that the top half of the cum. ω_f consisted of branched copolymers with absolute M_w in excess of 105 200 g mol^{-1}.

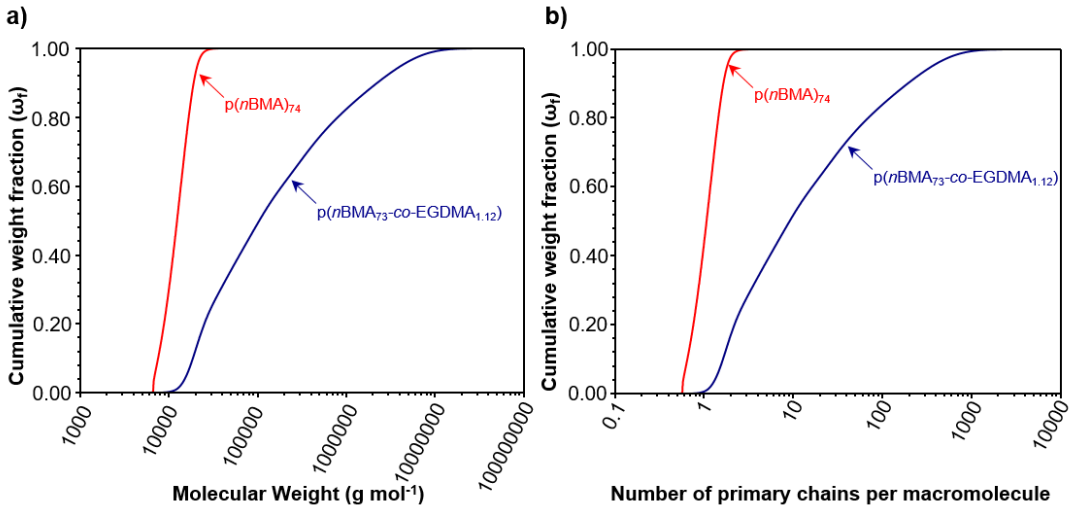

Figure 2.18 Understanding the extent of branching within (co)polymer molecular weight distributions obtained using TD-SEC. a) Plots of cum. ω_f *vs.* molecular weight and b) cum. ω_f *vs.* number of primary chains per macromolecule obtained by TD-SEC of a linear homopolymer, $p(n\text{BMA})_{74}$ (red lines), and a branched statistical copolymer, $p(n\text{BMA}_{73}\text{-}co\text{-EGDMA}_{1.12})$ (blue lines).

Given that ^{1}H NMR analyses and RI TD-SEC chromatograms suggested that branched copolymers consisted of primary chains identical to those generated in the absence of EGDMA, it was possible to probe the extent of branching across the molecular weight distribution. This required modification of cum. ω_f *vs.* M_w plots to account for the $M_{n(\text{TD-SEC})}$ of the primary chains from which branched copolymers are constructed. This was achieved using $M_{n(\text{TD-SEC})}$ values obtained for the equivalent linear homopolymer generated under identical polymerisation conditions. This allowed the construction of plots of cum. ω_f *vs.* the number of primary chains per macromolecule within the molecular weight distribution. As can be seen in Figure 2.18b, the plot obtained for *p*(*n*BMA)$_{74}$ showed a dramatic increase in cum. ω_f with 98 % of the branched copolymer mass consisting of species theoretically containing < 2.00 primary chains per polymer chain; this was expected for a polymer generated in the absence of a BFM capable of facilitating inter-chain branching reactions. In contrast, the plot obtained for *p*(*n*BMA$_{73}$-*co*-EGDMA$_{1.12}$) showed a broader range of species contributing to the copolymer mass. Analysis showed that cum. ω_f values of 0.25, 0.50 and 0.75 were occupied by species containing > 2.59, > 9.00 and > 47.31 primary chains per macromolecule respectively. In stark contrast to linear homopolymers, this highlighted high levels of branching achieved by some species within the molecular weight distribution, and indicates that the top 10 % of the *p*(*n*BMA$_{73}$-*co*-EGDMA$_{1.12}$) molecular weight distribution consisted of branched copolymers containing no fewer than 195 primary chains.

Whilst plots of cum. ω_f *vs.* number of primary chains per macromolecule demonstrated the extent of branching within copolymer samples, they also highlighted the statistical nature of the branching process which occurs during polymerisation. This was evident by the decreasing gradients observed in both plots obtained for *p*(*n*BMA$_{73}$-*co*-EGDMA$_{1.12}$) as M_w / number of primary chains per macromolecule increased. This indicated that, despite highly branched species having considerably larger absolute M_w, the contribution of branched copolymers to the total sample mass decreased as the M_w / number of primary chains per macromolecule increased. This suggested a decrease in the number of species present at each incremental increase in absolute M_w; this was confirmed *via* number distribution analysis of the species present within the *p*(*n*BMA$_{73}$-*co*-EGDMA$_{1.12}$) molecular weight distribution; specifically, plots were obtained for normalised mol fraction and cumulative mol fraction *vs.* number of primary chains per macromolecule (Figure 2.19). These plots showed the number of species present within each absolute M_w increment decrease as the level of branching increases.

This is an intrinsic feature of branched copolymers generated *via* copolymerisation of monofunctional and BFMs and arises as a result of the statistical uptake of BFMs across primary chains.[98] Failure to incorporate a BFM precludes primary chains from partaking in branching reactions and results in the presence of unbranched primary chains within the final molecular weight distribution. Whilst primary chains that incorporate a single BFM unit are capable of facilitating branching reactions, they can only partake in a maximum of one branching reaction. Therefore, in cases where this pendant vinyl group is consumed through an intermolecular branching reaction, such chains form the terminal units of branched statistical copolymers and suppress further growth *via* intermolecular branching. In contrast, primary chains which incorporate ≥ 2 BFMs per primary chain can facilitate multiple branching reactions and, providing that pendant vinyl groups are not consumed *via* intramolecular cyclisation, act as branch points within the branched copolymer architecture. The statistical copolymerisation of *n*BMA and EGDMA was conducted using an experimental $[B]_0/[I]_0$ of 1.12, it is therefore likely that the statistical nature of BFM uptake will produce high numbers of primary chains containing only 1 EGDMA unit. The probability of incorporating one of these primary chains during the ensuing statistical branching process increases dramatically with the number of primary chains per macromolecule and explains why the number of species present decrease with the level of branching observed.

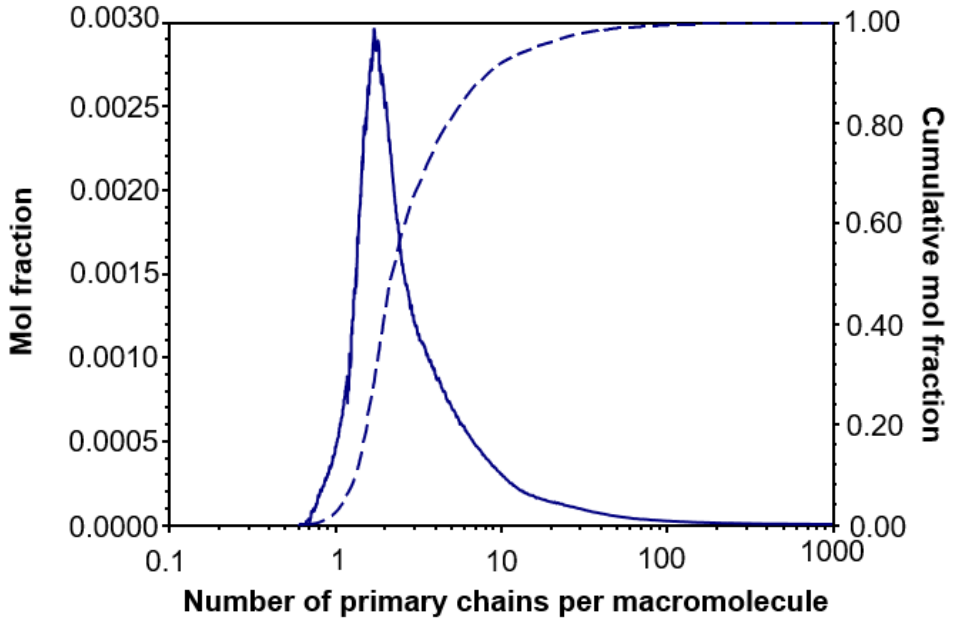

Figure 2.19 Analysis of the number distribution of species present within *p*(*n*BMA$_{73}$-*co*-EGDMA$_{1.12}$). Plots of mol fraction (solid blue) and cumulative mol fraction (dashed blue) *vs.* the number of chains per macromolecule obtained by TD-SEC.

2.4.2 Mark-Houwink-Sakurada Analysis of Branched Statistical Copolymers and Linear Homologues

The formation of branched copolymer architectures was also studied using comparative Mark-Houwink-Sakurada (MHS) analysis on both branched statistical copolymers and linear homologues which resemble the primary chains from which they are constructed. The MHS relationship describes the association between the absolute molecular weight of a polymer and the intrinsic viscosity, [η], of the solution formed when it is dissolved within a suitable organic solvent. The relationship between these two properties is described by the MHS equation (Equation 2.3) and is intrinsically linked to the topological structure of the polymer in solution.

$$[\eta] = KM^{\alpha} \qquad \textbf{Equation 2.3}$$

The MHS equation which describes the relationship between the intrinsic viscosity, [η], and absolute molecular weight, M, of a polymer; where K and α are known as MHS parameters which are dependent on the nature of polymer-solvent interaction. The [η] of a polymer solution typically increases with absolute M_w due to increased polymer-solvent interactions. However the degree of polymer-solvent interaction, and thus the relationship between [η] and M, is highly influenced by the topological structure of the polymer in solution (Figure 2.20). Linear polymers typically adopt a random coil conformation in solution. This relatively expanded state allows significant levels of polymer-solvent interaction; as a result, the [η] of a linear polymer solution shows increased sensitivity higher molecular weight species. In contrast, branched and hyper-branched polymers typically form spherical, shape-persistent structures in solution with higher density than linear random coils in solution, which reduce the level of polymer-solvent interaction and thus decrease the sensitivity of the [η] of branched polymer solutions to increases in absolute molecular weight (*M*).[99]

The MHS exponent, α, indicates the topological structure of a polymer in solution. TD-SEC allows measurement of the intrinsic viscosity of a polymer-eluent solution across the whole of the molecular weight distribution; this facilitates determination of the MHS exponent by construction of the MHS plot of log[η] *vs*. log *M*. For hyperbranched and branched polymers, the MHS exponent, α, typically varies between 0.2 and 0.5 depending on the degree of branching within the branched polymer architecture. In contrast, relatively expanded linear polymers typically give MHS exponents between 0.5 and 1.0.[99] MHS analysis therefore offers a useful characterisation technique for branched copolymers.

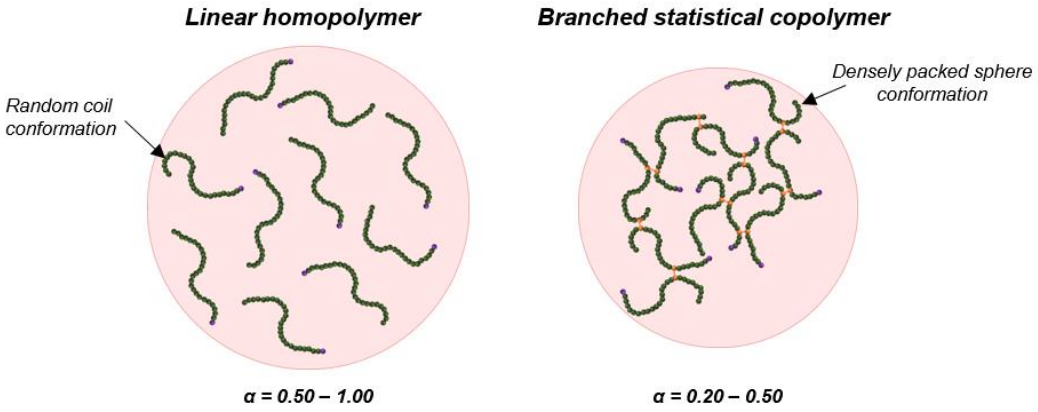

Figure 2.20 Schematic representation of the random coil and densely packed sphere conformations adopted by a linear homopolymers and a branched statistical copolymers in solution along with expected values.

To further validate claims that branched copolymer architectures were generated during Cu-RDRcP of hydrophobic methacrylates with EGDMA, MHS plots were constructed for all branched statistical copolymers as well as for the linear homopolymers generated under identical conditions but in the absence of EGDMA. In all cases, overlaid MHS plots obtained for branched statistical copolymers highlighted considerable differences between the topology of branched statistical copolymers in comparison with their linear homologues. MHS exponents described above were calculated by taking averaged gradients across the whole of the molecular weight distribution. Linear homopolymers gave α values ranging from 0.544 to 0.694, which are representative of linear polymers behaving as random coils within a theta solvent. In contrast, α values obtained for branched statistical copolymers were significantly lower, ranging from 0.378-0.471; these differences could be seen clearly when comparable MHS plots were overlaid (Figure 2.21a, and Appendix, Figure A2.5). This confirmed the formation of the branched copolymer architectures during all statistical copolymerisations and highlighted the significant role that the addition of small amounts of EGDMA plays in changing the architecture of the resulting copolymer.

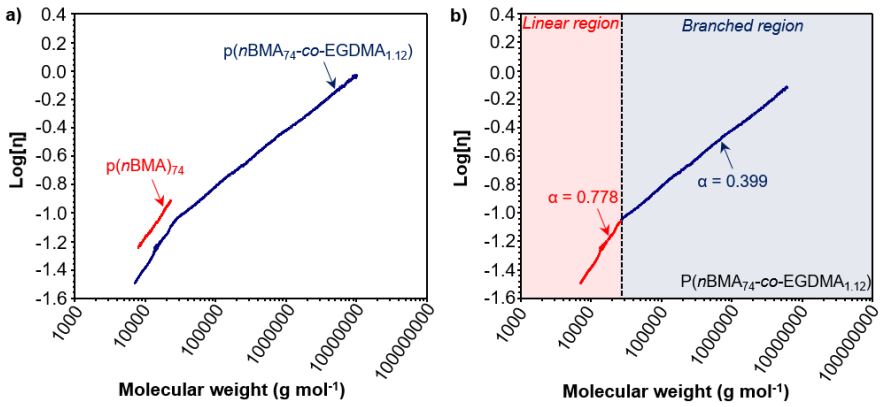

Figure 2.21 MHS analysis of linear homopolymers and branched statistical copolymers generated *via* Cu-RDRP in anhydrous MeOH. a) Overlaid MHS plots obtained by TD-SEC for linear homopolymer, $p(n\text{BMA})_{74}$, and branched statistical copolymer, $p(n\text{BMA}_{73}\text{-}co\text{-EGDMA}_{1.12})$. b) Deconvolution of the MHS plot obtained for $p(n\text{BMA}_{73}\text{-}co\text{-EGDMA}_{1.12})$, highlighting the architectural contrast between two distinct regions within the molecular weight distribution.

A detailed assessment of the MHS plots obtained for the branched statistical copolymers showed that, in all cases, the relationship between [η] and *M* varied across the molecular weight distribution (Appendix, Figure A2.6). This is demonstrated in the MHS analysis of $p(n\text{BMA}_{73}\text{-}co\text{-EGDMA}_{1.12})$ shown in Figure 2.21a. For low molecular weight species (*M* up to 12 000 g mol^{-1}), [η] showed a high sensitivity to increases in *M*. This section of the MHS plot obtained for $p(n\text{BMA}_{73}\text{-}co\text{-EGDMA}_{1.12})$ was comparable to that observed for its linear homologue, $p(n\text{BMA})_{74}$. At higher *M*, a significant change was observed in the MHS plot as increases in polymer M had a smaller impact on [η]. This *M* dependant variation in the MHS relationship indicated that the molecular weight distribution of $p(n\text{BMA}_{73}\text{-}co\text{-EGDMA}_{1.12})$ consisted of a complex mixture of polymer topologies.

The complex nature of the $p(n\text{BMA}_{73}\text{-}co\text{-EGDMA}_{1.12})$ molecular weight distribution was studied further *via* deconvolution of the MHS plot using intersectional analysis (Figure 2.21b). This allowed calculation of MHS exponents for each the two distinct regions within the molecular weight distribution, giving α values of 0.778 and 0.399 for low and high M_w regions respectively. The value obtained for low *M* species was comparable to that of $p(n\text{BMA})_{74}$ (0.690) and supported the conclusion that the low *M* fraction of branched copolymer molecular weight distributions consist of unbranched linear chains similar to those generated in the absence of EGDMA. In contrast, the α value obtained for the high *M* species was typical of branched polymers which adopt a densely packed spherical conformation in solution and confirmed the architectural transformation which occurs following linking of primary chains *via* intermolecular branching reactions during copolymerisation. This provided simplification of the

complex molecular weight distribution obtained for *p*(*n*BMA$_{73}$-*co*-EGDMA$_{1.12}$); allowing it to be divided into two distinct regions; a 'linear region' which consists of linear unbranched primary chains of low M_w and a 'branched region' containing high M_w species which consist of multiple co-joined primary chains. The deconvolution method was used to demonstrate the 'linear' and 'branched' regions within the molecular weight distributions of all branched statistical copolymers described above (Appendix, Figure A2.6).

The range of TD-SEC techniques described above permit detailed analysis of the complex nature of the molecular weight distributions of branched statistical copolymers generated *via* Cu-RDRcP in anhydrous alcohols. Such techniques therefore offered an effective characterisation tool to understand if and how a range of factors, such as copolymerisation concentration, experimental $[B]_0/[I]_0$ ratio and polymerisation mixture homogeneity, impact the levels of branching that occurs during statistical copolymerisations of hydrophobic methacrylates and EGDMA.

2.4.3 Understanding the Factors Affecting Branching During Cu-RDRcP

Having established a range of characterisation techniques capable of highlighting differences between materials containing complex molecular weight distributions, detailed analyses of branched statistical copolymers were conducted in order to identify the key factors which influence the level of branching during RDRcP in anhydrous alcohols. It is well established that the molar ratio of branching comonomer to initiator has a significant impact on the level of branching which occurs during RDRcP of monofunctional and BFMs.[66,71] This was studied for all hydrophobic monomers/alcohol pairings by conducting copolymerisations at increasing nominal $[B]_0/[I]_0$ ratios and subsequent comparison of copolymer compositions and molecular weight distributions. In all cases, a significant impact on the molecular weight distributions was observed by TD-SEC (Appendix, Figure A2.7), with M_w, $Đ$ and the weight fraction of primary chains incorporated *via* branching reactions all increasing with $[B]_0/[I]_0$ (Tables 2.4 and 2.5). This can be seen in Figure 2.22, which shows overlaid a) RI and b) RALS chromatograms obtained by TD-SEC of *p*(*n*BMA-*co*-EGDMA) copolymers generated at various experimental $[B]_0/[I]_0$ molar ratios. In both cases, chromatograms showed increases in the concentration and size of the species detected at lower elution volumes as the experimental $[B]_0/[I]_0$ ratios was increased from 0.95 to 1.12. These increases were accompanied by increases in M_w, M_n and $Đ$ from 242.2 kg mol^{-1}, 33.4 kg mol^{-1} and 7.25 to 798.0 kg mol^{-1}, 51.6 kg mol^{-1} and 15.46 respectively. This demonstrates the significant impact that increases in the experimental $[B]_0/[I]_0$ ratio has on the generation of high molecular weight branched copolymers during Cu-RDRcP.

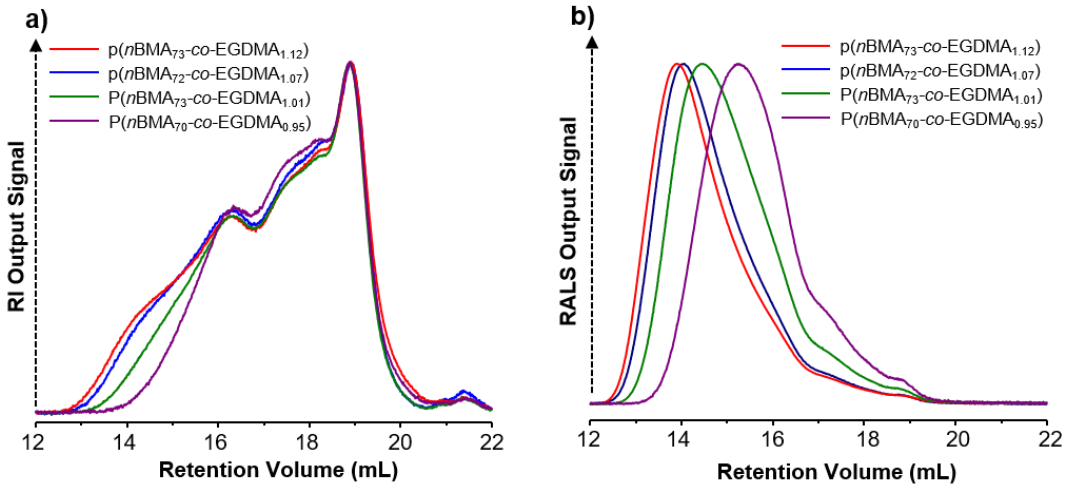

Figure 2.22 The impact of experimental $[B]_0/[I]_0$ ratio on the molecular weight distributions of *p*(*n*BMA-*co*-EGDMA) branched statistical copolymers. Overlaid a) RI and b) RALS chromatograms obtained by TD-SEC of *p*(*n*BMA$_{73}$-*co*-EGDMA$_{1.12}$) (red lines), *p*(*n*BMA$_{72}$-*co*-EGDMA$_{1.07}$) (blue lines), *p*(*n*BMA$_{72}$-*co*-EGDMA$_{1.01}$) (green lines) and *p*(*n*BMA$_{70}$-*co*-EGDMA$_{0.95}$) (purple lines).

Further TD-SEC analyses were conducted to understand how changes in the experimental $[B]_0/[I]_0$ ratio impacted branching reactions during copolymerisation. A logical explanation for the observed increases in M_w is that increases in the experimental $[B]_0/[I]_0$ ratio will strongly influence the statistical distribution of BFMs across primary chains during propagation. Specifically, this would likely reduce the fraction of primary chains unable to participate in branching reactions, due to failure to incorporate BFM units during propagation; it is also possible that this would increase the number of primary chains containing ≥ 2 BFM units which are therefore capable of forming branch points, rather than terminal units, within the resulting branched copolymer architectures. This was demonstrated by comparison of the MHS plots obtained from the 'branched regions' of *p*(*n*BMA-*co*-EGDMA) molecular weight distributions (Figure 2.23a). Calculation of the MHS exponents showed little difference in the α values, This indicated that, regardless of experimental $[B]_0/[I]_0$ ratio, there was little difference in the topology of the branched copolymers. Polymer topology is intrinsically linked, and is commonly associated, to the degree of branching of hyperbranched polymers; these data suggest that increases in the experimental $[B]_0/[I]_0$ ratio at which copolymerisations were conducted had minimal impact on the degree of branching of statistical copolymers towards the high molecular weight end of the molecular weight distribution. It appears that the impact of these increases in the experimental $[B]_0/[I]_0$ ratio disproportionately fell on chains at the lower end of the molecular weight distribution. This was supported by analysis of the cum. ω_f of unbranched linear chains within *p*(*n*BMA-*co*-EGDMA) branched copolymers, which decreased from 7.5 % to 0.7 % as the experimental $[B]_0/[I]_0$ increased from 0.95 to 1.12.

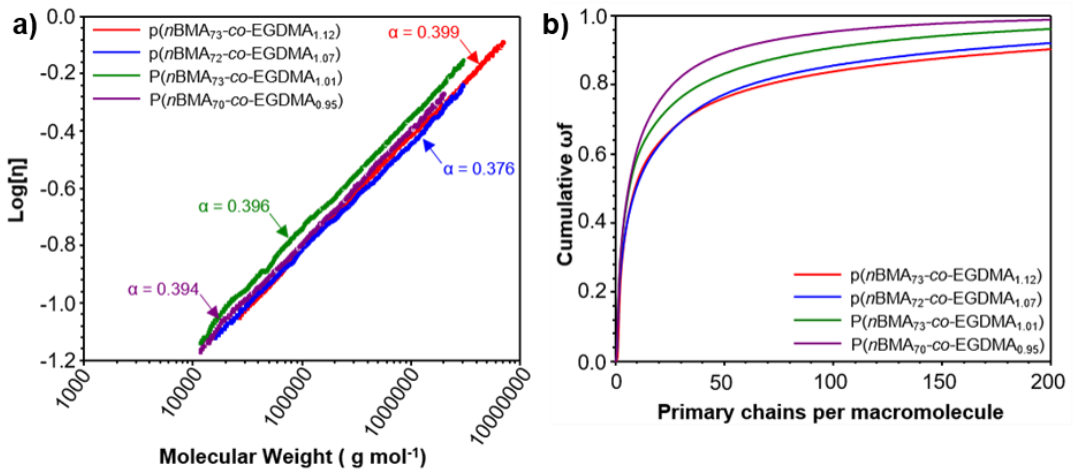

Figure 2.23 TD-SEC analysis on the impact of experimental $[B]_0/[I]_0$ ratio on the molecular weight distribution of *p*(*n*BMA-*co*-EGDMA) branched statistical copolymers. Overlaid a) MHS plots and b) Plots of cum. ω_f *vs.* number of primary chains per macromolecule obtained for: *p*(nBMA$_{73}$-*co*-EGDMA$_{1.12}$) (red lines), *p*(nBMA$_{72}$-*co*-EGDMA$_{1.07}$) (blue lines), *p*(nBMA$_{72}$-*co*-EGDMA$_{1.01}$) (green lines) and *p*(nBMA$_{70}$-*co*-EGDMA$_{0.95}$) (purple lines).

To support this hypothesis, plots of cum ω_f *vs.* number of primary chains per macromolecule were constructed for each of the *p*(*n*BMA-*co*-EGDMA) branched statistical copolymers generated at varied experimental $[B]_0/[I]_0$ ratios (Figure 2.23b). This showed that in copolymers generated at lower experimental $[B]_0/[I]_0$ ratios, unbranched linear chains and lightly branched copolymers made more significant contributions to the overall sample mass than was the case for branched copolymers generated at higher experimental $[B]_0/[I]_0$ ratios. For example, the lower quartile of the *p*(nBMA$_{70}$-*co*-EGDMA$_{0.95}$) sample mass consisted of species containing ≤ 2 primary chains; in contrast, the lower quartile of the mass of a *p*(nBMA$_{73}$-*co*-EGDMA$_{1.12}$) sample consisted of species containing up to 3 primary chains per macromolecule. This trend was reiterated at the high end of the molecular weight distribution as the upper quartile of *p*(nBMA$_{70}$-*co*-EGDMA$_{0.95}$) and *p*(nBMA$_{73}$-*co*-EGDMA$_{1.12}$) sample masses consisted of species consisting of ≥ 20 and 46 primary chains respectively.

The analyses outlined above reaffirmed the widely reported observations that the contributions of high M_w branched copolymers to the overall sample mass increased with experimental $[B]_0/[I]_0$ ratio. It must be noted, however, that despite the significant increases in M_w, MHS analysis on the branched copolymer molecular weight distributions provide evidence that increases in the experimental $[B]_0/[I]_0$ ratio have little impact on the degree of branching within high molecular weight species. Increases in M_w can therefore be attributed to increases in the extent of branching, rather than the degree of branching, achieved during copolymerisation. The extent of branching refers to the fraction of the primary chains, generated during Cu-RDRcP, which are incorporated into branched macromolecular architectures during polymerisation.

Alternatively, the degree of branching refers to the ratio between the average numbers of branching and terminal units to linear units within a branched copolymer sample.[100] Variation in the extent of branching observed occurs as a result of changes in the statistical distribution of EGDMA across propagating primary chains thus increasing the fraction of primary chains which can participate in branching reactions.

2.4.4 Comparison of Branching Observed Between Monomer-Solvent Systems

Branching copolymerisations utilising experimental $[B]_0/[I]_0$ ratios > 1.00 are expected to form insoluble crosslinked gels. Whilst ^{1}H NMR analysis of the branching copolymerisations described above gave nominal $[B]_0/[I]_0$ ratios ≤ 0.97, the varying initiation efficiencies observed during linear homopolymerisations indicated experimental $[B]_0/[I]_0$ ratios in excess of the theoretical gel point. Surprisingly, in many cases the formation of a gel network was avoided, and soluble branched polymers were obtained from branching copolymerisations conducted at experimental $[B]_0/[I]_0$ ratios in excess of the theoretical gel point. The high monomer conversions recorded, and the absence of unreacted methacrylate groups observed during analysis of purified polymers by ^{1}H NMR spectroscopy, indicated that gel formation was not suppressed due to incomplete polymerisation of pendant methacrylate groups. It is therefore probable that in copolymerisations with experimental $[B]_0/[I]_0$ >1.00, gelation was avoided due to the consumption of a fraction of pendant methacrylate vinyl groups (from EGDMA incorporation) *via* intramolecular cyclisation.

Increases in experimental $[B]_0/[I]_0$ ratio impacted the M_w of the resulting branched statistical copolymers differently for specific monomer-solvent systems. For example, in the copolymerisation of EMA and EGDMA in anhydrous MeOH, an increase in the experimental $[B]_0/[I]_0$ ratio from 0.89 – 1.04 resulted in an increase in M_w from 179 – 1,485 kg mol^{-1}, whereas in the copolymerisation of SMA with EGDMA in anhydrous IPA, similar increases in the experimental $[B]_0/[I]_0$ ratio resulted in only modest increases in the M_w of the resultant branched copolymers from 186 - 352 kg mol^{-1}.

Comparisons between the M_w of branched copolymers with M_n values obtained for their linear equivalents (M_w(Br)/M_n(L)) provides an indication of the weight-average number of chains that are conjoined during copolymerisation. Figure 2.24 demonstrates the impact that experimental $[B]_0/[I]_0$ ratios have on the extent of branching; M_w(Br)/M_n(L) generally increased with experimental $[B]_0/[I]_0$ in the branching copolymerisations of EGDMA with MMA, EMA, *n*BMA, *n*HMA and EHMA. In branching copolymerisations of the MMA-IPA and EHMA-MeOH systems, large increases in the extent of branching were observed shortly before gelation, which occurred when

polymerisations were attempted at experimental $[B]_0/[I]_0$ ratios of 1.00 and 1.05 respectively. A similar trend was observed in branched copolymers obtained from copolymerisation of EMA with EGDMA in MeOH; a sudden increase in M_w(Br)/M_n(L) occurred as experimental $[B]_0/[I]_0$ ratios were increased from 0.99 to 1.04, indicating that the latter copolymerisation is approaching the experimental gel point.

Surprisingly, sudden increases in the extent of branching were not observed in the copolymerisations of *n*BMA and *n*HMA with EGDMA in MeOH despite being conducted at experimental $[B]_0/[I]_0$ ratios of 1.12 and 1.03 respectively. This indicates that these reactions would likely tolerate experimental $[B]_0/[I]_0$ ratios greater than those reported here before the onset of gelation. In contrast to the monomer-MeOH systems described above, the relationship between the experimental $[B]_0/[I]_0$ ratio and the level of branching observed was significantly lower for copolymerisations of EGDMA with *t*BMA, CHMA, LMA or SMA. The copolymerisation of CHMA/EGDMA was studied across a wide range of experimental $[B]_0/[I]_0$ ratios ranging from 0.67 to 1.06 which gave increased M_w(Br)/M_n(L) from 2.77 to 16.66 chains. Much smaller differences in the extent of branching were recorded for the LMA/EGDMA and SMA/EGDMA systems. Copolymerisations of LMA with EGDMA at experimental $[B]_0/[I]_0$ ratios ranging from 0.88 to 1.04 resulted in an increase in the observed M_w(Br)/M_n(L) from 3.94 to 12.07 chains. Similar increases were observed in the SMA/EGDMA copolymerisation where M_w(Br)/M_n(L) increased from 5.24 to 9.93 chains as experimental $[B]_0/[I]_0$ ratios were raised from 0.89 to 1.06.

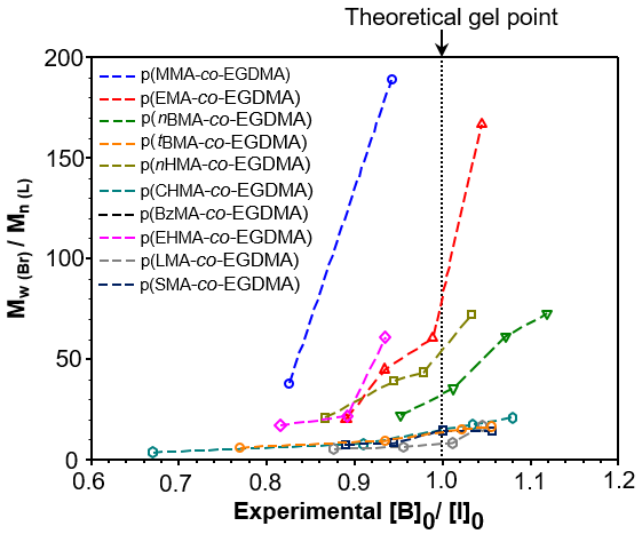

Figure 2.24 Understanding the extent of branching that occurred during Cu-RDRcP. Plots showing the variation observed in M_w(Br)/M_n(L) with increasing experimental $[B]_0/[I]_0$ ratio for all monomer/EGDMA copolymerisations.

This disparity in the extent of branching observed between monomer-alcohol systems was surprising. As other factors, such as failure to achieve high monomer conversion, had been ruled out, this indicated that the contrasting levels of branching may be due to variations in the nature of pendant vinyl group consumption; in particular, the relative contributions of intermolecular branching and intramolecular cyclisation which take place during copolymerisation. Characterisation of branched copolymers by ^{1}H NMR spectroscopy highlighted the samples which contained comparable monomer compositions and which should also, theoretically, contain identical branched copolymer architectures. These samples were selected for further TD-SEC analysis in order to understand the extent to which the level of branching varied between monomer-alcohol systems.

Analysis of the cum. ω_f versus absolute M, for the highest M_w branched copolymers obtained from each of the monomer-alcohol systems, were conducted to account for the M_n of the primary chains from which each macromolecule is constructed (Figure 2.25). This analysis unveiled the impact of varying the repeat unit mass, and therefore structure, on the resulting M_w (as judged by TD-SEC analysis), and provided an insight into the mass contributions of each branched species within the molecular weight distribution of each sample. The extent of branching observed in the samples studied followed the order of p(EMA$_{67}$-*co*-EGDMA$_{1.04}$) > p(MMA$_{70}$-*co*-EGDMA$_{0.94}$) > p(*n*BMA$_{73}$-*co*-EGDMA$_{1.12}$) ≈ p(*n*HMA$_{68}$-*co*-EGDMA$_{1.03}$) > p(EHMA$_{68}$-*co*-EGDMA$_{0.93}$) >> p(CHMA$_{69}$-*co*-EGDMA$_{1.06}$) > p(BzMA$_{78}$-*co*-EGDMA$_{0.91}$) > p(LMA$_{70}$-*co*-EGDMA$_{1.04}$) > p(*t*BMA$_{67}$-*co*-EGDMA$_{1.05}$) > p(SMA$_{65}$-*co*-EGDMA$_{1.06}$). This supports the trends seen in the M_w(Br)/M_n(L) analyses described above. This trend was reaffirmed when similar analyses were conducted using the cumulative mole fraction (Appendix, Figure A2.8). It must be stated however that some the samples studied were generated using differing experimental $[B]_0/[I]_0$ ratios. Therefore the ordering identified is only relevant to the samples described here and is not indicative of branching efficiency between monomer/ EGDMA systems.

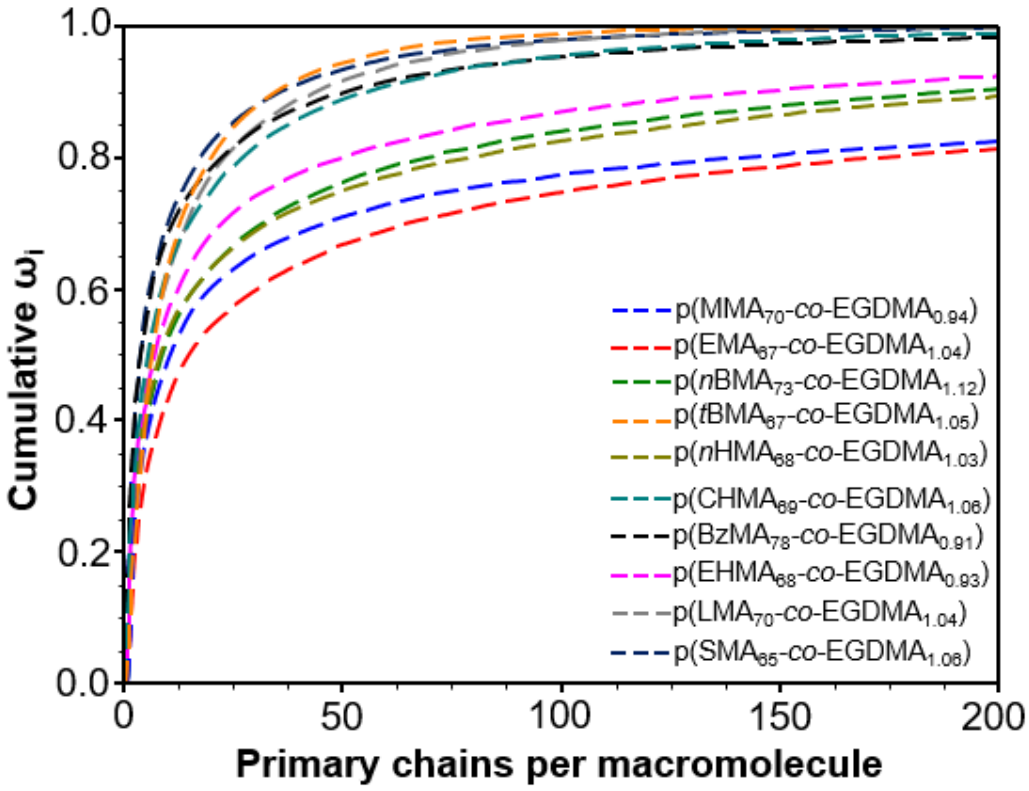

Figure 2.25 TD-SEC analyses comparing the levels of branching achieved during Cu-RDRcP within various monomer-alcohol systems. Plots showing the Cum. ω_f *vs.* number of primary chains per macromolecule for the highest M_w branched statistical copolymers obtained from each of the monomer-solvent systems.

In order to understand the extent to which the levels of branching varied between monomer-solvent systems, the cum. ω_f *vs.* number of primary chains per macromolecule plots of *p*(EMA$_{67}$-*co*-EGDMA$_{1.04}$) and *p*(SMA$_{65}$-*co*-EGDMA$_{1.06}$) were directly compared. Whilst these materials possessed the highest M_w (prepared by copolymerisation of EMA and SMA with EGDMA in MeOH and IPA respectively) and also contained comparable chain lengths and EGDMA contents as determined by ^{1}H NMR, they exhibited the highest and lowest levels of branching of all the monomer-solvent systems studied. TD-SEC analysis showed that the lowest 25 % of the cumulative weight fraction (ω_f = 0.25) was made up of branched copolymers containing no more than 4 and 2 primary chains in *p*(EMA$_{67}$-*co*-EGDMA$_{1.04}$) and *p*(SMA$_{65}$-*co*-EGDMA$_{1.06}$) respectively. In contrast, the same analysis showed that 75 % of the weight fraction (ω_f = 0.75) was made up of polymer chains containing up to 104 and 15 chains respectively. The upper quartile of the *p*(EMA$_{66}$-*co*-EGDMA$_{1.04}$) molecular weight distribution therefore has > 7-fold higher number of conjoined chains than *p*(SMA$_{65}$-*co*-EGDMA$_{1.06}$) (Figure 2.26).

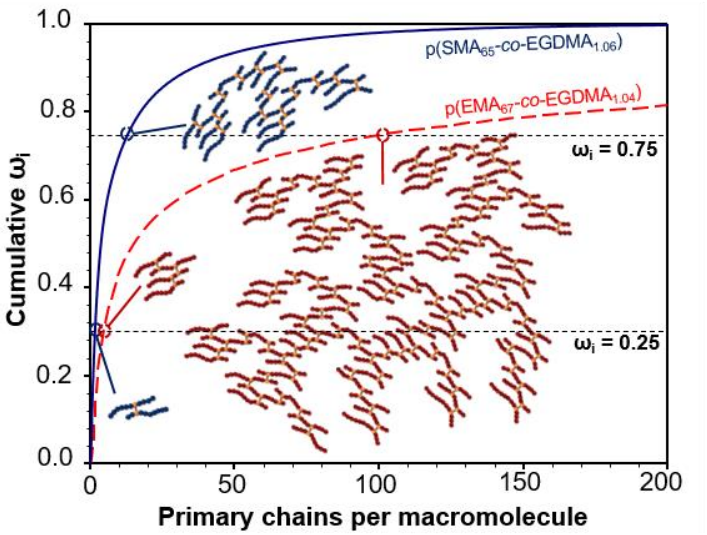

Figure 2.26 Direct comparison of the levels of branching observed in *p*(EMA$_{67}$-*co*-EGDMA$_{1.04}$) and *p*(SMA$_{65}$-*co*-EGDMA$_{1.06}$) by TD-SEC. Overlaid plots of cum ω_f *vs.* number of primary chains per macromolecule, accompanied by schematic representation of the branched copolymer architectures occupying the upper and lower quartiles of the *p*(EMA$_{67}$-*co*-EGDMA$_{1.04}$) (red) and *p*(SMA$_{65}$-*co*-EGDMA$_{1.06}$) (dark blue) sample masses.

The differences in the levels of branching observed between monomer-solvent systems can be explained by three key differences which arise, and most likely influence, branching reactions during copolymerisations targeting the same solids content and the same primary chain DP_n. Most strikingly, the active chain-end concentration, within the MMA to SMA copolymerisation series, decreases significantly when seeking to achieve constant solids content and identical chain length. The monomer M_r increase across the series can also be considered as a vinyl group weight fraction within the monomers as decreasing from 85 wt % to 25 wt % which necessitates a subsequent reduction in initiator concentration to target a fixed DP_n (Figure 2.27 and Appendix, Table A2.2). A normalised active chain-end concentration factor can be calculated for each branching copolymerisation studied. Across the extremes of the copolymerisations reported here, active chain-end concentrations for an MMA/EGDMA branched copolymerisation are 3.38-fold higher than the equivalent SMA/EGDMA reaction. Similar concentration factors arise when copolymerisations are conducted at lower solids contents. Based on theoretical calculations, Figure 2.27 (solid black line) shows the dependence of the relative $[I]_0$ on the solids content at which statistical copolymerisations of MMA and EGDMA are conducted (Appendix, Table A2.3). The impact of copolymerisation concentration on the prevalence of intramolecular cyclisation is well known and can likely explain the relatively low levels of branching observed in the copolymerisations of LMA and SMA with EGDMA, compared with those conducted under similar experimental $[B]_0/[I]_0$ ratios, at higher active chain-end concentrations.

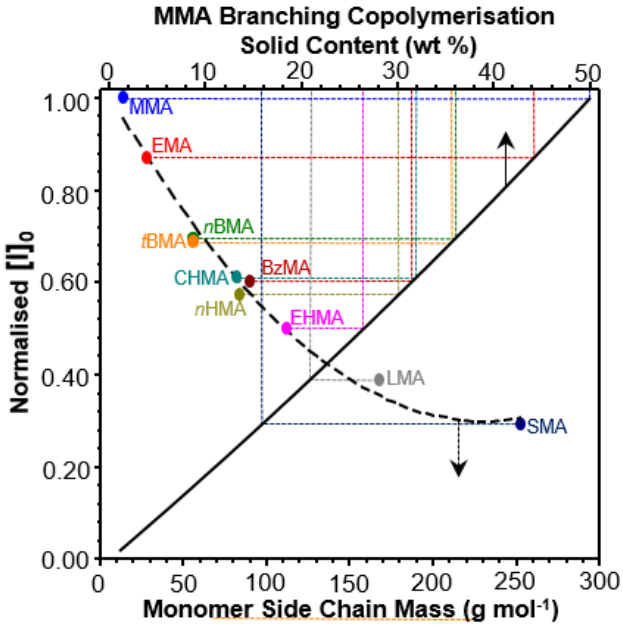

Figure 2.27 The inherent concentration factors which arise during branching copolymerisations. Graphical representations of the change in relative $[I]_0$ which accompany variations in monomer side chain mass in copolymerisations targeting a fixed DP_n, conducted at a constant total solids content (50 wt %, dashed black line); and the percent solids content at which MMA/EGDMA copolymerisations are conducted (solid black line). Dashed coloured lines show the reduction required, in the concentration at which a MMA/EGDMA copolymerisation is conducted, in order to produce a concentration equivalent to those experienced by each of the monomer-solvent systems.

Additionally, the variation in steric hindrance created by the methacrylate side-chain must also be considered. As the pendent group increases in size, the side-chains will ultimately exceed the length of the pendant methacrylate groups resulting from EGDMA incorporation (Figure 2.28a). Molecular modelling studies were conducted using Spartan'18™ software in order to understand the extent of steric hindrance around pendant methacrylate groups during copolymerisation. To achieve this, representative oligomers (DP_n = 10), derived from each of the hydrophobic methacrylate monomers used in this study, were constructed containing one EGDMA unit per primary chain; this allowed measurement of the distances that both pendant methacrylate groups and monomer side-chains protrude from the polymer backbone (Appendix, Figure A2.9). As expected, increases in the size of monomer side chains resulted in increased protrusion from the polymer backbone. However, despite significant differences in the size of the comonomer side-chain, little difference was observed in the protrusion distance of the EGDMA pendant methacrylate group, which gave an average protrusion distance of 0.889 nm from the polymer backbone. In contrast, repeat unit side-chains of MMA and LMA protruded distances of 0.427 nm and 1.619 nm respectively (Appendix A2.9, and Table A2.4). These simulations highlighted that steric hindrance around pendant EGDMA methacrylate groups

increases with the size of the monomer side-chain. However, it is unclear whether this would actually promote consumption of pendant methacrylate groups *via* intramolecular cyclisation over intermolecular branching reactions.[101] Whilst further studies may be required to determine the relative contributions of intermolecular branching and intramolecular cyclisation, increased steric hindrance remains one possible explanation for the variation in the levels of branching observed between monomer-solvent systems.

Finally, the varying solvent environment within these polymerisations, and the impact on the phase behaviour of the branched copolymers during propagation, may also be important. This may be highly specific to the copolymerisations discussed above. However, it has previously been hypothesised that for polymerisations where monomer consumption progressively leads to a bad solvent environment within the reaction mixture, the formation of densely-coiled structures is likely.[88] In the branching copolymerisations described here, it is likely that the conformations of the propagating primary chains within highly branched structures and the lightly branched fraction across the copolymerising monomer series differ significantly (Figure 2.28).

Branching copolymerisations of MMA with EGDMA gave homogeneous reactions mixtures, even after cooling, indicating that branched copolymers remained well-solvated throughout polymerisation. In contrast, *n*BMA/EGDMA branching copolymerisations remained homogeneous until these reaction mixtures were allowed to cool and *n*HMA/EGDMA copolymerisations remained homogenous until high monomer conversion. It is reasonable to envisage that, in relatively poor solvent environments, branched copolymers adopt more densely-packed conformations, reducing the availability of pendent methacrylate groups and reducing the overlap between neighbouring chains in solution. This would also hinder intermolecular branching. Several of the monomer/EGDMA copolymerisations studied formed biphasic reaction mixtures during copolymerisation, giving highly viscous polymer-rich phases. It is likely that such phase behaviour, and assumed associated conformational changes, negatively impact the creation of intermolecular branch points. This is supported by the high levels of branching observed for MMA/EGDMA and EMA/EGDMA systems in contrast to the lower levels of branching observed for the *n*BMA/EGDMA and *n*HMA/EGDMA systems. The lowest extent of branching were observed in copolymerisations of CHMA, LMA or SMA with EGDMA, which form biphasic reaction mixtures in the early stages of polymerisation with subsequent suppression of branching.

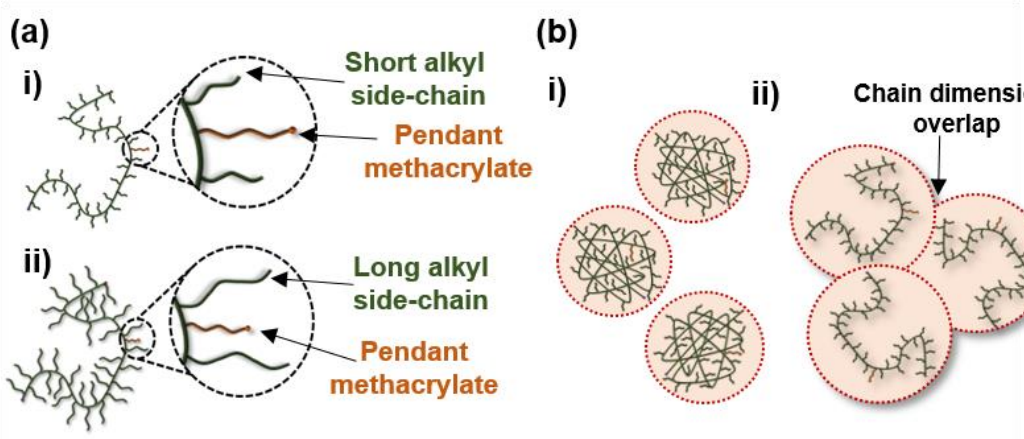

Figure 2.28 Factors affecting branching in the copolymerisation of hydrophobic methacrylates with EGDMA *via* Cu-RDRP in alcohols. (a) Schematic representation of the steric hindrance around pendant methacrylate groups in the presence of monomers containing i) short and ii) long alkyl side chains. (b) Schematic representation of proposed primary chain conformations in different solvent environments. i) collapsed polymer chains within a bad solvent environment and ii) expanded polymer chains within a good solvent environment.

2.5 Conclusions

This work aimed to expand the scope of Cu-RDRP of hydrophobic methacrylate monomers in alcoholic solvents and explore the viability of the synthesis of a range of linear homopolymer, AB block copolymer and branched statistical copolymer architectures using this unconventional approach. One attraction of RDRP reactions is the ability to conduct controlled polymerisations at high solids, leading to final polymer solutions of > 50 wt %. However, it is clear that monomer selection has the potential to impact the initial solvent environment. Monomer depletion during propagation, and formation of polymer, may lead to a transition from a "good" solvent environment to a "poor" solvent condition, as exploited by the so-called polymerization-induced self-assembly (PISA) reactions.[79] Equally, varying solvent/monomer mixture polarity may also impact the solubility of the catalytic systems employed and alterations of the reversible-deactivation equilibrium during different stages of polymerisation. These effects are readily overlooked within reactions where medium is a good solvent for all reagents and products. In the generation of linear homopolymers and AB block copolymers, reaction homogeneity is not a critical parameter and low degrees of phase separation do not appear to have a significant impact on the achievement of high conversions or low $Đ$ values. Further work to determine catalyst solubility within different monomer-solvent mixtures as well as kinetic monitoring of Cu-RDRP of other hydrophobic monomers in alcoholic media, is required to further understand the impact of phase separation on the polymerisation process.

The ability to conduct Cu-RDRP in anhydrous MeOH and IPA for a range of hydrophobic monomers from MMA to SMA, including cyclic aromatic/aliphatic and branched alkyl side chains, is remarkable. The low dispersity and M_n targeting to give linear homopolymers is highly interesting with value potentially in more environmentally favourable solvent systems being employed on large scales. Additionally, incorporation of EGDMA at low comonomer concentrations was not unduly impacted and offers a readily available route to the formation of branched vinyl polymers. To the best of the authors' knowledge, the work described here is the first report on the preparation of branched statistical copolymers containing either *n*HMA, CHMA, BzMA, EHMA, LMA or SMA using Cu-RDRP in alcoholic media. Again, further studies are required to optimise branching copolymerisations of this type under these conditions, but it may be possible to overcome poor branching efficiencies through simple changes to experimental design, including incremental increases to the $[B]_0/[I]_0$ ratios beyond those studied here to establish the experimental gel point, varying the chemistry and chain length of the BFM used (to overcome inter-chain steric issues) and variation in solids content and subsequent initial solvent environment.

2.6 References

1 M. De Malde, F. Minisci, U. Pallini, E. Volterra and A. Quilico, *La Chim. e l'Industria*, 1956, **38**, 371–382.
2 F. Minisci and R. Galli, *Tetrahedron Lett.*, 1962, **3**, 533–538.
3 F. Minisci and U. Pallini, *Gazz. Chim. Ital.*, 1961, **91**, 1030–1036.
4 M. Kato, M. Kamigaito, M. Sawamoto and T. Higashimura, *Macromolecules*, 1995, **28**, 1721–1723.
5 J.-S. Wang and K. Matyjaszewski, *J. Am. Chem. Soc.*, 1995, **117**, 5614–5615.
6 J.-S. Wang and K. Matyjaszewski, *Macromolecules*, 1995, **28**, 7572–7573.
7 J. Gromada and K. Matyjaszewski, *Macromolecules*, 2001, **34**, 7664–7671.
8 W. Jakubowski and K. Matyjaszewski, *Macromolecules*, 2005, **38**, 4139–4146.
9 W. Jakubowski, K. Min and K. Matyjaszewski, *Macromolecules*, 2006, **39**, 39–45.
10 K. Matyjaszewski, W. Jakubowski, K. Min, W. Tang, J. Huang, W. A. Braunecker and N. V Tsarevsky, *Proc. Natl. Acad. Sci.*, 2006, **103**, 15309–15314.
11 K. Matyjaszewski, S. Coca, S. G. Gaynor, M. Wei and B. E. Woodworth, *Macromolecules*, 1997, **30**, 7348–7350.
12 A. J. D. Magenau, N. C. Strandwitz, A. Gennaro and K. Matyjaszewski, *Science (80-.).*, 2011, **332**, 81–84.
13 V. Percec, A. V Popov, E. Ramirez-Castillo, M. Monteiro, B. Barboiu, O. Weichold, A. D. Asandei and C. M. Mitchell, *J. Am. Chem. Soc.*, 2002, **124**, 4940–4941.
14 M. A. Tasdelen, M. Uygun and Y. Yagci, *Macromol. Rapid Commun.*, 2011, **32**, 58–62.
15 A. Anastasaki, V. Nikolaou, Q. Zhang, J. Burns, S. R. Samanta, C. Waldron, A. J. Haddleton, R. McHale, D. Fox, V. Percec, P. Wilson and D. M. Haddleton, *J. Am. Chem. Soc.*, 2014, **136**, 1141–1149.
16 V. Percec, T. Guliashvili, J. S. Ladislaw, A. Wistrand, A. Stjerndahl, M. J. Sienkowska, M. J. Monteiro and S. Sahoo, *J. Am. Chem. Soc.*, 2006, **128**, 14156–14165.
17 C. Boyer, N. A. Corrigan, K. Jung, D. Nguyen, T.-K. Nguyen, N. N. M. Adnan, S. Oliver, S. Shanmugam and J. Yeow, *Chem. Rev.*, 2016, **116**, 1803–1949.

18 K. Matyjaszewski and J. Xia, *Chem. Rev.*, 2001, **101**, 2921–2990.
19 K. Matyjaszewski, T. E. Patten and J. Xia, *J. Am. Chem. Soc.*, 1997, **119**, 674–680.
20 K. A. Davis, H. Paik and K. Matyjaszewski, *Macromolecules*, 1999, **32**, 1767–1776.
21 J.-L. Wang, T. Grimaud and K. Matyjaszewski, *Macromolecules*, 1997, **30**, 6507–6512.
22 V. Percec, B. Barboiu and H.-J. Kim, *J. Am. Chem. Soc.*, 1998, **120**, 305–316.
23 L. Xue, U. S. Agarwal and P. J. Lemstra, *Macromolecules*, 2002, **35**, 8650–8652.
24 D. J. Siegwart, J. K. Oh and K. Matyjaszewski, *Prog. Polym. Sci.*, 2012, **37**, 18–37.
25 Y. Li, Y.-F. Wu, L. Yuan and S.-Q. Liu, *Chinese J. Anal. Chem.*, 2012, **40**, 1797–1802.
26 P. R. Rodrigues and R. P. Vieira, *Eur. Polym. J.*, 2019, **115**, 45–58.
27 F. J. Xu, K. G. Neoh and E. T. Kang, *Prog. Polym. Sci.*, 2009, **34**, 719–761.
28 J. K. Oh, S. A. Bencherif and K. Matyjaszewski, *Polymer.*, 2009, **50**, 4407–4423.
29 S. Watson, M. Nie, L. Wang and K. Stokes, *RSC Adv.*, 2015, **5**, 89698–89730.
30 Y. Kwak, R. Nicolaÿ and K. Matyjaszewski, *Aust. J. Chem.*, 2009, **62**, 1384–1401.
31 S. Coca, H. Paik and K. Matyjaszewski, *Macromolecules*, 1997, **30**, 6513–6516.
32 S. Coca and K. Matyjaszewski, *Macromolecules*, 1997, **30**, 2808–2810.
33 K. Matyjaszewski, K. L. Beers, A. Kern and S. G. Gaynor, *J. Polym. Sci. Part A Polym. Chem.*, 1998, **36**, 823.
34 H. Shinoda and K. Matyjaszewski, *Macromolecules*, 2001, **34**, 6243–6248.
35 H. Shinoda, P. J. Miller and K. Matyjaszewski, *Macromolecules*, 2001, **34**, 3186–3194.
36 S. G. Roos, A. H. Muller and K. Matyjaszewski, *Macromolecules*, 1999, **32**, 8331–8335.
37 J. Pyun, K. Matyjaszewski, T. Kowalewski, D. Savin, G. Patterson, G. Kickelbick and N. Huesing, *J. Am. Chem. Soc.*, 2001, **123**, 9445–9446.
38 S. Averick, A. Simakova, S. Park, D. Konkolewicz, A. J. D. Magenau, R. A. Mehl and K. Matyjaszewski, *ACS Macro Lett.*, 2012, **1**, 6–10.
39 P. Ritz, P. Látalová, M. Janata, L. Toman, J. Kříž, J. Genzer and P. Vlček, *React. Funct. Polym.*, 2007, **67**, 1027–1039.
40 C. Wang, K. Hashimoto, J. Zhang, Y. Kobayashi, H. Kokubo and M. Watanabe, *Macromolecules*, 2017, **50**, 5377–5384.
41 A. Ding, G. Lu, H. Guo and X. Huang, *Polym. Chem.*, 2017, **8**, 6997–7008.
42 W. Zhang and A. H. E. Müller, *Macromolecules*, 2010, **43**, 3148–3152.
43 W. Jakubowski, B. Kirci-Denizli, R. R. Gil and K. Matyjaszewski, *Macromol. Chem. Phys.*, 2008, **209**, 32–39.
44 J.-F. Lutz and K. Matyjaszewski, *J. Polym. Sci. Part A Polym. Chem.*, 2005, **43**, 897–910.
45 A. H. Soeriyadi, C. Boyer, F. Nyström, P. B. Zetterlund and M. R. Whittaker, *J. Am. Chem. Soc.*, 2011, **133**, 11128–11131.
46 F. Nyström, A. H. Soeriyadi, C. Boyer, P. B. Zetterlund and M. R. Whittaker, *J. Polym. Sci. Part A Polym. Chem.*, 2011, **49**, 5313.
47 F. Alsubaie, A. Anastasaki, P. Wilson and D. M. Haddleton, *Polym. Chem.*, 2015, **6**, 406–417.
48 C. Y. Lin, S. R. A. Marque, K. Matyjaszewski and M. L. Coote, *Macromolecules*, 2011, **44**, 7568–7583.
49 K. Matyjaszewski, D. A. Shipp, J.-L. Wang, T. Grimaud and T. E. Patten, *Macromolecules*, 1998, **31**, 6836–6840.
50 C.-H. Peng, J. Kong, F. Seeliger and K. Matyjaszewski, *Macromolecules*, 2011, **44**, 7546–7557.
51 N. O'Brien, A. McKee, D. C. Sherrington, A. T. Slark and A. Titterton, *Polymer.*, 2000, **41**, 6027–6031.
52 F. Isaure, P. A. G. Cormack and D. C. Sherrington, *J. Mater. Chem.*, 2003, **13**, 2701–2710.
53 G. Saunders, P. A. G. Cormack, S. Graham and D. C. Sherrington, *Macromolecules*,

2005, **38**, 6418–6422.
54 F. Isaure, P. A. G. Cormack, S. Graham, D. C. Sherrington, S. P. Armes and V. Bütün, *Chem. Commun.*, 2004, 1138–1139.
55 Y. Li and S. P. Armes, *Macromolecules*, 2005, **38**, 8155–8162.
56 C.-D. Vo, J. Rosselgong, S. P. Armes and N. C. Billingham, *Macromolecules*, 2007, **40**, 7119–7125.
57 J. C. Hernández-Ortiz, E. Vivaldo-Lima, L. M. F. Lona, N. T. McManus and A. Penlidis, *Macromol. React. Eng.*, 2009, **3**, 288–311.
58 H. Yang, Z. Wang, Y. Zheng, W. Huang, X. Xue and B. Jiang, *Polym. Chem.*, 2017, **8**, 2137–2144.
59 M. Liu, B. H. Tan, R. P. Burford and A. B. Lowe, *Polym. Chem.*, 2013, **4**, 3300–3311.
60 Z. Dong and Z. Ye, *Macromolecules*, 2012, **45**, 5020–5031.
61 F. L. Hatton, L. M. Tatham, L. R. Tidbury, P. Chambon, T. He, A. Owen and S. P. Rannard, *Chem. Sci.*, 2015, **6**, 326–334.
62 F. L. Hatton, P. Chambon, T. O. McDonald, A. Owen and S. P. Rannard, *Chem. Sci.*, 2014, **5**, 1844–1853.
63 A. R. Wang and S. Zhu, *Polym. Eng. Sci.*, 2005, **45**, 720–727.
64 B. Liu, A. Kazlauciunas, J. T. Guthrie and S. Perrier, *Macromolecules*, 2005, **38**, 2131–2136.
65 D. Taton, J. F. Baussard, L. Dupayage, J. Poly, Y. Gnanou, V. Ponsinet, M. Destarac, C. Mignaud and C. Pitois, *Chem. Commun.*, 2006, 1953–1955.
66 J. Rosselgong, S. P. Armes, W. R. S. Barton and D. Price, *Macromolecules*, 2010, **43**, 2145–2156.
67 J. Rosselgong and S. P. Armes, *Polym. Chem.*, 2015, **6**, 1143–1149.
68 J. Rosselgong and S. P. Armes, *Macromolecules*, 2012, **45**, 2731–2737.
69 I. Bannister, N. C. Billingham and S. P. Armes, *Soft Matter*, 2009, **5**, 3495–3504.
70 S. Liang, X. Li, W.-J. Wang, B.-G. Li and S. Zhu, *Macromolecules*, 2016, **49**, 752–759.
71 J. Rosselgong, S. P. Armes, W. Barton and D. Price, *Macromolecules*, 2009, **42**, 5919–5924.
72 W. Li, J. A. Yoon, M. Zhong and K. Matyjaszewski, *Macromolecules*, 2011, **44**, 3270–3275.
73 A. Moreno, S. Grama, T. Liu, M. Galià, G. Lligadas and V. Percec, *Polym. Chem.*, 2017, **8**, 7559–7574.
74 M. Enayati, R. L. Jezorek, R. B. Smail, M. J. Monteiro and V. Percec, *Polym. Chem.*, 2016, **7**, 5930–5942.
75 R. L. Jezorek, M. Enayati, R. B. Smail, J. Lejnieks, S. Grama, M. J. Monteiro and V. Percec, *Polym. Chem.*, 2017, **8**, 3405–3424.
76 M. Enayati, R. B. Smail, S. Grama, R. L. Jezorek, M. J. Monteiro and V. Percec, *Polym. Chem.*, 2016, **7**, 7230–7241.
77 S. Grama, J. Lejnieks, M. Enayati, R. B. Smail, L. Ding, G. Lligadas, M. J. Monteiro and V. Percec, *Polym. Chem.*, 2017, **8**, 5865–5874.
78 R. B. Smail, R. L. Jezorek, J. Lejnieks, M. Enayati, S. Grama, M. J. Monteiro and V. Percec, *Polym. Chem.*, 2017, **8**, 3102–3123.
79 N. J. Warren and S. P. Armes, *J. Am. Chem. Soc.*, 2014, **136**, 10174–10185.
80 Z. Ding, C. Gao, S. Wang, H. Liu and W. Zhang, *Polym. Chem.*, 2015, **6**, 8003–8011.
81 Z. Song, X. He, C. Gao, H. Khan, P. Shi and W. Zhang, *Polym. Chem.*, 2015, **6**, 6563–6572.
82 J. Jennings, G. He, S. M. Howdle and P. B. Zetterlund, *Chem. Soc. Rev.*, 2016, **45**, 5055–5084.
83 M. J. Derry, L. A. Fielding and S. P. Armes, *Prog. Polym. Sci.*, 2016, **52**, 1–18.
84 N. J. W. Penfold, J. R. Lovett, N. J. Warren, P. Verstraete, J. Smets and S. P. Armes, *Polym. Chem.*, 2016, **7**, 79–88.
85 T. Cuneo, R. W. Graff, X. Wang and H. Gao, *Macromol. Chem. Phys.*, 2019, **220**,

1800546.
86 R. W. Graff, X. Wang and H. Gao, *Macromolecules*, 2015, **48**, 2118–2126.
87 K. Min and H. Gao, *J. Am. Chem. Soc.*, 2012, **134**, 15680–15683.
88 A. B. Dwyer, P. Chambon, A. Town, T. He, A. Owen and S. P. Rannard, *Polym. Chem.*, 2014, **5**, 3608–3616.
89 F. Y. Hern, A. Hill, A. Owen and S. P. Rannard, *Polym. Chem.*, 2018, **9**, 1767–1771.
90 A. B. Dwyer, P. Chambon, A. Town, F. L. Hatton, J. Ford and S. P. Rannard, *Polym. Chem.*, 2015, **6**, 7286–7296.
91 Precis. Labware, https://www.precisionlabware.com/content/18-solvent-miscibility, (accessed 1 June 2016).
92 D. C. Dong and M. A. Winnik, *Can. J. Chem.*, 1984, **62**, 2560–2565.
93 Q. Zhang and R. Hoogenboom, *Prog. Polym. Sci.*, 2015, **48**, 122–142.
94 C. Pietsch, R. Hoogenboom and U. S. Schubert, *Polym. Chem.*, 2010, **1**, 1005–1008.
95 J. H. Liu, U. Wais, Y. M. Zuo, Y. Xiang, Y. H. Wang, A. W. Jackson, T. He and H. Zhang, *J. Mater. Chem. B*, 2017, **5**, 423–427.
96 M. Giardiello, F. L. Hatton, R. A. Slater, P. Chambon, J. North, A. K. Peacock, T. He, T. O. McDonald, A. Owen and S. P. Rannard, *Nanoscale*, 2016, **8**, 7224–7231.
97 I. Bannister, N. C. Billingham, S. P. Armes, S. P. Rannard and P. Findlay, *Macromolecules*, 2006, **39**, 7483–7492.
98 X. Xue, Y. Wang, W. Huang, H. Yang, J. Chen, J. Fang, Y. Yang, L. Kong and B. Jiang, *Macromol. Chem. Phys.*, 2015, **216**, 1555–1561.
99 H. Chen and J. Kong, *Polym. Chem.*, 2016, **7**, 3643–3663.
100 A. B. Cook and S. Perrier, *Adv. Funct. Mater.*, 2019, **30**, 1901001.
101 H. Cauldbeck, M. Le Hellaye, M. Long, S. M. Kennedy, R. L. Williams, V. R. Kearns and S. P. Rannard, *J. Control. Release*, 2016, **244**, 41–51.

Chapter 3

Expanding the Scope of Co-nanoprecipitation: Preparation of Novel Branched Vinyl Copolymer Nanoparticles and Understanding the Co-nanoprecipitation Process

3.1 Introduction

The production of polymer based nanoparticles is of considerable interest as it provides the opportunity to generate nanomaterials which typically possess different and often unobtainable physical and chemical properties to those of their bulk materials.[1–5] The preparation and utilisation of polymeric nanoparticles has therefore attracted significant scientific research interest in recent years.[6,7] Nanoprecipitation is one technique which has been used to generate nanoparticles using a wide range of polymeric materials.[8] The concept of nanoprecipitation, including an overview of the mechanisms of nanoparticle formation and colloidal stabilisation, was discussed in detail during Chapter 1, Section 1.4.2.1. In particular, research has focused on the optimisation of the nanoprecipitation process in order to generate polymeric nanoparticles which contain low dispersity whilst maintaining control over their hydrodynamic diameters.[9]

Nanoprecipitation of hydrophobic polymers has been used to generate aqueous polymer based nanoparticle dispersions. In the absence of steric or electrostatic stabilisation mechanisms, the inherent increase in interfacial surface area which accompanies a reduction in particle size make hydrophobic based polymeric nanoparticles unstable and prone to aggregation and sedimentation.[10] This is often overcome by using polymers which generate electrostatic charge at the nanoparticle surface and prevent particle-particle aggregation *via* electrostatic repulsion. However, such electrostatic stabilisation can be masked in the presence of electrolytes and the particles are prone to aggregation *via* flocculation even at low concentrations of salt.[11] Numerous alternative approaches have been made to stabilise hydrophobic polymer-based nanoparticles. These typically include surface modification of nanoparticles with amphiphilic copolymers and non-ionic surfactants.[12–19] The adsorption of such species at the nanoparticle surface provide nanoparticles with a degree of steric stabilisation and can delay or even completely prevent nanoparticle aggregation.

3.1.1 Co-nanoprecipitation

The synthesis of complex macromolecular architectures using RDRP has facilitated the production of novel nanoprecipitation based nanoformulation techniques.[20,21] In 2015, Rannard and co-workers reported the preparation of sterically stabilised branched vinyl copolymer nanoparticles *via* the simultaneous nanoprecipitation of high molecular weight, hydrophobic branched copolymers with their corresponding PEG-based amphiphilic block copolymers.[22] This approach was coined ‘co-nanoprecipitation’ and facilitated the production of highly monodisperse *p(*HPMA) based nanoparticles with intensity-average hydrodynamic diameters ranging from 72 – 293 nm. The use of PEG-based amphiphilic block copolymers in co-nanoprecipitation equipped the resulting hybrid nanoparticles with the steric stabilisation required to tolerate the addition of high concentrations of sodium chloride (NaCl).

The formation of branched vinyl copolymer nanoparticles *via* co-nanoprecipitation is presented in Figure 3.1. Briefly, amphiphilic AB block and branched copolymers, molecularly dissolved within a mutual good solvent are rapidly added to water, which is a bad solvent for the hydrophobic component of each copolymer. The rapid diffusion of water causes a state of supersaturation within the co-nanoprecipitation medium and drives nanoparticle formation *via* a diffusion-limited cluster-cluster aggregation (DLCA) growth mechanism. The co-nanoprecipitation process is reliant upon the simultaneous nucleation of amphiphilic block copolymers; this is achieved by ensuring that both hydrophobic components of the copolymers are derived from the same monomer, i.e. co-nanoprecipitation of PEG_{45}-*b*-*p(*$HPMA)_{120}$ with *p(*$HPMA_{50}$-*co*-$EGDMA_{0.90}$). Ford *et al.* demonstrated that nanoparticle formation occurred immediately after copolymer addition and gave stable aqueous nanoparticle dispersions following solvent removal *via* evaporation.[22]

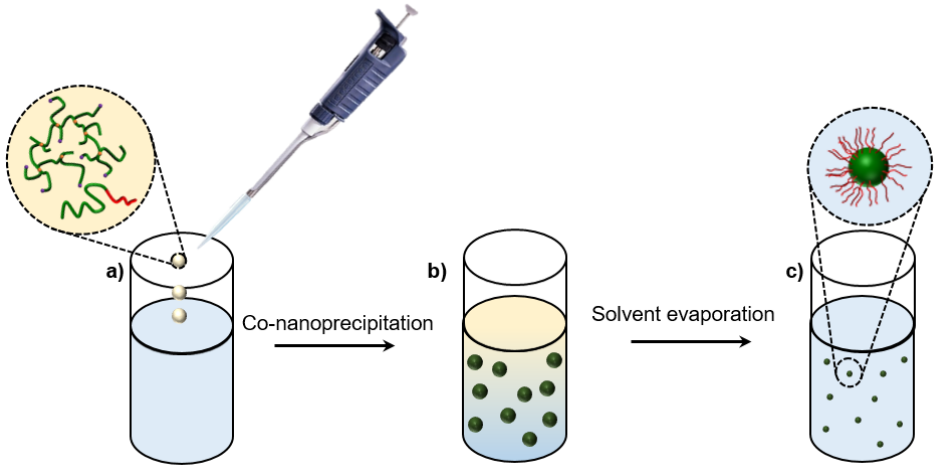

Figure 3.1 The formation of branched vinyl copolymer nanoparticles *via* co-nanoprecipitation as described by Rannard and co-workers.[22] a) Hydrophobic branched and amphiphilic AB block copolymers, dissolved within a good solvent, are rapidly added to water. b) Immediate nanoparticle formation *via* co-nanoprecipitation giving swollen *p(*HPMA) based within the nanoprecipitation media. c) Solvent removal *via* evaporation to give a sterically-stabilised aqueous branched vinyl copolymer nanoparticle dispersion.

The main advantage of the co-nanoprecipitation process is that, in the case of *p(*HPMA) based copolymers, it utilises the varied polymer architectures employed to generate optimal polymer nucleation and nanoparticle stabilisation during co-nanoprecipitation. *p(*HPMA) is considered a moderately hydrophobic polymer; as a result, the nanoprecipitation (*p(*HPMA-*co*-EGDMA) based copolymers typically show architecture-dependent nucleation.[23–25] Co-nanoprecipitation therefore relies on high molecular weight branched copolymers to drive nucleation during co-nanoprecipitation whilst utilising the hydrophilic domains of amphiphilic AB block copolymers to provide the resulting nanoparticles with steric stabilisation.

Co-nanoprecipitation allows the final composition of branched vinyl copolymer nanoparticles to be determined simply by controlling the copolymer stoichiometry within the initial

copolymer/good solvent solution. This allows the nanoparticle composition and therefore the level of steric stabilisation to be determined prior to synthesis. Furthermore, the capping of nanoparticle growth *via* a steric stabilisation mechanism allows multiple co-nanoprecipitations to be conducted without impact on the hydrodynamic diameters of the branched vinyl copolymer nanoparticles within the aqueous nanoparticle dispersion.[22]

3.1.2 Chapter Aims

The primary aim of the work depicted in this Chapter is to expand the scope and understanding of nanoparticle formation *via* co-nanoprecipitation. This was attempted through the individual nanoprecipitations and co-nanoprecipitations of a selection of the vast library of polymers generated in Chapter 2, and to build on the successful co-nanoprecipitations of *p(*HPMA) based copolymers previously reported. Here, the first report of the preparation and characterisation of branched vinyl copolymer nanoparticles consisting of a variety of hydrophobic methacrylate copolymers is presented.

The factors which influence nanoparticle formation *via* co-nanoprecipitation were studied; this was achieved through the manipulation of polymers used and experimental conditions in which co-nanoprecipitations are conducted, see Figure 3.2a.

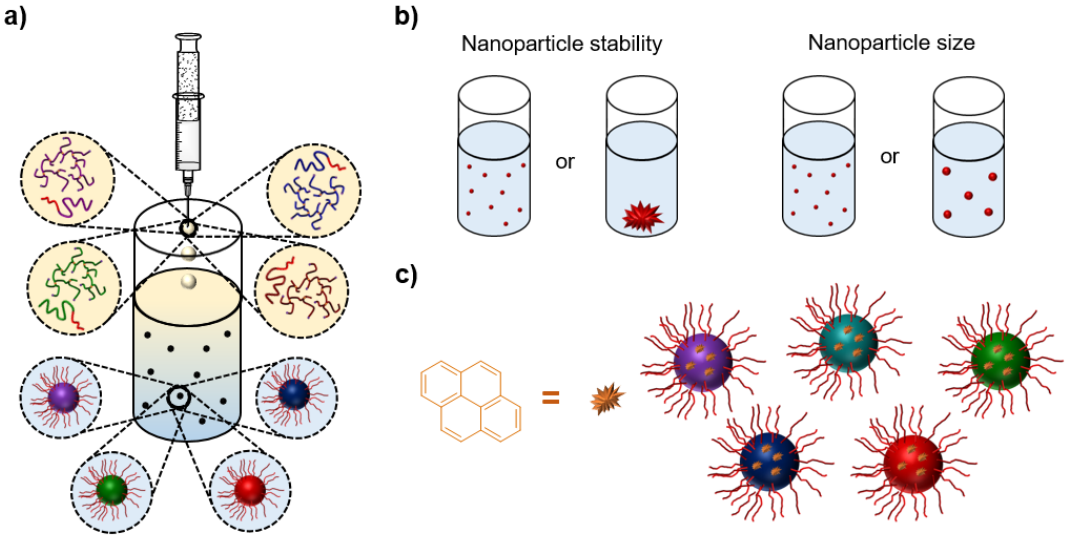

Figure 3.2 Schematic representation of the aims of the work conducted in Chapter 3. a) The preparation of branched vinyl copolymer nanoparticles *via* co-nanoprecipitation of various amphiphilic AB block and hydrophobic branched copolymers. b) Studying polymer and experimental factors which influence nanoparticle formation during co-nanoprecipitation and c) Encapsulation of hydrophobic guest molecule (pyrene) within the core of branched vinyl copolymer nanoparticles *via* co-nanoprecipitation.

In particular, the importance of the architecture, composition, and concentration of the copolymers used in nanoparticle formation during the co-nanoprecipitation process will be highlighted, and a mechanistic insight into the co-nanoprecipitation process will be discussed.

A series of studies will also be presented which correlate the physical properties of nanoparticles, including composition, size and surface charge, to the chemical and physical of the copolymers from which they are constructed.

The suitability of branched vinyl copolymer nanoparticles as prospective drug nanocarriers (DNCs) for the delivery of hydrophobic chemotherapeutics are evaluated. Preliminary studies were conducted to understand whether hydrophobic molecules could be encapsulated within the core of branched vinyl copolymer nanoparticles during the co-nanoprecipitation process. This was attempted *via* the addition of a small amount of hydrophobic pyrene into the solutions from which copolymers were co-nanoprecipitated, Figure 3.2c. Selection of pyrene as the hydrophobic guest molecule allowed the core polarity of branched vinyl copolymer nanoparticles constructed from various hydrophobic polymers to be assessed by fluorescence spectroscopy.

Finally this work aimed to explore whether branched vinyl copolymer nanoparticles formed *via* co-nanoprecipitation are suitable for application within biological environments. In particular, the stability of such nanomaterials to factors which may be experienced following IV administration, such as substantial dilution and the presence of high salt concentrations, were assessed.

3.2 Selection of Polymers for use in (Co)nanoprecipitation Studies

A selection of polymers from Chapter 2 were chosen to study the impact of the following polymer characteristics on their performance within the (co)nanoprecipitation processes: i) polymer functionality, i.e. the pendant group of the polymer methacrylic repeat unit, ii) polymer architecture in particular to draw comparisons between linear and branched equivalents and iii) polymer amphiphilicity and its role in nanoparticle stabilisation. Selections of the linear homopolymers, amphiphilic block copolymers and the highest M_w branched statistical copolymers presented in Chapter 2 were used. An overview of the polymers selected for nanoprecipitation and co-nanoprecipitation studies is presented in Figure 3.3 and full characterisation of the polymers used in this Chapter is provided in Chapter 2, Tables 2.1 - 2.4. In addition to the polymers generated in Chapter 2, a *p(*HPMA)-based linear homopolymer, amphiphilic branched copolymer and branched statistical copolymers were prepared *via* methanolic Cu-RDRP. Full characterisation of these materials is presented in Appendix, Figure A3.1 and Table A3.1.

Figure 3.3 Schematic representation of the library of polymers used in nanoprecipitation and co-nanoprecipitation studies in this Chapter. Specifically, the variations in polymer architecture and repeat unit pendant group functionality are highlighted.

3.3 Nanoprecipitation Studies

The preparation of polymer nanoparticles *via* a co-nanoprecipitation process provides additional complexity to traditional nanoprecipitation approaches which typically involve a sole component. In particular, understanding the role of individual polymer components in the co-nanoprecipitation process , or proving their presence within final nanoparticles can often be difficult. In an effort to evaluate the potential role that hydrophobic polymers may play within co-nanoprecipitation, all individual components were systematically studied as the sole components in nanoprecipitations.

3.3.1 Preliminary Nanoprecipitation Studies

Preliminary nanoprecipitation studies were conducted using all 33 of the polymers identified in Figure 3.3. It was desirable to generate a uniform nanoprecipitation process for all polymers which would therefore allow the individual polymers to be isolated. To achieve this, polymer solubility studies were conducted to find a common good solvent for all polymers. Solvent selection is of critical importance to the success of a nanoprecipitation. Organic solvents must be water-miscible in order to allow rapid mixing between good and bad solvents and thus create the state of supersaturation required to induce polymer nucleation. Whilst not a prerequisite it is also desirable if organic solvents are volatile to allow their removal under mild conditions post-nanoprecipitation. Following consideration of these criteria, acetone, MeOH, ethanol (EtOH), IPA and THF were considered suitable organic solvents. However; following the many cases of polymerisation-induced phase separation observed during Cu-RDRP in anhydrous alcohols reported in Chapter 2, MeOH, EtOH and IPA were disgarded at this point. Polymer solubility studies were therefore conducted using acetone and THF. This involved the attempted preparation of polymer solutions at a concentration of 10 mg mL^{-1} under constant agitation over a time period of 48 hours; the homogeneity of polymer solutions were inspected both visually and by passing them through a 0.25 µm PTFE filter. In all cases, polymers showed full solubility in THF whereas all *p(*LMA) and *p(*SMA) based polymers were insoluble in acetone at a concentration of 10 mg mL^{-1}. As a result, THF was selected as the good solvent for all aqueous nanoprecipitations and co-nanoprecipitations conducted throughout this research.

The design of the nanoprecipitation process is also of crucial importance. In particular, the initial concentration of polymer dissolved in good solvent ($[P]_0$), the volume ratio of good solvent to bad solvent, also known as the dilution ratio ($DR = V_{DI\ H2O} / V_{THF}$) and consequently the final polymer concentration in water ($[P]_f$) must all be taken into consideration. In order to ensure a uniform process, all nanoprecipitations were conducted using 1 mL of a starting solution comprising a $[P]_0$ of 5 mg mL^{-1} in THF into 5 mL of deionised (DI) H_2O. These conditions gave a DR of 5, which has been demonstrated as sufficient to drive the nucleation

and subsequent nanoparticle formation of a number of polymers containing similar structures and functionalities to the ones described here.[24–28] A general overview of the nanoprecipitation process employed is presented in Figure 3.4. Briefly, 1 mL of a THF solution the polymer was rapidly injected into 5 mL of DI H_2O under magnetic stirring using a Gilson® manual air displacement pipette; nanoprecipitations were left under magnetic stirring at ambient temperature for 48 hours to facilitate solvent removal *via* evaporation to give an aqueous nanoparticle dispersion at a $[P]_f$ of 1 mg mL^{-1}.

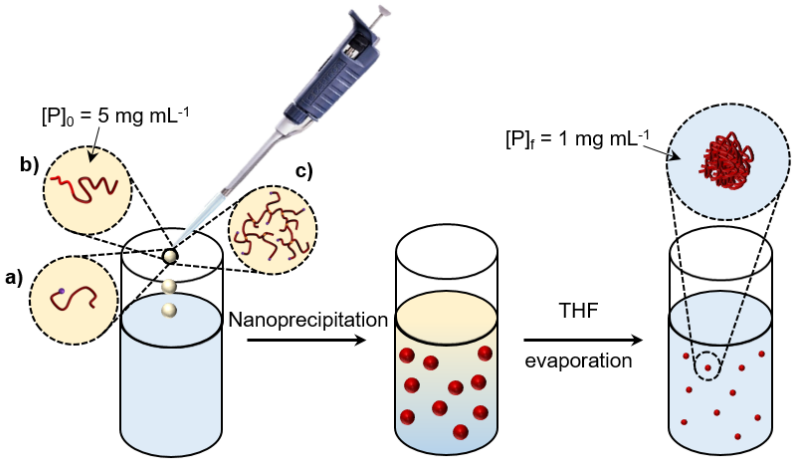

Figure 3.4 Schematic representation of the process by which the nanoprecipitation all 33 polymers was attempted. Firstly, 1mL of a THF solution containing either: a) linear homopolymer, b) AB block copolymer or c) branched copolymer ($[P]_0$ = 5 mg mL^{-1}) were added to 5 mL of DI H_2O causing rapid nanoprecipitation. THF was removed *via* evaporation over 48 hours leaving an aqueous nanoparticle dispersion at a $[P]_f$ of 1 mg mL^{-1}.

With the exception of *p(*$HPMA)_{65}$ and *p(*$HPMA_{63}$-*co*-$EGDMA_{0.90}$), nanoprecipitations of linear and branched copolymers resulted in the immediate formation of a turbid mixture. After 48 hours, visual inspection of the attempted nanoprecipitations of linear homopolymers and branched copolymers, with the exception of *p(*$HPMA_{63}$-*co*-$EGDMA_{0.90}$), indicated that nanoprecipitation had not been successful. This was evident by macroscopic polymer precipitation and subsequent sedimentation within the glass vials (Figure 3.5). In contrast, *p(*$HPMA_{63}$-*co*-$EGDMA_{0.90}$) formed a turbid, aqueous nanoparticle dispersion with no evidence of polymer sedimentation. The success of the nanoprecipitation of *p(*$HPMA_{63}$-*co*-$EGDMA_{0.90}$) was somewhat unsurprising given the prior reports of the formation of branched *p(*HPMA-*co*-EGDMA) based nanoparticles in the literature.[23,24] The size distribution of *p(*$HPMA_{63}$-*co*-$EGDMA_{0.90}$) nanoparticles was assessed using dynamic light scattering (DLS). Analysis showed intensity-derived hydrodynamic diameter (D_z) of 81 nm and a polydispersity index (*PDI*) of 0.041. The success of the nanoprecipitation of branched copolymers consisting of *p(*HPMA) has been attributed to the high surface charge of the nanoparticles formed. Whilst the explanation for this apparent charge stabilisation remains unclear, the zeta potential (ζ) values obtained for the *p(*$HPMA_{63}$-*co*-$EGDMA_{0.90}$) nanoparticles

generated here, - 34.7 mV, should provide a moderate level of charge stabilisation.[24] What perhaps was also unsurprising was the failure of the other predominantly lipophilic groups to provide any stabilisation for aqueous nanoparticle dispersions. However, this may seem less surprising when considering the relative polarity of repeat units containing short aliphatic or even aromatic groups such as those found in MMA and BzMA respectively.

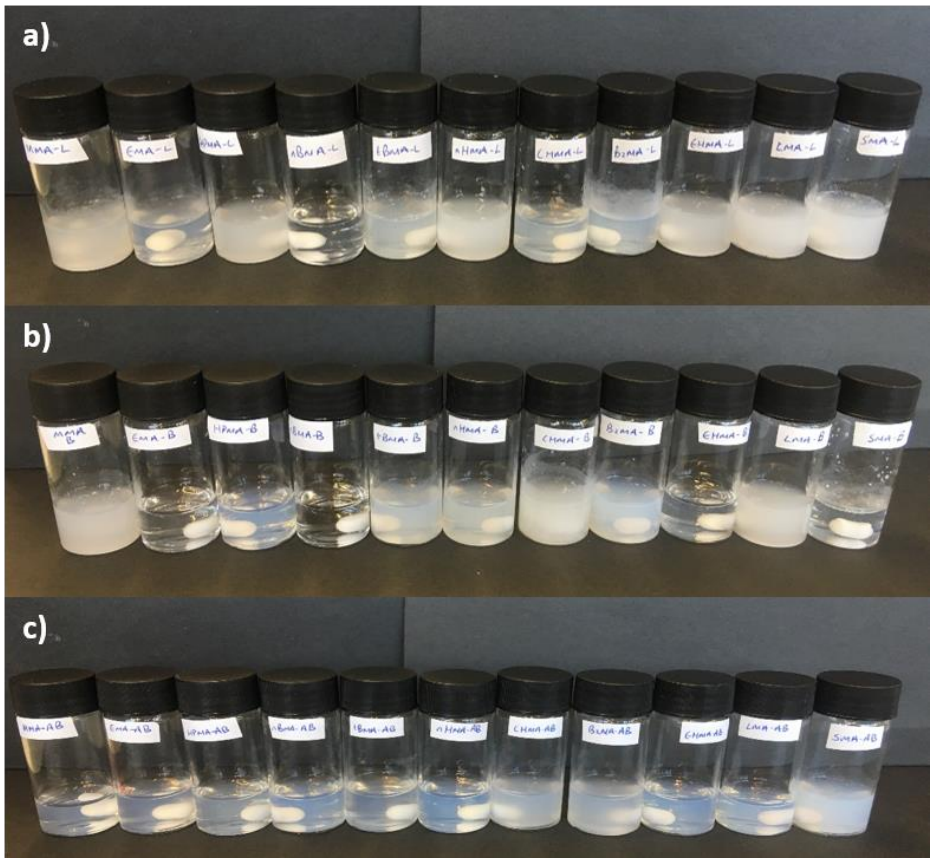

Figure 3.5 Visual observations of nanoprecipitation experiments conducted using a) linear homopolymers, b) branched statistical copolymers and c) amphiphilic AB block copolymers, 48 hours after polymer addition. (left to right) *p(*MMA), *p(*EMA), *p(*HPMA), *p(n*BMA), *p(t*BMA), *p(n*HMA), *p(*CHMA), *p(*BzMA), *p(*EHMA), *p(*LMA), *p(*SMA).

In contrast to nanoprecipitations consisting mainly of linear homopolymers and branched copolymers, all nanoprecipitations of amphiphilic block copolymers remained turbid and translucent immediately following polymer addition. However, the nanoprecipitation of PEG_{45}-*b*-*p(*$CHMA)_{123}$, PEG_{45}-*b*-*p(*$BzMA)_{123}$ and PEG_{45}-*b*-*p(*$SMA)_{122}$ formed macroscopic precipitates following solvent evaporation. These nanoprecipitations were repeated at a $[P]_0$ of 0.5 mg mL^{-1}, which resulted in the formation of stable PEG_{45}-*b*-*p(*$CHMA)_{123}$ nanoparticles. The remaining AB block copolymers formed turbid nanoparticle dispersions with no evidence of sedimentation (Figure 3.5c). The aqueous nanoparticle dispersions obtained from all successful nanoprecipitations were assessed by DLS and zeta potential measurements (Table 3.1).

Table 3.1 Characterisation of polymeric nanoparticles generated through successful nanoprecipitation of branched and amphiphilic AB block copolymers**.**

Architecture	Polymer	D_z (nm)[a]	D_n (nm)[a]	*PDI*[a]	Derived Count Rate (kcps)[a]	ζ (mV)[b]
Branched	*p(*HPMA$_{63}$-*co*-EGDMA$_{0.90}$)	81	65	0.041	486034	-34.7
AB Block	PEG$_{45}$-*b*-*p(*MMA)$_{120}$	97	45	0.239	221229	-*
	PEG$_{45}$-*b*-*p(*EMA)$_{120}$	99	49	0.313	227997	-*
	PEG$_{45}$-*b*-*p(*HPMA)$_{120}$	121	98	0.035	253390	-11.9
	PEG$_{45}$-*b*-*p(n*BMA)$_{120}$	78	58	0.079	395842	-12.0
	PEG$_{45}$-*b*-*p(t*BMA)$_{120}$	74	50	0.104	218123	-12.0
	PEG$_{45}$-*b*-*p(n*HMA)$_{120}$	77	58	0.066	379431	-3.4
	PEG$_{45}$-*b*-*p(*EHMA)$_{120}$	85	63	0.067	516357	-11.6
	PEG$_{45}$-*b*-*p(*LMA)$_{120}$	93	76	0.026	732780	-1.6

[a]Obtained using DLS analysis of aqueous nanoparticle dispersions at a concentration of 1 mg mL^{-1}. [b]Obtained *via* measurement of the electrophoretic mobility in 0.01M KCl aqueous nanoparticle dispersions. *Sample unstable, reliable zeta potential data could not be obtained.

Nanoparticle hydrodynamic diameters (D_z = 74 - 124 nm) were broadly comparable to number-average hydrodynamic diameters (D_n = 45 - 105 nm) throughout this series of materials. No trends were observed between nanoparticle size and the chemical nature of the methacrylate monomers from which AB block copolymers were constructed. With the exception of PEG$_{45}$-*b*-*p(*MMA)$_{122}$ and PEG$_{45}$-*b*-*p(*CHMA)$_{123}$ based nanoparticles, all aqueous nanoparticle dispersions had narrow size distributions ($PDI \leq 0.100$), which is indicative of homogeneous nucleation and rapid growth during the nanoprecipitation process. In all cases the zeta potentials obtained were generally low (-1.6 to -12.0 mV) which indicated that nanoparticle stability is not maintained by electrostatic stabilisation and thus is likely provided through steric stabilisation conferred by the hydrated PEG coronas of individual nanoparticles.

Interestingly there were varying levels of success observed during nanoprecipitation of copolymers which varied in monomer functionality and architecture. In all cases, the sole nanoprecipitation of linear homopolymers failed to generate stable nanoparticles. This may appear somewhat surprising in the case of *p(*HPMA)$_{65}$ whose corresponding branched copolymer generated monodisperse electrostatically stabilised nanoparticles. However, the role of high molecular weight *p(*HPMA-*co*-EGDMA) copolymers in promoting rapid homogeneous nucleation during co-nanoprecipitation has been reported previously.[23] In all other cases the failed nanoprecipitations were less surprising; the absence of groups capable of providing either electrostatic of steric stabilisation inevitably resulted in polymer aggregation due to uncontrolled growth during the nanoprecipitation process. This explanation can also be applied to the failed sole nanoprecipitations of all branched copolymers, with the exception of *p*(HPMA$_{65}$-*co*-EGDMA$_{0.90}$). In contrast, the sole nanoprecipitation of amphiphilic AB block copolymers generated stable aqueous nanoparticle dispersions for the

majority of polymers. It was assumed that the presence of the PEG block provided nanoparticles with steric stabilisation which could prevent nanoparticle-nanoparticle aggregation. This is supported by the relatively low zeta potentials obtained which would typically be considered insufficient to prevent such aggregation. The failed nanoprecipitations of PEG_{45}-*b*-*p(*$BzMA)_{123}$ and PEG_{45}-*b*-*p(*$SMA)_{122}$ were surprising. In the case of PEG_{45}-*b*-*p(*$SMA)_{122}$ it is possible that nanoparticle instability could be attributed to the relatively low weight fraction of PEG_{45} hydrophilic block. However, this hypothesis does not explain the failed nanoprecipitation of PEG_{45}-*b*-*p(*$BzMA)_{123}$, for which the hydrophilic PEG_{45} block has a higher weight fraction than that of PEG_{45}-*b*-*p(*$EHMA)_{115}$ and PEG_{45}-*b*-*(p(*$LMA)_{122}$ (which both produced stable aqueous nanoparticle dispersions).

It was evident from these experiments that stable aqueous nanoparticle dispersions could not be prepared *via* individual nanoprecipitation of all of the linear homopolymers or the vast majority of the branched copolymers studied here. The preparation of stable aqueous nanoparticle dispersions would therefore require the addition of a second component capable of conferring colloidal stabilisation. The success of nanoprecipitation with AB block copolymers demonstrated that these materials are capable of generating nanoparticles alone, which possess steric stabilisation and can therefore prevent nanoparticle-nanoparticle aggregation. Further studies therefore focused on generating stable aqueous nanoparticle dispersions *via* co-nanoprecipitation of linear homopolymers and branched copolymers with their corresponding amphiphilic block copolymers.

3.4 Co-nanoprecipitation Studies

Despite the failure of a significant number of nanoprecipitations described above, co-nanoprecipitation studies were conducted using combinations of all 33 polymers identified in Section 3.2. This approach was taken to understand whether materials which were unable to form stable nanoparticles unilaterally through nanoprecipitation, could be incorporated into stable aqueous nanoparticle dispersions *via* co-nanoprecipitation with another polymer. Co-nanoprecipitations were attempted using three (co)polymer combinations: i) linear homopolymers and branched copolymers, ii) linear homopolymers and AB block copolymers and iii) branched copolymers and AB block copolymers. An overview of the co-nanoprecipitation process is presented in Figure 3.6. Co-nanoprecipitations were attempted using compatible (co)polymers; for example, in the case of the co-nanoprecipitation of *p(*HPMA) based branched and AB block copolymers, *p(*$HPMA_{63}$-*co*-$EGDMA_{0.90}$) was co-nanoprecipitated with PEG_{45}-*b*-*p(*$HPMA)_{124}$. The combinations of (co)polymer architectures were selected to provide further confirmation of the importance of hydrophilic PEG blocks for the stabilisation of polymeric nanoparticles generated though co-nanoprecipitation.

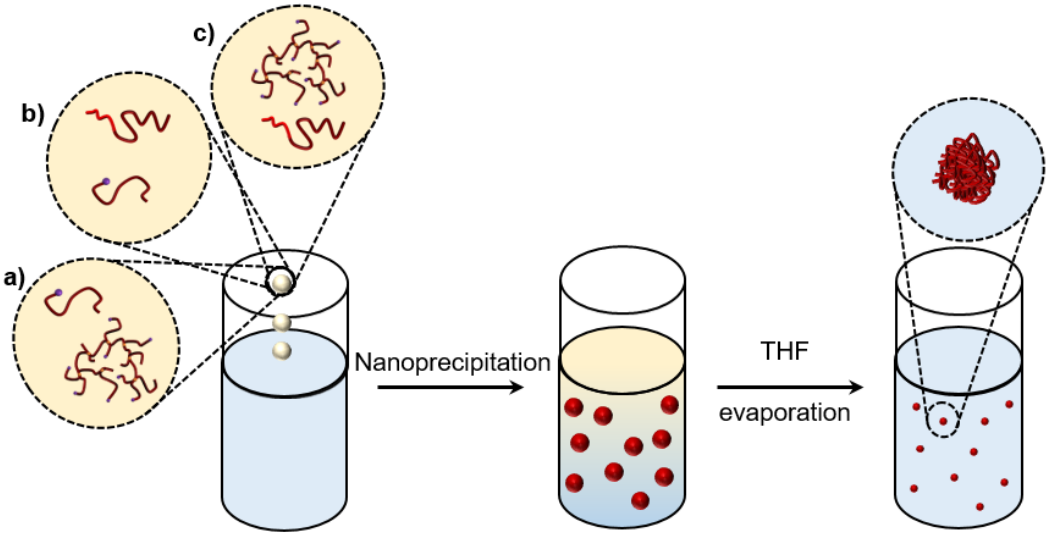

Figure 3.6 Schematic representation of the process by which co-nanoprecipitations of all 33 polymers combinations were attempted. Firstly, 1mL of a THF solution containing combinations of: a) linear homopolymer/branched copolymer, b) linear homopolymer/AB block copolymer or c) AB block copolymer/ branched copolymer were added to DI H_2O causing rapid nanoprecipitation. THF was subsequently removed *via* evaporation over 48 hours leaving an aqueous nanoparticle dispersion.

3.4.1 Initial Co-nanoprecipitation Studies

Initial co-nanoprecipitations were conducted *via* the addition of 1 mL of a polymer-THF solution at a $[P]_0$ of 5 mg mL^{-1} to 5 mL of DI H_2O (DR = 5). In all cases polymer-THF solutions consisted of equal weight fractions of the two (co)polymers being co-nanoprecipitated (ω_i = 0.50) and co-nanoprecipitations were left under magnetic stirring for 48 hours to facilitate solvent removal *via* evaporation.

Unsurprisingly, with the exception of the *p(*HPMA) based (co)polymers, all co-nanoprecipitations of linear homopolymers with branched copolymers were unsuccessful and resulted in macroscopic aggregation shortly after polymer addition (Figure 3.7a). Similar to the sole nanoprecipitations of linear homopolymers and branched copolymers, the absence of groups capable of providing electrostatic and/or steric stabilisation likely resulted in failure to prevent nanoparticle-nanoparticle aggregation processes during co-nanoprecipitation. In contrast, the co-nanoprecipitation of $p(HPMA)_{65}$ and $p(HPMA_{63}$-*co*-$EGDMA_{0.90})$ generated a colloidally stable near-monodisperse aqueous nanoparticle dispersion. Analysis of the nanoparticle size distribution by DLS showed that nanoparticles possessed near identical D_z, D_n and *PDI* values to those generated during the sole nanoprecipitation of $p(HPMA_{63}$-*co*-$EGDMA_{0.90})$, see Table 3.2. Once again, significant negative zeta potential (= -17.5 mV) suggested a moderate degree of electrostatic stabilisation. When considering the composition of branched copolymer molecular weight distributions, which were discussed in Chapter 2 Section 2.4, it is reasonable to suggest that the sole nanoprecipitation of $p(HPMA_{63}$-*co*-$EGDMA_{0.90})$ could itself be considered a co-nanoprecipitation of branched copolymers and linear homopolymers. The similarities observed between the nanoparticle size

distributions obtained were therefore anticipated. At this point, it was decided to abandon further co-nanoprecipitations of solely hydrophobic linear homopolymers and branched copolymers; this approach was not used throughout the remainder of the work discussed in this thesis.

Table 3.2 DLS and zeta potential analyses of aqueous nanoparticle dispersions produced *via* co-nanoprecipitation.

Architectures	Polymer repeat unit	D_z (nm)[a]	D_n (nm)[a]	*PDI*[a]	DCR (kcps)[a]	ζ (mV)[b]
Linear/ Branched	MMA			Aggregation		
	EMA			Aggregation		
	HPMA	81	63	0.041	486035	-30.8
	*n*BMA			Aggregation		
	*t*BMA			Aggregation		
	*n*HMA			Aggregation		
	CHMA			Aggregation		
	BzMA			Aggregation		
	EHMA			Aggregation		
	LMA			Aggregation		
	SMA			Aggregation		
Linear/ AB block	MMA*	112	84	0.105	182717	-*
	EMA*	99	69	0.126	342583	-*
	HPMA	100	79	0.063	404430	-17.4
	*n*BMA	97	72	0.086	587237	-11.7
	*t*BMA	78	54	0.121	269339	-21.3
	*n*HMA	109	94	0.011	1107125	-3.68
	CHMA			Aggregation		
	CHMA*	79	62	0.108	55927	-*
	BzMA			Aggregation		
	EHMA	110	97	0.010	1086538	-1.56
	LMA	122	106	0.014	1135586	-1.73
	SMA			Aggregation		
AB block/ Branched	MMA*	113	83	0.108	180289	-12.8
	EMA*	100	71	0.111	260780	-*
	HPMA	84	67	0.043	370713	-17.5
	*n*BMA	94	68	0.086	635687	-10.7
	*t*BMA	77	53	0.099	273918	-13.3
	*n*HMA	109	94	0.014	909072	-3.38
	CHMA			Aggregation		
	CHMA*	53	41	0.120	47157	-*
	BzMA			Aggregation		
	EHMA	107	91	0.021	890243	-2.04
	LMA	127	112	0.007	1077041	-1.56
	SMA			Aggregation		

[a]Obtained using DLS analysis of aqueous nanoparticle dispersions at a concentration of 1 mg mL^{-1}. [b]Obtained *via* measurement of the electrophoretic mobility within 0.01M KCl aqueous nanoparticle dispersions. *Sedimentation observed. Aqueous nanodispersion passed over a 0.25 μm PTFE filter prior to DLS analysis. –* Reliable z eta potentials could not be obtained.

In contrast, co-nanoprecipitations of hydrophobic linear homopolymers and amphiphilic AB block copolymers initially proved more successful, in all cases, nanoprecipitations remained turbid and translucent shortly after polymer addition. However, as was observed following the sole nanoprecipitations of amphiphilic AB block copolymers, *p(*CHMA), *p(*BzMA) and *p(*SMA) based co-nanoprecipitations did not remain colloidally stable following THF evaporation (Figure 3.7b). These results were not surprising given the corresponding amphiphilic block copolymers were unable to provide sufficient steric stabilisation to prevent nanoparticle aggregation when nanoprecipitated under identical conditions. Again, these nanoprecipitations were repeated at a decreased $[P]_0$ of 0.5 mg mL^{-1} which produced a stable *p(*CHMA) based aqueous nanodispersion. In addition to this, *p(*MMA) based co-nanoprecipitations showed small amounts of sedimentation. As a result, DLS analyses were conducted after passing the *p(*MMA) aqueous nanoparticle dispersion through a 0.25 µm PTFE filter. Turbid and translucent aqueous nanoparticle dispersions were obtained from co-nanoprecipitations of *p(*EMA), *p(*HPMA), *p(n*BMA), *p(t*BMA), *p(n*HMA), *p(*EHMA) and *p(*LMA) based linear homopolymers and amphiphilic AB block copolymers. Similar results were observed from co-nanoprecipitations of branched copolymers and AB block copolymers (Figure 3.7c); the only clear difference being the presence of small amounts of sedimentation in the *p(*EMA) based co-nanoprecipitation. *p(*EMA) nanoparticles were therefore passed through a 0.25 µm PTFE filter prior to DLS analysis. The *p(*EMA) co-nanoprecipitations were therefore repeated at a decreased $[P]_0$ of 0.5 mg mL^{-1} but this made little difference to nanoparticle stability.

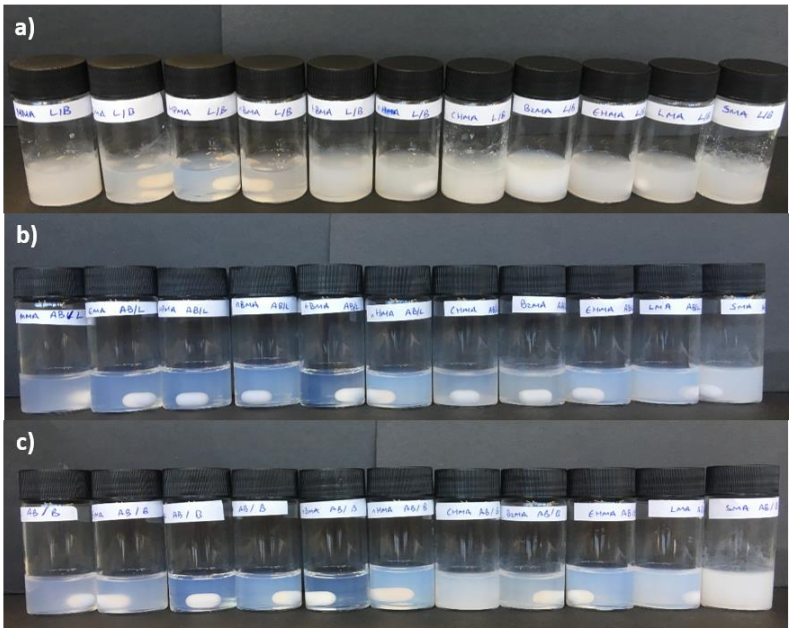

Figure 3.7 Visual observations of conanoprecipitation experiments conducted using combinations of a) linear homopolymers and branched copolymers, b) amphiphilic AB block copolymers and linear homopolymers, and c) amphiphillic AB block copolymers and branched copolymers, 48 hours after polymer addition. (left to right) *p(*MMA), *p(*EMA), *p(*HPMA), *p(n*BMA), *p(t*BMA), *p(n*HMA), *p(*CHMA), *p(*BzMA), *p(*EHMA), *p(*LMA), *p(*SMA).

Aqueous nanoparticle dispersions from co-nanoprecipitations were assessed *via* DLS and zeta potential analyses (Table 3.2). Co-nanoprecipitations generally created nanoparticles which possessed slightly larger hydrodynamic diameters compared to those produced by the sole nanoprecipitation of the corresponding amphiphilic AB block copolymer. For example, *p(n*BMA), *p(n*HMA), *p(*EHMA) and *p(*LMA) based co-nanoprecipitations of branched copolymers and amphiphilic AB block copolymers generated nanoparticles containing D_z values of 97, 109, 107 and 127 nm respectively, whereas nanoparticles generated *via* the analogous sole nanoprecipitations of the corresponding AB block copolymers gave D_z values of 78, 77, 85 and 93 nm respectively.

Similar increases in hydrodynamic diameters were observed for nanoparticles generated through co-nanoprecipitation of linear homopolymers with amphiphilic AB block copolymers. This can be explained by considering the role that each component plays during the co-nanoprecipitation process. As identified in Section 3.3, amphiphilic AB block copolymers are the only components capable of providing sufficient levels of steric stabilisation capable of preventing nanoparticle-nanoparticle aggregation. The role of amphiphilic AB block copolymers during co-nanoprecipitation must therefore be to stabilise the hydrophobic (co)polymers with which they are co-nanoprecipitated. This was supported by the low zeta potentials demonstrated through measurement of the electrophoretic mobility of aqueous nanoparticle dispersions. Initial co-nanoprecipitations were conducted using an amphiphilic AB block copolymer ω_i of 0.50. As a result, only half the number of stabilising AB block copolymer chains are present during co-nanoprecipitation; this lower number of chains are now required to stabilise hydrophobic domains which were not present during individual nanoprecipitations. It is therefore likely that the reduction in the amphiphilic AB block copolymer concentration during co-nanoprecipitation was responsible for the larger hydrodynamic diameters. Further investigation of this hypothesis is provided later in this chapter (Section 3.4.3.1).

What may appear to contradict this hypothesis are the results obtained from co-nanoprecipitations of *p(*HPMA) based nanoparticles. Nanoparticles generated *via* all forms of *p(*HPMA) based co-nanoprecipitations possessed lower hydrodynamic diameters than those obtained from the sole nanoprecipitation of PEG_{45}-*b*-*p(*$HPMA)_{124}$. In addition, significant variations were observed in the hydrodynamic diameters of nanoparticles generated *via* co-nanoprecipitations of different (co)polymer architectures. This contrasting behaviour can be explained by the chemical structure of both the *p(*HPMA) repeat unit and the architectures of the (co)polymers being nanoprecipitated. As demonstrated using pyrene fluorescence emission spectroscopy in Chapter 2 (Section 2.2.1), HPMA was the most polar methacrylate monomer used to generate the (co)polymers employed in (co)nanoprecipitations. *p(*HPMA)

based (co)polymers can therefore be considered the most polar – or least hydrophobic – (co)polymers used in this study.

It is well known that polymer hydrophobicity is a crucial parameter which governs the extent of supersaturation and thus the nucleation rate observed during nanoprecipitation.[19] The nucleation rate controls the number and therefore the size of the nanoparticles subsequently formed. It is therefore likely that the relatively low hydrophobicity of *p(*HPMA) based (co)polymers may influence nucleation during (co)nanoprecipitation. As a result, this could explain the architecture-dependent hydrodynamic diameters observed, which have also been reported previously.[23]

Given the aqueous solubility of its PEG block, it is likely that PEG_{45}-*b*-*p(*$HPMA)_{124}$ would express the lowest level of supersaturation within the (co)nanoprecipitation medium (5:1 v/v DI H_2O: THF) of all the *p(*HPMA) polymers studied. It is also possible that this would have hindered the nucleation process during the sole nanoprecipitation of PEG_{45}-*b*-*p(*$HPMA)_{124}$ and, as a result, generated aqueous nanoparticle dispersions possessing larger hydrodynamic diameters (D_z = 125 nm). In contrast, nanoparticles generated *via* co-nanoprecipitations of PEG_{45}-*b*-*p(*$HPMA)_{124}$ with hydrophobic domains of either linear homopolymers or branched copolymers, which do not possess hydrophilic PEG domains, exhibited smaller hydrodynamic diameters. It is possible that this may have occurred as a result of such hydrophobic domains driving the nucleation process during co-nanoprecipitation due to increased levels of supersaturation within the co-nanoprecipitation medium. Interestingly, smaller hydrodynamic diameters were observed for nanoparticles generated by co-nanoprecipitation of PEG_{45}-*b*-*p(*$HPMA)_{124}$ with *p(*$HPMA_{63}$-*co*-$EGDMA_{0.90}$) (D_z = 84 nm) than were obtained for nanoparticles produced *via* co-nanoprecipitation with *p(*$HPMA)_{65}$ (D_z = 100 nm). Furthermore, the size distribution of nanoparticles generated in the sole nanoprecipitation of *p(*$HPMA_{63}$-*co*-$EGDMA_{0.90}$) (D_z = 81 nm) was practically identical to that of nanoparticles formed during its co-nanoprecipitation with PEG_{45}-*b*-*p(*$HPMA)_{124}$. These results demonstrate the importance of the architecture of the hydrophobic domain in the co-nanoprecipitation of *p(*HPMA) based (co)polymers which is consistent with the previous reports.[23,24] These results therefore suggest that nanoparticles are formed *via* an architecture-dependent nucleation process which occurs as a result of the relatively low levels of supersaturation which exist due to the moderate hydrophobicity of *p(*HPMA) based (co)polymers.

Conversely, in all other cases, DLS analyses showed practically identical hydrodynamic diameters for nanoparticles generated *via* co-nanoprecipitations of amphiphilic AB block copolymers with either linear homopolymers or branched copolymers. This suggests that for

all polymers, with the exception of *p(*HPMA), co-nanoprecipitation proceeds *via* an architecture-independent nucleation process. It is likely that this is the result of greater degrees of supersaturation within the co-nanoprecipitation medium due to the increased hydrophobicity of polymers constructed from lower polarity monomers.

Nanoparticles generated *via* co-nanoprecipitation of amphiphilic block and branched copolymers were assessed using scanning electron microscopy (SEM). The physical properties of the polymers made imaging of nanoparticles difficult. Polymers containing long aliphatic side chains typically exhibit low T_g values. As a result, nanoparticles constructed of low T_g polymers were unable to retain their independent particle structure during the drying process therefore making such dried samples unrepresentative of nanoparticle morphology and rendering them unsuitable for SEM imaging (Appendix, Figure A3.2). Alternatively, higher T_g polymers maintained their original nanoparticle morphology during the drying process and, as a result, suitable images could be obtained for *p(*HPMA), *p(n*BMA), *p(t*BMA) and *p(*CHMA) based nanoparticles (Figure 3.8). SEM images showed that, in all cases, branched vinyl polymer nanoparticles possessed spherical morphologies and were able to maintain their structural integrity even at high concentration.

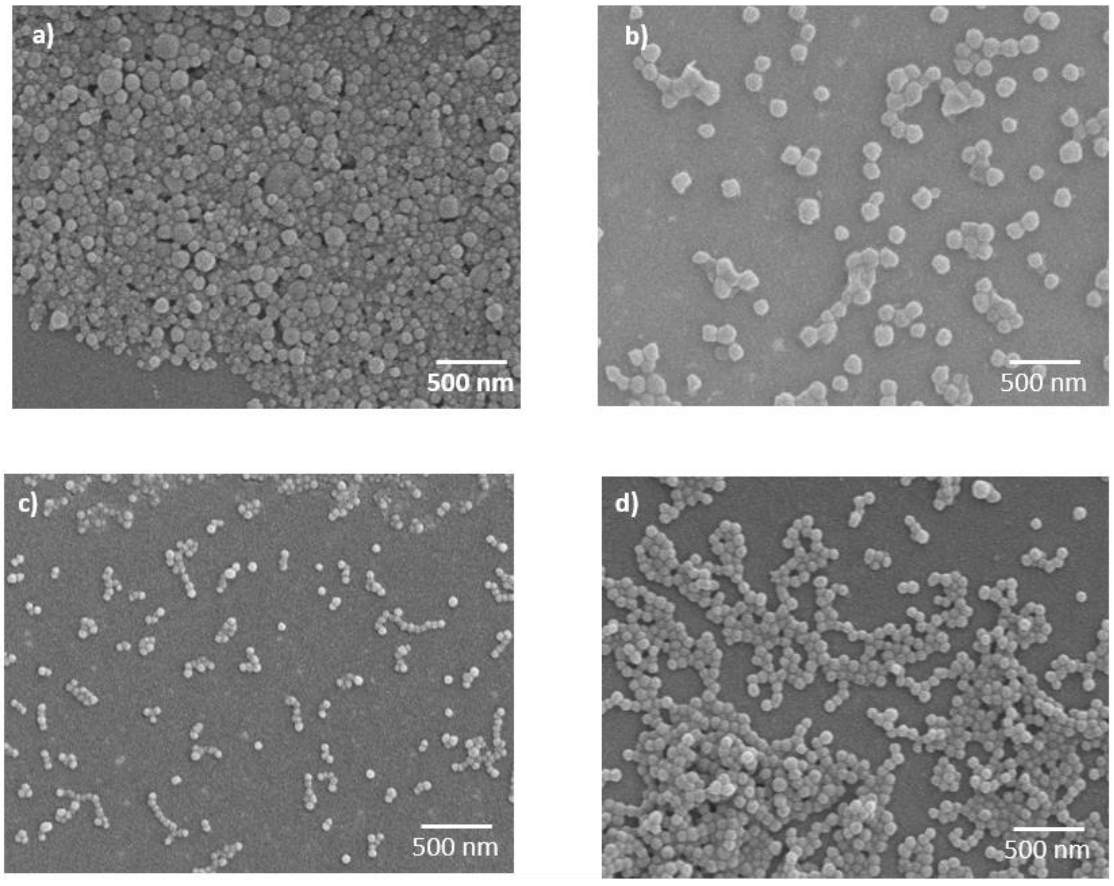

Figure 3.8 Scanning electron microscopy images of branched vinyl polymer nanoparticles generated *via* co-nanoprecipitation of AB block and branched copolymers consisting of: a) *p(*HPMA), b) *p(n*BMA), c) *p(t*BMA) and d) *p(*CHMA).

These experiments demonstrated many examples where stable aqueous nanoparticle dispersions can be generated *via* co-nanoprecipitation of both hydrophobic linear homopolymers and branched copolymers with amphiphilic block copolymers. In particular, the preparation of near-monodisperse *p(*MMA), *p(*HPMA), *p(n*BMA), *p(t*BMA), *p(n*HMA), *p(*CHMA), *p(*EHMA) and *p(*LMA) based aqueous nanoparticle dispersions could be achieved containing polymeric components which could not individually form stable aqueous nanoparticle dispersions in the absence of amphiphilic AB block copolymers. It was not possible to generate stable *p(*BzMA) or *p(*SMA) based nanoparticles under any circumstances therefore these materials were not studied further throughout the remainder of this work. Moreover, *p(*EMA), *p(*MMA) and *p(*CHMA) nanoparticles all required co-nanoprecipitation from a decreased $[P]_0$ of 0.5 mg mL^{-1}. Nevertheless, these materials still showed signs of polymer sedimentation over time, which is indicative of colloidal instability.

Whilst the ability to generate stable aqueous nanoparticle dispersions is a pre-requisite for the development of a novel DNC system, there is no guarantee that the formation of such desirable nanomaterials would be produced in the presence of a chemotherapeutic compound. Further studies were therefore required to determine (i) whether small molecules could be encapsulated using branched vinyl polymer nanoparticles during the co-nanoprecipitation process and (ii) to understand their impact, if any, on the co-nanoprecipitation process.

3.4.2 Encapsulation of a Hydrophobic Molecule during Co-nanoprecipitation

The preparation of a polymer-based DNC system must include a strategy to encapsulate hydrophobic drug molecules within the core of the DNC. A series of model drug encapsulation experiments were therefore conducted in order to determine whether it was possible to encapsulate a hydrophobic guest molecule within the core of branched vinyl copolymer nanoparticles.

3.4.2.1 Impact of a Guest Molecule on the (Co)nanoprecipitation process

Encapsulation experiments were conducted using pyrene as a small hydrophobic guest molecule. This was achieved by adding pyrene to the copolymer-THF solutions from which co-nanoprecipitations were typically attempted (Figure 3.9). It was expected that during this co-nanoprecipitation of an amphiphilic block copolymer, a hydrophobic branched copolymer and pyrene, the hydrophobic nature of pyrene would cause it to become entrapped and thus encapsulated within the core of branched vinyl copolymer nanoparticles during the nanoprecipitation process. These experiments aimed to answer two key questions: i) could a hydrophobic model drug, i.e. pyrene, be encapsulated without hindering the co-nanoprecipitation process and ii) could the environment-dependent fluorescence emission of pyrene be used to probe the internal polarities of branched vinyl copolymer nanoparticles.

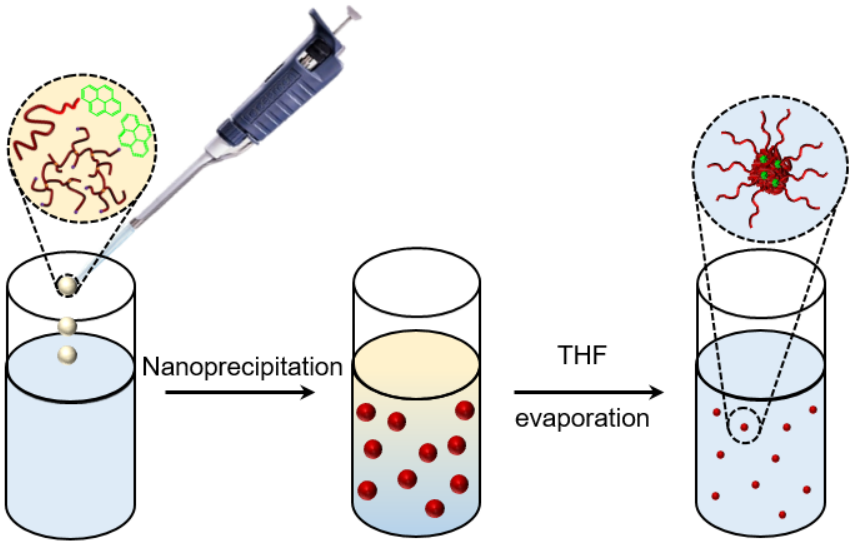

Figure 3.9 Schematic representation of the encapsulation of pyrene during co-nanoprecipitation.

Co-nanoprecipitations of amphiphilic block copolymers, hydrophobic branched copolymers and pyrene were conducted in a similar manner to those of the successful co-nanoprecipitations described above. Co-nanoprecipitations were conducted from a THF-solution containing a $[P]_0$ of 5 mg mL^{-1} which contained equal mass fractions of AB block and branched copolymers; in addition, a model drug loading of 1 weight percent (wt %) with respect to the total polymer mass was targeted by also ensuring a pyrene concentration of 0.05 mg mL^{-1} within the initial THF solution. Nanoprecipitations were conducted by addition of 1 mL of the polymer/ pyrene solution to 5 mL of DI H_2O (DR = 5). Following the improved co-nanoprecipitations observed at lower $[P]_0$ in THF co-nanoprecipitations of *p(*MMA), *p(*CHMA) and *p(t*BMA) based polymers were conducted from a $[P]_0$ of 0.5 mg mL^{-1} whilst maintaining a DR = 5 to give an aqueous nanoparticle dispersion of $[P]_f$ = 0.1 mg mL^{-1}.

In all cases, nanoprecipitations remained turbid/translucent after polymer addition and aqueous nanoparticle dispersions were obtained following THF removal *via* evaporation over 48 hours without macrophase separation. Nanoparticle size distributions were obtained using DLS. In all cases, the size distributions obtained largely resembled those produced *via* co-nanoprecipitation in the absence of pyrene (Figure 3.6); as a result, the D_z, D_n and *PDI* values were broadly comparable to the unloaded aqueous nanoparticle dispersions (Table 3.3). This indicated that the presence of small amounts of pyrene had little impact on the co-nanoprecipitation process.

Table 3.3 Analysis of branched vinyl copolymer nanoparticles obtained from co-nanoprecipitations of amphiphilic block copolymers, hydrophobic branched copolymers and pyrene.

AB Block copolymer	Branched copoylmer	D_z (nm)[a]	D_n (nm)[a]	*PDI*[a]	DCR (kcps)[a]
p(MMA$_{70}$-*co*-EGDMA$_{0.94}$)*	PEG$_{45}$-*b*-*p*(MMA)$_{122}$*	159	100	0.180	726635
p(HPMA$_{63}$-*co*-EGDMA$_{0.90}$)	PEG$_{45}$-*b*-*p*(HPMA)$_{124}$	87	69	0.044	232057
p(*n*BMA$_{73}$-*co*-EGDMA$_{1.12}$)	PEG$_{45}$-*b*-*p*(*n*BMA)$_{125}$	91	64	0.083	393311
p(*t*BMA$_{67}$-*co*-EGDMA$_{1.05}$)*	PEG$_{45}$-*b*-*p*(*t*BMA)$_{122}$*	85	60	0.098	12096
p(*n*HMA$_{68}$-*co*-EGDMA$_{1.03}$)	PEG$_{45}$-*b*-*p*(*n*HMA)$_{127}$	115	95	0.022	468489
p(CHMA$_{69}$-*co*-EGDMA$_{1.06}$)*	PEG$_{45}$-*b*-*p*(CHMA)$_{123}$*	55	43	0.049	27924
p(EHMA$_{68}$-*co*-EGDMA$_{0.93}$)	PEG$_{45}$-*b*-*p*(EHMA)$_{115}$	102	85	0.005	787508
p(LMA$_{70}$-*co*-EGDMA$_{1.04}$)	PEG$_{45}$-*b*-*p*(LMA)$_{121}$	133	114	0.009	595910

[a]Data obtained using DLS. [b]Data obtained using zeta potential measurement. *Co-nanoprecipitations conducted from a $[P]_0$ of 0.5 mg mL^{-1} in THF to a $[P]_f$ of 0.1 mg mL^{-1} in DI H_2O.

The similarities between nanoparticles generated *via* co-nanoprecipitation with and without the presence of pyrene gave a strong indication that pyrene encapsulation was successful during all co-nanoprecipitations. In all co-nanoprecipitations, the resulting pyrene concentration within aqueous nanoparticle dispersions (4.94×10^{-3} or 4.94×10^{-4} mol dm^{-3}) were in excess of the aqueous saturation concentration of pyrene (6.67×10^{-7} mol dm^{-3}).[29] The combination of this low aqueous solubility with the absence of sedimentation/ aggregation during DLS analyses indicate that pyrene was encapsulated within branched vinyl copolymer nanoparticles during co-nanoprecipitation.

Analysis of aqueous nanoparticle dispersions therefore confirmed that low loadings (1 wt %) of pyrene had little/negligible impact on nanoparticle formation during the co-nanoprecipitation process. The ability to generate colloidally stable, near-monodisperse nanoparticles in the presence of hydrophobic small molecules is a promising sign for the generation of DNC systems *via* co-nanoprecipitation of amphiphilic AB block and branched copolymers. However, it is important to state that these results only indicate rather than confirm the encapsulation of pyrene during co-nanoprecipitation. Further studies were therefore required to demonstrate that pyrene had in fact been encapsulated during co-nanoprecipitation.

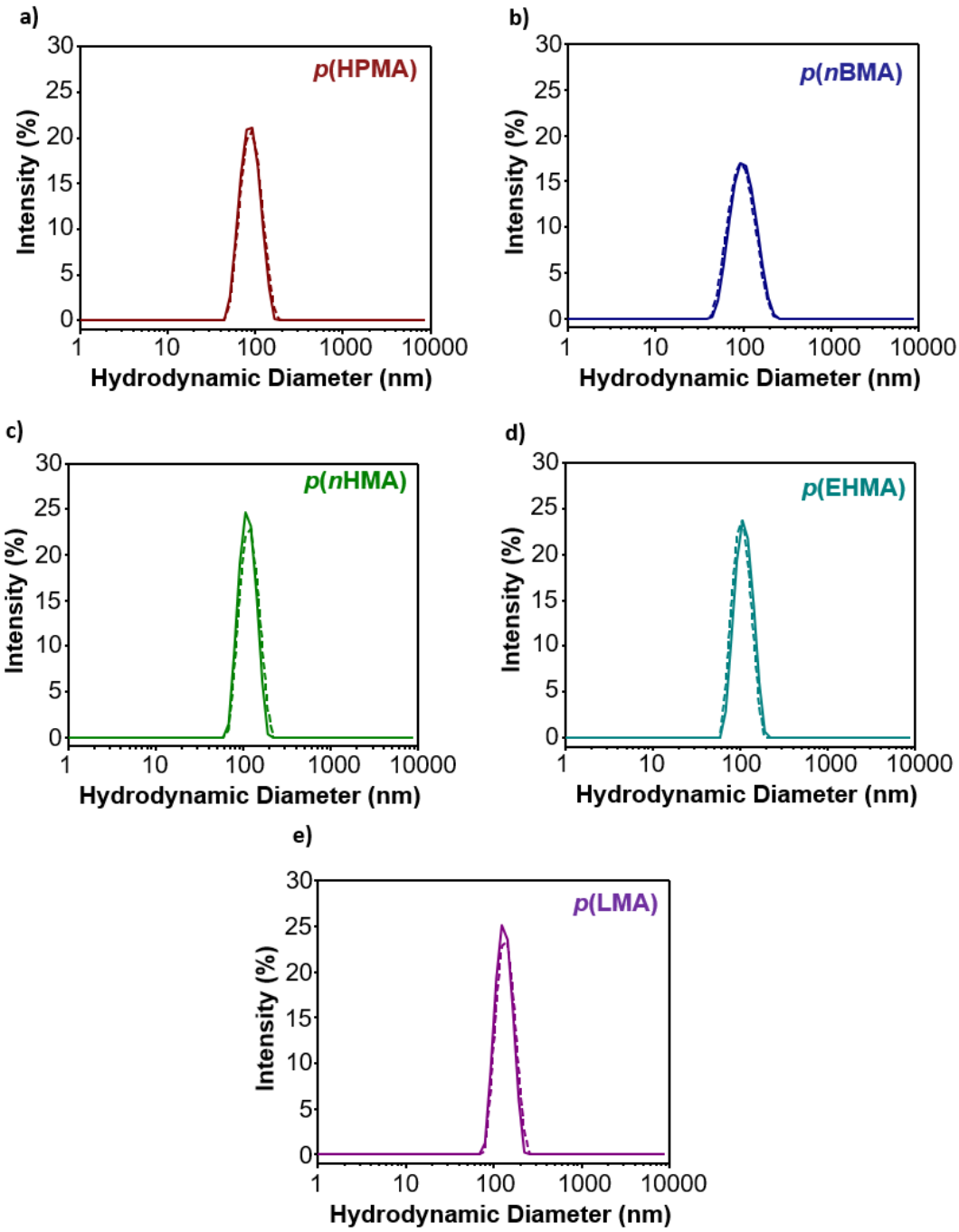

Figure 3.10 Overlaid nanoparticle size distributions obtained by DLS analysis of unloaded (dashed lines) and pyrene loaded (solid lines) aqueous nanoparticle dispersions prepared by co-nanoprecipitation of: a) *p*(HPMA), b) *p*(*n*BMA), c) *p*(*n*HMA), d) *p*(EHMA) and e) *p*(LMA).

3.4.2.2 Evaluation of Nanoparticle Core Polarity using Fluorescence Emission Spectroscopy

The selection of pyrene as a hydrophobic guest molecule during co-nanoprecipitation allowed confirmation of encapsulation using fluorescence emission spectroscopy. This was achieved through analysis of the fine structure of the fluorescence emission of pyrene, in particular the relative intensities of the first and third vibrational bands (I_1/I_3). Pyrene has often been used as a fluorescent probe to evaluate environmental polarity; for example, it has been used to

measure the relative polarities of organic solvents and to determine the critical micelle concentration of aqueous surfactant and block copolymer self-assembly processes.[30–32] In all cases, the fluorescence emissions of aqueous nanoparticle dispersions, obtained following excitation at $\lambda = 335$ nm, showed that the encapsulation of pyrene during co-nanoprecipitation had been successful. This was evident by the significantly lower I_1/I_3 ratios obtained from pyrene encapsulated in branched vinyl polymer nanoparticles (I_1/I_3 = 1.50 – 0.95) in comparison to that of pyrene dissolved in DI H_2O (I_1/I_3 = 1.80, Table 3.4). These results demonstrate that pyrene is located within an environment of considerably lower polarity following co-nanoprecipitation which is consistent with its encapsulation during co-nanoprecipitation.

Table 3.4 Polarity and hydrophobicity data obtained using molecular modelling calculations and pyrene emission spectroscopy.

Branched copolymer	AB block copolymer	CLogP (Monomer)[a]	I_1/I_3 (Monomer)[b]	I_1/I_3 (Core)[c]
p(MMA$_{70}$-*co*-EGDMA$_{0.94}$)	PEG$_{45}$-*b*-*p*(MMA)$_{122}$	0.99	1.44	1.39
p(HPMA$_{63}$-*co*-EGDMA$_{0.90}$)	PEG$_{45}$-*b*-*p*(HPMA)$_{124}$	0.79	1.48	1.60
p(*n*BMA$_{73}$-*co*-EGDMA$_{1.12}$)	PEG$_{45}$-*b*-*p*(*n*BMA)$_{125}$	2.23	1.30	1.20
p(*t*BMA$_{67}$-*co*-EGDMA$_{1.05}$)	PEG$_{45}$-*b*-*p*(*t*BMA)$_{122}$	1.86	1.25	1.24
p(*n*HMA$_{68}$-*co*-EGDMA$_{1.03}$)	PEG$_{45}$-*b*-*p*(*n*HMA)$_{127}$	3.07	1.23	1.10
p(CHMA$_{69}$-*co*-EGDMA$_{1.06}$)	PEG$_{45}$-*b*-*p*(CHMA)$_{123}$	2.54	1.27	1.18
p(EHMA$_{68}$-*co*-EGDMA$_{0.93}$)	PEG$_{45}$-*b*-*p*(EHMA)$_{115}$	3.88	1.17	1.05
p(LMA$_{70}$-*co*-EGDMA$_{1.04}$)	PEG$_{45}$-*b*-*p*(LMA)$_{121}$	5.77	1.16	1.00

[a]Obtained *via* QSAR calculations using Spartan'18 molecular modelling software. [b]Obtained using fluorescence emission spectroscopy of pyrene dissolved in neat monomer. [c]Obtained using fluorescence emission spectroscopy of aqueous nanoparticle dispersions following attempted encapsulation of pyrene during co-nanoprecipitation.

Pyrene encapsulation was further corroborated by the strong correlations observed between the I_1/I_3 ratios obtained from the fluorescence emission spectroscopy of encapsulated pyrene and the chemical structure of the polymers used in co-nanoprecipitation (Figure 3.11). A strong correlation was observed between the I_1/I_3 ratios obtained for encapsulated pyrene and those obtained for pyrene dissolved within the neat monomer from which the branched and AB block copolymers used during co-nanoprecipitation were constructed (Figure 3.11, a). These data support the encapsulation of pyrene during co-nanoprecipitation, but also raise two important points. Firstly, the high dependence of the pyrene fluorescence emission on monomer chemistry suggests that pyrene is in fact encapsulated within the nanoparticle core rather than adsorbed to the surface or even trapped within the hydrated corona of the nanoparticle. In the event that pyrene is located on the surface or even within the external hydrated corona of branched copolymer nanoparticles, a much weaker correlation between the polarity of the external environment of pyrene and that of the nanoparticle's hydrophobic domains would be expected. Secondly, these results strongly indicate that the internal polarity

of the nanoparticle core is highly dependent upon the chemical structure of the comonomers from which polymers are constructed. This demonstrates that, in the cases presented here, nanoparticle internal polarity is dominated by the low-polarity hydrophobic domains rather than the PEG-based hydrophilic domains.

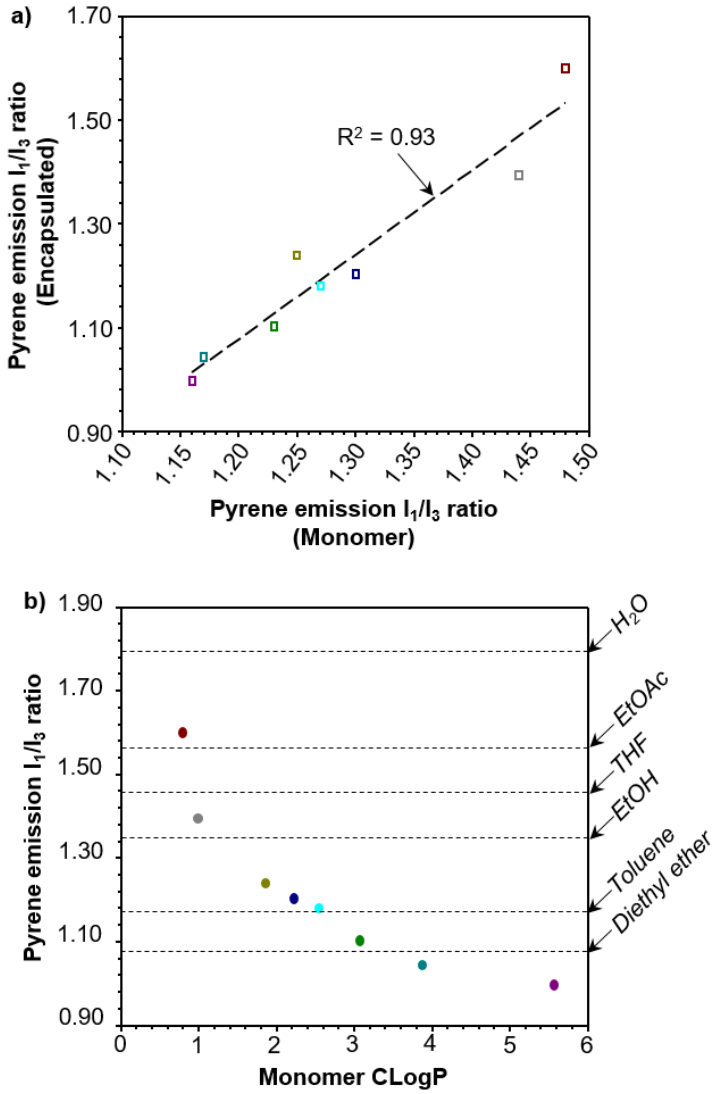

Figure 3.11 Graphical representations of the relationships between nanoparticle internal polarity and the chemical properties of the comonomers from which the polymers used during co-nanoprecipitation are constructed. a) A plot of the I_1/I_3 ratios of encapsulated pyrene *vs.* pyrene dissolved within neat monomer. b) A plot of the I_1/I_3 ratios of encapsulated pyrene *vs.* CLogP values for the comonomers from which nanoparticles are constructed.

Similar analyses were also made taking into account the hydrophobicity of the comonomers from which amphiphilic AB block and branched copolymers were constructed. Monomer hydrophobicity was measured according to their calculated water-octanol partition coefficients (CLogP) obtained using Spartan '18 molecular modelling software. (Table 3.4). As expected, CLogP values increased with increasing lipophilicity of the methacrylate monomer substituent. Plots of the I_1/I_3 ratio obtained for pyrene encapsulated within the core of branched

vinyl polymer nanoparticles against the CLogP of the monomer from which nanoparticles were constructed also showed a strong correlation. A general reduction in the polarity within the core of branched copolymer nanoparticles was observed with increasing CLogP. However, unlike the relationship observed between I_1/I_3 ratios described above, the relationship between the I_1/I_3 and CLogP values obtained was non-linear.

Changes in monomer CLogP appeared to have a more significant impact on nanoparticle core polarity at low CLogP values. For example, an increase in the size of the aliphatic chain length from 1 to 4 carbons, *p(*MMA) to *p(n*BMA), lowers the I_1/I_3 ratio of encapsulated pyrene from 1.39 to 1.20 (-0.19). A similar increase from 8 to 12 carbons, for *p(*EHMA) to *p(*LMA), caused a much smaller reduction from 1.05 to 1.00 (-0.05). Whilst this may initially seem surprising, these results are explained by the relative weight fractions of the aliphatic side chains. Increases to the aliphatic chain length constitute a higher weight fraction of the overall repeat unit mass in monomers containing low relative molecular mass. For example, the weight fraction of the aliphatic side chain increases from 0.15 to 0.40 with MMA to *n*BMA (+ 25 %). In contrast, a more modest increase in the weight fraction of the aliphatic side chain, from 0.57 to 0.67, is observed between EHMA and LMA (+ 9 %). This is supported by the strong correlation observed between encapsulated I_1/I_3 ratios and the weight fraction of the aliphatic side chain ($R^2 = 0.95$, Appendix, Figure A3.3).

Encapsulation of pyrene within branched vinyl polymer nanoparticles during co-nanoprecipitation was confirmed using fluorescence emission spectroscopy. The selection of pyrene provided a useful tool to probe the internal polarity of branched vinyl polymer nanoparticles; this allowed relationships between the specific chemical nature of polymers and the macroscopic properties of the resulting nanoparticles to be established. Pyrene encapsulation therefore offers a useful tool to study the internal structure of branched vinyl polymer nanoparticles and may prove useful in developing further understanding of the factors which influence the co-nanoprecipitation process.

3.4.3 Factors Affecting Co-nanoprecipitation

Given the expansion of the range of (co)polymers used to generate branched vinyl copolymer nanoparticles, further studies were conducted to acquire a deeper understanding of the factors which influence the co-nanoprecipitation processes. In particular, the impact of the composition of branched and AB block copolymers in the initial THF solution as well as the total mass of polymer being co-nanoprecipitated were studied in order to understand their significance within the co-nanoprecipitation process. At this point, the co-nanoprecipitations of *p(*HPMA), *p(n*BMA), *p(n*HMA), *p(*EHMA) and *p(*LMA) based copolymers were studied as they had produced the most consistent and stable aqueous nanoparticle dispersions.

3.4.3.1 Nanoparticle Composition

In the studies described above, co-nanoprecipitations have been conducted using equivalent weight fractions of the two constituent copolymers. Given the likely contrasting roles of branched and AB block copolymers during the co-nanoprecipitation process, it was expected that manipulation of the weight fractions of the copolymers within the initial THF solution would impact the properties of the resulting branched vinyl copolymer nanoparticles. A range of co-nanoprecipitations were therefore performed to develop an understanding of the importance of the composition of the initial THF solution on the physical properties of the branched vinyl copolymer nanoparticles formed; in particular, the impact on nanoparticle stability, size and internal polarity. A general overview of how nanoparticle compositions were varied during these studies is presented in Figure 3.12.

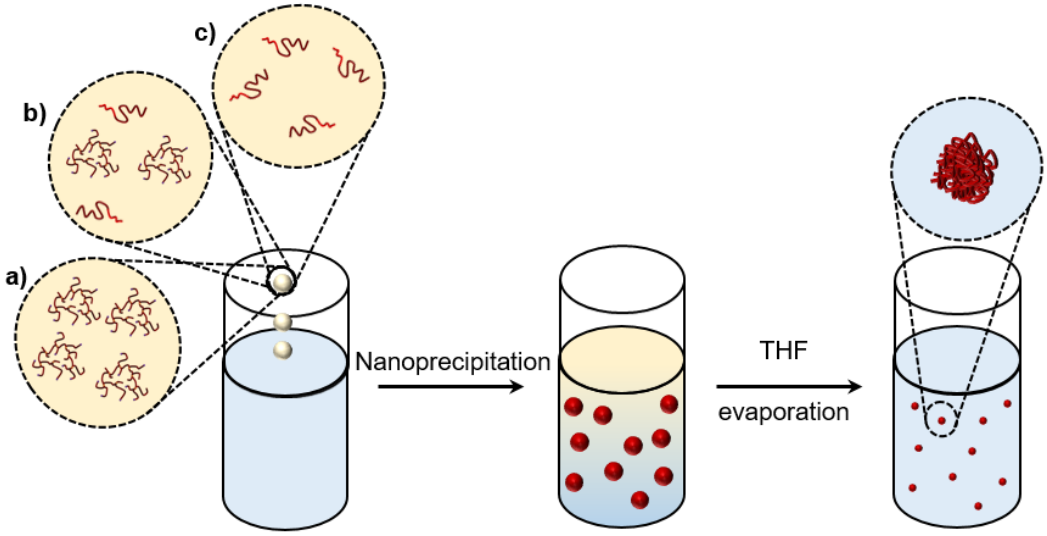

Figure 3.12 Schematic representation of the approach used to vary nanoparticle composition through co-nanoprecipitation. Demonstration of the manipulation of initial THF solutions, containing branched: AB block copolymer weight fractions of a) 1.0:0.0, b) 0.5:0.5, c) 0.0:1.0.

Co-nanoprecipitations were conducted using standard conditions; this included the addition of 1 mL of a copolymer-THF solution ($[P]_0$ = 5 mg mL^{-1}) to a fixed volume of DI H_2O (5 mL). THF removal *via* evaporation over 48 hours at ambient temperature gave aqueous nanoparticle dispersions at a $[P]_f$ of 1 mg mL^{-1}. In addition, low loadings of pyrene were encapsulated during the co-nanoprecipitation process in order to allow evaluation of nanoparticle internal polarity using fluorescence emission spectroscopy. It was expected that this would allow the impact of AB block: branched copolymer ratio on the internal polarity within branched vinyl copolymer nanoparticles to be understood. Pyrene at 1 wt% with respect to the total polymer mass was incorporated into the initial THF solution. In all cases, co-nanoprecipitations were conducted using AB block: branched copolymer weight fractions systematically varying from 1.0 to 0.0 (see Table 3.5). It is important to state that, due to the contrasting molecular weights

of AB block and branched copolymers, copolymer weight fractions were not representative of the actual molar ratio of AB block to branched copolymers. Nonetheless, systematic variation of the copolymer weight fractions used inherently varied the molar ratio of AB block:branched copolymers in the initial THF solution and within the resulting branched vinyl copolymer nanoparticles.

In line with what was observed during the sole nanoprecipitations of branched copolymers in Section 3.3, co-nanoprecipitations containing low weight fractions of the amphiphilic AB block copolymer resulted in macroscopic aggregation immediately after the addition of the copolymer-THF solution. This was generally observed for co-nanoprecipitations conducted using AB block copolymer weight fractions ≤ 20 %. The AB block copolymer weight fraction at which nanoprecipitations failed was dependent upon the methacrylic repeat unit of the copolymers. For example, all co-nanoprecipitations of PEG_{45}-*b*-*p(*$HPMA)_{124}$ and *p(*$HPMA_{65}$-*co*-$EGDMA_{0.90}$) were successful regardless of the AB block copolymer weight fraction used whereas *p(n*BMA), *p(n*HMA), *p(*EHMA) and *p(*LMA) based co-nanoprecipitations failed at AB block copolymer weight fractions of: 0.1, 0.1, 0.2 and 0.2 respectively. Regardless of the chemical nature of the copolymers used, stable aqueous nanoparticle dispersions were obtained from all co-nanoprecipitations conducted at AB block copolymer weight fractions ≥ 0.3.

The size distributions, hydrodynamic diameters and *PDI*s of aqueous nanoparticle dispersions were obtained using DLS analysis at a concentration of 1 mg mL^{-1} (Table 3.5). In the cases where macroscopic aggregation had occurred, where possible aqueous nanoparticle dispersions were passed through a 1 μm fibreglass filter to allow DLS analysis of any polymeric nanoparticles which remained in suspension after 48 hours.

In all cases, DLS analyses of aqueous nanoparticle dispersions generated from successful co-nanoprecipitations showed monomodal size distributions consisting of highly monodisperse nanoparticles with intensity-average hydrodynamic diameters ranging from 64 to 124 nm. Interestingly trends were observed between the hydrodynamic diameters of branched vinyl copolymer nanoparticles and the weight fraction of branched copolymer employed in co-nanoprecipitation (Figure 3.13). The nature of the relationship between branched copolymer weight fraction and the hydrodynamic diameters of branched copolymer nanoparticles were dependent upon the chemical nature of the polymers used in co-nanoprecipitation.

Table 3.5 Size and internal polarity analyses of branched vinyl copolymer nanoparticles containing varied branched and AB block copolymer compositions obtained by DLS and fluorescence emission spectroscopy.

Hydrophobic domain	AB block ω_i	Branched ω_i	D_z (nm)[a]	D_n (nm)[a]	*PDI*[a]	ζ (mV)	I_1/I_3[c]
	1.0	0.0	121	98	0.035	-11.9	1.39
	0.9	0.1	106	81	0.070	-11.0	1.45
	0.8	0.2	103	68	0.114	-11.6	1.48
	0.7	0.3	81	56	0.090	-13.0	1.52
	0.6	0.4	69	53	0.064	-17.0	1.60
*p(*HPMA)	0.5	0.5	68	51	0.063	-17.5	1.60
	0.4	0.6	67	49	0.068	-20.8	1.63
	0.3	0.7	67	48	0.082	-23.8	1.65
	0.2	0.8	65	45	0.090	-27.0	1.64
	0.1	0.9	65	43	0.110	-27.4	1.65
	0.0	1.0	64	41	0.109	-34.5	1.68
	1.0	0.0	66	44	0.121	-12.0	1.28
	0.9	0.1	69	46	0.109	-12.9	1.26
	0.8	0.2	74	50	0.109	-11.2	1.26
	0.7	0.3	81	57	0.095	-11.4	1.25
	0.6	0.4	85	64	0.076	-12.0	1.24
*p(n*BMA)	0.5	0.5	92	74	0.047	-11.7	1.23
	0.4	0.6	104	85	0.040	-11.0	1.22
	0.3	0.7	129	114	0.007	-10.3	1.21
	0.2	0.8	140	125	0.022	-11.2	1.20
	0.1*	0.9	166	153	0.012	-	1.30
	0.0*	1.0	191	167	0.105	-	1.19
	1.0	0.0	81	65	0.043	-3.44	1.19
	0.9	0.1	82	66	0.031	-3.64	1.18
	0.8	0.2	83	68	0.019	-3.24	0.17
	0.7	0.3	88	73	0.027	-3.87	1.17
	0.6	0.4	95	79	0.013	-3.53	1.16
*p(n*HMA)	0.5	0.5	105	90	0.006	-3.87	1.16
	0.4	0.6	124	109	0.015	-3.80	1.14
	0.3	0.7	136	121	0.022	-3.85	1.14
	0.2	0.8	157	144	0.012	-3.85	1.20
	0.1*	0.9	182	171	0.016	-	1.14
	0.0*	1.0	229	197	0.114	-	1.13
	1.0	0.0	88	73	0.020	-11.6	1.10
	0.9	0.1	95	79	0.006	-9.03	1.11
	0.8	0.2	98	82	0.011	-10.1	1.09
	0.7	0.3	104	89	0.012	-10.7	1.10
	0.6	0.4	119	103	0.009	-8.62	1.07
*p(*EHMA)	0.5	0.5	134	119	0.012	-9.84	1.05
	0.4	0.6	138	123	0.022	-10.9	1.09
	0.3	0.7	165	151	0.031	-10.3	1.06
	0.2*	0.8	Complete aggregation			-	1.08
	0.1*	0.9	Complete aggregation			-	1.02
	0.0*	1.0	Complete aggregation			-	1.03
	1.0	0.0	96	78	0.024	-1.64	1.00
	0.9	0.1	99	82	0.020	-1.79	0.99
	0.8	0.2	102	84	0.011	-2.40	0.98
	0.7	0.3	112	94	0.010	-2.04	1.01
	0.6	0.4	122	103	0.047	-2.60	0.96
*p(*LMA)	0.5	0.5	131	109	0.029	-2.56	0.98
	0.4	0.6	134	114	0.047	-2.50	0.99
	0.3	0.7	137	115	0.029	-2.70	0.96
	0.2*	0.8	143	123	0.049	-	0.94
	0.1*	0.9	169	149	0.019	-	0.96
	0.0*	1.0	284	232	0.175	-	0.93

[a]Measured using DLS analysis at a concentration of 1 mg mL^{-1}. [b]Obtained from fluorescence emission spectroscopy of aqueous nanoparticle dispersions at a concentration of 1 mg mL^{-1} (λex = 335 nm). *Macroscopic aggregation observed. Samples passed through a 1 µm fibreglass filter prior to DLS analysis.

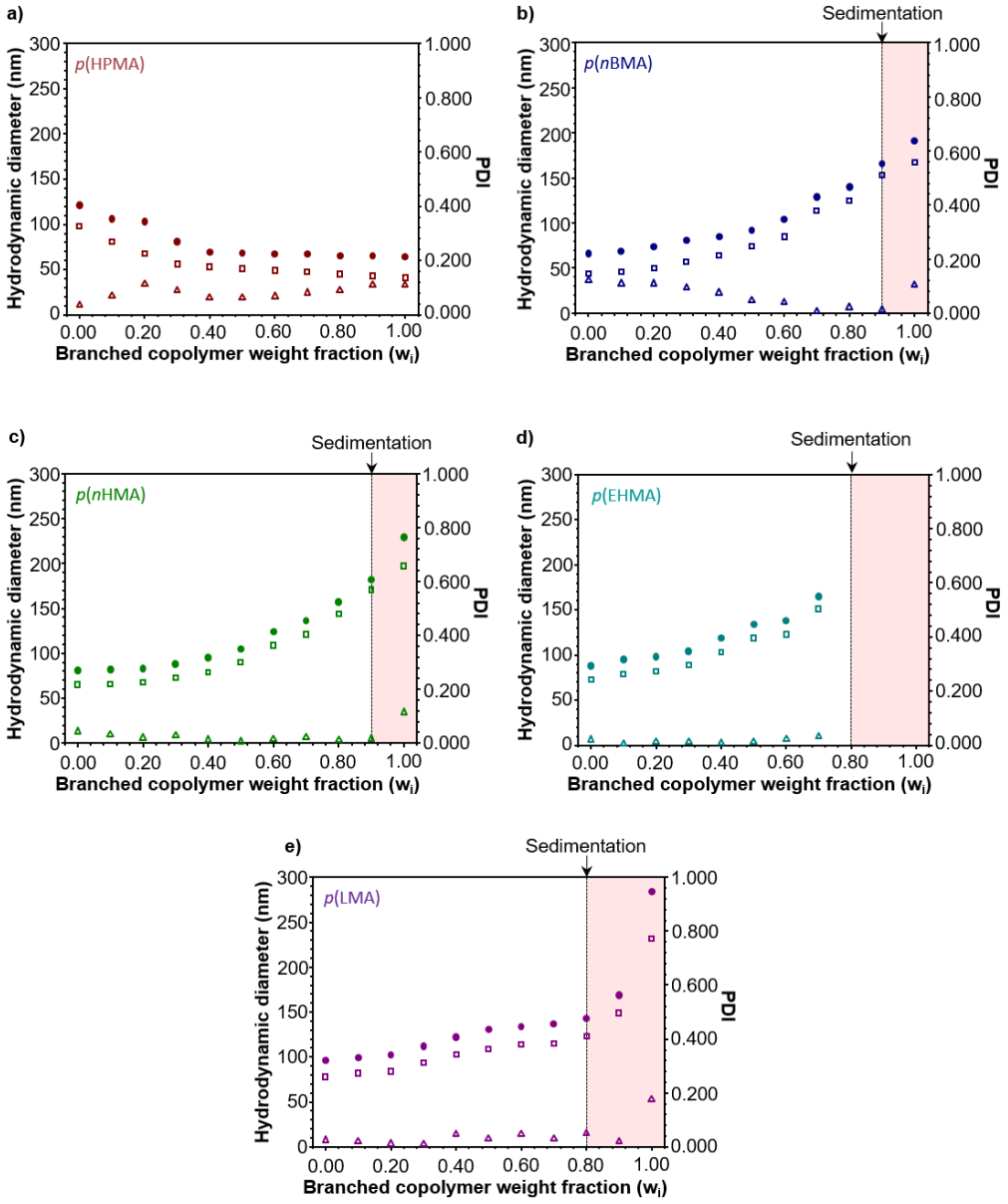

Figure 3.13 Graphical representation of the impact of the branched copolymer weight fraction on the intensity-average (closed circles) and number-average (open squares) hydrodynamic diameters as well as the *PDI* (open triangles) of branched vinyl copolymer nanoparticles generated *via* co-nanoprecipitation of: a) *p(*HPMA), b) *p(n*BMA), c) *p(n*HMA), d) *p(*EHMA) and e) *p(*LMA). The branched copolymer weight fraction at which sedimentation occurred is highlighted in red.

DLS analyses showed two contrasting relationships between the branched copolymer weight fraction and hydrodynamic diameter. The most common relationship showed a strong increase in both intensity-average and number-average hydrodynamic diameters with the increasing weight fraction of branched copolymer; this behaviour was observed for the co nanoprecipitations of *p(n*BMA), *p(n*HMA), *p(*EHMA), *p(*LMA) based copolymers. Interestingly, these relationships did not show linear increases in hydrodynamic diameter. Increases in the branched copolymer weight fraction from 0.0 to 0.5 typically had a relatively small impact on nanoparticle hydrodynamic diameter, whereas further increases resulted in

large increases in nanoparticle size until nanoprecipitations failed. For example, for the co-nanoprecipitation of PEG_{45}-*b*-*p(n*$HMA)_{123}$ and *p(n*HMA_{68}-*co*-$EGDMA_{1.03}$), increases in the branched copolymer weight fraction from 0.0 to 0.5 resulted in an increase in the intensity-average hydrodynamic diameter from 81 – 105 nm (ΔD_z = +24 nm) whereas further increases in the branched copolymer weight fraction to 0.8 saw the hydrodynamic diameter increase to 157 nm (ΔD_z = +52 nm) and finally the appearance of sediment at a branched copolymer weight fraction of 0.9.

The reduction in AB block copolymer weight fraction, which accompanies increasing branched copolymer weight fractions, can explain this as fewer AB block copolymer chains were available to stabilise the increasing mass of hydrophobic branched copolymer. As a result, nanoparticle growth continues until a sufficient level of steric stabilisation is provided by the hydrophilic domains of AB block copolymers, which prevent further nanoparticle-nanoparticle aggregation. It is likely that, in cases where low weight fractions of amphiphilic AB block copolymers were used, nanoparticles underwent longer growth periods owing to relatively low levels of steric stabilisation . In cases where exceptionally low levels of steric stabilisation were provided (AB block copolymer $\omega_i \leq 0.2$), nanoparticles could not achieve colloidal stability which resulted in macroscopic precipitation. These results emphasise the importance of AB block copolymers in nanoparticle stabilisation during co-nanoprecipitation.

In stark contrast to the co-nanoprecipitations described above, nanoparticles generated *via* co-nanoprecipitation of *p(*HPMA) based copolymers exhibited a reduction in hydrodynamic diameter as the weight fraction of the branched copolymer was increased. Increases in the weight fraction of *p(*$HPMA_{63}$-*co*-$EGDMA_{0.90}$) had the most significant impact as it was raised from 0.0 to 0.4. This was accompanied by a reduction in intensity-average hydrodynamic diameter from 121 to 69 nm (ΔD_z = 52 nm). Further increases up to and including the sole nanoprecipitation of *p(*$HPMA_{63}$-*co*-$EGDMA_{0.90}$), from ω_i = 0.4 to 1.0, had little impact on the size of nanoparticles formed (D_z = 64 nm, ΔD_z = 5 nm). These results may appear counter-intuitive given the role of amphiphilic AB block copolymers in the stabilisation of *p(n*BMA), *p(n*HMA), *p(*EHMA), *p(*LMA) based nanoparticles described above. However, there are two logical explanations for the trend observed in the hydrodynamic diameters of nanoparticles formed during *p(*HPMA) based co-nanoprecipitations. As demonstrated in Section 3.4.1, the high molecular weight branched copolymers play an important role in driving the nucleation process which occurs during *p(*HPMA) based co-nanoprecipitations. The results acquired here reiterate this hypothesis and suggest that it may be a reason for the variation observed in nanoparticle size. It is possible that nucleation is significantly hindered as a result of low amounts, or even the absence, of high molecular weight branched copolymers responsible for driving polymer nucleation within the initial THF solution. As a result, it is likely that fewer

stable nuclei capable of further growth would be formed, consequently leading to the generation of larger nanoparticles. Increases in the branched copolymer weight fraction therefore increased the proportion of stable nuclei forming high molecular weight branched copolymers within the initial THF solution. As a result, the hydrodynamic diameters of nanoparticles generated decreased as the weight fraction of branched copolymer increased.

Alternatively, the degree of electrostatic stabilisation provided by *p(*HPMA) could also be a contributing factor to the final hydrodynamic diameters of the *p(*HPMA) nanoparticles formed. When nanoprecipitating *p(*$HPMA_{63}$-*co*-$EGDMA_{0.90}$) in the absence of additional material, electrostatic stabilisation prevented nanoparticle-nanoparticle aggregation both during and after nanoprecipitation. In contrast, the low zeta potentials obtained for nanoparticles generated using low branched copolymer weight fractions suggest that such co-nanoprecipitations are reliant on the steric stabilisation provided by the hydrophilic domains of PEG_{45}-*b*-*p(n*$HMA)_{123}$ to cap nanoparticle growth. The impact of the branched copolymer weight fraction on nanoparticle stability is likely due to the relative contributions of electrostatic and steric to nanoparticle stabilisation during co-nanoprecipitation. It is therefore likely that the steric stabilisation mechanism is dominant at low branched copolymer weight fractions due to low amounts of *p(*$HPMA_{63}$-*co*-$EGDMA_{0.90}$); this suggestion is supported by the relatively low zeta potentials obtained for nanoparticles containing branched copolymer weight fractions ≤ 0.40. Whilst further increases in the branched copolymer weight fraction had little impact on nanoparticle size, significant increases were observed in the zeta potential of nanoparticles, which increased from -17.1 to -27 mV as the branched copolymer weight fraction was increased from 0.4 to 0.6. This indicated that at branched copolymer weight fractions ≥ 0.4, electrostatic stabilisation may become the predominant growth capping mechanism during co-nanoprecipitation.

These results highlight the differing roles played by branched and AB block copolymers containing varied repeat unit functionalities during co-nanoprecipitation. In all cases, the components play important roles in both the nucleation and growth stages of co-nanoprecipitation. The co-nanoprecipitation of highly hydrophobic copolymers which are incapable of providing electrostatic stabilisation is less complex as the increased hydrophobicity of such materials generally drive rapid nucleation, regardless of copolymer architecture. Amphiphilic AB block copolymers were the sole component responsible for arresting nanoparticle growth, therefore nanoparticle hydrodynamic diameters were dependent upon the amount of AB block copolymer stabiliser present within the initial THF solution.

In contrast, the co-nanoprecipitation of *p(*HPMA) based copolymers was more complex as it combined the architecture-dependent factors of copolymer nucleation and nanoparticle stabilisation. The relatively moderate hydrophobicity of *p(*HPMA) based copolymers resulted in an architecture-dependent nucleation process where high molecular weight branched copolymers were responsible for driving nucleation during co-nanoprecipitation. As a result, nanoparticle size depends on the composition of AB block and branched copolymers within the initial THF solution. Furthermore, competition between steric and electrostatic growth capping mechanisms appeared to be an important factor in the relationship between nanoparticle hydrodynamic diameter and branched copolymer composition. Based on the fundamental studies conducted and data produced here it would be difficult to correlate the relative contributions of nucleation and stabilisation mechanisms to the hydrodynamic diameter of *p(*HPMA) based nanoparticles. However, these studies clearly demonstrate that these factors should be considered when manipulating the branched copolymer weight fraction of *p(*HPMA) based copolymers for co-nanoprecipitation formulations.

Aqueous nanoparticle dispersions were assessed using fluorescence emission spectroscopy of pyrene encapsulated during co-nanoprecipitation (λ_{ex} = 335 nm). Assessment of the internal polarity within the core of branched vinyl copolymer nanoparticles should provide information on the impact of nanoparticle composition on core polarity. Similar studies had been conducted previously to demonstrate that reduction of the branched copolymer weight fraction from 1.0 to 0.5 had little impact on the internal polarity within the core of *p(*HPMA) based branched vinyl copolymer nanoparticles.[22] The authors suggested that AB block copolymers were solely located on the surface of branched vinyl copolymer nanoparticles rather than within their cores. It was hoped that similar analyses would provide information on the location of AB block copolymers within *p(n*BMA), *p(n*HMA), *p(*EHMA) and *p(*LMA) nanoparticles of varied copolymer composition.

Analysis of pyrene fluorescence emission spectra again showed two conflicting trends between nanoparticle internal polarity and the weight fraction of branched copolymer employed in co-nanoprecipitation (Figure 3.14). In the case of *p(*HPMA), I_1/I_3 ratios increased from 1.39 to 1.60 as branched copolymer weight fractions were increased from 0.0 to 0.4. Further increases in branched copolymer weight fraction above 0.4 had relatively little impact on internal polarity with nanoparticles consisting solely of *p(*$HPMA_{63}$-*co*-$EGDMA_{0.90}$) having an I_1/I_3 ratio of 1.68. The lack of a relationship between internal polarity and nanoparticle compositions at branched copolymer weight fractions $\geq$ 0.5 was consistent with data previously reported.[22] However, the additional data points obtained from nanoparticles containing branched copolymer composition between 0.0 and 0.4, along with the general trends in the size and zeta potentials obtained for *p(*HPMA) nanoparticles produced in this

work provide a new perspective on the location of PEG_{45}-*b*-*p(*$HPMA)_{124}$ within branched vinyl copolymer nanoparticles. These results can be explained by considering two factors: i) the relative polarities of PEG and *p(*HPMA) and ii) the stabilisation mechanism by which nanoparticle growth is arrested during co-nanoprecipitation.

Whilst it may appear counter-intuitive, the chemical functionality present on *p(*HPMA) repeat units, which provides a moderate level of electrostatic stabilisation for *p(*$HPMA_{63}$-*co*-$EGDMA_{0.90}$) based nanoparticles, will likely bring an associated polarity to the core of any *p(*HPMA) based branched vinyl copolymer nanoparticles. In contrast, whilst considered a relatively polar and hydrophilic polymer, PEG is known for its chemical neutrality. It is therefore possible that the relatively high composition of PEG in nanoparticles generated using low branched copolymer weight fractions influences the nanoparticle core polarity. Increases in the branched copolymer weight fraction significantly increase the nanoparticle internal polarity; it is possible that this occurred as a result of the inherent reduction in the chemically neutral PEG composition which accompany any increases in the branched copolymer weight fraction. The levelling of nanoparticle polarity at branched copolymer compositions > 0.5 may have arisen due to vastly diminished PEG compositions having negligible impact on nanoparticle core polarity. Whilst a possibility, quantification of the relative polarities of pure PEG and *p(*HPMA) would need to be conducted and validated.

Alternatively, the mechanism by which nanoparticle growth is arrested during co-nanoprecipitation must also be considered. The larger hydrodynamic diameters and low zeta potentials obtained for nanoparticles produced at low branched copolymer weight fractions were attributed to a steric stabilisation mechanism to halt nanoparticle growth. It is possible that combinations of varied nucleation rates between branched and AB block copolymers and a reliance on steric stabilisation could result in a disproportionate absence of PEG_{45}-*b*-*p(*$HPMA)_{124}$ within the core of branched vinyl copolymer nanoparticles. Furthermore, the increased nanoparticle size and the presence of a PEG corona may reduce the interaction between pyrene, encapsulated near or at the surface of branched copolymer nanoparticles, and surrounding water molecules. This would likely reduce the polarity of the environment in which pyrene is located. In contrast, the potential switch to an electrostatic growth capping mechanism resulted in a significant reduction in nanoparticle hydrodynamic diameter. It is therefore possible that due to the increased nanoparticle surface area and a reduced PEG corona, encapsulated pyrene molecules may have increased exposure to surrounding water molecules. At this point it is not possible to categorically state whether PEG_{45}-*b*-*p(*$HPMA)_{124}$ is located within the core of branched vinyl copolymer nanoparticles during co-nanoprecipitation, although it is likely.

The trends observed between branched copolymer composition and nanoparticle internal polarity appeared more straightforward in cases where there was a stark contrast between the polarities of the hydrophilic PEG and the hydrophobic methacrylic domains. This was the case for *p(n*BMA), *p(n*HMA), *p(*EHMA) and *p(*LMA) based co-nanoprecipitations. In all cases, modest reductions were observed in nanoparticle internal polarity as the weight fraction of branched copolymer was increased. This can be explained simply by considering the inherent decrease in the concentration of PEG chains located within branched vinyl copolymer nanoparticles as the branched copolymer weight fraction is increased. For example, the concentration of PEG within PEG_{45}-*b*-*p(n*$BMA)_{125}$ and *p(n*BMA_{73}-*co*-$EGDMA_{1.12}$) copolymers are 11 and 0 wt % respectively. Systematic increases in the proportion of *p(n*BMA_{73}-*co*-$EGDMA_{1.12}$) within initial THF solutions would therefore reduce the overall composition of PEG within the ensuing branched vinyl copolymer nanoparticles. The fact that these trends were observed for *p(n*BMA), *p(n*HMA), *p(*EHMA) and *p(*LMA) suggested that, in all cases, amphiphilic AB block copolymers are entrapped within the nanoparticle cores during the co-nanoprecipitation process. This may not be considered a surprise given that, again in all cases, amphiphilic AB block copolymers had exhibited effective nucleation during their individual nanoprecipitations, discussed in Section 2.3.

The relatively small impact of the branched copolymer weight fraction on nanoparticle internal polarity was initially surprising. For example, in the cases of *p(n*HMA) based co-nanoprecipitations, I_1/I_3 ratios decreased from 1.19 to 1.13 as the branched copolymer weight fraction was increased from 0.0 to 1.0. This can be explained by the low composition of PEG within branched vinyl copolymer nanoparticles regardless of the branched copolymer weight fraction employed. For example, PEG_{45}-*b*-*p(n*$BMA)_{125}$, PEG_{45}-*b*-*p(n*$HMA)_{127}$, PEG_{45}-*b*-*p(*$EHMA)_{115}$ and PEG_{45}-*b*-*p(*$LMA)_{122}$ based copolymers have PEG compositions of 11, 9, 9 and 7 wt % respectively. Systematic variation of branched copolymer weight fractions during co-nanoprecipitation thus only incorporated a maximum of 11 wt % of the polar hydrophilic PEG domains within the core of branched vinyl copolymer nanoparticle core. It was concluded that such small variations in the composition of the PEG domain produced only small changes in the internal polarity of the nanoparticle.

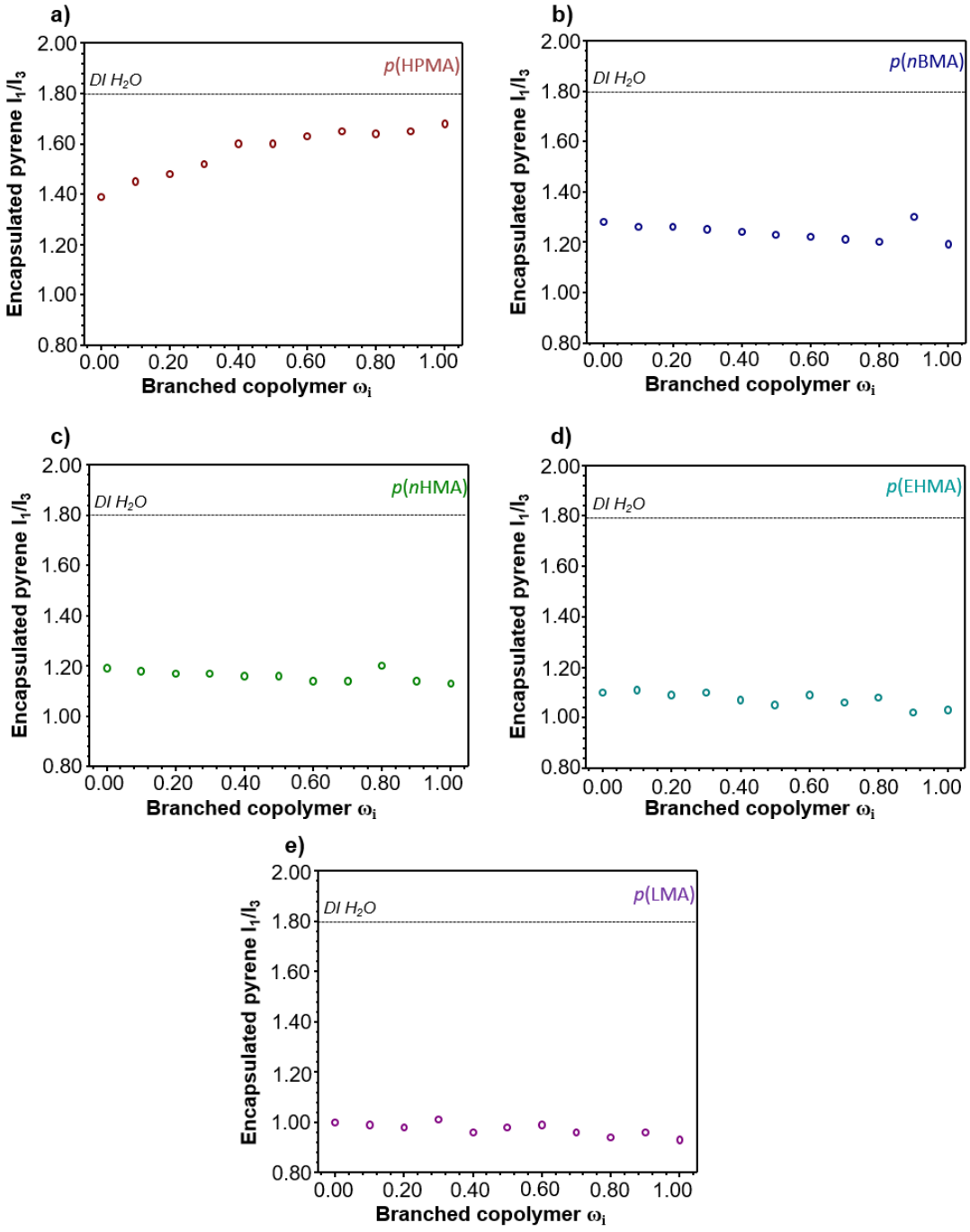

Figure 3.14 Graphical representation of the impact of the branched copolymer weight fraction on the internal polarity of branched vinyl copolymer nanoparticles generated *via* co-nanoprecipitation of: a) *p(*HPMA), b) *p(n*BMA), c) *p(n*HMA), d) *p(*EHMA) and e) *p(*LMA).

3.4.3.2 Impact of Initial Polymer Concentration on Co-nanoprecipitation

Polymer concentration was varied to study how this parameter affected the size of the nanoparticles. Co-nanoprecipitations conducted previously had produced nanoparticles with intensity-average hydrodynamic diameters ranging between 50 and 150 nm, depending on the chemical nature of the copolymers used in co-nanoprecipitation. It was hoped therefore that the co-nanoprecipitation process could be manipulated in order to allow nanoparticle sizes to

be tuned between 10 and 100 nm, which lead to enhanced drug delivery efficiencies *in vivo*.[33] Nanoparticle hydrodynamic diameters have been shown to increase with polymer concentration present within the water-miscible solvent used as the organic phase during nanoprecipitation.[34] Experiments were designed to investigate whether nanoparticle size could be influenced *via* manipulation of the total copolymer concentration in the good solvent (THF) prior to co-nanoprecipitation.

Given the strong influence that the branched:AB block copolymer ratio had on nanoparticle formation during co-nanoprecipitation, discussed in Section 3.4.3.1, all co-nanoprecipitations were conducted using equivalent weight fractions of the constituent copolymers employed in co-nanoprecipitation (ω_i (branched) = ω_i (AB block) = 0.50). As the hydrodynamic diameters being targeted were typically smaller than those achieved previously, co-nanoprecipitations were conducted using initial copolymer concentrations in THF that were less than or equal to those used previously ($[P]_0 = \leq 5.00$ mg mL^{-1}). A constant DR of bad:good solvent was used to generate uniform supersaturation conditions in all co-nanoprecipitations (DR = $V_{DI\ H2O}/V_{THF}$ = 5). Co-nanoprecipitations were conducted using THF solutions of *p(*HPMA), *p(n*BMA), *p(n*HMA), *p(*EHMA) and *p(*LMA) based copolymers containing incrementally decreasing $[P]_0$ ranging from 5.0 to 0.5 mg mL^{-1}. An overview of how co-nanoprecipitations were conducted is presented in Figure 3.15.

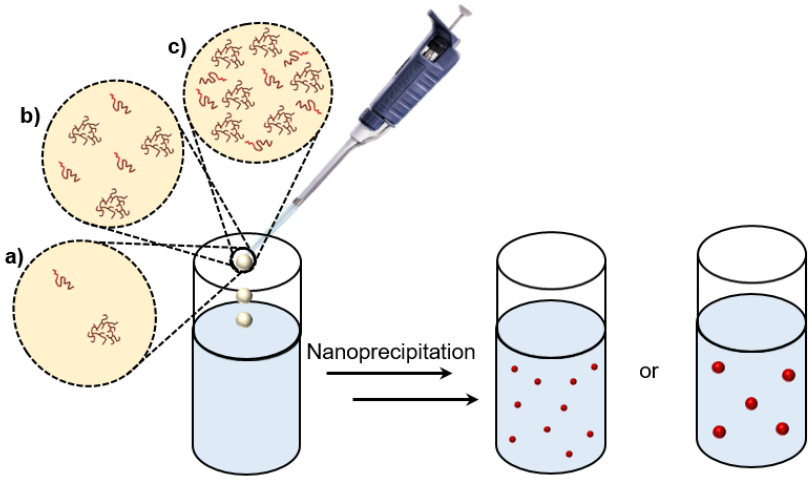

Figure 3.15 Schematic representation of the manipulation of copolymer concentration within the good solvent to conduct co-nanoprecipitations at: a) low, b) moderate or c) high concentration.

In all cases, co-nanoprecipitations formed uniform turbid/translucent mixtures immediately after polymer addition and remained as such following solvent removal *via* evaporation over 48 hours to give aqueous nanoparticle dispersions of varied $[P]_f$ in DI H_2O. Aqueous nanoparticle dispersions were assessed using DLS from which nanoparticle average hydrodynamic diameters, *PDI*s and DCRs were obtained. Nanoparticle concentrations and DLS characterisation data is presented in Table 3.5.

Table 3.5 The impact of polymer concentration on the size distribution of branched vinyl copolymer nanoparticles formed *via* co-nanoprecipitation.

Hydrophobic domain	$[P]_0$ (mg mL^{-1})[a]	$[P]_f$ (mg mL^{-1})[b]	D_z (nm)[c]	D_n (nm)[c]	*PDI*[c]	DCR (kcps)[c]
	5.000	1.000	76	61	0.030	181444
	4.950	0.990	70	56	0.050	165177
	4.875	0.975	70	56	0.027	163481
	4.750	0.950	75	61	0.024	201323
	4.500	0.900	72	58	0.031	185776
	4.250	0.850	73	58	0.037	160381
	4.000	0.800	73	53	0.024	148879
p(HPMA)	3.750	0.750	70	54	0.041	117829
	3.500	0.700	68	55	0.033	116873
	3.000	0.600	70	54	0.034	103683
	2.500	0.500	68	54	0.041	99219
	2.000	0.400	68	54	0.056	81094
	1.500	0.300	66	51	0.075	59235
	1.000	0.200	60	49	0.133	34437
	0.500	0.100	65	52	0.153	36659
	5.000	1.000	107	88	0.019	517987
	4.950	0.990	109	87	0.044	736903
	4.875	0.975	106	86	0.024	478355
	4.750	0.950	104	86	0.022	485867
	4.500	0.900	102	86	0.007	450092
	4.250	0.850	104	84	0.042	464043
	4.000	0.800	103	86	0.011	442725
p(*n*BMA)	3.750	0.750	102	84	0.027	421286
	3.500	0.700	104	85	0.035	402378
	3.000	0.600	101	82	0.027	349793
	2.500	0.500	97	80	0.016	296201
	2.000	0.400	97	79	0.021	265633
	1.500	0.300	98	80	0.022	226652
	1.000	0.200	93	76	0.002	91193
	0.500	0.100	77	61	0.040	24253
	5.000	1.000	106	87	0.033	495260
	4.950	0.990	109	89	0.024	521259
	4.875	0.975	108	89	0.024	484709
	4.750	0.950	106	88	0.019	473906
	4.500	0.900	107	87	0.023	474977
	4.250	0.850	106	88	0.017	439352
	4.000	0.800	104	86	0.023	419232
p(*n*HMA)	3.750	0.750	109	91	0.024	387608
	3.500	0.700	105	87	0.013	380172
	3.000	0.600	100	83	0.010	318753
	2.500	0.500	98	82	0.013	284270
	2.000	0.400	94	76	0.020	245017
	1.500	0.300	98	82	0.015	213560
	1.000	0.200	92	75	0.025	76897
	0.500	0.100	73	52	0.103	21989
	5.000	1.000	109	88	0.031	512757
	4.950	0.990	103	85	0.016	513437
	4.875	0.975	106	88	0.012	525057
	4.750	0.950	107	88	0.015	476623
	4.500	0.900	104	85	0.021	451986
	4.250	0.850	103	85	0.031	436791
	4.000	0.800	101	83	0.020	393764
p(EHMA)	3.750	0.750	100	83	0.021	378286
	3.500	0.700	96	77	0.048	310307
	3.000	0.600	101	85	0.025	349695
	2.500	0.500	92	73	0.048	206871
	2.000	0.400	93	77	0.013	215279
	1.500	0.300	83	66	0.050	78607
	1.000	0.200	74	49	0.139	33271
	0.500	0.100	79	88	0.200	18856

Table 3.5 *(cont.)* The impact of polymer concentration on the size distribution of branched vinyl copolymer nanoparticles formed *via* co-nanoprecipitation.

Hydrophobic domain	$[P]_0$ (mg mL^{-1})[a]	$[P]_f$ (mg mL^{-1})[b]	D_z (nm)[c]	D_n (nm)[c]	*PDI*[c]	DCR (kcps)[c]
	5.000	1.000	140	119	0.021	819851
	4.950	0.990	128	107	0.010	589548
	4.875	0.975	140	120	0.018	579082
	4.750	0.950	140	120	0.013	591223
	4.500	0.900	111	92	0.022	557191
	4.250	0.850	140	120	0.010	547231
	4.000	0.800	144	123	0.029	763449
*p(*LMA)	3.750	0.750	136	117	0.018	551351
	3.500	0.700	129	107	0.031	551402
	3.000	0.600	121	101	0.023	498301
	2.500	0.500	117	99	0.010	419086
	2.000	0.400	102	74	0.033	295089
	1.500	0.300	88	72	0.019	120926
	1.000	0.200	87	71	0.013	79987
	0.500	0.100	94	76	0.034	48672

[a]Polymer concentration in THF prior to co-nanoprecipitation. [b]Nanoparticle concentration in DI H_2O following solvent evaporation. [c]Determined by DLS of aqueous nanoparticle dispersions at $[P]_f$.

In the vast majority of cases, highly monodisperse aqueous nanoparticle dispersions were obtained. All series of co-nanoprecipitations showed small decreases in nanoparticle hydrodynamic diameters as $[P]_0$ was decreased. The extent to which nanoparticle hydrodynamic diameters varied was dependent upon the chemical nature of the hydrophobic domains of the copolymers used in co-nanoprecipitation. For example, in the case of *p(*HPMA) based co-nanoprecipitations, intensity-average hydrodynamic diameters decreased from 76 to 65 nm as the concentration at which co-nanoprecipitations were conducted was reduced from 5.0 to 0.5 mg mL^{-1} and number-average diameters decreased from 61 to 52 nm. This represented a 15 % decrease in the intensity-average diameter of *p(*HPMA) based nanoparticles. In contrast, nanoparticles generated through *p(*LMA) based co-nanoprecipitations saw a decrease in the intensity-average diameters from 140 to 94 nm which represented a 33 % decrease over the same reduction in $[P]_0$. Relatively consistent changes in nanoparticle hydrodynamic diameters were observed for nanoparticles generated through co-nanoprecipitation of *p(n*BMA), *p(n*HMA) and *p(*EHMA) based copolymers which saw their intensity-average diameters decrease by 28, 31 and 28 % respectively (Figure 3.16ai-v).

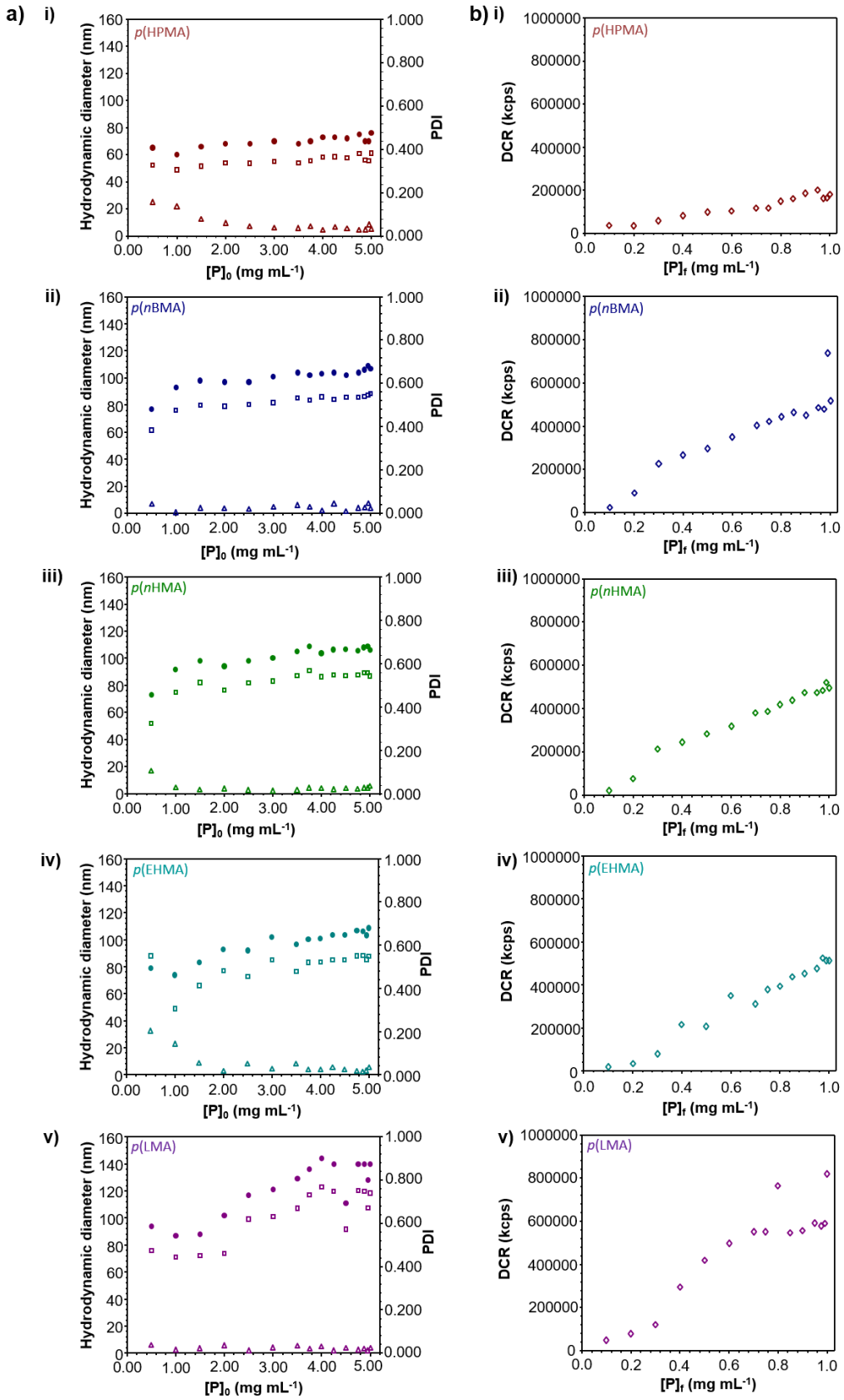

Figure 3.16 DLS analyses of branched vinyl copolymer nanoparticles. a) The impact of $[P]_0$ on nanoparticle PDI (open triangles), intensity- (closed circles) and number- (closed squares) diameters and b) The relationship between $[P]_f$ and derived count rates obtained from aqueous nanoparticle dispersions consisting of i) *p*(HPMA), ii) *p*(*n*BMA), iii) *p*(*n*HMA), iv) *p*(EHMA) and v) *p*(LMA).

The small changes observed in hydrodynamic diameter indicate that variation in the concentration at which co-nanoprecipitations were conducted did have an impact on nanoparticle size. It is likely that this occurred as a result of decreased nucleation and growth rates during co-nanoprecipitation due to suppressed polymers and nuclei concentrations within the THF/DI H_2O mixture. The data obtained by DLS provided some evidence of decreased nucleation and growth rates. Increased *PDI* values were obtained at low $[P]_0$ in *p(*HPMA) *p(n*HMA) and *p(*EHMA) based co-nanoprecipitations. Increases in *PDI* are typically associated with slow nucleation processes; this occurs due to lower levels of supersaturation within the good/bad solvent mixtures and typically results in the continuous formation of nuclei throughout the, albeit short, co-nanoprecipitation process. Nuclei formed at different stages of the co-nanoprecipitation have varied opportunities for nanoparticle growth and, as a result, larger disparities are observed in nanoparticle size. This was particularly evident in *p(*HPMA) based co-nanoprecipitations where, due to the relatively high polarity of the *p(*HPMA) repeat unit, the lowest levels of supersaturation would be expected.

The general increase observed in nanoparticle hydrodynamic diameters with $[P]_0$ could be attributed to lower rates of nanoparticle growth during co-nanoprecipitation. Given the high hydrophobicity of the copolymers used in co-nanoprecipitation and the low *PDI* values observed, it is likely that co-nanoprecipitations proceed *via* DLCA. Decreased concentrations of polymers within the initial THF/DI H_2O mixture likely decreased the number of nuclei (clusters) formed which in turn suppress the rate of nanoparticle growth *via* cluster-cluster aggregation. Slower growth rates would have provided opportunity for the stabilisation of nanoparticles *via* adsorption of stabiliser molecules which may nucleate at slow rates, thus allowing nanoparticle growth to be capped at a smaller size.

Interestingly, in all cases, nanoparticle hydrodynamic diameters appeared to level off at higher $[P]_0$. For example, negligible increases were observed in the hydrodynamic diameters of nanoparticles generated in *p(n*HMA) based co-nanoprecipitations as $[P]_0$ was increased from of 3.5 and 5.0 mg mL^{-1} (D_z = 105 and 106 nm). Whilst they may appear to contradict the hypotheses of decreased nucleation and growth rates described above, these results indicate that arrest of nanoparticle growth by the steric stabilisation provided by amphiphilic block copolymers proceeded independently of the nucleation and growth rates which occurred during co-nanoprecipitation. Whilst changes to $[P]_0$ did have an impact, changes in nanoparticle diameter were somewhat modest. It is possible that this occurred due to the limited $[P]_0$ ranges studied; however, the range of $[P]_0$ which could be studied was limited by the concentration limitations of DLS analysis. Nonetheless, the size analyses presented here demonstrate that, even under extreme dilution, stable branched vinyl copolymer nanoparticles can be generated *via* co-nanoprecipitation.

Plots of $[P]_f$ *vs.* derived count rate (DCR) were also constructed (Figure 3.16bi-v). In all cases, increases were observed in the DCRs obtained during DLS analyses of aqueous nanoparticle dispersions with $[P]_f$; DCRs can be indicative of changes in nanoparticle size or concentration and can also indicate simultaneous increases in both nanoparticle size and concentration. This was not surprising given the nature of this study ($[P]_f \sim [P]_0$), which produced aqueous nanoparticle dispersions at varying $[P]_f$ in DI H_2O. Nonetheless, given the limited changes in the hydrodynamic diameters obtained for nanoparticles generated across the concentration range specified, the strong relationships observed in plots of $[P]_f$ *vs.* DCR suggested that increases in observed DCRs were largely a result of higher nanoparticle concentrations rather than increases in nanoparticle size.

Small changes were observed in nanoparticle hydrodynamic diameters. However, these results demonstrate that the initial concentration at which co-nanoprecipitations were conducted was not an effective tool in controlling nanoparticle size over a wide range. The small decreases observed in the hydrodynamic diameters came with the associated cost of a lower polymer concentration within the final aqueous nanoparticle dispersion. This would be problematic for the use of such nanomaterials as prospective DNC systems as decreased aqueous nanoparticle dispersions would inherently increase the required therapeutic dose. For this reason, manipulation of the AB block:branched copolymer ratio offers a more practical alternative to vary the size of nanoparticles generated *via* co-nanoprecipitation. However, these results indicate that the $[P]_0$ at which co-nanoprecipitations are conducted could be increased above 5 mg mL^{-1} with minimal impact on nanoparticle size. This could allow the preparation of branched vinyl copolymer nanoparticles at higher concentrations which would decrease the volume of future drug-loaded aqueous nanoparticle dispersions required to achieve clinically relevant chemotherapeutic plasma concentrations. A preliminary study was conducted focussed on increased concentration which demonstrated that individual nanoprecipitations of *p(*$HPMA_{63}$-*co*-$EGDMA_{0.90}$) could be conducted at $[P]_0$ up to 100 mg mL^{-1} in THF whilst still producing monodisperse nanoparticles with an intensity-average diameter of 145 nm (Appendix, Figure A3.4). Alternatively, as discussed in Section 3.1.2, multiple co-nanoprecipitations offer another route to increasing nanoparticle concentration. Whilst multiple co-nanoprecipitations have not been attempted here, the steric stabilisation growth capping mechanism suggested by the results obtained within this study indicate that multiple co-nanoprecipitations should be possible for these novel *p(n*BMA), *p(n*HMA), *p(*EHMA) or *p(*LMA) based co-nanoprecipitation systems.

3.4.4 Nanoparticle Stability

Given the desired application of branched vinyl copolymer nanoparticles as DNC systems, it was important to subject nanoparticles to conditions similar to those encountered *in vivo*. In particular, it was essential to assess the stability of branched vinyl copolymer nanoparticles to dilution and also to the presence of salt. Studies were therefore designed to subject branched vinyl copolymer nanoparticles to biologically relevant conditions and determine whether such nanomaterials were able to maintain their structural integrity.

The nanoparticles used in stability studies were prepared *via* co-nanoprecipitation of a fixed total polymer mass consisting of equal weight fractions of amphiphilic AB block and hydrophobic branched copolymers. Co-nanoprecipitations were conducted from THF into DI H_2O using a fixed dilution ratio (V_{H2O}/V_{THF} = 5). THF removal occurred over 48 hours at ambient temperature to give *p(*HPMA), *p(n*BMA), *p(n*HMA), *p(*EHMA) and *p(*LMA) aqueous nanoparticle dispersions at a $[P]_f$ of 1 mg mL^{-1}.

3.4.4.1 Nanoparticle Stability to Dilution

The ability to maintain their structural integrity following high dilution is a pre-requisite for polymer-based nanoparticles as prospective applications for DNC systems. Stability to dilution is essential in preventing the burst release of encapsulated drug payloads shortly after IV administration into systemic circulation. The stability of branched vinyl copolymer nanoparticles to dilution was assessed *via* serial dilution of aqueous nanoparticle dispersions ($[P]_{H2O}$ = 1 mg mL^{-1}) over a 1000 fold dilution factor (DF). Aqueous nanoparticle dispersions were diluted and gently agitated (roller mixer) for 24 hours, in order to allow equilibration and/or sedimentation processes to occur, following which, nanoparticles were assessed using DLS (Appendix, Table A3.2).

In all cases, there was no evidence of polymer sedimentation as a result of dilution. DLS analyses showed negligible changes in the hydrodynamic diameters and *PDI* values obtained for all aqueous nanoparticle dispersions over a 1000-fold dilution. Plots of nanoparticle hydrodynamic diameters and *PDI* vs. $[P]_{H2O}$ were constructed to demonstrate the consistency in nanoparticle properties, despite the significant reduction in nanoparticle concentration (Figure 3.17). In all cases, DCR values showed linear increases with $[P]_f$. The absence of any change in hydrodynamic diameter combined with the linear relationships observed between DCR and $[P]_{H2O}$ therefore demonstrated that branched vinyl copolymer nanoparticles consisting of *p(*HPMA), *p(n*BMA), *p(n*HMA), *p(*EHMA) and *p(*LMA) based copolymers remained stable over a wide range of concentrations.

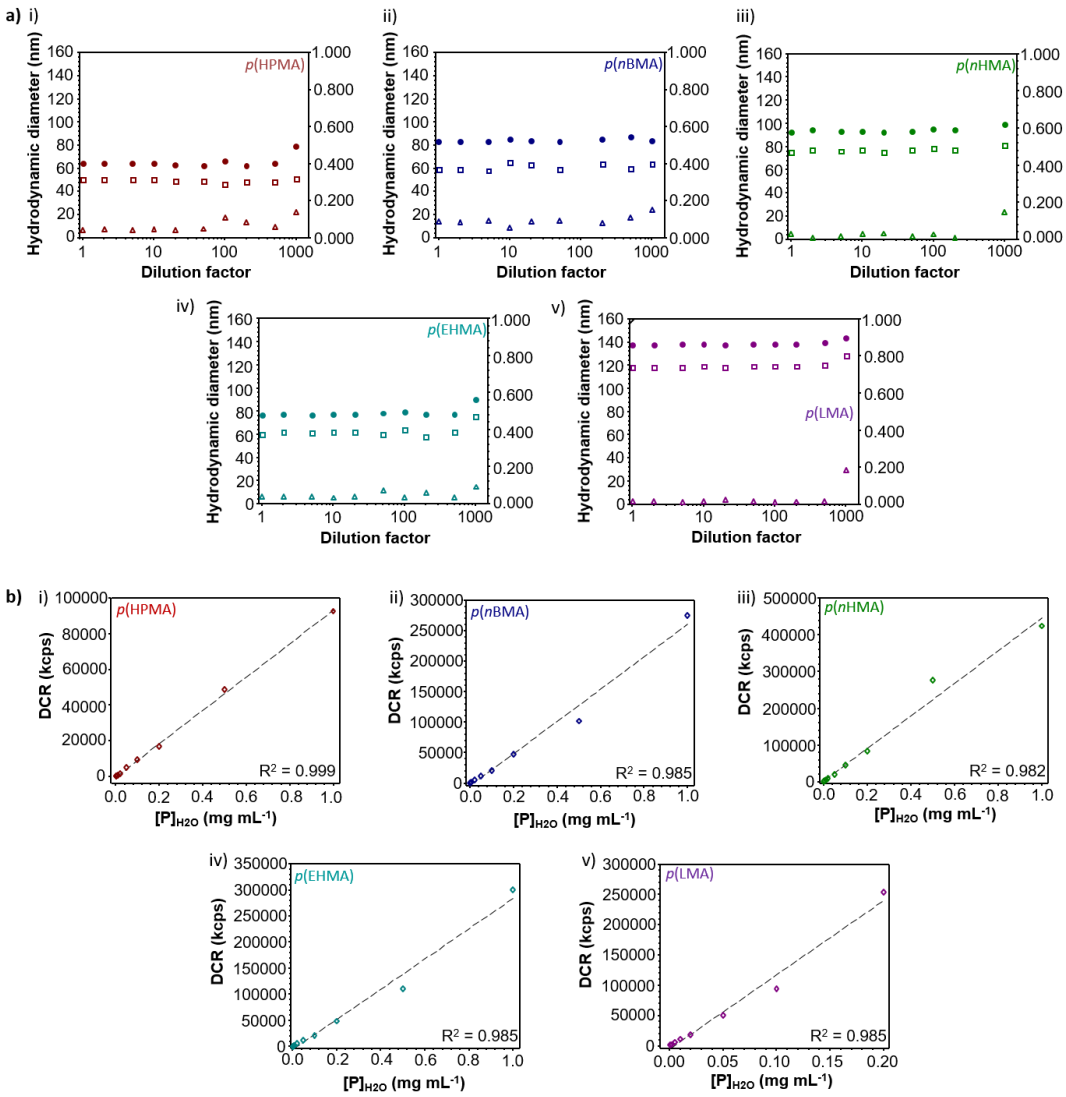

Figure 3.17 Graphical representation of nanoparticle stability to dilution. a) Plots of D_z (closed circles), D_n (open squares) and PDI (open triangles) *vs.* obtained for i) *p(*HPMA), ii) *p(n*BMA), iii) *p(n*HMA), iv) *p(*EHMA) and e) *p(*LMA) based branched vinyl copolymer nanoparticles. b) Plots of DCR vs. $[P]_{H2O}$.

Nanoparticle stability to dilution indicated that high molecular weight amphiphilic block copolymers, which confer stability *via* steric stabilisation, are kinetically frozen within the nanoparticle structure, presenting PEG chains at the surface of branched vinyl copolymer nanoparticles. It is likely that this is due to the high energy cost associated with the energetically unfavourable interactions of the highly hydrophobic domains of the amphiphilic block copolymer with the aqueous phase. The ability to maintain structural integrity whilst under extreme dilution is a promising sign for the use of branched vinyl copolymer nanoparticles as DNCs *in vivo*. Furthermore, these results indicate that, should these nanoparticles be loaded with hydrophobic chemotherapeutics, drug release rates would be governed by diffusion of drugs through the polymer matrix rather than concentration

gradient-induced rapid disassembly of the DNC system. Branched vinyl copolymer nanoparticles may therefore be able to offer controlled drug release of encapsulated payloads.

3.4.4.2 Nanoparticle Stability to Salt

Another factor which any DNC system would encounter during both *in vitro* and *in vivo* pharmacological evaluations is dilution in buffered media. The presence of metal ions in solution is particularly problematic for DNC systems whose colloidal stability is reliant on electrostatic repulsion-based stabilisation mechanisms. Given the steric stabilisation provided by the hydrophilic PEG domains of amphiphilic block copolymers it was expected that branched vinyl copolymer nanoparticles would remain stable in the presence of salt. Studies were therefore required to determine the resistance of branched vinyl copolymer nanoparticles to the addition of salt.

Nanoparticle stability to salt was assessed *via* dilution of aqueous nanoparticle dispersions in various concentrations of NaCl ranging from 0.01 – 1.00 mol dm^{-3}. Aqueous nanoparticle dispersions ($[P]_{H2O}$ = 1 mg mL^{-1}) were diluted in aqueous salt solutions (DR = 2) and gently agitated (roller mixer) for 24 hours.

The size distributions of aqueous nanoparticle dispersions were then obtained by DLS (Figure 3.18, Table 3.6). In all cases, aqueous nanoparticle dispersions showed stability to the addition of low concentrations of NaCl (≤ 0.05 mol dm^{-3}). Aqueous nanoparticle dispersions remained colloidally stable with no sign of sedimentation. In contrast, NaCl concentrations >0.05 mol dm^{-3} induced small amounts of polymer sedimentation for *p(n*HMA) and *p(*EHMA) based nanoparticles, therefore reliable DLS analyses could not be obtained. DLS analyses of nanoparticles exposed to <0.05 mol dm^{-3} NaCl solution showed monomodal size distributions for all aqueous nanoparticle dispersions analyses. Combined with the low *PDI* values obtained, this indicated that nanoparticles remained stable. These results reiterated the importance of the PEG shell in providing nanoparticles with the steric stabilisation as the predominant source of nanoparticle stability. This was reinforced by a comparative study of branched vinyl copolymer nanoparticles formed from the sole nanoprecipitation of *p(*$HPMA_{64}$-*co*-$EGDMA_{0.90}$). With the absence of the PEG-based amphiphilic AB block copolymers such nanoparticles are solely reliant on electrostatic repulsions to maintain colloidal stability. As a result, nanoparticle aggregation and sedimentation occurred immediately following the addition of even low concentrations of NaCl (Appendix Figure A3.5).

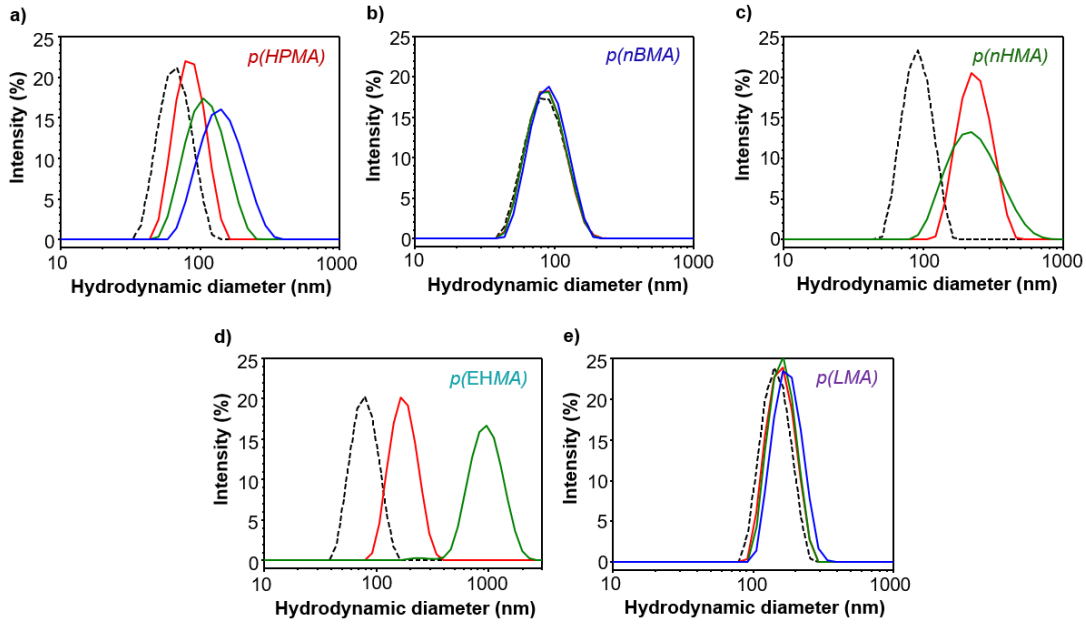

Figure 3.18 The impact of NaCl on the stability of branched vinyl copolymer nanoparticles. Overlaid DLS traces obtained for: a) *p(*HPMA), b) *p(n*BMA), c) *p(n*HMA), d) *p(*EHMA) and e) *p(*LMA). DLS analyses conducted on aqueous nanoparticle dispersions at [NaCl] of: 0.00 (black), 0.01 (red), 0.10 (green) and 1.00 (blue) mol dm^{-3}.

Interestingly, the addition of salt had a varied impact on the hydrodynamic diameters of branched copolymer nanoparticles. For example, little difference was observed in the sizes of *p(n*BMA) and *p(*LMA) based nanoparticles when the NaCl concentration was increased from 0.0 to 0.5 mol dm^{-3}; such nanoparticles saw increases in their intensity-average diameters from 82 – 86 nm and 143 – 172 nm over this concentration range. Alternatively, in the cases of *p(*HPMA), *p(n*HMA) and *p(*EHMA), nanoparticle size generally increased with the concentration of salt. The extent to which hydrodynamic diameters increased, however, varied between nanoparticles. For example, *p(*HPMA) based nanoparticles saw an increase in the intensity-average diameter from 64 to 104 nm as the concentration of NaCl increased from 0.0 to 0.05 mol dm^{-3}, whereas *p(*EHMA) nanoparticles saw an increase in the intensity-average diameter from 76 to 877 nm over the same concentration range.

These results may appear surprising as the addition of salt typically decreases hydrodynamic diameters obtained by DLS as the presence of electrolytes suppress the electrical double layer which surround nanoparticles. However, given the low surface charge due to the apparent neutrality of the PEG shell, it is possible that this may have little impact on branched vinyl copolymer nanoparticles. On the contrary, increases in the concentration of salt may result in non-covalent interactions between the, hydrogen/cation binding PEG shell of branched vinyl copolymer nanoparticles and the sodium cations within the aqueous nanoparticle dispersion. It is also likely that the addition of moderate concentrations of salt would increase the viscosity of the aqueous nanoparticle dispersion. Such increases in viscosity would be expected to

suppress nanoparticle translational coefficients and would therefore artificially inflate the increases observed in nanoparticle hydrodynamic diameters. Despite the increase in hydrodynamic diameter, the retention of monomodal size distributions and low *PDI*s indicate that branched vinyl copolymer nanoparticles maintain their structural integrity at moderate concentrations of NaCl.

Table 3.6 Visual and DLS analyses of the stability of aqueous nanoparticle dispersions to addition of NaCl.

Nanoparticle Hydrophobic domain	[NaCl] (mol dm^{-3})	Sedimentation[a]	D_z (nm)[b]	D_n (nm)[b]	*PDI*[b]
*p(*HPMA)	0.000	N	64	50	0.049
	0.005	N	83	67	0.029
	0.050	N	104	76	0.077
	0.500	N	134	97	0.102
*p(n*BMA)	0.000	N	82	59	0.083
	0.005	N	83	62	0.075
	0.050	N	83	62	0.079
	0.500	N	86	65	0.075
*p(n*HMA)	0.000	N	89	73	0.013
	0.005	N	225	205	0.044
	0.050	N	220	160	0.187
	0.500	N	-	-	-
*p(*EHMA)	0.000	N	76	59	0.055
	0.005	N	167	141	0.056
	0.050	N	877	779	0.107
	0.500	Y	-	-	-
*p(*LMA)	0.000	N	143	122	0.008
	0.005	N	156	137	0.022
	0.050	N	160	141	0.034
	0.500	N	172	154	0.028

[a]Sedimentation inspected visually. Y = Sedimentation observed and N = No sedimentation observed. [b]Obtained by DLS. *Reliable DLS data could not be obtained due to polymer sedimentation.

These studies demonstrate that in all cases aqueous nanoparticle dispersions remained stable to the addition of low concentrations of NaCl. *p(*HPMA), *p(n*BMA) and *p(*LMA) based nanoparticles demonstrated colloidal stability at NaCl concentrations up to 0.500 mol dm^{-3} which is in excess of that typically present within systemic circulation (0.150 mol dm^{-3}); it is therefore reasonable to suggest that these materials would be expected to maintain their colloidal stability in the presence of salt concentrations present within systemic circulation. In contrast, *p(n*HMA) and *p(*EHMA) showed colloidal stability at concentrations up to 0.05 mol dm^{-3} in this study. A more detailed study would therefore be required to determine the stability of such nanoparticles at NaCl concentrations between 0.05 and 0.50 mol dm^{-3} and

understand whether they can maintain their colloidal stability under biologically-relevant concentrations of NaCl. The presence of salt, however, is not the only factor which could impact nanoparticle stability *in vivo*. Further studies would therefore be required to show the level of interaction between branched vinyl copolymer nanoparticles and many of the biological proteins within the blood stream.

3.5 Conclusions

This work aimed to expand the scope of branched vinyl copolymer nanoparticles that can be produced v*ia* co-nanoprecipitation and explore the factors which influence nanoparticle formation during the co-nanoprecipitation process. In that sense, this was achieved, as demonstrated, by the formation of *p(n*BMA), *p(n*HMA), *p(*EHMA) and *p(*LMA) based nanoparticles *via* co-nanoprecipitation. One attraction of this nanoformulation approach is that it allows the incorporation of polymeric materials which themselves are incapable of forming stable aqueous nanoparticle dispersions. However, as shown during these studies, successful nanoparticle formation is highly dependent upon the chemical nature of the polymers used; for example, the preparation of stable aqueous nanoparticle dispersions using *p(*MMA), *p(*EMA), *p(t*BMA), *p(*CHMA), *p(*BzMA) and *p(*SMA) based copolymers could not be achieved using these methods. Interestingly, all (co)polymers which failed to form stable nanoparticles *via* (co)nanoprecipitation possessed a T_g above room temperature. It is therefore possible that glass transition temperature is a crucial polymer property that govern successful nanoprecipitation. Furthermore, it is possible that (co)nanoprecipitations at elevated temperature may yield better results.

The use of increasingly hydrophobic (co)polymers helped shed light on the role of individual polymeric components, as well as other parameters which influence the co-nanoprecipitation process. The use of copolymers with compatible hydrophobic domains appears to ensure comparable nucleation rates. As a result, hydrophobic components undergo architecture-independent nucleation processes; this allowed the previously unreported preparation of stable aqueous nanoparticle dispersions consisting of hydrophobic linear homopolymers and their corresponding amphiphilic block copolymers *via* co-nanoprecipitation. Furthermore, the entrapment of amphiphilic block copolymers within the core of branched vinyl copolymer nanoparticles during nanoparticle growth was confirmed for the first time.

The ability to encapsulate hydrophobic guest molecules during co-nanoprecipitation highlights this approach for the loading of hydrophobic chemotherapeutics within branched vinyl copolymer nanoparticles. The fluorescence emission of pyrene proved a useful tool for assessing encapsulation and allowed the internal environments of branched vinyl copolymer nanoparticles to be probed. Branched vinyl copolymer nanoparticles showed resistance to

excessive dilution over prolonged time periods. This indicates that the release of encapsulated payloads should be governed by the rate of diffusion through the nanoparticle core rather than by DNC disassembly and offers a promising prospect for sustained release of such hydrophobic payloads. Furthermore, stability to moderate concentrations of salt indicate that such nanoparticles may be capable of retaining colloidal stability within buffered and biological media.

3.6 References

1 C. Clavero, *Nat. Photonics*, 2014, **8**, 95.
2 M. Klapper, C. G. Clark Jr and K. Müllen, *Polym. Int.*, 2008, **57**, 181–202.
3 K. M. Gharpure, S. Y. Wu, C. Li, G. Lopez-Berestein and A. K. Sood, *Clin. Cancer Res.*, 2015, **21**, 3121 LP – 3130.
4 A. Dickherber, S. A. Morris and P. Grodzinski, *Wiley Interdiscip. Rev. Nanomedicine Nanobiotechnology*, 2015, **7**, 251–265.
5 M. Morgen, C. Bloom, R. Beyerinck, A. Bello, W. Song, K. Wilkinson, R. Steenwyk and S. Shamblin, *Pharm. Res.*, 2012, **29**, 427–440.
6 S. M. D'Addio and R. K. Prud'homme, *Adv. Drug Deliv. Rev.*, 2011, **63**, 417–426.
7 A. Kumari, S. K. Yadav and S. C. Yadav, *Colloids Surfaces B Biointerfaces*, 2010, **75**, 1–18.
8 W. S. Saad and R. K. Prud'homme, *Nano Today*, 2016, **11**, 212–227.
9 J. P. Rao and K. E. Geckeler, *Prog. Polym. Sci.*, 2011, **36**, 887–913.
10 E. Lepeltier, C. Bourgaux and P. Couvreur, *Adv. Drug Deliv. Rev.*, 2014, **71**, 86–97.
11 S. M. Moghimi, A. C. Hunter and J. C. Murray, *Pharmacol. Rev.*, 2001, **53**, 283–318.
12 S. M. D'Addio, W. Saad, S. M. Ansell, J. J. Squiers, D. H. Adamson, M. Herrera-Alonso, A. R. Wohl, T. R. Hoye, C. W. Macosko, L. D. Mayer, C. Vauthier and R. K. Prud'homme, *J. Control. Release*, 2012, **162**, 208–217.
13 Z. Zhu, *Biomaterials*, 2013, **34**, 10238–10248.
14 V. Kumar, L. Wang, M. Riebe, H.-H. Tung and R. K. Prud'homme, *Mol. Pharm.*, 2009, **6**, 1118–1124.
15 Z. Zhu, J. L. Anacker, S. Ji, T. R. Hoye, C. W. Macosko and R. K. Prud'homme, *Langmuir*, 2007, **23**, 10499–10504.
16 M. E. Matteucci, M. A. Hotze, K. P. Johnston and R. O. Williams, *Langmuir*, 2006, **22**, 8951–8959.
17 S. J. Budijono, B. Russ, W. Saad, D. H. Adamson and R. K. Prud'homme, *Colloids Surfaces A Physicochem. Eng. Asp.*, 2010, **360**, 105–110.
18 M. Akbulut, N. K. Reddy, B. Bechtloff, S. Koltzenburg, J. Vermant and R. K. Prud'homme, *Langmuir*, 2008, **24**, 9636–9641.
19 K. M. Pustulka, A. R. Wohl, H. S. Lee, A. R. Michel, J. Han, T. R. Hoye, A. V McCormick, J. Panyam and C. W. Macosko, *Mol. Pharm.*, 2013, **10**, 4367–4377.
20 K. Matyjaszewski and N. V Tsarevsky, *J. Am. Chem. Soc.*, 2014, **136**, 6513–6533.
21 K. Matyjaszewski and N. V Tsarevsky, *Nat. Chem.*, 2009, **1**, 276–288.
22 J. Ford, P. Chambon, J. North, F. L. Hatton, M. Giardiello, A. Owen and S. P. Rannard, *Macromolecules*, 2015, **48**, 1883–1893.
23 F. L. Hatton, P. Chambon, A. C. Savage and S. P. Rannard, *Chem. Commun.*, 2016, **52**, 3915–3918.
24 R. A. Slater, T. O. McDonald, D. J. Adams, E. R. Draper, J. V. M. Weaver and S. P. Rannard, *Soft Matter*, 2012, **8**, 9816–9827.
25 H. E. Rogers, P. Chambon, S. E. R. Auty, F. Y. Hern, A. wen and S. P. Rannard, *Soft Matter*, 2015, **11**, 7005–7015.
26 F. L. Hatton, L. M. Tatham, L. R. Tidbury, P. Chambon, T. He, A. Owen and S. P. Rannard, *Chem. Sci.*, 2015, **6**, 326–334.
27 F. L. Hatton, P. Chambon, T. O. McDonald, A. Owen and S. P. Rannard, *Chem. Sci.*,

2014, **5**, 1844–1853.
28 F. Y. Hern, A. Hill, A. Owen and S. P. Rannard, *Polym. Chem.*, 2018, **9**, 1767–1771.
29 M. M. Miller, S. P. Wasik, G. L. Huang, W. Y. Shiu and D. Mackay, *Environ. Sci. Technol.*, 1985, **19**, 522–529.
30 D. C. Dong and M. A. Winnik, *Photochem. Photobiol.*, 1982, **35**, 17–21.
31 D. C. Dong and M. A. Winnik, *Can. J. Chem.*, 1984, **62**, 2560–2565.
32 J. Aguiar, P. Carpena, J. A. Molina-Bolívar and C. Carnero Ruiz, *J. Colloid Interface Sci.*, 2003, **258**, 116–122.
33 S. Wilhelm, A. J. Tavares, Q. Dai, S. Ohta, J. Audet, H. F. Dvorak and W. C. W. Chan, *Nat. Rev. Mater.*, 2016, **1**, 16014.
34 W. S. Saad and R. K. Prud'Homme, *Nano Today*, 2016, **11**, 212–227.

Chapter 4

Encapsulation and Release of Docetaxel from Branched Vinyl Copolymer Nanoparticles formed *via* Co-Nanoprecipitation.

4.1 Introduction

4.1.1 Docetaxel Anticancer Chemotherapeutic Drug

Chemotherapy remains the most prevalent therapy for the treatment of a wide range of cancers. Significant research efforts have focused on platinum based chemotherapy treatments.[1] However, in recent years, there has been considerable interest in the development and application of non-metallic chemotherapy treatments. This has led to the discovery and development of a number of organic chemotherapeutics, including doxorubicin, daunorubicin, fluorouracil, SN38 and taxanes.[2] Docetaxel is one such chemotherapeutic which has received considerable interest since its discovery by Denis and co-workers in 1988.[3,4] Docetaxel is a member of the family of taxanes which are naturally occurring diterpenes generated by plants of the genus *Taxus* (yews).[4] The most common member of the taxane family is Paclitaxel; a naturally occurring product originally sourced from the bark of Pacific yew (*Taxus brevifolia*). The extraction of paclitaxel was, however, a labour-intensive, destructive and ecologically unsustainable process. Increased demand for paclitaxel, which arose following its successful clinical application as a chemotherapeutic, led to the species of Pacific yew at one point being considered "on the brink of extinction".[5] As a result, the need for highly efficient yet ecologically sustainable synthetic routes to taxanes was at the centre of organic chemistry research during the final two decades of the 20th century.

Numerous attempts were made to develop pure synthetic routes for the preparation of paclitaxel; however, such syntheses could not provide sufficient yields to be considered practically and thus commercially viable.[6,7] In the early 1980s, an ecologically sustainable synthetic route for the preparation of paclitaxel was developed (Figure 4.1).[8–10] This involved the isolation of large quantities of the naturally occurring precursor, 10-deacetylbaccatin-III, from the needles of *Taxus baccata* (European yew). The precursor was used for the preparation of paclitaxel, and later for the discovery of docetaxel in a process known as a semi-synthesis. Semi–syntheses are synthetic routes in which one, or more, of the compounds used are derived from natural sources. This is a commercially advantageous approach as the use of naturally occurring, complex and often high molecular weight building blocks can remove many of the synthetic and purification steps required for the production of a desired compound. Furthermore, the ability to isolate large qualities of 10-deacetylbaccatin-III allowed the targeting of other novel taxanes possessing chemical structures with high similarity to that of paclitaxel. It was this approach which led to the discovery of docetaxel, which is now one of the most commonly used non-platinum based chemotherapeutics for the treatment of breast, gastric, ovarian, prostate and non-benign lung cancer.[11–20]

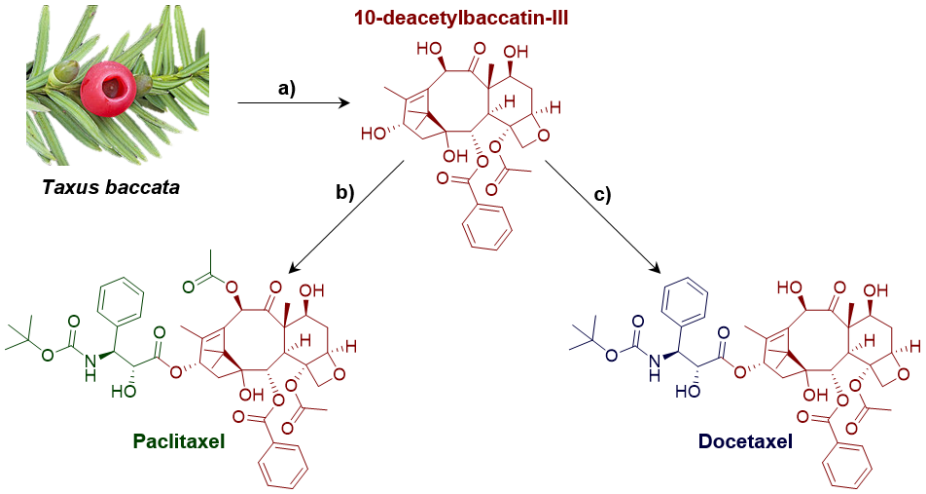

Figure 4.1 Schematic representation of the semi-synthesis of the taxanes paclitaxel and docetaxel. a) Precursor 10-diacetylbaccatin-III is extracted from the needles of Taxus baccata, followed by preparation of b) Paclitaxel and docetaxel *via* esterification of 10-diacetylbaccatin-III.

As demonstrated in Figure 4.1, docetaxel has a similar structure to paclitaxel with the only difference being the presence of the acetate group adjacent to the ketone on the 10-membered ring. Similar to paclitaxel, docetaxel functions as an anti-neoplastic agent by disrupting the microtubule networks which are responsible for mitotic and metabolic cell functions. Docetaxel's anti-cancer activity occurs *via* the following multistep mechanism. Firstly docetaxel molecules bind, with high affinity, to free tubulin within the cell cytoplasm. Polymerisation *via* self-assembly of docetaxel-bound tubulin result in the formation of stable microtubules which are unable to undergo the disassembly processes. The formation of stabilised microtubule bundles render such biomaterials incapable of performing normal cell functions; failure of microtubules to disassemble prevent cellular replication processes. Selective delivery of docetaxel to cancerous cells can therefore promote apoptosis and thus provide effective anti-cancer treatment. The subtle differences in the chemical structures of docetaxel and paclitaxel have resulted in varied anti-tumour and toxicity activities. Docetaxel is considered the more potent cytotoxic anti-microtubule agent and has demonstrated to be five times more effective in promoting microtubule formation and subsequently inhibiting the disassembly processes when compared to paclitaxel during *in vitro* studies.[21]

Despite the high potency of docetaxel as a chemotherapeutic, as well as the commercially viable semi-synthesis routes available for its production, the chemical properties of docetaxel have also hindered its translation to clinical applications. Docetaxel is a highly hydrophobic molecule which exhibits extremely low aqueous solubility.[22,23] Furthermore, the high cytotoxicity, which makes docetaxel such a potent chemotherapeutic, produces negative side effects within healthy tissues when docetaxel is not taken up selectively by cancer cells.[24,25] To overcome these issues, research efforts have moved towards the development of drug nanocarrier systems for the encapsulation and targeted delivery of docetaxel.[26–29]

4.1.2 Docetaxel Nanoformulation

The concept of nanoformulation, and the many forms of drug nanocarriers currently receiving increased attention in nanomedicine research, have been discussed in Chapter 1, alongside the associated benefits of such formulation approaches. Here, a more detailed discussion of docetaxel-specific nanoformulation approaches which either form the basis of academic research or are currently under clinical application will be discussed. Beside the main nanomaterial platforms which have been developed to overcome issues of low aqueous solubility and high cytotoxicity, others include: docetaxel-polymer conjugates, dendrimers, inorganic nanoparticles and liposomes.[30–37] Alternatively, a number of formulation strategies have been developed for the preparation of drug-polymer composites. In particular, this has involved the preparation of docetaxel-polymer composites using poly(lactic acid) and poly(lactic acid-*co*-glycolic acid) based (co)polymers *via* emulsification,[38–43] nanoprecipitation,[44] thin film hydration,[45] and ultrasonication.[46] Whilst many of these techniques indeed form docetaxel-polymer composites with hydrodynamic diameters on the nanoscale, these synthetic approaches typically utilise low drug loadings, where relatively low weight fractions of drug are encapsulated during the nanoformulation process. In contrast, novel technology based strategies such as the particle replication in non-wetting templates (PRINT) process has enabled the preparation of docetaxel-polymer composites with average hydrodynamic diameters *ca.* 250 nm whilst containing high drug loadings (up to 40 wt %).[47–51] Furthermore, quantitative encapsulation efficiencies have been achieved using the PRINT process.

BIND-014[52,53] is one docetaxel-polymer composite which has recently undergone Phase 2 clinical trials and showed mixed results depending on the specific clinical application;[54] BIND-014 gave positive outcomes for the treatment of prostate and non-small-cell lung cancers, whereas application of BIND-014 for the treatment of head and neck cancer was unsuccessful and clinical trials were terminated during Phase 2. Taxotere® is another commercially available docetaxel micelle formulation used for the treatment of a wide range of cancers. However, the continued pursuit for novel nanoformulation strategies for the preparation of DNCs which can produce optimal therapeutic effects will no doubt continue. Potential candidates for novel docetaxel nanocarriers must possess the following qualities: i) the ability to encapsulate high docetaxel payloads with near-quantitative encapsulation efficiency; ii) nanoparticles must retain colloidal stability following formulation; iii) encapsulated payloads must be maintained within the nanoparticle core until nanoparticles have accumulated at the target site; and iv) nanoparticles must be produced *via* facile and commercially viable formulation processes.

4.1.3 Chapter Aims

The aims of this Chapter were to study the encapsulation and release of docetaxel from branched vinyl copolymer nanoparticles. Comprehensive co-nanoprecipitation studies were conducted to discover the maximum docetaxel loadings that can be encapsulated within branched vinyl copolymer nanoparticles without disrupting the formation process. This work aimed to build on the successful co-nanoprecipitations of *p*(HPMA), *p*(*n*BMA), *p*(*n*HMA), *p*(EHMA) and *p*(LMA) based copolymers discussed in Chapter 3. Radiometric analyses were utilised to quantify the efficiency of docetaxel encapsulation which allows the impact of copolymer functionality to be assessed.

Docetaxel-loaded branched vinyl copolymer nanoparticles were subsequently studied to determine docetaxel release rates *in vitro*. The effect of the polarity and viscosity of each nanoparticle core on docetaxel release rates are presented. Detailed kinetic analyses were conducted to evaluate the temperature dependence of docetaxel release from branched vinyl copolymer nanoparticles; this was investigated with respect to the physical properties of the copolymers from which nanoparticles are constructed. Finally, factors which influence the potential of these nanoparticles, such as drug half-life, as prospective DNC systems for the site-specific delivery of docetaxel *in vivo* will be discussed.

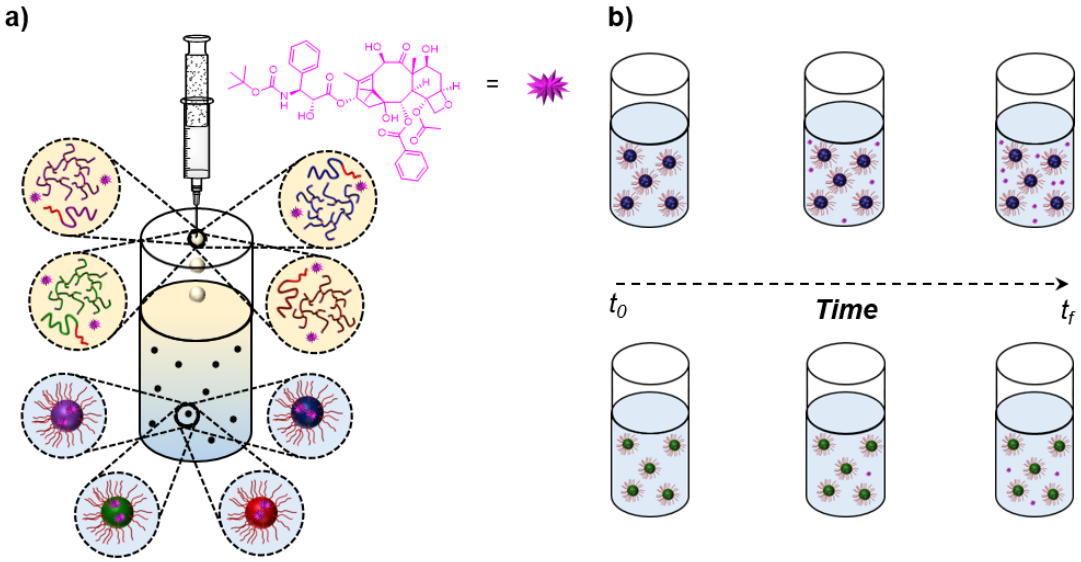

Figure 4.2 Schematic representation of the research aims of the work conducted in Chapter 4. a) Encapsulation of docetaxel within the core of branched vinyl copolymer nanoparticles during co-nanoprecipitation. b) Monitoring the rate of encapsulated docetaxel release from branched vinyl copolymer nanoparticles.

4.2 Docetaxel Encapsulation *via* Co-nanoprecipitation

The use of branched vinyl copolymer nanoparticles as prospective docetaxel DNC systems required a series of preliminary experiments to determine whether docetaxel could be encapsulated during the co-nanoprecipitation process. It was important to understand whether stable, docetaxel-loaded aqueous nanoparticle dispersions could be prepared as well as the maximum docetaxel loading that could be encapsulated without having a negative impact on the co-nanoprecipitation process. As they had proven to be the most robust and reproducible co-nanoprecipitation processes, docetaxel encapsulation experiments were conducted involving the addition of docetaxel into the co-nanoprecipitations of *p*(HPMA), *p*(*n*BMA), *p*(*n*HMA), *p*(EHMA) and *p*(LMA) based copolymers.

In order to generate comparable data, given the large number of co-nanoprecipitations being studied, it was important to determine standard conditions under which all docetaxel encapsulation experiments could be conducted. All co-nanoprecipitations were therefore performed from THF (1 mL, 5 mg mL^{-1}) into DI H_2O (1 mL, DR = 5). It was important to ensure that all encapsulation experiments involved co-nanoprecipitation of the same total solid mass therefore, in all cases, a constant total solid mass of 5 mg was present within the initial THF solution. The total solid mass consisted of varying ratios of docetaxel and the copolymers used in co-nanoprecipitation, in order to achieve target drug loadings ranging from 0 – 50 wt % of the total solid mass. This involved systematic variation of the weight fractions of the total polymer mass from 1.0 to 0.5 whilst simultaneously increasing the docetaxel weight fraction from 0.0 to 0.5 within the initial THF solution (Table 4.1). All co-nanoprecipitations were conducted using equal weight fractions of AB block and branched copolymers (ω_i = 0.5). A general overview of the docetaxel encapsulation experiments is presented in Figure 4.3.

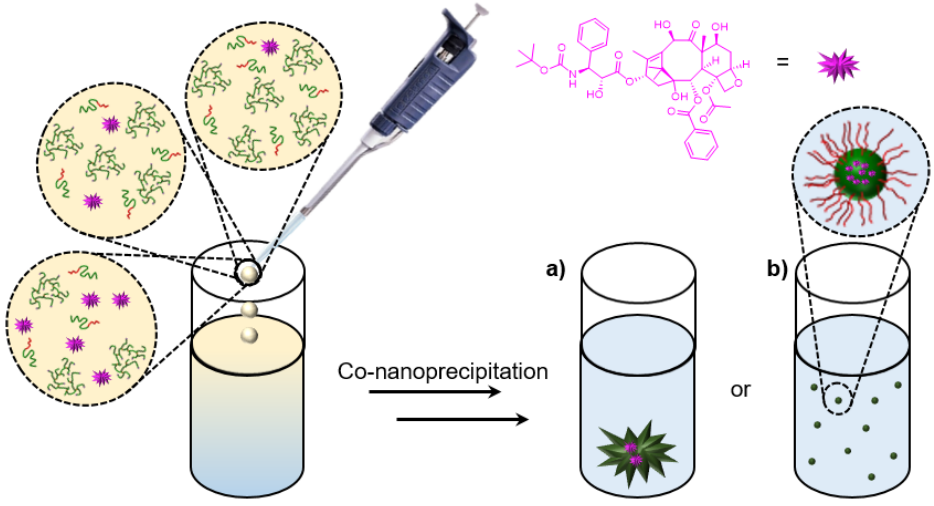

Figure 4.3 Schematic representation of the encapsulation of docetaxel at varied target drug loadings *via* co-nanoprecipitation of amphiphilic AB and branched copolymers. Co-nanoprecipitations conducted at varied target drug loadings can form a) macroscopic aggregation or b) Docetaxel-loaded aqueous nanoparticle dispersions.

Table 4.1 DLS analyses of docetaxel-loaded branched vinyl copolymer nanoparticle dispersions formed *via* co-nanoprecipitation. Co-nanoprecipitations conducted at target weight loadings ranging from 0 to 50 wt %.

Nanoparticle	Polymer ω_i[a]	Docetaxel ω_i[b]	Target loading (%)[c]	Sedimentation[d]	D_z (nm)[e]	D_n (nm)[e]	*PDI*[e]	DCR (kcps)[e]
	1.000	0.000	0.0	N	76	61	0.030	181444
	0.990	0.010	1.0	N	79	64	0.021	244478
	0.975	0.025	2.5	N	79	63	0.029	248334
	0.950	0.050	5.0	N	77	60	0.048	225962
	0.900	0.100	10.0	N	77	63	0.015	222840
p(HPMA)	0.850	0.150	15.0	N	82	66	0.022	238247
	0.800	0.200	20.0	N	79	64	0.029	224827
	0.750	0.250	25.0	N	77	61	0.026	215901
	0.700	0.300	30.0	Y*	-	-	-	-
	0.600	0.400	40.0	Y*	-	-	-	-
	0.500	0.500	50.0	Y*	-	-	-	-
	1.000	0.000	0.0	N	107	88	0.019	517987
	0.990	0.010	1.0	N	106	85	0.037	459493
	0.975	0.025	2.5	N	100	82	0.039	422213
	0.950	0.050	5.0	N	88	69	0.037	373594
	0.900	0.100	10.0	N	85	67	0.029	345979
p(*n*BMA)	0.850	0.150	15.0	N	84	66	0.050	337393
	0.800	0.200	20.0	N	87	66	0.051	322274
	0.750	0.250	25.0	Y*	-	-	-	-
	0.700	0.300	30.0	Y*	-	-	-	-
	0.600	0.400	40.0	Y*	-	-	-	-
	0.500	0.500	50.0	Y*	-	-	-	-
	1.000	0.000	0.0	N	106	87	0.033	495260
	0.990	0.010	1.0	N	109	89	0.019	536666
	0.975	0.025	2.5	N	103	86	0.014	512039
	0.950	0.050	5.0	N	97	79	0.025	479461
	0.900	0.100	10.0	N	86	69	0.023	358284
p(*n*HMA)	0.850	0.150	15.0	N	89	74	0.018	379010
	0.800	0.200	20.0	N	92	72	0.049	382924
	0.750	0.250	25.0	Y*	-	-	-	-
	0.700	0.300	30.0	Y*	-	-	-	-
	0.600	0.400	40.0	Y*	-	-	-	-
	0.500	0.500	50.0	Y*	-	-	-	-
	1.000	0.000	0.0	N	109	88	0.031	512757
	0.990	0.010	1.0	N	101	81	0.041	508852
	0.975	0.025	2.5	N	98	79	0.038	480232
	0.950	0.050	5.0	N	93	76	0.019	400514
	0.900	0.100	10.0	N	85	69	0.021	341935
p(EHMA)	0.850	0.150	15.0	N	85	69	0.031	351118
	0.800	0.200	20.0	Y*	-	-	-	-
	0.750	0.250	25.0	Y*	-	-	-	-
	0.700	0.300	30.0	Y*	-	-	-	-
	0.600	0.400	40.0	Y*	-	-	-	-
	0.500	0.500	50.0	Y*	-	-	-	-
	1.000	0.000	0.0	N	140	119	0.021	819851
	0.990	0.010	1.0	N	109	89	0.022	548381
	0.975	0.025	2.5	N	127	107	0.018	550903
	0.950	0.050	5.0	N	107	88	0.031	494591
	0.900	0.100	10.0	N	94	75	0.033	426528
p(LMA)	0.850	0.150	15.0	N	98	80	0.029	443566
	0.800	0.200	20.0	N	100	84	0.016	483511
	0.750	0.250	25.0	Y*	-	-	-	-
	0.700	0.300	30.0	Y*	-	-	-	-
	0.600	0.400	40.0	Y*	-	-	-	-
	0.500	0.500	50.0	Y*	-	-	-	-

[a]Polymer ω_i = (total polymer mass / (total polymer mass + docetaxel mass)). [b]Docetaxel ω_i = (docetaxel mass/(total polymer mass + docetaxel mass)) [c]Target drug loading = (docetaxel mass/(docetaxel mass + total polymer mass) x 100). [d]Determined visually. [e]Determined by DLS analysis at a concentration of 1 mg mL^{-1}. *Sedimentation observed therefore unsuitable for analysis by DLS.

For each copolymer system, docetaxel encapsulation experiments involved 11 co-nanoprecipitations conducted at targeted drug loadings of: 0.0, 1.0, 2.5, 5.0, 7.5, 10, 15, 20, 25, 30, 40 and 50 wt %. The success of co-nanoprecipitations were initially judged visually. In all cases, the addition of the drug/copolymer THF solution resulted in the formation of a turbid/translucent mixture and there was no evidence of sedimentation. However, following THF removal over 48 hours, only some formulations remained as almost clear nanodispersions, whilst others showed evidence of macroscopic precipitation. The success of such co-nanoprecipitations was clearly dependent on the drug loading targeted during the co-nanoprecipitation. In all cases, co-nanoprecipitations failed at high drug loadings (≥30 wt %) and this was evident from the appearance of large aggregates within the resultant aqueous nanoparticle dispersions (Appendix, Figure A4.1). In contrast, all co-nanoprecipitations conducted at target drug loadings ≤15 wt % were deemed successful. The drug loadings at which co-nanoprecipitations failed varied for each copolymer system. The maximum drug loadings at which stable aqueous nanoparticle dispersions were obtained, with the absence of larger aggregates, was at 25, 20, 20 15 and 20 wt % for *p*(HPMA), *p*(*n*BMA), *p*(*n*HMA), *p*(EHMA) and *p*(LMA) based co-nanoprecipitations respectively. The absence of large aggregates within aqueous nanoparticle dispersions produced *via* successful co-nanoprecipitation indicated that docetaxel undergoes rapid nucleation and growth following addition to DI H_2O due to a state of supersaturation within the THF/DI H_2O mixture.

The impact of targeted drug loading on the success of nanoparticle formation during co-nanoprecipitation was initially assumed to occur due to the inherent reduction in the number of AB block copolymer chains present as a proportion of the total solid mass being co-nanoprecipitated, as target drug loadings were increased. In all co-nanoprecipitations, increases in target docetaxel loading from 0 % to 50 % therefore caused a reduction in the overall AB block copolymer weight fraction from 0.50 to 0.25. As a result, fewer AB block copolymer chains are available to provide steric stabilisation and cap nanoparticle growth during co-nanoprecipitation. The importance of AB block copolymer composition in the stabilisation of branched vinyl copolymer nanoparticles was discussed in Chapter 3, Section 3.4.3.1 In the cases of *p(n*BMA), *p(n*HMA), *p(*EHMA) and *p(*LMA) based co-nanoprecipitations, AB block copolymer weight fractions ≤ 0.80 had a negative impact on the capping of nanoparticle growth and resulted in increases to the average hydrodynamic diameters of the resulting nanoparticles. It is therefore reasonable to suggest that the inherent decreases in AB block copolymer composition which accompanied co-nanoprecipitations conducted at higher target drug loadings were responsible for unsuccessful nanoparticle formation at AB block copolymer weight fractions ≤ 0.375 (target loading ≥25 wt %).

Aqueous nanoparticle dispersions which did not show any signs of sedimentation were assessed by DLS. One of the biggest concerns prior to docetaxel loading experiments was that docetaxel would not exhibit the similar levels of supersaturation as hydrophobic branched and amphiphilic AB block copolymers within the THF/DI H_2O mixture and would therefore nucleate at a different rate during co-nanoprecipitation. However, in all cases, monomodal nanoparticle size distributions were obtained with low PDI values (<0.100) which demonstrated that docetaxel-loaded nanoparticles were near-monodisperse. These data further supported claims that docetaxel undergoes rapid nucleation and/or growth during co-nanoprecipitation as slow or even heterogeneous nucleation processes do not typically produce monodisperse nanoparticles. It is therefore reasonable to suggest that, despite the presence of up to 25 wt % docetaxel, nanoparticle formation proceeds *via* a diffusion-limited cluster-cluster aggregation growth mechanism.

Nanoparticle sizes were relatively consistent and comparable to those produced in the absence of docetaxel with intensity-average diameters varying between 79 and 142 nm. Interestingly, for *p*(*n*BMA), *p*(*n*HMA), *p*(EHMA) and *p*(LMA) based co-nanoprecipitations, nanoparticle size decreased with the weight fraction of docetaxel. For example, in the case of *p*(*n*HMA) based co-nanoprecipitations, intensity-average hydrodynamic diameters decreased from 109 to 92 nm as target drug loadings were increased from 1 to 20 wt %. This was somewhat surprising given that, as discussed above, increases in target drug loading resulted in lower amphiphilic AB block copolymer concentrations during co-nanoprecipitation; nanoparticle sizes were therefore expected to increase with target drug loading. The relationship between target drug loading and nanoparticle size can be explained by consideration of the role of docetaxel within the co-nanoprecipitation process. Smaller nanoparticles indicated an increase in the number of nuclei formed during the early stages of co-nanoprecipitation. Combined with the low *PDI* values, which suggest that docetaxel undergoes rapid nucleation, the size data indicated that docetaxel formed higher numbers of nuclei per unit mass than the copolymers with which they were co-nanoprecipitated. This is not surprising given their contrasting molecular weights and thus the relative number of molecules dissolved within the initial THF solution. Increases in the number of nuclei formed during co-nanoprecipitation typically result in higher nanoparticle concentrations and would be expected to cause increases in the DCR. However, DCRs obtained by DLS decreased with drug loading; this was likely due to the simultaneous decrease in nanoparticle size. It is possible, however, that the simultaneous increase in the number of nuclei formed and the reduction in the AB block copolymer weight fraction may have led co-nanoprecipitations to fail at high target drug loadings. It was proposed that fewer AB block copolymer chains were able to provide the level of steric stabilisation required to arrest nanoparticle growth given the higher surface area created by

higher numbers of nuclei. Co-nanoprecipitations conducted using higher weight fractions of AB block copolymer may therefore allow the preparation of docetaxel-loaded aqueous nanoparticle dispersions at higher target drug loadings.

The impact of targeted drug loading on the hydrodynamic size was explored further in order to understand the role of docetaxel in the co-nanoprecipitation process. This was achieved by studying the intensity-average hydrodynamic diameters of nanoparticles generated in co-nanoprecipitations conducted in the presence and absence of docetaxel (Figure 4.4). This involved amalgamation of data obtained in the docetaxel loading experiments presented here (Table 4.1) with that obtained during the study of the influence of copolymer concentration at which co-nanoprecipitations are conducted, discussed in Chapter 3, Table 3.5. In both cases co-nanoprecipitations were conducted at varying copolymer concentrations within the initial THF solution. However, drug loading experiments also included the addition of docetaxel. This allowed direct comparison between aqueous nanoparticle dispersions produced under identical conditions in the presence and the absence of docetaxel.

Nanoparticles generated in the absence of docetaxel exhibited little difference in hydrodynamic diameter, regardless of the amount of copolymer within the initial THF solution, over the concentration range studied. For example, negligible differences were observed in the intensity-average hydrodynamic diameters obtained for *p*(EHMA) nanoparticles generated in co-nanoprecipitations conducted at copolymer concentrations ranging from of 4.99 and 4.25 mg mL^{-1}. In contrast, *p*(EHMA) co-nanoprecipitations conducted over an identical concentration range of copolymer concentration, in the presence of docetaxel, showed intensity-average hydrodynamic diameters decreasing from 101 to 85 nm. Interestingly, large decreases in nanoparticle diameter occurred as target docetaxel loadings were increased from 0 to 5 wt % with intensity-average hydrodynamic diameters becoming constant thereafter. Whilst this clearly supports the role of docetaxel in driving the nucleation process during co-nanoprecipitation, it is clear that changes in hydrodynamic diameter were not directly proportional to targeted drug loadings. Once again, this could be due to the trade-off between increasing numbers of nuclei formed during the initial stage of co-nanoprecipitation and the associated decreases in the AB block copolymer composition. It was hypothesised that low targeted drug loadings increased the number of nuclei present whilst having little effect on the AB block copolymer concentration; this allowed smaller nanoparticles to be formed as sufficient levels of AB block copolymer were present to cover the greater surface area generated by the presence of higher numbers of nuclei during co-nanoprecipitation. Further increases in the targeted drug loading, however, had a larger impact on the AB block copolymer concentration. Increases in the number of nuclei formed were met by lower AB block copolymer concentrations, which were therefore unable to arrest

nanoparticle growth at lower hydrodynamic diameters and resulted in no further change in nanoparticle size.

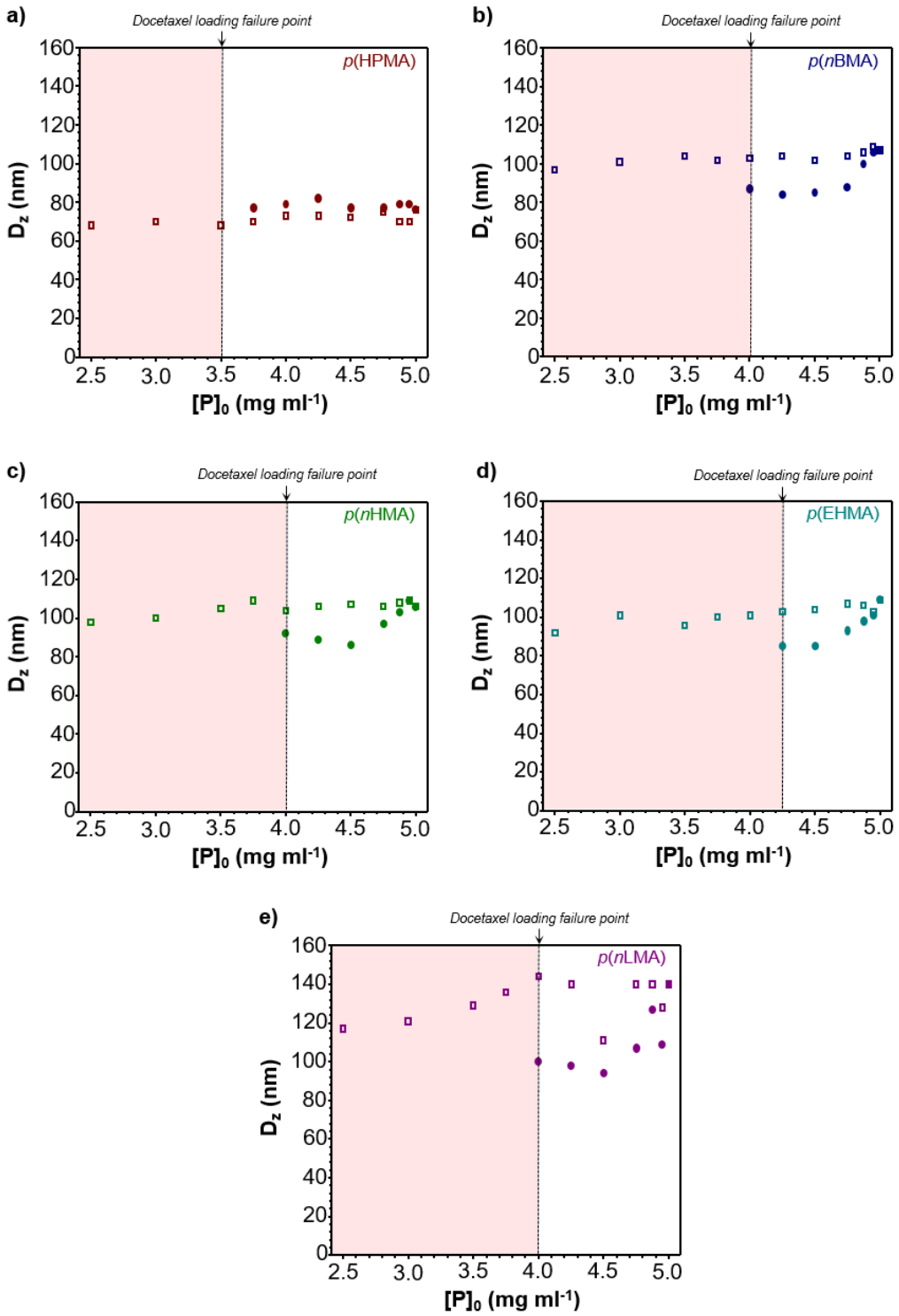

Figure 4.4 The impact of copolymer concentration on the hydrodynamic diameters of loaded nanoparticles formed *via* co-nanoprecipitation. Comparison of intensity-average hydrodynamic diameters obtained for docetaxcel loaded (solid circles) and unloaded (open squares) for a) *p*(HPMA), b) *p*(*n*BMA), c) *p*(*n*HMA), d) *p*(EHMA) and e) *p*(LMA) based nanoparticles generated at various copolymer concentrations.

In contrast, negligible changes in nanoparticle size were observed for *p*(HPMA) based co-nanoprecipitations as target drug loading was increased from 0 to 25 wt %. This was likely due to the dominance of electrostatic repulsion capping nanoparticle growth during *p*(HPMA) based co-nanoprecipitations. This supported findings in Chapter 3, Section 3.4.3.1, where the hydrodynamic diameters of nanoparticles formed were independent of the AB block copolymer composition at AB block copolymer weight fractions ≤ 0.60. It is therefore evident that nanoparticle growth capping mechanisms are equally important in the preparation of docetaxel loaded aqueous nanoparticle dispersions *via* co-nanoprecipitation.

The contrast in the maximum drug loadings at which stable aqueous nanoparticle dispersions could be achieved was initially thought to be due to increased copolymer hydrophobicity, which would generate favourable drug-copolymer association during co-nanoprecipitation. The maximum drug loading that could be tolerated was therefore expected to increase with polymer hydrophobicity. However, this was not the case as the highest targeted drug loadings were achieved in co-nanoprecipitations of *p*(HPMA) based co-polymers (25 wt %) which are considered the least hydrophobic copolymers. Furthermore co-nanoprecipitations of the remaining copolymers yielded broadly similar results, with stable aqueous nanoparticle dispersions formed at comparable maximum drug loadings which ranged between 15 and 20 wt %. Broadly speaking, the maximum drug loadings achieved were comparable and implied that monomer chemistry had little impact on docetaxel encapsulation during co-nanoprecipitation. This indicates that the encapsulation of docetaxel is largely under kinetic control. This may be considered unsurprising given the rapid rate at which nanoparticles are formed during co-nanoprecipitation and suggests that optimisation of drug encapsulation may not be possible *via* manipulation of copolymer chemistry.

The presence of strong non-covalent interactions between docetaxel and the copolymers which make up the nanoparticle core, as well as the physical properties of the core itself, are therefore more likely to play a role in controlling the rate at which docetaxel is released from branched vinyl copolymer nanoparticles. It may be possible, however, to achieve higher docetaxel drug loadings *via* manipulation of the experimental conditions under which co-nanoprecipitations are conducted. Under the conditions that co-nanoprecipitations were conducted in this study, successful nanoparticle formation at target docetaxel loadings of 15, 20 and 25 wt % allowed aqueous docetaxel concentrations, dispersed within branched vinyl copolymer nanoparticles, of 0.15, 0.20 and 0.25 mg mL^{-1} to be achieved. Previous reports have demonstrated an aqueous saturation concentration of 6.5 µg mL^{-1} for docetaxel at ambient temperature.[22,23] Encapsulation of docetaxel within stable branched vinyl copolymer nanoparticles at drug loadings of 15, 20 and 25 wt % therefore represent 23-, 31- and 39-fold increases in the aqueous concentration of docetaxel *via* nanoformulation within branched vinyl copolymer

nanoparticles relative to the aqueous saturation concentration. Co-nanoprecipitation also offers two formulation pathways through which the aqueous concentration of docetaxel could be increased further. Firstly, as discussed in Chapter 3, Section 3.4.3.1, co-nanoprecipitations could be conducted at higher concentrations with minimal impact on nanoparticle size and stability. Alternatively, multiple copolymer additions could be used to increase nanoparticle concentration with minimal impact on nanoparticle size or stability. Either of these approaches could be used to achieve higher aqueous docetaxel concentrations. However, given the preliminary stage of this research, and that docetaxel had successfully been encapsulated within the nanoparticles, obtaining the maximum aqueous concentration of docetaxel that could be achieved *via* co-nanoprecipitation was not investigated further at this point.

Encapsulation of docetaxel within branched vinyl copolymer nanoparticles therefore offers a number of advantages over the conventional administration of docetaxel. Firstly, due to the ability to achieve higher aqueous docetaxel concentrations, nanoformulation could increase the concentration of docetaxel within systemic circulation and therefore reduce the IV dose required. Furthermore, nanoformulations offer a more homogeneous form of docetaxel administration as aggregation of free docetaxel can result in opsonisation and subsequent clearance *via* the mononuclear phagocyte system. Secondly, it is highly likely that docetaxel is encapsulated within the core of branched vinyl copolymer nanoparticles. As a result, providing nanoparticles remain chemically inert, docetaxel would be protected from chemical degradation whether *via* opsonisation, enzymatic degradation or changes in the external environment such as pH. Encapsulation may therefore reduce the amount of docetaxel being removed from systemic circulation *via* physiological defence mechanisms. Finally, docetaxel is a relatively low molecular weight compound (808 g mol^{-1}); unencapsulated docetaxel molecules are therefore susceptible to size-dependent physiological filtration mechanisms within systemic circulation. It is therefore likely that encapsulation of docetaxel within nanoparticles with hydrodynamic diameters of ~100 nm would greatly reduce the clearance of docetaxel from systemic circulation *via* renal filtration pathways. Furthermore, due to prolonged circulation times, such nanoparticles would likely benefit from the enhanced permeation and retention effect, discussed in Chapter 1, Section 1.2.2.3. As a result, encapsulation of docetaxel within branched vinyl copolymer nanoparticles would likely greatly increase the accumulation of drug at a tumour site and, therefore, increase the efficacy of such chemotherapy treatments, whilst minimising toxic side effects which have a significant impact on the frequency and intensity of chemotherapy treatments that can be administered.

Whilst preliminary drug loading co-nanoprecipitations showed that aqueous nanoparticle dispersions could be formed in the presence of increasing concentrations of docetaxel, they provided no quantitative evidence of docetaxel encapsulation within the core of branched vinyl copolymer nanoparticles. Although the absence of sedimentation at docetaxel concentrations in excess of the aqueous saturation limit suggests docetaxel encapsulation, further quantitative analyses were required to determine whether, and what proportion of, docetaxel had been encapsulated during co-nanoprecipitation. Studies were therefore required to understand the relationship between the chemical structure of the hydrophobic nanoparticle cores and the rate at which docetaxel was released from branched vinyl copolymer nanoparticles.

4.3 Quantitative Analysis of Docetaxel Encapsulation and Release from Branched Vinyl Copolymer Nanoparticles formed *via* Co-Nanoprecipitations

The ability to encapsulate docetaxel within the core of branched vinyl copolymer nanoparticles during co-nanoprecipitation offered the opportunity for docetaxel release over prolonged time periods, and perhaps in a controlled manner. In order to demonstrate this potential, quantitative analyses were required to demonstrate that: i) docetaxel was in fact encapsulated within the core of branched vinyl copolymer nanoparticles; and ii) encapsulation within branched vinyl copolymer nanoparticles could be used to modulate docetaxel release. The research focus, therefore, moved towards the development of techniques which would provide facile and reproducible quantification of drug encapsulation and release rates.

4.3.1 Quantification of Docetaxel Encapsulation Efficiency and Drug Loading achieved during Nanoparticle Formation *via* Co-Nanoprecipitation

There are several possible fates for docetaxel molecules employed in co-nanoprecipitation. Perhaps the most obvious fate would be that docetaxel is encapsulated during the co-nanoprecipitation process and would therefore be located within the core of branched vinyl copolymer nanoparticles. Alternatively, docetaxel, likely accompanied by hydrophobic copolymers, can sediment from the aqueous nanoparticle dispersion. Sedimentation occurs when co-nanoprecipitation processes fail to encapsulate docetaxel within nanoparticles which would be capable of maintaining their colloidal stability both during and after the co-nanoprecipitation process. Finally, small amounts of docetaxel, $\leq$6.5 μg mL^{-1}, is likely to be dissolved within the DI H_2O in which branched vinyl copolymer nanoparticles were formed and dispersed. In order to gain an insight into the efficiency of docetaxel encapsulation, quantitative techniques were required to determine the amount of docetaxel within each of these environments.

Encapsulation efficiency (EE) and total drug loading (DL) are two key factors which must be considered when evaluating the efficiency of any drug encapsulation process. EE and DL are described in Equations 4.1 and 4.2. EE, also referred to as entrapment efficiency, refers to the

fraction of drug that has been encapsulated during nanoparticle formation (D_{encap}), as a proportion of the total amount used during the formulation process. The total docetaxel mass (D_{total}) consists of encapsulated docetaxel (D_{encap}) and free docetaxel (D_{free}) in aqueous solution ($D_{total} = D_{encap} + D_{free}$). Alternatively, the DL gives an indication of the nanoparticle composition and quantitatively represents the amount of encapsulated drug (m_{ED}) as a proportion of the total mass of the nanocarrier ($m_{total} = m_{polymer} + m_{ED}$). EE and DL are therefore both important factors required in order to provide a true representation of the efficiency of drug encapsulation process.

$$EE = \frac{D_{encap}}{D_{total}} \qquad \textbf{Equation 4.1}$$

$$DL = \frac{m_{ED}}{m_{polymer} + m_{ED}} \times 100 \qquad \textbf{Equation 4.2}$$

4.3.1.1 Quantifying the EE and DL of ^{3}H -labelled Docetaxel during Co-Nanoprecipitation

Initial research involved attempts to develop techniques which could be used for the quantification of the docetaxel EE and DL achieved during co-nanoprecipitation. Due to docetaxel's extremely low aqueous saturation solubility, quantification of aqueous docetaxel concentrations is a challenging task. A maximum solubility of 6.5 μg mL^{-1} meant that accurate analysis of aqueous nanoparticle dispersions could not be achieved using ^{1}H NMR spectroscopy. Similarly, reliable calibration curves could not be obtained for docetaxel in DI H_2O using ultraviolet-visible spectroscopy (UV-Vis). As a result, direct analysis of aqueous nanoparticle dispersions was not possible using either ^{1}H NMR or UV-Vis spectroscopy.

Alternatively, following removal of DI H_2O *via* freeze-drying and subsequent full dissolution in $CDCl_3$ and THF, docetaxel quantification was achieved by ^{1}H NMR and UV-Vis respectively. However, whilst this allowed the amount of docetaxel present to be quantified, this approach was labour-intensive and was generally incompatible with the low solid masses employed in co-nanoprecipitations and the high sensitivity required caused inconsistencies in results obtained using ^{1}H NMR and UV-Vis spectroscopy. As a result, this approach was not taken forward and radiometric analysis was explored as an alternative for the quantification and comparison of the EE and DL achieved during co-nanoprecipitations.

Tritium (^{3}H) radio-labelling of docetaxel and subsequent liquid scintillation counting (LSC) was used as the quantitative analytical technique to determine EE and DL achieved during co-nanoprecipitations. ^{3}H is a low energy (0.0186 MeV) beta (β) emitting radio nuclide with a half-life of more than 12 years; negligible radio-decay would therefore be expected over the time scales that docetaxel encapsulation and release studies were conducted during the course of this research. Furthermore, the low energy β-emission of ^{3}H nuclei results in low

penetration distances in air (6 mm) from emitted electrons and an inability to penetrate through the top layer of any exposed skin. Nonetheless, experiments conducted using ^{3}H-labelled molecules required basic radiation protection training at the University of Liverpool and all experiments were conducted within the Rannard Group Radio Materials Laboratory under the supervision of an accredited radiation protection supervisor, Dr. Helen Cauldbeck.

Co-nanoprecipitations were conducted using ^{3}H-labelled docetaxel containing specific activities ranging from 6.61 - 6.65 μCi mg^{-1}. Specific activity (SA) refers to the intensity of β-emissions from ^{3}H nuclei per unit mass of docetaxel. The relationship between total radioactivity (TR), SA and docetaxel mass ($m_{\text{Docetaxel}}$) is presented in Equation 4.3. It is important to clarify, however, that not every docetaxel molecule contained radioactive ^{3}H nuclei. Nevertheless, accurate quantification of the SA of a sample of ^{3}H-labelled docetaxel allows the total docetaxel mass to be calculated from the intensity of the β-emission observed during LSC analysis. The radio-purity of ^{3}H-labelled docetaxel was confirmed using radio-thin layer chromatography; this showed the presence of just one ^{3}H-labelled species which gave an identical R_f value to that obtained from regular thin-layer chromatography of non-labelled docetaxel using the same eluent system. This allowed quantification of the amount of docetaxel present within aqueous nanoparticle dispersions *via* LSC analysis and was essential for the calculation of the EE and DL achieved during co-nanoprecipitation.

$$m_{Docetaxel}(\text{mg}) = \text{TR}(\mu Ci)/SA\ (\mu Ci\ mg^{-1}) \qquad \textbf{Equation 4.3}$$

An overview of the encapsulation of ^{3}H-labelled docetaxel during the co-nanoprecipitation process is given in Figure 4.5. Co-nanoprecipitations were conducted using equal weight fractions of amphiphilic AB block and branched copolymers (ω_i = 0.5) from THF (1 mL), at a total solids concentration of 5 mg mL^{-1}, into DI H_2O (5 mL, DR = 5). In order to generate comparable drug release data, all co-nanoprecipitations were conducted at target drug loadings of 15 wt % as this was the maximum target drug loading at which stable docetaxel-loaded aqueous nanoparticle dispersions were produced from all copolymer co-nanoprecipitations. Co-nanoprecipitations were left for 48 hours to allow complete THF removal *via* evaporation to give aqueous nanoparticle dispersions at a concentration of 1 mg mL^{-1}.

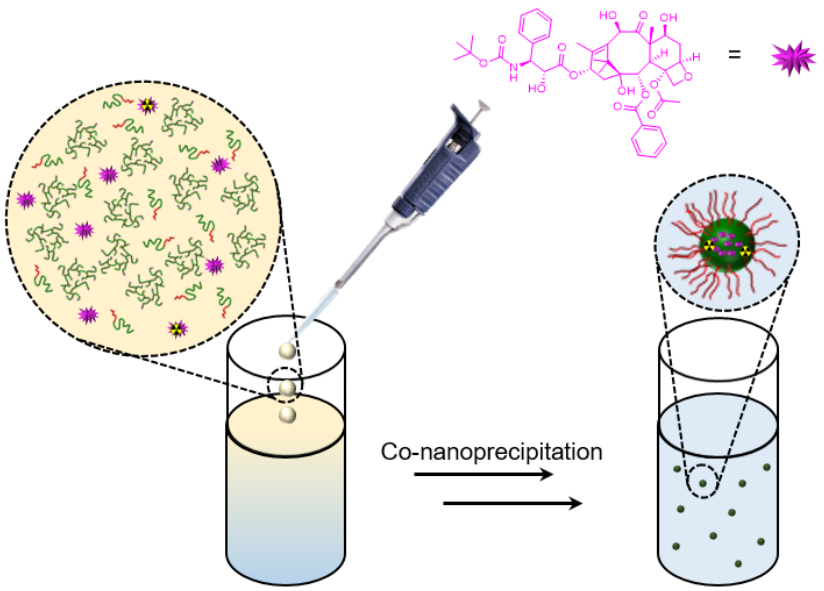

Figure 4.5 Schematic representation of the encapsulation of ^{3}H-labelled docetaxel within the core of branched vinyl copolymer nanoparticles *via* co-nanoprecipitation.

In all cases, co-nanoprecipitations resulted in the formation of turbid and translucent ^{3}H-docetaxel-loaded aqueous nanoparticle dispersions which showed no sedimentation. This was consistent with the observations made for the analogous co-nanoprecipitations conducted using unlabelled docetaxel, described in Section 4.2. ^{3}H-docetaxel-loaded nanoparticle dispersions were assessed by DLS, and in all cases had monomodal size distributions with intensity-average hydrodynamic diameters consistent with those generated previously (Table 4.2). Aqueous nanoparticle dispersions also showed low *PDI* values which, once again, confirmed the success of co-nanoprecipitations in the presence of 15 wt % targeted docetaxel loadings.

Table 4.2 Radiometric and DLS analyses of ^{3}H-docetaxel-loaded aqueous nanoparticle dispersions produced *via* co-nanoprecipitation.

Polymer	Target loading (wt %)[a]	EE[b]	DL (wt %)[c]	D_z (nm)[d]	D_n (nm)[d]	*PDI*[d]
p(HPMA)	14.3	0.769	11.0	86	58	0.111
p(*n*BMA)	13.6	0.954	13.0	88	57	0.126
p(*n*HMA)	13.5	0.955	12.9	109	75	0.098
p(EHMA)	13.0	0.974	12.7	81	54	0.095
p(LMA)	12.4	0.836	10.4	99	73	0.071

[a]Determined by radiometric analysis of aqueous nanoparticle dispersion prior to centrifugation. [b]Calculated using masses of encapsulated and free docetaxel determined using radiometric analyses following ultracentrifugation. [c]DL = Target loading x EE. [d]Determined by DLS at a concentration of 1 mg mL^{-1}.

Quantification of the EE and DL achieved during co-nanoprecipitation first required a process to separate free and encapsulated docetaxel. This was achieved *via* centrifugation of aqueous

nanoparticle dispersions through a 3.5 kDa membrane, allowing free docetaxel dissolved within the aqueous medium to be separated from the branched vinyl copolymer nanoparticles in which the remainder of the initial docetaxel loading was encapsulated. The purification process is presented in Figure 4.6. Briefly, LSC analysis was conducted on the initial aqueous nanoparticle dispersion (c_{total} = 1 mg mL^{-1}) in order to determine the total amount of docetaxel present (D_{total}) This allowed accurate quantification of the actual docetaxel concentration within the aqueous nanoparticle dispersion (i.e. the experimental target drug loading). 0.5 mL of the aqueous nanoparticle dispersion was then placed in the top of a centrifuge tube containing a 3.5 kDa filter. The sample was then centrifuged, which allowed the vast majority of the water, along with any free docetaxel to pass into the lower chamber of the centrifuge tube. The amount of free docetaxel (D_{free}) was then determined *via* LSC analysis of the liquid collected in the lower chamber of the centrifuge tube. EE was then calculated in accordance with Equation 4.1.

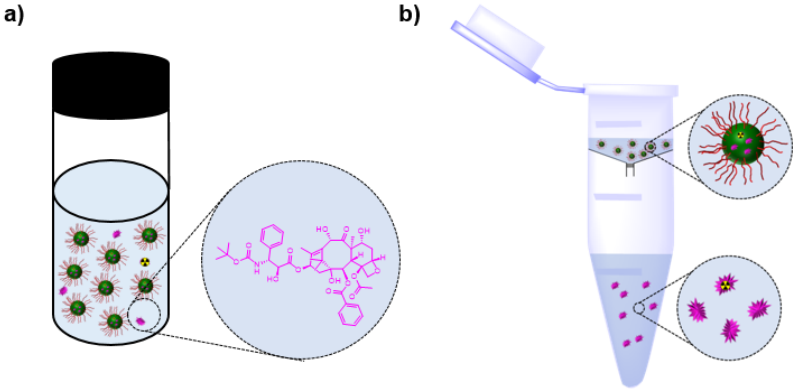

Figure 4.6 Schematic representation of nanoparticle purification *via* centrifugation. a) Aqueous nanoparticle dispersions consisting of both encapsulated and free docetaxel and b) Purification of aqueous nanoparticle dispersions by separation of encapsulated (top) and free (bottom) docetaxel.

Data obtained from LSC analyses were used to determine the EE and DL achieved during all co-nanoprecipitations (Table 4.2). In all cases, the experimental targeted drug loadings were slightly below the theoretical 15 wt %, possibly due to loss of initial solution of ^{3}H- docetaxel/ copolymer-THF solution on the pipette tip during co-nanoprecipitation or affinity of the drug for glass. In all cases, high docetaxel encapsulation efficiencies were observed during co-nanoprecipitation; this was evident by LSC analyses which showed ≥76.9 % docetaxel remained within branched vinyl copolymer nanoparticles following centrifugation. Exceptionally high encapsulation efficiencies were observed during co-nanoprecipitations of *p*(*n*BMA), *p*(*n*HMA) and *p*(EHMA) based copolymers (EE ≥0.954). As was observed during initial docetaxel encapsulation studies, no correlation was observed between EE and the chemical structure of the copolymers used during co-nanoprecipitation. For example, the lowest EE values were observed for *p*(HPMA) and *p*(LMA) based copolymers. These copolymers are considered the most and least hydrophobic of the copolymers used in this

study. This once again indicated that copolymer structure had little impact on docetaxel encapsulation during the co-nanoprecipitation process. This supports earlier indications that docetaxel encapsulation is a kinetically-driven process due to the high levels of supersaturation during co-nanoprecipitation and that, although copolymers are essential for successful nanoparticle formation, they have little impact on the level of small molecules encapsulated during co-nanoprecipitation.

The ability to determine both the experimental targeted drug loading and the EE of docetaxel using radiometric analyses allowed the actual docetaxel DL achieved during co-nanoprecipitation to be calculated. In all cases, the amount of docetaxel encapsulated was lower than the theoretical target, but DLs ranging between 10.4 and 13.0 % of the total nanoparticle mass were achieved during co-nanoprecipitation. Given the higher EE achieved during co-nanoprecipitation, the highest drug loadings, which ranged from 12.7 to 13.0 %, were achieved for *p*(*n*BMA), *p*(*n*HMA) and *p*(EHMA) based nanoparticles. In contrast, lower docetaxel DLs of 11.0 and 10.4 % were achieved during co-nanoprecipitations of *p*(HPMA) and *p*(LMA) based copolymers. Although accurate quantification of docetaxel encapsulation could be achieved using radiometric analyses, it was clear that manipulation of copolymer structure could not be used as a tool to increase docetaxel encapsulation or EE during co-nanoprecipitation.

The ^{3}H-docetaxel encapsulation experiments were conducted at a fixed target drug loading of 15 wt %. It is therefore possible that studying the EE across the full range of targeted drug loadings attempted in Section 4.2 could impact the EE and DLs achieved during co-nanoprecipitation. For example, 15 wt % was the highest targeted drug loading at which a suitable aqueous nanoparticle dispersion was generated during *p*(EHMA) based co-nanoprecipitations. It is therefore feasible that higher EE values could be achieved during co-nanoprecipitations conducted at lower targeted DL. The trade-off between target DL and EE may allow for the preparation of aqueous nanoparticle dispersions which have reduced amounts/no free drug present within the aqueous phase; and achieve higher overall DL due to increased EE. Such studies are outside the scope of this thesis.

The data obtained here further demonstrated the ability to encapsulate hydrophobic guest molecules within the core of branched vinyl copolymer nanoparticles during the co-nanoprecipitation process. Although the docetaxel encapsulation experiments yielded stable aqueous nanoparticle dispersions, with desirable size characteristics, it was evident that the co-nanoprecipitation failed to ensure complete docetaxel encapsulation at higher targeted drug loadings. Despite this, the encapsulation of relatively high loadings of docetaxel would be expected to modulate the docetaxel release profile during both *in vitro* and *in vivo*

experiments compared with administration of the free drug. The impact of docetaxel encapsulation, as well as that of the presence of free docetaxel, required further studies to monitor the release of docetaxel from branched vinyl copolymer nanoparticles. Fortunately, the presence of ^{3}H-docetaxel within the core of branched vinyl copolymer nanoparticles allowed this release to be studied using further radiometric analyses.

4.3.2 Monitoring Docetaxel Release *via* ^{3}H Radio-dialysis

The encapsulation of docetaxel during co-nanoprecipitation was expected to modulate the rates of docetaxel release from branched vinyl copolymer nanoparticles. The high sensitivity of radio experiments and LSC allows the detection and accurate quantification of the low docetaxel concentrations expected to be released following high dilution. A series of radio-dialysis experiments were therefore conducted to determine whether docetaxel was released from branched vinyl copolymer nanoparticles and, in particular, to understand whether the chemical nature of the nanoparticle core affected docetaxel release rates. Docetaxel release experiments were conducted using the ^{3}H-docetaxel-loaded aqueous nanoparticle dispersions generated in Section 4.3.1 and experiments to evaluate the impact of copolymer structure and temperature on the rate of docetaxel release from branched vinyl copolymer nanoparticles were undertaken.

An overview of the radio-dialysis procedure is presented in Figure 4.7. Briefly, 1 mL of docetaxel-loaded branched vinyl copolymer nanoparticles was added to a double-sided bio-dialyser and sealed with a 3.5 kDa molecular weight cut-off (MWCO) membrane. A bio-dialyser was considered more suitable for radio-dialysis experiments as its rigid structure provided more secure containment of ^{3}H-labelled compounds compared with conventional dialysis tubing. A bio-dialyser also provides conditions which are easily replicated which reduces inter-experiment variability with respect to surface area of nanoparticle dispersion exposed to the dialysis membrane. To ensure that sink conditions were achieved, the bio-dialyser was placed in a reservoir containing 100 mL of DI H_2O. Initial radio-dialyses were conducted over 24 hours at ambient temperature during which time the external reservoir was replaced at regular intervals of: 0.5, 1, 2, 3, 4, 5, 6, 7, 8 and 24 hours. LSC analysis conducted on samples of the external reservoir allowed quantification of the amount of docetaxel which had been released at each time point.

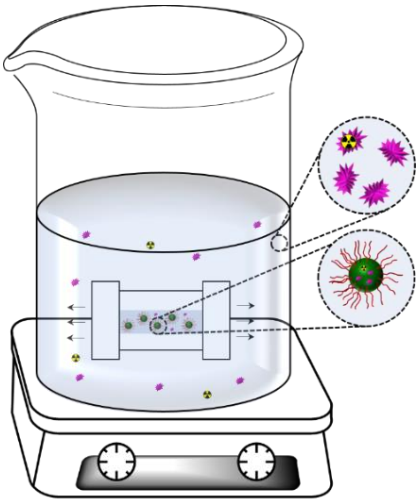

Figure 4.7 Schematic representation of the radio-dialysis experiments through which the rates of docetaxel release from branched vinyl copolymer nanoparticles were determined. Docetaxel loaded aqueous nanoparticle dispersions were loaded into a bio-dialyser (3.5 kDa MWCO) and placed in DI H_2O under sink conditions, allowing docetaxel diffusion into the external reservoir.

4.3.2.1 The Impact of Copolymer Structure on Docetaxel Release from Branched Vinyl Copolymer Nanoparticles

Initial radio-release studies sought to determine the impact of nanoparticle core chemistry on the rate of docetaxel release from branched vinyl copolymer nanoparticles. This was achieved by conducting identical radio-release experiments using aqueous nanoparticle dispersions consisting of *p*(HPMA), *p*(*n*BMA), *p*(*n*HMA), *p*(EHMA) and *p*(LMA) based copolymers. To remove any possible impact of temperature on docetaxel release rates, initial radio-dialyses were conducted at 20 °C over 24 hours.

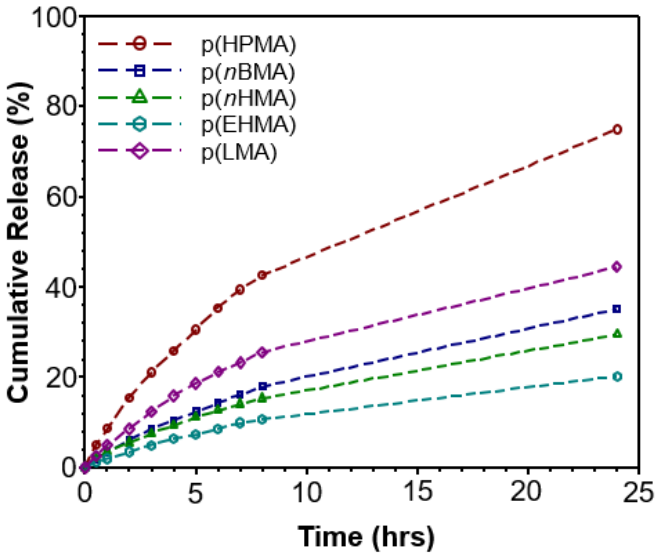

Figure 4.8 Cumulative ^{3}H-labelled docetaxel release data obtained over 24 hour *via* radio-dialyses of: *p*(HPMA) (red open circles), *p*(*n*BMA) (blue open squares), *p*(*n*HMA) (green open triangles), *p*(EHMA) (teal open hexagons) and *p*(LMA) (purple open diamonds) based branched vinyl copolymer nanoparticles at 20 °C.

Clear differences were observed between the docetaxel release rates obtained for branched vinyl copolymers consisting of various hydrophobic copolymers. For example, after 8 hours 43, 18, 15, 11 and 26 % of the initial docetaxel loading had been released from branched vinyl copolymer nanoparticles consisting of *p*(HPMA), *p*(*n*BMA), *p*(*n*HMA), *p*(EHMA) and *p*(LMA), respectively. The ^{3}H-labelled release curves, obtained from radio-dialysis of all docetaxel loaded aqueous nanoparticle dispersions at ambient temperature, are presented in Figure 4.8. Interestingly, DLS studies of branched vinyl copolymer nanoparticles before and after radio-dialyses indicated negligible impact on nanoparticle size or stability (Appendix, Table A4.1). This was somewhat surprising given that nanoparticles had lost a significant proportion of their original mass. This, however, supported earlier claims that, due to nanoparticle stability to dilution, docetaxel release most likely occurred *via* diffusion from the nanoparticle cores rather than as a result of complete disassembly of nanoparticle structure.

It is important to state that the total amount of docetaxel used in each radio-dialysis experiment (*ca*. 0.15 mg) was significantly below the docetaxel aqueous saturation limit within the 100 mL external reservoir (C_{max} = 0.65 mg, 6.5 µg mL^{-1}).[22,23] This suggests that under homogeneous conditions and rapid equilibration, that >99 % of docetaxel release could theoretically be achieved within 0.5 hours. It must be noted, however, that this would require complete equilibration of the concentration gradient within the first 30 minutes of radio-dialysis. Radio-dialysis of free docetaxel was attempted by addition of a docetaxel-EtOH solution directly into the bio-dialyser. This, however, did not show the expected burst release profile typically obtained for dialysis of free drugs. Instead, free docetaxel showed a comparable release profile to that obtained for *p*(HPMA) based nanoparticles (Appendix Figure A4.2). This likely occurred due to the formation of large aggregates within the bio-dialyser as the docetaxel concentration exceeded its aqueous saturation limit. As a result, docetaxel release was dependent upon the rate at which such aggregates dissolved, which was, in turn, limited by the aqueous docetaxel saturation limit. It was therefore not possible to obtain comparable release data for free docetaxel under the experimental conditions that radio-dialyses were conducted.

The highest docetaxel release rates were observed for branched vinyl copolymer nanoparticles consisting of *p*(HPMA) and *p*(LMA) based copolymers. This was somewhat unsurprising given the lower encapsulation efficiencies achieved during co-nanoprecipitation (0.769 and 0.836 respectively). It is therefore likely that high concentrations of free docetaxel within the aqueous nanoparticle dispersion were immediately able to permeate through the dialysis membrane into the external reservoir. In contrast, *p*(*n*BMA), *p*(*n*HMA) and *p*(EHMA) based nanoparticles, which showed higher encapsulation efficiencies (≥0.954) showed slower docetaxel release rates. This indicated that EE is a crucial factor in controlling drug release

rates from branched vinyl copolymer nanoparticles formed *via* co-nanoprecipitation. Interestingly, comparison between docetaxel release from *p*(*n*BMA), *p*(*n*HMA) and *p*(EHMA) based nanoparticles, which achieved comparable encapsulation efficiencies during co-nanoprecipitation, generally showed a strong correlation with the hydrophobicity of the copolymers from which nanoparticles were constructed. Release rates obtained at 20 °C decreased in the order of *p*(*n*BMA) > *p*(*n*HMA) > *p*(EHMA). This strongly suggested that the nanoparticle core chemistry had a significant influence on the rate at which docetaxel was released, at least within this series of materials. Furthermore, this implied that hydrophobic interactions between the aliphatic side chains of copolymer repeat units and encapsulated docetaxel were responsible for an aspect of drug release modulation.

In all cases, docetaxel release kinetics demonstrated first-order release. This indicated that release rates were proportional to the docetaxel concentration within the nanoparticle cores. Given that the initial concentration of docetaxel was known and that the amount of docetaxel released at each time point had been quantified, this allowed the concentration of encapsulated docetaxel ([Docetaxel]) to be calculated at each time point during the radio-dialysis. This data was used to determine the docetaxel release constants (*k*) for each of the branched vinyl copolymer nanoparticles studied. This was achieved using the integrated rate law for first order reactions to construct plots of ln[Docetaxel] *vs.* time (Equation 4.4). In order to eliminate any effects of varied concentration gradients, semi-logarithmic plots were constructed using data obtained between hours 1 and 8 of radio-dialysis experiments during which time the external reservoir was replaced at regular intervals. In all cases, this generated reliable data ($R^2 \geq 0.95$) which allowed determination of docetaxel release rate constants for each of the radio-dialyses. In ascending order, these rate constants of 47.9, 67.7, 82.4, 125.6 and 256.3 s^{-1} were obtained for *p*(EHMA), *p*(*n*HMA), *p*(*n*BMA), *p*(LMA) and *p*(HPMA) based nanoparticles respectively.

$$[Docetaxel]_t = [Docetaxel]_0 \, e^{-kt} \qquad \textbf{Equation 4.4}$$

The release rate constants obtained were used to determine the half-life ($t_{1/2}$) of docetaxel within the core of branched vinyl copolymer nanoparticles. In this sense, $t_{1/2}$ refers to the time taken for 50 % of the initial docetaxel loading to be released into the external reservoir. This is not to be confused with the plasma half-life, which refers to the time taken for the concentration of an active pharmaceutical ingredient to be reduced to 50 % of its initial value within systemic circulation. Given that, $t_{1/2}$ is proportional to *k* for processes that obey first-order kinetics (Equation 4.5), release rate constants could easily be converted into docetaxel half-lives. At ambient temperature, half-lives of 52.1, 36.9, 30.3, 19.9 and 9.7 hours were obtained for docetaxel release from *p*(EHMA), *p*(*n*HMA), *p*(*n*BMA), *p*(LMA) and *p*(HPMA) based nanoparticles respectively.

$$t_{1/2} = \frac{ln2}{k}$$

Equation 4.5 Calculation of the half-life ($t_{1/2}$) of docetaxel which remained in the core of branched vinyl copolymer nanoparticles.

The calculation of docetaxel half-lives provided context for the impact of nanoparticle core chemistry on the rate at which encapsulated payloads are released from branched vinyl copolymer nanoparticles. The calculated docetaxel half-lives indicated that branched vinyl copolymers are capable of retaining encapsulated payloads for prolonged time periods. For example, more than 50 % of encapsulated docetaxel would remain within the *p*(EHMA) nanoparticle cores for two days after dilution. In all cases, branched vinyl copolymer nanoparticles retained more than 50 % of their encapsulated payloads long after the time typically required for significant nanoparticle accumulation within tumour tissue as a result of the enhanced permeation and retention effect *in vivo* (6 hrs).[55] Initial radio-dialyses therefore demonstrated that docetaxel-loaded branched vinyl copolymer nanoparticles have the potential to modulate drug release *in vivo*. Whilst initial studies sought to understand the relationship between nanoparticle chemistry and docetaxel release rates, applications of drug nanocarriers within a clinical setting require nanoparticles to be able to modulate drug release at physiological temperatures. Further studies were therefore required to understand the impact of temperature on docetaxel release from branched vinyl copolymer nanoparticles.

4.3.2.2 The Impact of Temperature on Docetaxel Release Rates

It was predicted that temperature would have a significant impact on the rate of docetaxel release from branched vinyl copolymer nanoparticles. Increases in temperature were expected to produce (i) an increase in the aqueous solubility limit of docetaxel and (ii) higher rates of docetaxel diffusion from the nanoparticle cores. A series of radio-dialyses were conducted to evaluate the extent, if any, to which increases in temperature impacted docetaxel release rates. Further radio-dialyses were conducted at 37 °C and 50 °C under otherwise identical conditions to those discussed in Section 4.3.3, allowing comparison with the release data generated above and therefore enabling docetaxel release rates to be studied at temperatures ranging from 20 °C to 50 °C. In all cases, faster docetaxel release rates were observed at higher temperature. For example, *p*(*n*BMA)-based nanoparticles released 18, 30 and 39 % of their encapsulated docetaxel payloads over 8 hours during radio-dialyses conducted at 20, 37 and 50 °C respectively. Overlaid docetaxel release curves obtained for each nanoparticle type at various temperatures are presented in Figure 4.9.

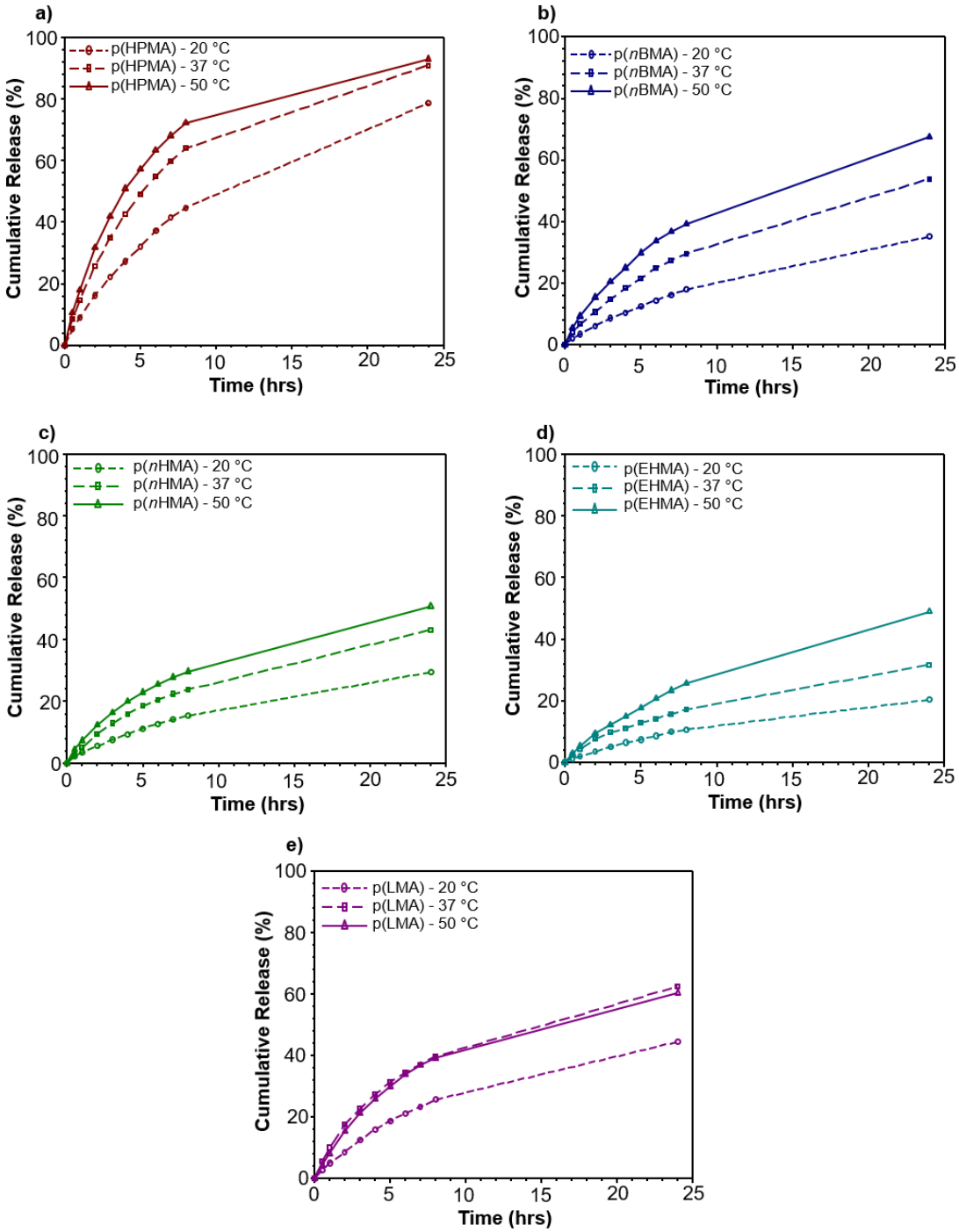

Figure 4.9 The effect of temperature on the rate of docetaxel release from branched vinyl copolymer nanoparticles. Overlaid docetaxel release curves obtained from radio-dialyses of a) *p*(HPMA), b) *p*(*n*BMA), c) *p*(*n*HMA), d) *p*(EHMA) and e) *p*(LMA) based branched vinyl copolymer nanoparticles at 20 ℃ (open circles, short dashed lines), 37 ℃ (open squares, medium dashed lines) and 50 ℃ (open triangles, solid lines) over 24 hours.

Release data demonstrated that, regardless of the chemical nature of the nanoparticle core, temperature had a profound effect on docetaxel release rates. Interestingly, nanoparticles for which high encapsulation efficiencies were achieved during co-nanoprecipitation saw docetaxel release rates increase at higher temperature. In contrast, *p*(HPMA) and *p*(LMA) based nanoparticles showed more noticeable increases in release rates as temperature was

increased from 20 to 37 °C than a similar increase from 37 to 50 °C. As suggested above, it is possible that the higher release rates are observed due to a higher proportion of free drug within the aqueous nanoparticle dispersions; initial increases in temperature may therefore have a disproportionate impact on aqueous nanoparticle dispersions containing higher concentrations of free drug. These data suggest that faster release rates likely occurred due to a combination of higher rates of docetaxel diffusion through the nanoparticle cores to the nanoparticle-water interface, and increased docetaxel solubility within the aqueous phase.

Docetaxel release rates obtained for nanoparticles comprising various core chemistries generally remained constant across the temperature range that radio-dialyses were conducted. This is demonstrated in Figure 4.10; release data have been replotted to show overlaid docetaxel release plots obtained for different nanoparticles consisting at each of the temperatures studied.

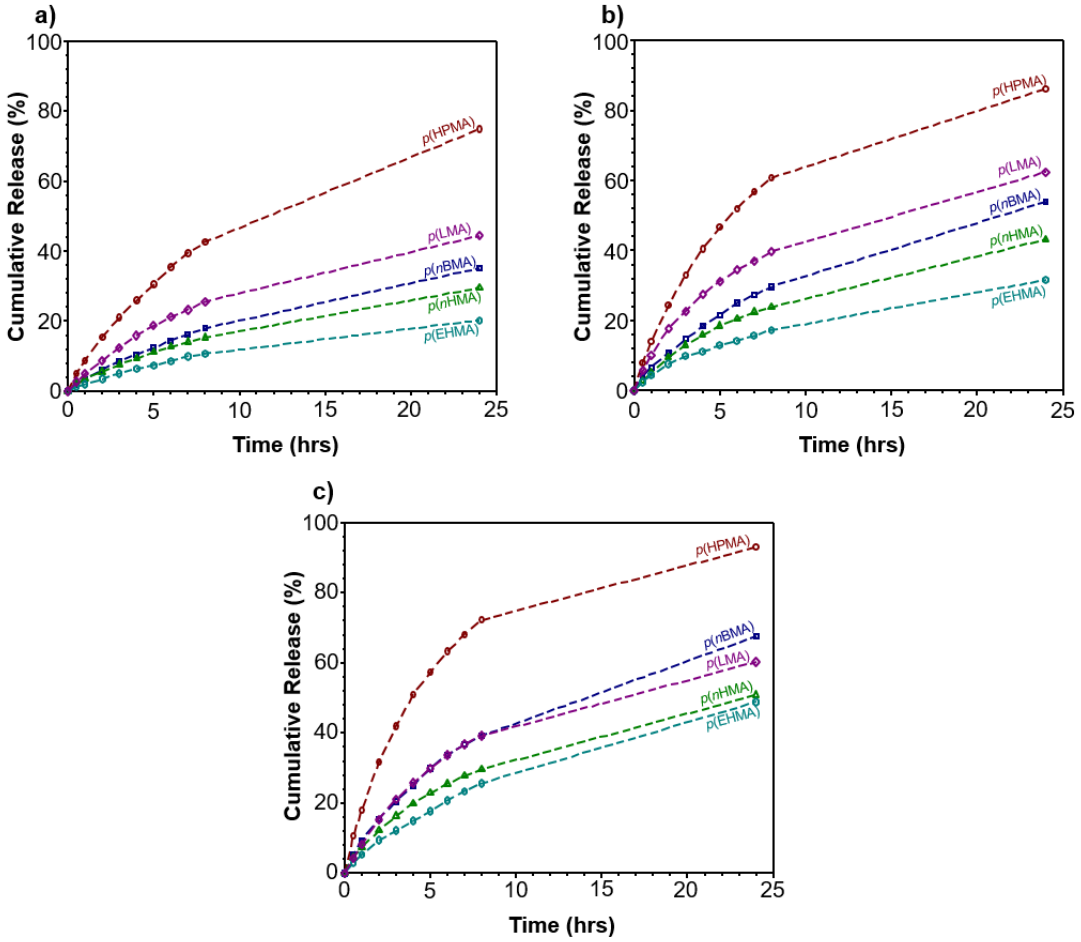

Figure 4.10 The effect of nanoparticle core chemistry on the rate of docetaxel release from branched vinyl copolymer nanoparticles at various temperatures. Overlaid docetaxel release curves obtained for *p*(HPMA) (red, open circles), *p*(*n*BMA) (blue, open squares), *p*(*n*HMA) (green, open triangles), *p*(EHMA) (teal, open hexagons) and *p*(LMA) (purple, open diamonds) during radio dialyses conducted over 24 hours at a) 20 °C, b) 37 °C and c) 50 °C.

Radio-dialyses conducted at 37 °C, Figure 4.10b, provided an indication of the docetaxel release rates that may be achieved at physiological temperature. The release rates observed at 37 °C increased in the order of *p*(EHMA), *p*(*n*HMA), *p*(*n*BMA), *p*(LMA) and *p*(HPMA), which was identical to the order observed at 20 °C. However, significantly higher amounts of docetaxel were released after 8 hours at 37 °C compared to the amounts released from the same nanoparticles at 20 °C. For example, cumulative docetaxel releases of 17, 24, 30, 40 and 61 wt % were achieved following 8 hours of radio-dialysis at 37 °C for *p*(EHMA), *p*(nHMA), *p*(nBMA), *p*(LMA) and *p*(HPMA)-based nanoparticles respectively. These values were significantly higher than the 11, 15, 18, 26 and 43 wt % of encapsulated docetaxel payloads that were cumulatively released during radio-dialysis of the same nanoparticles at 20 °C.

A further increase in the temperature at which radio-dialyses were conducted generally resulted in further increases in the rate at which docetaxel was released from branched vinyl copolymer nanoparticles. Surprisingly, however, docetaxel release from *p*(LMA) nanoparticles at 50 °C was almost identical to that observed for the same nanoparticles at 37 °C. For example, the same batch of *p*(LMA) nanoparticles showed comparable cumulative docetaxel release of 39.6 and 39.1 wt% of the initial encapsulated docetaxel payload following radio-dialysis over 8 hours. The factors that affect docetaxel release from *p*(LMA)-based branched vinyl copolymer nanoparticles will be discussed in more detail later in this Chapter. With the exception of *p*(LMA)-based nanoparticles, the order of docetaxel release rates obtained at 50 °C followed the same trend observed at lower tempeatures. This once again demonstrated the temperature dependence of docetaxel release from branched vinyl copolymer nanoparticles.

Detailed kinetic analyses were conducted using the data obtained from radio-dialysis of each of the branched vinyl copolymer nanoparticles at each of the temperatures studied. This analysis allowed further understanding of the effect of temperature on docetaxel release rates. Kinetic analysis first involved the construction of semi-logarithmic plots using release data obtained from radio-dialysis. This allowed determination of docetaxel release rate constants *via* calculation of the gradients obtained from plots of $\ln[\text{Docetacel}]_t$ *vs.* time. Kinetic plots obtained from radio-dialysis of each nanoparticle type at different remperatures were overlaid in order to demonstrate the impact of temperature on docetaxel release rates (Figure 4.11). In all cases, docetaxel release constants increased with temperature. For example, docetaxel release rate constants of 256.3, 441.7 and 552.2 s^{-1} were obtained for *p*(HPMA) nanoparticles during radio dialyses conducted at 20, 37 and 50 °C, respectively. In contrast to the general trends observed, comparable release rate constants of 200.9 and 211.0 s^{-1} were calculated from data obtained from radio-dialysis of *p*(LMA)-based nanoparticles at temperatures of 37 and 50 °C, respectively.

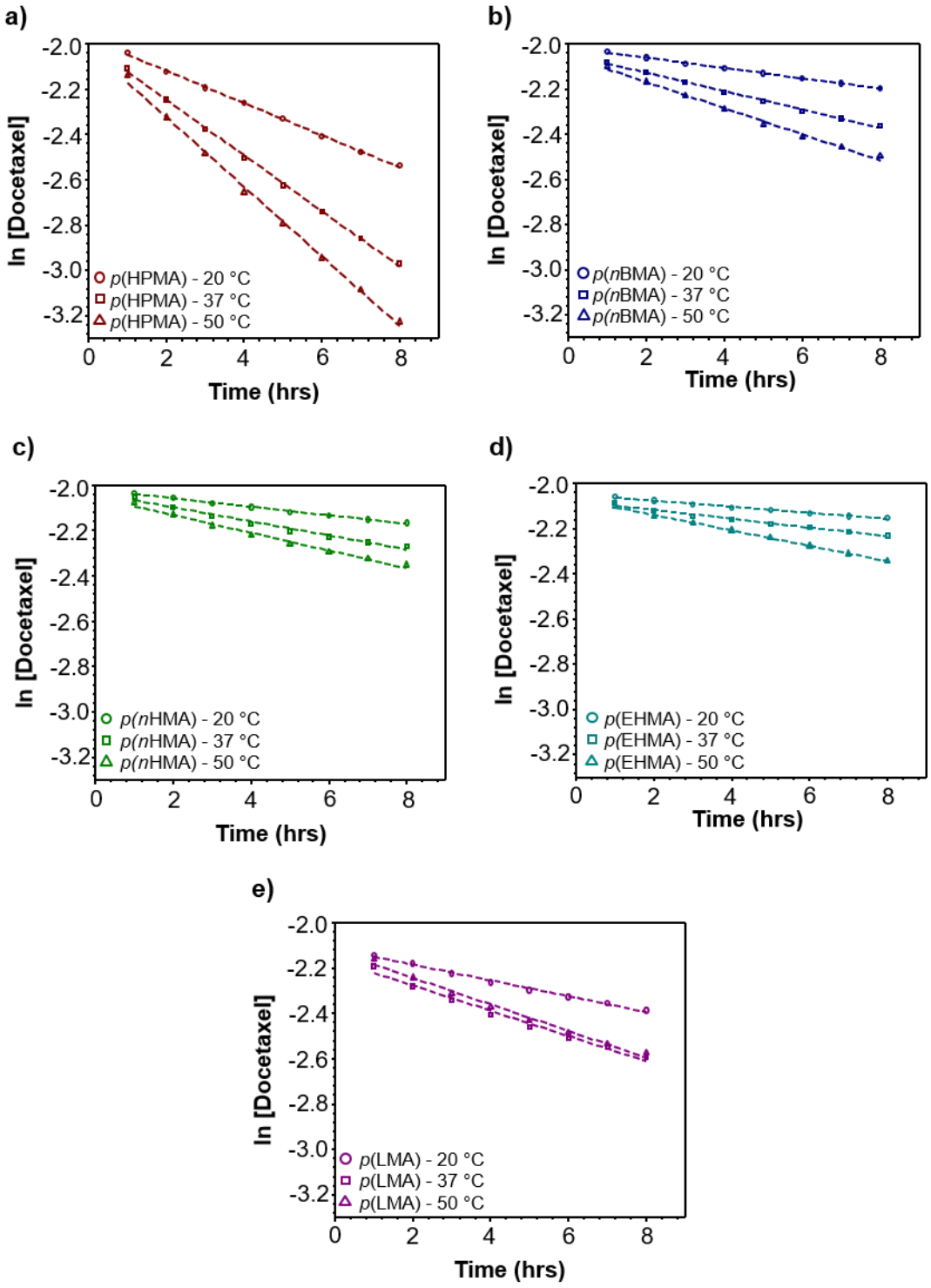

Figure 4.11 Calculation of docetaxel release rate constants at various temperatures. Semi-logarithmic kinetic plots constructed using data obtained from radio-dialysis of: a) *p*(HPMA), b) *p*(*n*BMA), c) *p*(*n*HMA), d) *p*(EHMA) and e) *p*(LMA)-based docetaxel-loaded branched vinyl copolymer nanoparticles at 20 °C (open circles), 37 °C (open squares) and 50 °C (open triangles) over 24 hours.

Release rate constants were used to calculate docetaxel half-lives within branched vinyl copolymers during radio-dialyses conducted at various temperatures. All calculated docetaxel release rate constants and half-lives are presented in Table 4.3. In all cases, docetaxel half-lives

decreased with temperature, as docetaxel release rates increased. For example, docetaxel half-lives of 36.9, 22.4 and 17.7 hours were calculated for docetaxel within the core of *p*(*n*HMA)-based nanoparticles during radio-dialysis conducted at temperatures of 20, 37 and 50 °C, respectively. Docetaxel half-lives calculated at 37 °C were perhaps of most significance due to their relevance to the physiological conditions with which branched vinyl copolymer nanoparticles would be exposed during *in vivo* release studies. Branched vinyl copolymer nanoparticles consisting of *p*(EHMA), *p*(nHMA), *p*(nBMA), *p*(LMA) and *p*(HPMA) gave docetaxel half-lives of 35.4, 22.4, 17.0, 12.4 and 5.65 hours respectively at 37 °C. With the exception of *p*(HPMA), all nanoparticles would be expected to release more than 50 % of their encapsulated payload after 12 hours dialysis at 37 °C. This is particularly significant for DNC systems which target the enhanced permation and retention effect in order to achieve high levels of nanoparticle accumulation within tumour tissue *in vivo*. It is therefore highly likely, should docetaxel half-lives translate to *in vivo* release studies, that the vast majority of encapsulated docetaxel payloads would be released either within the tumour tissues or within cancer cells if passive accumulation had occurred.

Table 4.3 Release rate constants and half-lives obtained from radio-dialysis of ^{3}H-labelled docetaxel-loaded aqueous nanoparticle dispersions at varied temperature.

Nanoparticle core	20 °C		37 °C		50 °C	
	k **(s^{-1})[a]**	**$t_{1/2}$ (hrs)[b]**	***k*** **(s^{-1})[a]**	**$t_{1/2}$ (hrs)[b]**	***k*** **(s^{-1})[a]**	**$t_{1/2}$ (hrs)[b]**
p(HPMA)	256.3	9.74	401.7	6.21	552.2	4.52
p(*n*BMA)	82.4	30.3	146.9	17.0	208.4	12.0
p(*n*HMA)	67.7	36.9	111.6	22.4	140.8	17.7
p(EHMA)	47.9	52.1	70.6	35.4	123.1	20.3
p(LMA)	125.6	19.9	200.9	12.4	211.0	11.8

[a]Calculated from plots of ln[Docetaxel] vs. time. [b]Calculated using docetaxel release rate constants obtained from radio release data ($t_{1/2} = \ln 2/k$.).

Whilst data obtained from radio-dialyses conducted at 50 °C may not have any clinical relevance to the application of branched vinyl copolymer nanoparticles as drug nanocarriers, such experiments were essential to understand the impact of temperature on docetaxel release from branched vinyl copolymer nanoparticles. Importantly, the avoidance of a "cold chain" in storage and supply is critical for the commercial viability of new drug delivery systems and storage temperatures can reach 50 °C in hot warehouse environments. It is noteworthy that branched vinyl copolymer nanoparticles were able to maintain their structural integrity following prolonged to temperatures up to 50 °C. As with experiments conducted at 20 and 37 °C, this was demonstrated by the negligible differences observed in the branched vinyl copolymer nanoparticle size distributions and intensity-average hydrodynamic diameters obtained by DLS analysis before and after radio-dialysis experiments (Appendix, Table A4.1).

Whilst docetaxel release rates from *p*(HPMA), *p*(nBMA), *p*(nHMA) and *p*(EHMA) based nanoparticles showed strong dependence upon the temperature at which radio-dialyses were conducted, the comparable docetaxel release rates obtained for *p*(LMA) based nanoparticles at temperatures ≥37 °C indicated that there may be a point at which docetaxel release rates become independent of temperature. Further analysis of release data and further copolymer analysis was therefore required in order to try to understand the factors governing docetaxel release rates from branched vinyl copolymer nanoparticles.

4.3.2.3 Understanding the Temperature Dependence of Docetaxel Release from Branched Vinyl Copolymer Nanoparticles

There are numerous chemical and physical factors which could have influenced docetaxel release rates from branched vinyl copolymer nanoparticles during radio-dialyses. Encapsulated docetaxel molecules must diffuse through the branched vinyl copolymer core in order to arrive at the polymer-water interface. The diffusion of small molecules through a polymer matrix is typically a temperature-dependent process; it is therefore likely that the rate of docetaxel release could be limited by the docetaxel diffusion to the polymer-water interface. Another factor which must be considered is the docetaxel solubility parameter within the nanoparticle core. In cases where favourable non-covalent interactions exist between docetaxel molecules and the hydrophobic domains of branched and amphiphilic AB block copolymers, which make up the nanoparticle core, high drug solubility within the copolymer matrix would be expected. High docetaxel-polymer compatibility would likely reduce the rate at which docetaxel molecules diffuse from the polymer phase into the surrounding aqueous environment. Furthermore, the docetaxel saturation limit within the surrounding aqueous environment would also likely influence the rate at which docetaxel molecules cross the polymer-water interface. Many of these factors are difficult to determine specifically for docetaxel encapsulated within different nanoparticle cores. Radio-release data was combined with copolymer characterisation, to develop a further understanding of the relationships between the physical properties of branched copolymers and docetaxel release rates from their ensuing branched vinyl copolymer nanoparticles.

The docetaxel release rate constants acquired from radio-dialyses conducted at varied temperatures were used to further demonstrate the impact of temperature on docetaxel release rates. This was achieved using an Arrhenius analysis. The Arrhenius equation is presented in Equation 4.6, which shows the relationship between the rate constant, *k*, and the activation energy (E_a), the universal gas constant (R) and temperature (T). The Arrhenius equation also involves the pre-exponential factor A, which is related to the frequency of collisions within the reaction medium.

$$k = Ae^{\left(\frac{-E_a}{RT}\right)}$$ **Equation 4.6**

Plots of ln *k vs.* 1/T were used to graphically demonstrate the relationship between the release rate constants and the temperature at which radio-dialyses were conducted. These plots were constructed using release data generated for all the branched vinyl copolymer nanoparticles studied (Figure 4.12). With the exception of data obtained from radio-dialyses of *p*(LMA) based nanoparticles, strong relationships were observed between temperature and the docetaxel release rates. The trend observed in data obtained from *p*(LMA)-based nanoparticles confirmed that the rate of docetaxel release became independent of temperature as it was increased from 37 to 50 ℃.

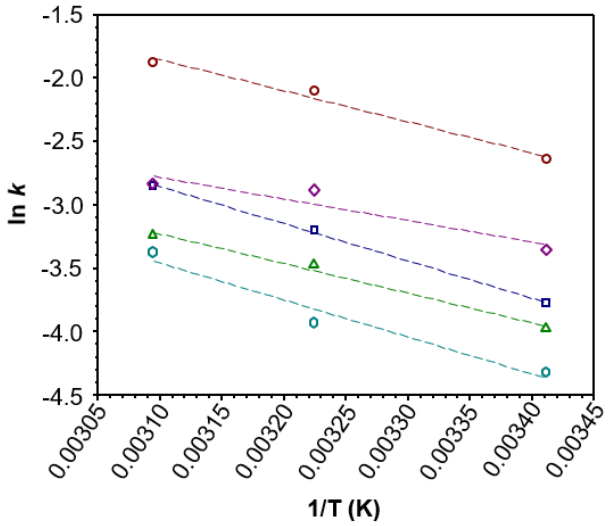

Figure 4.12 Analysis on the temperature dependence of docetaxel release rate constants obtained from radio-dialyses. Linear Arrhenius plots of ln*k vs.* 1/T showing the clear dependence of docetaxel release rates on the temperature that radio-dialyses were conducted. Arrhenius analyses were conducted on data obtained from: *p*(HPMA) (red, open circles), *p*(*n*BMA) (blue, open squares), *p*(*n*HMA) (green, open triangles), *p*(EHMA) (teal, open hexagons) and *p*(LMA) (purple, open diamonds) radio-dialyses at temperatures varying from 20 to 50 ℃.

Although the temperature-dependent docetaxel release rates were evident, the reason for such a relationship was less clear. It was hypothesised that an increase in temperature would promote docetaxel diffusion through the cores of the branched vinyl copolymer nanoparticles. Higher diffusion rates would therefore reduce the time taken for docetaxel molecules to permeate to the nanoparticle surface in order leave the nanoparticle and enter the aqueous surrounding environment. Interestingly, Arrhenius plots are also used to describe the temperature dependence of the rate of small molecule diffusion through polymer matrices.[56–58] The modified Arrhenius plot used to describe the temperature dependence of diffusion processes is described in Equation 4.7.

$$D = D_\infty e^{\left(\frac{-\Delta E_d}{RT}\right)}$$ **Equation 4.7**

This version of the Arrhenius plot demonstrates how small molecule diffusion rates increase with temperature. In particular, it shows that the diffusion rate (D) observed at temperature (T) is proportional to the exponential decay in the theoretical diffusion rate at infinite temperature (D∞), which occurs in proportion to the magnitude of the activation energy of diffusion (ΔE_d) and the gas constant (R).[59] Whilst the diffusion rates through the copolymer matrices were not quantified, the temperature dependence of both the diffusion and release rates are highly indicative that docetaxel diffusion through the nanoparticle core to the polymer-water interface is a key factor which drove the temperature dependence of the docetaxel release rates during radio-dialyses at varied temperatures.

All nanoparticles used in this study were constructed from amorphous copolymers. It was therefore initially expected that copolymer glass transition temperatures (T_g) would be a key factor in influencing the rate of docetaxel diffusion and, by extension, release rates from branched vinyl copolymer nanoparticles. The branched copolymers were therefore assessed using differential scanning calorimetry (DSC). T_g values of 70, 27, -7 and -11°C were obtained for *p*(HPMA$_{63}$-*co*-EGDMA$_{0.90}$), *p*(*n*BMA$_{73}$-*co*-EGDMA$_{1.12}$), *p*(*n*HMA$_{68}$-*co*-EGDMA$_{1.03}$) and *p*(EHMA$_{69}$-*co*-EGDMA$_{1.06}$) respectively. The T_g of *p*(LMA$_{70}$-*co*-EGDMA$_{1.04}$) could not be determined by DSC, however T_g values ranging from -65 to -53 °C have been reported in the literature.[60] It was therefore expected that radio-dialysis at temperatures above the T_g of the copolymers from which nanoparticles were constructed would result in faster release rates due to greater docetaxel diffusion. However, no evidence of any correlation between copolymer T_g and docetaxel release rates were observed. For example, all radio-dialyses were conducted above the T_g of *p*(LMA), *p*(*n*HMA), and *p*(EHMA) based copolymers whereas all dialyses were conducted below the T_g of *p*(HPMA) based copolymers. Nevertheless, docetaxel release rates were highest for *p*(HPMA) nanoparticles which, in theory, possessed more solid glass-like cores which would be expected to limit docetaxel diffusion and the observed release rates. Furthermore, a T_g of 27 °C was obtained from DSC analysis of *p*(*n*BMA$_{73}$-co-EGDMA$_{1.12}$) but the relationship between docetaxel release rate constants and the temperature remained consistent regardless of whether radio-dialyses of *p*(*n*BMA) nanoparticles were conducted below or above the *p*(*n*BMA) glass transition.

Another factor which was expected to impact docetaxel diffusion rates was the internal viscosity within the core of branched vinyl copolymer nanoparticles, especially at temperatures above their individual T_g values. Polymer viscosity typically decreases with temperature as polymer chains acquire more thermal energy to overcome the significant non-covalent interactions acting between large macromolecules. Although the glass transition defines the temperature at which polymer chains exhibit greater mobility, considerable non-covalent interactions still exist between polymer chains. As a result, at temperatures above

the T_g, polymers typically behave as highly viscous liquids. It is therefore unsurprising that the onset of the glass transition has little impact on docetaxel release rates as diffusion of docetaxel molecules through a highly viscous liquid would still require high amounts of energy. Rheological analyses were therefore conducted in order to understand the impact of temperature on the complex viscosity of each of the branched copolymers from which nanoparticles were constructed.

Rheological analyses involved performing reverse oscillatory temperature sweeps between temperatures of 150 to 25 °C. The use of reverse temperature sweeps ensured that all polymers initially formed low viscosity liquids of which the complex viscosity could be determined. Copolymer complex viscosities were then measured at 5 °C steps until either the temperature reached 25 °C or the minimum temperature at which reliable complex viscosity data could be obtained. This allowed graphical demonstration of the relationships between temperature and the complex viscosities of the branched copolymers from which each of the nanoparticles were constructed (Figure 4.13). Unsurprisingly, in all cases, lower temperatures caused significant increases in branched copolymer viscosity. For example, the complex viscosity of *p*(*n*HMA$_{68}$-*co*-EGDMA$_{1.03}$) increased from to 319 to 92477 Pa s^{-1} on cooling from 130 to 25 °C. In the cases of *p*(*n*BMA$_{73}$-*co*-EGDMA$_{1.12}$) and *p*(HPMA$_{63}$-*co*-EGDMA$_{0.90}$), reliable complex viscosity data could not be obtained as temperatures were lowered below 55 and 135 °C respectively. The order of complex viscosities observed were consistent with the T_g of the branched copolymers and, in all cases, exponential increases in copolymer complex viscosities were observed shortly before measurements failed. Interestingly, rheological analyses demonstrated that, in all cases, lower complex viscosities occurred at temperatures significantly higher than the T_g of the branched copolymers studied. For example, the lowest temperature at which complex viscosity of *p*(*n*BMA$_{73}$-*co*-EGDMA$_{1.12}$) could be measured was at 55 °C, which is 28 °C above the T_g recorded by DSC. Although bulk properties may not translate to copolymer behaviour at the nanoscale, these results clearly indicate that, although branched copolymers acquire greater chain mobility above their T_g, the significant reduction in copolymer viscosity required to increase docetaxel diffusion rates typically occurred at temperatures significantly higher than the T_g.

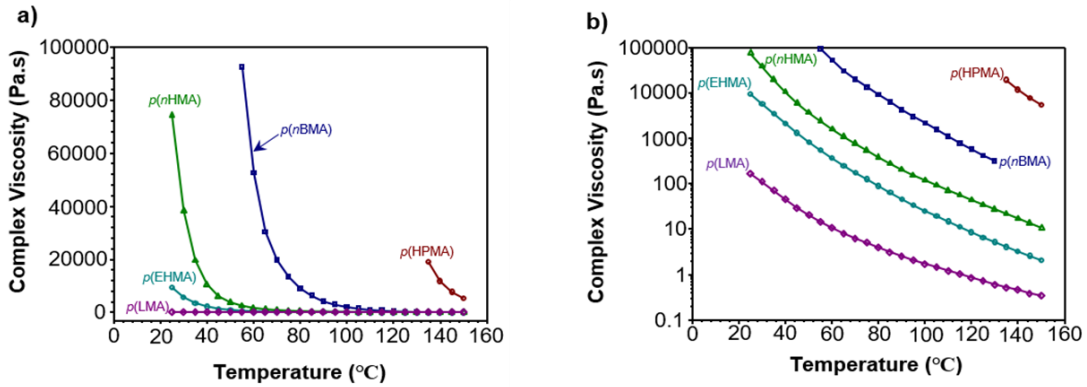

Figure 4.13 Rheological analysis of the branched copolymers which make up the core of branched vinyl copolymer nanoparticles. Change in the complex viscosity of branched vinyl copolymers using a reverse temperature sweep from 150 to 25 °C (or failure) at steps of 5 °C. Complex viscosity data was plotted on both a) linear and b) log scales. Analysis was conducted on *p*(HPMA) (red, open circles), *p*(*n*BMA) (blue, open squares), *p*(*n*HMA) (green, open triangles), *p*(EHMA) (teal, open hexagons) and *p*(LMA) (purple, open diamonds).

Analysis of the rheology data obtained for *p*(LMA$_{70}$-*co*-EGDMA$_{1.04}$) initially appeared to show that complex viscosity remained independent of temperature across the temperature range studied. However, a closer individual inspection of the *p*(LMA$_{70}$-*co*-EGDMA$_{1.04}$) complex viscosity data (Appendix, Figure A4.3) as well as replotting of complex viscosity data on a logarithmic scale (Figure 4.13b) showed, albeit still at extremely low complex viscosities ($\leq$ 170 Pa s^{-1}), exponential increases in complex viscosity in the temperature steps taken shortly before the reverse oscillatory temperature reached 25 °C. The exponential increase observed indicated that the core viscosity of *p*(LMA$_{70}$-*co*-EGDMA$_{1.04}$) based nanoparticles would most likely be significantly more viscous at 20 °C than at 37 or 50 °C. Furthermore, a negligible difference was observed between the complex viscosities of *p*(LMA$_{70}$-*co*-EGDMA$_{1.04}$) measured at 35 and 50 °C where, in both cases, complex viscosities were below 100 Pa s^{-1} and were indicative of low-viscosity liquids.

The significant reduction in complex viscosity of *p*(LMA$_{70}$-*co*-EGDMA$_{1.04}$) at higher temperature could explain the trend observed in docetaxel release rates observed from *p*(LMA) nanoparticles at various temperatures. The temperature increase from 20 to 37 °C would be expected to have had a profound impact on the core viscosity of *p*(LMA) based nanoparticles. This would likely cause a significant increase in the rate of docetaxel diffusion through the cores of branched vinyl copolymer nanoparticles and could explain the faster docetaxel release rates observed at 37 °C. The low viscosity of *p*(LMA$_{70}$-*co*-EGDMA$_{1.04}$) at 37 °C meant that further increases in temperature had a smaller impact on copolymer viscosity. As a result, comparable docetaxel diffusion rates would be expected at both 37 and 50 °C. This may explain the comparable docetaxel release rates observed during radio-dialysis of *p*(LMA) nanoparticles at temperatures $\geq$ 37 °C.

The non-linear temperature dependence of docetaxel release rates could be attributed to the plateau in the complex viscosity of the copolymer from which *p*(LMA) nanoparticles were constructed. This would suggest that, above 37 °C, the rate of docetaxel diffusion through the nanoparticle cores is dependent on both the viscosity within the nanoparticle core as well as the energy of individual docetaxel molecules. In the case of *p*(LMA), it appeared that core viscosity made the biggest contribution to docetaxel release rates. Radio-dialyses conducted above the temperature at which core viscosity appeared to reach a plateau demonstrated that docetaxel release rates became independent of temperature. In contrast, docetaxel release rates from nanoparticles consisting of branched copolymers which exhibited higher complex viscosities (>9400 Pa s^{-1}) showed linear temperature dependence across the temperature range studied. Rheology data obtained for branched copolymers suggests that, at these temperatures, nanoparticle core viscosities would be almost 2 orders of magnitude higher than that of *p*(LMA) nanoparticles. In such cases, docetaxel release rates would be expected to increase with temperature due to a simultaneous increase in the kinetic energy of docetaxel molecules as nanoparticle core viscosity decreased.

Another factor which may have influenced docetaxel release rates at higher temperature was the level of interaction between the hydrophobic domains within the core of branched vinyl copolymer nanoparticles. The reduction in core polarity observed in nanoparticles constructed from copolymers of greater hydrophobicity likely impacted the extent of host-guest interaction between aliphatic side-chains of copolymer repeat units and encapsulated docetaxel molecules. This would be expected to alter docetaxel release rates from branched vinyl copolymer nanoparticles. Evidence of this is clear upon comparison of the order of docetaxel release rates observed from *p*(HPMA), *p*(*n*BMA), *p*(*n*HMA) and *p*(EHMA) nanoparticles. The measurement of nanoparticle core polarities, conducted in Chapter 3, Section 3.4.2.2, showed that, with the exception of *p*(LMA) nanoparticles, docetaxel release rates correlated well with the nanoparticle core polarity. This implied that the rate at which docetaxel diffused to the polymer-water interface was affected by the chemical nature of the nanoparticle core. In cases where nanoparticle cores showed high polarity, docetaxel showed lower affinity for the polymer phase, which resulted in faster release rates. Alternatively, less polar cores provided a better environment for the hydrophobic chemotherapeutic, thus increasing its affinity for the polymer phase and reducing the rate at which it was released from branched vinyl copolymer nanoparticles. Higher temperature would therefore be expected to significantly reduce the prevalence of such host-guest interactions as docetaxel molecules acquire sufficient thermal energy to overcome non-covalent interactions with the copolymers which make up the nanoparticle core. Combined with the higher solubility within the aqueous phase, which typically accompany higher temperatures, the rate of docetaxel transport across the

polymer-water interface would likely increase and, therefore, increase docetaxel release rates from branched vinyl copolymer nanoparticles.

The main exception to the trend observed between core polarity and docetaxel release rates is that of *p*(LMA) nanoparticles. There are three possible reasons for this exception. As discussed above, these include the low EE observed during co-nanoprecipitation and the faster diffusion rates due to the low viscosity shown by *p*(LMA_{70}-*co*-$EGDMA_{1.04}$). The factors which govern docetaxel release from branched vinyl copolymer nanoparticles are clearly complex. It is evident that both core polarity and core viscosity may be associated with the variation in docetaxel release rates observed for branched vinyl copolymer nanoparticles; a highly hydrophobic environment within the core of branched vinyl copolymer nanoparticles appears to retard drug release and copolymer viscosity correlates with variation in docetaxel diffusion rates within the nanoparticle core. However, further studies would be required to determine the extent to which the release of encapsulated docetaxel was influenced by either of these macroscopic properties since they are dependent upon the length and/or functionality of aliphatic side chains of copolymer repeat units.

4.4 Conclusions

This work aimed to explore the behaviour of encapsulated docetaxel within the core of branched vinyl copolymer nanoparticles during co-nanoprecipitation. This was achieved *via* a comprehensive co-nanoprecipitation study which demonstrated that docetaxel loadings up to 25 wt % could be encapsulated without any impact on the stability and size distributions of the resultant nanoparticles. Furthermore, docetaxel loadings up to 15 wt % could be achieved regardless of the chemical nature of the copolymers used during co-nanoprecipitation. The ability to encapsulate up to 25 wt % drug makes co-nanoprecipitation an attractive approach for the preparation of DNC systems and allows the preparation of nanoparticle dispersions which contain more than a 20-fold increase in the aqueous docetaxel saturation limit to be formulated. Radiometric analyses determined the success of docetaxel encapsulation and demonstrated that not all of the initial docetaxel loading was encapsulated during co-nanoprecipitation. Simultaneous nanoparticle formation and drug encapsulation is a kinetically-driven process and, as a result, copolymer functionality has little impact on the encapsulation efficiency achieved during co-nanoprecipitation. Despite this, co-nanoprecipitation remains a robust and facile synthetic approach for the preparation of docetaxel-loaded aqueous nanoparticle dispersions.

^{3}H-labelled docetaxel loaded branched vinyl copolymers formed during co-nanoprecipitation studies were also used to determine docetaxel release rates *in vitro*. Radiometric analysis proved an excellent technique for direct analysis of aqueous nanoparticle dispersions without

the need for additional extraction and/or purification. This enabled quantitative comparison between the drug release rates from branched vinyl copolymer nanoparticles consisting of various core chemistries. Enhanced docetaxel release rates observed for nanoparticles formed *via* co-nanoprecipitations which achieved low EE highlighted the importance of preventing/removing free drug in order to prevent burst release during radio-dialysis. The variation observed in docetaxel release rates demonstrated that the macroscopic behaviour of branched vinyl copolymer nanoparticles depends on their chemical structure. Furthermore, the temperature dependence of docetaxel release rates highlighted the importance of nanoparticle core viscosity in controlling drug release.

Kinetic analysis of docetaxel release rates demonstrated that branched vinyl copolymer nanoparticles are able to modulate drug release over clinically-relevant time periods at physiological temperature. This highlighted the suitability of such materials for further application as DNC systems and indicated that they should be considered for *in vivo* analysis.

4.5 References

1 X. Kang, H.-H. Xiao, H.-Q. Song, X.-B. Jing, L.-S. Yan and R.-G. Qi, *Cancer Biol. Med.*, 2015, **12**, 362–374.
2 J. I. Hare, T. Lammers, M. B. Ashford, S. Puri, G. Storm and S. T. Barry, *Adv. Drug Deliv. Rev.*, 2017, **108**, 25–38.
3 J. N. Denis, A. Correa and A. E. Greene, *J. Org. Chem.*, 1990, **55**, 1957–1959.
4 J. N. Denis, A. E. Greene, D. Guenard, F. Gueritte-Voegelein, L. Mangatal and P. Potier, *J. Am. Chem. Soc.*, 1988, **110**, 5917–5919.
5 P. Zhao and D. Astruc, *ChemMedChem*, 2012, **7**, 952–972.
6 K. C. Nicolaou, R. K. Guy and P. Potier, *Sci. Am.*, 1996, **274**, 84–88.
7 Y.-F. Wang, Q.-W. Shi, M. Dong, H. Kiyota, Y.-C. Gu and B. Cong, *Chem. Rev.*, 2011, **111**, 7652–7709.
8 F. Lavelle, F. Gueritte-Voegelein and D. Guenard, *Bull. Cancer*, 1993, **80**, 326–338.
9 D. Guenard, F. Gueritte-Voegelein and P. Potier, *Acc. Chem. Res.*, 1993, **26**, 160–167.
10 H. Lataste, V. Senilh, M. Wright, D. Guénard and P. Potier, *Proc. Natl. Acad. Sci.*, 1984, **81**, 4090–4094.
11 I. Youm, X. Yang, J. B. Murowchick and B.-B. C. Youan, *Nanoscale Res. Lett.*, 2011, **6**, 630.
12 A. Inal, M. A. Kaplan, M. Kucukoner and A. Isikdogan, *Neoplasma*, 2012, **59**, 233–236.
13 T. Narita, A. Suzuki, E. Hashizume and M. Yajima, *Gan To Kagaku Ryoho.*, 2012, **39**, 119–122.
14 B. Sorbe, M. Graflund, G. Horvath, M. Swahn, K. Boman, R. Bangshöj, M. Lood and H. Malmström, *Int. J. Gynecol. Cancer*, 2012, **22**, 47–53.
15 Z. Mu, C. M. Ma, X. Chen, D. Cvetkovic, A. Pollack and L. Chen, *Phys. Med. Biol.*, 2012, **57**, 535–545.
16 S. J. Clarke and L. P. Rivory, *Clin. Pharmacokinet.*, 1999, **36**, 99–114.
17 D. H. L. Dal Yong Kim, S.-J. Jang, S.-W. Kim, C. Suh and J. S. Lee, *Cancer Res. Treat. Off. J. Korean Cancer Assoc.*, 2011, **43**, 212–216.
18 D. P. Petrylak, *Rev. Urol.*, 2006, **8**, S48–S55.
19 L. van Zuylen, J. Verweij and A. Sparreboom, *Invest. New Drugs*, 2001, **19**, 125–141.

20 V. Sanna, A. M. Roggio, A. M. Posadino, A. Cossu, S. Marceddu, A. Mariani, V. Alzari, S. Uzzau, G. Pintus and M. Sechi, *Nanoscale Res. Lett.*, 2011, **6**, 260–269.

21 A. Ray, N. Larson, D. B. Pike, M. Grüner, S. Naik, H. Bauer, A. Malugin, K. Greish and H. Ghandehari, *Mol. Pharm.*, 2011, **8**, 1090–1099.

22 W. Du, L. Hong, T. Yao, X. Yang, Q. He, B. Yang and Y. Hu, *Bioorg. Med. Chem.*, 2007, **15**, 6323–6330.

23 Y.-T. Ma, Y. Yang, P. Cai, D.-Y. Sun, P. A. Sánchez-Murcia, X.-Y. Zhang, W.-Q. Jia, L. Lei, M. Guo and F. Gago, *J. Nat. Prod.*, 2018, **81**, 524–533.

24 T. Ganesh, *Bioorg. Med. Chem.*, 2007, **15**, 3597–3623.

25 J. Crown, M. O'Leary and W.-S. Ooi, *Oncologist*, 2004, **9**, 24–32.

26 C. Mohanty, M. Das, J. R Kanwar and S. K Sahoo, *Curr. Drug Deliv.*, 2011, **8**, 45–58.

27 J. D. Byrne, T. Betancourt and L. Brannon-Peppas, *Adv. Drug Deliv. Rev.*, 2008, **60**, 1615–1626.

28 B. Haley and E. Frenkel, in *Urologic Oncology: Seminars and original investigations*, Elsevier, 2008, vol. 26, pp. 57–64.

29 L. E. Euliss, J. A. DuPont, S. Gratton and J. DeSimone, *Chem. Soc. Rev.*, 2006, **35**, 1095–1104.

30 J. M. Benito, M. Gómez-García, C. Ortiz Mellet, I. Baussanne, J. Defaye and J. M. García Fernández, *J. Am. Chem. Soc.*, 2004, **126**, 10355–10363.

31 U. Boas and P. M. H. Heegaard, *Chem. Soc. Rev.*, 2004, **33**, 43–63.

32 S.-S. Feng, L. Mei, P. Anitha, C. W. Gan and W. Zhou, *Biomaterials*, 2009, **30**, 3297–3306.

33 R. M. Straubinger and S. V Balasubramanian, in *Methods in enzymology*, Elsevier, 2005, vol. 391, pp. 97–117.

34 A. L. Klibanov, K. Maruyama, V. P. Torchilin and L. Huang, *FEBS Lett.*, 1990, **268**, 235–237.

35 M. V Lozano, D. Torrecilla, D. Torres, A. Vidal, F. Domínguez and M. J. Alonso, *Biomacromolecules*, 2008, **9**, 2186–2193.

36 H. Adachi, T. Irie, K. Uekama, T. Manako, T. Yano and M. Saita, *Eur. J. Pharm. Sci.*, 1993, **1**, 117–123.

37 C. K. Osborne, *Breast Cancer Res. Treat.*, 1998, **51**, 227–238.

38 F. Yan, C. Zhang, Y. Zheng, L. Mei, L. Tang, C. Song, H. Sun and L. Huang, *Nanomedicine Nanotechnology, Biol. Med.*, 2010, **6**, 170–178.

39 T. Musumeci, C. A. Ventura, I. Giannone, B. Ruozi, L. Montenegro, R. Pignatello and G. Puglisi, *Int. J. Pharm.*, 2006, **325**, 172–179.

40 M. Senthilkumar, P. Mishra and N. K. Jain, *J. Drug Target.*, 2008, **16**, 424–435.

41 D. Le Garrec, S. Gori, L. Luo, D. Lessard, D. C. Smith, M.-A. Yessine, M. Ranger and J.-C. Leroux, *J. Control. Release*, 2004, **99**, 83–101.

42 J. M. Chan, L. Zhang, K. P. Yuet, G. Liao, J.-W. Rhee, R. Langer and O. C. Farokhzad, *Biomaterials*, 2009, **30**, 1627–1634.

43 S. Murugesan, S. Ganesan, R. K. Averineni, M. Nahar, P. Mishra and N. K. Jain, *J. Biomed. Nanotechnol.*, 2007, **3**, 52–60.

44 R. Karnik, F. Gu, P. Basto, C. Cannizzaro, L. Dean, W. Kyei-Manu, R. Langer and O. C. Farokhzad, *Nano Lett.*, 2008, **8**, 2906–2912.

45 H.-C. Shin, A. W. G. Alani, D. A. Rao, N. C. Rockich and G. S. Kwon, *J. Control. Release*, 2009, **140**, 294–300.

46 X. Wang, Y. Wang, X. Chen, J. Wang, X. Zhang and Q. Zhang, *J. Control. Release*, 2009, **139**, 56–62.

47 E. M. Enlow, J. C. Luft, M. E. Napier and J. M. DeSimone, *Nano Lett.*, 2011, **11**, 808–813.

48 K. S. Chu, W. Hasan, S. Rawal, M. D. Walsh, E. M. Enlow, J. C. Luft, A. S. Bridges, J. L. Kuijer, M. E. Napier, W. C. Zamboni and J. M. DeSimone, *Nanomedicine Nanotechnology, Biol. Med.*, 2013, **9**, 686–693.

49 J. P. Rolland, B. W. Maynor, L. E. Euliss, A. E. Exner, G. M. Denison and J. M.

DeSimone, *J. Am. Chem. Soc.*, 2005, **127**, 10096–10100.
50 R. A. Petros, P. A. Ropp and J. M. DeSimone, *J. Am. Chem. Soc.*, 2008, **130**, 5008–5009.
51 T. J. Merkel, K. P. Herlihy, J. Nunes, R. M. Orgel, J. P. Rolland and J. M. DeSimone, *Langmuir*, 2009, **26**, 13086–13096.
52 R. F. Service, *Science.*, 2010, **330**, 314 LP – 315.
53 J. Hrkach, D. Von Hoff, M. M. Ali, E. Andrianova, J. Auer, T. Campbell, D. De Witt, M. Figa, M. Figueiredo and A. Horhota, *Sci. Transl. Med.*, 2012, **4**, 128ra39.
54 H. He, L. Liu, E. E. Morin, M. Liu and A. Schwendeman, *Acc. Chem. Res.*, 2019, **52**, 2445–2461.
55 J. Fang, H. Nakamura and H. Maeda, *Adv. Drug Deliv. Rev.*, 2011, **63**, 136–151.
56 T. Tsuji, T. Hiaki, M. Hongo and N. Itoh, *Ind. Eng. Chem. Res.*, 2004, **43**, 4428–4433.
57 B. S. Zolnik, P. E. Leary and D. J. Burgess, *J. Control. Release*, 2006, **112**, 293–300.
58 A. Lucero-Acuña, C. A. Gutiérrez-Valenzuela, R. Esquivel and R. Guzmán-Zamudio, *RSC Adv.*, 2019, **9**, 8728–8739.
59 L. W. McKeen, in *Plastics Design Library*, ed. L. W. B. T.-P. P. of P. and E. (Fourth E. McKeen, William Andrew Publishing, 2017, pp. 1–19.
60 M. Demetriou and T. Krasia-Christoforou, *J. Polym. Sci. Part A Polym. Chem.*, 2008, **46**, 5442–5451.

Chapter 5

Conclusions & Future Work

5.1 Conclusions

The primary aim of this research was to expand the scope of co-nanoprecipitation in order to generate nanomaterials which have the potential to modulate the release of hydrophobic chemotherapeutics *in vivo*. In many ways this research has created more questions that it has answered. However, it has, without doubt, achieved its primary objective and has produced 5 suitable candidates which can be now taken forward for *in vitro* and *in vivo* pharmacological evaluation. This research has provided fundamental understanding of the polymerisation and nanoprecipitation processes by which these polymers and nanoparticles were formed and allowed a number of factors which influence such processes to be identified.

5.1.1 Chapter 2

The research presented in Chapter 2 represents a significant advance in the expansion of the scope of Cu-RDRP of hydrophobic methacrylates in anhydrous alcohols. For the first time, successful Cu-RDRPs of EMA, *n*HMA, CHMA, BzMA and EHMA were achieved in anhydrous methanol at 60 °C. Successful Cu-RDRP of MMA, *t*BMA, CHMA, LMA and SMA were also conducted in anhydrous IPA at 60 °C. The successes of such Cu-RDRPs were attributed to the previously reported monomer co-solvency effect.[1,2] The use of pyrene as a fluorescent probe allowed assessment of polymerisation mixture polarities *via* fluorescence spectroscopy. These assessments revealed that polymerisations of hydrophobic monomers in anhydrous alcohols had a significant impact on reaction mixture polarity. The extent of this impact was dependent upon the relative polarities of the reaction mixture i.e. monomers and solvents used in Cu-RDRP. As a result, in cases where a contrast existed between the polarity of the monomer and solvent, large changes in the reaction mixture occurred as Cu-RDRPs proceeded. This research therefore reiterated the importance of monomer-co-solvency in facilitating Cu-RDRP of hydrophobic monomers in alcohols that their resulting polymers are typically insoluble in and, furthermore, highlighted the importance of conducting such polymerisations at high concentration (i.e. 50 wt %). Despite the co-solvency effect, many monomer-alcohol mixtures were unable to retain polymer solubility following monomer depletion and, as a result, many Cu-RDRPs underwent polymerisation-induced phase separation. This was particularly prevalent during Cu-RDRP of low polarity monomers due to the increased polymer sensitivity to increases in polymerisation mixture polarity. Furthermore, monomer polarity also influenced the point at which polymerisation-induced phase separation occurred. Remarkably, Cu-RDRP in anhydrous alcohols facilitated the synthesis of linear homopolymers of low dispersity with control over the molecular weight; Cu-RDRP in anhydrous alcohols was expanded further by the preparation of various copolymer architectures including AB block copolymers and branched statistical copolymers. The

preparation and subsequent use of a PEG macro-initiator permitted the preparation of amphiphilic block copolymers *via* Cu-RDRP.

The preparation of a wide range of branched copolymers was achieved *via* RDRcP of hydrophobic methacrylates with EGDMA in anhydrous alcohols. This was somewhat remarkable given the apparent onset of polymerisation-induced phase separation during copolymerisations. TD-SEC proved to be an effective technique for the characterisation of branched copolymers. Refitting of conventional molecular weight data allowed the development of new TD-SEC analyses which illustrated the broad distribution of macromolecular architectures which make up branched copolymer molecular weight distributions. However, despite the high monomer conversions achieved during copolymerisations, contrasting levels of branching were observed during these copolymerisations. As a result, many copolymerisations were able to avoid the formation of a gelled network despite being conducted at experimental $[B]_0/[I]_0$ ratios in excess of the theoretical gel points. Furthermore, the extent of branching appeared to be highly dependent upon the nature of the monomer used.

It is highly likely that these contrasting branching behaviours occurred as a result of variation in the relative levels of pendant group consumption *via* intermolecular and intramolecular cyclisation. There are three possible reasons which could explain the contrasting branching behaviours observed during Cu-RDRcP. These are: i) an inherent decrease in the concentration of active chain-ends/ methacrylate groups as a result of the increased weight fraction of the monomer side chain; ii) increased steric hindrance around pendant methacrylate groups due to the increased size of monomer repeat units; and iii) the conformation of primary chains in the polymerisation mixture and therefore the accessibility of pendant methacrylate groups. All of these factors naturally arise when conducting branching copolymerisations of EGDMA with different comonomers and each of these factors likely influence the consumption of EGDMA pendant methacrylate groups during copolymerisation. Whilst many reports of the impact of concentration on the extent of branching observed in copolymerisations of monofunctional and BFMs, have appeared in the literature,[3–5] they have typically studied the copolymerisation of EGDMA with only one monomer type. Studies are therefore required to understand how the size of the methacrylate side chain influences pendant methacrylate group consumption. However, given the nature of the copolymerisations presented in Chapter 2, it is not possible to determine which of these factors are responsible for the low levels of branching observed in some branching copolymerisations. Future research must therefore look to modify experimental conditions to allow each of these factors to be studied in isolation.

5.1.2 Chapter 3

The research presented in Chapter 3 showed an expansion of the scope of branched and AB block copolymers that can be used to form branched vinyl copolymer nanoparticles *via* co-nanoprecipitation. In particular, co-nanoprecipitations of *p*(*n*BMA), *p*(*n*HMA), *p*(EHMA) and *p*(LMA) based copolymers formed stable highly monodisperse aqueous nanoparticle dispersions and showed a robustness to changes in experimental conditions. This allowed the preparation of branched vinyl copolymer nanoparticles which possessed nanoparticle cores of significantly contrasting polarities than had been reported previously.[6] This is of particular significance given the desired application of such nanomaterials as nanocarriers of hydrophobic chemotherapeutics *in vivo*. This approach allows the macroscopic properties of branched vinyl copolymers to be designed at the initial stage of the production process and demonstrates how the advances in RDRP techniques have facilitated the bottom-up design of such nanomaterials. The encapsulation of low loadings of a hydrophobic guest molecule was achieved by simply adding small amounts of the compound to the initial THF solution from which copolymers were co-nanoprecipitated. The presence of small amounts of pyrene had minimal impact on nanoparticle formation *via* co-nanoprecipitation. This is particularly relevant as it offers a relatively facile synthetic approach for the encapsulation of hydrophobic chemotherapeutics during co-nanoprecipitation.

Surprisingly, nanoprecipitations and co-nanoprecipitations of *p*(*n*BMA), *p*(*n*HMA), *p*(EHMA) and *p*(LMA) based (co)polymers did not show the architecture dependent nucleation typically exhibited by (co)nanoprecipitations of *p*(HPMA) based copolymers; this likely occurred as a result of enhanced levels of (co)polymer supersaturation during co-nanoprecipitation. These results indicate that high molecular weight branched copolymers are not essential to drive (co)polymer nucleation during such co-nanoprecipitations and, as a result, are not compulsory for the formation of stable and highly monodisperse aqueous nanoparticle dispersions. This allowed the first report of successful nanoparticle formation from co-nanoprecipitations of linear homopolymers with amphiphilic AB block copolymers as well as the nanoprecipitations of amphiphilic AB block copolymers. These results are of considerable importance as they remove the need for relatively complex branched copolymer syntheses during preparation of aqueous nanoparticle dispersions consisting of *p*(*n*BMA), *p*(*n*HMA), *p*(EHMA) and *p*(LMA). These results demonstrate that it is the extent of excipient supersaturation not (co)polymer molecular weight which governs the rate of nucleation and subsequent nanoparticle formation during co-nanoprecipitation. This is of particular clinical relevance and should be taken into account when selecting excipients, which contain low to moderate levels of hydrophobicity, for use in the preparation of drug-loaded nanoparticles *via* (co)nanoprecipitation.

As well as the expansion of the scope of co-nanoprecipitation, the work presented in Chapter 3 provided a deeper understanding of the co-nanoprecipitation process and the factors which influence nanoparticle formation. In particular, this research showed the entrapment of amphiphilic AB block copolymers within the core of branched vinyl copolymers during co-nanoprecipitation. This is significant as previous studies had concluded that amphiphilic AB block copolymers led to the location of hydrophilic block segments solely at the surface of branched vinyl copolymer nanoparticles. However, the use of copolymers of increased hydrophobicity allowed the dependence of nanoparticle core polarity on AB block copolymer composition to be demonstrated and was highly indicative of polar PEG chains within the nanoparticle core. Co-nanoprecipitations conducted at varied branched to AB block copolymer ratios also showed the dependence of nanoparticle size on the concentration of amphiphilic block copolymers; this highlighted the importance of steric stabilisation in arresting nanoparticle growth during co-nanoprecipitation. This is of particular importance as it allows the composition of the initial THF solution to be used as a tool to control nanoparticle size, which is traditionally difficult to achieve through kinetically-controlled nanoprecipitation processes. Attempts to use copolymer concentration to control nanoparticle size were unsuccessful as steric stabilisation dominated the capping of nanoparticle growth during co-nanoprecipitation. This, however, brings alternative benefits as it allows aqueous nanoparticle dispersions to be prepared at a range of concentrations with negligible impact on nanoparticle size. This could allow the preparation of highly concentrated aqueous nanoparticle dispersions without having to compromise nanoparticle stability and uniformity, and would likely be of relevance in the preparation of drug-loaded aqueous nanoparticle dispersions at therapeutically relevant concentrations.

Finally, branched vinyl copolymer nanoparticles showed resistance to dilution and physiologically-relevant salt concentrations. This indicated that nanoparticles are likely to retain their structural integrity during pharmacological evaluations conducted in buffered and physiological media. This is important as it suggests that future *in vivo* studies of the pharmacology and immunology profiles of branched vinyl copolymer nanoparticles could be most likely conducted on intact, homogeneous nanoparticle dispersions rather than their aggregated or dissociated copolymer components. Furthermore, the resistance of branched vinyl copolymer nanoparticles to dilution ensures that drug release must occur *via* diffusion of encapsulated drug molecules through the copolymer matrix, rather than as a result of nanoparticle disassembly and subsequent burst release. This implies that such materials have the potential to modulate drug release over prolonged time periods.

5.1.3 Chapter 4

The primary aim of the research conducted throughout this thesis was to achieve the encapsulation and modulate the release of a hydrophobic chemotherapeutic, docetaxel, from branched vinyl copolymer nanoparticles formed *via* co-nanoprecipitation. This was achieved using 5 different branched vinyl copolymer systems. Docetaxel encapsulation experiments showed that relatively high loadings (15-25 wt %) of docetaxel could be achieved during co-nanoprecipitations of branched and amphiphilic AB block copolymers, with negligible impact on the stability and dispersity of branched vinyl copolymer nanoparticles. This is particularly noteworthy as the drug loadings achieved through co-nanoprecipitation are significantly higher than those previously reported using alternative nanoformulation approaches.[7–11] The ability to encapsulate high docetaxel payloads whilst maintaining nanoparticle size, monodispersity and stability is a promising sign for the use of branched vinyl copolymer nanoparticles as docetaxel nanocarriers. Interestingly, in many cases, increases in the weight fraction of docetaxel used in co-nanoprecipitation resulted in a reduction in nanoparticle hydrodynamic diameter. This was surprising given the reduced weight fraction of the AB block copolymer stabiliser and implied that docetaxel may participate in driving nucleation, or even arresting nanoparticle growth, during co-nanoprecipitation. This is particularly interesting for chemists conducting research on the formulation of water-insoluble chemotherapeutics. Drug encapsulation is often viewed as having negative impacts on nanoformulation approaches yet, in the case of co-nanoprecipitation, the presence of docetaxel appeared to aid nanoparticle formation.

Radiometric analyses proved to be an effective tool for the assessment of docetaxel encapsulation and release from branched vinyl copolymer nanoparticles formed *via* co-nanoprecipitation. Interestingly, significantly higher docetaxel encapsulation efficiencies (≥95.5 %) were achieved during co-nanoprecipitation of *p*(*n*BMA), *p*(*n*HMA) and *p*(EHMA)-derived copolymers although encapsulation efficiencies showed no correlation with the hydrophobicity of the copolymers from which nanoparticles were constructed. However, in all cases, encapsulation efficiencies ≥76.9 % were achieved during co-nanoprecipitations conducted at target drug loadings of 15 wt %. Docetaxel encapsulation was independent of branched copolymer hydrophobicity and therefore implied that docetaxel encapsulation during co-nanoprecipitation is under kinetic control. This may seem somewhat unsurprising given that nanoprecipitation processes are typically under kinetic control.[12] This poses real problems for the clinical translation of drug-loaded nanoformulations prepared by co-nanoprecipitation as the presence of free drugs within nanoformulations are often the main cause for sub-optimal burst release profiles observed both *in vivo* and within clinical settings.[13] It is therefore likely that aqueous nanoparticle dispersions will require either purification to remove free drug or

alternatively further development of formulation processes to increase the encapsulation efficiencies achieved during nanocarrier formation.

Radio-dialysis proved a simple and effective technique for measurement of docetaxel release rates from branched vinyl copolymer nanoparticles. Radio-dialyses clearly showed that the nanoparticle core hydrophobicity had a profound impact on docetaxel release rates. This was most apparent during comparisons of docetaxel release from *p*(*n*BMA), *p*(*n*HMA) and *p*(EHMA)-derived nanoparticles, which all achieved comparable encapsulation efficiencies, where release constants increased with repeat unit hydrophobicity. As would be expected, nanoparticles which achieved lower encapsulation efficiencies showed faster release rates, even in the case of *p*(LMA)-based nanoparticles which possessed the most hydrophobic repeat units. This highlighted the importance of ensuring high encapsulation efficiency during co-nanoprecipitation. Surprisingly, however, the strongest correlations were observed with copolymer viscosities. The rate of docetaxel release from branched vinyl copolymer nanoparticles was highly dependent on the temperature that radio-dialyses were conducted. This was linked to faster docetaxel diffusion rates caused by a reduction in the core viscosity of branched vinyl copolymer nanoparticles. The impact of copolymer viscosity is rarely mentioned in nanoparticle research papers. Although a more detailed study is required to further understand these relationships, it appears that this is an area of nanoparticle research that is not receiving significant attention. Given that polymer structure, architecture and molecular weight can all be manipulated without impacting the chemistry of the nanoparticle core, these polymer properties may offer a new tool which can be used to modulate hydrophobic payload release from polymer-based nanoparticles.

Kinetic analyses were used to determine docetaxel release constants for each of the nanoparticles studied. Release constants were then used to calculate docetaxel half-lives within the core of branched vinyl copolymer nanoparticles during radio-dialyses; this provided context for the observed release rates by showing that, at physiological temperature, over 50 % of docetaxel payloads remained encapsulated within branched vinyl copolymer nanoparticles after 12 hours. This demonstrated that significant amounts of docetaxel should remain within branched copolymer nanoparticles for sufficient time to allow nanoparticle accumulation within tumour tissues *via* the EPR effect. As a result significant increases in docetaxel internalisation within cancer cells would be expected when administered within branched vinyl copolymer nanoparticles. This may also reduce the associated toxicity due to reduced docetaxel uptake within healthy tissues.

5.2 Future Work

There are many ways that the research conducted in this thesis could be taken forward, here two future directions are highlighted: i) additional research to further develop the fundamental understanding of the specific materials presented in this thesis; and ii) expansion of preliminary research which aims to explore alternative functional handles to control the macroscopic behaviour of branched vinyl copolymer nanoparticles formed *via* co-nanoprecipitation. A series of recommendations for future work, including some data from preliminary experiments, are presented herein.

5.2.1 Further Development of the Research Conducted in this Thesis

Recommendations for the future development of this research can be broken down into three categories, these are: polymer chemistry, nanoparticle formulation *via* (co)nanoprecipitation and drug loading and release.

5.2.1.1 Chapter 2 – Polymer Chemistry

The work presented in Chapter 2 could open up numerous new avenues of polymer chemistry research. One being determination of the reasons behind the variation in control observed between Cu-RDRPs of different hydrophobic methacrylates. It is likely that the control exhibited during Cu-RDRP is related to the solubility of the $[Cu(bpy)_2]Cl$ catalytic system. Research should therefore aim to determine catalyst solubility within each of the monomer-alcohol mixtures. Furthermore, the use of ligands such as 4,4′-dinonyl-2,2′-bipyridine, could be used to prepare an alternative Cu-catalytic system which show higher solubility within low polarity monomer-alcohol mixtures. This would likely reduce the dispersity of polymers generated during Cu-RDRP of LMA and SMA. Kinetic studies of the Cu-RDRP of *n*HMA in anhydrous methanol showed that the onset of polymerisation-induced phase separation had negligible impact on polymerisation kinetics and the evolution of molecular weight. However, this was likely due to the onset of the phase separation occurring at high monomer conversion (92 %). Additional kinetic studies of the Cu-RDRP of all other hydrophobic methacrylates are therefore required to demonstrate the relationship between monomer polarity and the onset of polymerisation-induced phase separation. Furthermore, these studies can be used to understand the impact of phase separation on polymerisation kinetics and the evolution of molecular weight during Cu-RDRP in anhydrous alcohols.

The preparation of amphiphilic block copolymers *via* Cu-RDRP of hydrophobic methacrylates in polar alcohols offers the exciting prospect of the *in situ* preparation of block copolymer nanoparticles *via* polymerisation-induced self-assembly (PISA). The high solubility of hydrophobic methacrylates ranging from MMA to EHMA in anhydrous MeOH (≥ 50 wt %),

as well as that of LMA and SMA in IPA, combined with the low solubility of their resulting polymers would be expected to trigger PISA during Cu-RDRP. This research could be conducted using Cu-RDRP or alternatively *via* RAFT polymerisation using a MeOH-soluble macro-RAFT agent. This would allow the preparation of block copolymer nanoparticles consisting of hydrophobic domains which cannot be achieved *via* aqueous PISA.

Perhaps the most significant finding presented in Chapter 2 was the contrasting levels of branching observed during Cu-RDRcP of hydrophobic methacrylates with EGDMA in anhydrous alcohols. Future research must therefore look to further understand branching reactions both in Cu-RDRcP in anhydrous alcohols and more generally during statistical copolymerisations of monofunctional and bifunctional monomers. In particular, research must explore the experimental gel points for each of the copolymerisations of EGDMA with hydrophobic methacrylates ranging from MMA to SMA. This would facilitate the achievement of ideal branching behaviour during copolymerisation and would therefore permit the preparation of highly branched, high molecular weight copolymers using all of the hydrophobic methacylates studied in this Chapter. Future research in this area must seek to understand the impact of the following three factors: i) lower vinyl group concentration due to higher monomer side chain mass, ii) steric hindrance around pendant methacrylate groups and iii) the impact of polymer conformation within the polymerisation mixture. This will require the use of detailed branched copolymer characterisation techniques, i.e. quantification of the prevalence of intermolecular branching and intramolecular cyclisation *via* NMR spectroscopy.[14] Experimental conditions must be manipulated to allow each of these factors to be studied in isolation. Such experiments would therefore provide a detailed assessment of the impact of each of these factors on the nature of pendant methacrylate group consumption during copolymerisation.

5.2.1.2 Chapter 3 – Nanoparticle Formation via (Co)nanoprecipitation

The sole focus of the research presented in Chapter 3 was to develop branched vinyl copolymer nanoparticles *via* co-nanoprecipitation. As a result, alternative possibilities of (co)-nanoprecipitation research were not studied to the same level of detail as presented for branched vinyl copolymer nanoparticles. Future work should therefore look to explore such potential areas of nanoprecipitation research. The success of the nanoprecipitations of amphiphilic AB block copolymers is one area which should be studied further. This is especially relevant for amphiphilic AB block copolymers where hydrophobic domains consisted of *p*(*n*BMA), *p*(*n*HMA), *p*(EHMA) and *p*(LMA), which formed stable highly monodisperse aqueous nanoparticle dispersions with hydrodynamic diameters <100 nm. Research should therefore look to understand how factors such as experimental conditions and

copolymer properties influence nanoparticle formation *via* nanoprecipitation. Given the success of AB block copolymer nanoprecipitation, these materials should be considered as prospective nanocarriers of docetaxel, as well as a series of other hydrophobic active pharmaceutical ingredients.

Further research should also be conducted to improve the properties of nanoparticles formed *via* co-nanoprecipitation. Chapter 3 involved manipulation of experimental factors which impact nanoparticle formation. Future research should therefore look to understand the impact of polymer structure on the co-nanoprecipitation process. In particular, this should involve manipulation of the respective block lengths of the hydrophobic and hydrophilic domains of amphiphilic AB block copolymers. This should provide control over the size and density of the hydrophilic PEG shells which stabilise branched vinyl copolymer nanoparticles; furthermore, this may impact the nanoparticle formation process and could provide an enhanced level of control over nanoparticle size than was achieved *via* manipulation of experimental conditions. Further characterisation and imaging techniques are required to fully understand branched vinyl copolymer nanoparticles. Development of cryo-SEM techniques are ongoing and should be developed further to allow representative imaging of branched vinyl copolymer nanoparticles constructed from low T_g copolymers. Furthermore, analysis of nanoparticles in their aqueous state, for example using small-angle X-ray scattering,[15] could provide further evidence of the spherical morphology of branched vinyl copolymer nanoparticles.

Given the desire to use branched vinyl copolymer nanoparticles as docetaxel nanocarriers *in vivo*, pharmacological evaluation of such materials is an essential component of future research. Pharmacological evaluations must focus on assessing the safety and suitability of such nanomaterials to their application within physiological environments. This should involve determination of nanoparticle resistance to opsonisation and cytotoxicity to both healthy and cancerous cell lines. As they will likely be administered intravenously, the haematological behaviour of branched vinyl copolymer nanoparticles, such as their impact on blood coagulation, should also be assessed. It is important to determine the level of nanoparticle interaction with plasma proteins. Flow cytometry may therefore be used to determine the level of interaction between branched vinyl copolymer nanoparticles and proteins of the complement system.[16] This will provide an evaluation of the possible immunogenic properties of such nanomaterials and in particular should provide evidence for the role of the PEG shell in preventing opsonisation by plasma proteins. Nanoparticle cytotoxicity must be assessed for both healthy endothelial cells as well as for cancerous cell lines, and will provide an indication of whether branched vinyl copolymer nanoparticles are capable of acting as benign nanocarriers *in vivo*.

5.2.1.3 Chapter 4 – Understanding Drug Encapsulation and Release

The research presented in Chapter 4 showed that the use of ^{3}H-labelled docetaxel in drug loading co-nanoprecipitations allowed docetaxel encapsulation efficiencies (EE) and drug loadings (DL) to be determined *via* liquid scintillation counting (LSC). Future research should look to use this technique to investigate how EE and, by extension, DL vary with the targeted drug loading used in co-nanoprecipitation. This should allow optimisation of drug encapsulation for each of the copolymer systems studied in Chapter 4. This may allow the preparation of branched vinyl copolymer nanoparticle dispersions containing minimal free docetaxel, which could prevent initial burst release and high cytotoxicity typically associated with low encapsulation efficiencies of chemotherapeutics. Further efforts should also be made to increase the docetaxel concentration within aqueous nanoparticle dispersions. This should involve increasing the concentration at which co-nanoprecipitations are conducted and/or conducting multiple additions of the THF-copolymer-docetaxel solutions.[6] The potential to encapsulate hydrophobic chemotherapeutics during co-nanoprecipitation extends beyond docetaxel; studies should therefore be conducted using a range of other chemotherapeutics such as SN-38, paclitaxel and doxorubicin.

Future experiments should aim to further understand the links between copolymer properties and drug release rates. In particular, focus should move away from the functionality of the copolymer repeat unit and should consider the physical properties of the polymer materials. In particular, research should seek to understand the impact of copolymer crystallinity, viscosity and polarity on the release of encapsulated payloads. This research should involve systematic variations in copolymer properties in order to isolate individual physical properties and aid the identification of trends with drug release rates; in particular, this could be achieved *via* copolymerisation of monomers which generally produce copolymers of varied physical and chemical properties. Where possible, this should be supported with physical and chemical characterisation techniques. Preliminary work has been conducted in this area and is presented in Section 5.2.2.1.

Finally, pharmacological evaluation should also be conducted for docetaxel-loaded branched vinyl copolymer nanoparticles. This would allow assessment of the cytotoxicity and the extent of cellular internalisation of nanoformulated docetaxel encapsulated within branched vinyl copolymer nanoparticles, in comparison to unformulated docetaxel. *In vivo* tumour models would also allow the impact of encapsulation on the accumulation of docetaxel within tumour tissues to be understood. Furthermore, this would allow comparison with similar experiments conducted using unloaded branched vinyl copolymer nanoparticles, recommended in Section 5.2.1.2.

5.2.2 Alternative Approaches to Manipulation of Nanoparticle Properties

Whilst the work discussed in Chapters 2 – 4 focused on the manipulation of nanoparticle core chemistry using copolymers consisting of a sole type of hydrophobic monomer, alternative strategies were also studied to manipulate the properties of branched vinyl copolymer nanoparticles. These included: i) systematic variation of nanoparticle properties *via* co-nanoprecipitations of statistical copolymers; ii) using branched copolymer end-groups to modify the core of branched vinyl copolymer nanoparticles; and iii) preparation of branched vinyl copolymers containing varied hydrophilic shell functionality. Preliminary experiments were conducted in order to assess the feasibility of future research in each of these areas.

5.2.2.1 Optimisation of Nanoparticle Properties using Bespoke Copolymers

In Chapters 3 and 4, the hydrophobic repeat units of branched and AB block copolymers made up the vast majority of the mass of branched vinyl copolymer nanoparticles formed *via* co-nanoprecipitation. It was for this reason that the hydrophobic repeat unit functionality had such a significant impact on the macroscopic properties of the branched vinyl copolymers formed. For example, large contrasts were observed in nanoparticle formation, core polarity and docetaxel release rates between branched vinyl copolymer nanoparticles constructed from HPMA and EHMA. It is therefore possible that control over nanoparticle properties could be achieved by systematic variation of the structures and compositions of the copolymers from which they are constructed. Preliminary research was therefore conducted to see if this could be achieved *via* statistical copolymerisation of different hydrophobic monomers used in this thesis. Given that *p*(HPMA) and *p*(EHMA) based nanoparticles showed the fastest and slowest docetaxel release rates during radio-dialyses conducted in Chapter 4, preliminary research aimed to prepare statistical branched and AB block copolymers, constructed from HPMA and EHMA, across a range of monomer compositions.

Given the success of Cu-RDRP of both HPMA and EHMA in anhydrous MeOH, presented in Chapter 2, this approach was used for the preparation of branched and AB block statistical copolymers. The synthetic approaches used to prepare branched and AB block copolymers are presented in Figure 5.1. Branching copolymerisations targeted a DP_n of 60 monomer units ($[M]_0/[I]_0 = 60$) and a nominal branching ratio of 0.90 molar equivalents of EGDMA per unit of the BzBiB initiator ($[B]_0/[I]_0 = 0.90$). AB block copolymerisations were conducted using the PEG_{45}-Br macro-initiator, synthesised in Chapter 2, and targeted a total number average degree of polymerisation of 120 monomer units ($[M]_0/[I]_0 = 120$). Branched and AB block copolymers were prepared containing varied molar ratios of HPMA and EHMA; this was achieved by conducting copolymerisations using mole fractions (X_f) of HPMA:EHMA of 1.00: 0.00, 0.90: 0.10, 0.75: 0.25, 0.50: 0.50, 0.25: 0.75, 0.10: 0.90 and 0.00: 1.00.

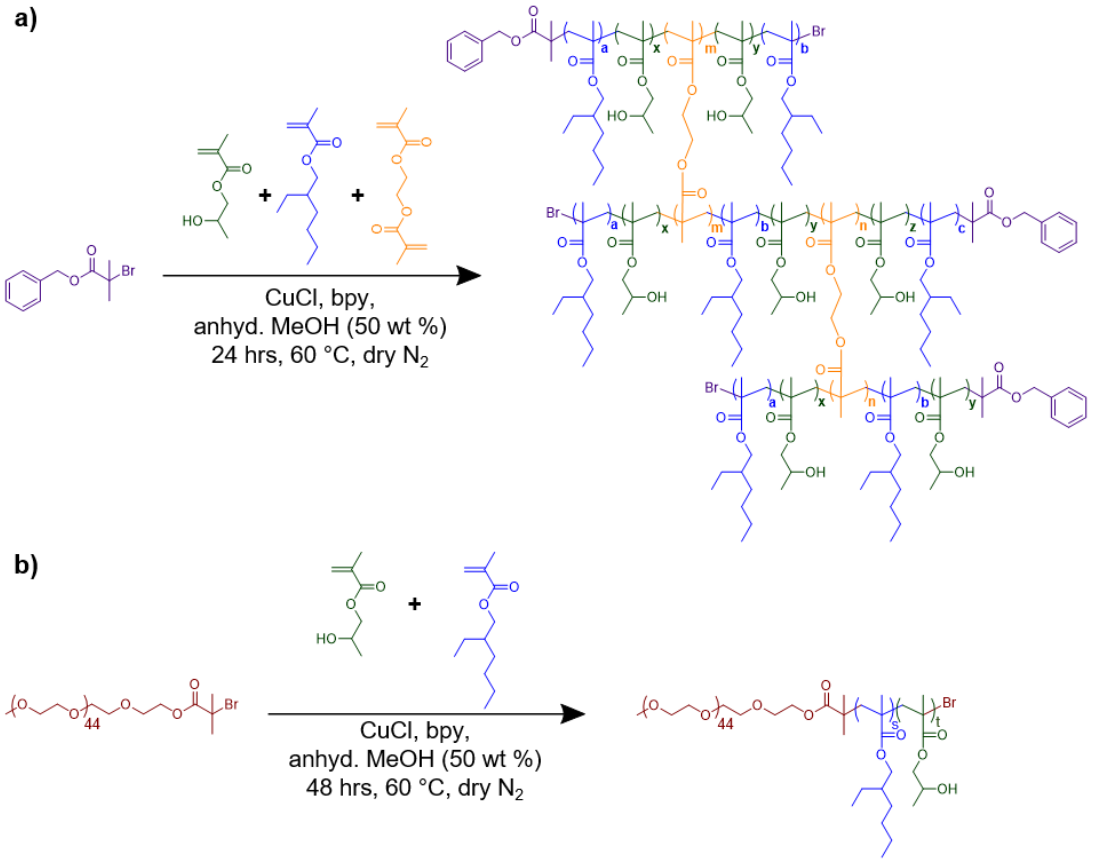

Figure 5.1 Schematic representation of the synthesis routes used for the preparation of a) branched and b) AB block statistical copolymers *via* Cu-RDRP at 50°C in anhydrous MeOH.

Interestingly, comonomer composition had a profound impact on the homogeneity of reaction mixtures observed during copolymerisations. In the preparation of both branched and AB block copolymers, copolymerisations conducted using HPMA $X_f \geq 0.10$ remained homogeneous throughout the course of the copolymerisation, whereas polymerisation-induced phase separation occurred in copolymerisations conducted at HPMA $X_f \leq 0.10$. This was somewhat unsurprising given the high EHMA content, especially as polymerisation-induced phase separation was observed during branching copolymerisations of EHMA conducted in Chapter 2. Despite the occurrence of polymerisation-induced phase separation, branching copolymerisations achieved high monomer conversion (≥97 %) in all cases. The purified branched copolymers were assessed by TD-SEC (Table 5.1). In all cases, the number-average molecular weights obtained were significantly higher than theoretical number-average molecular weights. This indicates the formation of branched macromolecular architectures by coupling of primary chains during copolymerisation, as supported by the low MHS exponents ($\alpha \leq 0.50$), representative of densely-packed structures, obtained from MHS plots. This demonstrated that branched statistical copolymer architectures containing more than one hydrophobic methacrylate monomer can be achieved *via* Cu-RDRcP in anhydrous MeOH at 60 °C.

Table 5.1 Branched and AB block statistical copolymers prepared *via* RDRcP of HPMA and EHMA in anhydrous MeOH at 60 °C.

	^{1}H NMR					TD-SEC (THF/TEA)			
	$[M]_0$ /$[I]_0$[a]	$[B]_0$ /$[I]_0$[a]	HPMA X_f[a]	EHMA X_f[a]	Conv. (%)[b]	M_w (g mol^{-1})[c]	M_n (g mol^{-1})[c]	$Đ$[c]	α[c]
p(EHMA$_{60}$-*co*-EGDMA$_{0.90}$)	60	0.90	1.00	0.00	>99	698 200	33 300	20.96	0.378
p(EHMA$_{54}$-*co*-HPMA$_6$-*co*-EGDMA$_{0.90}$)	60	0.90	0.90	0.10	>99	794 500	42 500	18.69	0.378
p(EHMA$_{45}$-*co*-HPMA$_{15}$-*co*-EGDMA$_{0.90}$)	60	0.90	0.75	0.25	98	185 000	37 600	4.92	0.403
p(EHMA$_{30}$-*co*-HPMA$_{30}$-*co*-EGDMA$_{0.90}$)	60	0.91	0.50	0.50	97	155 000	38 300	4.05	0.406
p(EHMA$_{15}$-*co*-HPMA$_{45}$-*co*-EGDMA$_{0.90}$)	60	0.90	0.25	0.75	99	254 600	57 200	4.45	0.389
p(EHMA$_6$-*co*-HPMA$_{54}$-*co*-EGDMA$_{0.90}$)	61	0.90	0.10	0.90	>99	485 300	57 100	8.49	0.281
p(HPMA$_{60}$-*co*-EGDMA$_{0.90}$)	60	0.90	0.00	1.00	98	302 500	28 000	10.82	0.349
PEG$_{45}$-*b*-*p*(EHMA)$_{120}$	120	-	1.00	0.00	99	33 400	28 100	1.19	0.574
PEG$_{45}$-*b*-*p*(EHMA$_{108}$-*co*-HPMA$_{12}$)	120	-	0.90	0.10	97	40 800	31 200	1.31	0.460
PEG$_{45}$-*b*-*p*(EHMA$_{90}$-*co*-HPMA$_{30}$)	120	-	0.75	0.25	97	35 200	27 700	1.27	0.498
PEG$_{45}$-*b*-*p*(EHMA$_{60}$-*co*-HPMA$_{60}$)	120	-	0.50	0.50	97	37 300	26 300	1.41	0.466
PEG$_{45}$-*b*-p(EHMA$_{30}$-*co*-HPMA$_{90}$)	120	-	0.25	0.75	98	34 000	29 100	1.17	0.571
PEG$_{45}$-*b*-*p*(EHMA$_{12}$-*co*-HPMA$_{108}$)	120	-	0.10	0.90	99	35 300	30 600	1.15	0.582
PEG$_{45}$-*b*-*p*(HPMA)$_{120}$	120	-	0.00	1.00	98	23 000	18 500	1.22	0.409

[a]Determined by ^{1}H NMR studies of the polymerisation prior to addition of the CuCl. [b]Determined by ^{1}H NMR studies of the polymerisation mixture at t_f. [C]Obtained by TD-SEC analysis of the purified copolymer in THF/TEA (98/2 v/v%) at 35 °C and a flow rate of 1 mL min^{-1}.

The preparation of AB block copolymers were conducted over 48 hours in order to accommodate the higher target DP_n of 120 monomer units. As a result, copolymerisations achieved high monomer conversion (≥97 %) in all cases. Analysis of AB block copolymers by TD-SEC showed good agreement between experimental and theoretical number-average molecular weights. Furthermore, molecular weight distributions generally showed low dispersity, which is indicative of a controlled RDRP process. However, high molecular weight shoulders within the RI chromatograms were observed for all copolymerisations involving HPMA. Similar observations have been made during polymerisations of hydroxyl-functional methacrylates containing low amounts of BFM impurities.[17] It is also possible that the formation of a high molecular weight fraction occurred as a result of small amounts of termination by combination due to prolonged exposure to monomer-starved conditions over the 48 hour reaction time. Nonetheless, these reactions showed that AB block copolymers containing hydrophobic blocks of varied monomer composition could be prepared with a degree of control over copolymer molecular weight *via* Cu-RDRcP in anhydrous MeOH.

Statistical copolymerisations were conducted in order to manipulate the chemical and physical properties of branched vinyl copolymer nanoparticles. In particular, given the contrast in the core polarities and branched copolymer complex viscosities identified in Chapter 4, preliminary studies sought to demonstrate whether systematic variation in copolymer composition could be used to influence the macroscopic behaviour. Branched copolymers were therefore subjected to the same rheological analyses shown in Chapter 4 (Figure 5.2).

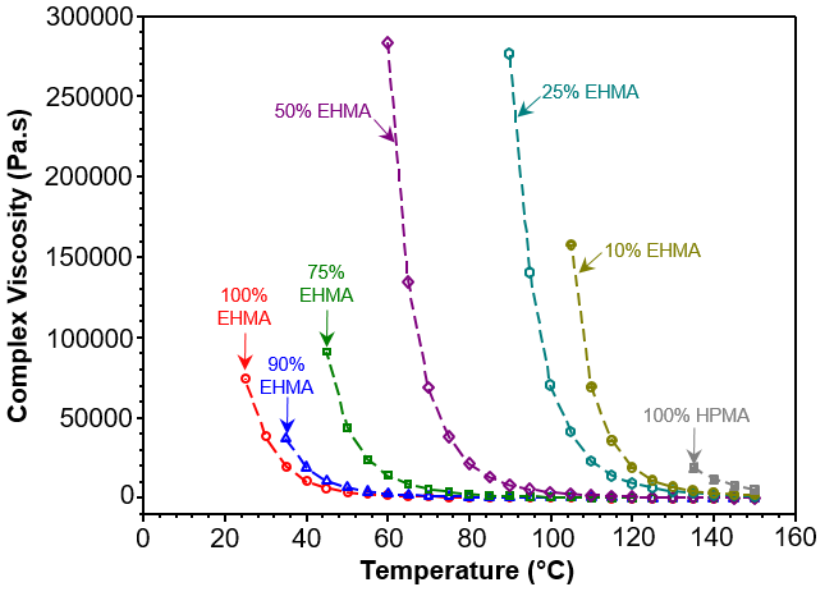

Figure 5.2 The impact of monomer composition on the complex viscosity of branched statistical copolymers formed *via* Cu-RDRcP. Rheological analyses of branched statistical copolymers containing varied monomer compositions using an oscillatory reverse temperature sweep from 150 – 25 °C.

Rheological analysis on cooling from 150 to 25 °C showed that copolymer complex viscosities were highly dependent upon branched copolymer composition. The temperature at which dramatic increases in complex viscosity were observed increased as the EHMA composition was decreased. This demonstrated that branched copolymer complex viscosity can be influenced by the composition and type of hydrophobic monomers distributed along the primary chain backbone. By extension, this indicated that it is possible to use monomer composition to manipulate the core viscosity of branched vinyl copolymer nanoparticles formed *via* co-nanoprecipitation. However, it must be noted that all branched copolymer complex viscosities recorded at 25 °C were significantly higher than that of the *p*(LMA$_{70}$-*co*-EGDMA$_{1.22}$) studied in Chapter 4. As a result, it is unlikely that the changes in complex viscosity shown here would be sufficient to influence docetaxel release rates from branched vinyl copolymer nanoparticles. Future studies could therefore look to replace EHMA with a hydrophobic methacrylate monomer that would form branched copolymers containing lower complex viscosities than those observed for *p*(EHMA$_{60}$-*co*-EGDMA$_{0.90}$).

Co-nanoprecipitation of the corresponding statistical branched and AB block copolymers were conducted in order to understand whether the variation in copolymer properties, which arise as a result of manipulation of monomer composition, translate to the macroscopic properties of branched vinyl copolymer nanoparticles. Co-nanoprecipitations were conducted using branched and AB block copolymers containing identical weight fractions of EHMA and HPMA. For example, the branched copolymer, *p*(EHMA$_{30}$-*co*-HPMA$_{30}$-*co*-EGDMA$_{0.90}$), was co-nanoprecipitated with the AB block copolymer, PEG$_{45}$-*b*-*p*(EHMA$_{60}$-*co*-HPMA$_{60}$). This allowed the overall hydrophobic X_f of each monomer within the core of the resulting branched vinyl copolymers to be known. Co-nanoprecipitations utilised equal weight fractions of branched and AB block copolymers ($\omega_i = 0.5$) and were conducted from THF (1 mL, $[P]_0 = 5$ mg mL^{-1}) into DI H_2O (5 mL, DR = 5) under magnetic stirring. In addition, pyrene (1 wt %) was added into the initial THF-copolymer solution in order to facilitate measurement of the core polarity of branched vinyl copolymer nanoparticles using fluorescence emission spectroscopy. In all cases, co-nanoprecipitations were successful and showed no sign of copolymer sedimentation. The resulting aqueous nanoparticle dispersions were assessed using DLS, zeta potential measurements and fluorescence emission spectroscopy (Table 5.2).

Table 5.2 Analysis of aqueous nanoparticle dispersions formed through co-nanoprecipitations of branched and AB block statistical copolymers containing varied molar ratios of EHMA and HPMA repeat units.

EHMA X_f	HPMA X_f	D_z (nm)[a]	D_n (nm)[a]	*PDI*[a]	ζ (mV)[b]	I_1/I_3[c]
1.00	0.00	131	116	0.014	-9.84	1.07
0.90	0.10	112	95	0.019	-14.3	1.09
0.75	0.25	103	85	0.037	-13.6	1.10
0.50	0.50	91	69	0.071	-10.4	1.17
0.25	0.75	89	65	0.083	-12.9	1.22
0.10	0.90	84	69	0.023	-10.1	1.34
0.00	1.00	77	59	0.055	-23.8	1.60

[a]Obtained by DLS analysis of aqueous nanoparticle dispersions at a concentration of 1 mg mL^{-1}. [b]Zeta potentials measured at a concentration of 0.01 M KCl. [c]Obtained *via* fluorescence emission spectroscopy of encapsulated pyrene.

In all cases, stable and highly monodisperse nanoparticles were produced from co-nanoprecipitations of branched and AB block copolymers across the whole monomer composition range studied. This showed that it is possible to manipulate nanoparticle core chemistry without having a negative impact on nanoparticle formation *via* co-nanoprecipitation. In all cases, highly monodisperse branched vinyl copolymer nanoparticles were formed. This indicated nanoparticle formation *via* homogeneous nucleation and subsequent diffusion-limited cluster-cluster aggregation (DLCA) growth mechanism. Interestingly, copolymer composition had a significant impact on the hydrodynamic diameter and the internal polarity of branched vinyl copolymer nanoparticles (Figure 5.3). Both intensity- and number-average hydrodynamic diameters showed a general increase with EHMA composition; for example, intensity-average hydrodynamic diameters of 77, 91 and 131 nm were recorded for branched vinyl copolymer nanoparticles containing EHMA X_f of 0.0, 0.5 and 1.0 respectively. In contrast, nanoparticle core polarities decreased with increasing EHMA composition with obtained I_1/I_3 ratios showing a general decrease from 1.60 to 1.07 over the range of copolymer compositions studied. This demonstrated that copolymer composition could be used to achieve a significant level of control over the macroscopic properties of branched vinyl copolymer nanoparticles formed *via* co-nanoprecipitation.

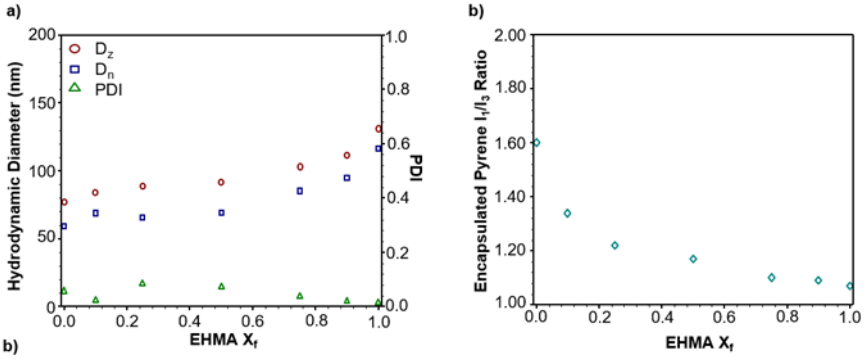

Figure 5.3 Analysis of branched vinyl copolymer nanoparticles formed *via* co-nanoprecipitation of branched and AB block copolymers containing varied comonomer compositions. a) The impact of copolymer composition on nanoparticle size and dispersity. b) The impact of copolymer composition on the internal polarity of branched vinyl copolymer nanoparticles.

Given that copolymer composition had a profound effect on nanoparticle properties, docetaxel encapsulation and release studies were conducted to determine whether these effects influenced their performance as potential docetaxel nanocarriers. Co-nanoprecipitations were conducted using equal weight fractions of branched and AB block copolymers ($\omega_i = 0.425$), a docetaxel weight fraction of 0.15 and were conducted from THF (1 mL, $[P]_0 = 5$ mg mL^{-1}) into DI H_2O (5 mL, DR = 5) under magnetic stirring. Co-nanoprecipitations were conducted using ^{3}H labelled docetaxel (targeted specific activity = 6.5 μCi mg^{-1}) in order to allow measurement of docetaxel EE, DL and release rates using radiometric analyses (Table 5.3).

Table 5.3 Analysis of the encapsulation and release of ^{3}H-labelled docetaxel from branched vinyl copolymer nanoparticles of varied monomer composition.

EHMA X_f	HPMA X_f	D_z (nm)[a]	D_n (nm)[a]	*PDI*[a]	EE[b]	DL (%)[b]	k (s^{-1})[c]	$t_{1/2}$ (hrs)[c]
1.00	0.00	81	54	0.095	0.974	12.7	70.6	35.3
0.90	0.10	126	96	0.067	0.972	11.9	83.1	30.0
0.75	0.25	104	70	0.111	0.807	11.0	152.3	16.4
0.50	0.50	121	88	0.079	0.837	11.9	138.2	18.1
0.25	0.75	102	83	0.045	0.889	11.7	137.5	18.1
0.10	0.90	107	88	0.027	0.865	10.7	318.6	7.80
0.00	1.00	86	58	0.111	0.769	11.0	401.7	6.21

[a]Obtained by DLS analysis of aqueous nanoparticle dispersions at a concentration of 1 mg mL^{-1}. [b]Determined by radiometric analyses following purification *via* centrifugation. [C]Obtained from radio-dialyses of ^{3}H-docetaxel loaded branched vinyl copolymer nanoparticles at 37 °C.

The resulting ^{3}H labelled aqueous nanoparticle dispersions were also assessed by DLS. The size trends observed in branched vinyl copolymer nanoparticles produced *via* co-nanoprecipitation in the absence of docetaxel were not observed during docetaxel loading co-nanoprecipitations. As was shown in Chapter 4, this indicated that the presence of docetaxel impacted nanoparticle formation during the co-nanoprecipitation process. Interestingly, the docetaxel EE generally increased with EHMA X_f which, contrary to observations made in

Chapter 4, indicated that the functionality of branched copolymer repeat units did impact the EE achieved during co-nanoprecipitation in this case.

Radio-dialyses of ^{3}H-docetaxel loaded branched vinyl copolymer nanoparticles were conducted at 37 °C over 24 hours in order to determine the impact of copolymer composition on the docetaxel release rates (Figure 5.4). Radio dialyses showed that copolymer composition had a profound impact on docetaxel release. Results generally showed that docetaxel release rates decreased as the EHMA X_f was increased. This reiterated findings in Chapter 4 which showed that the chemistry of copolymer repeat units had a significant impact on the release of docetaxel from branched vinyl copolymer nanoparticles. The order of docetaxel release rates were comparable for nanoparticles containing EHMA X_f from 0.25 to 0.75. This can be explained by the lower EE observed for nanoparticles containing EHMA X_f of 0.75. Docetaxel release rates can therefore be thought of as products of both the EE achieved during co-nanoprecipitation and the rates at which encapsulated docetaxel is released from branched vinyl copolymer nanoparticles. This demonstrated that, although the nanoparticle core functionality is an important factor in docetaxel release rates, a high EE is essential to allow modulation of docetaxel release from branched vinyl copolymer nanoparticles.

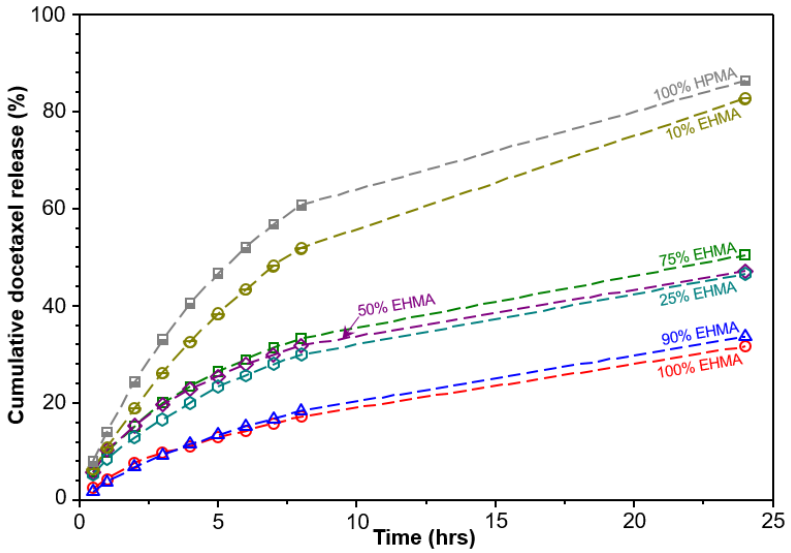

Figure 5.4 Release of ^{3}H-labelled docetaxel from branched vinyl copolymer nanoparticles consisting of varied comonomer compositions during radio-dialysis over 24 hours.

These preliminary results demonstrate that it is possible to influence the properties of branched vinyl copolymer nanoparticles *via* systematic variation of the composition of copolymers used in co-nanoprecipitation. As a result, this approach can be used to influence the EE achieved during co-nanoprecipitation and modulate docetaxel release profiles from branched vinyl copolymer nanoparticles. These results may inspire future research aiming to optimise the encapsulation and release of docetaxel, or other hydrophobic drugs, from branched vinyl copolymer nanoparticles formed through co-nanoprecipitation. Research should look at using

alternative monomer pairings to influence specific nanoparticle properties (i.e. core polarity, viscosity or nanoparticle size); this approach could be used to manipulate each of these nanoparticle properties in isolation and may therefore allow their impact on drug encapsulation and release to be studied. Furthermore, this approach could be used to incorporate repeat units which, alone, are incapable of forming stable branched vinyl copolymer nanoparticles through co-nanoprecipitation. For example, statistical copolymerisation of EHMA with BzMA may allow aromatic character to be incorporated into the core of branched vinyl copolymer nanoparticles. This may have a further impact on influencing the encapsulation and release of hydrophobic chemotherapeutics.

5.2.2.2 Copolymer End-Groups to Modulate Docetaxel Release

The work presented in Chapters 2, 3 and 4 focused on the use of monomer functionality to influence the core chemistry of branched vinyl copolymer nanoparticles. Future research must therefore look to exploit alternative functional handles and assess their impact on influencing the macroscopic behaviour of branched vinyl copolymer nanoparticles. As identified in Chapter 1, polymer end-groups enable chemical functionality to be integrated into both polymers and the resultant nanomaterials that they are used to construct. Future research should therefore look to assess whether end-group chemistry can be used to influence the rate of docetaxel release from branched vinyl copolymer nanoparticles. This could be achieved by the selection of chemical functionalities which can promote host-guest interactions between branched copolymers and docetaxel, which make up the nanoparticle core, and encapsulated docetaxel molecules. There are many directions that this research could take. Hyper-branched polydendrons are an established macromolecular architecture designed to amplify chemical functionality at branched copolymer end-groups;[18–22] this approach therefore offers one potential synthetic route to influence docetaxel release rates via control over the functionality of branched copolymer end-groups.

The research presented in this thesis focused on modulating the docetaxel release. It was hypothesised that, in order to influence docetaxel release from branched vinyl copolymer nanoparticles, branched copolymer end-groups must possess a high affinity for docetaxel. Preliminary studies therefore aimed to incorporate docetaxel at the end-groups of branched copolymers formed *via* Cu-RDRcP. The synthetic route taken to prepare such docetaxel functional branched copolymers is outlined in Figure 5.5.

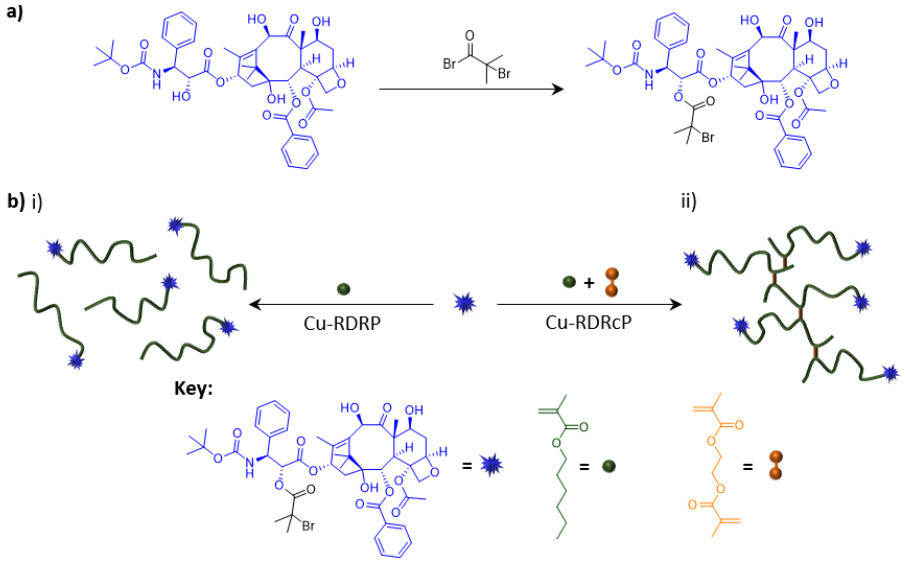

Figure 5.5 Schematic representation of the incorporation of docetaxel at the end-groups of branched copolymers prepared by Cu-RDRP. a) The preparation of a monofunctional docetaxel initiator *via* esterification of docetaxel with α–bromoisobutyryl bromide. b) The preparation of docetaxel-polymers conjugates containing i) linear homopolymer and ii) branched copolymer architectures.

Briefly, this involved preparation of a docetaxel functional alkyl bromide initiator, which was subsequently employed for both the homopolymerisation of *n*HMA and its copolymerisation with EGDMA. The docetaxel-based initiator was prepared *via* esterification of docetaxel with α-bromoisobutyryl bromide, using a similar approach to those described for the preparation of benzyl- and PEG-based initiators in Chapter 2. The presence of multiple docetaxel hydroxyl groups meant that a mixture of products were isolated from the reaction. Purification *via* column chromatography confirmed the formation of monofunctional, bifunctional and trifunctional docetaxel initiators, which were characterised *via* electrospray ionisation mass spectrometry, ^{1}H and ^{13}C NMR spectroscopy (Appendix, Figures A5.1 – A5.3). ^{1}H and ^{13}C NMR of the monofunctional adduct showed that the initiating moiety was exclusively located at the hydroxyl β to the amide group, as shown in Figure 5.5. This was consistent with the order of hydroxyl reactivity identified during previously reported functionalisation of docetaxel and other taxanes.[23–25]

The monofunctional docetaxel initiator was later employed in the Cu-RDRP of *n*HMA at 60 °C in anhydrous MeOH (Table 5.4). Cu-RDRP was facilitated by a $[Cu(bpy)_2]Cl$ catalytic system and targeted a DP_n of 50 monomer units. As had been observed for Cu-RDRP of *n*HMA in anhydrous MeOH using a benzyl-based initiator, polymerisation-induced phase separation occurred during polymerisation and resulted in the formation of a biphasic reaction mixture. Despite the onset of polymerisation-induced phase separation, the polymerisation achieved high monomer conversion (> 99 %) and subsequent analysis of the purified polymer by TD-SEC showed a monomodal molecular weight distribution of low dispersity ($Đ$ = 1.14).

TD-SEC analysis showed that docetaxel initiators achieved high initiation efficiency ($IE_{(TD\text{-}SEC)}$ = 93 %). This was higher than had been achieved during Cu-RDRP conducted using BzBiB in Chapter 2 (77 %). This highlighted that the docetaxel-based macro-initiator was able to facilitate polymerisation of *n*HMA without hindering the RDRP process. Branching copolymerisations were also conducted by addition of small amounts of EGDMA under identical polymerisation conditions and showed identical phase behaviour to linear homopolymerisations.

Table 5.4 Characterisation of (co)polymers produced from linear polymerisation and branched statistical copolymerisation of *n*HMA using a monofunctional docetaxel initiator.

Polymer	^{1}H NMR ($CDCl_3$)			IE	TD-SEC (THF/TEA)			
	$[M]_0/[I]_0$[a]	$[B]_0/[I]_0$[a]	Conv. (%)[b]	(%)[c]	M_w (g mol^{-1})[d]	M_n (g mol^{-1})[d]	$Đ$[d]	α[d]
dctx-*p*(*n*HMA)$_{55}$	51	-	>99	93	11 900	10 400	1.14	0.676
dctx-*p*(*n*HMA$_{54}$-*co*-EGDMA$_{0.97}$)	50	0.90	>99	-	185 200	32 000	6.59	0.384

[a]Obtained from ^{1}H NMR spectroscopy of the polymerisation mixture prior to initiation. [b]Obtained from ^{1}H NMR spectroscopy of polymerisation mixture following deactivation of the Cu-catalyst. [c]Obtained by comparison of theoretical and experimental M_n values determined by ^{1}H NMR and TD-SEC respectively. [d]Determined *via* TD-SEC in THF/TEA at a flow rate of 1 mL min^{-1}.

In contrast to the linear homopolymer, the branched copolymer exhibited a broad molecular weight distribution ($Đ$ = 6.59, Figure 5.6) and had a significantly higher molecular weight (M_w = 185 200 g mol^{-1}). This demonstrated that the onset of phase separation had not prevented the formation of branched copolymers during Cu-RDRcP of *n*HMA with EGDMA. The branched copolymer architecture was further confirmed by the lower MHS exponents. However, the overlap between the RI output signals obtained for *dctx*-*p*(*n*HMA)$_{55}$ and the low molecular weight fraction of *dctx*-*p*(*n*HMA$_{54}$-*co*-EGDMA$_{0.97}$) highlight the presence of linear primary chains within the molecular weight distribution. This indicated that further work is required to manipulate reaction conditions in order to promote optimal branching reactions during copolymerisation.

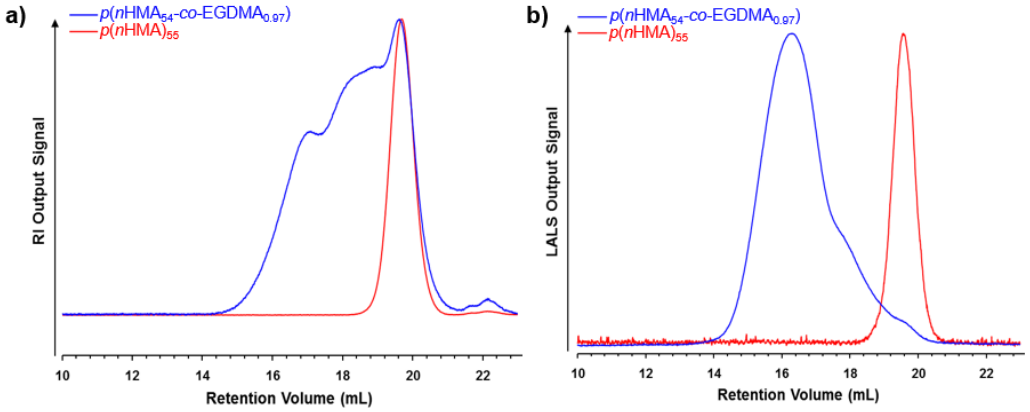

Figure 5.6 TD-SEC analysis of linear and branched (co)polymers generated *via* Cu-RDRP from a docetaxel-based macro-initiator. Overlaid a) RI and b) LALS chromatograms obtained for *p*(*n*HMA)$_{55}$ (red) and *p*(*n*HMA$_{54}$-*co*-EGDMA$_{0.97}$) (blue).

Co-nanoprecipitation studies were conducted to investigate whether docetaxel-functional branched copolymers could be successfully incorporated into the core of branched vinyl copolymer nanoparticles (Figure 5.7). This involved co-nanoprecipitation of *dctx*-*p*(*n*HMA$_{54}$-*co*-EGDMA$_{0.97}$) with the amphiphilic AB block copolymer, PEG$_{45}$-*b*-*p*(*n*HMA)$_{127}$, prepared in Chapter 2. The co-nanoprecipitation was conducted using equal weight fractions of *dctx*-*p*(*n*HMA$_{54}$-*co*-EGDMA$_{0.97}$) and PEG$_{45}$-*b*-*p*(*n*HMA)$_{127}$. Co-nanoprecipitations were conducted from THF (1 mL, $[P]_0$ = 5 mg mL^{-1}) into DI H_2O (5 mL, DR = 5). The co-nanoprecipitation of *dctx*-*p*(*n*HMA$_{54}$-*co*-EGDMA$_{0.97}$) and PEG$_{45}$-*b*-*p*(*n*HMA)$_{127}$ yielded a turbid, translucent aqueous nanoparticle dispersion. Analysis by DLS showed that the nanoparticles formed were highly monodisperse (*PDI* = 0.028) and possessed intensity- and number-average hydrodynamic diameters of 97 and 78 nm respectively. This showed that the presence of docetaxel end-group functionality had little impact on nanoparticle formation. Furthermore, the size distributions and hydrodynamic diameters were comparable to that obtained from the co-nanoprecipitation of PEG$_{45}$-*b*-*p*(*n*HMA)$_{127}$ with the branched copolymer, *p*(*n*HMA$_{68}$-*co*-EGDMA$_{1.03}$), which contained benzyl end-group functionality (Figure 5.7b).

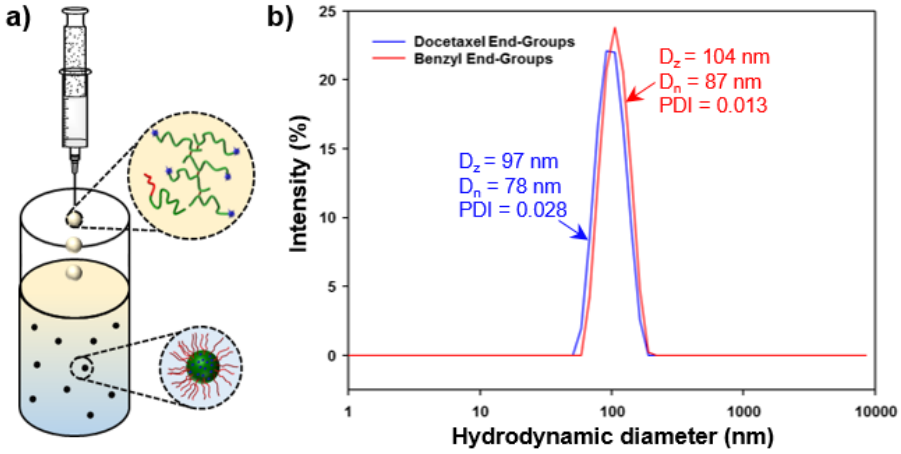

Figure 5.7 Incorporation of *dctx*-*p*(*n*HMA$_{54}$-*co*-EGDMA$_{0.97}$) into branched vinyl copolymer nanoparticles *via* co-nanoprecipitation. a) Schematic representation of the co-nanoprecipitation process through which nanoparticles are formed and b) overlaid nanoparticle size distributions obtained from DLS analysis of aqueous nanoparticle dispersions constructed from branched copolymers containing docetaxel and benzyl end-group functionalities.

The preliminary results demonstrate that docetaxel can be incorporated into the core of branched vinyl copolymer nanoparticles *via* covalent attachment at branched copolymer end-groups. Interestingly, at a primary chain DP_n of 54 monomer units, docetaxel occupied 9.4 wt % of the branched copolymer mass. As a result, branched copolymer nanoparticles were formed containing a *dctx*-*p*(*n*HMA$_{54}$-*co*-EGDMA$_{0.97}$) weight fraction of 0.5, and a docetaxel loading of 4.7 wt % and 100 % encapsulation efficiency would be expected during co-nanoprecipitation.

The preliminary results presented here demonstrate that covalent conjugation of docetaxel at the end-groups of branched copolymers can be used to incorporate this drug within the core of branched vinyl copolymer nanoparticles formed *via* co-nanoprecipitation. This approach can therefore be used to drive future research. In particular, research should look to understand whether i) the presence of docetaxel moieties at branched copolymer end-groups affects the encapsulation efficiency of unbound docetaxel during co-nanoprecipitation; and ii) the presence of docetaxel end-groups impact the release of unbound docetaxel from branched vinyl copolymer nanoparticles during radio-dialysis. Furthermore, research should look to understand whether the ester linkages between docetaxel and α-terminus of primary chains can be cleaved in the presence of esterase enzymes. This research also suggests that it may be possible to incorporate docetaxel at alternative points on different macromolecular architectures. For example, the reaction of docetaxel with methacryloyl chloride should produce a docetaxel monomer which would place docetaxel units along the polymer (co)backbone. Research should also look to increase the composition of docetaxel within branched vinyl copolymer nanoparticles. This could be achieved in two ways: i) decreasing the primary chain DP_n or ii) increasing the weight fraction of *dctx*-*p*(*n*HMA$_{54}$-*co*-EGDMA$_{0.97}$) used during co-nanoprecipitation.

5.2.2.3 Alternative Block Copolymers to Modify Nanoparticle Shell Functionality

The work presented in this thesis demonstrated that it is possible to encapsulate and modulate the release of docetaxel from branched vinyl copolymers formed through co-nanoprecipitation. Future research should begin to explore how such nanoparticles behave in biological and physiological environments; in particular, how nanoparticles interact with plasma proteins, cell membranes and over-expressed receptors on cell surfaces. The hydrophilic shell which surrounds the hydrophobic core of branched vinyl copolymer nanoparticles is the component which has the highest level of interaction with the external environment. Future research could therefore look to explore the significance of the chemical functionality of the hydrophilic components that make up the nanoparticle shell, and should look to understand how they influence the macroscopic behaviour of such nanoparticles.

Preliminary research has been conducted to assess the feasibility of varying the shell functionality of branched vinyl copolymer nanoparticles. This involved the preparation of a series of amphiphilic AB block copolymers which contain varied hydrophilic functionalities. These materials were then used as stabilisers in co-nanoprecipitations with the hydrophobic branched copolymer, *p*(*n*HMA$_{68}$-*co*-EGDMA$_{1.03}$). The synthetic approach employed in the preparation of amphiphilic AB block copolymers is presented in Figure 5.8.

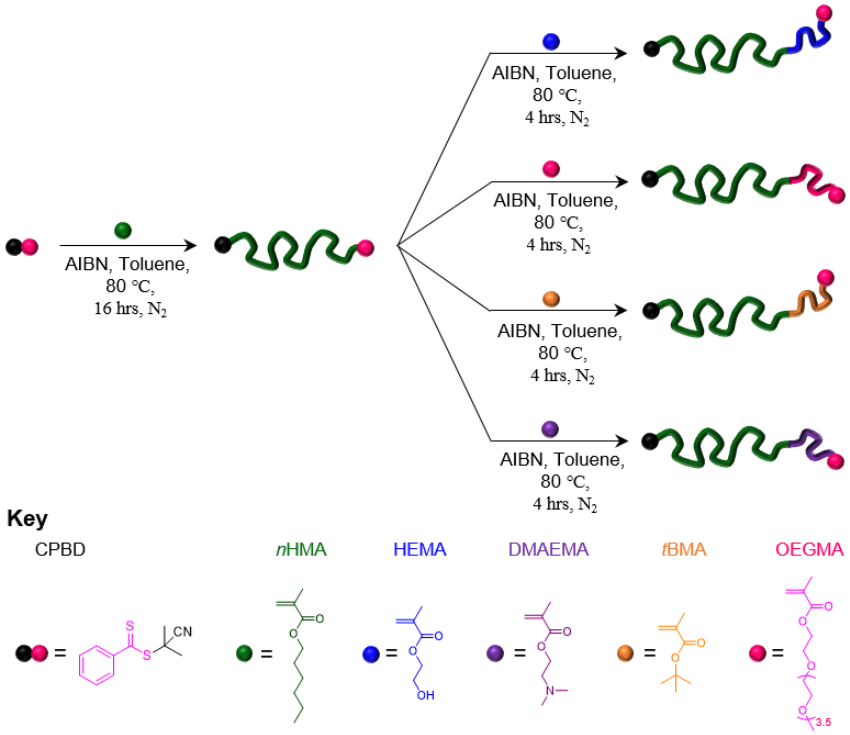

Figure 5.8 Schematic representation of the preparation of AB block copolymers *via* RAFT polymerisation. i) Preparation of a *p*(*n*HMA) macro-RAFT agent *via* polymerisation of *n*HMA using RAFT. ii) A series of separate chain extensions of the *p*(*n*HMA) macro-RAFT agent using a range of different methacrylate monomers.

The preparation of a *p*(*n*HMA) based macro-RAFT agent was achieved *via* RAFT polymerisation of *n*HMA in toluene at 80 °C for 16 hours. ^{1}H NMR analysis of the purified macro-CTA showed a DP_n of 122 and, more importantly, high retention of the dithiobenzoate end-group. Further characterisation by TD-SEC showed a narrow molecular weight distribution ($Đ$ = 1.12) which was indicative of a controlled polymerisation (Table 5.5). The purified macro-RAFT agent was then used in the preparation of AB block copolymerisation *via* separate chain extensions with oligo(ethylene glycol) monomethacrylate (OEGMA, M_n = 300 g mol^{-1}), 2-(dimethylamino) ethyl methacrylate (DMAEMA), 2-hydroxyethyl methacrylate (HEMA) and *t*BMA. The decision to chain-extend with *t*BMA was made as it was hypothesised that if co-nanoprecipitations involving *p*(nHMA$_{122}$-*b*-*t*BMA$_{16}$) fail, the importance of conducting chain extensions with a hydrophilic monomer would be highlighted; this would therefore reiterate the importance of hydrophilic domains of AB block copolymers in stabilising branched vinyl copolymer nanoparticles during co-nanoprecipitation. Short chain lengths were targeted for the second copolymer block in order to retain sufficient overall hydrophobicity and therefore to ensure that AB block copolymers experience a state of supersaturation during co-nanoprecipitation. Chain extensions were conducted in toluene at 80 °C and were stopped after 4 hours, following which AB block copolymers were purified and characterised by TD-SEC. In all cases, an increase in molecular weight was observed in comparison to that of the original macro-RAFT agent. Furthermore, AB block copolymers

exhibited low dispersities ($Đ$ = ≤1.22) which again showed that RAFT polymerisations had proceeded in a controlled manner. In all cases, AB block copolymers showed negligible solubility in DI H_2O which indicated that all AB block copolymers should experience a state of supersaturation during co-nanoprecipitation.

Table 5.5 Characterisation of the *p*(*n*HMA) macro-RAFT agent and AB block copolymers formed during subsequent chain extension using a number of methacrylate monomers.

	^{1}H NMR ($CDCl_3$)				TD-SEC (THF/TEA)		
	$[M]_0$ /$[CTA]_0$[a]	Conv. (%)[b]	DP_n[c]	Time (hrs)	M_w (g mol^{-1})[d]	M_n (g mol^{-1})[d]	$Đ$[d]
p(*n*HMA)$_{122}$	125	95	122	16	17 000	15 200	1.12
p(*n*HMA$_{122}$-*b*-OEGMA$_{11}$)	20	57	122, 11	4	24 700	21 100	1.18
p(*n*HMA$_{122}$-*b*-*t*BMA$_{16}$)	20	82	122, 16	4	21 200	18 800	1.13
p(*n*HMA$_{122}$-*b*-HEMA$_{14}$)	20	70	122, 14	4	23 750	19 400	1.22
p(*n*HMA$_{122}$-*b*-DMAEMA$_{19}$)	20	97	122, 19	4	22 850	19 350	1.18

[a] Calculated through ^{1}H NMR analysis of the polymerisation mixture prior to initiation. [b] Calculated through ^{1}H NMR analysis of the polymerisation mixture after the polymerisation had been stopped. [C] Macro-RAFT agent DP_n calculated from ^{1}H NMR of the purified polymer. DP_n of second block calculated as DPn = ($[M]_0$/$[CTA]_0$ x conv.)/100. Dd Obtained from TD-SEC analysis in THF/TEA (98/2 v/v %) conducted at 35 °C at a flow rate of 1 mL min^{-1}.

The AB block copolymers prepared by RAFT polymerisation were studied as stabilisers in co-nanoprecipitation with the hydrophobic branched copolymer *p*(*n*HMA$_{68}$-*co*-EGDMA$_{1.03}$). An overview of the co-nanoprecipitations conducted is presented in Figure 5.9. Briefly, co-nanoprecipitations involved equal weight fractions of *p*(*n*HMA$_{68}$-*co*-EGDMA$_{1.03}$) and the respective AB block copolymer (ω_i = 0.5) and were conducted from THF (1 mL, $[P]_0$ = 5 mg mL^{-1}) into DI H_2O (5 mL, DR = 5, $[P]_f$ = 1 mg mL^{-1}) under magnetic stirring and were left for 48 hours to ensure complete THF removal *via* evaporation. In addition to the AB block copolymers produced using RAFT polymerisation, separate co-nanoprecipitations were also conducted using PEG$_{45}$-*b*-*p*(*n*HMA)$_{127}$ and the *p*(*n*HMA)$_{122}$ macro-RAFT agent.

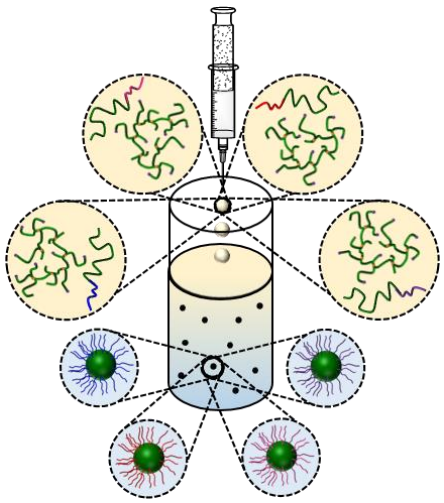

Figure 5.9 A general overview of the co-nanoprecipitations of *p*(*n*HMA$_{68}$-*co*-EGDMA$_{1.03}$) with a range of AB block copolymer stabilisers to produce branched vinyl copolymer nanoparticles containing varied shell functionalities.

With the exception of those conducted using *p*(*n*HMA$_{122}$-*b*-*t*BMA$_{16}$) and the *p*(*n*HMA)$_{122}$ macro-RAFT agent as the stabiliser blocks, all co-nanoprecipitations were successful and created turbid, translucent aqueous nanoparticle dispersions with no signs of sedimentation. In contrast, co-nanoprecipitations conducted using *p*(*n*HMA$_{122}$-*b*-*t*BMA$_{16}$) and the *p*(*n*HMA)$_{122}$ macro-RAFT agent as stabilisers resulted in (co)polymer sedimentation and were deemed to have failed. This reiterated the importance of the hydrophilic components of amphiphilic AB block copolymers in the stabilisation of growing nanoparticles during co-nanoprecipitation with hydrophobic branched polymers. All aqueous nanoparticle dispersions generated from successful co-nanoprecipitations were assessed using DLS. Interestingly, little size difference was observed between nanoparticles generated using different AB block copolymer stabilisers, which were comparable to that of the aqueous nanoparticle dispersion of PEG$_{45}$-*b*-*p*(*n*HMA)$_{127}$ and *p*(*n*HMA$_{68}$-*co*-EGDMA$_{1.03}$), also discussed in Chapter 3. DLS studies showed that all aqueous nanoparticle dispersions were highly monodisperse (*PDI* ≤0.090), which indicated growth *via* a DLCA growth mechanism.

Sole nanoprecipitations were conducted to investigate the role of AB block copolymers during co-nanoprecipitation. Despite the absence of *p*(*n*HMA$_{68}$-*co*-EGDMA$_{1.03}$), sole nanoprecipitations were performed using identical conditions to those used for the co-nanoprecipitations described above. As would be expected for an AB block copolymer that does not contain a hydrophilic block, the nanoprecipitation of *p*(*n*HMA$_{122}$-*b*-*t*BMA$_{16}$) was unsuccessful and resulted in macroscopic aggregation and subsequent copolymer sedimentation. This reiterated claims, made in Chapter 3, that the success of the sole nanoprecipitation of an AB block copolymer is highly indicative of its ability to stabilise growing nanoparticles during co-nanoprecipitation. In contrast, nanoprecipitations of *p*(*n*HMA$_{122}$-*b*-OEGMA$_{11}$), *p*(*n*HMA$_{122}$-*b*-HEMA$_{14}$) and *p*(*n*HMA$_{122}$-*b*-DMAEMA$_{19}$) produced translucent/turbid and colloidally stable aqueous nanoparticle dispersions and showed no sign of copolymer sedimentation. Nanoparticles were assessed using DLS (see Table 5.6) and showed slightly reduced hydrodynamic diameters to their corresponding branched vinyl copolymer nanoparticles produced *via* co-nanoprecipitation with *p*(*n*HMA$_{68}$-*co*-EGDMA$_{1.03}$). This indicated that the inherent increase in stabiliser concentration, which accompanied the increase in the AB block copolymer weight fraction from 0.5 to 1.0, produced smaller nanoparticles. Interestingly, aqueous nanoparticle dispersions formed *via* the sole nanoprecipitation of *p*(*n*HMA$_{122}$-*b*-OEGMA$_{11}$) and *p*(*n*HMA$_{122}$-*b*-HEMA$_{14}$) exhibited higher *PDI* values compared to those formed from co-nanoprecipitation with *p*(*n*HMA$_{68}$-*co*-EGDMA$_{1.03}$). This indicated that these AB block copolymers underwent slower nucleation in the absence of *p*(*n*HMA$_{68}$-*co*-EGDMA$_{1.03}$). It is possible that the use of alternative hydrophilic blocks, which would undoubtedly have contrasting levels of interaction with and therefore

solubility in DI H_2O, could influence the state of supersaturation achieved during co-nanoprecipitation.

Table 5.6 DLS analysis of aqueous nanoparticle dispersions produced *via* co-nanoprecipitation of *p*(*n*HMA$_{68}$-*co*-EGDMA$_{1.03}$) with polymeric stabilisers and sole nanoprecipitations of AB block copolymers.

	Hydrophobic domain	Stabiliser	D_z (nm)	D_n (nm)	*PDI*
Co-nanoprecipitation	*p*(*n*HMA$_{68}$-*co*-EGDMA$_{1.03}$)	*p*(*n*HMA)$_{122}$	-[a]	-[a]	-[a]
	p(*n*HMA$_{68}$-*co*-EGDMA$_{1.03}$)	*p*(*n*HMA$_{122}$-*b*-OEGMA$_{11}$)	100	79	0.049
	p(*n*HMA$_{68}$-*co*-EGDMA$_{1.03}$)	*p*(*n*HMA$_{122}$-*b*-HEMA$_{14}$)	110	78	0.090
	p(*n*HMA$_{68}$-*co*-EGDMA$_{1.03}$)	*p*(*n*HMA$_{122}$-*b*-DMAEMA$_{19}$)	104	86	0.036
	p(*n*HMA$_{68}$-*co*-EGDMA$_{1.03}$)	PEG$_{45}$-*b*-*p*(*n*HMA)$_{127}$	99	78	0.035
	p(*n*HMA$_{68}$-*co*-EGDMA$_{1.03}$)	*p*(*n*HMA$_{122}$-*b*-*t*BMA$_{16}$)	-[a]	-[a]	-[a]
Sole nanoprecipitation	-[b]	*p*(*n*HMA$_{122}$-*b*-OEGMA$_{11}$)	90	50	0.196
	-[b]	*p*(*n*HMA$_{122}$-*b*-HEMA$_{14}$)	98	67	0.107
	-[b]	*p*(*n*HMA$_{122}$-*b*-DMAEMA$_{19}$)	78	63	0.034
	-[b]	*p*(*n*HMA$_{122}$-*b*-*t*BMA$_{16}$)	-[a]	-[a]	-[a]

[a]Co-nanoprecipitation failed – sedimentation observed. Reliable DLS analysis could not be obtained. [b]Sole nanoprecipitation of AB block copolymer - no branched copolymer used.

The work presented here demonstrates that it is possible to prepare branched vinyl copolymer nanoparticles containing shell functionalities beyond the PEG$_{45}$ used throughout this thesis. This approach could therefore be used to control the surface functionality of branched vinyl copolymer nanoparticles and hence allow their interactions with biological and physiological components to be influenced. Synthetic polymer chemistry should be used to vary the functionality, density and length of the hydrophilic blocks that make up the shell of branched vinyl copolymer nanoparticles. Future research should involve pharmacological evaluation of the impact of shell functionality on nanoparticle behaviour in both biological and physiological environments. In particular, research should seek to understand the impact of shell functionality on the cytotoxicity, cellular uptake and opsonisation of branched vinyl copolymer nanoparticles *in vitro*.

5.3 References

1 A. B. Dwyer, P. Chambon, A. Town, T. He, A. Owen and S. P. Rannard, *Polym. Chem.*, 2014, **5**, 3608–3616.

2 A. B. Dwyer, P. Chambon, A. Town, F. L. Hatton, J. Ford and S. P. Rannard, *Polym. Chem.*, 2015, **6**, 7286–7296.

3 H.-J. Yang, B.-B. Jiang, W.-Y. Huang, D.-L. Zhang, L.-Z. Kong, J.-H. Chen, C.-L. Liu, F.-H. Gong, Q. Yu and Y. Yang, *Macromolecules*, 2009, **42**, 5976–5982.

4 P. Polanowski, J. K. Jeszka, W. Li and K. Matyjaszewski, *Polymer.*, 2011, **52**, 5092–5101.

5 J. Rosselgong, S. P. Armes, W. R. S. Barton and D. Price, *Macromolecules*, 2010, **43**, 2145–2156.

6 J. Ford, P. Chambon, J. North, F. L. Hatton, M. Giardiello, A. Owen and S. P. Rannard, *Macromolecules*, 2015, **48**, 1883–1893.

7 J. M. Benito, M. Gómez-García, C. Ortiz Mellet, I. Baussanne, J. Defaye and J. M. García Fernández, *J. Am. Chem. Soc.*, 2004, **126**, 10355–10363.
8 U. Boas and P. M. H. Heegaard, *Chem. Soc. Rev.*, 2004, **33**, 43–63.
9 P. K. Jain, I. H. El-Sayed and M. A. El-Sayed, *Nano Today*, 2007, **2**, 18–29.
10 A. S. Mikhail and C. Allen, *Biomacromolecules*, 2010, **11**, 1273–1280.
11 S.-S. Feng, L. Mei, P. Anitha, C. W. Gan and W. Zhou, *Biomaterials*, 2009, **30**, 3297–3306.
12 W. S. Saad and R. K. Prud'Homme, *Nano Today*, 2016, **11**, 212–227.
13 B. Sharma, R. M. Crist and P. P. Adiseshaiah, *AAPS J.*, 2017, **19**, 1632–1642.
14 J. Rosselgong and S. P. Armes, *Macromolecules*, 2012, **45**, 2731–2737.
15 E. E. Brotherton, F. L. Hatton, A. A. Cockram, M. J. Derry, A. Czajka, E. J. Cornel, P. D. Topham, O. O. Mykhaylyk and S. P. Armes, *J. Am. Chem. Soc.*, 2019, **141**, 13664–13675.
16 N. J. Liptrott, M. Giardiello, J. W. Hunter, L. Tatham, L. R. Tidbury, M. Siccardi, S. Rannard and A. Owen, *Nanomedicine*, 2014, **10**, 1407–1421.
17 L. Ratcliffe, A. Blanazs, C. N. Williams, S. L. Brown and S. Armes, *Polym. Chem.*, 2014, **5**, 3643–3655.
18 F. L. Hatton, L. M. Tatham, L. R. Tidbury, P. Chambon, T. He, A. Owen and S. P. Rannard, *Chem. Sci.*, 2015, **6**, 326–334.
19 F. L. Hatton, P. Chambon, A. C. Savage and S. P. Rannard, *Chem. Commun.*, 2016, **52**, 3915–3918.
20 F. L. Hatton, P. Chambon, T. O. McDonald, A. Owen and S. P. Rannard, *Chem. Sci.*, 2014, **5**, 1844–1853.
21 F. Y. Hern, A. Hill, A. Owen and S. P. Rannard, *Polym. Chem.*, 2018, **9**, 1767–1771.
22 H. E. Rogers, P. Chambon, S. E. R. Auty, F. Y. Hern, A. Owen and S. P. Rannard, *Soft Matter*, 2015, **11**, 7005–7015.
23 Y. Bao, E. Guégain, J. Mougin and J. Nicolas, *Polym. Chem.*, 2018, **9**, 687–698.
24 B. Louage, M. J. van Steenbergen, L. Nuhn, M. D. P. Risseeuw, I. Karalic, J. Winne, S. Van Calenbergh, W. E. Hennink and B. G. De Geest, *ACS Macro Lett.*, 2017, **6**, 272–276.
25 A. S. Mikhail and C. Allen, *Biomacromolecules*, 2010, **11**, 1273–1280.

Chapter 6

Experimental

6.1 Materials

Methyl methacrylate (MMA, 99 %) ethyl methacrylate (EMA, 99%), *n*-butyl methacrylate (*n*BMA 99 %), *t*-butyl methacrylate (*t*BMA 99 %), *n*-hexyl methacrylate (*n*HMA, 99 %), cyclohexyl methacrylate (CHMA, 99 %), benzyl methacrylate (BzMA, 96 %), 2-ethyl hexyl methacrylate (EHMA, 99 %), lauryl methacrylate (LMA, 99 %), stearyl methacrylate (SMA, 99 %), copper (I) chloride (Cu(I)Cl, 99 %), deuterated chloroform ($CDCl_3$, 98.8 atom % D), pyrene (99 %), α-bromo isobutyryl bromide (99 %), benzyl alcohol (99 %), anhydrous tetrahydrofuran (a. THF, 99.8 %) anhydrous triethyl amine (TEA, 99 %), dimethyl amino pyridine (DMAP, 99 %), 2,2' – bipyridine (bpy, 99%), anhydrous methanol (a. MeOH, 99.8 %), anhydrous propan-2-ol (a. IPA, 99.8 %) and aluminium oxide (activated, neutral) were purchased from Sigma Aldrich. Tetrahydrofuran (THF, reagent grade), chloroform ($CHCl_3$, reagent grade), methanol (MeOH, reagent grade), acetone (reagent grade), ethyl acetate (reagent grade), ethanol (reagent grade), toluene (reagent grade), hexane (reagent grade) and petroleum ether (40 - 60 ° C, reagent grade) were purchased from Fisher Scientific. Docetaxel was purchased from Chemleader Biochemical. ProSafe+ scintillation cocktail (Meridian Biotechnologies Ltd.). All materials were used as received. Tritiated docetaxel was purchased from American Radiolabelled Chemical, Inc.in an ethanol solution. Ethanol was removed before experiments conducted.

6.2 Characterisation

^{1}H and ^{13}C nuclear magnetic resonance (NMR) spectra were recorded in $CDCl_3$ using a Bruker Avance spectrometer operating at 400 and 100 MHz respectively. Chemical shifts (δ) are reported in parts per million (ppm) and TMS was used as an internal standard for both ^{1}H and ^{13}C NMR spectra. Triple detection size exclusion chromatography (SEC) was conducted using a Malvern Viscotek instrument equipped with a GPCmax VE2001 auto-sampler, two viscotek T6000 columns (and a guard column), a refractive index (RI) detector VE3580 and a dual 270 detector (light scattering and viscometer). SEC was performed at a flow rate of 1 mL min^{-1} using THF (containing 2 v/v % of TEA) as the mobile phase. Fluorescence spectra were obtained using a Shimadzu RF-5301PC spectrofluorophotometer. Emission spectra for pyrene were recorded between 350 and 500 nm. An excitation wavelength of λ_{ex} = 335 nm was used for all studies as well as an excitation slit width of 2.5 nm and an emission slit width of 2.5 nm with a scan rate of 60 nm min^{-1}. Electrospray (ESI) mass spectrometry data were recorded in the Mass Spectrometry Laboratory at the University of Liverpool using a MicroMass LCT mass spectrometer using electron ionisation and direct infusion syringe pump sampling. All materials were diluted with methanol. Elemental analyses were obtained from a Thermo FlashEA 1112 series CHNSO elemental analyser.

Dynamic light scattering (DLS) and zeta potential measurements were performed at 25 °C using a Malvern Zetasizer Nano ZS instrument (laser wavelength = 630 nm) at a nanoparticle concentration, unless otherwise stated, of 1 mg mL^{-1}. Scanning electron microscopy (SEM) images were obtained using a Hitachi S-4800 FE-SEM. Sample preparation involved dropping the aqueous samples on to silicon wafers mounted on an aluminium stub with a carbon tab. Samples were dropped directly onto SEM stubs and left to dry overnight. Samples were then subjected to gold sputter coating at 20 mA for 2 minutes prior to imaging. All radiation measurements were carried out using a liquid scintillation counter (Packard Tri-Carb 3100TR; Isotech) and radio-TLC analysed on an AR-2000 radio-TLC imaging scanner (Bioscan Inc.)

6.3 Methods

6.3.1 Chapter 2

6.3.1.1 Monomer-Alcohol Miscibility Studies

Monomer-solvent miscibility studies were conducted at a monomer concentration of 50 weight percent (50 wt %) with respect to the total mass of the monomer-solvent mixture. Solvent miscibility was assessed visually at both ambient and elevated (60 °C) temperatures. In a typical experiment, MMA (1.00 g, 9.99 mmol) and anhydrous methanol (1.00 g, 1.26 mL) were added to a glass vial and sealed. The vial was agitated gently in order to give ample opportunity for mixing, after which monomer-solvent miscibility at ambient temperature was assessed visually. A magnetic stirrer bar was then added, the vial was re-sealed with a rubber septum and placed in an oil bath at 60 °C under magnetic stirring. After 10 minutes, the vial was withdrawn from the oil bath and monomer-alcohol miscibility at an elevated temperature was assessed visually.

6.3.1.2 Pyrene Fluorescence Emission Spectroscopy of Monomer, Solvent and Monomer-Alcohol Solutions

Pyrene emission fluorescence spectroscopy was conducted at a pyrene concentration of 10 nM. Solutions were prepared with pyrene dissolved in: neat methacrylic monomers, common organic solvents, monomer-MeOH mixtures or monomer-IPA mixtures. As in the miscibility studies described in Section 6.3.1.1, monomer-alcohol mixtures were prepared at a monomer concentration of 50 wt %. In a typical experiment, an acetone stock solution of pyrene was added to a glass vial (300 µL, 0.1 mg mL^{-1}). The vial was left in a low velocity fumehood overnight, allowing complete evaporation of acetone, to give a known quantity of solid pyrene (0.03 mg, 1.48 x 10^{-4} mmol). Following addition of the MMA-MeOH mixture (14.8 mL, 50 wt %), the vial was sealed and placed on an orbital mixer to ensure full dissolution of pyrene. The solution (ca. 1.00 mL) was added to a quartz cuvette and placed in a Shimadzu RF-5301PC spectrofluorophotometer. A fluorescence emission spectrum was

recorded between 350 nm and 500 nm following excitation at 335 nm. The polarity of all pyrene solutions were determined using the I_1/I_3 ratio, by comparison of the relative intensities of the first (I_1, *ca.* 373 nm) and third (I_3, *ca.* 384 nm) vibrational bands of the pyrene fluorescence emission (Appendix, Figure A6.1).

6.3.1.3 Synthesis of Benzyl Initiator

Benzyl alcohol (5.00 g, 46.2 mmol), anhydrous TEA (7.02 g, 69.4 mmol) and DMAP (0.565g, 4.62 mmol) were added to an oven dried round bottomed flask containing a magnetic stirrer bar and was equipped with a pressure equalising dropping funnel. The round bottom flask was purged with nitrogen followed by addition of anhydrous THF (100 mL), the solution was cooled to 0 ℃ in an ice bath. α-bromo isobutyryl bromide (13.8 g, 7.43 mL, 60.1 mmol) and anhydrous THF (25.0 mL) were added dropwise over 30 minutes *via* the pressure equalising dropping funnel and the reaction could be observed to occur immediately by the formation of the of a white precipitate. After one hour the ice bath was removed and the reaction was allowed to proceed for a further 23 hours. The precipitate was removed by filtration and the THF from the filtrate was removed *in vacuo*. The product was then extracted using diethyl ether and dried *in vacuo* to give a colourless oil. The pure product was isolated by silica gel column chromatography using a hexane/ethyl acetate mobile phase (95/5 volume %), R_f = 0.44, giving a colourless oil (71 %). ^{1}H NMR (400 MHz, $CDCl_3$) δ ppm 7.40 – 7.30 (m, 5H), 5.21 (s, 2H), 1.95 (s, 6H). ^{13}C NMR (100 MHz, $CDCl_3$) δ ppm 171.5, 135.4, 128.6, 128.4, 127.9, 67.6, 55.7, 30.8. m/z (ES MS) 274.0 $[M^+NH4]^+$ m/z required 256.01 $[M]^+$. $C_{11}H_{13}BrO_2$ requires C, 51.38; H, 5.98; Br, 18.96; O, 15.19 %. Found C, 51.62; H, 5.75 %

6.3.1.4 Synthesis of Poly(Ethylene Glycol) Macro-Initiator (PEG_{45}-Br)

This synthesis was conducted in accordance with the method previously reported.[1–3] Poly(ethylene glycol) methyl ether (20.5 g, 10.3 mmol), anhydrous TEA (3.14 mL, 22.5 mmol) and DMAP (158 mg, 1.30 mmol) were added to an oven dried round bottomed flask containing a magnetic stirrer bar and was equipped with a pressure equalising dropping funnel. The round bottom flask was purged with nitrogen followed by addition of anhydrous DCM (100 mL) and the solution was cooled to 0 ℃ in an ice bath. α-bromo isobutyryl bromide (3.69 g, 2.78 mL, 22.5 mmol) and anhydrous DCM (25.0 mL) were added dropwise over 30 minutes *via* the pressure equalising dropping and the reaction could be observed immediately by the formation of the of a white precipitate. After one hour the ice bath was removed and the reaction was allowed to proceed at ambient temperature for a further 23 hours. The precipitate was removed by filtration and the resulting solution was diluted in DCM and passed over a basic alumina column. The product was dried *in vacuo*, re-dissolved in a minimum amount of acetone and precipitated three times from acetone into petroleum ether

(B.P. = 40 - 60 °C). The resulting white solid was dried *in vacuo* at 40 °C for 72 hours to give poly(ethylene glycol)$_{45}$ 2-bromo-2-methyl propanoate (PEG$_{45}$-Br). Purified PEG$_{45}$-Br was assessed by ^{1}H NMR in order to determine the number average degree of polymerisation (DP_n) and molecular weight (Mn). DP_n (NMR) = 45, M_n (NMR) = 2130 (Appendix, Figure A6.2). ^{1}H NMR (400 MHz, D_2O) δ ppm: 4.40 (t, 2H), 3.90 – 3.60 (s, 182 H), 3.40 (s, 3H), 1.98 (s, 6H).

6.3.1.5 General Procedure for the Synthesis of Linear Homopolymers by Cu-RDRP (MMA, EMA, nBMA, tBMA, nHMA, CHMA, BzMA, EHMA, LMA and SMA)

Prior to use, all monomers and initiators were deoxygenated *via* gentle bubbling with N_2 for 60 minutes. In a typical synthesis of a methacrylic linear homopolymer targeting DP_n = 60 monomer units, *n*HMA (5.00 g, 29.4 mmol), bpy (153 mg, 0.979 mmol) and BzBiB (126 mg, 0.489 mmol) were added to an oven dried round bottom flask (25 mL) equipped with a magnetic stirrer bar. The reaction solvent, either anhydrous MeOH (6.73 mL, 50 wt %) or anhydrous IPA (6.74 mL, 50 wt %), was added and the resulting solution was purged with N_2 for a further 15 minutes. At this point a sample was withdrawn (ca. 100 µL) and diluted in $CDCl_3$ allowing quantification of $[M]_0/[I]_0$ by ^{1}H NMR (Figure 6.1).

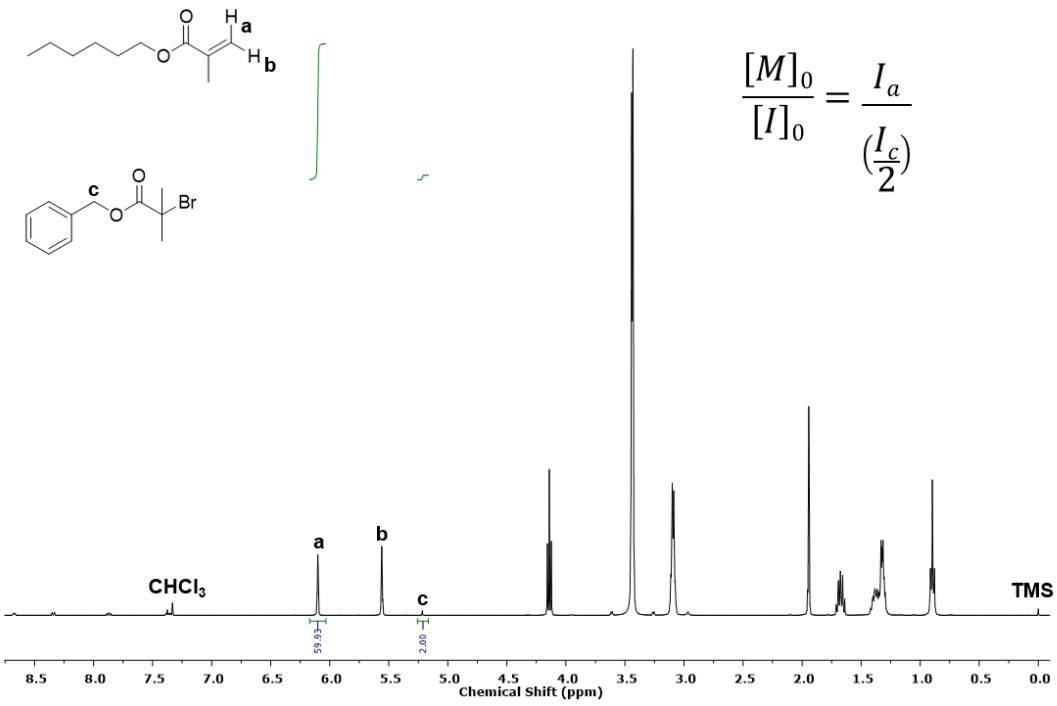

Figure 6.1 Quantification of $[M]_0/[I]_0$ for the polymerisation of *n*HMA by analysis of the reaction mixture, prior to initiation, using ^{1}H NMR spectroscopy ($CDCl_3$, 400 MHz).

Cu(I)Cl (48.5 mg, 0.489 mmol) was added rapidly to the flask, and instantly formed a brown solution. The reaction was then purged with N_2 for a further 60 seconds, sealed and swiftly submerged into an oil bath preheated at 60 °C. In some cases (MMA, *t*BMA and *n*BMA) the

reaction mixture remained homogeneous throughout the reaction and phase separation only occurred on cooling following removal from the oil bath at 60 °C. In all other cases (*n*HMA, CHMA, EHMA, LMA and SMA) phase separation occurred during polymerisation and the reaction proceeded as a biphasic mixture. The reaction was stopped after 24 hours by dilution with $CDCl_3$ until a homogeneous blue/green solution was obtained, at this point a sample (*ca.* 500 μL) was taken for quantification of monomer conversion by ^{1}H NMR (Figure 6.2).

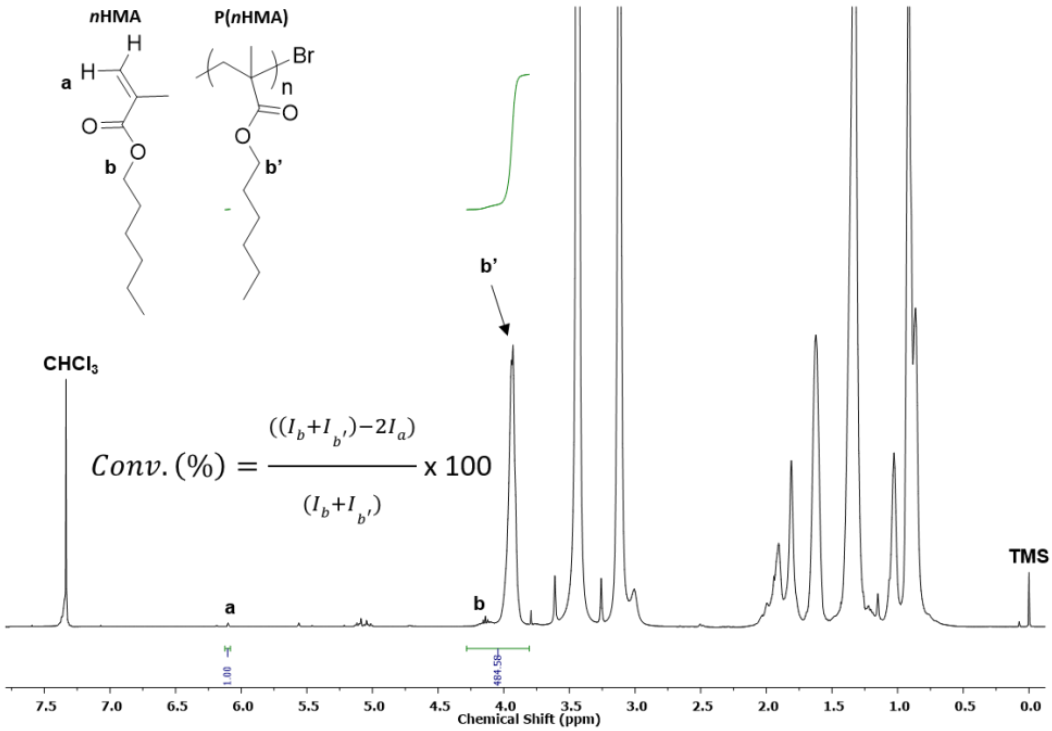

Figure 6.2 Quantification of the monomer conversion achieved during Cu-RDRP of *n*HMA by ^{1}H NMR analysis of the reaction mixture after 18 hours ($CDCl_3$, 400 MHz).

The solution was further diluted in $CHCl_3$, passed over a neutral alumina column to remove the copper catalyst and dried *in vacuo*. The polymer was re-dissolved in a minimum amount of THF and precipitated twice from THF into cold methanol, or another suitable anti-solvent (Appendix, Table A6.1) to give *p*(*n*HMA) as a clear viscous oil. The polymer was then dried *in vacuo* at 40 ° C for 48 hours and characterised *via* ^{1}H NMR in $CDCl_3$ (Figure 6.3) and triple detection SEC using a THF/TEA eluent (98/2 v/v %) using a narrow poly(styrene) standard calibration.

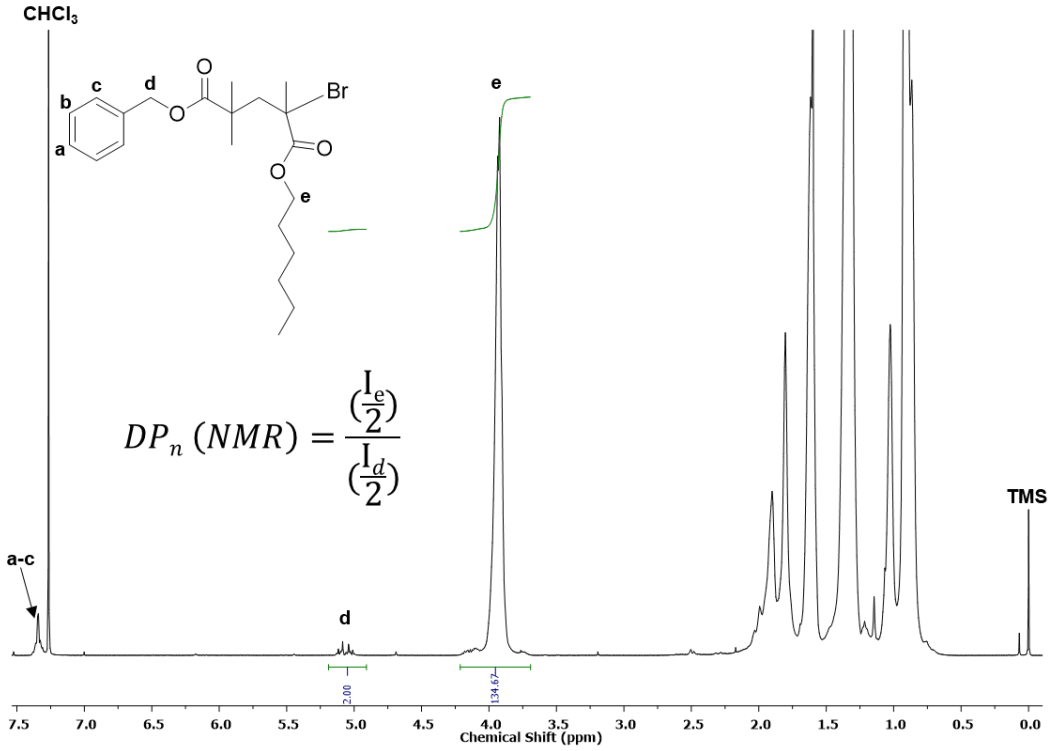

Figure 6.3 Quantification of the number average degree of polymerisation of *p*(*n*HMA) using ^{1}H NMR spectroscopy ($CDCl_3$, 400 MHz).

6.3.1.6 Kinetic Studies of the Cu-RDRP of nHMA at 60 °C in MeOH

Kinetic studies were conducted largely in accordance with the procedure outlined above (Section 6.3.1.5). Prior to use, all monomers and initiators were deoxygenated *via* gentle bubbling with N_2 for 60 minutes. Kinetic studies of the Cu-RDRP of *n*HMA targeted a DP_n = 60 monomer units. *n*HMA (25.0 g, 147 mmol), bpy (765 mg, 2.45 mmol) and BzBiB (630 mg, 2.45 mmol) were added to an oven dried round bottom flask (100 mL) equipped with a magnetic stirrer bar. The reaction solvent, either anhydrous MeOH or anhydrous IPA (33.7 mL, 50 wt %), was added and the resulting solution was purged with N_2 for a further 15 minutes. A sample was withdrawn (ca. 100 µL) and diluted in $CDCl_3$ allowing quantification of $[M]_0/[I]_0$ by ^{1}H NMR. Cu(I)Cl (48.5 mg, 0.489 mmol) was added rapidly to the flask, and instantly formed a brown solution. The reaction was purged with N_2 for a further 60 seconds; the Cu-RDRP was then rapidly transferred to 15 individual 10 mL RBFs, *via* a syringe under N_2, which were each sealed and quickly submerged into an oil bath preheated at 60 °C. At pre-determined time points individual Cu-RDRP were removed from the oil bath and stopped *via* simultaneous dilution with $CDCl_3$ and exposure of oxygen, following which a sample (*ca.* 500 µL) was taken for quantification of monomer conversion by ^{1}H NMR. Solutions were then passed over a neutral alumina column and dried *in vacuo*. The molecular weights of *p*(HMA), isolated at each time point, were then obtained *via* TD-SEC using average dn/dc values.

6.3.1.7 General Procedure for the Synthesis of AB Block Copolymers by Cu-RDRP (MMA, EMA, nBMA, tBMA, nHMA, CHMA, BzMA, EHMA, LMA and SMA)

In a typical synthesis, targeting DP_n = 120 monomer units and using PEG_{45}–Br as the macro-initiator, PEG_{45}-Br (526 mg, 0.245 mmol), *n*HMA (5.00 g, 29.4 mmol) and bpy (76.5 mg, 0.489 mmol) were added to a 25 mL single-neck round bottom flask equipped with a magnetic stirrer bar. Anhydrous MeOH (7.07 mL, 50 wt % wrt. monomer) was added and the resulting solution was sparged with N_2 for a further 15 minutes. At this point a sample was withdrawn (ca. 100 µL) and diluted in $CDCl_3$ allowing quantification of $[M]_0/[I]_0$ by ^{1}H NMR, as described in Figure 6.1. Cu(I)Cl (24.3 mg, 0.245 mmol) was rapidly added to the flask, and a brown solution instantly formed. The reaction was then purged with N_2 for a further 60 seconds, sealed and quickly submerged into an oil bath preheated at 60 °C. Cu-RDRPs were then allowed to proceed for 48 hours. The polymerisation was stopped by cooling the flask to room temperature, exposing its contents to air and diluting the reaction medium with $CDCl_3$. The polymer solution was passed through a neutral alumina column to remove the catalyst using DCM as the mobile phase and the resulting solution was concentrated under reduced pressure. The AB block copolymer was purified *via* precipitation from THF into cold MeOH and subsequently dried *in vacuo* at 40 °C over 48 hours. The pure AB block copolymer was then characterised *via* ^{1}H NMR ($CDCl_3$) and TD-SEC (THF/TEA), in accordance with the procedures outlined above, to determine DP_n and molecular weights.

6.3.1.8 General Procedure for the Synthesis of Branched Statistical Copolymers by Cu-RDRP (MMA, EMA, nBMA, tBMA, nHMA, CHMA, BzMA, EHMA, LMA and SMA)

In a typical branching statistical copolymerisation of *n*HMA and EGDMA targeting a primary chain DP_n of 60 monomer units and a branching ratio ($[B]_0/[I]_0$) of 0.90, *n*HMA (5.00 g, 29.4 mmol), EGDMA (87.3 mg, 0.441 mmol), bpy (153 mg, 0.978 mmol) and BzBiB (126 mg, 0.489 mmol) were added to a round bottom flask (25 mL) equipped with a magnetic stirrer bar. The reaction solvent, either anhydrous MeOH (6.84 mL, 50 wt %) or anhydrous IPA (6.86 mL, 50 wt %) was added and the resulting solution purged with N_2 for a further 15 minutes. A sample was withdrawn (*ca.* 100 µL) and diluted in $CDCl_3$ allowing quantification of $[M]_0/[I]_0$ and $[B]_0/[I]_0$ by ^{1}H NMR spectroscopy (Figure 6.4).

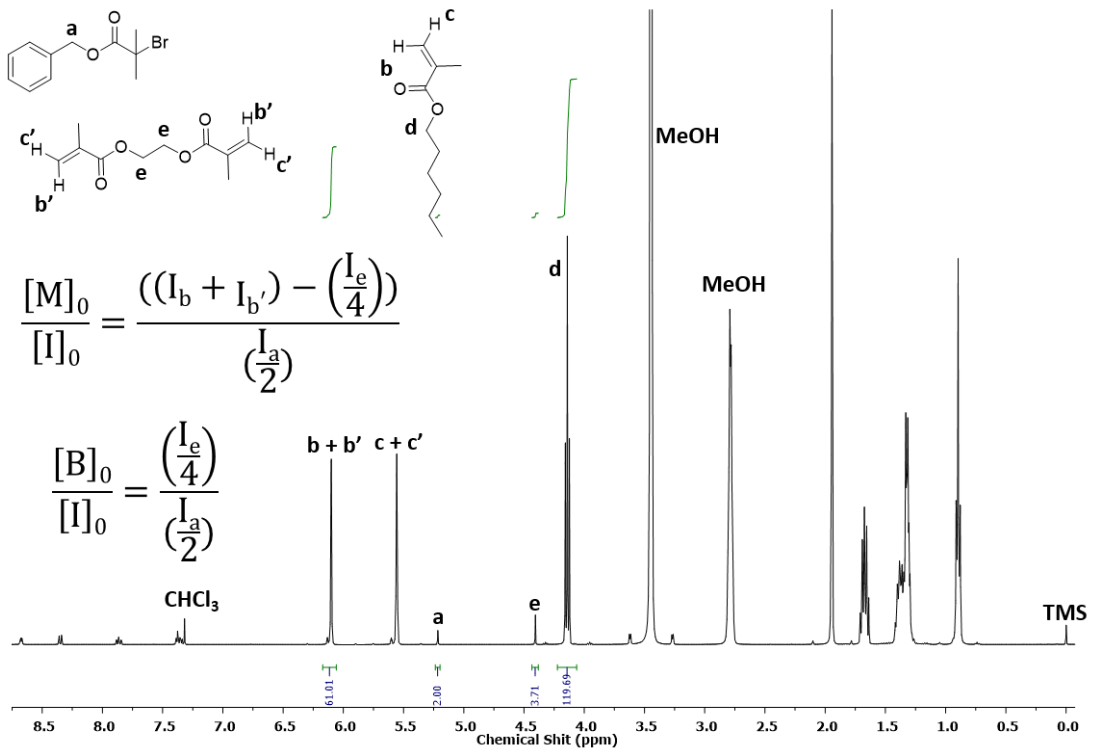

$$\frac{[M]_0}{[I]_0} = \frac{((I_b + I_{b'}) - (\frac{I_e}{4}))}{(\frac{I_a}{2})}$$

$$\frac{[B]_0}{[I]_0} = \frac{(\frac{I_e}{4})}{(\frac{I_a}{2})}$$

Figure 6.4 Quantification of $[B]_0/[I]_0$ for the polymerisation of *n*HMA *via* analysis of the reaction mixture at t_0 using ^{1}H NMR spectroscopy ($CDCl_3$, 400 MHz).

Cu(I)Cl (48.5 mg, 0.978 mmol) was rapidly added to the flask, instantly forming a brown coloured solution. The reaction was purged with N_2 for a further 60 seconds and submerged into a preheated oil bath at 60 ° C. The reaction was stopped after 24 hours by dilution with $CDCl_3$ until a homogeneous blue/green solution was obtained, at this point a sample (*ca.* 500 μL) was taken for quantification of monomer conversion by ^{1}H NMR. The solution was further diluted in $CHCl_3$, passed over a neutral alumina column to remove the copper catalyst and dried *in vacuo*. The branched copolymer was then dissolved in a minimum amount of THF and precipitated twice from THF into cold methanol to give *p*(*n*HMA$_{65}$-*co*-EGDMA$_{0.95}$) as a viscous clear liquid. *p*(*n*HMA$_{65}$-*co*-EGDMA$_{0.95}$) was then dried *in vacuo* at 40 °C for 48 hours and characterised by ^{1}H NMR in $CDCl_3$ (Figure 6.5) and triple detection SEC using a THF/TEA eluent (98/2 v/v %) using narrow and broad poly(styrene) standard calibrations.

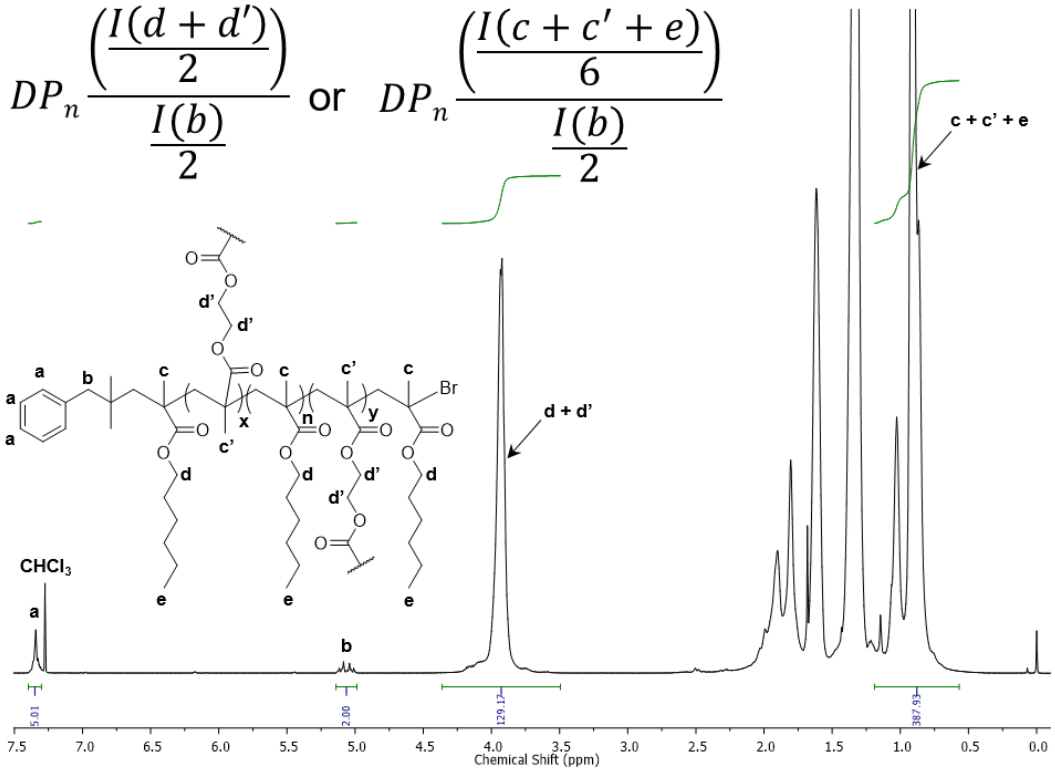

Figure 6.5 Quantification of the DP_n of the primary chains of which branched statistical copolymers, in this case *p*(*n*HMA$_{65}$-*co*-EGDMA$_{0.98}$), are constructed. Analyses were conducted *via* ^{1}H NMR spectroscopy of branched copolymers following purification ($CDCl_3$, 400 MHz).

6.3.1.9 Analysis of Branched Copolymer Architecture by TD-SEC

Plots of cumulative weight fraction (cum. ω_f) *vs.* number of primary chains per macromolecule were constructed by modification of the original cum. ω_f vs. molecular weight plots generated *via* TD-SEC. the absolute molecular weights (M) obtained were divided by the M_n of their linear homologues, generated in the absence of EGDMA under identical polymerisation conditions, which provided suitable representation of the primary chains from which the branched copolymers were constructed (Equation 6.1). For example, the modification of the cum. ω_f vs. M plot obtained for *p*(MMA$_{70}$-*co*-EGDMA$_{0.94}$), calculation of the number of primary chains per macromolecule was achieved by dividing each incremental increase in M by the M_n of *p*(MMA)$_{67}$ obtained from the homopolymerisation of MMA in anhydrous IPA (Mn = 6 700 g mol^{-1}). Similar modifications were made to generate plots of cumulative mole fraction (X_f) *vs.* number of primary chains per macromolecule (Appendix, Figure A2.8).

$$Primary\ chains\ per\ macromolecule = \frac{M}{m_n(LH)}$$

Equation 6.1 Calculation of the number of primary chains per macromolecule where M = absolute molecular weight of the species contributing towards the cum. ωf and Mn (LH) = the number average molecular weight of the linear homopolymer generated in the absence of EGDMA under identical polymerisation conditions.

6.3.2 Chapter 3

6.3.2.1 Polymer Solubility Studies

Polymer solubility studies were conducted in acetone and THF with the branched statistical copolymers used in Chapter 3. In a typical solubility study, *p*($EHMA_{68}$-*co*-$EGDMA_{0.93}$) (50 mg) was added to a glass vial followed by THF (5 mL). The glass vial was then sealed and placed on a roller mixer at ambient temperature for 48 hours. The homogeneity of the THF/ *p*($EHMA_{68}$-*co*-$EGDMA_{0.93}$) solution ([P] = 10 mg mL^{-1}) was inspected visually. In cases where the polymers had not dissolved the sample was disregarded. THF/ *p*($EHMA_{68}$-*co*-$EGDMA_{0.93}$) solution which appeared to have dissolved were passed over a 0.25 μm PTFE filter to test for the presence of small aggregates. In any samples which caused resistance on the syringe filter, the polymer/solvent mixture was deemed incompatible.

6.3.2.2 Initial Nanoprecipitation Studies

Initial nanoprecipitations were conducted from THF (1 mL) into DI H_2O (5 mL) (dilution ratio = 5). (Co)polymers were nanoprecipitated from an initial concentration of 5 mg mL^{-1} in THF ($[P]_0$ = 5 mg mL^{-1}) which, following solvent removal, gave a final (co)polymer concentration of 1 mg mL^{-1} in DI H2O ($[P]_f$ = 1 mg mL^{-1}). In a typical nanoprecipitation *p*($HPMA_{63}$-*co*-$EGDMA_{0.90}$) (25 mg) and THF (5 mL) were added to a glass vial and sealed. The vial was placed on a roller mixer and the polymer allowed to dissolve over 48 hours at ambient temperature to give a *p*($HPMA_{63}$-*co*-$EGDMA_{0.90}$)/ THF solution at a concentration of 5 mg mL^{-1}. The *p*($HPMA_{63}$-*co*-$EGDMA_{0.90}$)/ THF solution (1 mL, 5 mg mL^{-1}) was added to a glass vial containing DI H_2O (5 mL) under magnetic stirring. The sample was then left for 48 hours at ambient temperature to allow solvent removal *via* evaporation resulting in an aqueous nanoparticle dispersion at a concentration of 1 mg mL^{-1}. Aqueous nanoparticle dispersions were assessed visually for signs of polymer sedimentation following which, nanoparticles were assessed *via* DLS, zeta potential measurements taken and SEM. This method was employed for: sole nanoprecipitations of linear homopolymers, branched statistical copolymers and AB block copolymers.

6.3.2.3 Initial Co-Nanoprecipitation Studies

Initial co-nanoprecipitations were conducted from THF (1 mL) into DI H_2O (5 mL) (dilution ratio = 5). Equal weight fractions of each of the two components (ω_i = 0.5) were used during co-nanoprecipitations. (Co)Polymers were nanoprecipitated from an initial concentration of 5 mg mL^{-1} in THF ($[P]_0$ = 5 mg mL^{-1}) which, following solvent removal, gave a final (co)polymer concentration of 1 mg mL^{-1} in DI H_2O ($[P]_f$ = 1 mg mL^{-1}). In a typical co-nanoprecipitation of *p*(*n*BMA) based AB block and branched copolymers,

PEG_{45}-*b*-*p*(*n*BMA)$_{125}$ and *p*(*n*BMA_{73}-*co*-$EGDMA_{1.12}$) (50 mg) were added into separate glass vials followed by THF (10 mL). Each of the vials were then sealed and placed on a roller mixer for 48 hours at ambient temperature. The resulting THF/ copolymer solutions (3 mL, 5 mg mL^{-1}) were added to a separate glass vial; this was then sealed and placed on an orbital mixer for 1 minute at ambient temperature to ensure complete homogenisation. The resulting copolymer/ THF solution contained AB block and branched copolymer weight fractions of 0.50 and a total copolymer concentration of 5 mg mL^{-1} ($[P]_0$ = 5 mg mL^{-1}). The copolymer/ THF solution (1 mL, 5 mg mL^{-1}, branched copolymer ω_i = 0.50) was then rapidly added to DI H_2O (5 mL) under magnetic stirring. The co-nanoprecipitation was then stirred at ambient temperature for 48 hours in order to allow complete THF removal *via* evaporation, to give an aqueous nanoparticle dispersion at a concentration of 1 mg mL^{-1} ([P]f = 1 mg mL^{-1}). Aqueous nanoparticle dispersions were visually evaluated for signs of polymer sedimentation following which, nanoparticles were assessed *via* DLS, zeta potential measurements and SEM. This approach was used for the co-nanoprecipitations of linear homopolymers and branched copolymers, linear homopolymers and AB block copolymers and branched copolymers and AB block copolymers.

6.3.2.4 Nanoparticle Imaging via Scanning Electron Microscopy

SEM images of branched vinyl copolymer nanoparticles were prepared from a solution with initial nanoparticle concentration of 0.1 mg mL^{-1}. In a typical preparation of a sample for SEM analysis, a *p*(*n*BMA) based aqueous nanoparticle dispersion (1 mL, 1 mg mL^{-1}) was added to a glass vial containing DI H_2O (9 mL) to give a diluted aqueous nanoparticle dispersion at a concentration of 0.1 mg mL^{-1}. The sample was agitated gently on a roller mixer for approximately 5 minutes following which the aqueous nanoparticle dispersion (0.1 mg mL^{-1}) was dropped on to a glass cover slide mounted on an aluminium stub with a carbon tab and left to dry overnight. Dried samples were gold sputter coated at 20 mA for 2 minutes prior to imaging.

6.3.2.5 Pyrene Encapsulation Studies

Pyrene encapsulation studies were conducted using standard co-nanoprecipitations of AB block and branched copolymers outlined in Section 6.3.2.3. Co-nanoprecipitations were conducted using a target pyrene loading of 1 wt % with respect to the total copolymer mass. In a typical pyrene encapsulation experiment, a stock solution of pyrene in acetone (250 µL, 1 mg mL^{-1}) was added to a glass vial and left at ambient temperature for 48 hours to allow complete acetone removal *via* evaporation resulting in a solid pyrene mass of 0.25 mg. THF stock solutions of PEG_{45}-*b*-*p*(*n*BMA)$_{125}$ (2.5 mL, 5 mg mL^{-1}) and *p*(*n*BMA_{73}-*co*-$EGDMA_{1.12}$) (2.5 mL, 5 mg mL^{-1}) were added to the glass vial which was then sealed and placed on a roller

mixer for 2 hours to allow complete homogenisation. The resulting THF/ copolymer/ pyrene solution (1 mL, $[P]_0$ = 5 mg mL^{-1}, $[pyrene]_0$ = 0.05 mg mL^{-1}) was rapidly added to DI H_2O (5 mL, DR = 5) under magnetic stirring. The co-nanoprecipitation was then stirred at ambient temperature for 48 hours to allow complete THF removal *via* evaporation, resulting in an aqueous nanoparticle dispersion at a concentration of 1 mg mL^{-1} ([P]f = 1 mg mL^{-1}). Aqueous nanoparticle dispersions were assessed visually for signs of polymer sedimentation; nanoparticles were assessed *via* DLS and fluorescence emission spectroscopy (λ_{ex} = 335 nm).

6.3.2.6 Nanoparticle Composition Co-Nanoprecipitation Studies

Nanoparticle composition studies were conducted using standard co-nanoprecipitations of AB block and branched copolymers, outlined in Section 6.3.2.3. Co-nanoprecipitation studies were conducted using AB block and branched copolymer weight fractions of: 1.0:0.0, 0.9:0.1, 0.8:0.2, 0.7:0.3, 0.6:0.4, 0.5:0.5, 0.4:0.6, 0.3:0.7, 0.2:0.8, 0.1: 0.9 and 0.0:1.0. A typical co-nanoprecipitation of PEG_{45}-*b*-*p*(*n*BMA)$_{125}$ and *p*(*n*BMA_{73}-*co*-$EGDMA_{1.12}$), targeting AB block and branched copolymer weight fractions of 0.4 and 0.6 respectively was conducted as follows. Stock solutions of PEG_{45}-*b*-*p*(*n*BMA)$_{125}$ and *p*(*n*BMA_{73}-*co*-$EGDMA_{1.12}$) were prepared at a copolymer concentration of 5 mg mL^{-1} in THF. The PEG_{45}-*b*-*p*(*n*BMA)$_{125}$ (1.2 mL, 5 mg mL^{-1}) and *p*(*n*BMA_{73}-*co*-$EGDMA_{1.12}$) (1.8 mL, 5 mg mL^{-1}) stock solutions were added to a glass vial containing pyrene (0.15 mg). The vial was then sealed and placed on a roller mixer for 24 hours to ensure complete homogenisation. The resulting THF solution contained a total copolymer concentration of 5 mg mL^{-1} with a PEG_{45}-*b*-*p*(*n*BMA)$_{125}$ ω_i of 0.4 and a *p*(*n*BMA_{73}-*co*-$EGDMA_{1.12}$) ω_i of 0.6. The THF solution (1 mL) was then added to DI H_2O (5 mL, DR = 5) under magnetic stirring and left at ambient temperature for 48 hours, to allow complete THF removal *via* evaporation. The resultant aqueous nanoparticle dispersion was at a concentration of 1 mg mL^{-1} ($[P]_f$ = 1 mg mL^{-1}). Aqueous nanoparticle dispersions were assessed visually for signs of polymer sedimentation; nanoparticles were assessed *via* DLS, zeta potential measurements and fluorescence emission spectroscopy (λ_{ex} = 335 nm).

6.3.2.7 Co-Nanoprecipitation Concentration Studies

Co-nanoprecipitation concentration studies were conducted using co-nanoprecipitations of AB block and branched copolymers, outlined in Section 6.3.2.3. Co-nanoprecipitations were conducted using stock solutions containing varied copolymer concentrations ranging from 5.0 to 0.5 mg mL^{-1} in THF. All co-nanoprecipitations were conducted using equal weight fractions of AB block and branched copolymers (ω_i = 0.5). A typical co-nanoprecipitation of PEG_{45}-*b*-*p*(*n*BMA)$_{125}$ and *p*(*n*BMA_{73}-*co*-$EGDMA_{1.12}$) from a $[P]_0$ of 1 mg mL^{-1} was conducted as follows. Separate stock solutions of PEG_{45}-*b*-*p*(*n*BMA)$_{125}$ and *p*(*n*BMA_{73}-*co*-$EGDMA_{1.12}$) in THF were prepared at a copolymer concentration of 5 mg mL^{-1}. The solutions (3 mL,

5 mg mL^{-1}) were added to a glass vial and homogenised using an orbital mixer for 1 minute at ambient temperature. The stock solution (1 mL, 5 mg mL^{-1}) was then added to a separate glass vial followed by THF (4 mL); the vial was then sealed and placed on an orbital mixer for 1 minute to give a copolymer concentration of 1 mg mL^{-1}. The stock solution (1 mL, 1 mg mL^{-1}) was then added to DI H_2O (5 mL, DR = 5) under magnetic stirring and was left at ambient temperature for 48 hours, in order to allow complete THF removal *via* evaporation. An aqueous nanoparticle dispersion at a concentration of 1 mg mL^{-1} ($[P]_f$ = 0.20 mg mL^{-1}) resulted. Aqueous nanoparticle dispersions were assessed visually for signs of polymer sedimentation following which, nanoparticles were assessed *via* DLS.

6.3.2.8 Nanoparticle Stability to Dilution Studies

Nanoparticle dilution studies were conducted using aqueous nanoparticle dispersions (1 mg mL^{-1}) prepared by co-nanoprecipitations of AB block and branched copolymers. Co-nanoprecipitations were conducted from THF (1 mL) into DI H_2O (5 mL) (dilution ratio = 5). Equal weight fractions of each of the two components (ω_i = 0.5) were used during co-nanoprecipitation. In a typical co-nanoprecipitation of *p*(*n*BMA) based AB block and branched copolymers, PEG_{45}-*b*-*p*(*n*BMA)$_{125}$ and *p*(*n*BMA_{73}-*co*-$EGDMA_{1.12}$) (50 mg) were added into separate glass vials followed by THF (10 mL). Each of the glass vials were then sealed and placed on a roller mixer for 48 hours at ambient temperature. The resulting THF/ copolymer solutions (2 mL, 5 mg mL^{-1}) were added to a separate glass vial; this was sealed and placed on an orbital mixer for 1 minute at ambient temperature to ensure complete homogenisation. The resulting copolymer THF solution contained AB block and branched copolymer weight fractions of 0.5 and a total copolymer concentration of 5 mg mL^{-1} ($[P]_0$ = 5 mg mL^{-1}). The copolymer/ THF solution (1 mL, 5 mg mL^{-1}, branched copolymer ω_i = 0.5) was then rapidly added to DI H_2O (5 mL) under magnetic stirring. The co-nanoprecipitation was stirred at ambient temperature for 48 hours in order to allow complete THF removal *via* evaporation, resulting in an aqueous nanoparticle dispersion at a concentration of 1 mg mL^{-1} ($[P]_f$ = 1 mg mL^{-1}).

Aqueous nanoparticle dispersions were then diluted in DI H_2O using a serial dilution method over a dilution factor of 1000. For example, to achieve a 100 fold dilution, an aqueous *p*(*n*BMA) nanoparticle dispersion (1 mL, $[P]_f$ = 1 mg mL^{-1}) was added to a glass vial along with 9 mL of DI H_2O, the diluted sampled was then placed on a roller mixer for approximately 30 minutes. The resulting diluted aqueous nanoparticle dispersion (1 mL, $[P]_{H2O}$ = 0.1 mg mL^{-1}) was added to a glass vial along with 9 mL DI H_2O. The vial was sealed and placed on a roller mixer for 24 hours to give a final dilution factor of 100

($[P]_{H2O}$ = 0.01 mg mL^{-1}). The diluted aqueous nanoparticle dispersion was then assessed using DLS.

6.3.2.9 Nanoparticle Salt Stability Studies

Nanoparticle dilution studies were conducted using aqueous nanoparticle dispersions (1 mg mL^{-1}) prepared by co-nanoprecipitations of AB block and branched copolymers. Co-nanoprecipitations were conducted from THF (1 mL) into DI H_2O (5 mL) (dilution ratio = 5). Equal weight fractions of each of the two components (ω_i = 0.5) were used during co-nanoprecipitations. In a typical co-nanoprecipitation, PEG_{45}-*b*-*p*$(LMA)_{121}$ and *p*$(LMA_{70}$-*co*-$EGDMA_{1.04})$ (50 mg) were added into separate glass vials followed by THF (10 mL). Each of the glass vials were then sealed and placed on a roller mixer for 48 hours at ambient temperature. The resulting THF/ copolymer solutions (2 mL, 5 mg mL^{-1}) were added to a separate glass vial, this was then sealed and placed on an orbital mixer for 1 minute at ambient temperature to ensure complete homogenisation. The resulting copolymer THF solution contained AB block and branched copolymer weight fractions of 0.5 and a total copolymer concentration of 5 mg mL^{-1} ($[P]_0$ = 5 mg mL^{-1}). The copolymer/ THF solution (1 mL, 5 mg mL^{-1}, branched copolymer ω_i = 0.5) was then rapidly added to DI H_2O (5 mL) under magnetic stirring. The co-nanoprecipitation was stirred at ambient temperature for 48 hours in order to allow complete THF removal *via* evaporation, to give an aqueous nanoparticle dispersion at a concentration of 1 mg mL^{-1} ($[P]_f$ = 1 mg mL^{-1}).

Nanoparticle dispersions were diluted in NaCl solutions of varied concentration whilst maintaining a constant nanoparticle concentration of 0.5 mg mL^{-1}. For example, to achieve a salt concentration of 0.5 mol dm^{-3}, an aqueous *p*(LMA) nanoparticle dispersion (1 mL, $[P]_0$ = 1 mg mL^{-1}) and an aqueous solution of NaCl (1 mL, 1.0 mol dm^{-3}) were added a glass vial. The vial was sealed and placed on a roller mixer for 24 hours to give an aqueous nanoparticle dispersion with a $[P]_{H2O}$ = 0.5 mg mL^{-1} and a [NaCl] = 0.5 mol dm^{-3}. The stability of the aqueous nanoparticle dispersion was first assessed visually and, where there were no signs of copolymer sedimentation, this was followed by DLS analysis.

6.3.3 Chapter 4

6.3.3.1 Initial Docetaxel Encapsulation Study

Initial docetaxel loading experiments were conducted using a constant fixed total mass during co-nanoprecipitation. The total solid mass consisted of branched and AB block copolymers, which contained equal weight fractions (ω_i = 0.50), and docetaxel. Co-nanoprecipitations were conducted using a constant dilution ratio of 5 (V_{H2O}/V_{THF} = 5) from an initial total solid concentration of 5 mg mL^{-1} in THF. Docetaxel loadings of 1.00, 2.50, 5.00, 10.0, 15.0, 20.0,

25.0, 30.0, 40.0 and 50.0 wt % with respect to the total solid mass were attempted during initial docetaxel encapsulation studies. A typical co-nanoprecipitation, targeting a docetaxel loading of 25 wt % was conducted as follows. Docetaxel (50 mg) and dichloromethane (DCM) were added to a glass vial. The vial was sealed and placed on a roller mixer at ambient temperature overnight. The resulting docetaxel stock solution (375 μL, 10 mg mL^{-1}) was added to a separate glass vial and left at ambient temperature for 24 hours to allow complete DCM removal via evaporation, leaving a solid docetaxel mass of 0.375 mg. Stock solutions of *p*($HPMA_{63}$-*co*-$EGDMA_{0.90}$) and PEG_{45}-*b*-*p*$(HPMA)_{124}$ (1.5 mL, 3.75 mg mL^{-1}) were added to the vial which was then sealed and placed on a roller mixer for 24 hours. The stock solution (1 mL, 5 mg mL^{-1} docetaxel ω_i = 0.25) was then rapidly added to DI H_2O (5 mL) under magnetic stirring. The co-nanoprecipitation was left at ambient temperature for 48 hours to allow complete THF removal via evaporation to give an aqueous docetaxel loaded nanoparticle dispersion at a concentration of 1 mg mL^{-1}. Aqueous nanoparticle dispersions were initially assessed visually for signs of copolymer/ drug sedimentation. Co-nanoprecipitations were deemed to have failed in any cases where sedimentation was observed. Aqueous nanoparticle dispersions that showed no evidence of sedimentation were assessed using DLS.

6.3.3.2 Calculation of Drug Loading via ^{1}H NMR Spectroscopy

Analysis of docetaxel encapsulation by ^{1}H NMR spectroscopy required co-nanoprecipitations to be conducted on a larger scale to those reported above. In a typical large-scale co-nanoprecipitation, PEG_{45}-*b*-*p*(*n*$BMA)_{125}$ and *p*(*n*BMA_{73}-*co*-$EGDMA_{1.12}$) (45 mg) were added to separate glass vials followed by THF (10 mL). The glass vials were sealed and placed on a roller mixer for 48 hours to ensure complete copolymer dissolution. The resulting copolymer-THF stock solutions (6 mL, 4.5 mg mL^{-1}) were added to a separate glass vial containing docetaxel (3 mg); the vial was sealed and placed on a roller mixer for a further 24 hours. The resulting stock solution (5 mL, total solid mass = 5 mg mL^{-1}, docetaxel ω_i = 0.1) was added to DI H_2O (25 mL, DR = 5) under magnetic stirring and was left for 72 hours at ambient temperature to allow complete THF removal. The resulting aqueous nanoparticle dispersion (25 mL, 1 mg mL^{-1}, docetaxel ω_i = 0.1) was inspected visually for signs of sedimentation and was subsequently assessed using DLS.

In a typical drug loading analysis by ^{1}H NMR spectroscopy, an aqueous nanoparticle dispersion (5 mL, 1 mg mL^{-1}) was added to a glass vial and cooled under liquid N_2 for 5 minutes and freeze-dried over 72 hours. A separate sample of the same aqueous nanoparticle dispersion (5 mL, 1 mg mL^{-1}) was added to a Amicon® Ultra-15 Centrifugal filter unit and placed under high centrifugation (4000 xg, swing bucket rotor) for 60 minutes. The aqueous

nanoparticle dispersion remaining at the top of the centrifuge chamber was transferred to a glass vial, rapidly cooled in liquid N_2 and was also freeze-dried for 72 hours. Following freeze drying, both samples were assessed using ^{1}H NMR spectroscopy (400 MHz, $CDCl_3$). The molar ratio of copolymer to docetaxel was determined by comparison of the relative intensities of chemical shifts of the: docetaxel allylic unit, the PEG methyl end-group and the ethylene protons of methacrylate repeat units (Figure 6.6).

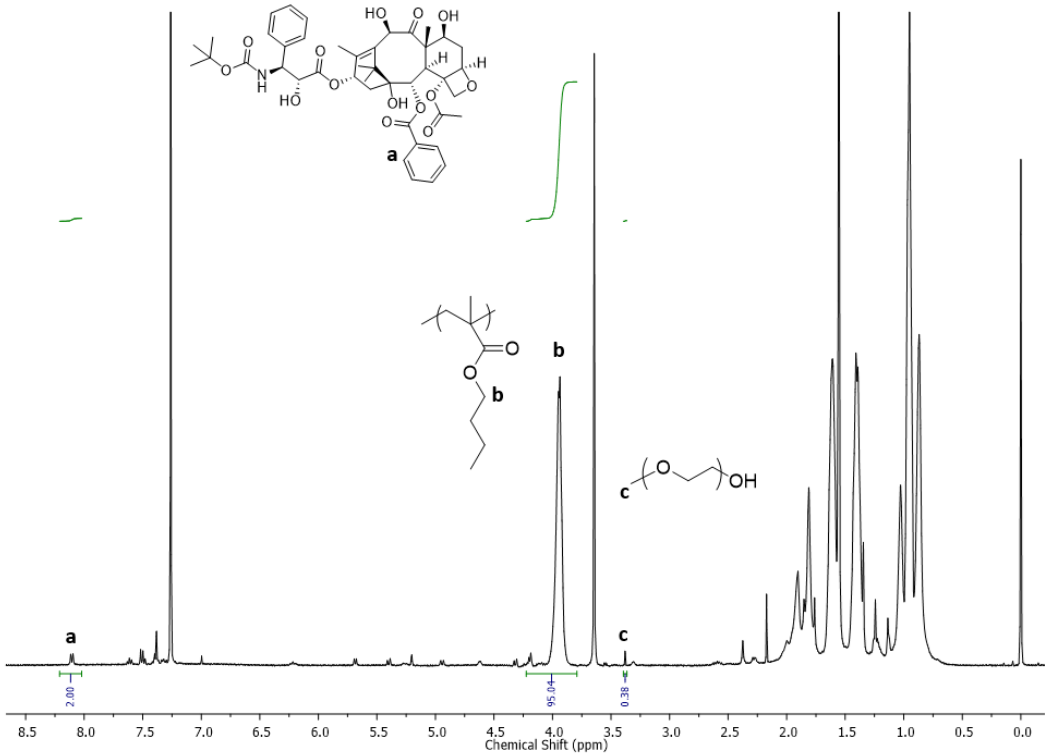

Figure 6.6 An exemplary ^{1}H NMR spectrum obtained for docetaxel loaded *p*(*n*BMA) nanoparticles following water removal *via* freeze drying.

Molar ratios were converted into mass ratio using the molecular weights of: docetaxel (808 g mol^{-1}), the PEG_{45}-Br macro initiator (2150 g mol^{-1}) and that of the repeat unit (142.2 g mol^{-1}) respectively. Drug loading was calculated by comparison of the mass of docetaxel in proportion with that of the overall mass, in accordance with Equation 6.2, where m_D = docetaxel mass, m_{RU} = the mass of the methacrylate repeat unit and m_{PEG} = the mass of the PEG domains of amphiphilic block copolymers.

$$DL\ (\%) = \left(\frac{m_D}{m_D + m_{RU} + m_{PEG}}\right) \times 100$$

Equation 6.2 Calculation of drug loading of docetaxel with respct to overall mass where m_D = docetaxel mass, m_{RU} = the mass of the methacrylate repeat unit and m_{PEG} = the mass of the PEG domains of amphiphilic block copolymers.

Encapsulation efficiencies were calculated *via* comparison of the of docetaxel weight fractions in freeze dried samples obtained before and after nanoparticle purification *via* centrifugation. Encapsulation efficiencies were therefore calculated in accordance with Equation 6.3.

$$EE = \frac{DL_{(filtered)}}{DL_{(unfiltered)}}$$

Equation 6.3 Calculation of encapsulation efficiency as a fraction of docetaxel weight in freeze dried samples before and after filtration.

6.3.3.3 Calculation of Drug Loading via Ultraviolet-Visible Spectroscopy

Analysis of docetaxel encapsulation by ^{1}H NMR spectroscopy required co-nanoprecipitations to be conducted on a larger scale to those reported above. In a typical large-scale co-nanoprecipitation, PEG_{45}-*b*-*p*(*n*BMA)$_{125}$ and *p*(*n*BMA_{73}-*co*-$EGDMA_{1.12}$) (45 mg) were added to separate glass vials followed by THF (10 mL). The glass vials were sealed and placed on a roller mixer for 48 hours to ensure complete copolymer dissolution. The resulting copolymer-THF stock solutions (6 mL, 4.5 mg mL^{-1}) were added to a separate glass vial containing docetaxel (3 mg); the vial was sealed and placed on a roller mixer for a further 24 hours. The resulting stock solution (5 mL, total solid mass = 5 mg mL^{-1}, docetaxel ω_i = 0.1) was added to DI H_2O (25 mL, DR = 5) under magnetic stirring and was left for 72 hours at ambient temperature to allow complete THF removal. The resulting aqueous nanoparticle dispersion (25 mL, 1 mg mL^{-1}, docetaxel ω_i = 0.10) was inspected visually for signs of sedimentation and was subsequently assessed using DLS.

UV-Vis measurements were conducted in THF. Docetaxel concentrations were calculated using an extinction coefficient (ε) obtained from a calibration curve for docetaxel in THF. In a typical drug loading analysis by UV-Vis spectroscopy, an aqueous nanoparticle dispersion (5 mL, 1 mg mL^{-1}) was added to a glass vial and cooled under liquid N_2 for 5 minutes and freeze-dried over 72 hours. A separate sample of the same aqueous nanoparticle dispersion (5 mL, 1 mg mL^{-1}) was added to a Amicon® Ultra-15 Centrifugal filter unit and placed under high centrifugation (4000 xg, swing bucket rotor) for 60 minutes. The filtrate, located in the lower compartment of the centrifugal filter unit transferred to a glass vial, rapidly cooled in liquid N_2 and was also freeze-dried for 72 hours. Following freeze-drying, both the unfiltered nanoparticle-drug and the filtrate were dissolved in a known volume of THF and the docetaxel mass concentration was calculated from the UV-vis absorption at 244 nm. The drug loading was determined using Equations 6.4 and 6.5, where mD_{encap} is the mass of encapsulated docetaxel, mD_{total} is the total mass of docetaxel in the aqueous nanoparticle dispersion and mD_{free} is the mass of free docetaxel which was not encapsulated during co-nanoprecipitation.

$$mD_{encap} = mD_{total} - mD_{free}$$

Equation 6.4 Calculation of mass of encapsulated docetaxel within aqueous nanoparticle dispersion where $m\mathrm{D}_{total}$ is the total mass of docetaxel in the aqueous nanoparticle dispersion and $m\mathrm{D}_{free}$ is the mass of free docetaxel which was not encapsulated during co-nanoprecipitation.

$$DL\ (\%) = \left(\frac{mD_{encap}}{mD_{total}+m_{polymer}}\right) \times 100$$

Equation 6.5 Calculation of drug loading as a percentage of mass of docetaxel encapsulated compared to total mass of docetaxel and polymer within the aqueous nanoparticle dispersion.

Encapsulation efficiencies (EE) were calculated *via* comparison of the docetaxel concentrations in freeze dried samples obtained before and after nanoparticle purification *via* ultracentrifugation. Docetaxel concentrations, determined by UV-Vis spectroscopy, within the filtrate ($[\mathrm{D}]_{free}$) were compared to the total docetaxel concentration within the unfiltered sample ($[\mathrm{D}]_{total}$). This allowed encapsulation efficiencies to be determined in accordance with Equation 6.6.

$$EE = \left(\frac{[D]_{total} - [D]_{free}}{[D]_{total}}\right)$$

Equation 6.6 Calculation of encapsulation efficiency of docetaxel within aqueous nanoparticle dispersion *via* freeze-drying samples before and after ultracentrifugation to determine $[\mathrm{D}]_{free}$ (amount of docetaxel in filtrate, unencapsulated) compared to $[\mathrm{D}]_{total}$ (the total docetaxel concentration within the unfiltered sample) measured by UV-Vis spectroscopy.

6.3.3.4 Assessment of ^{3}H-Labelled Radio Purity via Radio Thin-Layer Chromatography

Thin-layer chromatography (TLC) analysis was conducted of unlabelled docetaxel in order to establish a suitable eluent system and R_f value; these were determined to be ethyl acetate/ hexane (30/70 v/v %) and Rf = 0.40. Radio-TLC was then conducted using the same mobile phase to define radio-purity of tritiated docetaxel. TLC of tritiated docetaxel was analysed in parallel to analogous unlabelled docetaxel. Once the TLC plate had been exposed to the eluent system for a sufficient amount of time it was dried and placed on a radio-TLC imaging scanner. The scanner contained a gas-filled proportional counter which provided a direct digital counting of tritium and a corresponding Rf value of the radioisotope. The Rf value obtained for tritiated docetaxel concurred with that of the unlabelled analogue, therefore the tritiated docetaxel was deemed pure.

6.3.3.5 Preparation of ^{3}H-Docetaxel Loaded Branched Vinyl Copolymer Nanoparticles via Co-Nanoprecipitation

All ^{3}H-docetaxel co-nanoprecipitations were conducted using equal weight fractions of AB block and branched copolymers (ω_i = 0.50) targeting a docetaxel loading of 15 wt % with

respect to the total solid mass. Co-nanoprecipitations were conducted from THF into DI H_2O using a dilution ratio of 5.

A typical preparation of ^{3}H-docetaxel loaded *p*(*n*HMA) branched vinyl copolymer nanoparticles was conducted as follows. A stock solution of docetaxel (5 mg, 6.189 μmol) and ^{3}H labelled docetaxel (33 μCi, 6.6 μCi/mg^{-1}) was prepared in EtOH. This stock solution (225 μL, 1.125 mg, 6.6 μCi/mg^{-1}) was added to a glass vial and left at ambient temperature overnight to allow complete EtOH *via* evaporation. Stock solutions of *p*(*n*HMA$_{68}$-*co*-EGDMA$_{1.03}$) (0.75 mL, 4.25 mg mL^{-1}) and PEG$_{45}$-*b*-*p*(*n*HMA)$_{127}$ (0.75 mL, 4.25 mg mL^{-1}) in THF were added to the glass vial containing dried docetaxel (1.125 mg, 6.6 μCi/mg^{-1}); the vial was then sealed and homogenised by placing the vial on an vortex mixer for 1 minute. This solution (1 mL) was then added to DI H_2O (5 mL) under magnetic stirring and was left at ambient temperature for 48 hours to allow complete THF removal *via* evaporation to give an aqueous nanoparticle dispersion at a solids concentration of 1 mg mL^{-1}. Aqueous nanoparticle dispersions were assessed by DLS at a concentration of 1 mg mL^{-1} at 25 °C.

6.3.3.6 Measurement of Encapsulation Efficiency and Drug Loading of ^{3}H-Labelled Docetaxel Using Radiometric Analysis

Docetaxel drug loadings were determined *via* liquid scintillation counting (LSC) analysis of known volumes of aqueous nanoparticle dispersions prior to centrifugation and the resulting filtrate. In a typical analysis of docetaxel loading and encapsulation efficiency, an aqueous nanoparticle dispersion (1 mL, 1.000 g) was analysed using LSC in order to determine the total mass of docetaxel present. A separate sample of the same aqueous nanoparticle dispersion (0.500 mL, 1 mg mL^{-1}) was added to a centrifugal filter unit and was placed under high centrifugation (14,000 rpm) for 60 minutes. Analysis of untreated aqueous nanoparticle dispersions allowed the total docetaxel concentration ([D]$_{total}$) and therefore the total docetaxel mass (mD_{total}) to be determined by LSC analysis. Alternatively, LSC analysis of the filtrate, collected at the bottom of the centrifuge tube, allowed the concentration [D]$_{free}$ and thus the mass (mD_{free}) of free docetaxel to be determined. Docetaxel encapsulation efficiencies were calculated in accordance with Equation 6.7.

$$EE = \frac{mD_{total} - mD_{free}}{mD_{total}}$$

Equation 6.7 Calculation of encapsulation efficiency of docetaxel within aqueous nanoparticle dispersion *via* radiometric analysis before and after ultracentrifugation to determine mD$_{free}$ (amount of docetaxel in filtrate, unencapsulated) compared to mD$_{total}$ (the total docetaxel concentration within the unfiltered sample) measured by LSC.

Given that the aqueous nanoparticle dispersion mass and the copolymer concentrations were known and that the concentration of docetaxel could be determined *via* LSC analysis, docetaxel drug loadings were be calculated using Equation 6.8, where mP_{total} is the total mass of branched and AB block copolymers. mP_{total} was based on a copolymer concentration of 0.85 mg mL^{-1}

$$DL = \frac{mD_{total} - mD_{free}}{mD_{total} + mP_{total}}$$

Equation 6.8 Calculation of drug loading of mass of docetaxel encapsulated compared to total mass of docetaxel and polymer within the aqueous nanoparticle dispersion.

6.3.3.7 Monitoring Release of ^{3}H-Labelled Docetaxel from Branched Vinyl Copolymer Nanoparticles during Radio-Dialyses

Radio-dialysis of aqueous nanoparticle dispersions was conducted using a nanoparticle concentration of 1 mg mL^{-1}, at a docetaxel loading of 15 wt %. Radio-dialyses were conducted using a 1:100 dilution. Dialyses were conducted at ambient temperature (20 ℃), 37 ℃ and 50 ℃. Docetaxel release was monitored at set time points of: 0.5, 1, 2, 3, 4, 5, 6, 7, 8 and 24 hours. In a typical radio-dialysis, a ^{3}H labelled aqueous nanoparticle dispersion (1 mL) was added to a double sided bio-dialyser fitted with 3.5 kDa MWCO membranes. The bio-dialyser was placed in DI H_2O 100 mL and stirred at 100 rpm; the reservoir was placed in an oil bath at the desired temperature. At regular time intervals, the bio-dialyser was transferred to a fresh reservoir (100 mL). A sample was then taken from the previous external reservoir (1 mL) to determine docetaxel release using LSC.

6.3.3.8 Determination of Branched Copolymer Complex Viscosities Using Rheological Analysis

Branched copolymer complex viscosities were determined using a reverse oscillatory temperature sweep from 150 ℃ to 25 ℃. All samples were tested using a 40 mm cross-hatched stainless steel parallel plate and were subjected to the same conditions during reverse oscillatory temperature sweeps, these included: i) a time sweep to probe the stability of each sample at 150 ℃ during which measurements were taken at 5 second intervals over a time period of 180 seconds using an oscillatory frequency of 1 Hz. ii) A temperature sweep from a start temperature of 150 ℃ to an end temperature of 25 ℃ which included measurement of complex viscosities at an oscillatory frequency of 1 Hz at 5 ℃ steps across the temperature range.

6.3.4 Chapter 5

6.3.4.1 Preparation of Branched Statistical Copolymers of HPMA, EHMA and EGDMA via Cu-RDRP at 60 °C in Anhydrous Methanol

In a typical branching statistical copolymerisation of HPMA, EHMA and EGDMA targeting a primary chain DP_n = 60 monomer unit, a branching ratio ($[B]_0/[I]_0$) of 0.9 and a HPMA X_f of 0.5, HPMA (2.12 g, 14.7 mmol), EHMA (2.92 g, 14.7 mmol), EGDMA (87.3 mg, 0.441 mmol), bpy (153 mg, 0.978 mmol) and BzBiB (126 mg, 0.489 mmol) were added to a round bottom flask (25 mL) equipped with a magnetic stirrer bar. The reaction solvent, anhydrous MeOH (5.40 g, 6.83 mL, 50 wt %), was then added and the resulting solution was purged with N_2 for a further 15 minutes. A sample was withdrawn (*ca.* 100 µL) and diluted in $CDCl_3$ allowing quantification of $[M]_0/[I]_0$ and $[B]_0/[I]_0$ by ^{1}H NMR spectroscopy. Cu(I)Cl (48.5 mg, 0.978 mmol) was rapidly added to the flask, and a brown coloured solution instantly formed. The reaction was purged with N_2 for a further 60 seconds and submerged into a preheated oil bath at 60 °C. After 24 hours, a sample (*ca.* 500 µL) was taken for quantification of monomer conversion by ^{1}H NMR and the polymerisation was then stopped by dilution with THF until a homogeneous blue/green solution was obtained. The solution was then further diluted in THF, passed over a neutral alumina column to remove the copper catalyst and dried *in vacuo*. The branched copolymer was then re-dissolved in a minimum amount of THF and precipitated twice from THF into cold petroleum ether to give *p*($EHMA_{30}$-*co*-$HPMA_{30}$-*co*-$EGDMA_{0.90}$). The branched copolymer was then dried *in vacuo* at 40 °C for 48 hours and characterised by triple detection SEC using a THF/TEA eluent (98/2 v/v %) using narrow and broad poly(styrene) standard calibrations.

6.3.4.2 Preparation of Statistical AB Block Copolymers of PEG_{45} EHMA and HPMA via Cu-RDRP at 60 °C in Anhydrous Methanol

In a typical synthesis, targeting DP_n = 120 monomer units and a HPMA X_f of 0.5, using PEG_{45}-Br as the macro-initiator; PEG_{45}-Br (526 mg, 0.245 mmol), HPMA (2.12 g, 14.7 mmol), EHMA (2.92 g, 29.4 mmol) and bpy (76.5 mg, 0.489 mmol) were added to a 25 mL single-neck round bottom flask equipped with a magnetic stirrer bar. Anhydrous MeOH (5.67 g, 7.16 mL, 50 wt % w.r.t. monomer) was added and the resulting solution was sparged with N_2 for a further 15 minutes. At this point a sample was withdrawn (ca. 100 µL) and diluted in $CDCl_3$ allowing quantification of $[M]_0/[I]_0$ by ^{1}H NMR. Cu(I)Cl (24.3 mg, 0.245 mmol) was rapidly added to the flask, and a brown solution instantly formed. The reaction was then purged with N_2 for a further 60 seconds, sealed and quickly submerged into an oil bath preheated at 60 °C. The polymerisation was then allowed to proceed for 48 hours. After 48 hours, a sample (ca. 500 µL) was taken for quantification of monomer conversion by ^{1}H NMR

and the polymerisation was then stopped by dilution with THF and exposure to air until a homogeneous blue/green solution was obtained. The polymer solution was passed through a neutral alumina column to remove the catalyst using THF as the mobile phase and the resulting solution was concentrated under reduced pressure. The AB block copolymer was purified *via* precipitation from THF into cold petroleum ether and subsequently dried *in vacuo* at 40 °C over 48 hours. The pure AB block copolymer was then characterised *via* TD-SEC using THF/TEA eluent (98/2 v/v %) and a narrow poly(styrene) standard calibration.

6.3.4.3 Rheological Analyses of Branched Statistical Copolymers

Branched copolymer complex viscosities were determined using a reverse oscillatory temperature sweep from 150 °C to 25 °C. All samples were tested using a 40 mm cross-hatched stainless steel parallel plate and were subjected to the same conditions during reverse oscillatory temperature sweeps, these included: i) a time sweep to probe the stability of each sample at 150 °C during which measurements were taken at 5 second intervals over a time period of 180 seconds using an oscillatory frequency of 1 Hz. ii) A temperature sweep from a start temperature of 150 °C to an end temperature of 25 °C which included measurement of complex viscosities at an oscillatory frequency of 1 Hz at 5 °C steps across the temperature range.

6.3.4.4 Co-nanoprecipitations of Statistical Branched and AB Block Copolymers

All co-nanoprecipitations were conducted from THF (1 mL) into DI H_2O (5 mL) (dilution ratio = 5). Equal weight fractions of each of the hydrophobic branched and amphiphilic AB block copolymers (ω_i = 0.5) were used during co-nanoprecipitations. Copolymers were nanoprecipitated from an initial concentration of 5 mg mL^{-1} in THF ($[P]_0$ = 5 mg mL^{-1}) which, following solvent removal, gave a final copolymer concentration of 1 mg mL^{-1} in DI H_2O ($[P]_f$ = 1 mg mL^{-1}). In a typical co-nanoprecipitation of statistical branched and AB block copolymers, PEG_{45}-*b*-*p*(EHMA$_{60}$-*co*-HPMA$_{60}$)$_{125}$ and *p*(EHMA30-*co*-HPMA$_{30}$-*co*-EGDMA$_{1.12}$) (50 mg) were added into separate glass vials followed by THF (10 mL). Each of the vials were then sealed and placed on a roller mixer for 48 hours at ambient temperature. The resulting THF/ copolymer solutions (3 mL, 5 mg mL^{-1}) were added to a separate glass vial; this was then sealed and placed on an orbital mixer for 1 minute at ambient temperature to ensure complete homogenisation. The resulting copolymer/ THF solution contained AB block and branched copolymer weight fractions of 0.5 and a total copolymer concentration of 5 mg mL^{-1} ($[P]_0$ = 5 mg mL^{-1}). The copolymer/ THF solution (1 mL, 5 mg mL^{-1}, branched copolymer ω_i = 0.5) was then rapidly added to DI H_2O (5 mL) under magnetic stirring. The co-nanoprecipitation was then stirred at ambient temperature for 48 hours in order to allow complete THF removal *via* evaporation, to give an aqueous nanoparticle dispersion at a

concentration of 1 mg mL^{-1} ([P]f = 1 mg mL^{-1}). Aqueous nanoparticle dispersions were visually evaluated for signs of polymer sedimentation following which, nanoparticles were assessed *via* DLS.

6.3.4.5 Monitoring ^{3}H-Docetaxel Release from Branched Vinyl Copolymer Nanoparticles during Radio-Dialyses

The preparation of *p*(HPMA-*co*-EHMA) based ^{3}H-docetaxel loaded branched vinyl copolymer nanoparticles were conducted in accordance with the procedures outlined in Chapter 6, Section 6.3.3.5. Docetaxel encapsulation efficiencies and total drug loadings were determined in accordance with the procedures and calculations outlined in Chapter 6, Section 6.3.3.6. Radio-dialyses, docetaxel release, determination of release constants and docetaxel half-lives were conducted in accordance with the procedures and outlined in Chapter 6, Section 6.3.3.7.

6.3.4.6 Preparation of a Docetaxel Based Macro-Initiator

Docetaxel (1.00 g, 1.24 mmol, 1 equiv.), anhydrous TEA (187 mg, 1.86 mmol, 1.5 equiv.) and DMAP (30 mg, 0.248 mmol, 0.2 equiv.) were added to an oven dried 25 mL round bottom flask containing a magnetic stirrer bar. The round bottom flask was purged with N_2 followed by addition of anhydrous DCM (10 mL), the solution was cooled to 0 °C in an ice bath. A solution of α-bromo isobutyryl bromide (285 mg, 1.86 mL, 1.24 mmol, 1.00 equiv.) in anhydrous DCM (2.5 mL) were added dropwise, using a syringe under N_2, over 30 minutes. After one hour the ice bath was removed and the reaction was allowed to proceed for a further 23 hours. After a total of 24 hours, the reaction was quenched by addition of DI H_2O (0.5 mL). The crude reaction mixture was dried *in vacuo* and the pure product was isolated using silica gel column chromatography using a hexane/ethyl acetate mobile phase (50/50 volume %), R_f = 0.27, giving docetaxel 2-bromo methyl propanoate (Doc-BiB) as a solid white powder. m/z (ES MS) 980.3 $[MNa]^+$ m/z required 980.3 $[MNa]^+$. ^{1}H NMR (400 MHz, $CDCl_3$) δ(ppm) 8.11, 8.09, 7.62, 7.50, 7.38, 7.26, 6.21, 5.68, 5.66, 5.47, 5.27, 5.21, 4.95, 4.93, 4.62, 3.91, 3.89, 3.47, 2.57, 2.37, 2.27, 2.25, 1.85, 1.75, 1.71, 1.34, 1.23, 1.13. ^{13}C NMR (101 MHz, $CDCl_3$) δ(ppm) 211.33, 172.74, 170.34, 167.02, 155.36, 138.47, 138.33, 135.89, 133.73, 130.17, 129.11, 128.84, 128.72, 128.06, 126.74, 84.14, 81.05, 80.23, 78.78, 74.79, 74.52, 73.66, 72.42, 71.99, 57.63, 56.17, 46.46, 43.06, 36.96, 35.68, 28.19, 26.43, 22.57, 20.64, 14.39, 9.86.

6.3.4.7 Linear Polymerisation of nHMA via Cu-RDRP at 60 °C in Anhydrous Methanol using a Docetaxel Based Macro-Initiator

Prior to use, all monomers and initiators were deoxygenated *via* gentle bubbling with N_2 for 60 minutes. In a typical synthesis of a *p*(*n*HMA) linear polymer targeting DP_n = 50 monomer

units, *n*HMA (1.00 g, 5.87 mmol), bpy (37 mg, 0.235 mmol) and Doc-BiB (112 mg, 0.117 mmol) were added to an oven dried round bottom flask (5 mL) equipped with a magnetic stirrer bar. Anhydrous MeOH (1.186 g, 1.50 mL, 50 wt %) was added and the resulting solution was purged with N_2 for a further 15 minutes. At this point a sample was withdrawn (ca. 100 μL) and diluted in $CDCl_3$ allowing quantification of $[M]_0/[I]_0$ by ^{1}H NMR. Cu(I)Cl (11.5 mg, 0.117 mmol) was added rapidly to the flask, and instantly formed a brown solution. The reaction was then purged with N_2 for a further 60 seconds, sealed and swiftly submerged into an oil bath preheated at 60 °C. The reaction was stopped after 24 hours by dilution with $CDCl_3$ and exposure to air until a homogeneous blue/green solution was obtained, at this point a sample (*ca.* 500 μL) was taken for quantification of monomer conversion by ^{1}H NMR. The solution was further diluted in $CHCl_3$, passed over a neutral alumina column to remove the copper catalyst and dried *in vacuo*. The polymer was re-dissolved in a minimum amount of THF and precipitated twice from THF into cold MeOH, to give Doc-*p*(*n*HMA)$_{50}$ as a clear viscous oil. The polymer was then dried *in vacuo* at 40 °C for 48 hours and characterised *via* ^{1}H NMR in $CDCl_3$ and triple detection SEC using a THF/TEA eluent (98/2 v/v %) and a narrow poly(styrene) standard calibration.

6.3.4.8 Branched Copolymerisation of nHMA and EGDMA via Cu-RDRP at 60 °C in Anhydrous Methanol using a Docetaxel Based Macro-Initiator

In a typical branching statistical copolymerisation of *n*HMA and EGDMA targeting a primary chain DP_n = 60 monomer units and a branching ratio ($[B]_0/[I]_0$) of 0.9, *n*HMA (1.00g, 5.87 mmol), bpy (37 mg, 0.235 mmol) EGDMA (21 mg, 0.105 mg) and Doc-BiB (112 mg, 0.117 mmol) were added to an oven dried round bottom flask (5 mL) equipped with a magnetic stirrer bar. Anhydrous MeOH (1.186 g, 1.50 mL, 50 wt %) was added and the resulting solution was purged with N_2 for a further 15 minutes. At this point a sample was withdrawn (ca. 100 μL) and diluted in $CDCl_3$ allowing quantification of $[M]_0/[I]_0$ by ^{1}H NMR. Cu(I)Cl (11.5 mg, 0.117 mmol) was added rapidly to the flask, and instantly formed a brown solution. The reaction was then purged with N_2 for a further 60 seconds, sealed and swiftly submerged into an oil bath preheated at 60 °C. The reaction was stopped after 24 hours by dilution with $CDCl_3$ and exposure to air until a homogeneous blue/green solution was obtained, at this point a sample (*ca.* 500 μL) was taken for quantification of monomer conversion by ^{1}H NMR. The solution was further diluted in $CHCl_3$, passed over a neutral alumina column to remove the copper catalyst and dried *in vacuo*. The polymer was re-dissolved in a minimum amount of THF and precipitated twice from THF into cold methanol, to give Doc-*p*(*n*HMA$_{50}$-*co*-EGDMA$_{0.90}$) as a clear viscous oil. The polymer was then dried *in vacuo* at 40 ° C for 48 hours and characterised *via* ^{1}H NMR in $CDCl_3$ and triple

detection SEC using a THF/TEA eluent (98/2 v/v %) and a narrow poly(styrene) standard calibration.

6.3.4.9 Co-Nanoprecipitation of Branched Docetaxel Copolymer Conjugates and Amphiphilic AB Block Copolymers

Co-nanoprecipitations were conducted from THF (1 mL) into DI H_2O (5 mL) (dilution ratio = 5). Equal weight fractions of Doc-*p*(*n*HMA$_{50}$-*co*-EGDMA$_{0.90}$) and PEG$_{45}$-*b*-*p*(*n*HMA)$_{127}$ (ω_i = 0.5) were used during co-nanoprecipitations. Copolymers were nanoprecipitated from an initial concentration of 5 mg mL^{-1} in THF ($[P]_0$ = 5 mg mL^{-1}) which, following solvent removal, gave a final copolymer concentration of 1 mg mL^{-1} in DI H_2O ($[P]_f$ = 1 mg mL^{-1}). In a typical co-nanoprecipitation, Doc-*p*(*n*HMA$_{50}$-*co*-EGDMA$_{0.90}$) and PEG$_{45}$-*b*-*p*(*n*HMA)$_{127}$ (50 mg) were added into separate glass vials followed by THF (10 mL). Each of the vials were then sealed and placed on a roller mixer for 48 hours at ambient temperature. The resulting THF/ copolymer solutions (3 mL, 5 mg mL^{-1}) were added to a separate glass vial; this was then sealed and placed on an orbital mixer for 1 minute at ambient temperature to ensure complete homogenisation. The resulting copolymer/ THF solution contained AB block and branched copolymer weight fractions of 0.5 and a total copolymer concentration of 5 mg mL^{-1} ($[P]_0$ = 5 mg mL^{-1}). The copolymer/ THF solution (1 mL, 5 mg mL^{-1}, branched copolymer ω_i = 0.5) was then rapidly added to DI H_2O (5 mL) under magnetic stirring. The co-nanoprecipitation was then stirred at ambient temperature for 48 hours in order to allow complete THF removal *via* evaporation, to give an aqueous nanoparticle dispersion at a concentration of 1 mg mL^{-1} ($[P]_f$ = 1 mg mL^{-1}). Aqueous nanoparticle dispersions were visually evaluated for signs of polymer sedimentation following which nanoparticles were assessed *via* DLS.

6.3.4.10 Preparation of a p(nHMA) Based Macro-RAFT Agent

Prior to polymerisation *n*HMA and anhydrous toluene were deoxygenated *via* gentle N_2 bubbling for 60 minutes. AIBN (32 mg, 0.196 mmol, 0.2 equiv.), CPBD (217 mg, 0.979 mmol, 1 equiv.), *n*HMA (20.0g, 0.117 mol, 120 equiv.) and anhydrous toluene (20.25 g, 23.4 mL, 50 wt %) were added to a round bottom flask (50 mL). The reaction was deoxygenated *via* gentle nitrogen bubbling for a further 30 minutes following which an aliquot of the reaction mixture was taken for determination of $[M]_0$ / $[CTA]_0$ by ^{1}H NMR in $CDCl_3$. This was achieved by comparison of the integrals from CPBD aromatic resonances (7.90ppm, 2H) with those of the O-CH_2 adjacent to the ester of the *n*HMA monomer (4.20ppm, 2H). The flask was placed in an oil bath at 80 °C for 16 hours, after which the reaction was stopped rapidly *via* placement in an ice bath; an aliquot was taken for analysis of monomer conversion by ^{1}H NMR as has been previously described. The reaction mixture was concentrated *in vacuo*, diluted in

acetone and precipitated three times from cold methanol giving a pale pink viscous oil. The polymer was dried *in vacuo* at 40 ° C for 48 hours and was characterised by TD-SEC (THF/TEA) and ^{1}H NMR ($CDCl_3$). DP_n (NMR) was determined by comparison of the aromatic resonances from the RAFT end-group (7.90 ppm, 2H) with those from the O-CH_2 group adjacent to the ester of the *p*(*n*HMA) repeat unit (4.00 ppm, 2H).

6.3.4.11 Chain Extension of a p(nHMA)$_{122}$ Macro-RAFT Agent

All monomers and solvents were deoxygenated *via* gentle N_2 bubbling for 60 minutes prior to synthesis. In a typical chain extension of a *p*(*n*HMA)$_{122}$ macro-RAFT agent with OEGMA, OEGMA (0.50 g, Mn = 300 g mol^{-1}, 1.67 mmol, 20 equiv.), *p*(*n*HMA)$_{122}$ (1.75 g, $Mn_{(NMR)}$ = 21 000 g mol^{-1}, 0.083 mmol, 1 equiv.) and AIBN (2.74 mg, 0.0167 mmol, 0.2 equiv.) and anhydrous toluene (3.41 g, 3.93 mL, 60 wt %) were added to a round bottom flask (5 mL). The mixture was deoxygenated *via* gentle nitrogen bubbling for a further 30 minutes following which an aliquot of the reaction mixture was taken for determination of $[M]_0$ / $[CTA]_0$ by ^{1}H NMR in $CDCl_3$. This was achieved by comparison of the integrals from aromatic resonances of the macro-RAFT agent (7.90 ppm, 2H) with those of the vinyl protons of the OEGMA monomer (6.05 ppm, 2H). The flask was placed in an oil bath at 80 °C for 4 hours, after which the reaction was stopped rapidly by placement of the reaction flask in an ice bath; an aliquot was taken for analysis of monomer conversion by ^{1}H NMR. The reaction mixture was concentrated *in vacuo*, diluted in acetone and precipitated three times from cold methanol which gave a pale pink viscous oil. The polymer was dried *in vacuo* at 40 °C for 48 hours and was characterised using a THF/TEA eluent (98/2 v/v %) and a narrow poly(styrene) standard calibration.

6.3.4.12 Sole Nanoprecipitations of Amphiphilic AB Block Copolymers

Nanoprecipitations of amphiphilic AB block copolymers were conducted from THF (1 mL) into DI H_2O (5 mL) (dilution ratio = 5). Copolymers were nanoprecipitated from an initial concentration of 5 mg mL^{-1} in THF ($[P]_0$ = 5 mg mL^{-1}) which, following solvent removal, gave a final copolymer concentration of 1 mg mL^{-1} in DI H2O ($[P]_f$ = 1 mg mL^{-1}). In a typical nanoprecipitation *p*(*n*HMA)$_{122}$-*b*-*p*(OEGMA)$_{11}$ (25 mg) and THF (5 mL) were added to a glass vial and sealed. The vial was placed on a roller mixer and the polymer allowed to dissolve over 48 hours at ambient temperature to give a *p*(*n*HMA)$_{122}$-*b*-*p*(OEGMA)$_{11}$/ THF solution at a concentration of 5 mg mL^{-1}. The *p*(*n*HMA)$_{122}$-*b*-*p*(OEGMA)$_{11}$/ THF solution (1 mL, 5 mg mL^{-1}) was added to a glass vial containing DI H_2O (5 mL) under magnetic stirring. The sample was then left for 48 hours at ambient temperature to allow solvent removal *via* evaporation resulting in an aqueous nanoparticle dispersion at a concentration of 1 mg mL^{-1}. Aqueous

nanoparticle dispersions were assessed visually for signs of polymer sedimentation following which, nanoparticles were assessed *via* DLS.

6.3.4.13 Co-nanoprecipitations of p(nHMA$_{68}$-co-EGDMA$_{1.03}$) with Amphiphilic AB Block Copolymers

Co-nanoprecipitations were conducted from THF (1 mL) into DI H_2O (5 mL) (dilution ratio = 5). Equal weight fractions of each of the two components (ω_i = 0.5) were used during co-nanoprecipitations. Copolymers were nanoprecipitated from an initial concentration of 5 mg mL^{-1} in THF ([P]$_0$ = 5 mg mL^{-1}) which, following solvent removal, gave a final (co)polymer concentration of 1 mg mL^{-1} in DI H_2O ([P]$_f$ = 1 mg mL^{-1}). In a typical co-nanoprecipitation *p*(*n*HMA$_{68}$-*co*-EGDMA$_{1.03}$) and *p*(*n*HMA)$_{122}$-*b*-*p*(OEGMA)$_{11}$ (50 mg) were added into separate glass vials followed by THF (10 mL). Each of the vials were then sealed and placed on a roller mixer for 48 hours at ambient temperature. The resulting THF/ copolymer solutions (3 mL, 5 mg mL^{-1}) were added to a separate glass vial; this was then sealed and placed on an orbital mixer for 1 minute at ambient temperature to ensure complete homogenisation. The resulting copolymer/ THF solution contained *p*(*n*HMA$_{68}$-*co*-EGDMA$_{1.03}$) and *p*(*n*HMA)$_{122}$-*b*-*p*(OEGMA)$_{11}$ weight fractions of 0.5 and a total copolymer concentration of 5 mg mL^{-1} ([P]$_0$ = 5 mg mL^{-1}). The copolymer/ THF solution (1 mL, 5 mg mL^{-1}) was then rapidly added to DI H_2O (5 mL) under magnetic stirring. The co-nanoprecipitation was then stirred at ambient temperature for 48 hours in order to allow complete THF removal *via* evaporation, resulting in an aqueous nanoparticle dispersion at a concentration of 1 mg mL^{-1} ([P]f = 1 mg mL^{-1}). Aqueous nanoparticle dispersions were visually evaluated for signs of polymer sedimentation following which, nanoparticles were assessed *via* DLS.

6.4 References

1 A. B. Dwyer, P. Chambon, A. Town, F. L. Hatton, J. Ford and S. P. Rannard, *Polym. Chem.*, 2015, **6**, 7286–7296.

2 F. L. Hatton, L. M. Tatham, L. R. Tidbury, P. Chambon, T. He, A. Owen and S. P. Rannard, *Chem. Sci.*, 2015, **6**, 326–334.

3 J. Ford, P. Chambon, J. North, F. L. Hatton, M. Giardiello, A. Owen and S. P. Rannard, *Macromolecules*, 2015, **48**, 1883–1893.

Appendix

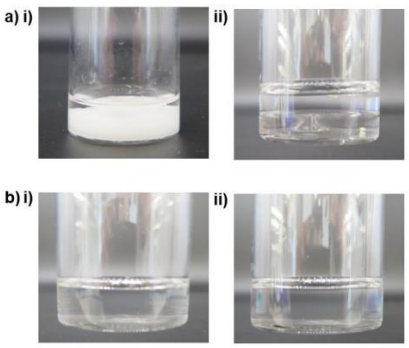

Figure A2.1 Monomer SMA in anhydrous methanol miscibility studies at ambient and elevated temperatures. a) SMA-MeOH (50 wt %) at i) 20 ℃ and ii) 60 ℃. b) SMA-IPA mixtures (50 wt %) at i) 20 ℃ and ii) 60 ℃.

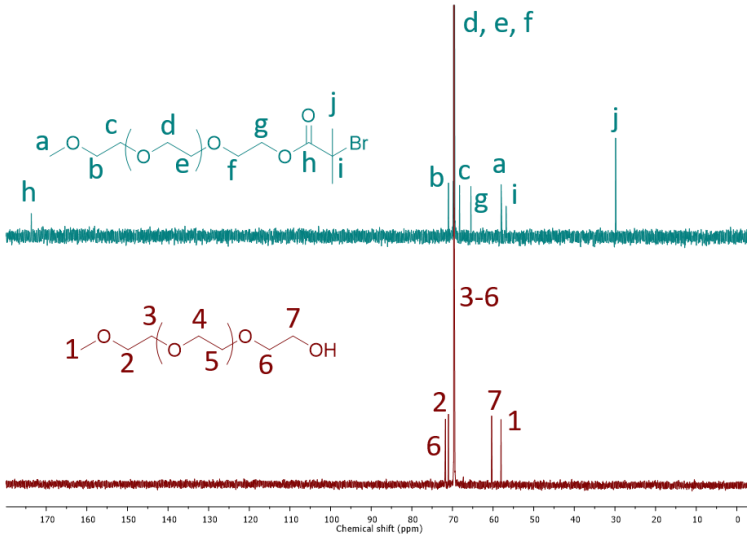

Figure A2.2 Overlaid ^{13}C NMR spectra (D_2O, 100 MHz) of (a) PEG_{45}-Br and (b) PEG_{45}-OH.

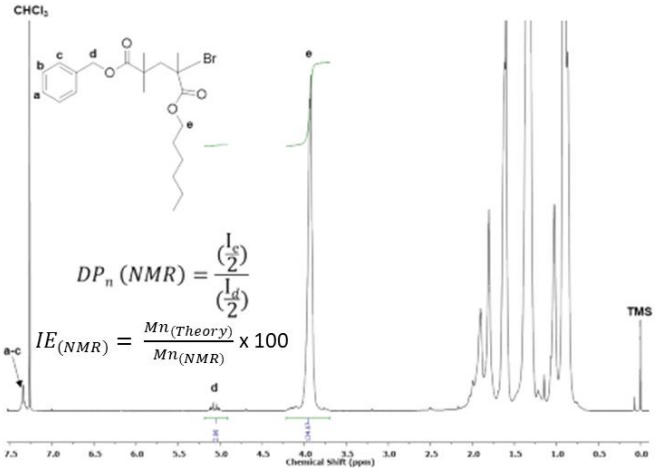

Figure A2.3 ^1H NMR spectra ($CDCl_3$, 400 MHz) of *p*(*n*HMA) to quantify the degree of polymerisation and $IE_{(NMR)}$.

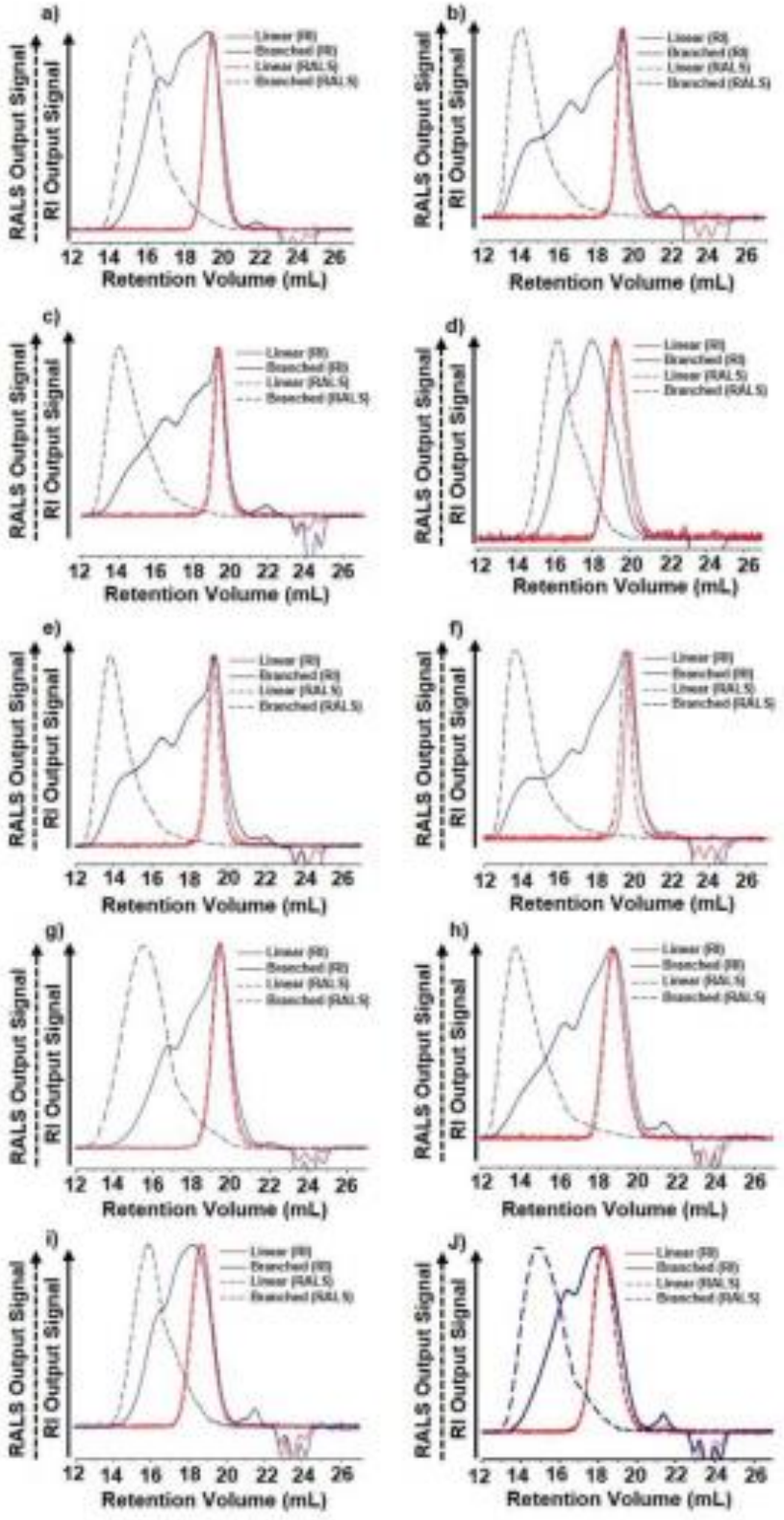

Figure A2.4 Comparison of molecular weight distributions obtained by TD-SEC. Overlaid refractive index (RI; solid lines) and right-angle light scattering (RALS; dotted lines) chromatograms obtained for linear homopolymers (red) and the highest molecular weight branched statistical copolymers (blue) obtained for the following monomer-alcohol systems: a) MMA-IPA, b) EMA-MeOH, c) *n*BMA-MeOH, d) *t*BMA-MeOH, e) *n*HMA-MeOH, f) BzMA MeOH, g) CHMA-IPA, h) EHMA-MeOH, i) LMA-IPA and j) SMA-IPA.

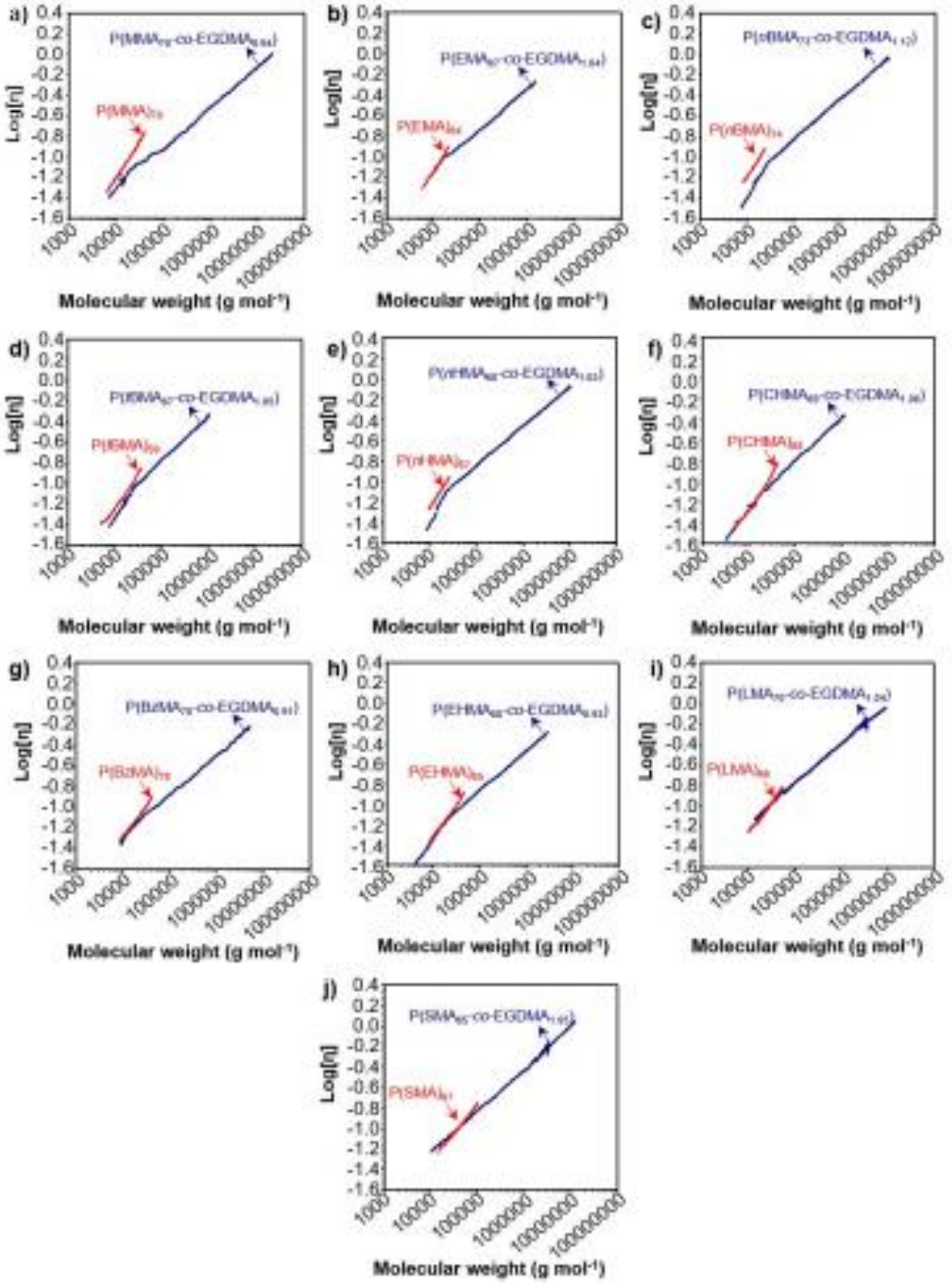

Figure A2.5 Overlaid Mark-Houwink-Sakurada (MHS) plots obtained for linear homopolymers and branched statistical copolymers consisting of a) *p*(MMA) b) *p*(EMA), c) *p*(*n*BMA), d) *p*(*t*BMA), e) *p*(*n*HMA), f) *p*(CHMA), g) *p*(BzMA), h) *p*(EHMA), i) *p*(LMA), j) *p*(SMA) produced *via* Cu-catalysed RDRP.

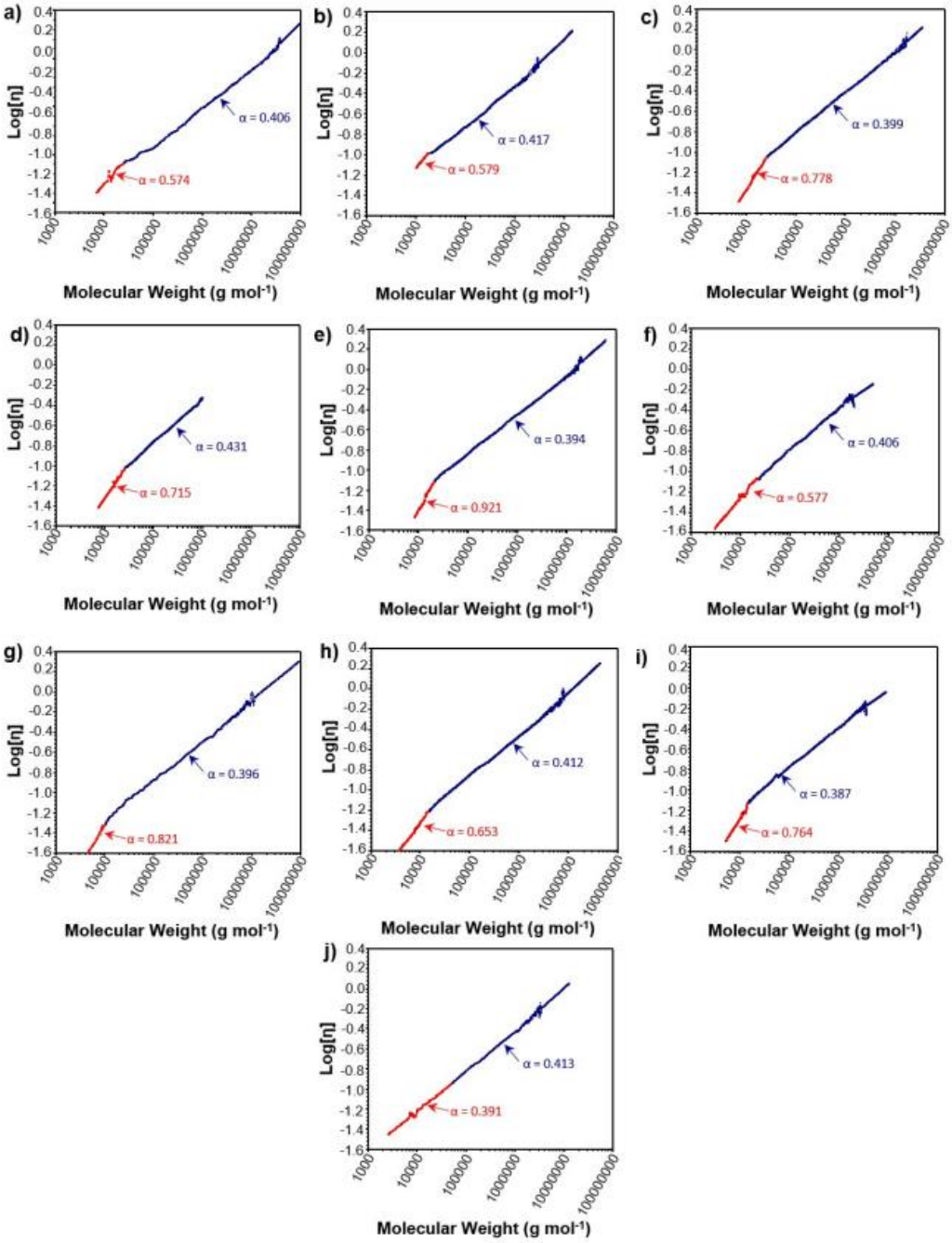

Figure A2.6 Deconvolution of MHS plots obtained for branched statistical copolymers consisting of a) *p*(MMA$_{66}$-*co*-EGDMA$_{0.90}$), b) *p*(EMA$_{66}$-*co*-EGDMA$_{0.90}$), c) *p*(nBMA$_{66}$-*co*-EGDMA$_{0.90}$), d) *p*(*t*BMA$_{66}$-*co*-EGDMA$_{0.90}$), e) *p*(*n*HMA$_{66}$-*co*-EGDMA$_{0.90}$), f) *p*(CHMA$_{66}$-*co*-EGDMA$_{0.90}$), g) *p*(BzMA$_{66}$-*co*-EGDMA$_{0.90}$), h) *p*(EHMA$_{66}$-*co*-EGDMA$_{0.90}$), i) *p*(LMA$_{66}$-*co*-EGDMA$_{0.90}$), j) *p*(SMA$_{66}$-*co*-EGDMA$_{0.90}$) produced *via* Cu-catalysed RDRP.

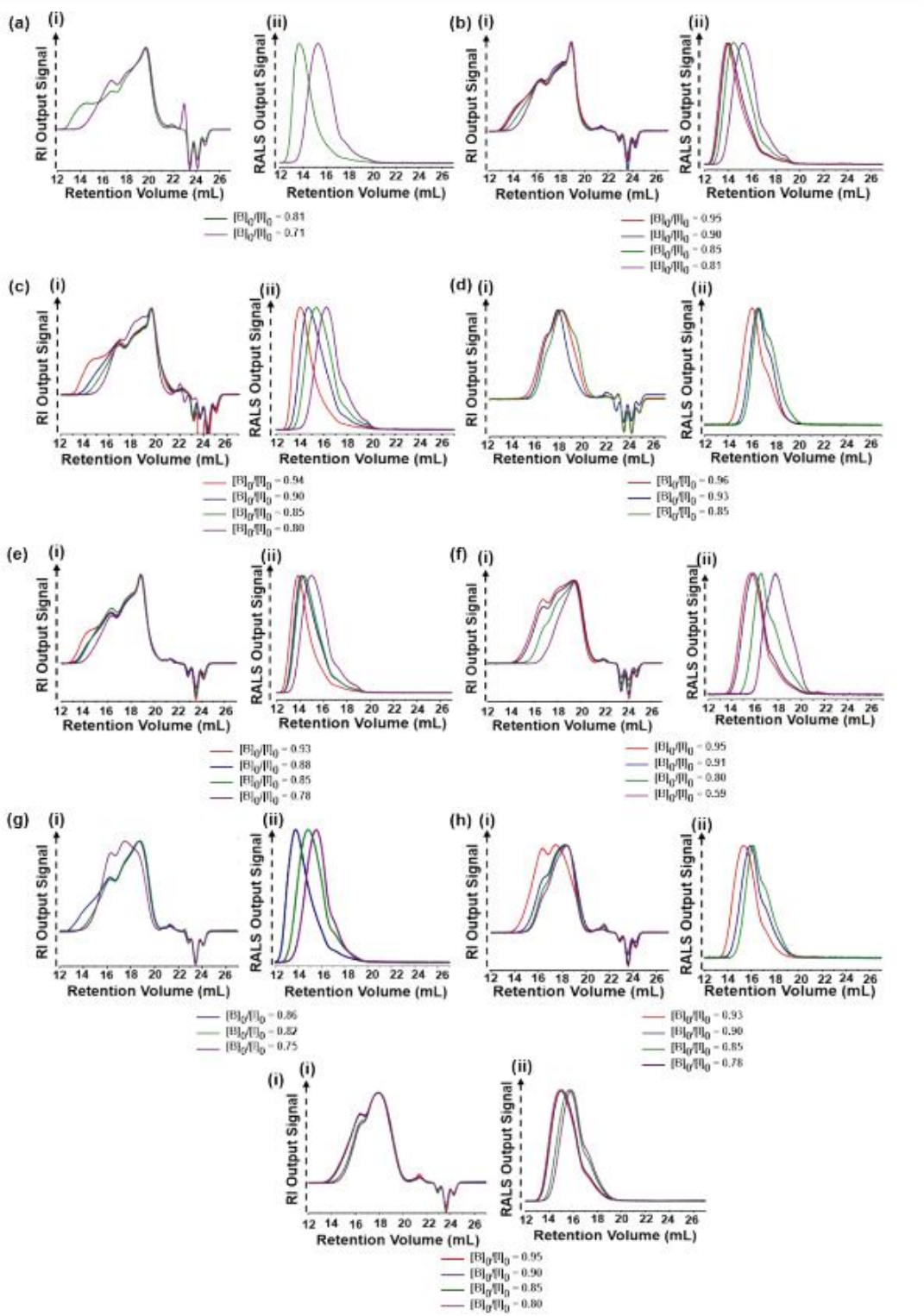

Figure A2.7 Overlaid (i) RI and (ii) RALS chromatograms for branched copolymers obtained from statistical copolymerisations of EGDMA with (a) MMA, (b) EMA, (c) *n*BMA. (d) *t*BMA, (e) *n*HMA, (f) CHMA, (g) BzMA, (h) EHMA, (i) LMA, (j) SMA produced *via* Cu catalysed RDRP at varied $[B]_0/[I]_0$ ratios.

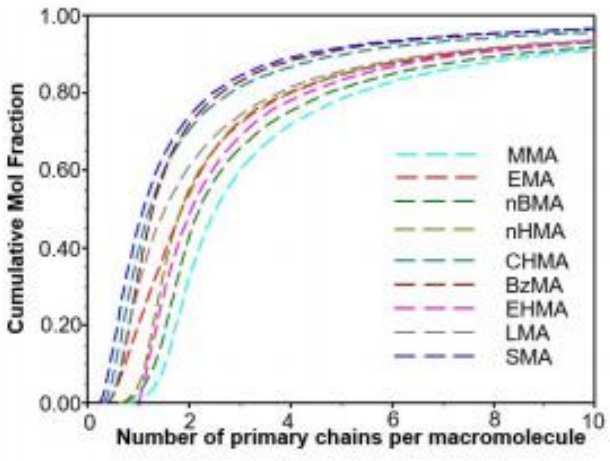

Figure A2.8 Plots of primary chains per macromolecule vs. cumulative mol fraction (cum. x_f) for branched statistical copolymers: a) *p*(MMA_{66}-*co*-$EGDMA_{0.90}$), b) *p*(EMA_{66}-*co*--$EGDMA_{0.90}$), c) *p*($nBMA_{66}$-*co*-$EGDMA_{0.90}$), d) *p*(*t*BMA_{66}-*co*-$EGDMA_{0.90}$), e) *p*(*n*HMA_{66}-*co*-$EGDMA_{0.90}$), f) *p*($CHMA_{66}$-*co*-$EGDMA_{0.90}$), g) *p*($BzMA_{66}$-*co*-$EGDMA_{0.90}$), h) *p*($EHMA_{66}$-*co*-$EGDMA_{0.90}$), i) *p*(LMA_{66}-*co*-$EGDMA_{0.90}$), j) *p*(SMA_{66}-*co*-$EGDMA_{0.90}$) produced *via* Cu-catalysed RDRP.

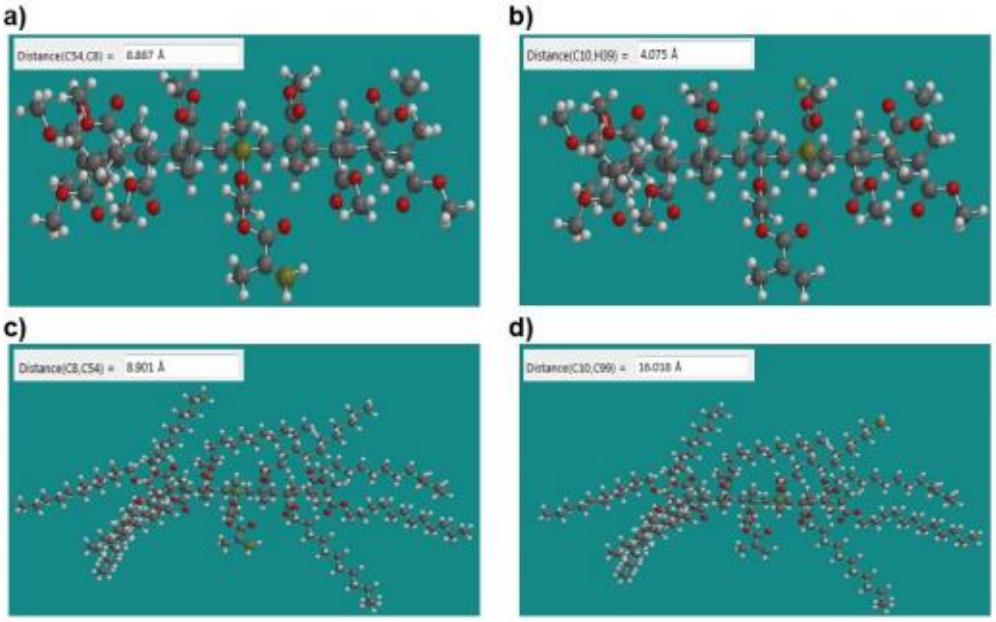

Figure A2.9 Spartan simulations of pendant group and repeat unit protrusion distances in *p*(MMA) and *p*(LMA) oligomers (DP = 10) containing one EGDMA unit per chain. Distances were measured between the polymer backbone and the: a) pendant methacrylate group in *p*(MMA_{10}-*co*-$EGDMA_1$), b) pendant CH_3 of a *p*(MMA) repeat unit, c) pendant methacrylate group in *p*(MMA_{10}-*co*-$EGDMA_1$), d) terminal CH_3 of a *p*(LMA) repeat unit.

Table A2.1 I_1/I_3 ratios obtained by fluorescence emission spectroscopy of pyrene dissolved within: neat methacrylic monomers, monomer-MeOH mixtures, monomer-IPA mixtures and common organic solvents.

	Neat Monomer	Monomer-MeOH	Monomer-IPA	Solvent
HPMA	1.48	1.49	1.37	
MMA	1.44	1.49	1.39	
EMA	1.39	1.48	1.37	
*n*BMA	1.30	1.42	1.32	
*t*BMA	1.25	1.41	1.29	
*n*HMA	1.23	1.37	1.27	
BzMA	1.39	1.46	1.35	
CHMA	1.27	1.39	1.29	
EHMA	1.17	1.33	1.22	
LMA	1.16	1.24	1.15	
SMA	0.95	-[a]	1.06	
MeOH				1.53
THF				1.46
Ethanol				1.36
IPA				1.21
Toluene				1.16
Diethyl Ether				1.09

[a] An I_1/I_3 ratio could not be obtained for the SMA-MeOH mixture due to monomer-alcohol immiscibility.

Table A2.2 Calculation of the differences in initiator ($[I]_0$) and methacrylate group ($[M]_0$) concentrations which arises as a result of the increased contribution of the pendant side group to the overall monomer mass.

			Monomer			Initiator		EGDMA	
Monomer	M_r	Side Chain	Mass (g)	mmol	Volume (mL)	Mass (mg)	mmol	Mass (mg)	mmol
MMA	100	14	1.000	9.99	1.06	42.80	0.166	29.70	0.150
EMA	114	28	1.000	8.76	1.09	37.55	0.146	26.05	0.131
*n*BMA	142	56	1.000	7.03	1.12	30.14	0.117	20.91	0.105
*t*BMA	142	56	1.000	7.03	1.14	30.14	0.117	20.91	0.105
*n*HMA	170	84	1.000	5.87	1.16	25.17	0.098	17.46	0.088
CHMA	168	82	1.000	5.94	1.04	25.47	0.099	17.67	0.089
BzMA	176	90	1.000	5.68	0.96	24.32	0.095	16.87	0.085
EHMA	198	112	1.000	5.04	1.13	21.61	0.084	14.99	0.076
LMA	254	168	1.000	3.93	1.15	16.84	0.066	11.69	0.059
SMA	339	253	1.000	2.95	1.16	12.66	0.049	8.78	0.044

	Solvent				Conc. (mol dm^{-3})		Conc (normalised)	
Monomer	Weight %	Mass (g)	Volume (mL)	Total Volume (mL)	$[I]_0$	$[M]_0$	Initiator	Monomer
MMA	50	1.07	1.35	2.42	0.069	4.131	1.00	1.00
EMA	50	1.06	1.34	2.43	0.060	3.600	0.87	0.87
*n*BMA	50	1.05	1.33	2.44	0.048	2.877	0.70	0.70
*t*BMA	50	1.05	1.33	2.47	0.047	2.847	0.69	0.69
*n*HMA	50	1.04	1.32	2.48	0.040	2.373	0.57	0.57
CHMA	50	1.04	1.32	2.35	0.042	2.525	0.61	0.61
BzMA	50	1.04	1.31	2.28	0.042	2.493	0.60	0.60
EHMA	50	1.04	1.31	2.44	0.034	2.068	0.50	0.50
LMA	50	1.03	1.30	2.45	0.027	1.604	0.39	0.39
SMA	50	1.02	1.29	2.45	0.020	1.207	0.29	0.29

Table A2.3 Calculation of the differences in initiator ($[I]_0$) and methacrylate group ($[M]_0$) concentrations which arises as a result of the increased contribution of the pendant side group to the overall monomer mass.

Conc. (wt %)	Monomer		Initiator	EGDMA	Solvent		$[I]_0$		$[M]_0$	
	Mass (g)	V (mL)	Mass (mg)	Mass (mg)	Mass (mg)	V (mL)	mmol dm^{-3}	Normalised	mmol dm^{-3}	Normalised
50	1.00	1.06	43	30	1.07	1.35	69	1.00	4131	1.00
40	1.00	1.06	43	30	1.61	2.03	54	0.78	3227	0.78
30	1.00	1.06	43	30	2.50	3.16	39	0.57	2365	0.57
20	1.00	1.06	43	30	4.29	5.42	26	0.37	1541	0.37
10	1.00	1.06	43	30	9.65	12.2	13	0.18	754	0.18
1	1.00	1.06	43	30	106	134	1	0.02	74	0.02

Table A2.4 Calculated pendant group and repeat unit protrusion distances from the methacrylic polymer backbone using Spartan molecular modelling software.

Polymer	Pendant Methacrylate (Å)	Repeat Unit (Å)	Repeat Unit (Å)	Repeat Unit (Å)	Repeat Unit (Å)	Average Repeat Unit (Å)
p(MMA)	8.887	4.071	4.461	4.073	4.462	4.267
p(LMA)	8.901	16.018	16.255	15.056	17.411	16.185

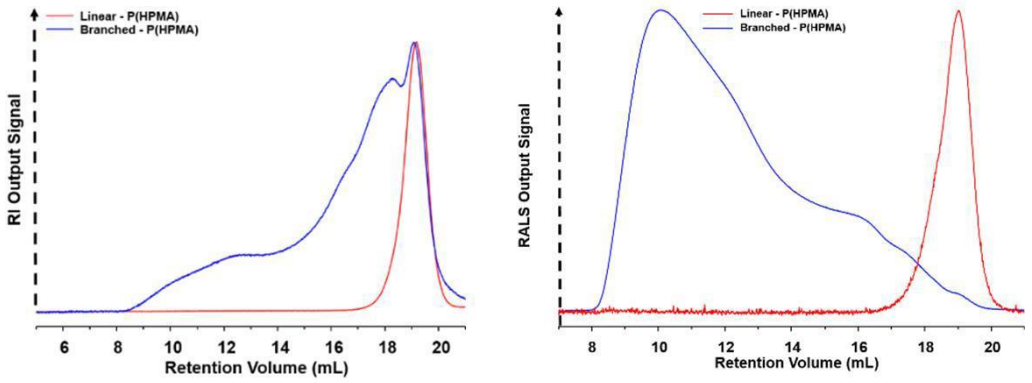

Figure A3.1 TD-SEC analysis of *p*(HPMA) based: linear homopolymer, amphiphilic branched copolymer prepared *via* methanolic Cu-RDRP.

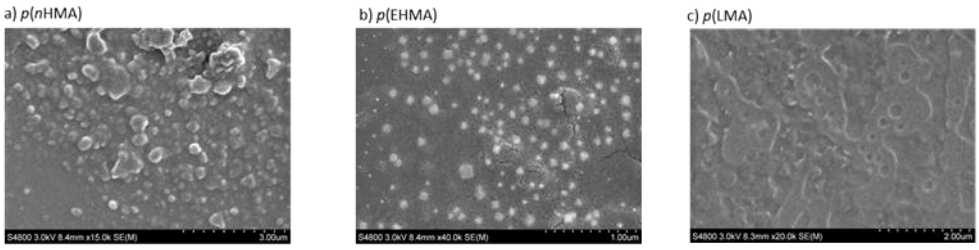

Figure A3.2 Scanning electron microscopy images of nanoparticles constructed of low T_g polymers which were unable to retain their structural integrity during the drying process.

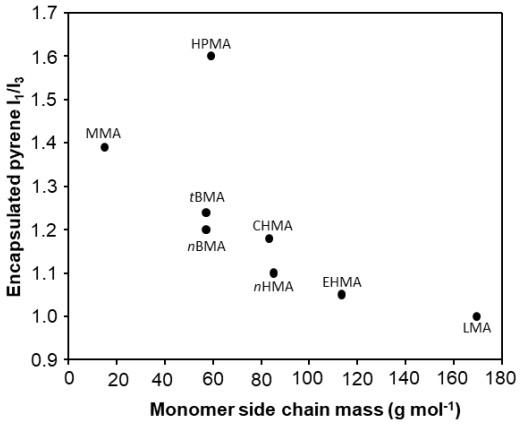

Figure A3.3 Graphical representation of the relationship between I_1/I_3 ratios and the weight fraction of the aliphatic side chain of the monomers from which the polymers used during co-nanoprecipitation are constructed.

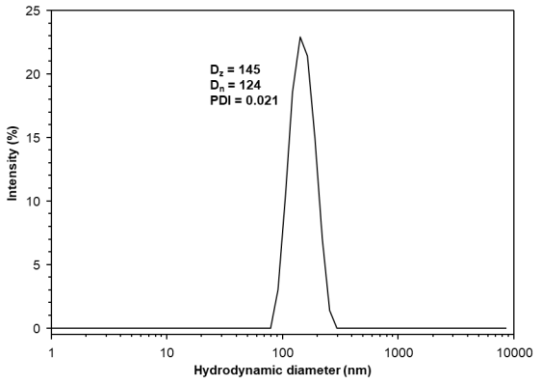

Figure A3.4 DLS analysis of the sole nanoprecipitation of *p*(HPMA$_{63}$-*co*-EGDMA$_{0.90}$) at $[P]_0$ =100 mg mL^{-1} in THF.

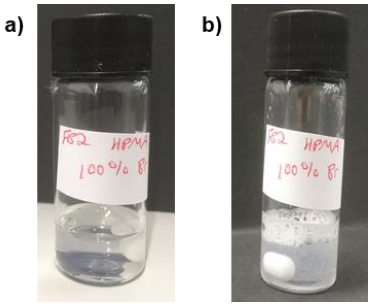

Figure A3.5 Aqueous nanoparticle dispersion without the PEG-based amphiphilic AB block copolymers which have been exposed to a low concentration of NaCl.

Table A3.1 Characterisation of *p*(HPMA) based: linear homopolymer, amphiphilic branched copolymer and branched statistical copolymers prepared *via* methanolic Cu-RDRP.

	$[M]_0$ /$[I]_0$	$[B]_0$ /$[I]_0$	Conv.	DP_n	*Mw* (g mol^{-1})	*Mn* (g mol^{-1})	*Đ*	α
p(HPMA)$_{65}$	60	-	98	65	26 000	20 700	1.26	0.490
p(HPMA$_{63}$-*co*-EGDMA$_{0.90}$)	60	0.90	99	63	704 300	55 000	12.80	0.345
PEG$_{45}$-*b*-*p*(HPMA)$_{124}$	120	-	99	124	23 000	18 500	1.22	0.409

Table A3.2 DLS analysis to show the impact of a serial dilution on aqueous nanoparticle dispersions ($[P]_{H2O}$ = 1 mg mL^{-1}) up to a 1000 fold dilution factor (DF).

Hydrophobic domain	Dilution Factor	$[P]_{(H2O)}$ (mg mL^{-1})	D_z (nm)[a]	D_n (nm)	*PDI*	DCR (kcps)
*p(*HPMA)	1	1.000	64	50	0.041	92823
	2	0.500	64	50	0.044	48697
	5	0.200	64	50	0.041	16885
	10	0.100	64	50	0.045	9208
	20	0.050	63	49	0.040	4844
	50	0.020	62	49	0.046	1382
	100	0.010	66	46	0.109	744
	200	0.005	62	48	0.082	321
	500	0.002	64	48	0.055	139
	1000	0.001	79	51	0.135	82
*p(n*BMA)	1	1.000	83	59	0.086	274752
	2	0.500	83	59	0.083	101591
	5	0.200	83	58	0.089	47517
	10	0.100	85	65	0.052	20559
	20	0.050	84	63	0.084	11107
	50	0.020	83	59	0.089	5255
	100	0.010	113	48	0.231	4052
	200	0.005	85	64	0.077	1156
	500	0.002	87	60	0.106	490
	1000	0.001	84	64	0.148	220
*p(n*HMA)	1	1.000	92	75	0.028	424110
	2	0.500	94	77	0.007	276294
	5	0.200	93	76	0.016	82576
	10	0.100	93	77	0.026	44437
	20	0.050	92	75	0.029	19635
	50	0.020	93	77	0.013	9362
	100	0.010	95	78	0.025	5137
	200	0.005	94	77	0.007	1938
	500	0.002	115	97	0.190	1035
	1000	0.001	99	81	0.146	470
*p(*EHMA)	1	1.000	76	60	0.036	299966
	2	0.500	77	62	0.036	110756
	5	0.200	76	61	0.035	48299
	10	0.100	77	62	0.029	21175
	20	0.050	77	62	0.034	11423
	50	0.020	78	60	0.069	5498
	100	0.010	79	64	0.032	2195
	200	0.005	77	58	0.057	1016
	500	0.002	77	62	0.030	478
	1000	0.001	90	75	0.088	264
*p(*LMA)	1	1.000	137	118	0.015	589909
	2	0.500	137	118	0.012	441019
	5	0.200	138	118	0.007	253568
	10	0.100	138	119	0.014	94073
	20	0.050	137	118	0.020	50593
	50	0.020	138	119	0.012	17694
	100	0.010	138	119	0.008	10990
	200	0.005	138	119	0.011	5811
	500	0.002	139	120	0.013	1792
	1000	0.001	143	128	0.182	1029

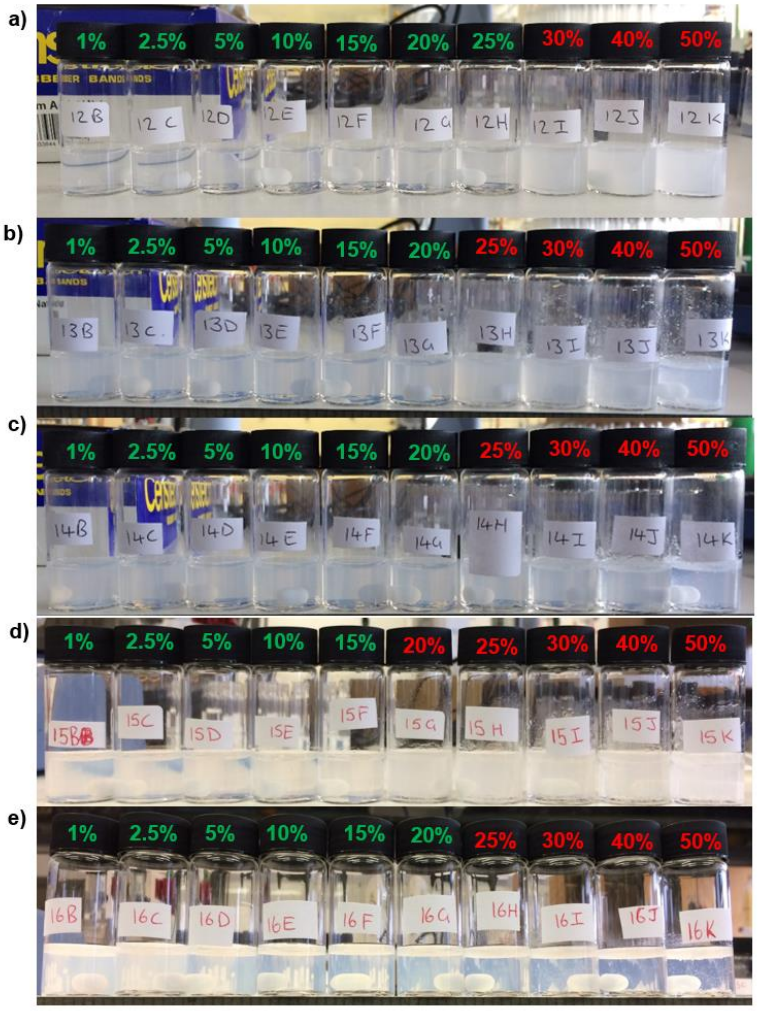

Figure A4.1 Failed docetaxel-loaded branched vinyl copolymer nanoparticle dispersions formed *via* co-nanoprecipitation at drug loadings ≥ 30 wt % of a) *p*(HPMA), b) *p*(*n*BMA), c) *p*(*n*HMA), d) *p*(EHMA) and *p*(LMA).

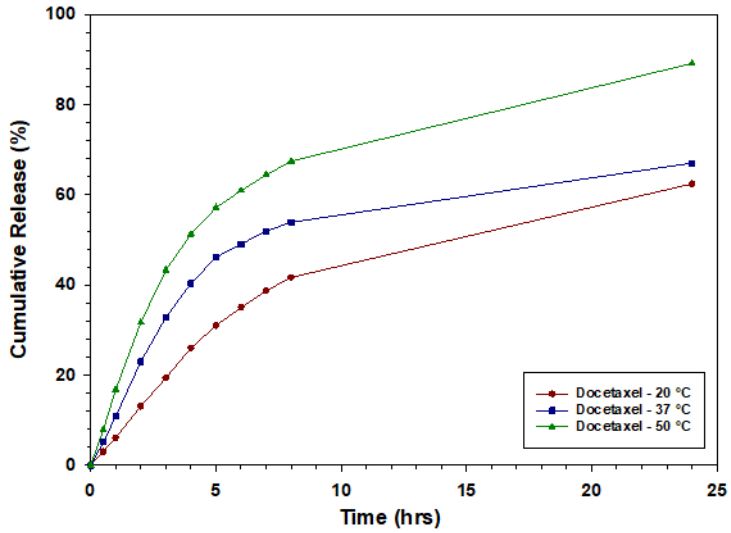

Figure A4.2 Cumulative ^{3}H-labelled docetaxel release data obtained over a 24 hour radio-dialysis of unencapsulated docetaxel.

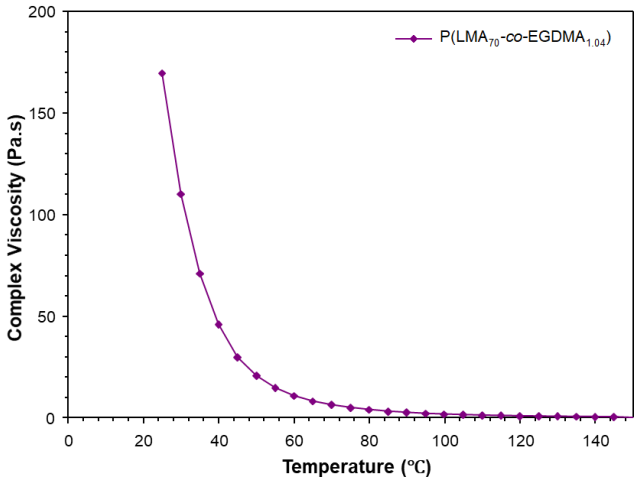

Figure A4.3 A closer individual inspection of the *p*(LMA$_{70}$-*co*-EGDMA$_{1.04}$) complex viscosity data showing an exponential increase in copolymer viscosity between 50 – 25 °C.

Table A4.1 DLS analysis of ^{3}H-docetaxel loaded aqueous nanoparticle dispersions produced *via* co-nanoprecipitation before and after radio-dialyses.

Hydrophobic domain	Temp. (°C)	Time (hrs)	D_z (nm)	D_n (nm)	*PDI*
p(EHMA)	20	0	81	55	0.101
	20	24	82	57	0.100
	37	24	82	55	0.099
	50	24	81	58	0.100

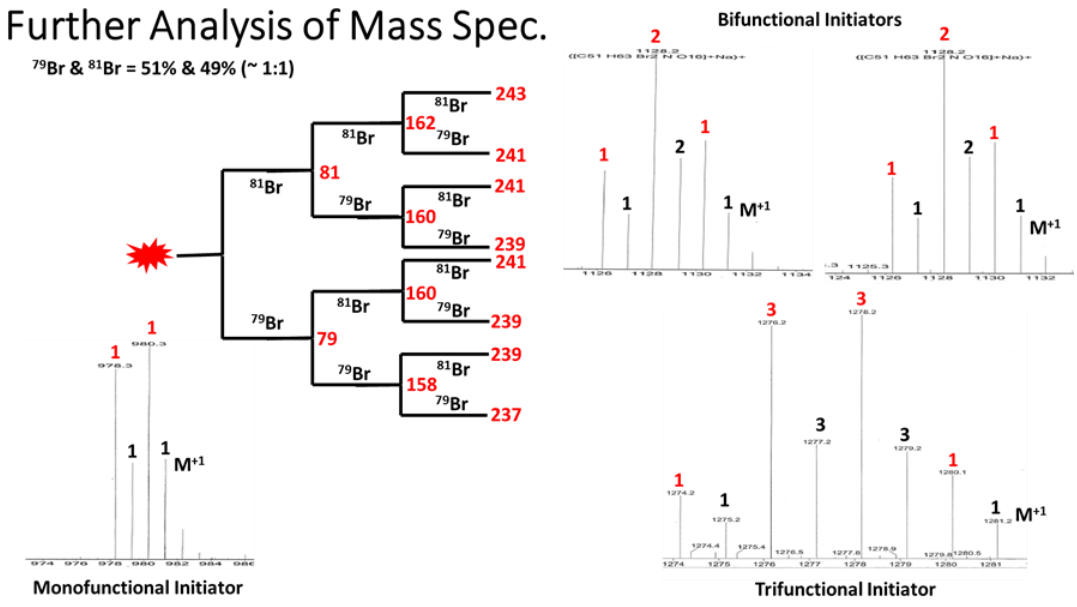

Figure A5.1 Electrospray ionisation mass spectrometry of monofunctional, bi-functional and trifunctional docetaxel initiators which have been isolated from the reaction *via* column chromatography.

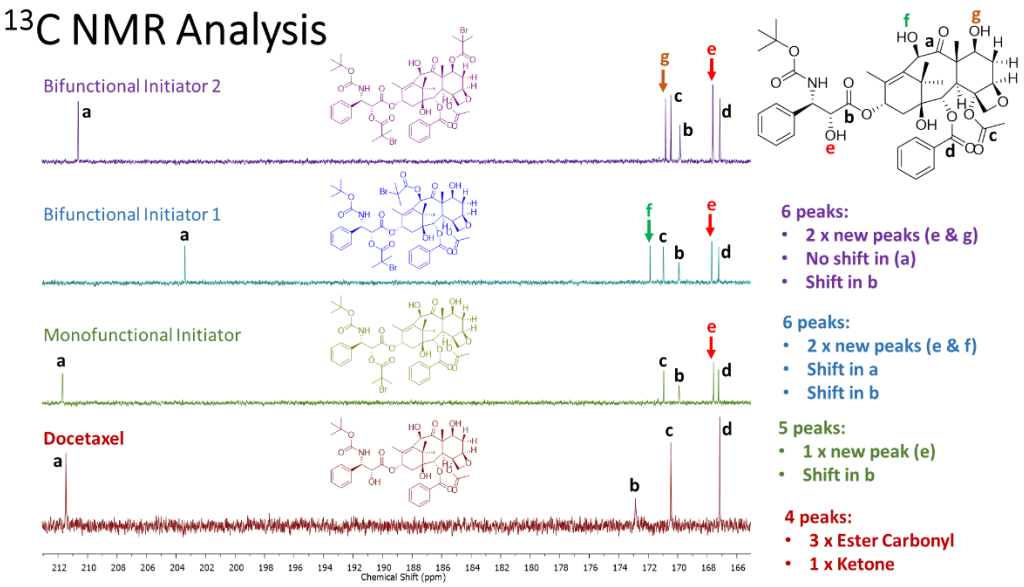

Figure A5.2 ^{13}C NMR ($CDCl_3$, 100 MHz) analysis of monofunctional, bi-functional and trifunctional docetaxel initiators which have been isolated from the reaction *via* column chromatography.

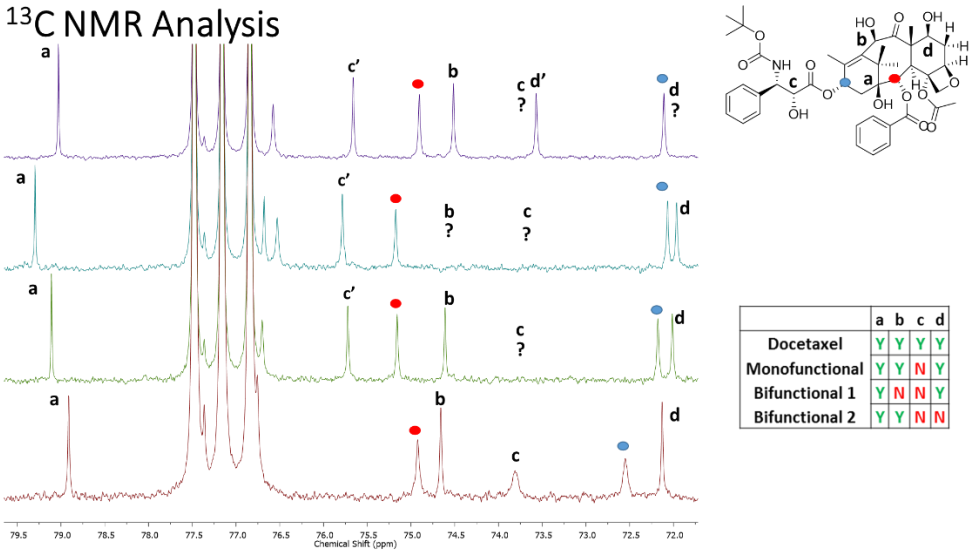

Figure A5.3 ^{13}C NMR ($CDCl_3$, 100 MHz) analysis of monofunctional, bi-functional and trifunctional docetaxel initiators which have been isolated from the reaction *via* column chromatography.

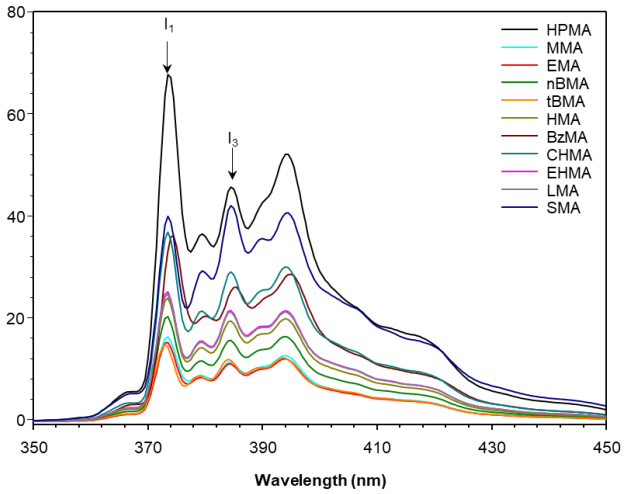

Figure A6.1 Determination of the polarity of pyrene solutions using the I_1/I_3 ratio; comparison of the relative intensities of the first (I_1, *ca.* 373 nm) and third (I_3, *ca.* 384 nm) vibrational bands of the pyrene fluorescence emission.

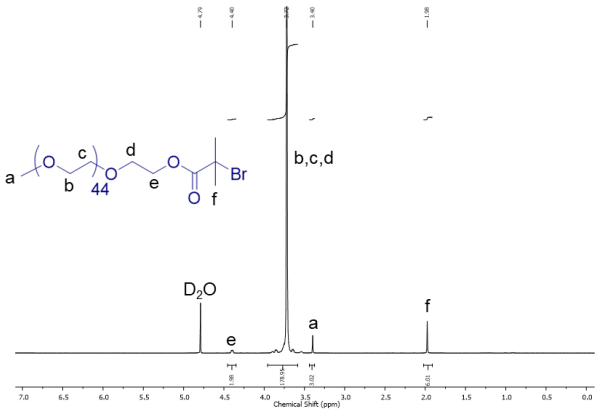

$$DP_n = \left(\frac{\left(\frac{I_e + I_{b,c,d}}{4} \right)}{\frac{I_f}{6}} \right) \text{ or } DP_n = \left(\frac{\left(\frac{I_e + I_{b,c,d}}{4} \right)}{\frac{I_a}{3}} \right)$$

Figure A6.2 ^{1}H NMR ($CDCl_3$, 400 MHz) analysis to determine the number average degree of polymerisation (DP_n) and molecular weight (Mn) of purified PEG_{45}-Br.

Table 6.1 Good and bad solvents identified for purification of linear homopolymers and branched statistical copolymers.

Polymer	Polymer Good Solvents	Polymer Bad Solvent(s)
p(MMA)^{B,L}	**Acetone**, THF, DCM	MeOH^c, **MeOH/H_2O^{c*}**, Hexane^c
p(EMA)^{B,L}	**Acetone**, THF, DCM	MeOH^c, **MeOH/H_2O^{c*}**, Hexane^c
p(*n*BMA)^{B,L}	Acetone, **THF**, DCM	MeOH^c, **MeOH/H_2O^{c*}**, Hexane^c
p(*t*BMA)^{B,L}	Acetone, **THF**, DCM	MeOH^c, **MeOH/H_2O^{c*}**
p(*n*HMA)^{B,L}	Acetone, **THF**, DCM	**MeOH,**
p(CHMA)^{B,L}	Acetone, **THF**, DCM	**MeOH^c,**
p(BzMA)^{B,L}	Acetone, **THF**, DCM	**MeOH^c,**
p(EHMA)^{B,L}	**THF**, DCM	**MeOH,**
p(LMA)^{B,L}	**THF**, DCM	**MeOH,** IPA
p(SMA)^{B,L}	**THF**, DCM	MeOH, EtOH, IPA, **Acetone**

Solvent used for polymer purification by precipitation highlighted in bold. ^{B} Branched copolymer. ^{L} Linear homopolymer.
^{c} Precipitation conducted in a solid CO_2 ice bath. * Conducted at a MeOH/H_2O composition of 80/20 (v/v %).